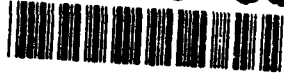


WL-TR-93-2116

PLASMA CHEMISTRY OF VIBRATIONALLY  
NONEQUILIBRIUM MOLECULES

AD-A279 630



5



1

J. WILLIAM RICH

DEPARTMENT OF MECHANICAL ENGINEERING  
THE OHIO STATE UNIVERSITY  
206 W. 18TH AVENUE  
COLUMBUS OH 43210-1107

OCTOBER 1993

FINAL REPORT FOR 07/09/90-07/08/93

DTIC  
ELECTRONIC  
MAY 26 1994  
S F D

APPROVED FOR PUBLIC RELEASE; DISTRIBUTION IS UNLIMITED.

94-15736



AEROPROPULSION AND POWER DIRECTORATE  
WRIGHT LABORATORY  
AIR FORCE MATERIEL COMMAND  
WRIGHT PATTERSON AFB OH 45433-7650

94 5 25 03 4

DTIC QUALITY INSPECTED 1

**Best  
Available  
Copy**

## NOTICE

When Government drawings, specifications, or other data are used for any purpose other than in connection with a definitely Government-related procurement, the United States Government incurs no responsibility or any obligation whatsoever. The fact that the government may have formulated or in any way supplied the said drawings, specifications, or other data, is not to be regarded by implication, or otherwise in any manner construed, as licensing the holder, or any other person or corporation; or as conveying any rights or permission to manufacture, use, or sell any patented invention that may in any way be related thereto.

This report is releasable to the National Technical Information Service (NTIS). At NTIS, it will be available to the general public, including foreign nations.

This technical report has been reviewed and is approved for publication.



CHARLES A. DEJOSEPH JR  
Research Physicist  
Advanced Plasma Research Section  
Power Components Branch  
Aerospace Power Division  
Aero Propulsion and Power Directorate



CHARLES W. ANDERSON  
Chief, Power Components Branch  
Aerospace Power Division  
Aero Propulsion and Power Directorate



MICHAEL D. BRAYDICH, Lt Col, USAF  
Deputy Chief  
Aerospace Power Division

If your address has changed, if you wish to be removed from our mailing list, or if the addressee is no longer employed by your organization please notify WL/POOC, WPAFB, OH 45433-7919 to help us maintain a current mailing list.

Copies of this report should not be returned unless return is required by security considerations, contractual obligations, or notice on a specific document.

**REPORT DOCUMENTATION PAGE**Form Approved  
OMB No. 0704-0188

Public reporting burden for this collection of information is estimated to average 1 hour per response, including the time for reviewing instructions, searching existing data sources, gathering and maintaining the data needed, and completing and reviewing the collection of information. Send comments regarding this burden estimate or any other aspect of this collection of information, including suggestions for reducing this burden, to Washington Headquarters Services, Directorate for Information Operations and Reports, 1215 Jefferson Davis Highway, Suite 1204, Arlington, VA 22202-4302, and to the Office of Management and Budget, Paperwork Reduction Project (0704-0188), Washington, DC 20503.

1. AGENCY USE ONLY (Leave blank)		2. REPORT DATE November 1993		3. REPORT TYPE AND DATES COVERED Final 09 July 1990 - 08 July 1993	
4. TITLE AND SUBTITLE Plasma Chemistry of Vibrationally Nonequilibrium Molecules				5. FUNDING NUMBERS C F33615-90-C-2039 PE 61102F PR 2301 TA S2 WU 09	
6. AUTHOR(S) J. William Rich					
7. PERFORMING ORGANIZATION NAME(S) AND ADDRESS(ES) Department of Mechanical Engineering The Ohio State University 206 W. 18th Avenue Columbus, Ohio 43210-1107				8. PERFORMING ORGANIZATION REPORT NUMBER	
9. SPONSORING/MONITORING AGENCY NAME(S) AND ADDRESS(ES) Aero Propulsion and Power Directorate Wright Laboratory Wright-Patterson AFB, OH 45433-7650				10. SPONSORING/MONITORING AGENCY REPORT NUMBER WL-TR-93-2116	
11. SUPPLEMENTARY NOTES					
12a. DISTRIBUTION / AVAILABILITY STATEMENT Approved for public release; distribution is unlimited.				12b. DISTRIBUTION CODE	
13. ABSTRACT (Maximum 200 words) The present report describes experimental and analytical studies of energy transfer and chemical reaction in diatomic and small polyatomic gases under conditions of extreme disequilibrium of the vibrational modes. Primary emphasis is on collision-dominated environments with relatively low translational/rotational mode temperatures, which are characteristic of a variety of gas discharges, plasma chemical reactors and high enthalpy supersonic gas dynamic expansions. Some additional work has also been directed to the complementary environment in which the translational/rotational mode temperatures are high, and the vibrational mode energy content is initially low. This latter environment is characteristic of strong shock waves in gases, such as occurs during planetary entry of hypersonic aerospace vehicles. The report details vibration-translation (V-T), vibration-electronic (V-E), associative ionization, and dissociation processes in CO and NO. There are some data and rate models for related diatomic and small polyatomic species. Emphasis is placed on energy transfer processes involving high quantum states.					
14. SUBJECT TERMS Molecular Energy Transfer; Plasma Chemistry; Ionization; Vibrational Relaxation; Nitric Oxide; Carbon Monoxide; Associative Ionization; Vibration-Vibration Processes				15. NUMBER OF PAGES 433	
				16. PRICE CODE	
17. SECURITY CLASSIFICATION OF REPORT Unclassified	18. SECURITY CLASSIFICATION OF THIS PAGE Unclassified	19. SECURITY CLASSIFICATION OF ABSTRACT Unclassified	20. LIMITATION OF ABSTRACT Unlimited		



## TABLE OF CONTENTS

	List of Figures	iv
	List of Tables	xv
•	1. Summary	1
	2. Introduction	2
	3. Carbon Monoxide Studies I: Nonequilibrium Vibrational Kinetics of CO at High Translational Mode Temperatures.	7
	4. Carbon Monoxide Studies II: Vibrationally-Stimulated Ionization of CO.	55
	5. Carbon Monoxide Studies III: UV Radiation After Preparation of CO $a^3\Pi$ , $v=2$ State.	98
	6. Nitric Oxide Studies I: Vibrational and Electronic Excitation of NO in Optical Pumping Experiments	144
	7. Nitric Oxide Studies II: Development of a 15 W c.w. Single Line CO Laser for NO Vibrational Excitation.	174
	8. Energy Transfer in CO/OCS Mixtures; The Possibility of c.w. Lasing.	279
	9. Modeling Studies I: Strong Vibrational Nonequilibrium in Supersonic Flows.	348
10.	Modeling Studies II: Nonequilibrium Dissociation Rates Behind Strong Shock Waves: Classical Model.	386

Accession For	
NTIS CRA&I	<input checked="" type="checkbox"/>
DTIC TAB	<input type="checkbox"/>
Unannounced	<input type="checkbox"/>
Justification	
By	
Distribution/	
Availability Codes	
Dist	Avail and/or Special
A-1	

## LIST OF FIGURES

3.1. Schematic of experimental apparatus used at Ohio State. The CO/Ar mixture in the absorption cell (7) is optically pumped by the radiation of a CO laser (11) and the emission spectra of the gas are analyzed with an UV/visible (14) and an infrared monochromator (4). The laser pulse is monitored by means of a fast pyroelectric detector (6) .....	39
3.2. CO multiple-line laser spectrum, Centrale Paris, 27 W cw conditions, intensity in arbitrary units .....	40
3.3. Absorption cell schematics a. Ohio State b. Centrale Paris .....	41
3.4. CO potential energy diagram. Shown are the main energy transfer processes between the vibrational levels of the $X^1\Sigma$ ground state, the first excited singlet state $A^1\Pi$ and the lowest triplet state $a^3\Pi$ .....	42
3.5. $C_2$ Swan bands, $d^3\Pi_g \rightarrow a^3\Pi_u$ , $\Delta v=0$ sequence, OSU experiment .....	43
3.6. Determination of rotational temperature from $\Delta v=0$ $C_2$ Swan band component intensities .....	44
3.7. Theoretical and experimental CO 1 <sup>st</sup> overtone emission on selected bands at an inferred rotational temperature $T=1500K$ , Centrale Paris experiment. Predicted decrease in transmission by water vapor at 300K is also shown .....	45
3.8. $C_2$ Swan bands, $d^3\Pi_g \rightarrow a^3\Pi_u$ , $\Delta v=0, -1, -2$ sequences, Centrale Paris experiment .....	46
3.9. Q-switched laser pulse oscillograms a. Laser pulse shape observed with the fast pyroelectric detector b. Enlarged initial position of the laser pulse and 15 $\mu m$ gate signal .....	47

3.10. Time dependence of the first overtone emission (intensity normalized) after pulsed excitation for selected wavelengths, laser pulse duration of 2.5 ms .....	48
3.11. 1 <sup>st</sup> overtone spectra for selected CO concentrations. Shown are all bands from $v=2-0$ to approximately $v=40-38$ (2.3-4.4 $\mu\text{m}$ ). The rotational structure is not resolved. The amplifier gain for curve No.2 is twice that of curves 1,3, and 4 .....	49
3.12. Measured current in the absorption cell vs. applied electric field over total cell pressure P. The cell pressure was varied from 60 to 500 Torr at a CO/Ar concentration ratio of 4/69 .....	50
3.13. Time dependence of the current and the overtone emission after pulsed laser excitation: a. Laser pulse shape (L) and Current response (C) b. Laser pulse shape (L) and subsequent overtone emission on $v=22-20$ .....	51
3.14. Kinetic modeling calculation: predicted steady-state vibrational population densities of the V-V pumped CO for two different focal diameters (power densities) of the laser beam, for $T=1500\text{ K}$ .....	52
3.15. Kinetic modeling calculation: predicted time-dependent 1 <sup>st</sup> overtone radiative intensities after pulse excitation (0-2.5 ms); laser power density = $22\text{ W/cm}^2$ ....	53
3.16. Kinetic modeling calculation: predicted time-dependent 1 <sup>st</sup> overtone radiative intensities after pulse excitation (0-2.5 ms); laser power density = $2.2\text{ W/cm}^2$ ...	54
4.1. Schematic of the experimental setup: 1, infrared CO laser; 2, d.c. power supply; 3, microammeter; 4, gas supply and gas mixing manifold; 5, impurity trap; 6, optical cell; 7, exhaust pump; 8, infrared spectro- meter; 9, laser power meter .....	86

4.2. Typical CO laser spectrum .....	87
4.3. Optical cell with probe .....	88
4.4. CO first overtone emission spectra at different He pressures .....	89
4.5. Comparison of experimental and synthetic CO vibrational spectra .....	90
4.6. Comparison of experimental and synthetic CO rotational spectra .....	91
4.7. Inferred CO vibrational distribution functions at different He pressures .....	92
4.8. Experimental and theoretical voltage-current characteristics of the Thomson discharge .....	93
4.9. Saturation current and number of "active CO molecules" dependencies on the He pressure .....	94
4.10. Charged species distributions in the Thomson dis- charge in the absence of the field and in the satu- ration regime. $P=100$ torr, $CO:Ar=3:97$ , $d/L=0.25$ ; $q_1(0) = 10^{-21} \text{ cm}^3/\text{s}$ (see Eqs. 6, A2-A4). $L$ - inter- electrode distance .....	95
4.11. Electric field influence on different CO vibrational level populations .....	96
4.12. Qualitative demonstration of the $V \rightarrow e \rightarrow V-\Delta V$ effect (strongly exaggerated). $\epsilon$ - electron energy, $T_e$ - electron temperature .....	97
5.1. Optics arrangement on optical cell, top view .....	103
5.2. Gas handling system for the optical cell .....	105
5.3. Schematic of setup used to take steady-state calibration spectra .....	107
5.4. Typical spectral response of the PMT (a) and grating efficiency (b) .....	108

5.5. Schematic of setup used to take time integrated measurements .....	111
5.6. Schematic of setup used to take time dependent measurements .....	112
5.7. $\text{CO}(X^1\Sigma^+) \rightarrow \text{CO}(a^3\Pi)$ absorption lines with the typical width of the pump laser line .....	115
5.8. Energy level diagram of CO illustrating the 193 nm pump laser transition .....	116
5.9. Boxcar specifications with respect to time .....	117
5.10. Signal processing diagram for Boxcar and oscilloscope ....	118
5.11. Results found at 1 $\mu\text{sec}$ delay .....	121
5.12. Quasi steady-state results .....	127
5.13. 3440 A system at higher resolution (600 $\mu\text{m}$ slits) illustrating its two bands .....	129
5.14. Relative rise times of the 3856 A band and 3440 A band ...	131
5.15. Relative decay times of the 3856 A band and 3440 A band ..	131
6.1. The experimental setup. 1, CO laser; 2, laser mirror, 3, grating; 4, focusing mirror; 5, absorption cell; 6, monochromator, 7, InSb infrared detector, 8, photomultiplier, 9, lock-in amplifier; 10, computer; 11, powermeter .....	166
6.2. The first overtone infrared NO spectra; solid lines - experimental spectra, dashed line - synthetic spectrum ....	167
6.3. Einstein coefficients for NO infrared spontaneous radiation; 1,2 - [19], 1',2' - [20]; 1,1' - $\Delta v=1$ , 2,2' - $\Delta v=2$ .....	168
6.4. The experimental NO vibrational distribution functions (points); 1,2, Treanor distributions for $T_v=2500\text{K}$ , $T=300\text{K}$ , and $T_v=2500\text{K}$ , $T=700\text{K}$ , respectively; 3, Boltzmann distribution, $T=700\text{K}$ .....	169
6.5. The visible/ultraviolet NO spectrum .....	170

6.6. The experimental profile of the NO 0,2 $\gamma$ band (points); the synthetic profile at different temperatures (lines) ...	171
6.7. Comparison of the master equation calculation with the experiment [14] .....	172
6.8. Comparison of the NO V-T rates measured by optical pumping [13] and by SEP [5] (the point for v=1 is the result of [3]) .....	173
7.1. Molecular Energy Lab's CO laser constructed by Bulent Mehmetli [Meister] .....	185
7.2. Fast-Axial-Flow Electric Discharge (FAFED) CO laser basic layout. External view of trough and Brewster window assemblies .....	188
7.3. Fast-Axial-Flow Electric Discharge (FAFED) CO laser tube .....	189
7.4. Fast Axial Flow gas swirl injector .....	193
7.5. Injector used in V=1 $\rightarrow$ 0 laser by J.P. Martin and later used in Mehmetli's CO laser [Martin] .....	194
7.6. Male taper joint construction showing details of the internal purge and electrode arrangement .....	197
7.7. Inner purge gas restrictor .....	198
7.8. Cryogenic bellows end seal for connecting laser discharge tube to trough .....	202
7.9. Half-symmetric resonator arrangement, stability diagram and waist size as a function of the well-known g-parameters [Seigman] .....	207
7.10. Near-hemispheric resonator arrangement, stability diagram and waist size as a function of the well-known g-parameters [Seigman] .....	208
7.11. Typical Littrow configuration for a laser .....	211
7.12. FAFED CO laser optical resonator .....	212

7.13. Typical grating first order efficiency curves for a $46^{\circ}04'$ blaze angle echelette grating. Solid curve, S plane; dashed curve, P plane [Loewen et al.] .....	213
7.14. FAFED CO laser Brewster window holder .....	216
7.15. Fractional losses from incident S and P planes, $\lambda=5200$ nm, on a $\text{CaF}_2$ window ( $n_1=1$ , $n_2=3.975$ ) as a function of Brewster angle .....	217
7.16. Gas handling and pressure measurements for FAFED CO laser .....	219
7.17. FAFED CO laser exhaust tube /common anode/ pressure tap male taper joints .....	220
7.18. Typical all line operation of FAFED CO laser .....	224
7.19. Variation of laser power as a function of discharge current .....	226
7.20. Present external purge arrangement .....	226
7.21. Stability of FAFED CO laser with and without semi-Littrow zeroth order return .....	231
7.22. Typical cw single line $8\rightarrow7$ P(11) line spectrum with and without semi-Littrow reflector .....	232
7.23. Typical single line mode shapes with and without semi-Littrow zeroth order return .....	233
7.24. Standing wave patterns for a stable optical resonator [Seigman] .....	238
7.25. Laser beam detection and optical cell setup .....	239
7.26. Possible arrangements of the half-symmetric resonator prior to fine tuning .....	241
7.27. Laser spectrum of misaligned half-symmetric resonator .....	241
7.28. Losses of P-plane at the Brewster window set at a Brewster angle of $35.5^{\circ}$ .....	244

7.29. First overtone infrared NO spectra; solid line - experimental spectrum; dashed line - synthetic spectrum [Saupe et al.] .....	249
7.30. Experimental and master equation calculation of the NO vibrational distribution function .....	250
7.31. Visible/ultraviolet NO spectrum .....	251
7.32. Alternate FAFED CO laser discharge tube and cooling system .....	257
7.33. Diagram showing phase relation between rays diffracted from two adjacent grating grooves .....	266
7.34. Illustration of the Raleigh criterion [Feynam] .....	270
8.1. The normal modes of OCS. Directions and length of arrows indicate relative motions of the nuclei for the three vibrations. $\nu_3$ is degenerated, a vibration of the same frequency perpendicular to the page is also possible. /Townes & Schawlow 55/ .....	280
8.2. Vibrational levels in OCS. Lines indicate possible interactions between nearby levels. /Townes & Schawlow 55/ .....	281
8.3. Schematic CO <sub>2</sub> -N <sub>2</sub> laser energy transfer /Kneubel & Sigrist/ .....	283
8.4. Schematic setup .....	295
8.5. Optical properties of BaF <sub>2</sub> /Janos 89/ .....	297
8.6. Brewster window holder .....	300
8.7. Gas handling system for OCS laser setup .....	301
8.8. CO-OCS spectrum .....	304
8.9. Pure CO spectrum .....	304
8.10. Relative population of OCS(001) at different OCS partial pressures .....	307



8.11. Spectra of CO-OCS mixture for two different OCS partial pressures. Curve A: partial pressure 12.5 mtorr; Curve B: partial pressure 82.7 mtorr .....	308
8.12. Relative population of OCS(001) at different currents .....	309
8.13. Relative population of OCS(001) at different CO partial pressures .....	310
8.14. Relative population of OCS(001) at different nitrogen partial pressures .....	311
8.15. CO-He vibrational-rotational energy transfer rates /Verter 76/ .....	311
8.16. Relative population of OCS(001) at different helium partial pressures .....	312
8.17. Relative population of OCS(001) at different temperatures .....	313
8.18. Schematic of the pathways included in the code for the case of discharge and V-V transfer from CO .....	318
8.19. Pure OCS discharge. Populations in % of the total OCS population .....	329
8.20. OCS optically pumped. Populations in % of the total OCS population .....	331
8.21. Ratio A/S depending on the He partial pressure. OCS optically pumped .....	332
8.22. Ratio A/S depending on the He partial pressure. OCS excitation by CO V-V transfer .....	332
8.23. Ratio A/S depending on the partial pressure of vibrationally excited CO (torr) .....	333
8.24. Ratio A/S depending on the different gases in the experimental situation .....	334

8.25. Experimental situation. Populations in % of the total OCS population .....	334
8.26. Relative A state population depending on the different gases in the experimental situation .....	335
9.1. Normalized vibrational populations vs. vibrational quantum number. Pure CO, $P_0=100$ atm, $T_0=2000$ K. outlet: $P=17.5$ torr, $T=199$ K, $M=7.1$ , $A/A^*=110$ .....	371
9.2. Normalized vibrational populations vs. vibrational quantum number. Pure CO, $P_0=100$ atm, $T_0=3000$ K. outlet: $P=17.7$ torr, $T=327$ K, $M=6.9$ , $A/A^*=110$ .....	372
9.3. Normalized vibrational populations vs. vibrational quantum number. 20% CO - 80% Ar, $P_0=100$ atm, $T_0=3000$ K. reg.noз.outlet: $P=5.7$ torr, $T=59$ K, $M=11.5$ , $A/A^*=111$ opt.noз.outlet: $P=31.4$ torr, $T=116$ K, $M=7.8$ , $A/A^*=41$ .....	373
9.4. Normalized vibrational populations vs. vibrational quantum number. $H_2$ impurity influence. CO-Ar- $H_2$ , optimized nozzle .....	374
9.5. Vibrational populations vs. vibrational quantum number. 20% CO - 20% $N_2$ - 60% Ar; reg.noз.outlet: $P=8.7$ torr, $T=90.9$ K, $M=9.1$ , $A/A^*=111$ .....	375
9.6. Vibrational populations vs. vibrational quantum number. 20% CO - 20% $N_2$ - 60% Ar; opt.noз.: $P=103$ torr, $T=209$ K, $M=5.8$ , $A/A^*=22$ .....	376
9.7.1. Average vibrational mode energy vs. nozzle position. Mixture CO- $N_2$ -Ar .....	377
9.7.2. Average vibrational mode energy vs. nozzle position. Mixture $^{12}CO$ - $^{13}CO$ - Ar .....	378
9.7.3. Average vibrational mode energy vs. nozzle position. Mixture $^{12}CO$ - $^{13}CO$ - $N_2$ - Ar .....	379
9.8. Normalized vibrational populations vs. vibrational quantum number. 25% CO - 25% $N_2$ - 50% Ar. outlet: $P=8.2$ torr, $T=109$ K, $M=8.4$ , $A/A^*=111$ .....	380

9.9. Vibrational populations vs. vibrational quantum number. 25% CO - 25% N <sub>2</sub> - 50% Ar. outlet: P=8.2 torr, T=109 K, M=8.4, A/A <sub>0</sub> =111 .....	381
9.10. <sup>13</sup> C isotopic enrichment vs. vibrational quantum number. Natural abundance: 1.1% .....	382
9.11. Vibrational populations vs. vibrational quantum number. Influence of excited electronic states. 10% CO - 10% N <sub>2</sub> - 80% Ar. S <sub>VE</sub> <sup>0</sup> = 5·10 <sup>-13</sup> cm <sup>3</sup> /s and S <sub>VE</sub> <sup>0</sup> /k <sub>0</sub> =100 .....	383
9.12. CO and NO energy levels .....	384
9.13. CO/NO V-E/E-E transfer laser. Small signal gain for NO-β at 200 K. NO(B <sup>2</sup> Π, v=0, J) → NO(X <sup>2</sup> Π, v=8, J+1) .....	385
10.1. Collinear diatom-atom collision. Arrows indicate velocities of atoms .....	424
10.2. Threshold line E <sub>t</sub> =F(E <sub>v</sub> ) for dissociation in diatom-atom collisions .....	425
10.3. Dissociation rate coefficient for N <sub>2</sub> -N <sub>2</sub> or N <sub>2</sub> -N collisions versus vibrational temperature at constant translational temperature T=10000 K. 1, 1' -Park model [8-10] with s=0.5 (1) and s=0.7 (1'); 2, 2' - Marrone-Treanor model [4] with U=D/6 (2) and U=D/3 (2'); 3, 3' - present theory with "exact" evaluation of Ψ and k <sub>0</sub> (3) and using the steepest descent method (3') .....	426
10.4. Relative contribution of dissociation from low (1), intermediate (2), and high (3) levels to the overall nitrogen dissociation rate at constant T=10000 K. Solid lines - "exact" evaluation of Ψ and k <sub>0</sub> , dashed lines - calculations using the steepest descent method .....	427

10.5. Average energy removed from vibrational mode in a single dissociation act as a fraction of dissociation energy versus vibrational temperature at different gas temperatures .....	428
10.6a. Diatom-diatom collision in collinear geometry .....	429
10.6b. Diatom-diatom collision in perpendicular geometry .....	430
10.7. Threshold line for dissociation in collinear diatom-diatom collisions .....	431

## LIST OF TABLES

3.1. Parameters used in the VV, VT, VE and SRD rate models .....	35
3.2. Spontaneous electronic radiative transfer Frank-Condon factors (1/s) .....	36
3.3. Spectroscopic constants and PL rate parameters .....	37
3.4. Output of the CO laser .....	38
4.1. Typical laser conditions .....	85
5.1. Experimental set-up equipment list .....	109
5.2. Scanning functions of the SPEX 1870 spectrometer with 2500 Å blaze grating (1200 grooves/mm) .....	119
5.3. UV emission from CO/Ar mixture .....	133
5.A1. Vibrational energy levels of $\text{CO}(X^1\Sigma^+)$ .....	135
5.A2. Vibrational energy levels of $\text{CO}(a^3\Pi)$ .....	136
5.A3. Vibrational energy levels of $\text{CO}(A^1\Pi)$ .....	136
5.A4. Vibrational energy levels of $\text{CO}(b^3\Sigma)$ .....	137
5.A5. Vibrational transitions of $\text{CO}(a^3\Pi)$ (across) → $\text{CO}(X^1\Sigma^+)$ (down) .....	138
5.A6. Vibrational transitions of $\text{CO}(A^1\Pi)$ (across) → $\text{CO}(X^1\Sigma^+)$ (down) .....	139
5.A7. Vibrational transitions of $\text{CO}(b^3\Sigma)$ (down) → $\text{CO}(X^1\Sigma^+)$ (across) .....	142
6.1. Laser parameters optimized for $P(11) 8 \rightarrow 7$ .....	164
6.2. Experimental regimes .....	164
7.1. Absorption of CO laser radiation by a 2% NO/Ar mixture at $P=0.118$ atm, $T=300\text{K}$ and atmospheric absorption (km=kilometers) .....	182
7.2. Kan and Whitney's spectral distribution of their laser in the convective and diffusion modes [Kan and Whitney] ..	191

7.3. Parameters for selecting optimum output coupler .....	209
7.4. Broad-band lasing conditions for 0.8W on the 2→1 P(12) transition .....	222
7.5. 92 W broad-band lasing conditions .....	223
7.6. 15 W single line lasing conditions for the 8→7 P(11) transition .....	229
7.7. 10 W single line lasing conditions for the 8→7 P(11) transition .....	230
8.1. Rovibrational constants (in $\text{cm}^{-1}$ ) for $^{16}\text{O}^{12}\text{C}^{32}\text{S}$ /Maki & Wells 91/ .....	282
8.2. Integral cross-section for $\text{e}^- + \text{OCS}$ elastic scattering and vibrational excitation. All cross-sections in $10^{-16}$ $\text{cm}^2$ . /Sohn 87/ .....	289
8.3. Number of collisions required to cause V-V transfer from CO(n) to OCS, depending on CO vibrational quantum number n. /Hancock 71, Lev-On 72/ .....	290
8.4. Relaxation rates for OCS(001) /Hancock 74, Zittel 88/ .....	292
9.1. Parameters used in the VT and VV rate models .....	370
9.2. Parameters used in the VE rate model .....	370

## 1. SUMMARY

The present report describes experimental and analytical studies of energy transfer and chemical reaction in diatomic and small polyatomic gases under conditions of extreme disequilibrium of the molecular vibrational modes. Primary emphasis is on collision-dominated environments with relatively low translation/rotational mode temperatures, which are characteristic of a variety of gas discharges, plasma chemical reactors, and high enthalpy supersonic gas dynamic expansions. Some additional work has also been directed to the complementary environment in which the translational/rotational mode temperatures are high, and the vibrational mode energy content is initially low. This latter environment is characteristic of strong shock waves in gases, such as occurs during planetary entry of hypersonic aerospace vehicles. This research has been conducted by staff of the Physical Gas Dynamics Program of the Department of Mechanical Engineering at the Ohio State University, under the sponsorship of the Aero Propulsion and Power Directorate of Wright Laboratory of the U.S. Air Force, Wright-Patterson AFB, Ohio. The contract has been technically monitored by the Plasma Research Section of the Power Components Branch of the Aerospace Power Division of that Directorate.

In most of the experimental studies in the program, the molecular vibrational mode(s) have been energized by the resonant absorption of CO laser radiation, with subsequent rapid redistribution of vibrational energy in vibration-vibration (V-V) exchange collisions. Vibrational mode energy inputs of the order of 1 eV per molecule are easily attainable together with low translational/rotational mode temperatures. These conditions have been observed to favor efficient vibrational-nonequilibrium-driven chemical reactions in a variety of plasma reactors. The experimental environment therefore serves as a model for some typical plasma chemistry reactors. However, this experimental environment affords the possibility of controlling or suppressing the influence of free electrons which are present in a plasma reactor. The nonequilibrium-vibrational chemical and energy transfer processes can be studied in a controlled system, independently of complicating side reaction and excitation channels driven by the high energy tail of the electron gas. In addition to these CO-laser energized experiments, some complementary studies in: 1) CO/OCS plasmas excited by a glow discharge, and in 2) CO gas excited by an ArF excimer laser, are also reported. Finally, complementary master equation kinetic models of vibrational energy transfer and chemical reaction in these environments (and in corresponding gas dynamic flow environments) have also been developed, and are reported in detail.

The report details experimental and theoretically-derived rate data for certain specific vibration-vibration (V-V), vibration-translation (V-T), vibration-electronic (V-E), associative ionization, and dissociation processes in CO and NO. There are some data and rate models for related diatomic and small polyatomic species. Emphasis is placed on energy transfer processes involving relatively high vibrational quantum states.

## 2. INTRODUCTION

It has long been established that a special type of extreme thermodynamic disequilibrium exists in the vibrational energy modes of cool molecular plasmas. Specifically, for environments in which the average energy of the vibrational modes is a few tenths of an electron volt per oscillator, and the gas kinetic temperatures are a fraction of the characteristic vibrational mode temperature, the population distribution of most diatomic and small polyatomic molecular gases is strikingly non-Boltzmann. This population distribution, when compared with a Boltzmann distribution corresponding to the same energy, is characterized by extreme overpopulation of the higher vibrational quantum states. Upper state populations may be many orders of magnitude greater than the populations of the corresponding Boltzmann distribution. Such nonequilibrium distributions are variously called Treanor Distributions, Vibration-Vibration (V-V) Pumped Distributions, or Anharmonic Pumped Distributions, and have an extensive literature <sup>(1-3)</sup>.

The nonequilibrium plasma conditions necessary to create V-V pumped distributions are pervasive in most electric glow discharges. Since many plasma chemical, ionic, and electronic energy transfer processes proceed from higher molecular vibrational states, the influence of this type of disequilibrium is critical, and its detailed consideration is essential to predicting a variety of plasma-chemical phenomena.

V-V pumped nonequilibrium is also created in many supersonic flows of high enthalpy gases<sup>(4)</sup>, and in the optical excitation of cool absorption cells<sup>(5-8)</sup>, in addition to its creation in electric discharges. In absorption cells, the phenomenon has been observed in both solid<sup>(6-7)</sup> and liquid<sup>(8)</sup> phase materials, in addition to gases. At this writing, V-V pumped nonequilibrium and its effects has been detected in a variety of diatomic and small polyatomic systems, including N<sub>2</sub>, CO, NO, H<sub>2</sub>, D<sub>2</sub>, HF, I<sub>2</sub>, CO<sub>2</sub>, H<sub>2</sub>O, N<sub>2</sub>O and <sup>13</sup>CH<sub>3</sub>F<sup>(2,3)</sup>. Indeed, in the type of environments cited, it is usually difficult to inhibit the creation of a V-V pumped distribution in these small molecules.

Despite their ubiquity, the role and influence of V-V pumping effects has tended to be largely ignored in molecular discharge plasma studies, outside of directed research in carbon monoxide gas lasers and closely related laser work. There are some notable and recent exceptions to this, however, we cite the research of Capitelli and his co-workers at the Institute for Plasma Chemistry at the University of Bari, Italy<sup>(9,10)</sup>, the work of Rusanov and his co-workers at the I.V. Kurchatov Institute of Atomic Energy in the Soviet Union<sup>(11,12)</sup>, and studies in the Plasma Research Section at the Aeropropulsion Laboratory at Wright Laboratories, including the recent results in silane chemistry initiated by V-V pumped N<sub>2</sub><sup>(13,14)</sup>.

At the inception of the present study, there was strong evidence from the work of the groups cited above, and from the previous work of the group at the Ohio State University<sup>(15,16,17)</sup> that V-V pumped nonequilibrium systems afforded a major avenue to drive unique plasma chemical reaction paths, and



also afforded a method to strongly populate excited molecular electronic states in a collision dominated, high density plasma. The plasma chemical applications have, for example, great potential importance in microelectronics and detector fabrication processes<sup>(14)</sup>, and in atomic-hydrogen power engineering<sup>(11)</sup>. The control of excited molecular electronic state populations has a corresponding potential for high voltage switching applications and high energy gas lasers<sup>(13,18,19,20)</sup>. The major goal of the research program reported here was to develop insight into the basic kinetic mechanisms of vibrationally nonequilibrium plasmas. It is hoped that these insights will aid in the design of new electric discharge plasma reactors.

A major difficulty in studying these V-V pumped processes in detail in electric discharges is that the relatively small fraction of rather high energy electrons can initiate many excited electronic state, ionization, and chemical processes, independently of the more dominant, vibrationally excited state processes. It is difficult to sort out the major energy storage and transfer paths in such a plasma, in view of the large number of relatively minor plasma processes occurring, which contribute to radiation signal from the plasma, often giving a misleading picture of the true energy partition in the environment. For this reason the largest part of the present research effort has centered on experiments in optically pumped, V-V nonequilibrium gases. A carbon monoxide (CO) gas laser is used to excite the vibrational mode(s) of various diatomic and small polyatomic molecules in a reaction cell by resonant absorption of the laser radiation and subsequent redistribution of vibrational energy by V-V exchange collisions. In such experiments, the influence of free electron-molecule collision processes is generally negligible, and the major vibration-to-vibration, vibration-to-electronic, and chemical reaction channels can be conveniently studied. In the present report, an experimental and analytic program of research in such optically pumped environments is described.

Each of the following chapters in this report is based on either papers already published in the journal literature during the course of the project, or on recently-completed theses. An appendix gives the complete list of journal publications, meeting presentations, and theses completed under this study.

The following Chapter 3, describes experiments on the optical pumping of vibrationally nonequilibrium CO, with emphasis on extension of the range of accessible translational/rotational mode temperatures. The work was performed in collaboration with the group at Ecole Centrale Paris, and some of their complementary results are described. Chapter 4 continues the CO experimental studies, but the emphasis here is on measurements of vibrational-quantum-state resolved associative ionization rates in this molecule. Chapter 5 concludes the CO investigations, presenting Chapter 5 a study in which an ArF excimer laser was used to directly prepare a specific vibrational level of the  $a^3\Pi$ , the lowest-lying excited electronic state of CO. Chapter 6 extends the optical pumping studies to NO, and gives upper state rate data for this species. Chapter 7 gives the details of the unique line-selected CO laser that was developed to optically pump NO. Chapter 8 discusses the use of V-V pumped

CO to transfer energy to the carbonyl sulfide (OCS) molecule, and describes and investigation to ascertain the possibility of continuous wave infrared laser action on that molecule. Finally, Chapters 9 and 10 detail theoretical kinetic models developed under the program to describe nonequilibrium energy transfer and reaction kinetic processes in these vibrationally excited environments.

## REFERENCES

1. C.E. Treanor, J.W. Rich, and R.G. Rehm, J. Chem. Phys. 48, 1798 (1968).
2. J.W. Rich, Relaxation of Molecules Exchanging Vibrational Energy . Chap. 4 in E.W. McDaniel and W.L. Nighan, Applied Atomic Collision Physics . Vol. 3, Gas Lasers , Academic Press, N.Y. (1982).
3. M. Capitelli, Ed., Nonequilibrium Vibrational Kinetics , Springer-Verlag, Berlin (1986).
4. J.D. Anderson, Jr., Gasdynamic Lasers: An Introduction , Academic Press, N.Y., (1976).
5. J.W. Rich and R.C. Bergman, Chem. Phys., 44, 53 (1979).
6. N. Leagay-Sommaire and F. Legay, IEEE J. Quantum Electron. QE-16, 308 (1980).
7. J.P. Galaup, J.Y. Harbec, R. Charneau, and H. Dubost, Chem. Phys. Lett. 120, 188 (1985).
8. D.S. Anex and G.E. Ewing, J. Phys. Chem. 90, 1604 (1986).
9. S. De Benedictis, M. Capitelli, F. Cramarossa, and C. Gorse, Chem. Phys. 111, 361 (1987).
10. M. Cacciatore, M. Capitelli, and G.D. Billing, Chem. Phys. 157, 305 (1989).
11. V.D. Rusanov, A.A. Fridman, and G.V. Sholin, Sov. Phys. Usp. 24, 447 (1981).
12. T.M. Grigor'eva, et al., High Temperature Chemistry, 18, 268 (1984).
13. W.F. Bailey and A. Garscadden, J. Physique, 40, C7-377, (1979).
14. C.A. DeJoseph, Jr., Reactions of Silane in Active Nitrogen , Dissertation University of Oklahoma, Norman, OK (1989).
15. H. Dunnwald, E. Siegel, W. Urban, J.W. Rich, G.F. Homicz, and M.J. Williams, Chem. Phys. 94, 195 (1985).
16. R.L. Deleon and J.W. Rich, Chem. Phys. 107, 283 (1986).
17. W. Urban, J.X. Lin, V.V. Subramaniam, M. Havenith, and J.W. Rich, Chem. Phys. 130, 389 (1989).

18. N.G. Basov, V.F. Gavrikov, S.A. Pozdneev, and V.A. Shcheglov Sov. J. Quantum Electronics 17, 1130 (1987).
19. J.W. Rich, R.C. Bergman, and M.J. Williams, Vibration to Electronic Energy Transfer Laser , Calspan Report No. 6678-A-2, Calspan Corp., Buffalo, N.Y. (1984).
20. L.G. Piper and W.J. Marinelli, J. Phys. Chem 93, 4033 (1989).

**3. CARBON MONOXIDE STUDIES I:  
Nonequilibrium Vibrational Kinetics of CO  
at High Translational Mode Temperatures**

\*This chapter adapted from C. Flament, T. George, K.A. Meister, J.C. Tufts, J.W. Rich, V.V. Subramaniam, J.-P. Martin, B. Piar, and M.-Y. Perrin, Chem. Phys. **163**, 241 (1993)

### 3.1. Introduction

In this chapter, the results of the program for the vibrational excitation of CO by CO laser optical pumping are presented. The results at both Ohio State and at the laboratory of our collaborator, C.N.R.S Centrale Paris, will be described. Previous work with this technique has been published for both CO [1-3] and for NO [4].

### 3.2. Experimental

#### 3.2.1 Apparatus

Fig. 3.1 shows the typical setup for the experiment, as used at Ohio State. The infrared and visible UV emission spectra of the observed molecules (CO and C<sub>2</sub>) can be observed simultaneously as shown on the figure. At C.N.R.S. Centrale Paris only one port of the cell is used and the diagnostic apparatus is not the same; notably a larger 1.15 m focal length SOPRA monochromator is used. This monochromator is equipped with an IR (4  $\mu\text{m}$ ) or UV (2500  $\text{\AA}$ ) blazed grating so that the spectra emitted by the different molecules at different wavelength regions are recorded successively. As the pump laser is used in the c.w. mode only, the mechanical chopper is placed in front of the entrance slit of the monochromator. The lock-in amplifier is connected to a PC type micro-computer for further processing and display; the computer also drives the stepping motor of the monochromator so that the spectrum can be recorded directly as a function of the wavelength.

The pump laser is a flowing-gas electric discharge CO laser, wall-cooled by a liquid nitrogen bath. The laser combines several features reported in the literature [5-9] for enhancing short wavelength operation, i.e., forcing lasing on the lowest fundamental vibrational band components, including  $v=1-0$ . These features include: precooling of the laser gases before they are introduced into the discharge tube; pure helium gas injection at the tube ends to prevent absorption losses due to partially relaxed CO; small gas injectors which introduce the laser gases at sonic velocity into the tube, and impart a swirling motion to the gases; a mechanical chopper to provide intra-cavity Q-switching; selectively coated laser mirrors; and optimization of the laser gas partial

pressures and discharge operating current. With these features, the Ohio State laser, which has 1 meter active discharge length, can produce 3 watts average multiline power when lasing on  $v=1-0$  transitions, and up to 12 watts multiline when  $v=2-1$  is the shortest wavelength lasing band component. The longest wavelength band component typically lasing is  $v=12-11$ . The short wavelength operation is essential for optically exciting room temperature CO; if the shortest wavelength lasing band component is  $v=5-4$  or higher, it is impossible to initiate the CO vibrational excitation process. The Centrale Paris laser, which has a 1.64 meter active discharge length, has mostly been operated in the c.w. mode for the present experiments, which have been conducted as discussed below, at powers up to 27 Watts. Fig. 3.2, taken from the Centrale Paris laser, shows the typical output spectrum from these lasers under 27 W c.w. conditions. Note that the rotational number of the lasing lines decreases with vibrational band; this is a consequence of lasing-induced cascade [3].

Under Q-switched operation, the pulse-to-pulse broadband power output stability is quite good, with variations being less than  $\pm 2.5\%$  over the entire pulse shapes. Long time amplitude stability, over periods up to a few hours, is of the same magnitude as long as the liquid nitrogen level is maintained in the cooling baths. The single-line stability of the laser is poorer than the numbers just mentioned. For the present purposes of optically exciting the vibrational mode of the CO in the absorption cell, however, the broadband stability is the important parameter, and is quite satisfactory.

The development of a multiwatt, slow-flow, wall-cooled CO laser, providing a significant fraction of its output on the  $v=1-0$  and  $v=2-1$  band components, affords a novel opportunity to study V-V pumped gases. Relatively high pump laser powers are necessary to excite significant volumes of gas at pressures of several Torr and above. Most previous detailed spectroscopic studies of V-V pumped CO gas used large, supersonic-flow CO lasers [10], which were expensive to run for long times [1, 2, 11-12]. Except for the recent work of Urban, et al. [3], other attempts to excite V-V pumping in CO with a slow flow laser required auxiliary discharge excitation [3]. The present experiments can be operated continuously, permitting sampling times of hours, if necessary.

After some preliminary studies done to test the efficiency of the pumping of CO by the infrared CO laser as a function of laser power, Q-switch and c.w. modes, Ar-CO gas mixture composition, pressure and flow rate through the cell, we decided to build two complementary set-ups. The details of the absorption cells are given in Fig. 3.3. At Ohio State (Figure 3.3a) the cell is built to achieve CO pumping at low flowing rate, medium laser power and relatively low temperature 300 to 700K. The cell is a 6-armed stainless steel cross (Varian Corp.) of 1.5" diameter tubing, permitting optical access on three axes. One or more of the six windows can be replaced by a flange mounting diagnostic equipment, if desired. The cell has gas fill and purge ports, and fittings for pressure measurements. It can be operated either with static gas fills, or in a flowing-gas mode; CO fills the entire volume of the cell. In the flowing gas mode the gas mixture flows in the direction of the incoming laser beam.

At Centrale Paris (Figure 3.3b), the cell makes it possible to run at the higher translational temperatures associated with a more powerful laser. The temperature can vary from 600K to 1500K as described later. It is a four-armed stainless steel cross of 25mm diameter tubing, allowing access in two perpendicular directions. The viewing axis is perpendicular to the direction of the laser beam. The output window on the laser beam is adjusted at Brewster's angle in order to avoid reflection of the high power laser beam back into the cell. The gas CO-Ar mixture is injected perpendicularly to both the optical axis of the laser and to the detection direction through a 4mm diameter stainless steel tube. The mixture is extracted through a similar tube placed at 8mm distance opposite the injector exit. A buffer gas (Ar) is injected by a third inlet to fill the entire cell and pumped out by the same tube as the CO-Ar mixture. With this arrangement CO is present and excited only in the 4mm ID region located between the injection and the evacuation tubes. Pressure is measured in the injection tube 2cm before injection in the cell.

As shown, diagnostics include infrared and visible/ultraviolet monochromators, for emission spectroscopy. Steady-state signals are processed with lock-in amplifiers, and pulsed signals with a boxcar averager. C.w. and average laser powers and laser pulse energies are measured with a Coherent Corp. "Labmaster" system. Laser pulse shapes are determined with a Molelectron P5-00 ultra-fast pyroelectric detector. Modifications from this basic setup are noted in the discussions of specific measurements in the following sections.



### 3.2.2 Operation and Energy Flow Channels

With this setup, the CO laser beam is focused by a 2.5 cm dia., 20 cm focal length zinc selenide lens into the absorption cell. A mixture of CO and Ar is slowly flowing through the cell. As discussed subsequently, the partial pressures of the CO and Ar can be varied over a large range; a typical condition is a 1/9 CO/Ar volumetric ratio at 100 Torr total pressure, with a flow velocity of 1 cm/sec. Under such conditions, the CO in the cell readily absorbs the laser energy into its lowest vibrational states,  $v \leq 12$ . Higher CO vibrational states,  $v > 12$ , are populated by V-V exchange. One result of this V-V up-pumping is immediately seen in the absorption cell: there is a quite intense blue light emission visible, centered at the focal point of the laser beam, and extending for approximately 2 to 3 centimeters along the optical axis. The diameter of this luminous region varies with cell and laser conditions; it is of the order of 1 to 2 mm. This blue emission is due to visible band components of the C<sub>2</sub> Swan system,  $d^3\Pi_g \rightarrow a^3\Pi_u$ . The C<sub>2</sub> is generated by chemical reaction of the V-V pumped CO. It has been observed and discussed in previous work using this excitation technique [1, 2-3, 11-12].

Fig.3.4 is a simplified energy level diagram for CO, showing the ground electronic state,  $X^1\Sigma^+$ , the lowest excited electronic state,  $a^3\Pi$ , and the lowest excited singlet state,  $A^1\Pi$ . Several additional triplet states with energies between those of the  $a^3\Pi$  and the  $A^1\Pi$  states have not been shown. Some of the energy transfer mechanisms occurring in the cell are shown, based on both the present work and the previous studies referenced above. We show the primary excitation transitions, which involve resonance absorption of the laser radiation by the  $v=0-1$  to  $v=11-12$  fundamental infrared band components of the CO in the cell. Note that in the excitation of CO initially in equilibrium at 300K, some laser output on the  $v=1-0$  or, at least, the  $v=2-1$  band component, is needed; levels above  $v=1$  are negligibly populated at this temperature, and hence do not absorb. In our case, if the laser does not operate c.w. on these lowest band components, Q-switching the laser can often force these components. Q-switching the laser created higher peak powers on the higher bands than in the c.w. case. With the Q-switching, lasing-induced cascade can force gain on the lowest vibrational band components. Such use of Q-switching

to achieve CO pumping in an optical absorption cell was first demonstrated by Urban et al., who discuss the phenomenon [3]. In the present experiments, if the laser is operating c.w., with no lasing output on the lowest two band components, the cell gases will not absorb the laser radiation. However, it is usually possible to trigger the initial absorption by merely briefly blocking one laser mirror intra-cavity. The cascade induced by this Q-switch is sufficient to trigger absorption and the subsequent V-V up-pumping; the cell gases will continue to absorb in the steady state, until the laser beam is interrupted. We emphasize that the laser excitation mechanism is, indeed, resonance absorption. The focused laser fields are relatively weak. Strong absorption and subsequent V-V up-pumping occur with focused laser field intensities of only a few hundred  $\text{W}/\text{cm}^2$ . The strongest fields in the present experiments are  $2.7 \times 10^5 \text{ W}/\text{cm}^2$ , reached in some of the Centrale Paris studies. We believe that even with these intensities, negligible multiphoton absorption is occurring, given the low density of states in the CO molecular absorber.

Also shown on Fig. 3.4 are the V-V pumping transitions, created when two CO molecules collide and exchange a quantum of vibrational energy. These processes are typically much more rapid than the rate of energy absorption from the excitation laser, and very much more rapid than V-T deactivating collisions or spontaneous radiative decay. As indicated on the figure, vibrational levels up to approximately  $v=40$  have been observed to be populated by the V-V process. It was first specifically noted by Farrenq, et al. [14] in V-V pumped CO in an electric discharge that levels above  $v=42$  are not populated in the V-V pump. This same limit appeared to occur in previous optically excited experiments [3, 11-12], despite the fact that the dissociation energy of the CO  $X^1\Sigma^+$  state is 11.09 eV, and there are 40 additional bound vibrational levels above  $v=42$  in the Morse oscillator model of CO. This limit on the up-pump appears to be a consequence of rapid V-E transfer into the  $A^1\Pi$  state, which is approximately isoenergetic with  $v=42$ . It should be emphasized, however, that the mechanism coupling the  $X^1\Sigma^+$  and  $A^1\Pi$  states has not yet been detailed. In any case, the CO  $A^1\Pi$  state rapidly radiates on the CO 4th Positive UV emission bands (10 nsec lifetime), effectively putting a cap on the V-V up-pump [2-3, 11-12, 14]. In the present experiments, emission from vibrational bands to  $v=40$  have been observed at O.S.U., and to  $v=27$  at

Centrale Paris. The highest significantly populated vibrational level has not yet been determined for either of these experiments.

Also shown in Fig. 3.4 is the  $a^3\Pi$  state. There is also some energy transfer into this state from the V-V pumped  $X^1\Sigma^+$  states; reaction from the  $a^3\Pi$  is presumably a major channel for the production of the  $C_2$  that is observed in emission [1, 3, 11-12, 14]. Unlike the transfer into the  $A^1\Pi$ , however, transfer into the  $a^3\Pi$  does not stop the V-V up-pump; the radiative lifetime of the  $a^3\Pi$  state is long (4 msec) and the chemical reaction and any other quenching channels are not sufficiently rapid to provide a major energy sink. Nevertheless, perturbation of the steady-state V-V pumped  $X^1\Sigma^+$  state vibrational populations due to this transfer have been observed in high resolution FTIR spectroscopic studies in electric discharges [14].

Our previous studies of CO laser-excited, V-V pumped, gaseous CO have yielded data on the rates for some of these processes at moderate translational/rotational mode temperatures, below 370K [2]. More recent work has indicated that the V-V up-pump can occur at higher temperatures, of the order of 800K [3]. The present study independently confirms that the results of Ref. 3 are at 800K, and extends results to 1500K translational/rotational mode temperature; strong up-pumping is still occurring at these surprisingly elevated temperatures. This is discussed further in Section 4.

### 3.2.3 Translational/Rotational Mode Temperature Measurement

#### $C_2$ Swan Emission - OSU

In contrast to the emission from electric-discharge-excited CO plasmas [15], there are few band systems emitting in the visible and near-ultraviolet wavelength regions from the vibrationally pumped gases in the present experiments. By far the strongest system at these wavelengths is the  $C_2$  Swan. Fig.3.5 shows a typical spectrum from one sequence ( $\Delta v=0$ ) of this band system. The R-branch of the  $v=0-0$  sequence is rotationally resolved; the closely-spaced multiplet structure is not separated. The values of  $J'$  for each line are indicated on the figure. The radiative lifetime of the  $C_2$   $d^3\Pi_g$  state is sufficiently long ( $O[1 \mu\text{sec}]$ ) to ensure that these states are rotationally

equilibrated, and, therefore, the intensity distribution of these lines can be used to infer the rotational mode temperature. Under the entire range of operating densities of the absorption cell, rotational mode relaxation is sufficiently rapid to insure that this temperature is equilibrated to the translational mode temperature and the CO rotational mode temperature. Fig. 3.6 shows the usual semilogarithmic plot to determine this temperature, for the spectrum of Fig. 3.5. The pump laser was operating at 7.5 W c.w. power, and the gas pressures in the cell were 9 Torr CO and 51 Torr Ar. The gas temperature is inferred as 753K. Over the range of cell temperatures in the present (OSU) experiments, accuracy of this measurement is estimated to be  $\pm 50\text{K}$ .

### CO 1st Overtone Emission - Centrale Paris

At Centrale Paris, temperature measurements have been performed by fitting the CO first overtone emission. The cell is filled with Ar under a total pressure of 240 Torr, and pure CO is injected at the center of the absorption cell at a speed of  $1\text{ ms}^{-1}$ . The pump laser is operating at 27 watts c.w. power. Fig. 3.7 shows a portion of the first overtone spectrum, which corresponds to emission from CO vibrational levels  $v=4$  to 8. The apparatus function of the monochromator is a triangle with a half width at mid height (HWMH) of  $1.3\text{cm}^{-1}$ , so that the lines of a given vibrational transition, which are distant about  $4\text{ cm}^{-1}$ , should be well separated. Nevertheless, the badly resolved rotational structure demonstrates that there is a significant overlapping of the different bands and gives evidence that the levels of high  $J$  are populated. This is confirmed by the large emission in the band heads and proves that the temperature is high.

In order to deduce the rotational temperature and the vibrational distribution, we make a fit of the experimental spectra, as primarily suggested by Horn and Oettinger [16]: when assuming that the rotational mode is at equilibrium at the translational temperature  $T$ , the theoretical intensity of the emission is given by:

$$I^{\text{TH}}(\sigma) = \sum_{\substack{\text{all bands} \\ (v, v-2)}} N_v U_v(\sigma, T) \quad (1)$$

where  $N_v$  is the total population of level  $v$ ,  $\sigma$  is the wavenumber,  $U_v(\sigma, T)$  results from the contribution of all the rotational lines within the band  $(v, v-2)$ ,

and is convoluted with the apparatus function. Under our experimental conditions, the line shape is a Voigt profile with HWMH of typically  $10^{-2} \text{ cm}^{-1}$ . Since this value is much smaller than the width of the spectrometer apparatus function ( $1.3 \text{ cm}^{-1}$ ), one can calculate  $U_V(\sigma, T)$  by using Dirac lines; this leads to:

$$U_V(\sigma, T) = \sum_{\text{all } J} \sum_{J'=J\pm 1} \left[ A_{v-2, J'}^{v, J} \frac{2J+1}{Q_{\text{rot}}(T)} e^{-F_v(J)/kT} \right] h\sigma_{v-2, J'}^{v, J} \tau_{\text{mono}}(\sigma - \sigma_{v-2, J'}^{v, J}) \quad (2)$$

$J'=J+1$  for the P lines and  $J'=J-1$  for R lines;  $\sigma_{v-2, J'}^{v, J}$  is the wavenumber of the transition  $(v, J) \rightarrow (v-2, J')$  [17],  $A_{v-2, J'}^{v, J}$  is the Einstein coefficient for spontaneous emission [18],  $F_v(J)$  is the rotational part of the energy of the level  $(v, J)$  [17] and  $\tau_{\text{mono}}$  is the apparatus function.

$N_V$  and  $T$  are then deduced from the experimental spectra, sampled in  $n$  points  $\{\sigma_i, I^{\text{EXP}}(\sigma_i)\}$ , by using equations (1) and (2) and by minimizing the quantity:

$$\sum_{i=1}^n \left[ I^{\text{TH}}(\sigma_i) - I^{\text{EXP}}(\sigma_i) \right]^2 \quad (3)$$

In order to solve this separable nonlinear least square problem ( $N_V$  are linear parameters and  $T$  is a non linear one), we use a technique based on the theoretical developments by Golub and Pereyra [19]. This method, contrary to that of Horn and Oettinger [16] or De Benedictis and al. [20] has the advantage of being noniterative, and thus does not require an arbitrary assumption for the initial shape of the  $N_V$  distribution.

Fig. 3.7 shows the experimental spectrum (EXP) and the calculated spectrum with the fitted values of  $N_V$  and  $T$  (TH). The discrepancies remain lower than 5% except in spectral regions where absorption lines of water vapor in the optical path coincide with emission lines of CO. The regions, like that between  $4000$  and  $4160 \text{ cm}^{-1}$ , where the absorption by laboratory air does not perturb the fitting procedure, are unfortunately too narrow to allow a correct determination of all the vibrational populations, but permit a reliable measurement of temperature. In the conditions of Fig. 3.7, the deduced temperature is  $1500\text{K} (\pm 100\text{K})$ .

Recordings of experimental spectra between 3100 and 3300  $\text{cm}^{-1}$  show that levels up to  $v=27$  are significantly populated. This efficiency of VV pumping is remarkable when considering the high rotational temperature obtained in the present experiment.

### **C<sub>2</sub> Swan Emission - Centrale Paris**

The rotational temperature has also been inferred from the R branch of the C<sub>2</sub> Swan  $\Delta v=0$  emission spectrum, as discussed in section 2.3, C<sub>2</sub> Swan Emission - OSU. This leads to a temperature of  $1450\text{K} \pm 100\text{K}$  in very good agreement with that obtained from IR measurements. Fig.3.8 shows the C<sub>2</sub> Swan band emission spectra for these elevated rotational temperatures. It is important to note that when the pump laser power is set to that used in OSU (6 Watts c.w.), rotational temperature deduced from C<sub>2</sub> spectra is  $660\text{K} \pm 50\text{K}$ . This value is in quite good agreement with the OSU measurements given the different flow geometry.

### **3.2.4 Vibrational Band Emission Measurements**

The rate of the V-V up pump is of considerable interest, in view of the high rotational/translational mode temperatures of the present experiments. Previous measurements of V-V exchange rates among high vibrational levels in CO have been at temperatures of 370K and less [2]. In the O.S.U. apparatus, the excitation laser was Q-switched with an intracavity chopper, and the response of the CO in the cell to the pulsed energy input was investigated. Fig.9 shows the shape of the Q-switched laser pulse, when the laser was chopped with a 50% duty-cycle chopper at 200 Hz. Fig.9a shows the entire pulse shape; pulse duration is 2.5 msec. The initial spike created by the cavity dumping is evident.

To investigate the rate of V-V up-pumping, the infrared monochromator was positioned at a wavelength centered on a preselected 1st overtone vibrational band component. The output of the InSb detector on the monochromator was directed to a gated boxcar averager. This infrared signal was monitored at selected time intervals during the laser excitation pulse. A 15  $\mu\text{sec}$  gate was typically used, and 3000 pulses were averaged at each time interval. Fig. 3.9b

shows an enlargement of the initial portion of the laser pulse, and shows the 15  $\mu$ sec gate positioned at approximately 0.2 msec before the pulse.

Fig. 3.10 shows the time-dependent 1st overtone emission signal obtained by this means, with the monochromator centered at four selected wavelengths. As indicated on the figure, the selected wavelengths correspond to the centers of the  $v=4-2$ ,  $v=19-17$ ,  $v=35-33$ , and  $v=39-37$  band components. The cell conditions for these data are given on the figure. It is important to note that for these pulse conditions, 100% modulation is not attained at any of the four selected wavelengths; vibrational relaxation times, even when catalyzed by reaction products, are sufficiently long so that even the highest vibrational states monitored remain partially populated during the 2.5 msec laser-off period. This rather large vibrational heat capacity effect insures relatively small fluctuations in the rotational/translational mode temperature during the pulse. The average rotational/translational mode temperature, measured by the  $C_2$  emission diagnostic discussed above, is 740K. The sequential rise of each progressively higher band component can be seen; the rise times, of the order of 0.1 msec, are in contrast to those observed in lower temperature experiments [2]. These fast rise times are a consequence of the faster V-V rates at the present temperature.

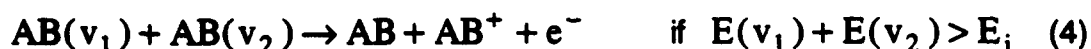
Very high energy loading of the vibrational mode can be obtained in these experiments, which permit the V-V up-pump despite the high translational/rotational mode temperatures. Fig. 3.11 shows low-resolution first overtone emission spectra from the pumped CO for CO concentrations varying over two orders of magnitude. For these data, the cell gases are diluted by Ar; Ar concentration is approximately constant at  $3 \times 10^{18} \text{ cm}^{-3}$ . The centers of the vibrational band components are indicated on the figure. The maximum bandpass for this resolution is approximately 0.25 micron; this implies that approximately five adjacent vibrational states contribute to the emission at a given wave-length. Emission is measured to  $\approx 4.4$  microns, at which wavelength the R-branch of the  $v=1-0$  band component of the CO fundamental begins, and swamps signal from the overtone, as can be seen. Air in the optical path causes significant  $H_2O$  absorption in the 2.4 to 2.8 micron region, and significant  $CO_2$  absorption from 4.2 to 4.4 microns. The  $CO_2$  absorption and the overlap of the fundamental are particularly unfortunate diagnostic

complications, since they prevent determination of the highest populated vibrational level from these low-resolution spectra. Nevertheless, it is evident that levels to at least  $v=40$  are populated for all CO densities shown in the spectra of Fig. 3.11.

For the data of Fig. 3.11, the absorbed power decreased slightly with the increasing number density, varying from 1.2 W at the highest CO concentration to 1.0 W at the lowest concentration. This near-constant absorbed power for the greatly varying number density implies that the vibrational mode energy loading per CO molecule is greatly increasing with decreasing concentration. This is confirmed by the emission spectra. It can be noted that although overall emission intensity can decrease with decreasing CO concentration, there is a marked increase in the relative population of the higher states with such decreasing concentration. For example, ratioing intensities at 2.40 and 3.25 microns implies an increase in  $n_{25}/n_4$  of more than a factor of 2 as the CO density is decreased over the range shown.

### 3.2.5 Ionization Measurements

It was proposed by Polack et al. [21] that an associative ionization mechanism involving vibrationally excited diatomic molecules could occur by the following scheme:



where  $AB(v)$  is the molecule in the  $v^{\text{th}}$  vibrational state with energy  $E(v)$  and  $E_i$  is the ionization energy. The reverse of this reaction is a form of the well-known dissociative recombination mechanism which is a major mechanism controlling the electron concentration in many molecular plasmas [22]. The work of Ref.21 specifically studied  $N_2$  plasmas, and a specific rate of the ionization of  $N_2$  by this mechanism was inferred experimentally. A major difficulty in studying this process in an electric discharge plasma is that there are several ionization mechanisms operating in addition to Eq.4, and separation of this single ionization process can be ambiguous. However, Achasov et al. [23] have made ionization measurements in the adiabatic supersonic nozzle expansion of shock heated  $N_2$  and CO. As noted in Sect.1,



such rapid expansions of high enthalpy flows can create the requisite nonequilibrium conditions (high vibrational mode energy, low translational/rotational mode temperature) strongly favoring the V-V up-pump. This study, having been conducted in a discharge-free environment with negligible thermal ionization, clearly showed electron production in both N<sub>2</sub> and CO by the Eq.4 mechanism. Electron concentrations several orders of magnitude above the concentration predicted by Saha equilibrium were measured in the expansion.

The present experiment also shows ionization in CO by the mechanism of Eq.4. For these ionization measurements, two parallel brass plate electrodes were placed in the absorption cell. One plate was on each side of the luminous region of the V-V pumped gas, centered about the focal point of the laser beam. The total plate separation was 2 cm; each plate was a 1 cm x 2 cm rectangle. The long dimension of the plates was along the laser beam axis. A d.c. voltage was applied to these electrodes. Under all cell operating conditions in which significant V-V pumping was produced, a current could be drawn through the gas with moderate voltages applied; voltages were much below breakdown threshold for the cell gases. Currents were measured with a microammeter. Fig.12 shows typical voltage-current characteristics for one experiment. For this case, CO/Ar concentration ratio was 4/69, and the cell pressure was varied from 60 to 500 Torr. Laser power was 5.1 W c.w. From the measured currents, the electron concentration can be estimated from:

$$n_e = \frac{I}{A_e u_e} \quad (5)$$

where  $I$  is the measured current,  $A_e$  is the estimated collection area, and  $u_e$  is the electron drift velocity for the applied  $E/N$ . Electron densities calculated from Eq.5 are in the range of  $10^7 \text{ cm}^{-3}$  to  $10^8 \text{ cm}^{-3}$  for a plasma area of  $0.1 \text{ cm}^2$ , for the data of Fig. 3.12.

The measured currents, though small, can definitely be correlated with the volume ionization created by the laser excitation, via the mechanism of Eq.4. The possibility of photo-ionization of the plates, by U.V. radiation from excited CO electronic states (Fig. 3.4), was excluded by surrounding the active pumped

region in the cell by a 1 cm diameter U.V. grade quartz tube. Negligible currents could be drawn at all applied voltages with this arrangement. Some checks were also made for the possibility of an easily ionizable impurity creating electrons by ionizing collisions with highly vibrationally excited CO. Measurements with ultra high purity CO, and with liquid nitrogen trapping of the test gases before the cell did not show substantially lower ionization.

Finally, some preliminary experiments were performed to examine the response of the current to the pulsed operation of the laser. Fig. 3.13a is an oscillogram of the laser pulse, taken with the fast photodiode, and the current response. The modulation of the population of vibrational level  $v=22$  was simultaneously monitored in these experiments by use of a narrow bandpass filter centered at 3.05 microns. This response is shown in Fig. 3.13b. In all cases, the rise in the current was subsequent to the rise in  $v=22$  emission. The plasma decays after the laser pulse with times of the order of a few milliseconds. This is unexpectedly rapid when compared to known associative recombination times for CO molecular plasmas [24]. The presence of an impurity which is a strong electron attacher is suspected. As discussed in [24], iron pentacarbonyl,  $\text{Fe}(\text{CO})_5$ , generated during storage of the CO test gas in a steel cylinder is suspected. Further experiments with traps to eliminate electron-attaching impurities are planned.

### 3.3. Kinetic modeling

A master equation kinetic model has been previously developed and applied to V-V pumping experiments in CO and NO [2-4]. The earlier work in CO had been used to correlate experiments at temperatures below 370K [2], and led to specific V-V rate model expressions valid over a temperature range  $150\text{K} \leq T \leq 370\text{K}$ , and a vibrational quantum number range  $0 \leq v \leq 35$ . This rate expression is also in agreement with the experiments and model rates of Powell [25], which includes some data to 500K.

The previous model has been further developed and applied to the present experiments. A major question is whether the V-V rate expressions, obtained from lower temperature data, are valid for the present elevated temperatures.

We have applied the model to two of the experimental cases discussed in the previous section: the steady-state experiment at 1500K (Sect.2.3) and the Q-switched pulse experiment at 740K (Sect.2.4).

The numerical results presented in this section were obtained with a computer program which integrates the full set of kinetic equations describing the vibrational level populations in each electronic state as a function of time. Rapid integration of some seventy vibrational level equations relies upon efficient "stiff" equation integration routines [26, 27].

### 3.3.1. Equations

A description of the master equation kinetic model employed in the present study has been given previously [2-4]; therefore, only a brief summary is included here. The time dependence of each vibrational level in up to two coupled electronic manifolds is expressed as a sum of five rate processes:

$$dn_{i,v} / dt = VV_{i,v} + VT_{i,v} + SRD_{i,v} + VE_{i,v} + PL_{i,v} \quad (6)$$

$$i = 1,2 \quad \text{and} \quad v = 0, 1, \dots, (vmax)_i$$

where  $n_{i,v}$  (also written  $n_i(v)$ ) is the number density of molecules  $i$  in vibrational quantum level  $v$ , in  $\text{cm}^{-3}$ ;  $i = 1,2$  represents the ground state and one electronically excited state of CO respectively; and  $(vmax)_i$  is the highest level included in the vibrational manifold, where  $(vmax)_i < 80$ . Allowance is also made for an inert diluent, which in the present case is argon. The translational and rotational modes of the system are assumed to be in equilibrium at temperature  $T$ .

In the right hand side of the above equation  $VV_{i,v}$  is the vibration-vibration exchange rate,  $VT_{i,v}$  is the vibration-translation exchange rate,  $SRD_{i,v}$  is the spontaneous radiative decay rate,  $VE_{i,v}$  is the vibration-electronic exchange rate, and  $PL_{i,v}$  is the absorption and stimulated emission rates due to the CO pump laser. In our calculations the  $VV$  term is the sum of a long-range dipole-dipole Sharma-Brau term and a short range impulsive Schwartz-Slawsky-Herzfeld (SSH) term [28]. The  $VT$  rate used is a modified SSH model [29, 30]. The  $VE$  term employs an analytical form based on a collision-induced near-

resonance exchange mechanism [4]. The appendix gives the actual VV, VT, VE, SRD and PL expressions used.

### 3.3.2. Input values

All the parameters needed in the calculation of the VV, VT, VE and SRD rates are given in Table 1 and Table 2. Table 2 in particular gives the spontaneous electronic radiative transition rates from the electronic excited  $A^1\Pi$  state to the electronic ground level of CO. The spectroscopic parameters used in the computation of PL are given in Table 3. These parameters are directly taken from Huber and Herzberg [21].

The input values characterizing the experiment are the temperature, the gas partial pressures in the cell, and a precise description of the laser pulse, which includes the power, the focus, the shape and the wave-lengths used. These input values are given for each application of the code (see below). The beam focus is a significant input parameter that is not directly measured in the experiment and is therefore treated parametrically in these model calculations.

### 3.3.3. C.w. case

We first apply the code to the calculation of the c.w. experiments. The cell conditions are:  $P_{CO} = 24$  Torr,  $P_{Ar} = 216$  Torr. The wavelengths and spectral power distribution of the excitation laser are listed in table 4 (see also the spectrum in Fig.2). For these conditions, the calculation was begun with the gases initially in a 1500K equilibrium state. Eq.6 was integrated until steady state was achieved for the vibrational populations. Calculation was done for two focal diameters, 3.0 and 1.0 mm. Fig.14 shows the calculated steady state distribution for these two cases. As can be seen, the model rates predict strong pumping to  $v \approx 35$  for the 3 mm focus, and to  $v \approx 40$  for the stronger 1.0 mm focus. 1.0 mm is the focal diameter estimated for the experiments of Sect.2.3.

### 3.3.4. Q-switched case

This case models the pulsed experiment of Section 2.4, the results of which are given in Fig. 3.10. The cell conditions are:  $P_{CO} = 6.14$  Torr,  $P_{Ar} = 103.9$  Torr,  $T = 740$ K. The laser is Q-switched at 200 Hz, with a 50% chopper, giving a 2.5 msec duration pulse, with a 2.5 msec off-period. The model pulse shape closely approximates the experimentally measured shape of Fig. 3.9. Note that the laser pulse intensity starts to decrease at 2 msec. The simplifying assumption is made that each lasing spectral line has the same temporal dependence as the total power pulse shape of Fig. 3.9. Total laser power is 2.2 W. Results are calculated for a range of power densities,  $W/cm^2$ , corresponding to varying focal diameters. The solution is started from initial conditions for the cell gas in equilibrium at 740K. The calculation is continued until there is no pulse-to-pulse variation in the vibrational state populations. Figs. 3.15 and 3.16 show the predicted first overtone radiative intensities from four vibrational levels,  $v=4$ , 19, 35 and 39. Intensity is calculated from:

$$I_v = (E_v - E_{v-2}) A_{v,v-2} n_v \quad (7)$$

where  $I_v$  is the intensity from vibrational level  $v$ ,  $E_v$  is the energy of this level, and  $A_{v,v-2}$  is the Einstein coefficient. Fig. 3.15 shows these intensities for a power density of  $22.0 W/cm^2$ , and Fig. 3.16 for a lower density of  $2.2 W/cm^2$ . The calculated intensities have been referenced to a common zero and then normalized. It can be seen that at the higher power density, the radiative intensity follows the shape of the excitation laser pulse (Fig. 3.15). The lower power density case, for which the laser excitation rates ( $PL_{i,v}$ ) are much smaller than the V-V rates ( $V-V_{i,v}$ ) for all levels, do not reflect the shape of the pump pulse, and are in reasonable correspondence with the experimental intensities of Fig. 3.10.

### 3.4. Discussion and Conclusions

V-V pumping of vibrational nonequilibrium is generally regarded as a low temperature phenomenon. It is certainly true that some of the most extreme nonequilibrium vibrational population distributions created by this mechanism have been observed in solid and liquid CO [32-34]. Nevertheless, the key criteria for such disequilibrium are [35]:

(a) The translational temperature must be less than the characteristic vibrational temperature of the gas, to ensure that the vibrational exchange mechanism is dominant :  $T < \theta_{\text{char}}$ , where  $\theta_{\text{char}} = h \nu / k$

(b) The vibrational "temperature" parameter  $\theta_1^*$  must be at least a considerable fraction of the characteristic vibrational temperature if there is to be any significant influence of the excited vibrational states:

$$\theta_1^* / \theta_{\text{char}} \approx [\ln(n_0 / n_1)]^{-1} = O[1] \quad (8)$$

(c) The ratio of the vibrational temperature parameter  $\theta_1^*$  to the translational temperature must be considerably greater than 1:  $\theta_1^* / T \gg 1$ .

It can be seen from this that if the vibrational mode energy loading is sufficiently high, pumping will occur even if the translational mode temperature is a sizable fraction of the characteristic vibrational temperature,  $\theta_{\text{char}}$ , which is 3,120K for CO. This is what is occurring in the present experiments. The focused, multiwatt laser excitation powers provide sufficient vibration mode energy loading to create V-V up-pumping even at translational/rotational mode temperatures up to approximately  $\theta_{\text{char}} / 2$ .

A related issue is the rate of the V-V up-pump. The laser is directly coupled only to the lowest vibrational states,  $v \leq 12$ . Indeed, at initiation of the V-V pump, beginning with 300K CO, there is significant energy absorption only into level  $v=1$  and 2. Higher states, up to at least  $v=35$ , are populated by the V-V pumping mechanism. It is important to note that for most of the approach to the steady-state nonequilibrium vibrational population distribution, the dominant rates are relatively near-resonant processes [3]. For such processes, the specific V-V rate constant,  $Q_{jk_{w-1,w}}^{v,v-1}$  (see Appendix) has  $|v - w|$  a small integer. These rates are quite rapid, and increase with increasing vibrational quantum number. Both the long-range and short range processes contribute to the overall rate; the total rates increase rapidly with increasing translational mode temperature. The present specific rate model, as detailed in the Appendix, gives pumping times in good agreement with experimental time-dependent emission measurements to translational temperatures of 750K.

The final feature of the present experiments is the observation of ionization accompanying the production of strongly V-V pumped nonequilibrium distributions. The ionization, although slight, is clearly a consequence of the high-level vibrational excitation of CO. The rapid plasma decay after the laser pulse suggests as we have noted, that a strongly-attaching impurity is present in the cell gases, which is likely to be  $\text{Fe}(\text{CO})_5$ . Further experiments with trapping of this impurity will be conducted; it is probable that with the removal of impurity attachers, the steady-state electron concentration will be much higher than is measured here. We note however, that the present low electron concentrations insure that molecule-electron collision processes cannot have a significant influence on the basic energy transfer processes studied in these experiments.

In conclusion, the high rotational/translational mode temperature at which extreme vibrational disequilibrium can be produced in CO has implications for the chemistry of those plasma reactors using CO and those using  $\text{N}_2$ , which has a characteristic vibrational temperature and long V-T relaxation times similar to CO. Such plasma reactors include both  $\text{CO}_2/\text{H}_2\text{O}$  reactors for  $\text{H}_2$  production [36] and  $\text{N}_2/\text{SiH}_4$  reactors for silicon deposition [37]. Despite the high rotational/translational mode temperature which can exist in such reactors, V-V pumped nonequilibrium processes can control the reaction kinetics.

## **Appendix**

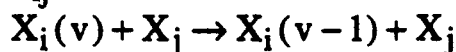
We introduce  $n_{i,v}$  the number density of the primary species  $i$ , in vibrational state  $v$ , in part/cc;  $n_{j,w}$  the number density of the secondary species  $j$  in vibrational state  $w$ , in part/cc;  $n_i = \sum_v n_{i,v}$  the total number density of species  $i$ , in part/cc; and  $n_T = \sum_i n_i$  the total number density of the mixture. In the following, we use the internal energy of molecule  $i$  in vibrational level  $v$  of species  $i$  (in  $\text{cm}^{-1}$ ):  $E_{i,v} = T_{e_i} + \omega_{e_i} \left(v + \frac{1}{2}\right) - \omega_{e_i} x_{e_i} \left(v + \frac{1}{2}\right)^2$  where  $T_{e_i}$  (in  $\text{cm}^{-1}$ ) is the electronic energy, and where  $\omega_{e_i}$  (in  $\text{cm}^{-1}$ ) and  $x_{e_i}$  (dimensionless) are the spectroscopic constants (fundamental vibrational frequency and anharmonicity, respectively) for the molecule  $i$  (see Table 3.3).

### Vibration-translation term:

The VT term of equation (6) is written as

$$VT_{i,v} = \sum_j n_j \{ P_{ij}^{v+1,v} [n_{i,v+1} - \exp(-\Delta E_i^v / kT) n_{i,v}] - P_{ij}^{v,v-1} [n_{i,v} - \exp(-\Delta E_i^{v-1} / kT) n_{i,v-1}] \}$$

where  $P_{ij}^{v,v-1}$  is the rate constant (in cm<sup>3</sup>/s) of the V-T transition:



$X_i(v)$  refers to species  $i$  in vibrational state  $v$ . The rate constant can be expressed as follows [22,52]:

$$P_{ij}^{v,v-1} = P_{ij}^0(T) \cdot \frac{v}{1 - x_{e_i} v} \cdot F_{ij}^{v,v-1} (\lambda_{ij}^{v,v-1})$$

$F$  is a function given by [49]:

$$F(\lambda) = \frac{1}{2} \cdot \left[ 3 - e^{-\frac{2}{3}\lambda} \right] \cdot e^{-\frac{2}{3}\lambda}$$

$$\lambda_{ij}^{v,v-1} = 2^{-\frac{3}{2}} \cdot \sqrt{\frac{\Theta_{ij}}{T}} \cdot \frac{|\Delta E|}{k\Theta_i}$$

$\Delta E$  is the energy difference (in Joules) between the products and the reactants in the V-T transition;

$\Theta_i = hc\omega_{e_i} / k$  is the vibrational characteristic temperature of species  $j$  where  $c$  is the speed of light (in cm.s<sup>-1</sup> in all the appendix);

$\Theta_{ij} = 16\pi^4 \mu_{ij} c^2 \omega_{e_i}^2 l^2 / k$  is in Kelvin [38] where  $\mu_{ij}$  is the reduced mass (in kg) and  $l$  ( $= 0.2 \cdot 10^{-10}$  m) is the range parameter.

In the rate constant expression,  $P_{ij}^0(T)$  is a coefficient which allows fitting to experimental relaxation time data. It is expressed (in cm<sup>3</sup>/s) as :

$$P_{ij}^0(T) = \frac{10^{-7} (1 - x_{e_i}) kT}{\left\{ (\tau_{ij} p) \cdot F_{ij}^{1,0} \cdot \left[ 1 - \exp\left(-\frac{\Theta_i}{T}\right) \right] \right\}}$$

Here  $\tau_{ij} p$  is the vibrational relaxation time in atm.μs ( $10^{-7}$  J s cm<sup>-3</sup>) and is given by:

$$\ln(\tau_{ij} p) = A_{ij} + B_{ij} T^{-\frac{1}{3}} + C_{ij} T^{-\frac{2}{3}}$$

$A_{ij}$ ,  $B_{ij}$ ,  $C_{ij}$  are chosen in order to fit the experimental data (see Table 1).

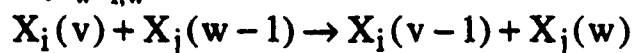


### Vibration-vibration term:

The VV term, including only the single quantum transitions, is written as:

$$VV_{i,v} = \sum_j \sum_{w=0}^w \{ Q_{ij,w,w+1}^{v+1,v} [n_{i,v+1} n_{j,w} - \exp(-\Delta E_{ij}^{v,w} / kT) n_{i,v} n_{j,w+1}] \\ - Q_{ij,w,w+1}^{v,v-1} [n_{i,v} n_{j,w} - \exp(-\Delta E_{ij}^{v-1,w} / kT) n_{i,v-1} n_{j,w+1}] \}$$

where  $Q_{jk,w-1,w}^{v,v-1}$  is the rate constant (in cm<sup>3</sup>/s) of the V-V transition:



The rate constant is the sum of two terms, the first being the contribution of the short-range interactions, and the second the contributions of the long-range forces due to dipole-dipole interaction. The rate is expressed as [2]:

$$Q_{ij,w-1,w}^{v,v-1} = Z_{ij} \left[ S_{ij,w-1,w}^{v,v-1} + L_{ij,w-1,w}^{v,v-1} \right] e^{-\frac{\Delta E}{2kT}} \\ Z_{ij} = 400 \sigma_{ij}^2 \sqrt{\frac{\pi kT}{2\mu_{ij}}}$$

where  $Z_{ij}$  is the collision number in cm<sup>3</sup>/s and  $\pi\sigma_{ij}^2$  is the cross section in cm<sup>2</sup> (see Table 3.3).

The dimensionless short-range contribution is given by [38]:

$$S_{ij,w-1,w}^{v,v-1} = S_{ij}^0 T \frac{v}{1-x_{ei}v} \frac{w}{1-x_{ej}w} F_{ij,w-1,w}^{v,v-1} \left( \lambda_{ij,w,w-1}^{v,v-1} \right)$$

$F(\lambda)$ ,  $\lambda$ , and  $\Delta E$  have the same definitions as above.

The dimensionless long-range contribution is given by [39]:

$$L_{ij,w-1,w}^{v,v-1} = \frac{L_{ij}^0}{T} \left( \frac{g_i^{v,v-1}}{g_i^{1,0}} \right)^2 \left( \frac{g_j^{w-1,w}}{g_j^{1,0}} \right)^2 \exp \left( -\frac{\Delta E^2}{k^2 b_{ij} T} \right)$$

$S_{ij}^0$  (in K<sup>-1</sup>),  $L_{ij}^0$  (in K) and  $b_{ij}$  (in K) are empirical parameters matched to experimental data (see Table 1) and:

$$\left( \frac{g_i^{v,v-1}}{g_i^{1,0}} \right)^2 = \left[ \frac{a_i + 1}{a_i + 3 - 2v} \right]^2 \left[ \frac{v(a_i + 2 - 2v)(a_i + 4 - 2v)}{a_i(a_i + 3 - v)} \right]$$

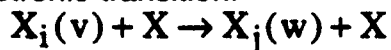
where  $a_i = 1/x_{ei}$

### Vibration-electronic term:

The collision-induced V-E terms are retained only here:

$$VE_{i,v} = n_T \sum_{j \neq i} \sum_{w=0}^{w_{\max}} S_{ij}^{v,w} \left\{ n_{j,w} + n_{i,v} \exp \left[ -hc(E_{j,w} - E_{i,v}) / kT \right] \right\}$$

where  $S_{ij}^{v_i, v_j}$  is the rate constant (in  $\text{cm}^3/\text{s}$ ) for the collision induced vibration-to-electronic transition:



$X_i(v)$  and  $X_j(w)$  are two electronic manifolds of the same species. Their vibrational states are  $v$  and  $w$  respectively. It is assumed that collisions can induce the transition from  $X_i(v)$  to  $X_j(w)$  when the energy of these molecules are very close. The rate constant is modeled with a Gaussian function of the energy defect; the width and the maximum of the Gaussian rate are empirical parameters.

$$S_{ij}^{v,w} = S_{VE}^0 \cdot \exp \left( - \left( \frac{\Delta E}{C_{VE} hc \omega_e} \right)^2 \right) \cdot \exp \left( - \frac{\Delta E}{2kT} \right)$$

The vibrational spectroscopic constant,  $\omega_e$ , is taken to be the larger of the constants for the two electronic states involved. The adjustable parameters are  $S_{VE}^0$  (in  $\text{cm}^3/\text{s}$ ) and  $C_{VE}$  (dimensionless). In the case of  $\text{CO}(X^1\Sigma) \rightarrow \text{CO}(A^1\Pi)$  transfer, values of these parameters were obtained by fitting kinetic rate models to V-V up-pumping experiments in optical cells [2-4]. The range of validity of the resonance model above remains to be determined, in detailed state-resolved experiments. The value of these parameters are indicated in Table 1.

### Spontaneous radiative decay term:

The spontaneous radiative transfer term is written as:

$$\text{SRD}_{i,v} = \text{SRVD}_{i,v} + \text{SRED}_{i,v}$$

where

$$\text{SRVD}_{i,v} = \sum_{u=1}^{u^*} \left[ A_i^{v+u,v} n_{i,v+u} - A_i^{v,v-u} n_{i,v} \right]$$

is the radiative transition between vibrational levels with the same electronic state, using the Einstein coefficient [40]:

$$\frac{A_i^{v,v-u}}{A_i^{1,0}} = \frac{1}{(a_i - 2)(a_i - 3)} u \frac{v!}{(v-u)!} \frac{b_v(b_v + u)(b_v + 2u)}{\prod_{q=0}^{u-1} (b_v - v + q)}$$

with  $b_v = a_v - 2v - 1$ , and  $u^*$ ,  $A_i^{1,0}$  (in 1/s) given in Table 1;  
and where:

$$SRED_{CO(X^1\Sigma),v} = \sum_{w=w_{\min}}^{w=w_{\max}} A_{CO(A^1\Pi),CO(X^1\Sigma)}^{w,v} n_{CO(A^1\Pi),w}$$

and

$$SRED_{CO(A^1\Pi),v} = -n_{CO(A^1\Pi),v} \sum_{w=w_{\min}}^{w=w_{\max}} A_{CO(A^1\Pi),CO(X^1\Sigma)}^{v,w}$$

using the Frank-Condon factors  $A^{v,w}$  (in 1/s) given in Table 2.

#### Stimulated emission/absorption term:

The stimulated emission/absorption term is written [4]:

$$PL_{i \neq CO(X^1\Sigma^+),v} = 0$$

$$PL_{CO(X^1\Sigma^+),v} = [T_{v+1,v} n_{i,v+1} - T_{v,v+1} n_{i,v}] - [T_{v,v-1} n_{i,v} - T_{v-1,v} n_{i,v-1}]$$

where  $T_{v+1,v}$  and  $T_{v,v+1}$  are the rate constant (in 1/s) of the PL term [24]:

$$T_{v+1,v} = \frac{1}{8\pi kT} \left( \frac{c}{v_{v+1,v}} \right)^3 A_{v+1,v} B_{v+1} \sum_{j_1}^{j_2} I_{v_j}(t) * \left[ \sum_{j=0}^{j_{\max}} (J+1) Q_{nl}^P(v_j) \exp\left(-\frac{hc}{kT} F_{J,v+1}\right) + \sum_{j=1}^{j_{\max}} J Q_{nl}^R(v_j) \exp\left(-\frac{hc}{kT} F_{J,v+1}\right) \right]$$

$$T_{v,v+1} = \frac{1}{8\pi kT} \left( \frac{c}{v_{v+1,v}} \right)^3 A_{v+1,v} B_v \sum_{j_1}^{j_2} I_{v_j}(t) * \left[ \sum_{j=0}^{j_{\max}} (J+1) Q_{nl}^P(v_j) \exp\left(-\frac{hc}{kT} F_{J+1,v}\right) + \sum_{j=1}^{j_{\max}} J Q_{nl}^R(v_j) \exp\left(-\frac{hc}{kT} F_{J-1,v}\right) \right]$$

and  $v_{v+1,v} = c(E_{i,v+1} - E_{i,v})$  (in 1/s) is the band center frequency,  $I_{v_j}(t)$  is the pulse height (in W/cm<sup>2</sup>),  $B_v = B_e - \alpha_e(v + 1/2) + \gamma_e(v + 1/2)^2$  (in 1/cm) is the vibrational constant, and the Lorentzian line shape factor is written (in s) [55]:

$$Q_{nl}^{P,R}(v_j) = \frac{1}{\pi} \frac{\Delta v_c}{2} \left( (v_j - v_{nl}^{P,R})^2 + (\Delta v_c/2)^2 \right)^{-1}$$

where  $\Delta v_c = 10^2 \sum_k n_k d_{CO,k}^2 \sqrt{8kT/\pi \mu_{CO,k}}$  (in 1/s) is the pressure-broadened line width,  $d_{CO,k}$  being the optical collision diameter (in cm) and where  $v_{nl}^{P,R} = v_{v+1,v}^{P,R}(J) = v_{v+1,v} + c[F_{J,v+1} - F_{J\pm 1,v}]$  (in 1/s) is the center of the absorbing line, with  $F_{J,v} = B_v J(J+1) - D_v (J(J+1))^2$  the rotational-vibrational contribution (in 1/cm) and  $D_v = D_e + \beta_e (v+1/2)$  the rotational constant (in 1/cm).

All the different parameters are given in Table 3.3.

### **References:**

- [1] J. W. Rich and R. C. Bergman, Chem. Phys. 44 (1979) 53.
- [2] R. L. Deleon and J. W. Rich, Chem. Phys. 107 (1986) 283.
- [3] W. Urban, J.-X. Lin, V. V. Subramaniam, M. Havenith and J. W. Rich, Chem. Phys. 130 (1989) 389.
- [4] H. Dünwald, E. Siegel, W. Urban, J. W. Rich, G. F. Homicz, and M. J. Williams, Chem. Phys. 94 (1985) 195.
- [5] P. Brechignac and J.-P. Martin, IEEE J. Quantum Electron., QE-12, 2 (1976) 80.
- [6] N. Djeu, Appl. Phys. Lett., 23, 6 (1973) 309.
- [7] M. A. Gutin and A. P. Kolchenko, Sov. J. Quantum Electron, 18, 1 (1988).
- [8] J. Puerta, W. Hermann, G. Bourauel and W. Urban, Appl. Phys., 19 (1979), 439.
- [9] E. Samimy, Optimization of Short Wavelength Operation in the Carbon Monoxide Laser, MS Thesis, Mechanical Engineering Department, The Ohio State University, (1989).
- [10] J. W. Rich, R. C. Bergman, and J. A. Lordi, AIAA Journal, V13, 1 (1975) 95-101.
- [11] R. C. Bergman, G. F. Homicz, J. W. Rich and G. L. Wolk, J. Chem. Phys. 78 (1983) 1281.
- [12] G. L. Wolk and J. W. Rich, J. Chem. Phys. 79 (1983) 12.

- [13] D. B. Cohn, C. G. Parazzoli, D. G. Beck and F. N. Mastrup, *IEEE Quantum Electron*, QE-22, 5 (1986) 723.
- [14] R. Farrenq, C. Rossetti, G. Guelachvilli and W. Urban, *Chem. Phys.* 92 (1985) 389.
- [15] C. E. Little, *The Interaction of Stimulated Emission and Gain Medium in the CO laser*, PhD Dissertation, School of Mathematics and Physics, Macquaire University, North Ryde, N. S. W., Australia (1987).
- [16] K. P. Horn and P. E. Oettinger, *J. Chem. Phys.*, 54 (1971) 3040.
- [17] G. Guelachvilli, D. De Villeneuve, R. Farrenq, W. Urban and J. Verges, *J. Mol. Spec.*, 98 (1983) 64.
- [18] C. Chackerian, Jr. and R. M. Tipping, *J. Mol. Spec.* 99 (1983) 431.
- [19] G. H. Golub and V. Pereyra, *SIAM, J. Numer. Anal.* 10 (1973).
- [20] S. De Benedictis, R. D'Agostino and F. Cramarossa, *Chem. Phys.*, 71 (1982) 247.
- [21] L. S. Polak, I. A. Sergeev and D. I. Slovetsky, *Templofiz. Vysok. Temp.*, 15 (1977) 15.
- [22] E. M. McDaniel, *Collision Phenomena in Ionized Gases*, John Wiley & Sons, Inc., New York-London-Sydney (1964).
- [23] O. V. Achasov, N. A. Fomin, D. S. Ragozin, R. I. Soloukhin and S. A. Zhdanok, *Revue Phys. Appl.* 17 (1982) 15.
- [24] R. E. Center, *J. Appl. Phys.*, 44 (1973) 3538.
- [25] H. T. Powell, *J. Chem. Phys.* 63 (1975) 2635.
- [26] A. C. Hindmarsh, *ACM SIGNUM Newsletter*, 15 (1980) 10.
- [27] E. S. Oran and J. P. Boris, eds, *Numerical Simulation of Reactive Flow*, Elsevier Science Publishing Co., N. Y. (1987).
- [28] W. Q. Jeffers and J. D. Kelley, *J. Chem. Phys.*, 55 (1971) 4533.
- [29] J. Keck and G. Carrier, *J. Chem. Phys.* 43 (1965) 2284.
- [30] K. N. C. Bray, *J. Phys.*, B1, (1968) 705.
- [31] K. P. Huber and G. Herzberg, "Molecular Spectra and Molecular Structure," V4 : "Constants of Diatomic Molecules", Van Nostrand Reinhold Co., New York 1978.
- [32] N. Legay-Sommaire and F. Legay, *IEEE J. Quantum Electron*, QE-16, (1980) 308.
- [33] J. P. Galaup, J. Y. Harbec, R. Chameau, and H. Dubost, *Chem. Phys. Lett.* 120 (1985) 188.
- [34] D. S. Anex and G. E. Ewing, *J. Phys. Chem.* 90 (1986) 1604.

[35] J. W. Rich, *Relaxation of Molecules Exchanging Vibrational Energy*, Chap.4 in E. W. McDaniel and W. L. Nighan, *Applied Atomic Collision Physics*, Vol.3, Gas Lasers, Academic Press, N. Y. (1982).

▪ [[36] V. D. Rusanov, A. A. Fridman, and G. V. Sholin, *Sov. Phys. Usp.*, 24 (1981) 447.

▼ [37] C. A. DeJoseph, Jr, *Reactions of Silane in Active Nitrogen*, Dissertation, University of Oklahoma, Norman, OK (1989).

[38] R. N. Schwartz and K. F. Herzfeld, *J. Chem. Phys.* 22 (1954) 767.

[39] R. D. Sharma and C. A. Brau, *J. Chem. Phys.* 51 (1969) 924.

[40] H. S. Heaps and G. Herzberg, *Z. Physik* 133 (1953) 49.

[41] S. S. Penner, *Quantitative Molecular Spectroscopy and Gas Emissivities*, Addison-Wesley Pub. Co., Inc. (1959).

## **List of Figures**

- 3.1. Schematic of experimental apparatus used at Ohio-State. The CO/Ar gas mixture in the absorption cell (7) is optically pumped by the radiation of a CO laser (11) and the emission spectra of the gas are analysed with an UV/visible (14) and an infrared monochromator (4). The laser pulse is monitored by means of a fast pyroelectric detector (6).
- 3.2. CO multiple-line laser spectrum, Centrale Paris, 27 W c.w. conditions, intensity in arbitrary units.
- 3.3. Absorption cell schematics
- a. Ohio State
  - b. Centrale Paris
- 3.4. CO potential energy diagram. Shown are the main energy transfer processes between the vibrational levels of the  $X^1\Sigma$  ground state, the first excited singlet state  $A^1\Pi$  and the lowest triplet state  $a^3\Pi$ .
- 3.5. C<sub>2</sub> Swan bands,  $d^3\Pi_g \rightarrow a^3\Pi_u$ ,  $\Delta v=0$  Sequence, OSU experiment
- 3.6. Determination of Rotational Temperature from  $\Delta v=0$  C<sub>2</sub> Swan Band Component Intensities
- 3.7. Theoretical and experimental CO 1st overtone emission on selected bands at an inferred rotational temperature  $T=1500K$ , Centrale Paris Experiment. Predicted decrease in transmission by water vapor at 300 K is also shown.
- 3.8. C<sub>2</sub> Swan Bands,  $d^3\Pi_g \rightarrow a^3\Pi_u$ ,  $\Delta v=0, -1, -2$  Sequences, Centrale Paris Experiment
- 3.9. Q-Switched laser pulse oscillograms
- a. Laser pulse shape observed with the fast pyroelectric detector.
  - b. Enlarged initial position of the laser pulse and 15  $\mu s$  gate signal.
- 3.10. Time dependence of the first overtone emission (intensity normalized) after pulsed excitation for selected wavelengths, laser pulse duration of 2.5 ms.
- 3.11. 1st overtone spectra for selected CO concentrations. Shown are all bands from  $v=2-0$  to approximately  $v=40-38$  (2.3-4.4  $\mu m$ ). The rotational structure is not resolved. The amplifier gain for curve No.2 is twice that of curves 1,3, and 4.
- 3.12. Measured current in the absorption cell vs. applied electric field  $E$  over total cell pressure  $P$ . The cell pressure was varied from 60 to 500 Torr at a CO/Ar concentration ratio of 4/69.

**3.13. Time dependence of the current and the overtone emission after pulsed laser excitation:**

**a. Laser pulse shape (L) and Current response (C).**

**b. Laser pulse shape (L) and subsequent overtone emission on  $v=22-20$ .**

**3.14. Kinetic modeling calculation: predicted steady state vibrational population densities of the V-V pumped CO for two different focal diameters (power densities) of the laser beam, for  $T=1500$  K**

**3.15. Kinetic modeling calculation: predicted time-dependent 1st overtone radiative intensities after pulse excitation (0-2.5 ms); laser power density =  $22 \text{ W/cm}^2$**

**3.16. Kinetic modeling calculation: predicted time-dependent 1st overtone radiative intensities after pulse excitation (0-2.5 ms); laser power density =  $2.2 \text{ W/cm}^2$**



**Table 3.1: Parameters used in the VV, VT, VE and SRD rate models**

species\VT	A <sub>jk</sub>	B <sub>jk</sub>	C <sub>jk</sub>	$\Theta_{jk} / \Theta_j^2$ (K <sup>-1</sup> )
CO-CO	-15.23	280.5	-549.6	45.6E-02
CO-Ar	10.38	0.0	0.0	1.335E-03
species\VV	S <sub>jk</sub> <sup>o</sup> (K <sup>-1</sup> )	L <sub>jk</sub> <sup>o</sup> (K)	b <sub>jk</sub> (K)	$\Theta_{jk} / \Theta_j^2$ (K <sup>-1</sup> )
CO-CO	1.64E-06	1.6142	40.36	45.6E-02
species\VE	C <sub>VE</sub>	SVE <sup>o</sup> (cm <sup>3</sup> /s)		
CO-CO	5.49E-02	9.94E-13		
species\SRD	u*	A 10 (1/s)		
CO	4	30.3		

**Table 3.2: Spontaneous electronic radiative transfer  
Frank Condon factors (1/s)**

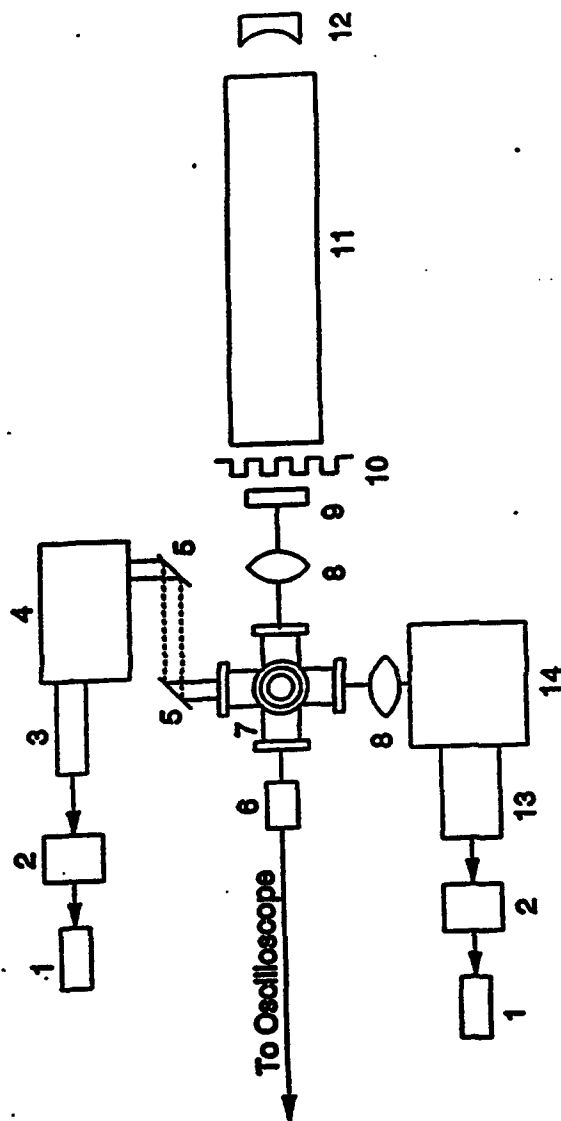
v \ w	0	1	2	3	4	5	6
0	1.387E+08	2.775E+08	3.062E+08	2.484E+08	1.664E+08	9.785E+08	5.24
1	2.785E+08	1.624E+08	8.263E+06	3.789E+07	1.361E+08	1.867E+08	1.74
2	2.648E+08	8.511E+05	1.097E+08	1.288E+08	2.942E+07	4.349E+06	6.37
3	1.586E+08	8.077E+07	1.045E+08	1.161E+05	7.815E+07	1.047E+08	3.77
4	6.717E+08	1.625E+08	1.289E+06	9.435E+07	5.513E+07	1.691E+06	6.41
5	2.142E+07	1.314E+08	5.637E+07	6.175E+07	1.286E+07	8.476E+07	3.05
6	5.348E+06	6.514E+07	1.224E+08	2.202E+05	8.478E+07	1.072E+07	3.29
7	1.075E+06	2.277E+07	1.019E+08	5.733E+07	2.837E+07	3.649E+07	5.48

**Table 3.3: spectroscopic constants and PL rate parameters**

<b>species</b>	<b>spectroscopic constants (in 1/cm except v)</b>
CO(X <sup>1</sup> Σ <sup>+</sup> )	$v_{\max}=55$ , $\omega_e=2169.8$ , $\omega_e x_e=13.288$ , $T_e=0.0$
CO(A <sup>1</sup> Π)	$v_{\max}=10$ , $\omega_e=1518.24$ , $\omega_e x_e=19.4$ , $T_e=6.5E+4$
<b>species</b>	<b>PL rate parameters (in 1/cm except d)</b>
CO(X <sup>1</sup> Σ <sup>+</sup> )	$\omega_e y_e=1.0511E-2$ , $\omega_e z_e=5.74E-5$ , $\omega_e a_e=9.83E-7$ , $\omega_e b_e=3.166E-8$ , $B_e=1.9313$ , $\alpha_e=1.75E-2$ , $\gamma_e=5.487E-2$ , $D_e=6.12E-6$ , $\beta_e=-9.66E-10$ , $d_{\text{CO-CO}}=5.119E-8$ cm, $d_{\text{CO-Ar}}=5.0E-8$ cm, $\sigma_{\text{CO-CO}}=3.75E-8$ cm

**Table 3.4: output of the CO laser**

frequency lines		% of power
Vibrational number	rotational number	
V(2-1)	P15	4.8
	P16	3.3
V(3-2)	P14	5.2
	P15	5.9
V(4-3)	P13	3.4
	P14	9.3
	P15	1.0
V(5-4)	P13	16.5
	P14	4.6
V(6-5)	P12	14.8
	P14	3.4
V(7-6)	P11	2.1
	P12	10.5
	P13	5.2
V(8-7)	P10	0.6
	P12	3.5
V(9-8)	P10	0.4
	P11	2.5
V(10-9)	P9	1.5
V(11-10)	P8	0.3
	P9	0.7
V(12-10)	P10	0.5



1. Dual Channel Chart Recorder, Kipp and Zonen Model BD41
2. Stanford Research Systems SR510 Lock-In Amplifier or SR250 Gated Integrator & Boxcar Averager.
3. IR photovoltaic InSb Detector, EG&G Judson #J10D-M204-R01M-60
4. Infrared .34m Spectrometer, Spex Model 340E
5. Mirror
6. Molelectron P5-00 Ultra-Fast Pyroelectric Detector
7. Absorption Cell, Varian Corp. Six Arm Cross
8. Lens
9. 97.5% Output Coupler
10. SR540 Optical Chopper, 50/50, 200Hz
11. CO Laser Cavity
12. Total Reflector
13. Blakkall Photomultiplier Tube, Thorn EMI Gencom Model 9635-QB
14. UV/Visible .5m Spectrometer, Spex Industries, Inc. Model 1870

Figure 3.1. Schematic of experimental apparatus used at Ohio-State. The CO/Ar gas mixture in the absorption cell (7) is optically pumped by the radiation of a CO laser (11) and the emission spectra of the gas are analysed with an UV/visible (14) and an infrared monochromator (4). The laser pulse is monitored by means of a fast pyroelectric detector (6).

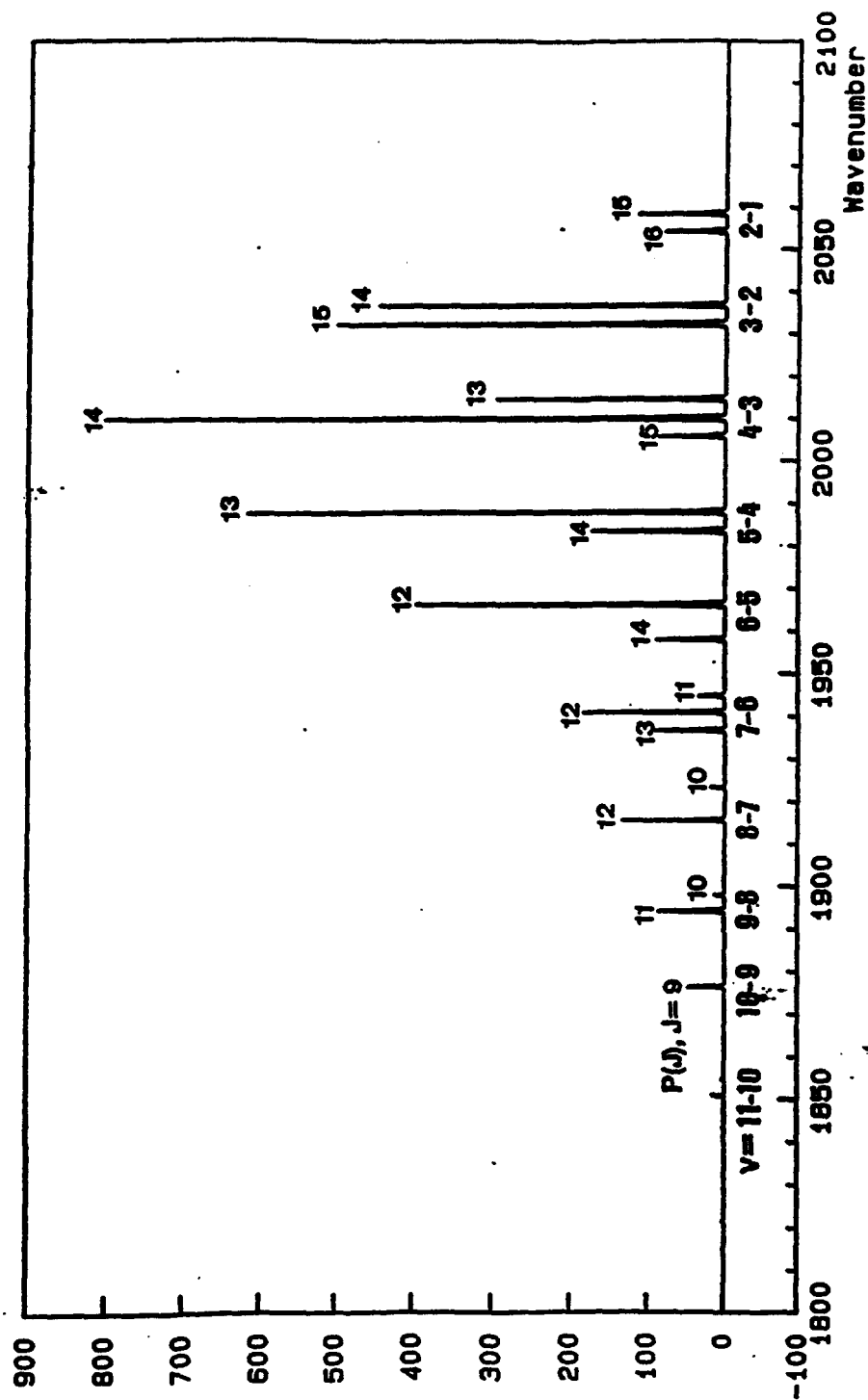
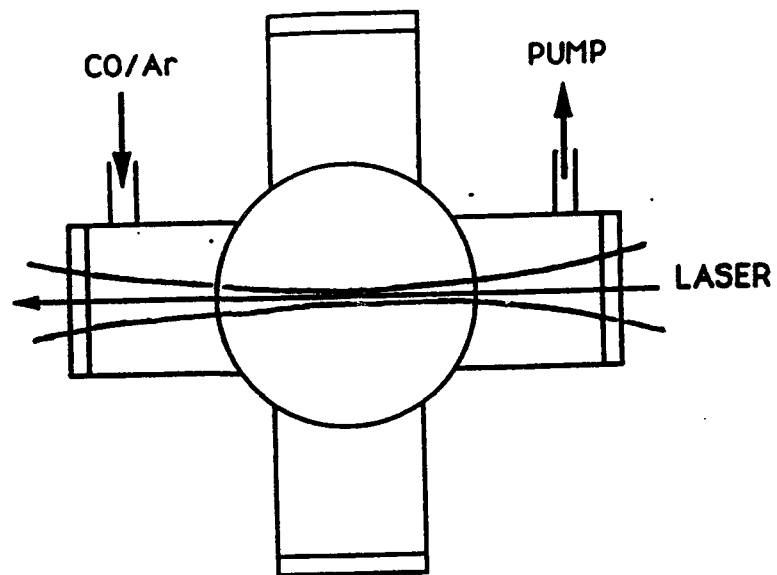
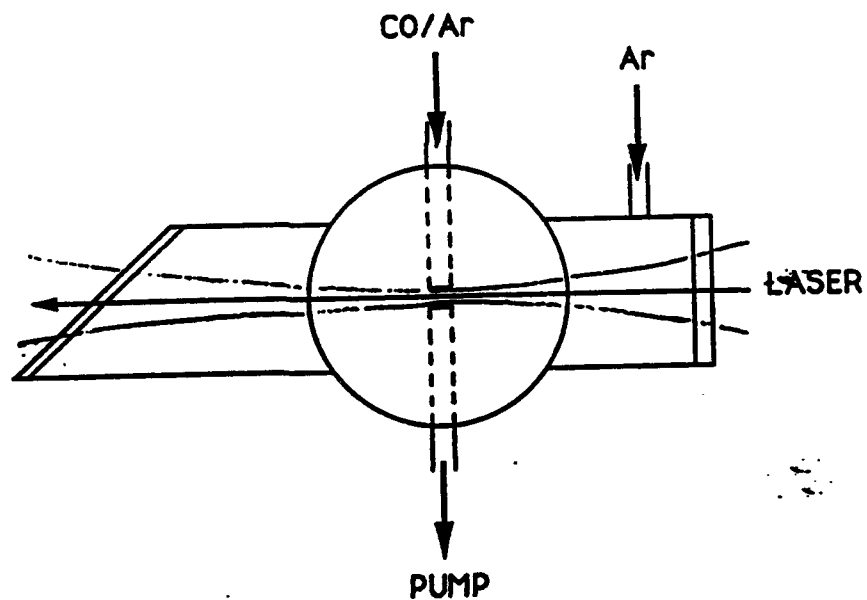


Figure 3.2. CO multiple-line laser spectrum, Centrale Paris, 27 W c.w. conditions, intensity in arbitrary units.



**a) Ohio State cell**



**b) Centrale Paris cell**

**Figure 3.3. Absorption cell schematics**

**a. Ohio State**

**b. Centrale Paris**

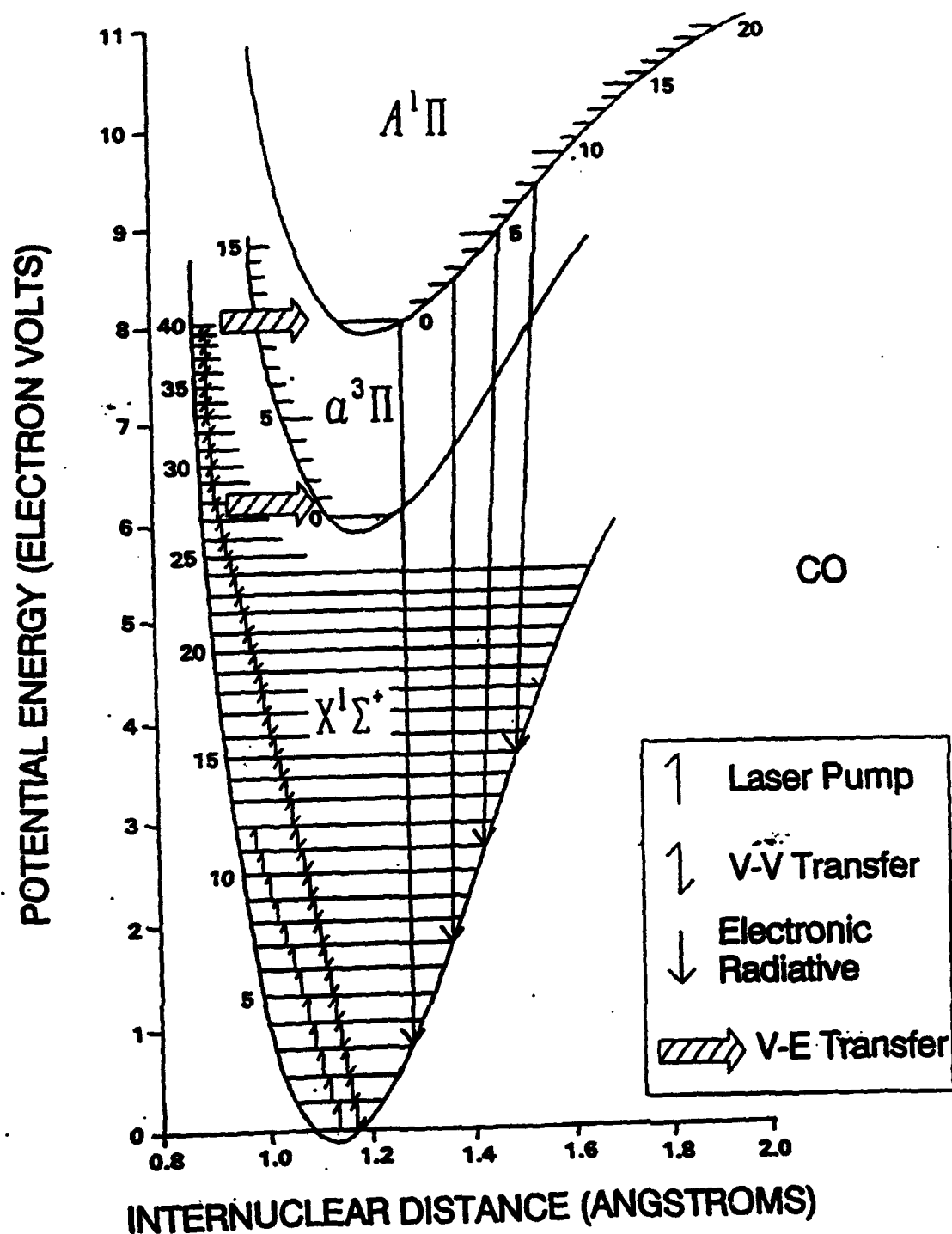


Figure 3.4. CO potential energy diagram. Shown are the main energy transfer processes between the vibrational levels of the  $X^1\Sigma$  ground state, the first excited singlet state  $A^1\Pi$  and the lowest triplet state  $a^3\Pi$ .



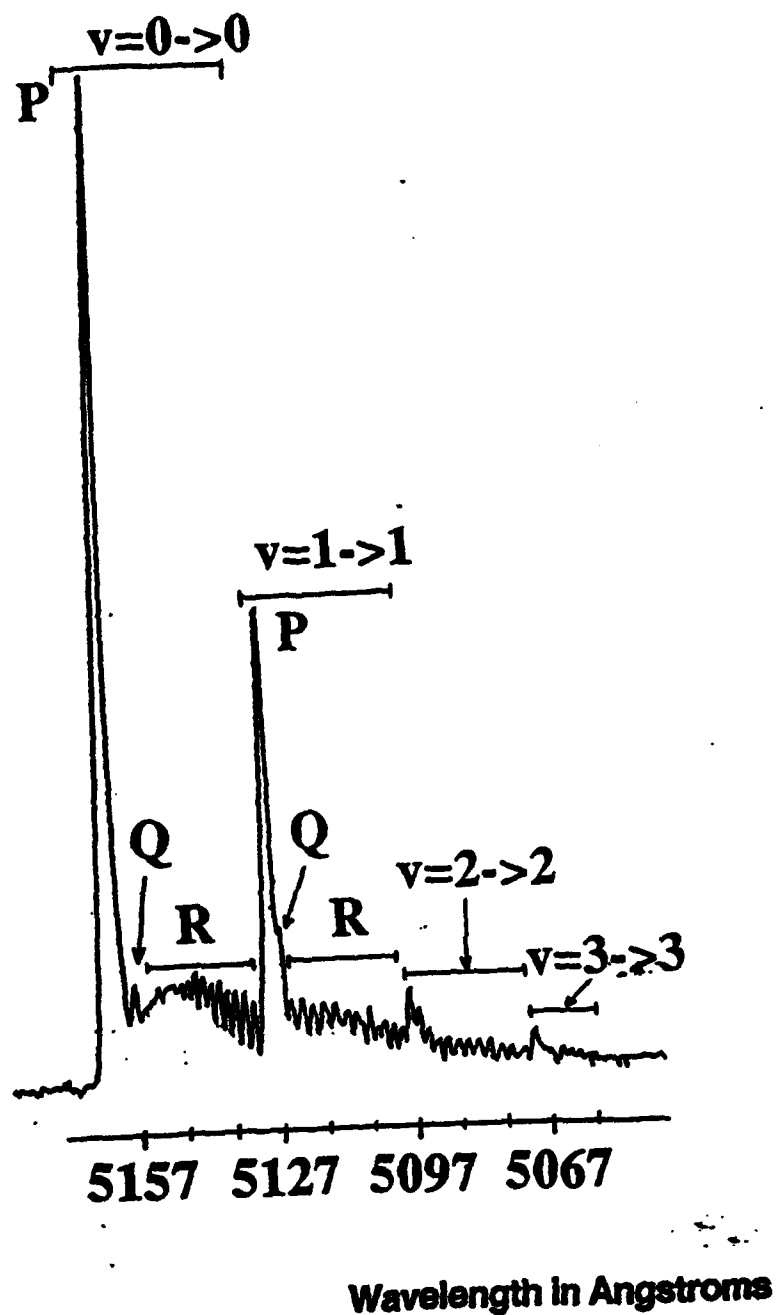


Figure 3.5. C<sub>2</sub> Swan bands,  $d^3\Pi_g \rightarrow a^3\Pi_u$ ,  $\Delta v=0$  Sequence, OSU experiment

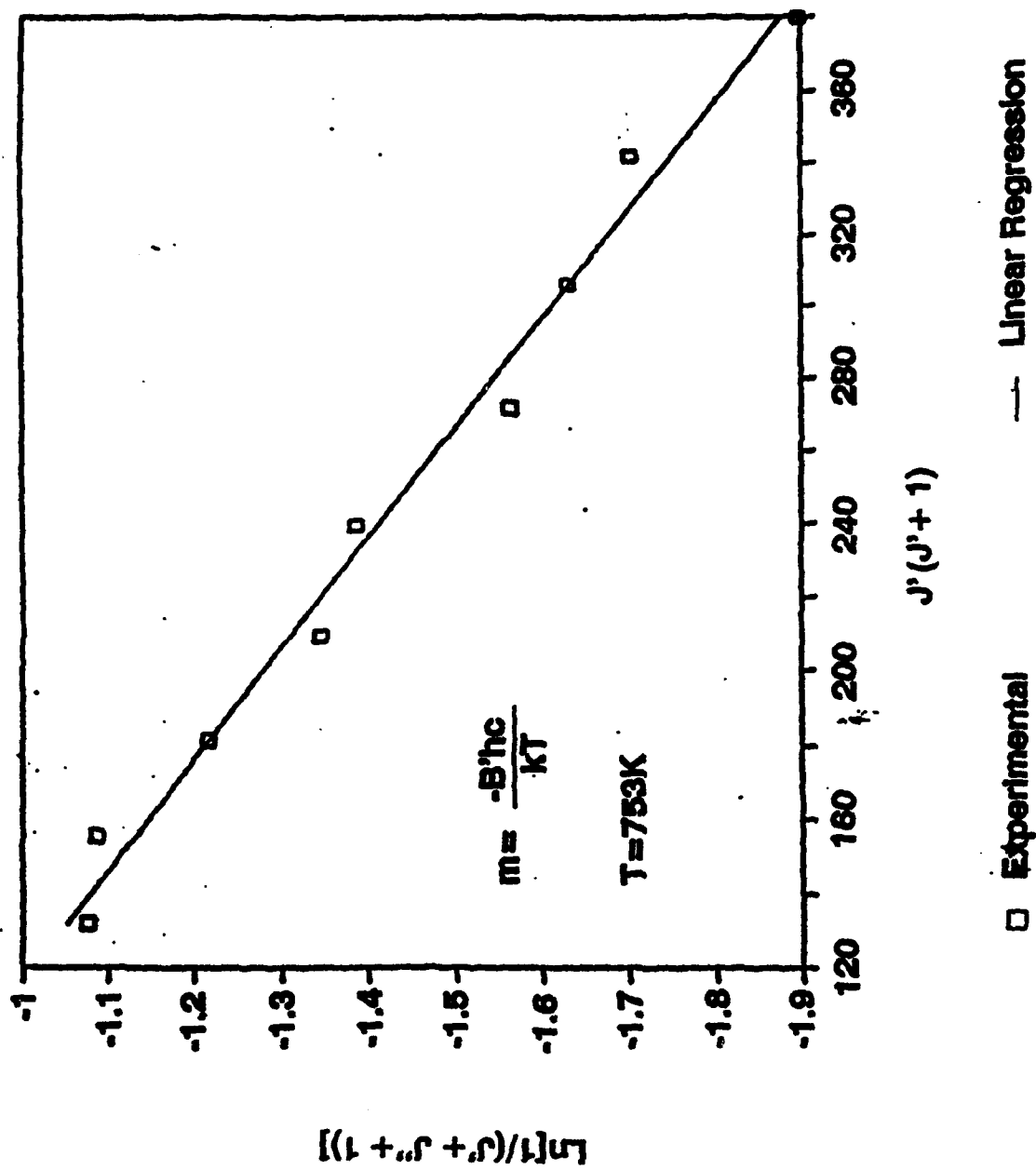


Figure 3.6. Determination of Rotational Temperature from  $\Delta v=0$  C<sub>2</sub> Swan Band Component Intensities

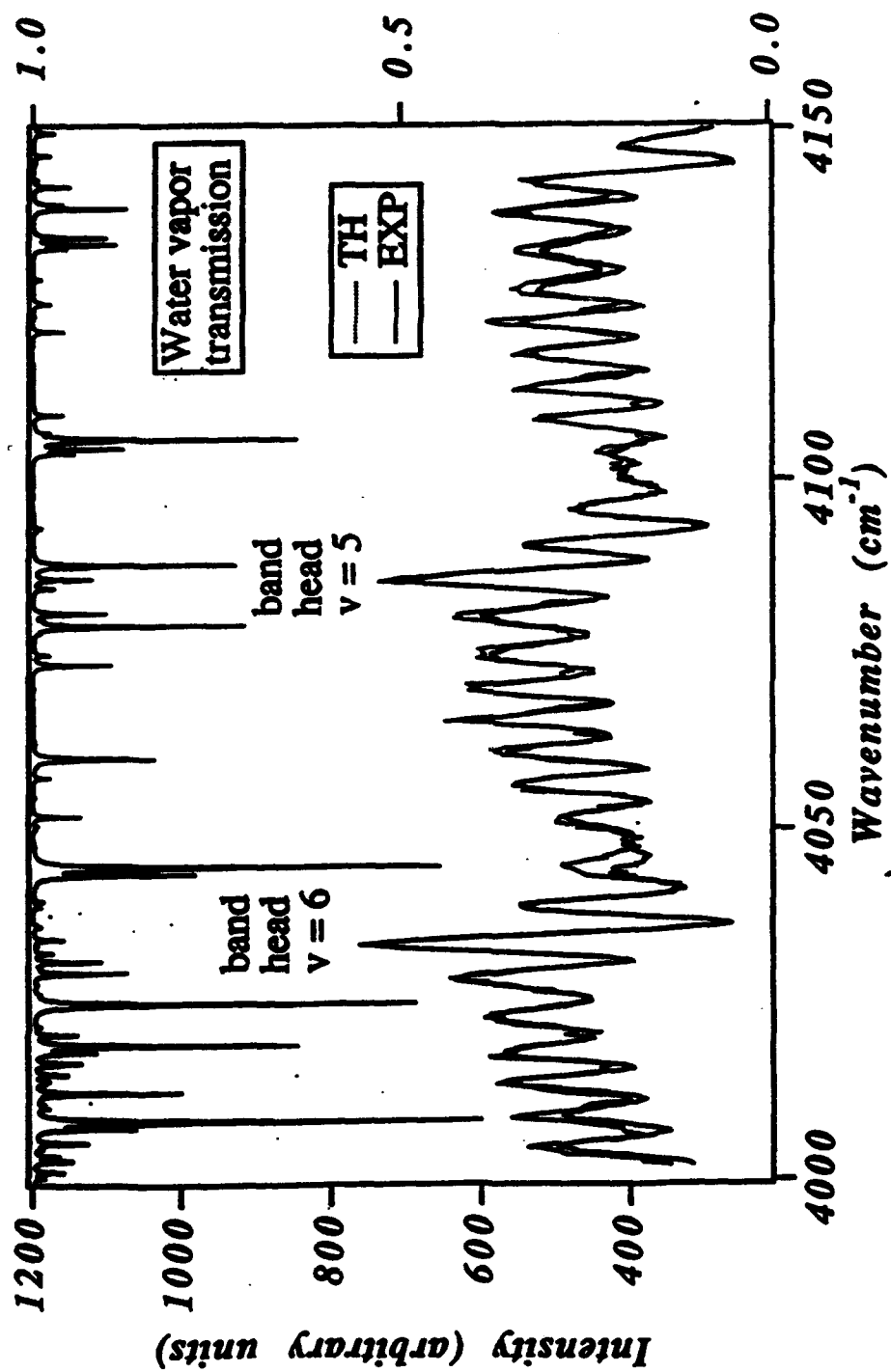


Figure 3.7. Theoretical and experimental CO 1st overtone emission on selected bands at an inferred rotational temperature  $T=1500\text{K}$ , Centrale Paris Experiment. Predicted decrease in transmission by water vapor at  $300\text{K}$  is also shown.

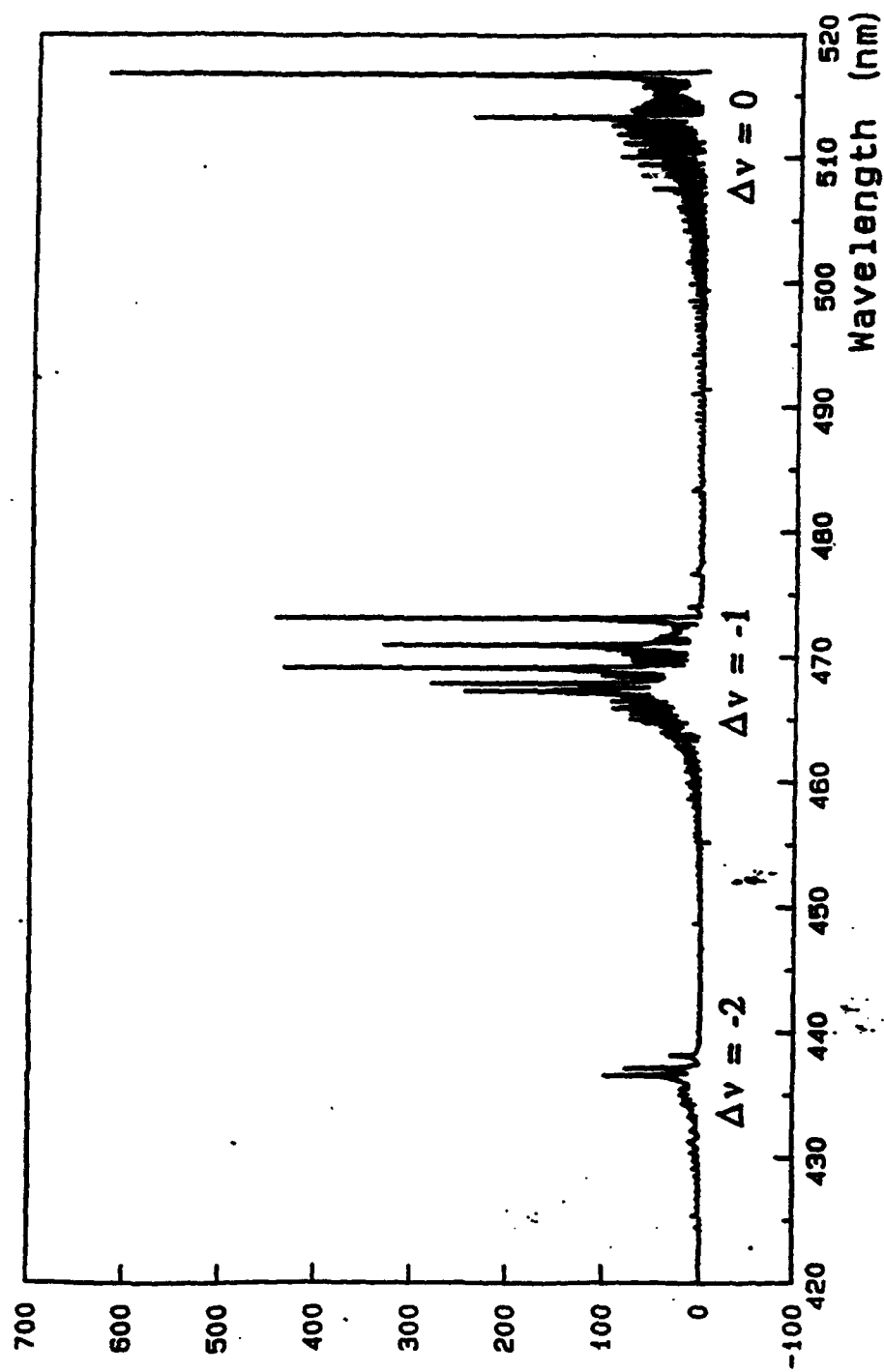
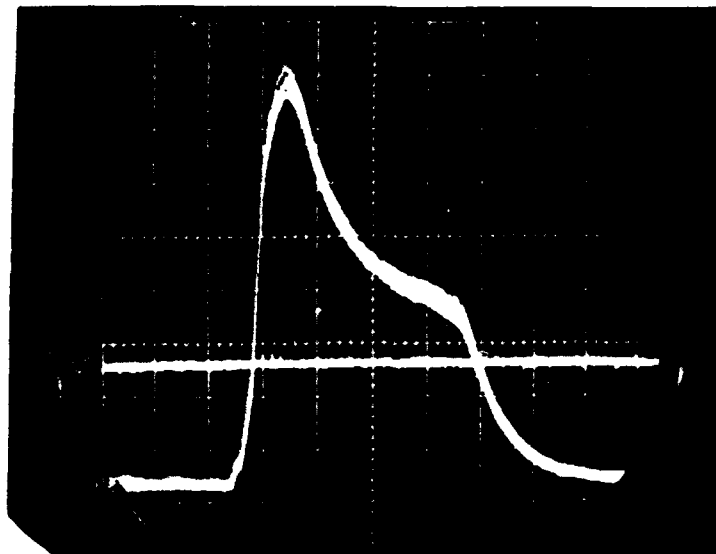
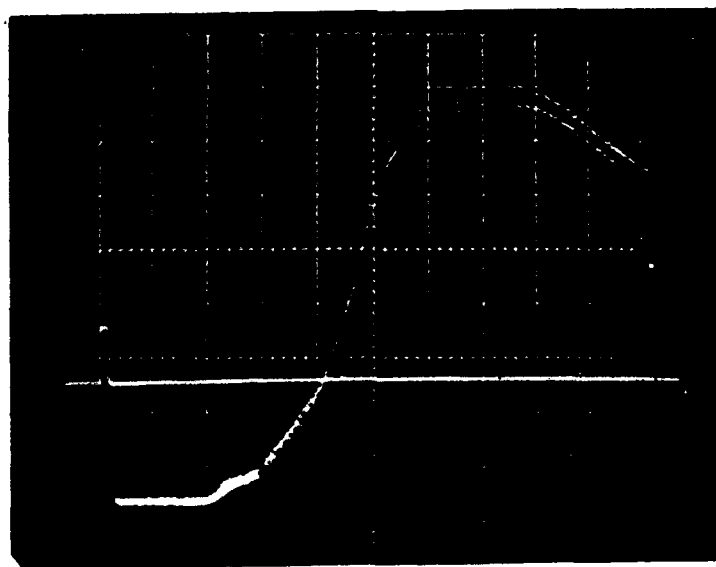


Figure 3.8. C2 Swan Bands,  $d^3\Pi_g \rightarrow a^3\Pi_u$ ,  $\Delta v=0, -1, -2$  Sequences, Centrale Paris Experiment



**a) 0.5 msec/div**



**b) 0.1 msec/div**

**Figure 3.9. Q-Switched laser pulse oscillograms**

- a. Laser pulse shape observed with the fast pyroelectric detector.
- b. Enlarged initial position of the laser pulse and 15  $\mu$ s gate signal.

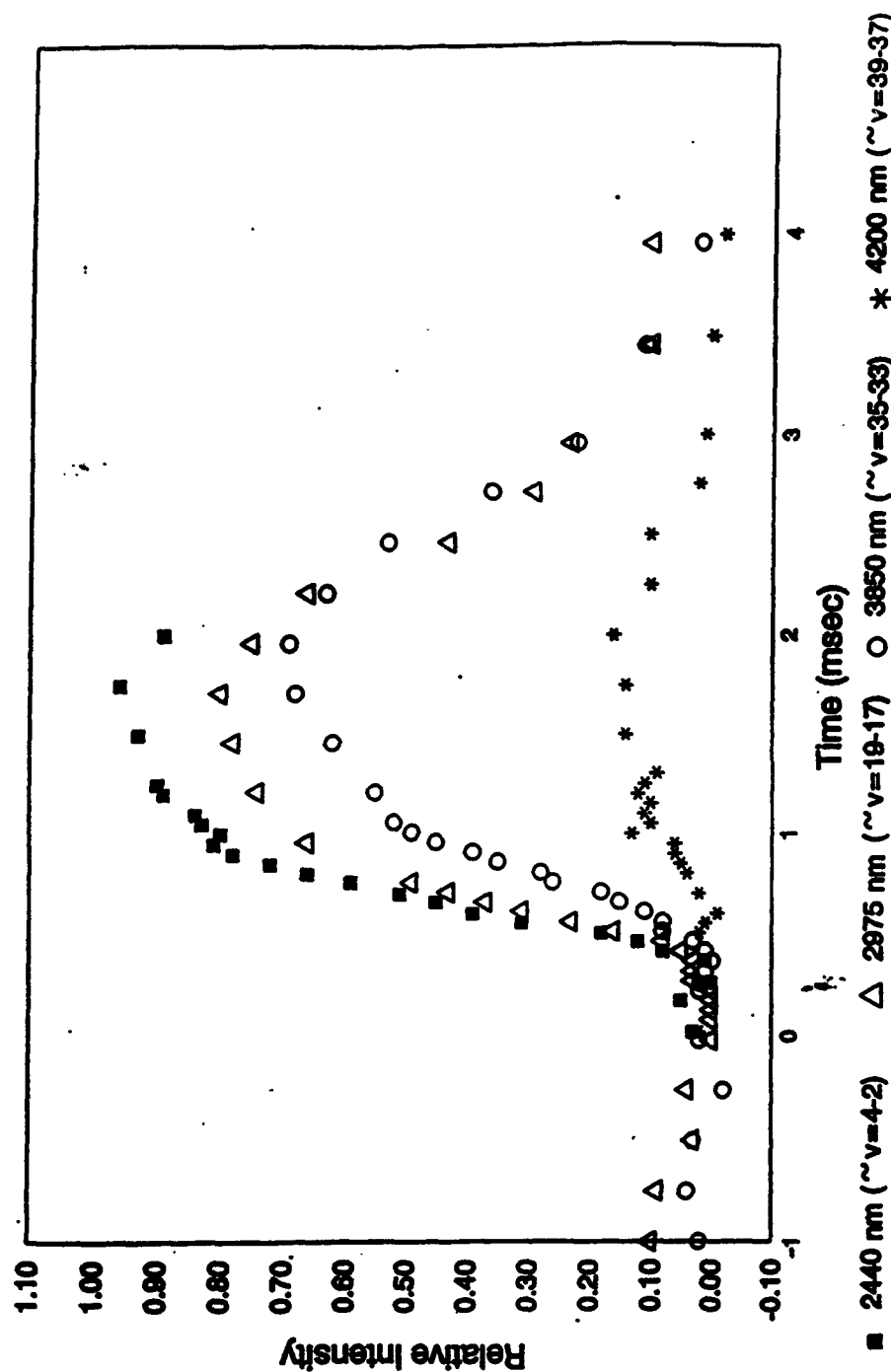


Figure 3.10. Time dependence of the first overtone emission (intensity normalized) after pulsed excitation for selected wavelengths, laser pulse duration of 2.5 ms.

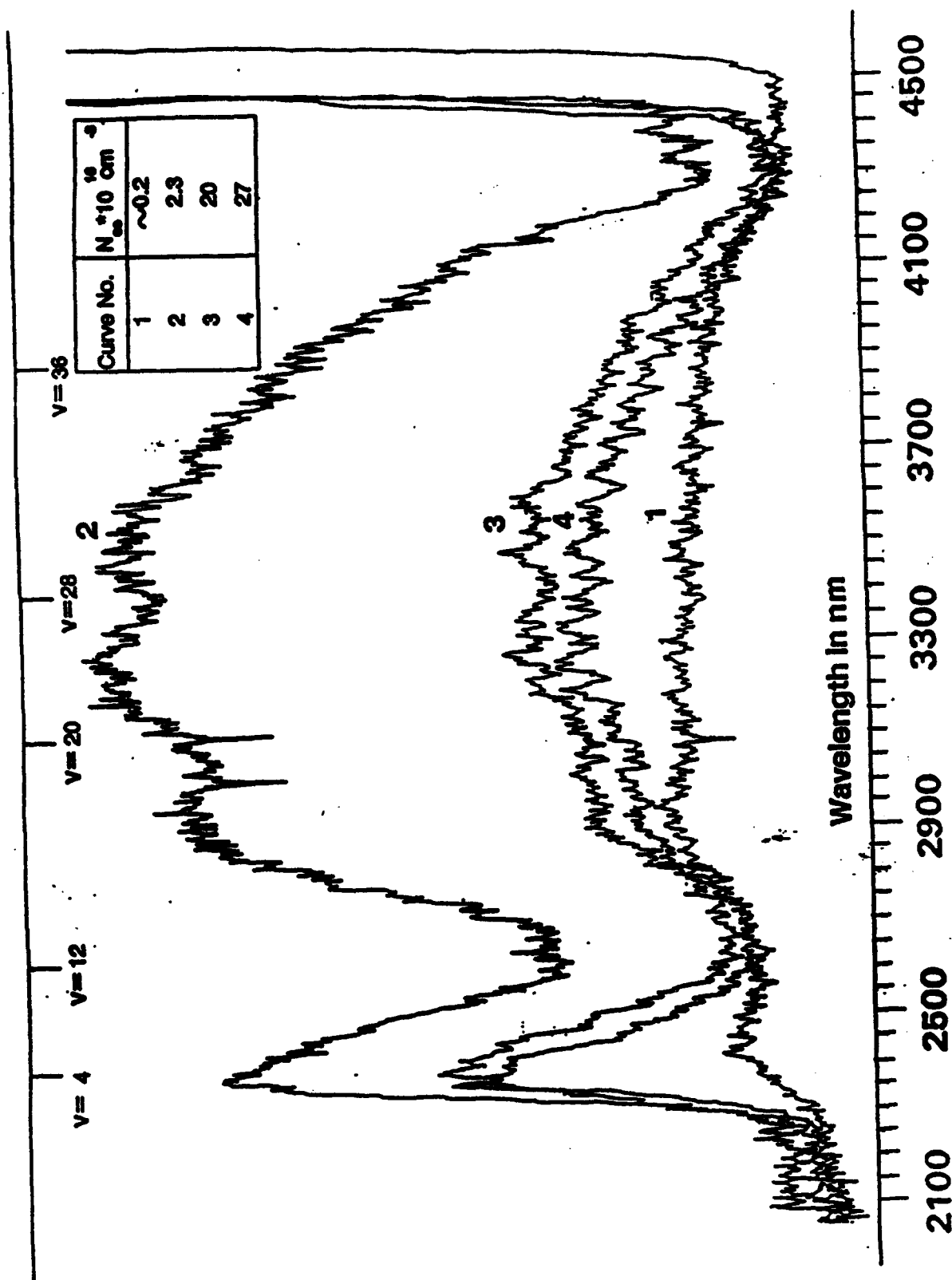


Figure 3.11. 1st overtone spectra for selected CO concentrations. Shown are all bands from  $v=2-0$  to approximately  $v=40-38$  ( $2.3-4.4 \mu\text{m}$ ). The rotational structure is not resolved. The amplifier gain for curve No.2 is twice that of curves 1,3, and 4.

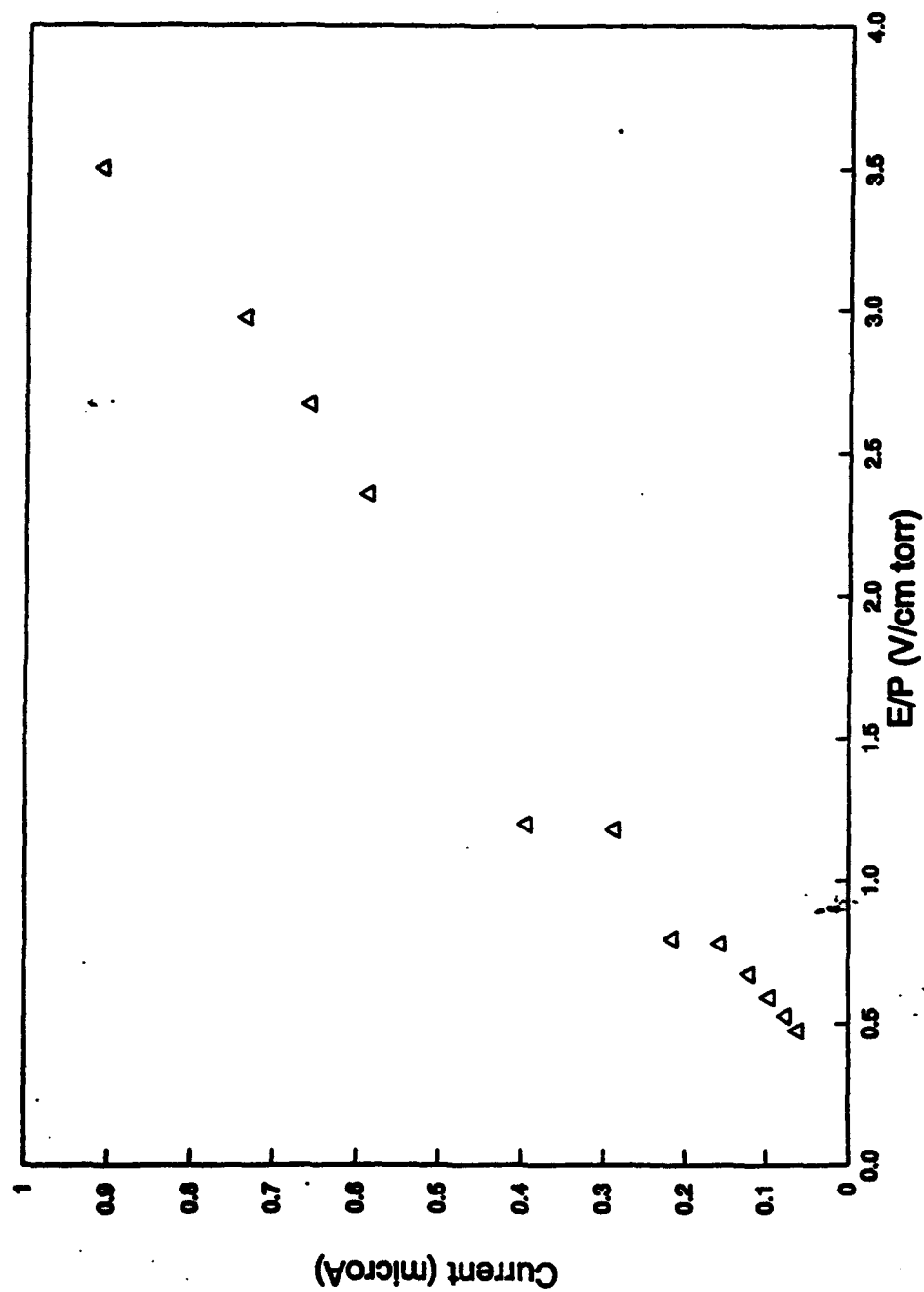
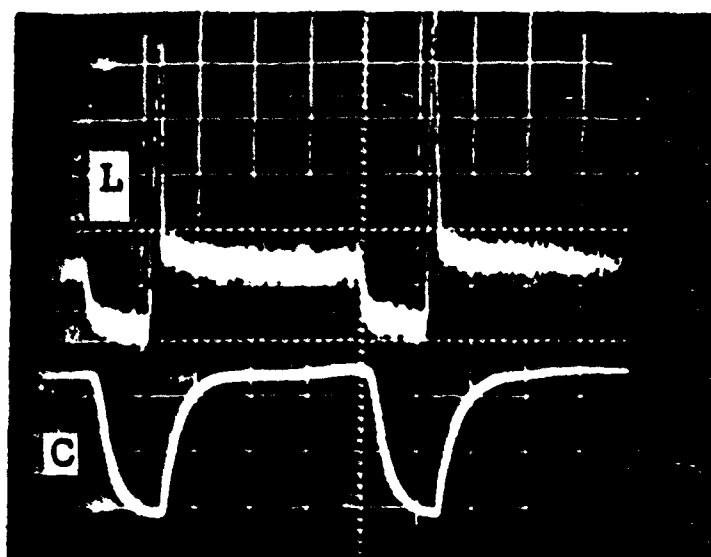
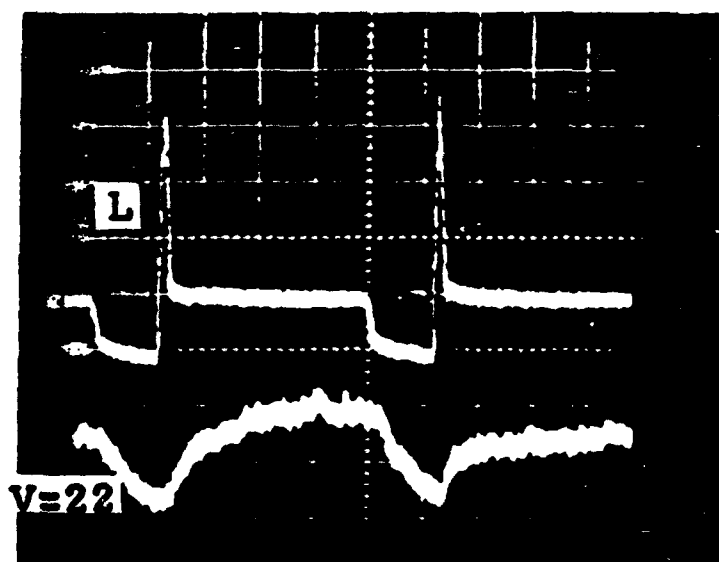


Figure 3.12. Measured current in the absorption cell vs. applied electric field E over total cell pressure P. The cell pressure was varied from 60 to 500 Torr at a CO/Ar concentration ratio of 4/69.





**a) Laser and Current Pulses**



**b) Laser and  $v=22$  Emission Pulses**

**Figure 3.13.** Time dependence of the current and the overtone emission after pulsed laser excitation:

- a. Laser pulse shape (L) and Current response (C).
- b. Laser pulse shape (L) and subsequent overtone emission on  $v=22-20$ .

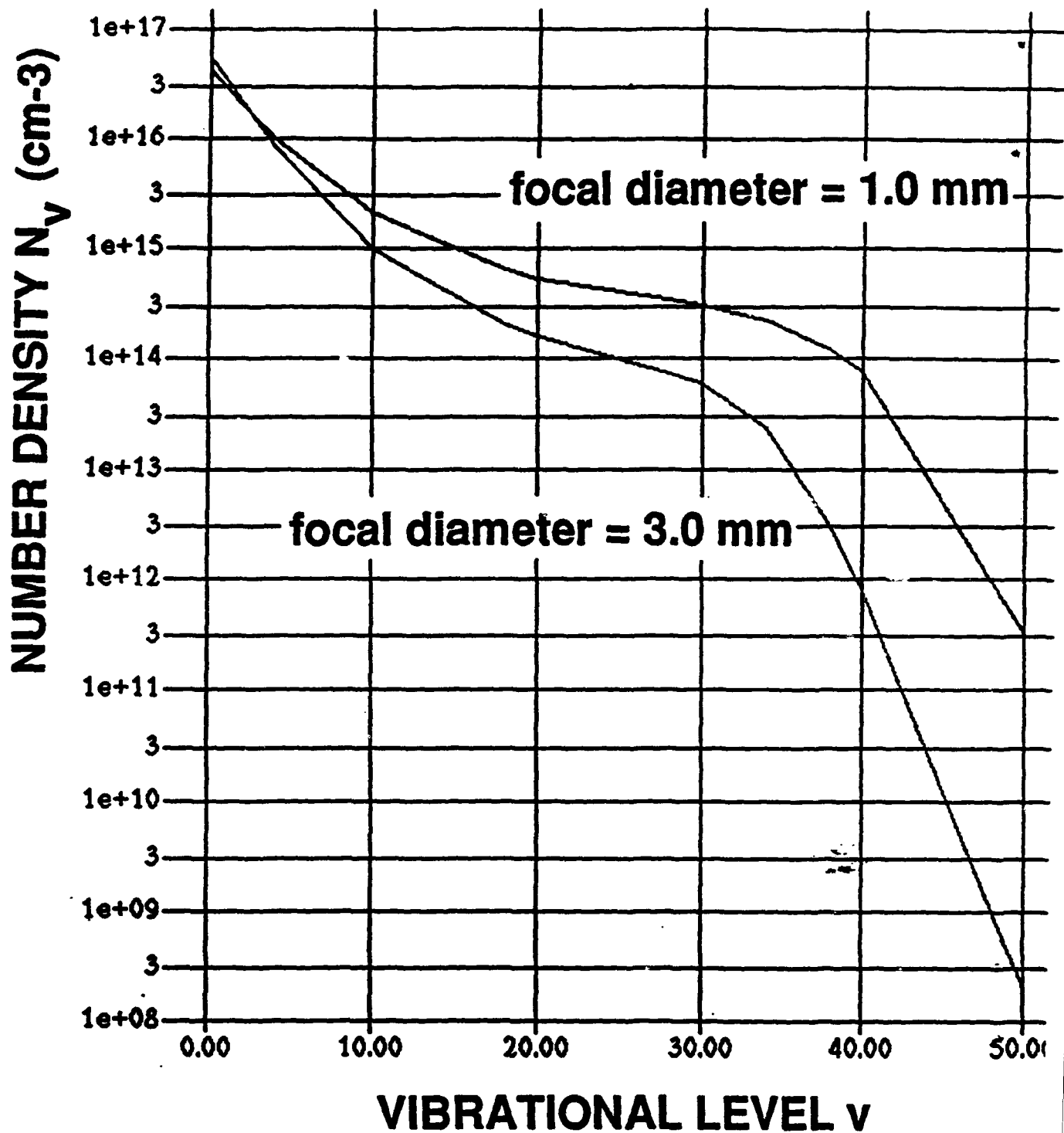


Figure 3.14. Kinetic modeling calculation: predicted steady state vibrational population densities of the V-V pumped CO for two different focal diameters (power densities) of the laser beam, for  $T=1500$  K

**1st OVERTONE RADIATIVE INTENSITIES  
POWER DENSITY = 22.0 W/cm<sup>2</sup>**

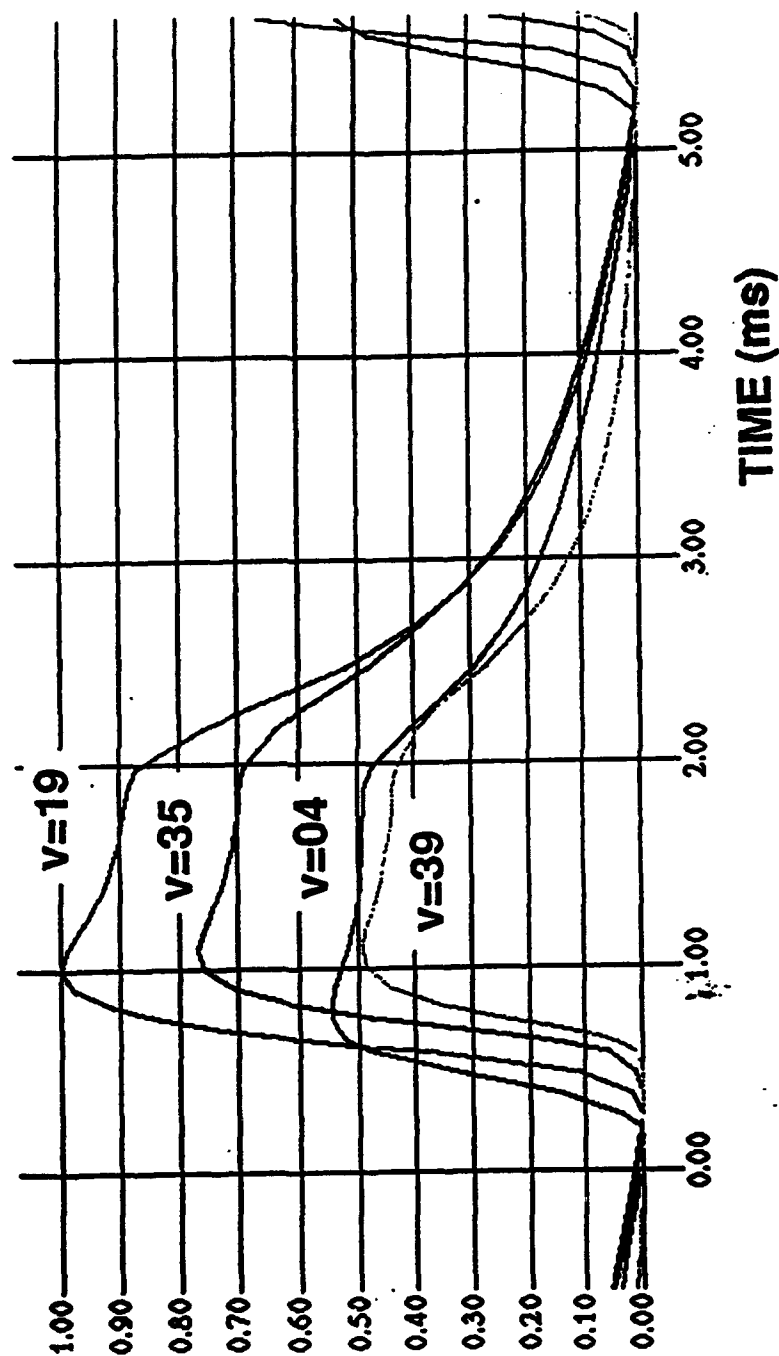


Figure 3.15. Kinetic modeling calculation: predicted time-dependent 1st overtone radiative intensities after pulse excitation (0-2.5 ms); laser power density = 22 W/cm<sup>2</sup>

# **1st OVERTONE RADIATIVE INTENSITIES** **POWER DENSITY = 2.2 W/cm<sup>2</sup>**

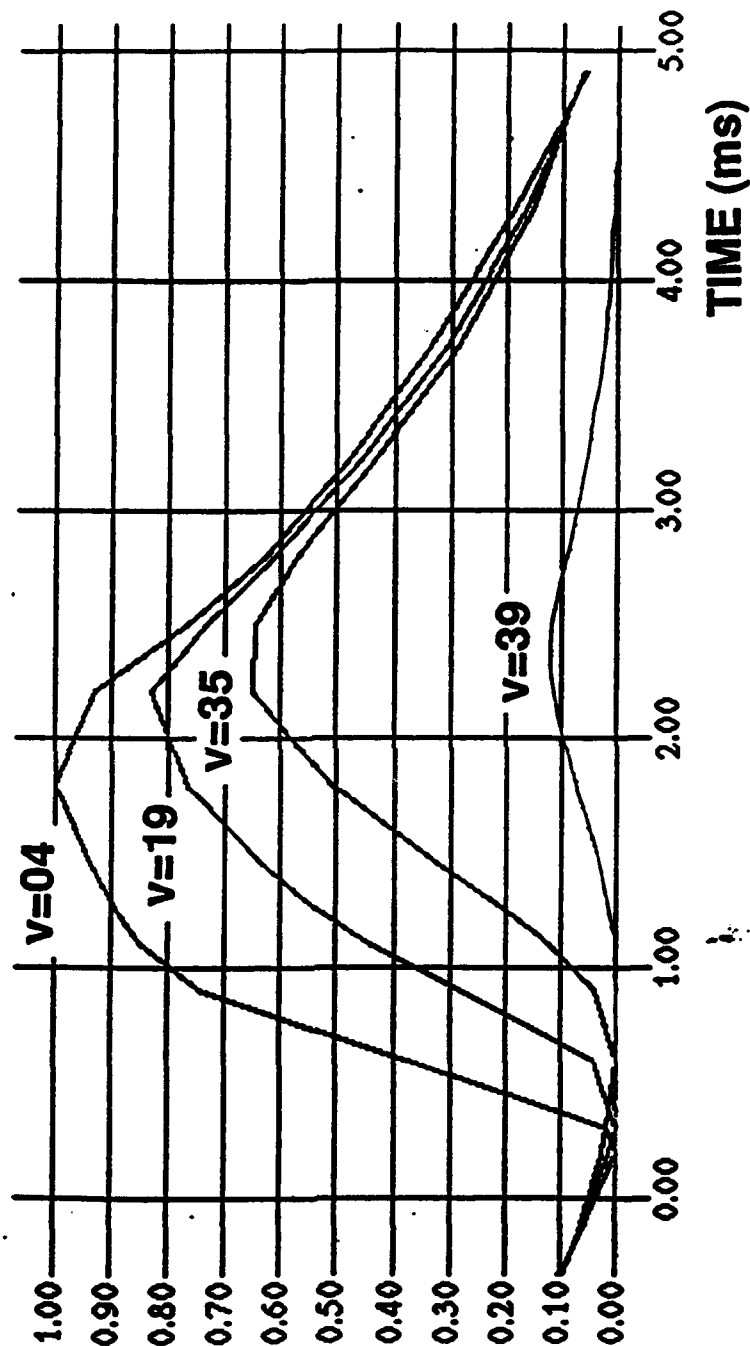


Figure 3.16. Kinetic modeling calculation: predicted time-dependent 1st overtone radiative intensities after pulse excitation (0-2.5 ms); laser power density = 2.2 W/cm<sup>2</sup>

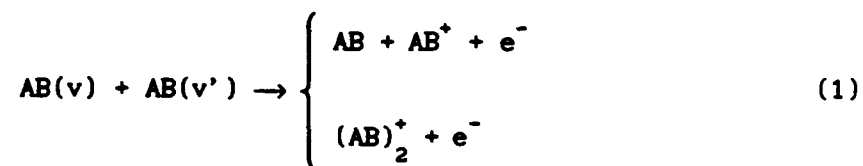
**4. CARBON MONOXIDE STUDIES II:**  
**Vibrationally Stimulated Ionization of CO<sup>\*</sup>**

• This chapter adapted from I. Adamovich, S. Saupe, M.J. Grassi, O. Shulz, S. Macheret, and J.W. Rich, Chem. Phys. 173, 491 (1993)

## 4.1 Introduction

Ionization mechanisms in diatomic gases are widely studied due to their applications to high-enthalpy gas dynamic flows, to electric discharge phenomena, and to gas laser development. There is a large literature on the study of ionization in diatomics by electron impact and by photoionization (see, for example, [1] and references therein).

The present chapter addresses an additional ionization mechanism which may well be a major electron source in gas environments in which the vibrational mode energy is high. It can be described by the following kinetic equation:



where:

$$E_v + E_{v'} > E_i$$

Here,  $AB(v)$  represents a diatomic gas molecule in the  $v^{\text{th}}$  vibrational quantum state,  $AB(v')$  is the molecule in the  $v'^{\text{th}}$  state,  $E_v$  and  $E_{v'}$  are the energies of the molecule in the  $v^{\text{th}}$  and  $v'^{\text{th}}$  states, respectively.  $E_i$  is the ionization energy of the molecule. Basically the preceding scheme states that ionization can occur by two-body collisions of the diatomics, if their total energy exceeds the ionization energy of  $AB$  (or the dimer  $(AB)_2$ ). Such ionization can occur in vibrationally nonequilibrium environments, for which the energy in the vibrational mode greatly exceeds the translational or rotational mode energies. Ionization can occur in gases where the translational/rotational modes are in equilibrium at near room temperature or lower, if the vibrational modes have sufficient energy. Such a situation

can readily occur in supersonic expansion flows and in molecular gas glow discharges.

Ionization by this mechanism has been previously studied by Polak et al. [2] in an  $N_2$  glow discharge, and shown to be the dominant mode of ionization in the environment studied. A major difficulty with such measurements in a glow discharge, however, is that alternative ionization channels, such as direct electron impact ionization or ionization by electronically excited molecular collisions, are simultaneously present. This makes isolation of key mechanisms difficult. A somewhat more recent study by Ahasov et al. [3] avoided this difficulty by studying the process in the supersonic expansion of a high-stagnation-enthalpy gas in a shock tunnel apparatus. In this work, both  $N_2$  and CO were heated to stagnation temperatures in the 2000 to 4000 K range, and cooled in a rapid supersonic expansion. In the expansion, a substantial degree of the stagnation energy was frozen in the vibrational mode, and relatively low translation-rotation temperatures were achieved. The vibrational mode is vibration-vibration (V-V) pumped [4]. Substantial amounts of ionization were measured in the expansion, and attributed to the associative ionization mechanism. Detailed exploration of the role of the vibrational nonequilibrium processes in the ionization mechanism was made difficult, however, due to the short test times available in the shock tunnel.

Theoretical studies of ionization by the vibrationally-induced mechanism (1) have also been made by Cacciatore et al. for a glow discharge in  $N_2$  [5] and by Capitelli et al. for a nitrogen afterglow [6], using the master equation simulation [4] and the rate constant recommended in [2].

In the present experiments, the associative ionization mechanism is studied, again in a discharge-free environment, but one which can be operated for hours duration. Radiation from a carbon monoxide (CO) infrared

gas laser is focused into a flowing-gas optical absorption cell. The cell contains a mixture of CO, Ar and He. Laser radiation is resonantly absorbed by the CO vibrational mode, and vibrational levels approximately up to  $v=40$  become strongly overpopulated. The CO vibrational distribution function (VDF) is determined by infrared (IR) emission spectroscopic diagnostics. The translational-rotational modes are in Boltzmann equilibrium at temperatures in the range 600-800 K. These temperatures are determined from rotationally resolved IR spectra. Such relatively low temperatures are maintained by the heat capacity effect of the Ar-He diluent and by the convective cooling effect of the gas flow. Ionization, induced by the CO vibrational excitation and presumably occurring by the mechanism (1), is studied by using the Thomson discharge [7] in the cell, supported by the laser beam. A preliminary report of ionization studies with this experimental approach was given recently as part of [8,9].

In the present chapter, the experimental setup is described in Section 4.2. Section 4.3 discusses the results of the measurements, as well as their comparison to theoretical predictions. The final Section, 4.4, gives a summary and conclusions.

#### 4.2. Experimental

The apparatus used in the present experiments is quite similar to that described in Chapter 3 and in Ref. [8]. Fig. 4.1 gives a schematic of the experimental equipment used in these studies. Radiation from the CO gas laser (1) is focused into the flowing-gas absorption cell (6). Extensive details of the CO pump laser construction and operation are given in [8,10]. Briefly, the laser is an electrically excited, slow-flow, CO gas laser. The



active discharge tube is 1 meter long and 2.5 cm in diameter. Power is supplied by a regulated d.c. power supply. The ends of the discharge tube are sealed by  $\text{CaF}_2$  windows at Brewster's angle; external 2.5 cm diameter laser mirrors are used. The walls of the tube are cooled by a liquid-nitrogen bath. In the present experiments the laser works in the cw regime. Table 4.1 gives the typical laser gas partial pressures, discharge current, and output power for the present experiments.

The laser operates with broad bandwidth reflectivity mirrors, and, typically, the beam consists of approximately 20 vibrational-rotational lines on the CO 5-micron infrared fundamental band, extending from the  $v = 3 \rightarrow 2$  component to  $v = 12 \rightarrow 11$ . Fig. 4.2 gives a typical laser output spectrum. The laser is optimized to run on low-lying vibrational transitions, which is essential to start V-V pumping of the cold (T=300K) CO. The usual procedure for starting the experiment is to operate the laser at relatively low powers (approximately 3 W), for which there is considerable  $v = 3 \rightarrow 2$  output on low rotational lines (~0.6 W). The up-pumping starts by spontaneous fluctuations of the laser lines to the band  $v = 2 \rightarrow 1$  or by intra-cavity chopping [8,10]. After substantial absorption occurs in the CO, the laser power is increased to 14 W, with about 1 W on the  $v = 3 \rightarrow 2$  band, and the system is allowed to reach steady state. The amplitude stability of the steady state broadband power is within  $\pm 3\%$ . The laser beam is focused into the absorption cell by a 30 cm focal length mirror. The reflecting angle is kept small to reduce astigmatism. The focusing area is approximately  $1 \text{ mm}^2$ .

The absorption cell, shown in Fig. 4.3, is a six-arm stainless steel tubing cross. Tubing inside diameter is 4 cm, and the ends of the cross arms along the pump beam axis are closed by  $\text{CaF}_2$  optical windows. The total length of the cell, window to window, along the laser beam axis is 15 cm. The sidearms perpendicular to the laser beam have been shortened to

increase the aperture for emission spectroscopy.

A mixture of CO, Ar and He is admitted into the cell through a 6 mm diameter port on the side of one arm; the gas mixture is exhausted through a similar port on the opposing cell arm. The cell gases are premixed before entering the cell.

The gas trapping system ((5) of the schematic of Fig. 4.1) is based on the findings of Center [11], who developed it to remove strongly electron-attaching iron pentacarbonyl  $\text{Fe}(\text{CO})_5$  from bottled CO. The iron and nickel carbonyls  $\text{Fe}(\text{CO})_5$  and  $\text{Ni}(\text{CO})_4$ , being strong attachers, are also capable of producing Fe and Ni atoms. The trap consists of a 15 cm long copper tube, 12 mm in diameter, filled with a 5 Å molecular sieve material (zeolite). The trap is operated at room temperature and can be by-passed. Gases used were Matheson CP grade CO (99.5% min), prepurified grade Ar (99.98%) and high purity grade He (99.995%). Some preliminary tests were made with UHP CO (99.9%) and with trapped gases processed with a liquid-nitrogen-cooled trap preceding the molecular-sieve-containing trap. No significant differences were observed in these tests from the results reported here.

The gas flow and the cell pressure can be varied by means of flowmeters and by a throttling valve before the pump. The gas flow through the cell is quite slow - less than 0.03 g/sec in all cases for the measurements reported here. It is estimated that the local gas flow velocity does not exceed 10 cm/sec in the region of the current measurement, which insures that the gas residence time is long enough to achieve steady-state CO vibrational distribution. On the other hand, any further throttling of the gas flow makes convective cooling ineffective, which leads to a significant temperature increase in the cell. The vibration-translation (V-T) relaxation rates also increase with temperature, so the vibrational

nonequilibrium under very slow-flow or non-flowing conditions is not as strong.

The pressures of CO, Ar and He in the cell can be varied over a wide range; for the present studies the CO partial pressure was constant  $P_{\text{CO}}=3$  torr, with the Ar-He mixture pressure being  $P_{\text{Ar-He}}=97$  torr. The He partial pressure has been changed from zero to 97 torr.

With the gases flowing through the cell under these conditions, the vibrational mode of the CO in the cell readily absorbs some of the pump laser energy into the lowest CO vibrational states,  $v \leq 12$ .

Higher CO vibrational states,  $v > 12$ , are populated by collision-induced vibration-to-vibration energy exchange [4,8]. One result of this V-V pumping is immediately seen in the absorption cell: there is a quite intense blue light emission visible, centered at the focal point of the laser beam. For the experiments described here, the glow starts approximately 4 cm before the focus and extends to the exit window, thus spreading for about 10 cm. The diameter of this luminous region varies with cell and laser conditions; it is approximately 2-3 mm for the present measurements. This blue emission is due to visible band components of the  $\text{C}_2$  Swan system,  $d^3\Pi_g \rightarrow a^3\Pi_u$ . The  $\text{C}_2$  is generated by chemical reaction of the V-V pumped CO. It has been observed and discussed in previous work using this excitation technique [8,12].

The infrared radiation from the cell is observed perpendicular to the laser beam. The IR signal is focused onto the entrance slit of a 0.34 m scanning IR monochromator ((8) of the schematic of Fig.1), by a two-mirror arrangement. It is analyzed by a 4  $\mu\text{m}$  blaze grating and observed with an InSb detector. All the spectra are stored in and processed by an IBM PC 486 computer.

Under these excitation conditions, ionization occurs in the cell

gases, presumably by the mechanism (1), as we shall discuss. For the ionization measurements, two parallel plate brass electrodes are placed in the absorption cell. Fig. 4.3 shows a detail of this arrangement. The plates are 2cm x 1cm with the long axis parallel to the laser beam. For the measurements reported here, the plates are separated by 1 cm. The axis of the pump laser beam is centered in the space between the plates. Insulated leads connect the plates to the exterior of the cell, as shown in Fig. 4.1.

The plates are connected to a regulated d.c. power supply (2), which can deliver an output voltage of up to 3000 V. In series with the supply is a microammeter (3) which can record the steady state current to within 10 nanoamperes.

Finally, the transmitted laser power is measured by a power meter (Fig. 4.1, (9)) positioned in the laser beam after the cell. Comparing the transmitted power under steady-state pumping conditions and after the CO is removed from the cell, one obtains the absorbed power. The incident power can be easily changed by using a beamsplitter, without changing the laser beam diameter and the laser spectrum. The absorbed power has been varied from 1.7 to 5 W for typical cell conditions as described above.

#### 4.3. Results and discussion

##### 4.3.1. Infrared measurements

Fig. 4.4 shows three typical infrared emission spectra, generated by the V-V pumped CO in the cell, when operating under the conditions described above, at three different helium pressures. The first overtone,  $\Delta v=2$ , emission bands of CO are shown under low resolution, ranging

from 2.3 to 4.4  $\mu\text{m}$  wavelength. The approximate centers of some of the radiating vibrational transitions are shown. As can be seen, vibrational states to  $v=40$  are populated and radiating. The abrupt signal rise at  $\lambda > 4.4 \mu\text{m}$  is due to overlapping with the fundamental,  $\Delta v=1$ , spectrum. The signal at  $\lambda < 2.3 \mu\text{m}$  is generated by the second overtone,  $\Delta v=3$ , radiation.

The observed IR radiation signal intensity  $I(\lambda)$  is a superposition of the first and the second CO overtones (the latter - in the two first orders of the grating). In this case  $I(\lambda)$  can be expressed in terms of absolute intensities of the overtones  $I_{\text{abs}}^{\text{I}}(\lambda)$  and  $I_{\text{abs}}^{\text{II}}(\lambda)$ , respectively, and the total InSb detector and 4  $\mu\text{m}$  monochromator grating response function  $\Phi(\lambda)\Psi_{\alpha}(\lambda)$ :

$$I(\lambda) = \left[ I_{\text{abs}}^{\text{I}}(\lambda) + I_{\text{abs}}^{\text{II}}(\lambda) \right] \Phi(\lambda)\Psi_{\text{I}}(\lambda) + I_{\text{abs}}^{\text{II}}(\lambda/2)\Phi(\lambda/2)\Psi_{\text{II}}(\lambda/2) \quad (2)$$

Here  $\Phi(\lambda)$  is the detector sensitivity, and  $\Psi_{\text{I}}(\lambda)$  and  $\Psi_{\text{II}}(\lambda)$  are the grating response functions in the first and in the second order, respectively. The product of  $\Phi(\lambda)$  and  $\Psi_{\alpha}(\lambda)$  was determined from a black-body source calibration of the spectrometer.

With known response functions, equation (2) allows comparison of the experimental CO spectrum and the computer-generated spectrum, based on a synthetic carbon monoxide VDF. Thus, the vibrational distribution functions of CO in the optical cell were inferred, as previously been done by Rich and Bergman [12]. The procedure was first suggested by Horn and Oettinger [13]. Details of the method we followed are described in [8]. CO molecular spectroscopic constants were taken from Huber and Herzberg [14]; Einstein coefficients for CO spontaneous radiation were obtained from Chackerian and Tipping [15]. Fig. 4.5 shows the typical agreement obtained between the experimental and the synthetic spectra. Note that the periodic structure of

these spectra at  $3.8 \mu\text{m} < \lambda < 4.4 \mu\text{m}$  is second overtone/second order signal, and it is not attributed to the radiation from the high vibrational levels  $v > 35$ . The same remark is also true for the curves 2,3 in Fig. 4.4.

The rotational temperature of the cell gases  $T_r$  was obtained from comparison of the experimental rotationally resolved CO fundamental spectrum on low vibrational transitions  $1 \rightarrow 0$  and  $2 \rightarrow 1$  with the appropriate synthetic spectrum (see Fig. 4.6). The relative error in  $T_r$  was estimated to be about 25%, both because of the strong self-absorption and because of the non-uniform temperature profile across the cell. There is no doubt, however, that the inferred  $T_r$  for all measured regimes is in the range  $T = 600\text{--}800$  K. This result is also confirmed by our earlier rotationally resolved spectra of the  $\text{C}_2$  Swan emission  $d^3\Pi_g \rightarrow a^3\Pi_u$  in the cell (see [8]). It was shown that the  $\text{C}_2$  rotational mode is in Boltzmann equilibrium. The inferred  $\text{C}_2$  rotational temperature for similar cell conditions was in the same range,  $T = 600\text{--}800$  K, as that obtained from the present infrared measurements.

Fig. 4.7 presents the CO vibrational distribution functions inferred from the experimental spectra. One can see that high vibrational levels of CO, up to level  $v \sim 30\text{--}40$ , are strongly overpopulated. The rate constant of V-T relaxation CO-He is much higher than that of CO-Ar or CO-CO, and thus the total V-T rate increases with the helium concentration ( $0 \leq n_{\text{He}}/n \leq 0.97$ ). Therefore by adding helium to the CO-Ar mixture, we succeeded in changing the plateau fall-off level  $v^*$ , where the V-T relaxation rate is equal to the local V-V rate, decreasing the plateau length. Note that the relative populations at  $v < v^*$  did not significantly change, so we just cut the "tail" of the VDF, as it has earlier been done in [12]. It should be pointed out that quite fine control of the plateau length can be obtained by this means. The distributions shown in Fig. 4.7 represent only some of the VDF's measured. Measurable, reproducible plateau lengths are obtained for

every 3% change in the  $n_{\text{He}}/n$  ratio. The rotational temperature of the gas mixture remains nearly unaffected by the helium concentration change, as was found from the rotational spectra. Obviously, the effect of the higher helium thermal conductivity is compensated by the also higher V-T energy transfer rate.

We note, however, that the shape of the CO VDF differs from that predicted by theory. Simple estimates show that the lower level populations should follow the Treanor distribution with some vibrational temperature  $T_v$ , since the nonresonant V-V exchange for these levels is much faster than the laser pumping or the V-T relaxation. But the best Treanor fit for levels  $v \leq 5$ , at  $T = 700\text{K}$ ,  $T_v = 3200\text{K}$  gives a strongly underestimated plateau population at levels  $v \geq 10$  (see the lower dashed curve in Fig. 4.7). On the other hand, the Treanor distribution corresponding to the inferred plateau,  $T = 700\text{K}$ ,  $T_v = 3900\text{K}$  (the upper dashed curve in Fig. 4.7), does not fit to populations of levels  $v < 10$ . A similar effect, but not so strong, was observed by Martin et al. [16], also in CO optical pumping experiments.

This anomaly can be qualitatively explained by the spatial nonuniformity of the cell gas. The infrared signal is collected from the entire optical path across the cell, while the energy is absorbed only in the near-axis area. The relaxation rates of the high CO vibrational levels are much faster than those of the low levels. This means that the molecules which contribute to the longer wavelength part of the IR spectrum (which corresponds to the plateau region of the VDF), are concentrated near the optical axis. At the same time, the shorter wavelength part of the spectrum (the Treanor region of the VDF) is a superposition of the signals both from the central and from the peripheral areas of the cell. Obviously, this decreases the effective vibrational temperature of the inferred Treanor-like population. The major contribution to these two parts of the distribution

function comes from different cell regions. This spatial nonuniformity brings substantial error in determination of the absolute populations of the high CO vibrational levels, because the VDF should be normalized by unity. The effect can be reduced only by decreasing the cell diameter. In the experiments of [16] the effect was minimized by removing partially-relaxed CO from the cell by Ar flow, which decreased the optical path to several mm.

#### 4.3.2. Ionization measurements

In these optical pumping experiments we have measured the electric current induced between two plane electrodes placed in the cell. It should be mentioned that the voltage applied to the electrodes was usually considerably lower than the breakdown voltage  $U_b$ ; the voltage-current characteristics were measured for  $U \leq U_b$  at different helium partial pressures (see Fig. 4.8). The typical value of the measured current was several microamperes. Obviously, a non-self-sustained electric discharge, supported by the laser beam, is ignited in the cell. The theory of this type of discharge was developed by Thomson as early as in 1928 [7]. It assumes that ionization by electron impact is negligible, because of the low energy of electrons. Then, the production of charge in the interelectrode region can be described by the ionization rate  $q_i$ , which is independent of the electron density.

The Thomson theory gives simple analytical relations for the current-voltage (I-U) characteristic of the discharge  $I(U)$ , the saturation voltage and current  $U_s$  and  $I_s$ , the electric field and the charge species distributions (see Appendix). The I-U characteristics are different for two specific cases of distributed ionization ( $q_i = \text{const}$  in the entire discharge



area) and concentrated ionization, when the external ionization layer width  $d$  is much smaller than the interelectrode distance  $L$ . In the first case the induced current is proportional to the square root of the applied voltage:

$$I = \left( 4\mu_+ \epsilon_0 e^3 q_1^3 \right)^{1/4} \cdot S \cdot U^{1/2}, \quad (3)$$

where  $\mu_+$  is the ion mobility, and  $S$  is the electrode surface area. For the concentrated source, placed on the symmetry axis of the discharge, the current is proportional to the square of the voltage:

$$I = \frac{9\mu_+ \epsilon_0 S}{L^3} U^2, \quad (4)$$

where  $L$  is the interelectrode distance. Note that in the case of the concentrated ionization source, which we are especially interested in, the  $I$ - $U$  characteristic (4) is independent of the ionization rate  $q_1$ . Also, if the ionization source is shifted from the symmetry axis by a distance  $\delta \ll L$ , ( $\delta > 0$  toward the positive electrode), the equation (4) becomes

$$I = \frac{9\mu_+ \epsilon_0 S}{(L+2\delta)^3} U^2, \quad (4')$$

which means that the alignment symmetry (and therefore the applicability of equation (4)) can be controlled by switching the voltage polarity.

It can be seen from Fig. 4.8 that the shape of the experimental  $I$ - $U$  characteristics reasonably corresponds to the theoretical curve  $I \sim U^2$  for the Thomson discharge supported by a concentrated ionization source (see equation 4). This supports the conclusion that the ionization of the cell gases occurs in the central area of the cell surrounding the laser beam. Furthermore, it is possible to show that if the ionization rate is not equal to zero in the vicinity of the electrodes, then

$$\lim_{U \rightarrow 0} dI/dU = \infty, \quad (5)$$

as is the case, for example, for the distributed ionization source (see equation (3)). Therefore, since the observed U-I characteristic does not reveal a noticeable sharp current increase at low voltages, one can conclude that surface ionization is negligible in the present experiments.

Further evidence supporting a gas-phase ionization process was obtained in the experiment by using a quartz tube. The laser beam was surrounded by the tube which allowed the UV radiation from the CO excited electronic states to pass, while the near-axis region was completely isolated from the electrodes. No current was measured in this case, which shows that the photoelectric effect on the electrodes is also negligible [8]. Also, no current can be measured in an Ar-He mixture or when the pump laser is turned off.

It also can be seen that at some voltage  $U_s$  the slope of the current curve substantially decreases, although the current nevertheless continues to grow linearly. This part of the I-U characteristic is associated with saturation. The fact that the current is not completely saturated is explained by the finite size of the electrodes.

If we assume that the ionization in the plasma is catalyzed by the laser radiation, and the ionization rate  $q_i$  follows the laser beam power distribution (Gaussian profile), then we can write:

$$q_i(x) = q_i(0) \exp \left[ - \left( \frac{x-L/2}{0.5d} \right)^2 \right], \quad (6)$$

where  $d$  is the characteristic profile width ( $d \ll L$ ). For this distribution of  $q_i$  the saturation current and voltage are given by the following relationships:

$$I_s = eq_1(0)d \frac{\pi^{1/2}}{2} S, \quad (7)$$

$$U_s = \left[ \frac{eq_1(0)d}{\mu_s \epsilon_0} \right]^{1/2} \frac{\pi^{1/4}}{3 \cdot 2^{1/2}} L^{3/2} \quad (8)$$

As can be seen, these equations do not contain rate constants of any collisional process in the plasma, except the external ionization rate. Therefore, the product  $q_1(0)d$  can be unambiguously inferred from the experimental values of  $I_s$  and  $U_s$ .

For the present situation of CO optical pumping by resonance absorption of CO-laser radiation, when one can neglect multiphoton ionization (the estimated energy fluence is far too weak), the ionization occurs in collisions of two heavy particles, and we can write:

$$q_1 = \kappa_1 n_{CO}^2, \quad (9)$$

where  $n_{CO}$  is the CO molecules concentration, and  $\kappa_1$  is the reduced ionization rate. To express  $\kappa_1$  in terms of the ionization rate constant  $k_1$  and relative concentrations of colliding molecules, one has to make an additional assumption on the process mechanism.

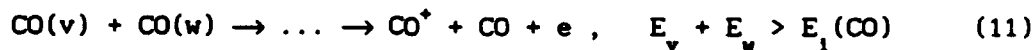
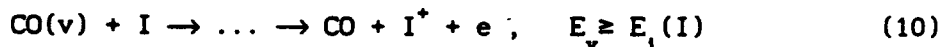
It is clear from Fig. 4.8, that the experimental I-U characteristics for different He concentrations at  $U < U_s$  are very close, while the saturation voltages and currents are substantially different. This is also in good agreement with the theoretical prediction that for the concentrated ionization source the I-U characteristic is independent of the ionization rate  $q_1$  (see equation (4)). Obviously,  $q_1$ , determined by relations (7,8), varies for different regimes in Fig. 4.8.

Recent time-resolved measurements, where the Q-switched CO laser was used to pump CO in the cell, have shown that the measured current pulse

occurs with some delay after the laser pulse. On the other hand, the current pulse is synchronized with the CO  $v=22 \rightarrow 20$  IR pulse, emitted from the cell [8]. Finally, the present experiments in the CO-Ar-He mixture with different helium concentration confirm that a definite correlation exists between vibrational excitation and ionization. An analysis of Fig. 4.7 and 4.8 shows that the lower the population of high CO vibrational levels, the lower is the saturation current. These measurements were carried out at constant laser power, total pressure, and CO concentration.

The sum of these arguments leads to the following conclusions: i) the observed ionization, stimulated by the CO laser, occurs in the gas phase, in the narrow near-axis area of the cell, occupied by the laser beam; and ii) it is induced by highly vibrationally excited CO molecules, which are also concentrated near optical axis.

Generally, ionization is allowed when the total energy of reactants is high enough to overcome the ionization potential of one of them. The previous discussion leaves us with two possible mechanisms of ionization:



where  $I$  is some easily ionizable impurity,  $E_v$  is the energy of the  $v^{\text{th}}$  CO vibrational level,  $E_i(I)$  and  $E_i(\text{CO})$  are the ionization potentials of the  $I$  and CO molecules, respectively. Ellipses in the reaction equations (10), (11) mean that the detailed mechanism of the ionization is still uncertain. For example, it is not clear how metastable  $\text{CO}(a^3\pi)$  molecules, which can be also created in the collision of vibrationally excited  $\text{CO}(X^1\Sigma, v)$  molecules

(see Farrenq et al., [17]), affect the ionization. The metastables could be an intermediate stage of the process.

The present phenomenological approach cannot resolve questions about the importance of intermediates in the vibrationally-induced ionization of CO. However, it is possible to make a choice between the first-order mechanism (10) and the second-order reaction (11). The reduced ionization rate  $\kappa_1$  (see equation (9)) in these two cases can be written as follows:

$$\kappa_1 = (k_1 f_I) \sum f_v, \quad E_v \geq E_1(I) \quad (12)$$

$$\kappa_1 = k_1 \sum f_v f_w, \quad E_v + E_w > E_1(\text{CO}) \quad (13)$$

where  $k_1$  is the ionization rate constant,  $f_I$  is the impurity fraction in the mixture ( $f_I = n_I/n_{\text{CO}}$ ), and  $f_v$  is the relative population of the CO  $v^{\text{th}}$  vibrational level.

Since the saturation voltage and current of the Thomson discharge are functions of the reduced ionization rate  $\kappa_1$  (see equations (7-9)), and the CO VDF in equations (12-13) is known from the infrared measurements, it is possible to determine the ionization rate constant  $k_1$  (or the product  $k_1 f_I$  for the first-order mechanism) from the experimental values of the saturation current  $I_s$ .

Fig. 4.9 gives the dependence of the saturation current, determined in the junction point of the parabolic and the linear parts of the I-U characteristics in Fig. 4.8, as well as the dependencies of the first order and the second order sums in equations (12) and (13):

$$S_1 = \sum f_v; \quad S_2 = \sum f_v f_w, \quad (14)$$

on the helium concentration. The first order sum  $S_1$  was calculated for several different threshold energies  $E_i(I)$ , which would correspond to different ionization potentials of impurities. One can see that the second-order sum  $S_2$  reasonably corresponds to the current curve. On the other hand, it is clear, that the first order sum is also in reasonable agreement with the current curve if the impurity ionization potential is about 7 eV ( $v \approx 35$ ), which is characteristic for some metal atoms (Fe - 7.90 eV, Ni - 7.64 eV, Cu - 7.73 eV). These metals can be present in the cell because the cell gases are stored in steel cylinders, and copper tubes are also used in the experimental setup. Besides that, such impurities as chemical reactions products  $\text{CO}_2$ ,  $\text{C}_2\text{O}$ ,  $\text{C}_2$ ,  $\text{C}_3\text{O}_2$  and their polymers are always present in the vibrationally excited CO because of chemical reactions (see Rich, Bergman [12]). On the other hand, we can definitely exclude impurities whose ionization potentials are lower or much higher than ~7 eV.

If we assume that ionization does occur in collisions of two vibrationally excited CO molecules, then the ionization rate constant inferred from the infrared spectra and the saturation current measurements is  $k_i = (6 \pm 2) \cdot 10^{-15} \text{ cm}^3/\text{s}$ . Otherwise, if the first-order mechanism is assumed, one gets the product  $k_i f_i \sim 10^{-17} \text{ cm}^3/\text{s}$ , which in the gas-kinetic limit for the ionization rate constant ( $k_i < 10^{-10} \text{ cm}^3/\text{s}$ ) gives  $f_i = n_i/n_{\text{CO}} > 10^{-7}$ , or for the present cell conditions,  $N_i > 10^{10} \text{ cm}^{-3}$ . It is disappointing that the possible influence of ionizable impurities cannot be eliminated on the basis of the preceding estimates on the lower bound of their concentrations. However, the trapping system described previously is specific for eliminating  $\text{Fe}(\text{CO})_5$  and also has been observed to remove  $\text{Ni}(\text{CO})_4$  from similar cell experiments (with the trap atomic Ni lines disappeared from the cell radiation spectrum) [18]. Such metal carbonyls are definitely present when the gases are untrapped, and form a ready source of Fe and Ni atoms

when in the presence of vibrationally pumped CO. Their concentration is significantly reduced when the trap is used. We observed that when the trap is in use, both the populations in the  $v > 20$  plateau and the electric current are slightly increased.

This result is inconsistent with such species being the source of impurity ionization. The observed increase in the  $v > 20$  concentrations when the trap is used is an expected consequence of the reduced V-T rates, as the fast-relaxing metal atoms are eliminated. The increase in current is consistent with the slightly higher plateau populations, if ionization occurs in collisions of two vibrationally excited CO molecules. On the other hand, the current would decrease significantly when the trap was used if impurity metal ionization were a major source of electrons. We conclude that the ionization is indeed due to the mechanism of equation (1).

The electron concentration and the ionization fraction in the field-free case can be estimated on the assumption that the dominant channel of electron loss is CO dissociative recombination ( $\beta \sim 10^{-7} \text{ cm}^3/\text{s}$ , [11]). This gives the electron concentration to be  $n_e \sim 10^{10} \text{ cm}^{-3}$ , with an ionization fraction about  $y_e = n_e/n \sim 10^{-8}$ .

Equations (7, 8) allow determination only of the product  $q_1(0)d$ . We therefore require an independent determination of the characteristic width,  $d$ . Since the ionization is localized in the region of substantial concentration of highly excited CO molecules  $\text{CO}(v \geq 25)$ ,  $d$  can be found from the experimentally determined width of the visible blue glow ( $\text{C}_2$  Swan band radiation observed in the cell). The  $\text{C}_2$  molecules are produced in chemical reactions which are started by a vibrationally stimulated reaction:



with an activation energy corresponding to CO vibrational level  $v \sim 25$ . One

can neglect diffusion of the excited  $C_2$  at the present cell pressures (~100 torr), and thus the glow diameter approximately corresponds to the ionization region width  $d$ . This parameter can be easily estimated visually within an accuracy of ~50%, and it is usually 2-3 mm for the present conditions. Taking into account the uncertainty in the rotational temperature of ~25%, we get an accuracy in  $\kappa_1$  of a factor of 2.

The accuracy of the inferred ionization rate constant  $k_1$  depends on the accuracy of determination of the VDF. Due to the spatial nonhomogeneity effect, discussed above, the uncertainty in the inference of populations of zero and the first vibrational levels can reach a factor of 2. The combination of uncertainties in the  $\kappa_1$  and VDF determinations gives the overall range for the inferred rate constant  $k_1 = (8 \pm 5) \cdot 10^{-15} \text{ cm}^3/\text{s}$ . This uncertainty can be substantially diminished by changing the cell design, thus reducing the nonuniformity of the flow across the cell, and this work is being done. This result for  $k_1$  corresponds to within an order of magnitude to that obtained by Polak et al [2] for associative ionization of nitrogen:

$$k_{N_2} = 1.9 \cdot 10^{-15} \cdot \exp(-1160/T) \text{ cm}^3/\text{s}$$

#### 4.3.3. Vibration-to-electron coupling measurements

To better understand how the electrons can affect the CO VDF, we also carried out a series of experiments where the relative populations of different vibrational levels of carbon monoxide were measured twice - with and without the electric field. Here we used an interesting property of the Thomson discharge, that is a strong difference of the electron and ion concentrations, due to their different mobilities (see Fig. 4.10 and



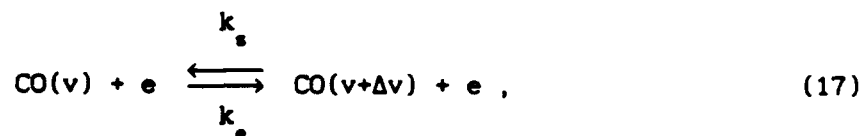
Appendix). One can easily show (see Appendix, equations (A1-A4)) that in the saturation regime:

$$\frac{n_{e \text{ max}}}{n_{+ \text{ max}}} \approx \left( \frac{\mu_e}{\mu_+} \right)^{1/2} \ll 1 \quad (16)$$

In other words, the electron concentration  $n_e$  in the saturation regime is much lower than the concentration of ions,  $n_+$ . Since in the absence of the electric field  $n_e = n_+$  (see Fig. 4.10),  $n_e$  can obviously be reduced by orders of magnitude just by increasing the applied voltage, without changing the energy loading in the plasma by the external source. Moreover, in the saturation regime the remaining electrons do not contribute to the energy loading, because the estimated electric field power  $P_e \sim U_e I_e \sim 1 \text{ mW}$ , which is much lower than the absorbed laser power  $P_l > 1 \text{ W}$ . For this reason, the removal of the electrons is the only direct result of the applied voltage. The influence of ions can be neglected because the electron-to-vibration (e-V) energy transfer cross-sections in CO are of the order of the atomic cross-section [19] and therefore the appropriate rate constants can considerably exceed the gas-kinetic limit.

Fig. 4.11 represents the results of these measurements. It is clear that the electron removal (field ON in Fig. 4.11) increases the populations of high vibrational levels,  $v \geq 15$ . The effect is not very dramatic, about 10% variation at the beginning of the plateau region, increasing with the vibrational quantum number to attain 70% variation at  $v=30$ . On the contrary, the populations of the levels below  $v=10$  decrease when the electrons are eliminated from the discharge area. Here again the effect does not exceed 10% variation. The qualitative change in the VDF is shown in Fig. 4.12, where the effect is strongly exaggerated for illustrative purposes.

The following approximate analysis can interpret qualitatively the observed dependence of the CO VDF on the electron concentration. The interaction of the CO molecules with electrons can be expressed by the reaction:



where the forward process is the vibrational excitation by electron impact, and the reverse one is the effect of superelastic collision. Let us approximately assume that the electron energy distribution function (EEDF) is Maxwellian, so that we can write:

$$k_e = k_s \cdot \exp\left(\frac{-\Delta E_{v+\Delta v, v}}{T_e}\right), \quad (18)$$

where  $\Delta E_{v+\Delta v, v} = E_{v+\Delta v} - E_v$  is the difference in energies of vibrational levels  $v+\Delta v$  and  $v$ , and  $T_e$  is electron temperature. The CO VDF can be represented as follows:

$$f_v \sim \exp(-E_v / T_{vib}^v), \quad (19)$$

where  $T_{vib}^v$  is the "local" vibrational temperature. This temperature obviously increases with vibrational quantum number, because the measured VDF at the high  $v$ 's has much higher values than the corresponding Boltzmann distribution at  $T_{vib}^1$ .

Now, one can easily show that the detailed balance for the process (17) is attained at  $T_e = T_{vib}^v$ . If the electron temperature exceeds the local vibrational temperature, the vibrational excitation by electron impact is a dominant process. On the contrary, for the high vibrational temperatures the superelastic collisions prevail. Since  $T_{vib}^v$  strongly increases with  $v$ , this

means that the low CO levels are populated by electron collisions, while for the very high  $v$ 's the effect is quite opposite (see Fig. 4.12). In other words, the influence of this vibrational-electron interaction is as it was observed in our experiments, where  $T_{vib}^1 \sim 3-4$  kK.

This analysis gives a simple estimate of the electron temperature from the measured VDF, from which the value  $T_e \sim 6$  kK is obtained (see straight line in Fig. 4.12). Since the perturbation of the VDF is the strongest in the absence of the field, this means that the electrons acquire energy from the high vibrational levels (otherwise they would be quickly thermalized) and return it to the lower levels ( $V \rightarrow e \rightarrow V-\Delta V$  process).

The effect of the acceleration of the remaining electrons, when the field is on, on the VDF should be considered as completely negligible. The typical value of the reduced electric field between the electrodes is  $E/N < 40$  Td, which implies the electron temperature to be  $T_e \sim 1$  eV [20]. This means that the concentration of the high-energy electrons ( $\epsilon \geq 5$  eV), which are able to excite high vibrational levels  $v \sim 20$ , is still low,  $n_e^* \sim 10^{-2} n_e$ . Taking into account the fact that  $n_e$  drops by approximately 3 orders of magnitude, when the field is on (see Fig. 4.10), one has  $n_e^* \sim 10^5$  cm $^{-3}$  for typical experimental conditions, when  $n_{CO} \sim 10^{17}$  cm $^{-3}$ . Now one can see that the excitation of the high CO levels by the high-energy electrons is insignificant compared to the resonant V-V exchange:

$$k_{ev} n_e^* n_{CO} \ll k_{vv} n_{CO}^2 f_v^2 \quad (20)$$

Here  $k_{ev} \sim 10^{-8}$  cm $^3$ /s [20] - rate constant of vibrational excitation by electron impact,  $k_{vv} \sim 10^{-10}$  cm $^3$ /s [21] - rate constant of the resonant V-V exchange at  $v \sim 20$ , and  $f_v \sim 10^{-3}$  - relative population of level  $v \sim 20$  in our experiments. Electron impact ionization of highly vibrationally excited CO molecules can be neglected for the same reason.

More detailed interpretation of the effect can be obtained by a self-consistent solution of the master equation for the CO VDF and the Boltzmann equation for the EEDF. Some results in this direction are already obtained (see, for example, work of Capitelli et al. [20]), but a complete kinetic model for this problem still requires the cross-sections of the process (17) for the high  $v$ 's.

Finally, we want to emphasize that the using of the Thomson discharge in an optical pumping experiment allows direct observation of the e-V energy transfer effects, arbitrarily changing the electron concentration, which is definitely impossible in self-sustained electric discharge systems.

#### 4.4 Summary

Ionization occurring in collisions of two excited CO molecules is investigated in steady-state conditions of optical pumping. This mechanism appears to be the same "associative ionization" process studied in vibrationally excited  $N_2$  by Polak, Sergeev and Slovetskii [2], and in  $N_2$  and in CO by Achasov et al [3]. The present experiments allow the study of this process by using a non-self-sustained discharge (Thomson discharge), supported by a CO laser beam. The ionization rate constant  $k_1$  is inferred from CO VDF measurements and the experimental saturation current of the discharge. A specific ionization rate constant of  $k_2 = (8 \pm 5) \cdot 10^{-15} \text{ cm}^3/\text{s}$  is measured, which reasonably corresponds to the result of [2], obtained for nitrogen.

The influence of low-energy electrons on the CO vibrational distribution function is also investigated, by varying the discharge

voltage, which allows elimination of the electrons from the discharge area. The effect of energy transfer from higher to lower vibrational levels of CO via collisions with electrons ( $V \rightarrow e \rightarrow V-\Delta V$  process) is observed for the first time.

The experimental technique used in the present work permits further studies of ionization and e-V processes in strongly excited, translationally cold gases, and such measurements are being pursued.

The detailed interpretation of the observed effects requires further theoretical study of elementary processes of interaction of highly vibrationally excited molecules and electrons.

#### Appendix: The Thomson Discharge [5]

For Gaussian distribution of the external ionization source power, (6), the distributions of the ionic and the electronic currents are:

$$\left\{ \begin{array}{l} j_+(x) = \frac{eq_1(0)d \pi^{1/2}}{4} \left[ \Phi(L/d) + \Phi(2x/d) \right] \\ j_-(x) = \frac{eq_1(0)d \pi^{1/2}}{4} \left[ \Phi(L/d) - \Phi(2x/d) \right] \end{array} \right. , \quad -L/2 \leq x \leq L/2 \quad (A1)$$

where:

$$\Phi(x) = \frac{2}{\pi^{1/2}} \int_0^x e^{-\xi^2} d\xi, \quad (A2)$$

The electric field distribution is:

$$E(x) = \left[ \frac{eq_1 d}{\mu_+ \epsilon_0} \right]^{1/2} \left[ \frac{\pi^{1/2}}{2} x \left( \Phi(L/d) + \Phi(2x/d) \right) + \frac{d}{4} e^{-\frac{4x^2}{d^2}} \right]^{1/2} \\ + \left[ \frac{eq_1 d}{\mu_- \epsilon_0} \right]^{1/2} \left[ \frac{\pi^{1/2}}{2} x \left( -\Phi(L/d) + \Phi(2x/d) \right) + \frac{d}{4} e^{-\frac{4x^2}{d^2}} \right]^{1/2} \quad (A3)$$

Finally, the ion and the electron distributions (excluding the near-electrode regions) are

$$n_+(x) = \frac{j_+(x)}{e\mu_+ E(x)}, \quad n_-(x) = \frac{j_-(x)}{e\mu_- E(x)}, \quad (A4)$$

The characteristic width of these near-electrode layers where the charge diffusion is significant, in the saturation regime is

$$\frac{\Delta x_\alpha}{L} \sim \frac{D_\alpha}{\mu_\alpha EL} = \frac{T_\alpha \text{ (eV)}}{U_s} \sim 10^{-2} - 10^{-3}, \quad (A5)$$

or  $\Delta x_\alpha$  is much smaller than  $L$ .

## References

- [1] Yu. P. Raizer, Gas Discharge Physics, Springer-Verlag, Berlin Heidelberg, 1991.
- [2] L. S. Polak, P. A. Sergeev and D. I. Slovetskii, Sov. High Temperature Physics, 15, (1977), 15.
- [3] O. V. Achasov, N. A. Fomin, D. S. Ragozin, R. I. Soloukhin and S. A. Zhdanok, Revue Phys. Appl. 17, (1982), 15.
- [4] J. W. Rich, Relaxation of Molecules Exchanging Vibrational Energy, Chap.4 in: E. W. McDaniel and W. L. Nighan, Applied Atomic Collision Physics, Vol.3, Gas Lasers, Academic Press, NY, 1982.
- [5] M. Cacciatore, M. Capitelli and C. Gorse, Chem.Phys., 66, (1982), 141.
- [6] M. Capitelli, C. Gorse and A. Ricard, J. Physique - Lett. 43, (1982), L-417.
- [7] J. J. Thomson and G. P. Thomson, Conduction of Electricity Through Gases, Vol.1, Cambridge, University Press, 1928.
- [8] C. Flament, T. George, K. A. Meister, J. C. Tufts, J. W. Rich, V.V. Subramaniam, J.-P. Martin, B. Piar and M.-Y. Perrin, Chem.Phys., 163, (1992), 241.
- [9] I. Adamovich, J. Hiltner, S. Macheret and J. W. Rich, Vibrationally Induced Ionization of Carbon Monoxide in Optical Pumping Experiments, AIAA Paper 92-3028, AIAA 23<sup>rd</sup> Plasmadynamics & Lasers Conference, Nashville, TN, USA, 1992.
- [10] W. Urban, J.-X. Lin, V. V. Subramaniam, M. Havenith and J. W. Rich, Chem.Phys., 94, (1985), 195.
- [11] R. E. Center, J. Appl.Phys., 44, (1973), 3538.
- [12] J. W. Rich and R. C. Bergman, Chem.Phys, 44, (1979), 53.
- [13] K. P. Horn and P. E. Oettinger, J. Chem.Phys., 54, (1971), 3040.

- [14] K. P. Huber and G. Herzberg, Molecular Spectra and Molecular Structure. IV. Constants of Diatomic Molecules , Van Nostrand - Reinhold, New-York, 1979.
- [15] C. Chackerian Jr. and R. M. Tipping, J. Mol. Spectry, 99, (1983), 431.
- [16] J. P. Martin, Private Communication, 1992.
- [17] R. Farrenq, C. Rosetti, G. Guelashvili and W. Urban, Chem. Phys, 92, (1985), 589.
- [18] J. P. Martin, V. V. Subramaniam, Private Communication, 1992.
- [19] J. M. Wadehra, Vibrational Excitation and Dissociative Attachment, Chap.7 in: Nonequilibrium Vibrational Kinetics , ed. by M. Capitelli, Springer-Verlag, 1986.
- [20] M. Capitelli, C. Gorse and A. Ricard, Coupling of Vibrational and Electronic Energy Distributions in Discharge and Post-Discharge Conditions , Chap.11 in: Nonequilibrium Vibrational Kinetics, ed. by M. Capitelli, Springer-Verlag, 1986.
- [21] G.D. Billing, Vibration-Vibration and Vibration-Translation Energy Transfer, Including Multiquantum Transitions in Atom-Diatom and Diatom-Diatom Collisions, Chap.4 in: Nonequilibrium Vibrational Kinetics, ed. by M. Capitelli, Springer-Verlag, 1986.



## Figure captions

Figure 4.1. Schematic of the experimental setup: 1, infrared CO laser; 2, d.c. power supply; 3, microammeter; 4, gas supply and gas mixing manifold; 5, impurity trap; 6, optical cell; 7, exhaust pump; 8, infrared spectrometer; 9, laser power meter

Figure 4.2. Typical CO laser spectrum

Figure 4.3. Optical cell with probe

Figure 4.4. CO first overtone emission spectra at different He pressures

Figure 4.5. Comparison of experimental and synthetic CO vibrational spectra

Figure 4.6. Comparison of experimental and synthetic CO rotational spectra

Figure 4.7. Inferred CO vibrational distribution functions at different He pressures

Figure 4.8. Experimental and theoretical voltage-current characteristics of the Thomson discharge

Figure 4.9. Saturation current and number of "active CO

molecules" dependencies on the He pressure

Figure 4.10. Charged species distributions in the Thomson discharge in the absence of the field and in the saturation regime.  $P=100$  torr,  $\text{CO:Ar}=3:97$ ,  $d/L=0.25$ ;  $q_1(0) = 10^{-21} \text{ cm}^3/\text{s}$  (see Eqs. 6, A2-A4).  $L$  - inter-electrode distance.

Figure 4.11. Electric field influence on different CO vibrational level populations

Figure 4.12. Qualitative demonstration of the  $V \rightarrow e \rightarrow V-\Delta V$  effect (strongly exaggerated).  $\epsilon$  - electron energy,  $T_e$  - electron temperature

**Table 4.1. Typical laser conditions**

Species	Partial pressure (torr)	
He	6.00	
$N_2$	0.50	
CO	0.03	
Discharge current		30 mA
Laser power		14.0 W

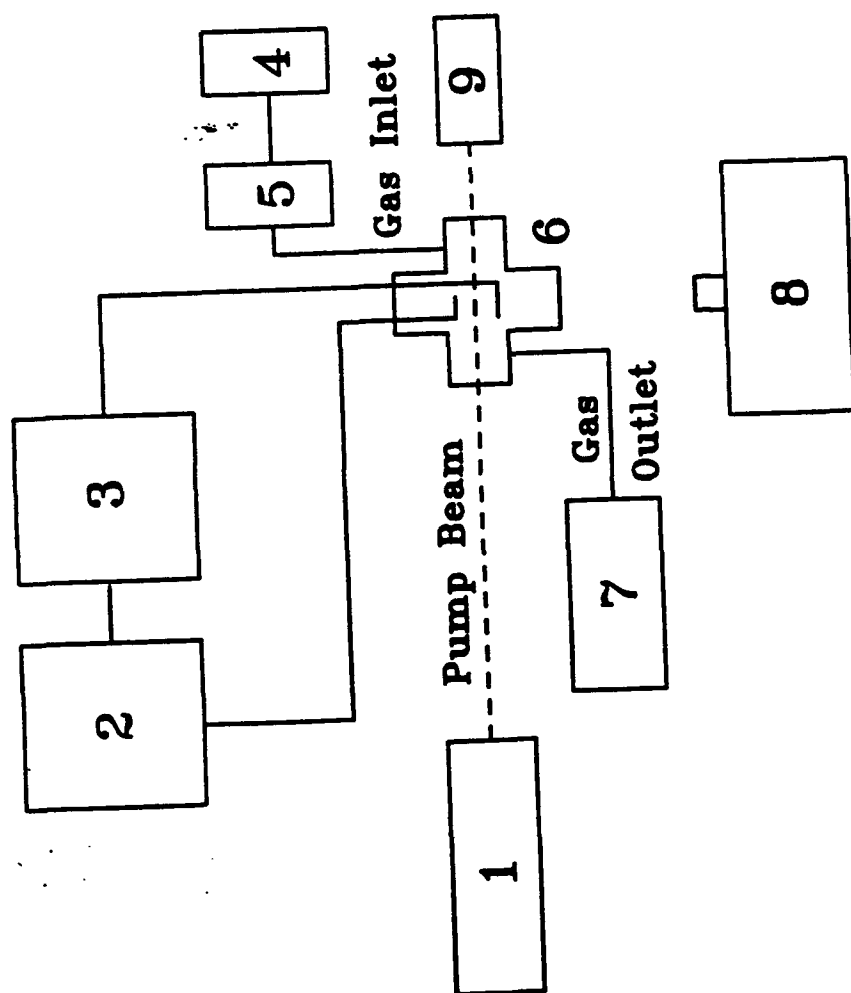


Figure 4.1. Schematic of the experimental setup: 1, infrared CO laser; 2, d.c. power supply; 3, microammeter; 4, gas supply and gas mixing manifold; 5, impurity trap; 6, optical cell; 7, exhaust pump; 8, infrared spectro-meter; 9, laser power meter

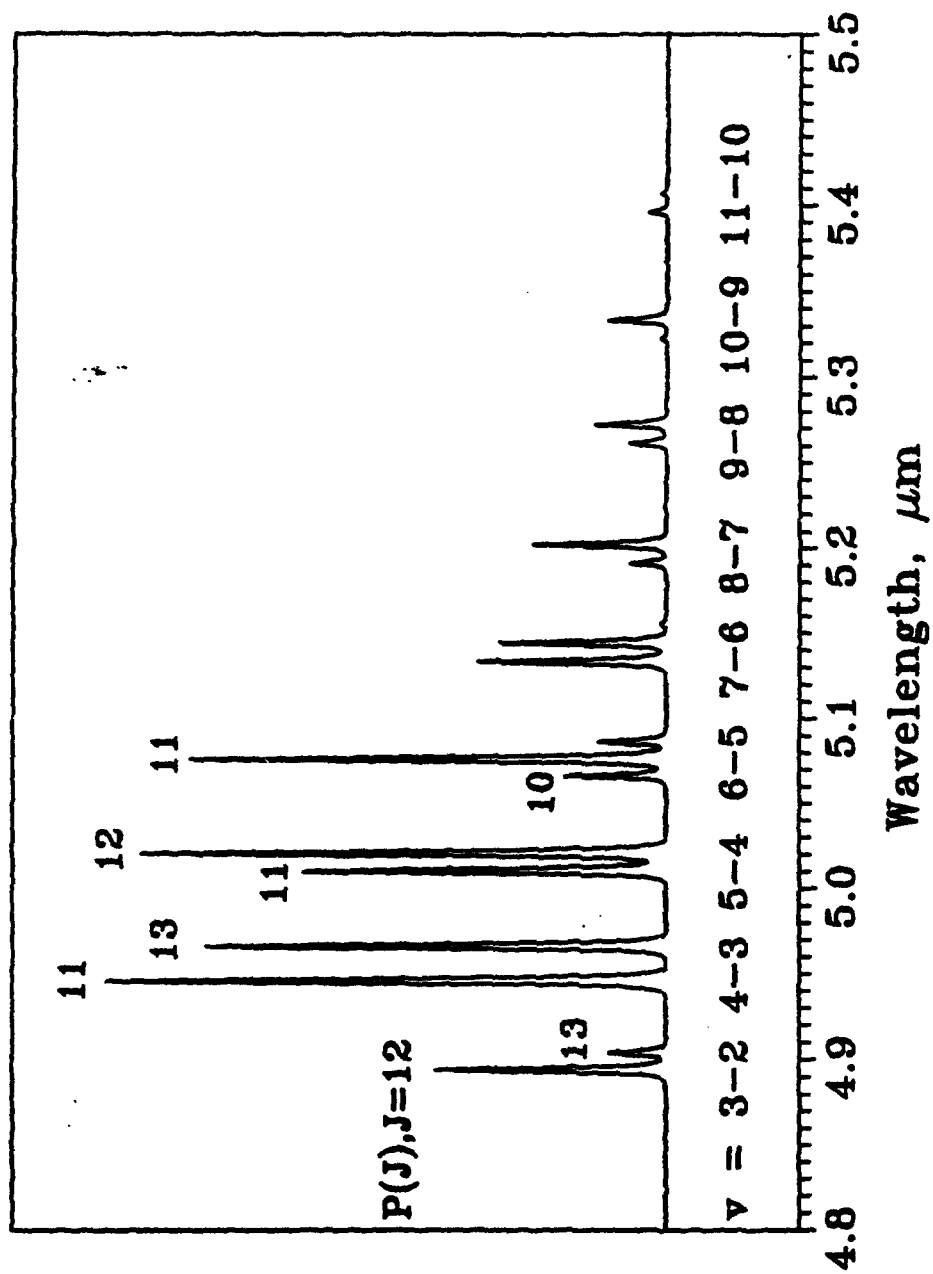


Figure 4.2. Typical CO laser spectrum

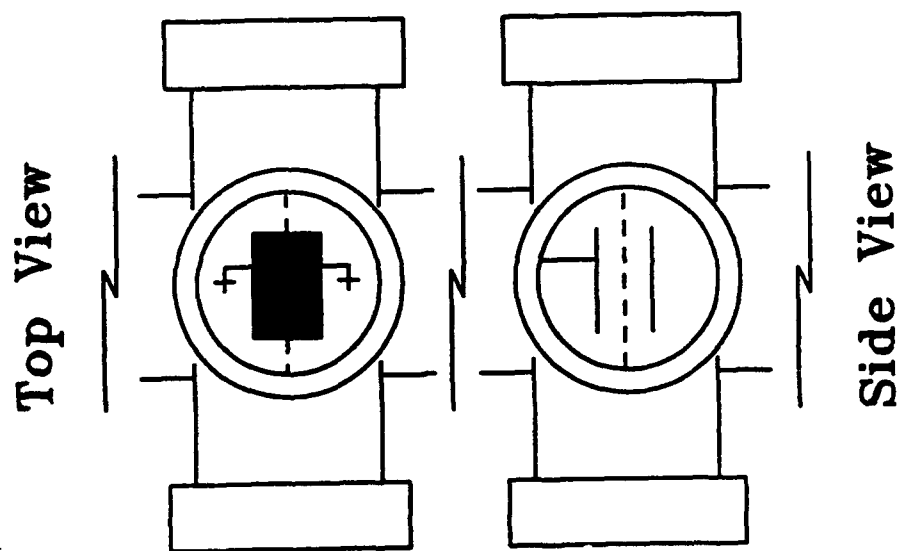


Figure 4.3. Optical cell with probe

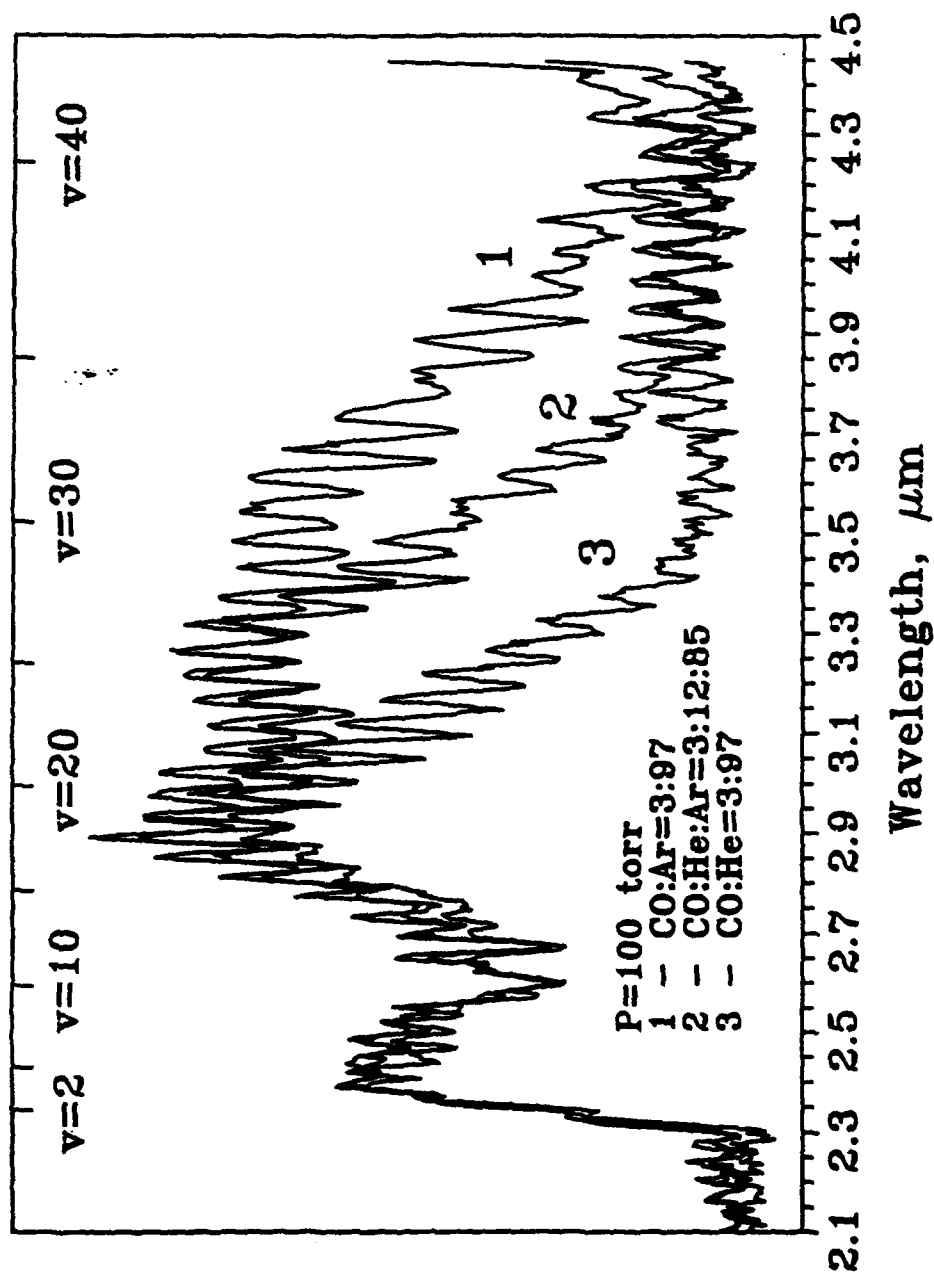


Figure 4.4. CO first overtone emission spectra  
at different He pressures

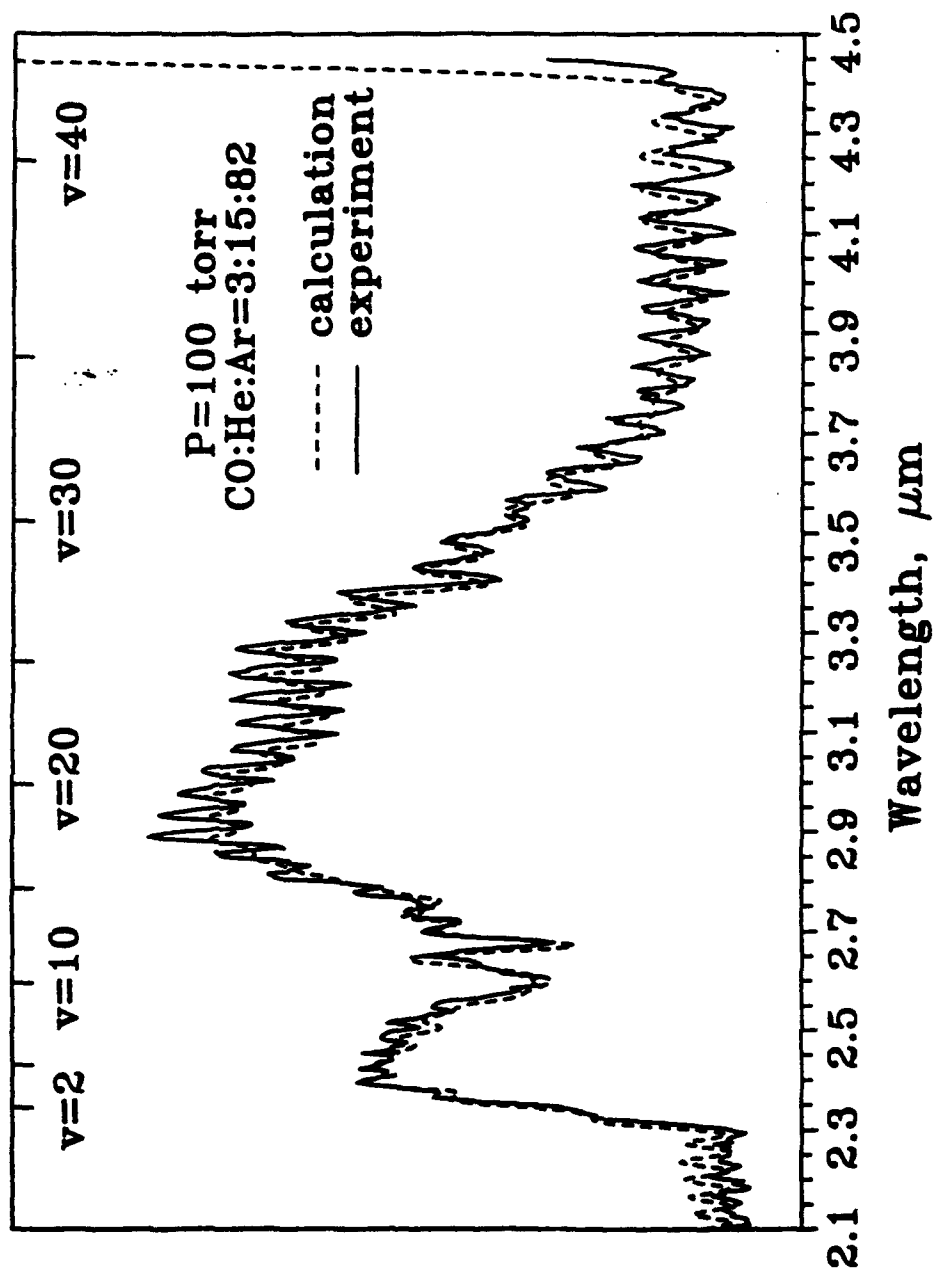


Figure 4.5. Comparison of experimental and synthetic  
CO vibrational spectra



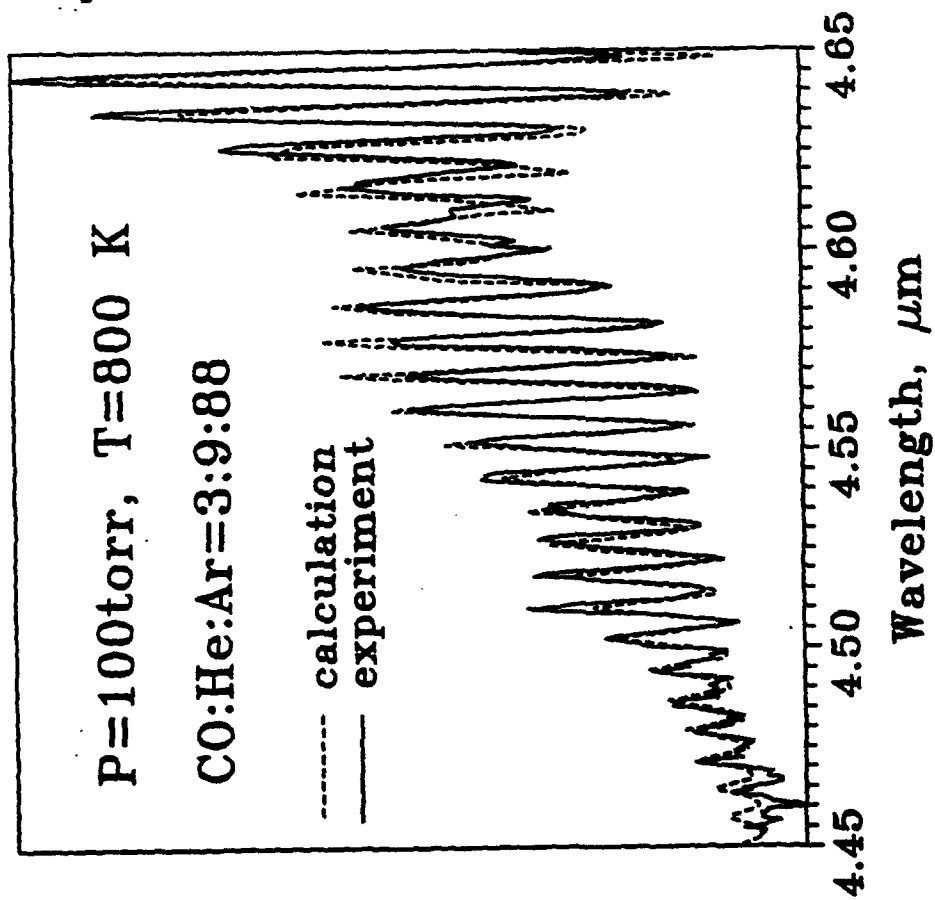


Figure 4.6. Comparison of experimental and synthetic  
CO rotational spectra

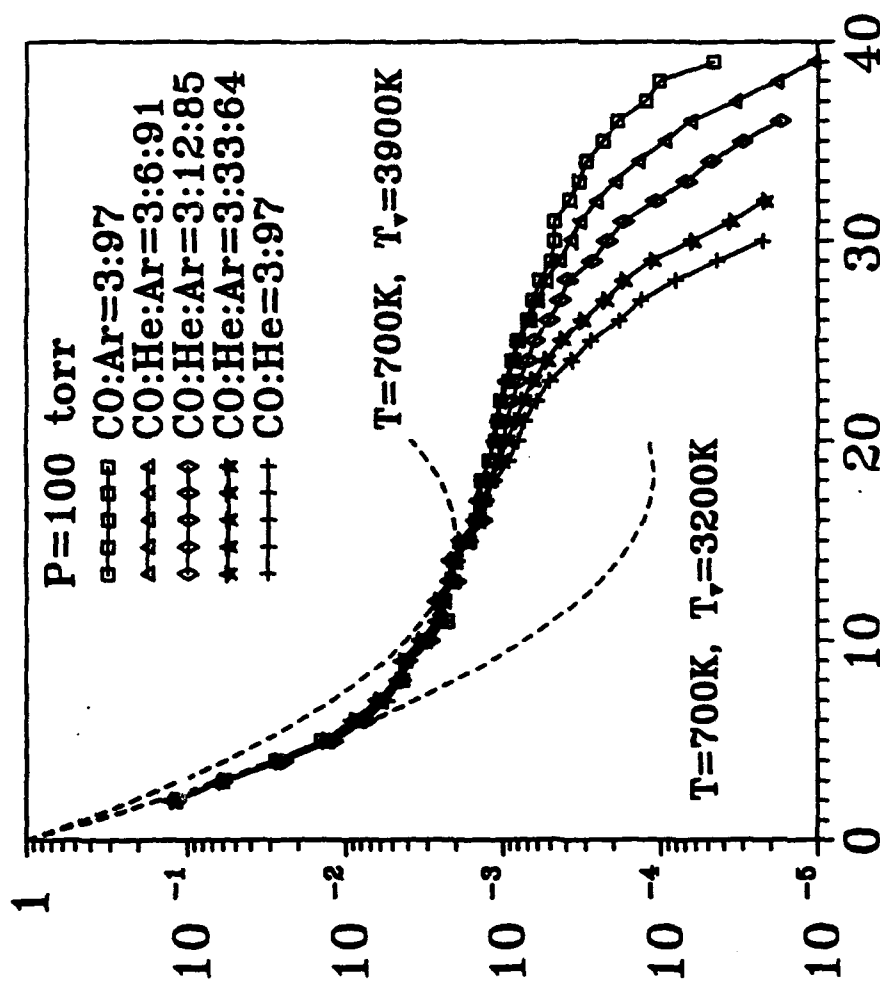


Figure 4.7. Inferred CO vibrational distribution functions at different He pressures

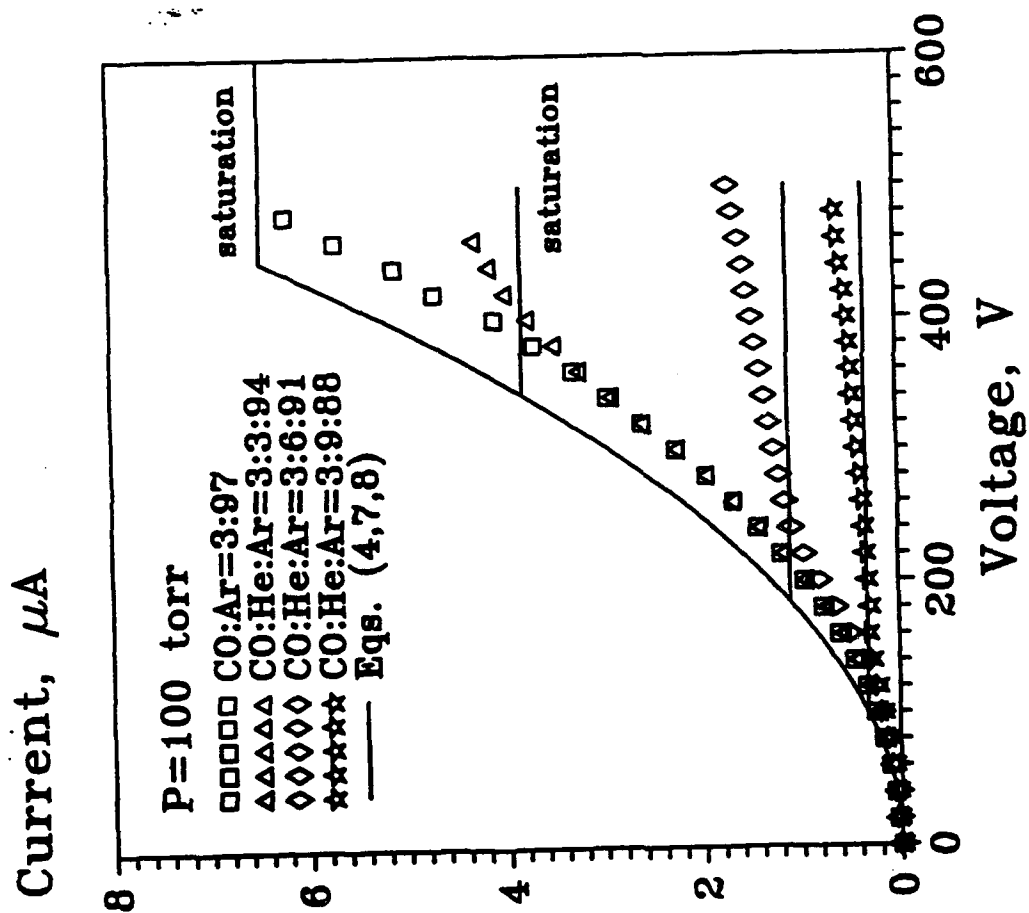
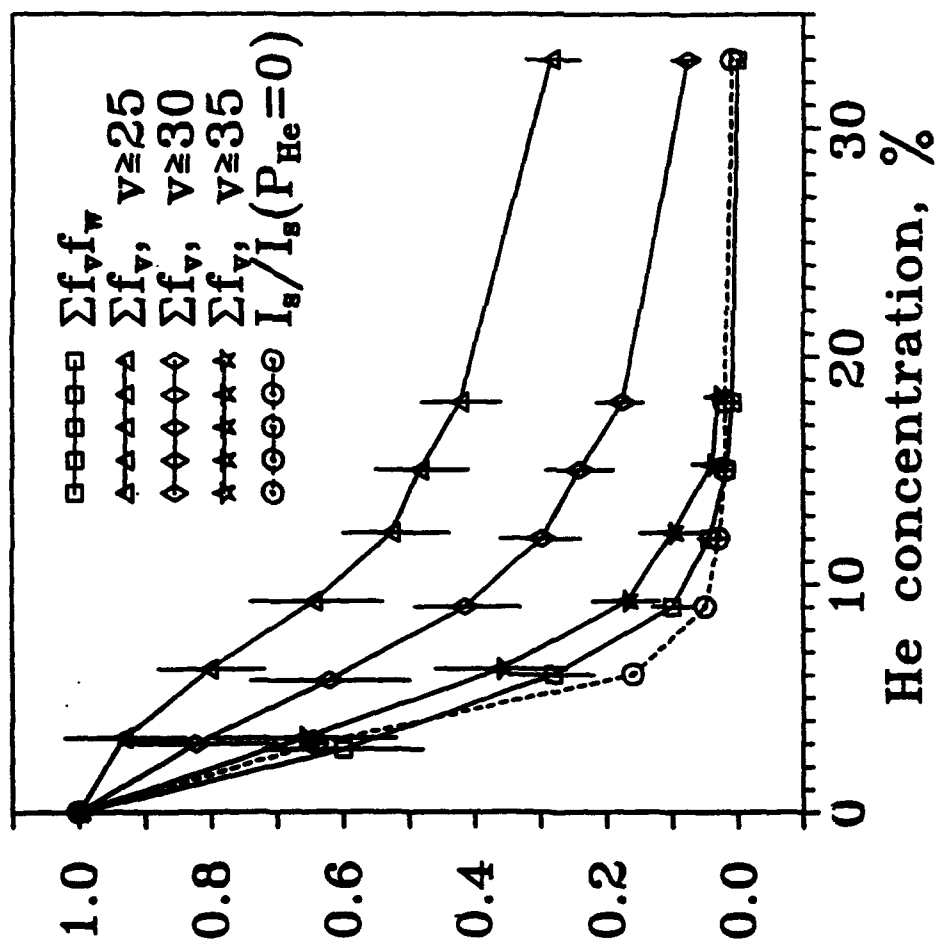


Figure 4.8. Experimental and theoretical voltage-current characteristics of the Thomson discharge



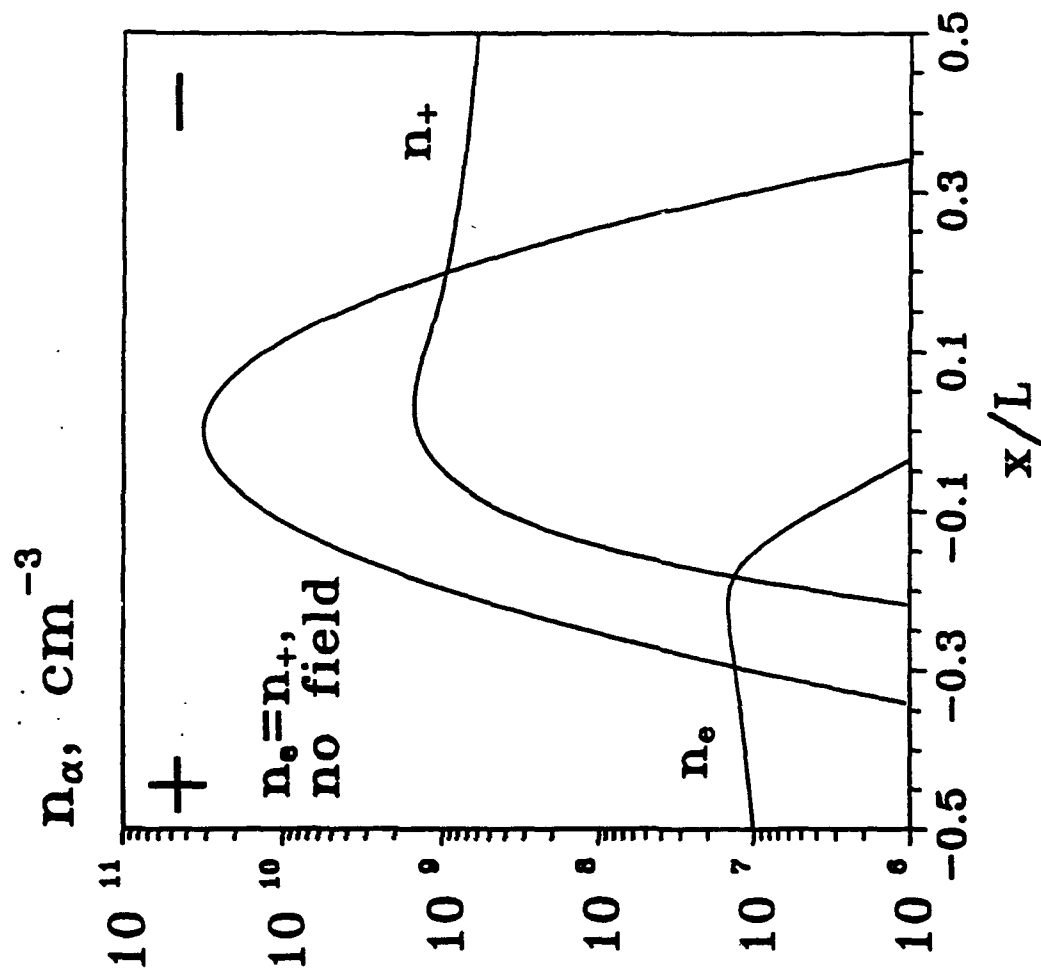


Figure 4.10. Charged species distributions in the Thomson discharge in the absence of the field and in the saturation regime.  $P=100$  torr,  $\text{CO:Ar}=3:97$ ,  $d/L=0.25$ ;  $q_1(0) = 10^{-21} \text{ cm}^3/\text{s}$  (see Eqs. 6, A2-A4).  $L$  - inter-electrode distance.

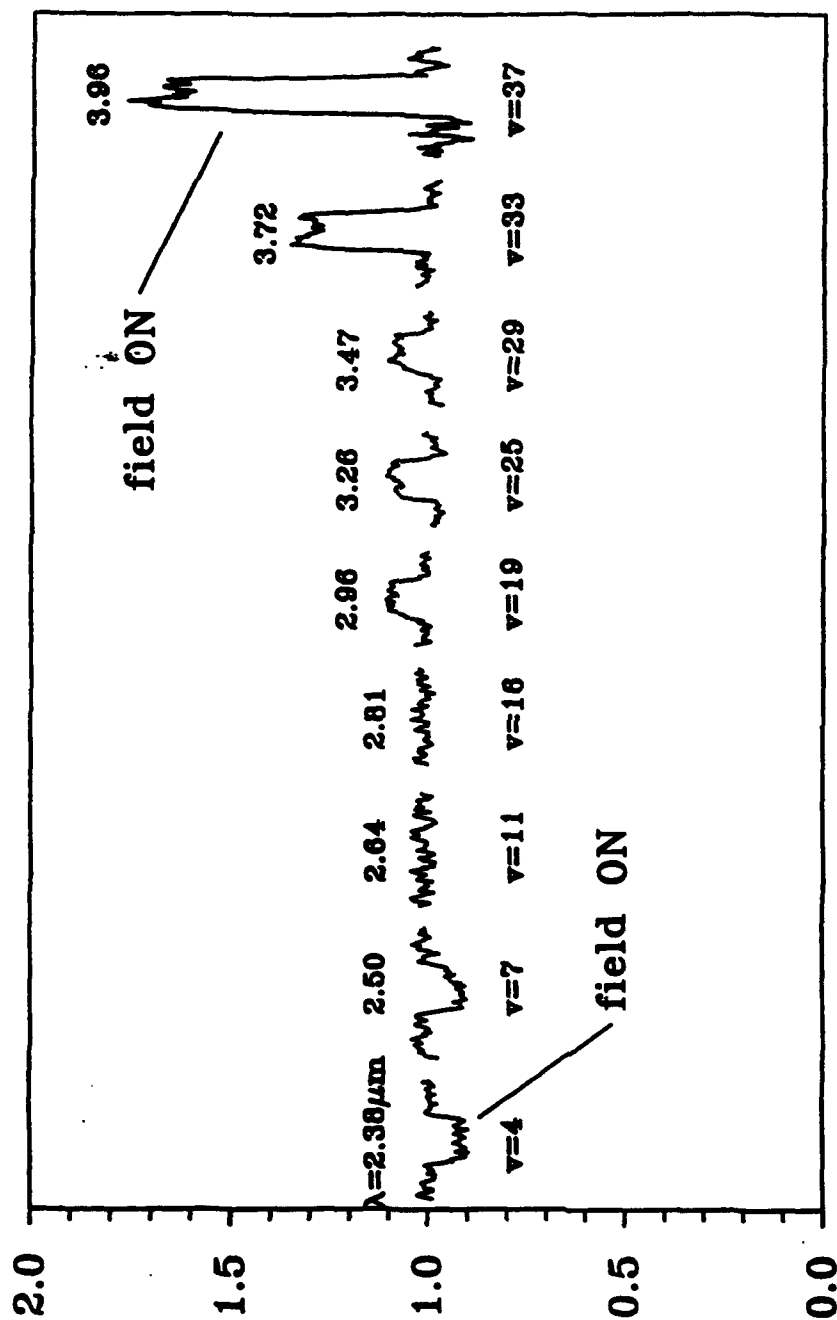


Figure 4.11. Electric field influence on different vibrational level populations

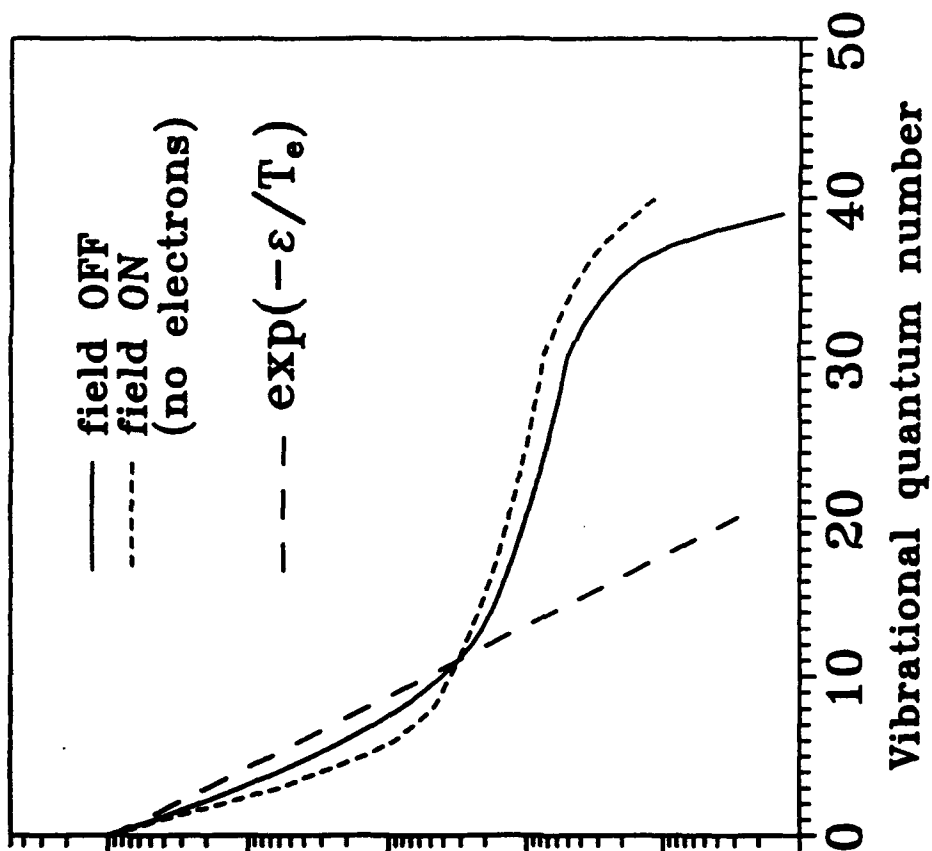


Figure 4.12. Qualitative demonstration of the  $V \rightarrow e \rightarrow V-\Delta V$  effect (strongly exaggerated).  $\epsilon$  - electron energy,  $T_e$  - electron temperature

**5. CARBON MONOXIDE STUDIES III:**  
**UV Radiation After Preparation of CO ( $a$ ,  $v=2$ ) State**

\*This chapter adapted from L.L. Cortney, "Ultraviolet Emission from Carbon Monoxide Excitation by an ArF Excimer Laser", M.S. Thesis, Ohio State Univ., Summer, 1993



## 5.1 Introduction

In these experiments, an ArF excimer laser (193 nm) was used to irradiate a CO / Ar mixture flowing through an optical cell. The resulting UV and visible fluorescence was collected and time dependent measurements taken.

The object of this work was to complete the first phase of a larger study whose purpose is to investigate how vibrational energy in the CO electronic ground state ( $X^1\Sigma^+$ ) is transferred with the low lying vibrational states,  $v$ , of excited electronic states ( $a^3\Pi$ ) and ( $A^1\Pi$ ), during V-V (vibration - vibration) pumping of the CO( $X^1\Sigma^+$ ).

In order to study this in a controlled manner, the overall plan is to observe the reverse process by preparing a significant population of CO ( $a^3\Pi$ ). Infrared and UV / visible diagnostics are to be used to observe the radiation resulting from any and all collisionally induced exchange or radiative processes. From these results, details of the original energy transfer processes under consideration are to be deduced.

The object of this phase of the study is to establish the experimental setup and obtain time dependent results of the UV/ visible emission from the CO mixture following irradiation by the laser pulse. This was done by using a commercial ArF excimer pump laser to irradiate an optical cell containing a gaseous mixture of CO and Ar as an inert diluent. The 193 nm wavelength output by the excimer laser is in near resonance with the  $v=2$  vibrational level of CO( $a^3\Pi$ ) and therefore populates that energy level of CO (Figure 5.8). Once the CO( $a^3\Pi$ ,  $v=2$ ) level is adequately populated, UV diagnostic equipment was used to observe the expected transfer of energy back into the ground electronic state. A gated integrator and boxcar averager was used to obtain the time

dependent traces of emission. From these results and other observations, some details of a few of the processes resulting from the  $a^3\Pi$  preparation have been concluded.

Electronic to vibrational energy transfer, one of the several modes of vibrational energy transfer that control the energy distributions in nonequilibrium gases, is the main focus of the study reported in this chapter. Slanger and Black (1975) [1] studied the efficiency of E-V transfer in three systems, one of which ( $\text{CO}(a^3\Pi)_{v=0} + \text{CO}$ ) is of direct importance to the present study. The basis of their technique relies on the phenomenon that in systems having sufficiently low total energy, all vibrational energy, no matter from which electronic level, eventually funnels into the ground  $v=1$  state. Therefore, after preparing the  $\text{CO}(a^3\Pi)$  using an iodine lamp, the radiation from the  $\text{CO}(X^1\Sigma^+)_{v=1}$  state with respect to time was observed. By comparing delay times with that of a control reaction, a determination of the efficiency of the collisionally induced energy transfer back into the ground state was made.

A simple model of E-V energy exchange during an atom - molecule collision has been developed (Schmalz , 1981 [2]) and although it does not include molecule - molecule collisions, it has the advantage of having exact solutions. Schmalz solves the model for two cases, one including the electronic level coupling due to curve crossing effects, the other representing parallel electronic potentials with no direct coupling. The model begins with the Schrödinger equation and uses a simple harmonic oscillator model for the diatom. From the solutions, transition probabilities are obtained and compared for the two models. As would be expected, the curve crossing model gives higher transition probabilities.

Ionikh and coworkers, 1986 [3], determined the rate constant for the E-V process of CO colliding with CO( $a^3\Pi$ ) which is the process studied in this thesis. The  $a^3\Pi$  state was prepared in a glow discharge and the rate of quenching of that state by collisions with other CO molecules was determined:



This was done by measuring the CO overtone distribution and comparing it with a calculated one which did not include the effects of the preceding reaction.

Some previous work on the preparation of the  $a^3\Pi$  state of CO includes Bokor et al. (1980) [4] who used an ArF laser at 193 nm to multiphoton dissociate CO. They reported reaction yielding excited carbon atoms, detected by absorbing a third photon and then emitting at 247.8 nm wavelength, and reported observing C<sub>2</sub> Swann band emission. Several years later (1988), Meijer and coworkers [5] showed that the C atom transition suggested by Bokor et al is actually an envelope of rotational lines in the CO( $a^3\Pi$ )  $v'=2 \rightarrow$  CO( $X^1\Sigma^+$ )  $v''=0$  transition.

Peterson and Woods (1990) [6] calculated the potential energy and dipole moment functions for the first two excited electronic states of CO, including the  $a^3\Pi$ . Markov et al. (1992) [7] determined the excitation function of the CO( $a^3\Pi$ ) by electron impact, and recently, Drabbles, Stolte and Meijer [8] excited CO to the  $v''=0$ ,  $a^3\Pi$  state using 206 nm pulsed laser radiation and produced an oriented pulsed beam of the metastable.

The Section 5.2 presents a description of the experimental setup and sections 5.3 and 5.4 discuss results and conclusions.

## **5.2 Experimental Set-up**

### **5.2.1 Gas Handling System**

A stainless steel, 6 - arm, Varian cross (Figure 5.1) optical cell was used. The gases flowed through the cell in the direction of the incoming laser beam. This direction was chosen such that the excited gases would flow away from the critical lithium fluoride (LiF) window at the laser beam entrance to the cell. This was done to help reduce the amount of carbon deposit built up on the LiF window surface. The laser then exited the cell through a  $\text{CaF}_2$  window (Figure 5.1). The emission was collected through a  $\text{MgF}_2$  lens on an axis perpendicular to that of the laser beam. Opposite this lens, a  $\text{CaF}_2$  window allowed for visual inspection of the emission (Figure 5.1), for example, to check for a visible glow.

Flowing through the cell was a gas mixture consisting of carbon monoxide in an argon bath. Argon was chosen, over helium, as the inert diluent

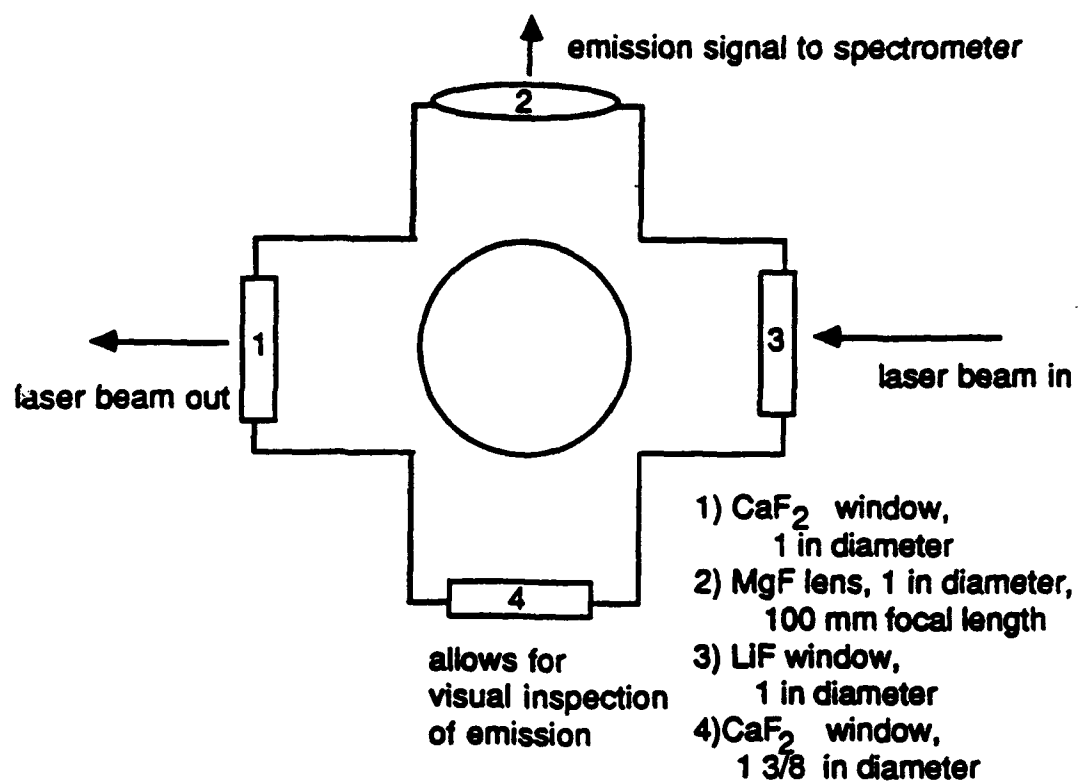


**Figure 5.1** Optics arrangement on optical cell, top view

because helium is a much stronger V-T relaxer, thus it removes energy from the vibrational mode, which is undesirable for the present purposes.

The gas handling system consists of 1/4 inch PVC tubing and various valves and flow metering devices as shown in Figure 5.2. The rotameter used for the CO was a Porter model B-250-2 tube with a spherical glass float. Argon flowed through a Brooks Instrument Division type 1110-06-F1D1-A rotameter with a size R-6-15-B tube with what appears to be a stainless steel spherical float. These rotameters were chosen for their availability.

The gases were pumped through the cell and exhausted to the atmosphere outside the lab by a Cenco Hyvac 14 vacuum pump (Figure 5.2). A valve to the atmosphere allowed for bleeding air into the inlet of the pump after shutting it off to prevent sucking pump oil back into the gas handling lines. An additional shut off valve (Nupro plug valve) was installed, near the pump shut off valve (Figure 5.2), to allow for throttling of the gas flow if desired.

A pressure tap on the vertical arm of the optical cell allowed for continuous monitoring of cell pressure by two Wallace & Tiernan analog pressure gages (Figure 5.2). One allowed for reading pressures from 0 to 20 torr with better resolution than the other which read pressure up to 800 torr. A valve to atmosphere here (Figure 5.2) allowed for bleeding air into the cell when it was desired to bring it up to atmospheric pressure, such as when removing the windows for cleaning.

### 5.2.2 Steady State Spectral Measurement Set-Up

During calibration of the UV spectrometer or during determination of the spectral line width function for a given slit setting, scans of steady state spectra

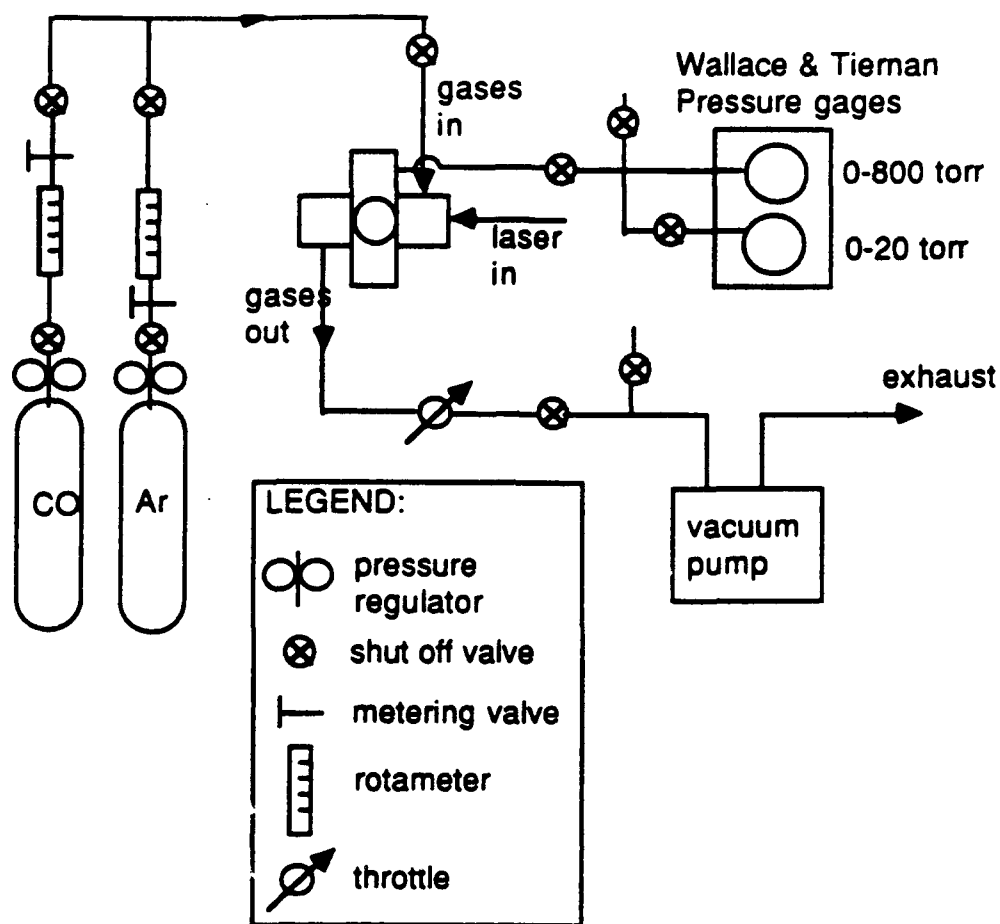


**Figure 5.2** Gas Handling System for the Optical Cell

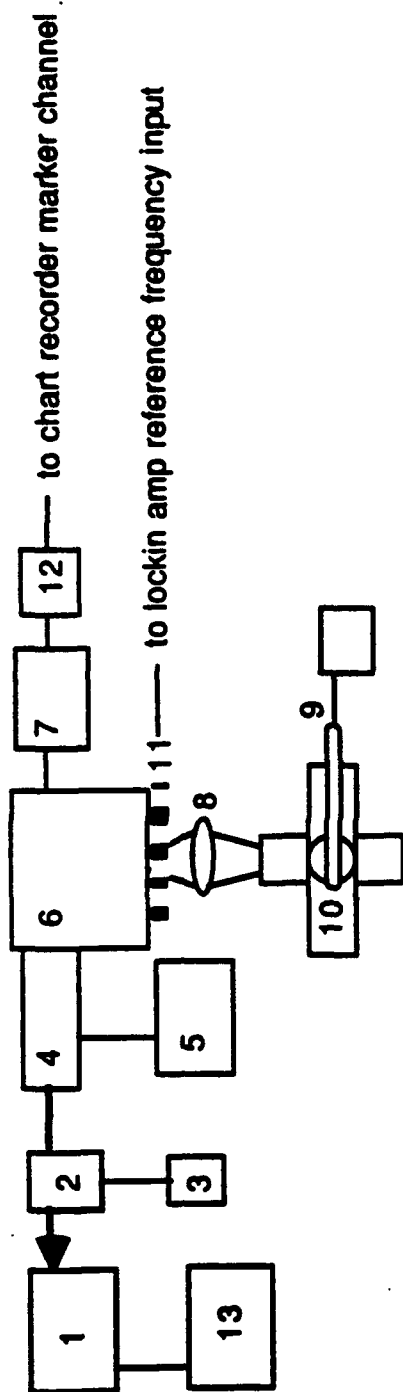
from a mercury - argon (HgAr) lamp were taken. The setup for these scans is shown in Figure 5.3 with equipment as listed in Table 5.1.

The LiF window (Figure 5.1) was removed from the cell and the HgAr lamp inserted to simulate emission along the same path as the laser beam. Lamp emission was focused as best as possible, given the fixed positions of the cell and spectrometer, with available lenses. A  $\text{MgF}_2$  lens with a 100 mm focal length was mounted on the cell and one with a 200 mm focal length was mounted between the cell and the Spex Model 1870 spectrometer (Figure 5.3). A Stanford Research Systems (SRS) Model SR540 optical chopper placed just before the entrance slit of the spectrometer, chopped the incoming emission signal and sent a reference frequency to the SRS Model SR510 Lockin Amplifier.

The 1/2 meter spectrometer is equipped with a Bausch & Lomb diffraction grating blazed at 2500 Å, with 1200 grooves / mm. The grating is scanned with a Spex Model 1872 Minidrive. A Thorn EMI Model 9635-QB bialkali photomultiplier tube (PMT) powered by a Thorn EMI Model 3000R high voltage power supply, detected the signal from the spectrometer. PMT output voltage was amplified by a Thorn EMI Model A1 preamplifier, and powered by a Lambda Model LZD-32 low voltage power supply. The typical spectral response of the PMT is given in Figure 5.4 a along with the grating efficiency (Figure 5.4 b).

The preamplified signal was then sent into the lockin amplifier which amplified only that component of the signal that entered at the reference frequency sent by the chopper. Amplified signal from the lockin was then recorded by a Kipp & Zonen Model BD41 chart recorder. In order to record the

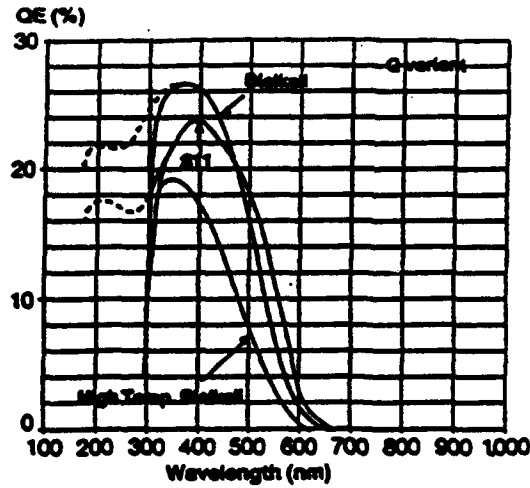




- |                              |                              |
|------------------------------|------------------------------|
| 1) LOCKIN AMPLIFIER          | 8) LENS                      |
| 2) PRE AMPLIFIER             | 9) HgAr LAMP w/ POWER SUPPLY |
| 3) LOW VOLTAGE POWER SUPPLY  | 10) OPTICAL ABSORPTION CELL  |
| 4) PHOTOMULTIPLIER TUBE      | 11) OPTICAL CHOPPER          |
| 5) HIGH VOLTAGE POWER SUPPLY | 12) PULSE GENERATOR          |
| 6) UV / VISIBLE SPECTROMETER | 13) CHART RECORDER           |
| 7) SPECTROMETER CONTROLLER   |                              |

**Figure 5.3** Schematic of set up used to take steady state calibration spectra

(a) Spectral Response



(b)

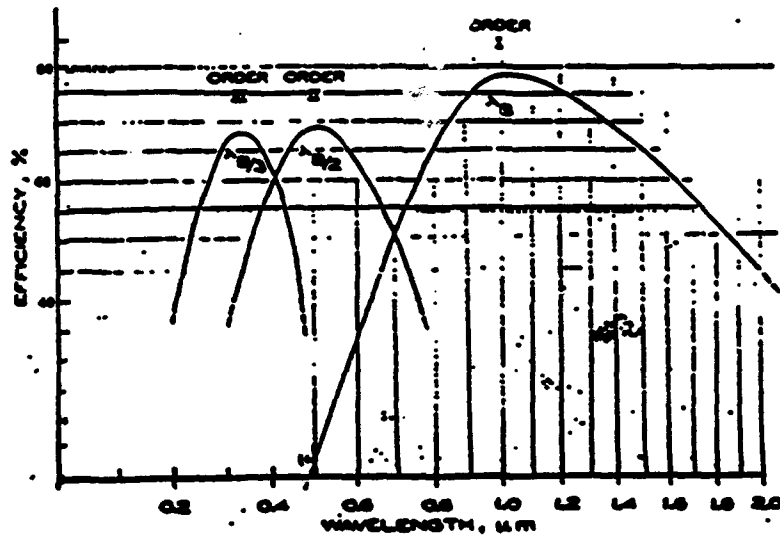


**Figure 5.4** Typical spectral response of the PMT (a) and grating efficiency (b). Note that the grating efficiency is typical, to be applied to the 2500 Å blaze grating used in these experiments, one must multiply the wavelengths by 0.25

**TABLE 5.1 . Experimental Set-Up Equipment List.**

<b>EQUIPMENT</b>	<b>MANUFACTURER</b>	<b>MODEL</b>
Excimer Laser (ArF)	Questek	2640
Chart Recorder	Kipp & Zonen	BD41
Gated Integrator and Boxcar Averager	Stanford Research Systems	SR250
Lock-in Amplifier	Stanford Research Systems	SR510
Optical Chopper	Stanford Research Systems	SR540
Digitizing Oscilloscope	Hewlett Packard	54501A 100 MHz
Spectrometer	Spex Industries	1870
Spectrometer Controller, Minidrive	Spex Industries	1872
Photomultiplier Tube	Thorn EMI	9635-QB bialkali
HV Power Supply for PMT	Thorn EMI	3000R
Pre Amplifier	Thorn EMI	A1
LV Power Supply for Pre Amp	Lambda	LZD-32

corresponding wavelengths, an event marker, linked to the scanning drive, provides a wavelength scale (see Appendix ).

### 5.2.3 Time Integrated (Quasi- Steady State) Measurement Setup

To provide a quick, overall picture of the emission from the CO mixture over a range of approximately 1700 Å to 5200 Å, a "quasi steady state" setup was used (Figure 5.5). The Pulse Energy BNC output from the excimer laser provided the necessary reference frequency for the lockin to amplify the signal from the Thorn EMI preamp. A scan through a given range then provided a time integrated picture of the emission spectra, realizing that only the strongest and/or longest lived signals would be observable.

### 5.2.4 Time Dependent Measurement Set Up

In order to study the emission generated by the pulsed laser excitation, a time dependent measurement system was set up (Figure 5.6). A modification of this setup (Figure 5.3) has been presented in Section 5.2.2 as the steady state spectra set-up.

A Questek Model 2640 Excimer Laser in ArF mode, emitting pulsed laser radiation at 193 nm in bursts of 10 ns duration, was used to excite CO molecules from the  $X^1\Sigma^+$ ,  $v=0$  to the  $a^3\Pi$ ,  $v=2$  state. The laser beam was apertured to approximately 5/8 inch diameter and then it entered the optical cell through a 1" diameter LiF window (Figure 5.1). Upon exiting the cell, the unabsorbed portion of the beam was stopped using a fire brick. Here, a pulsed head for a Coherent Labmaster power meter could be inserted periodically to check transmitted laser power.

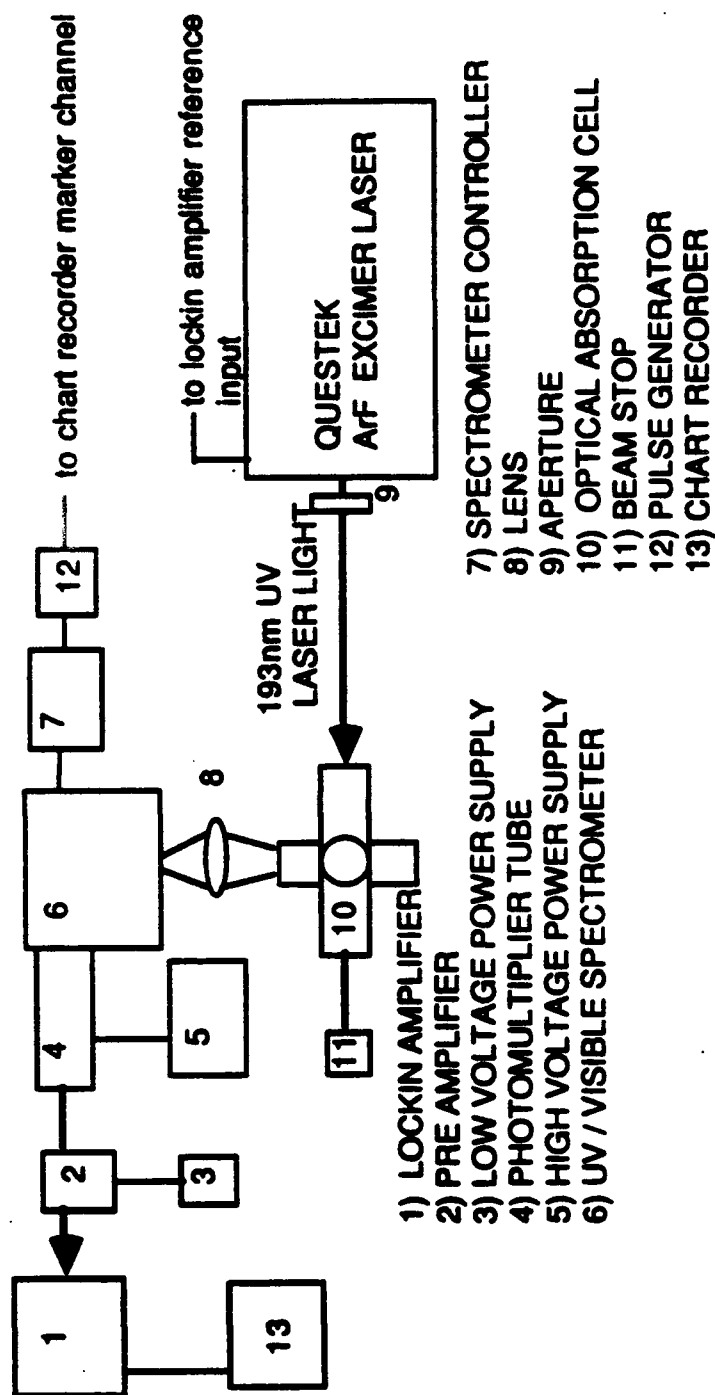


**Figure 5.5** Schematic of set up used to take time integrated measurements

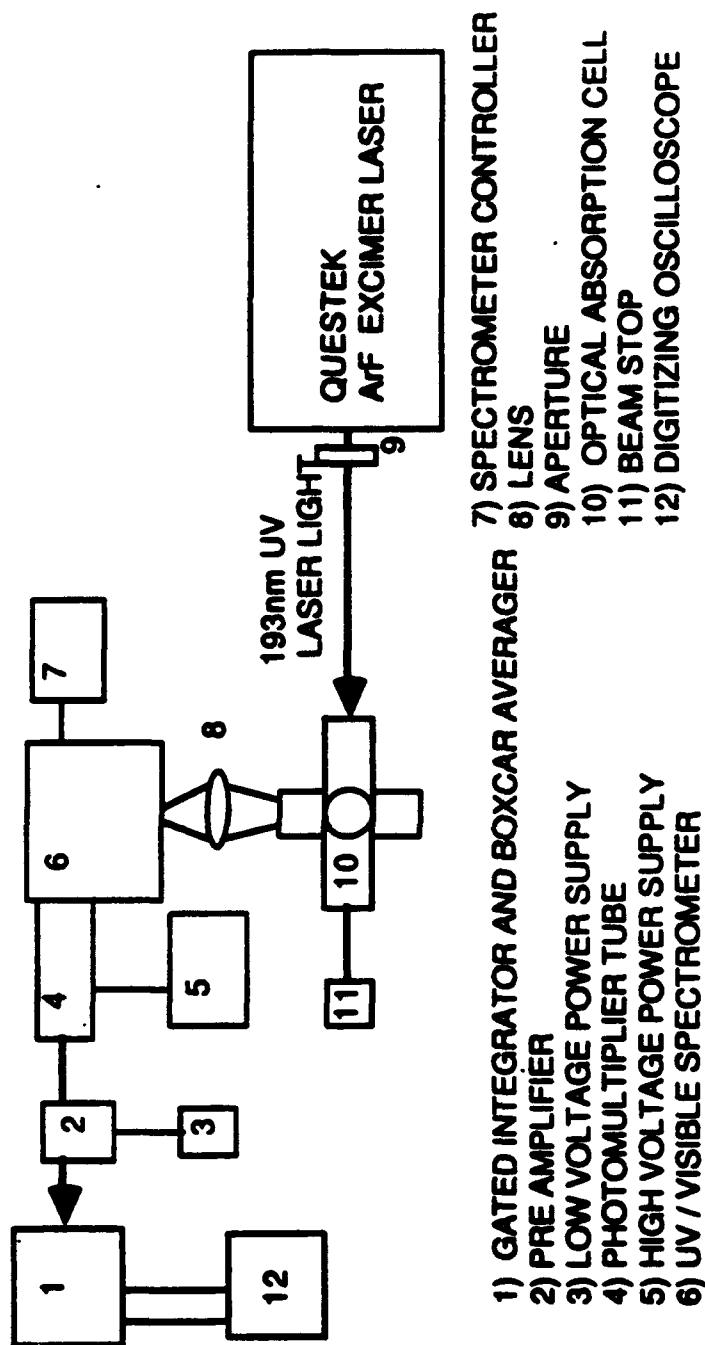


**Figure 5.6** Schematic of set up used to take time dependent measurements

Upon irradiation from the incident laser beam, CO in the cell was excited to the  $a^3\Pi, v=2$  state (Figure 5.8). Figure 5.7 illustrates the rotational level transitions in CO that absorb the incident laser pulse. The vertical axis is merely the absorption coefficient given in arbitrary units. The computer code calculates the absorption based on conditions such as CO partial pressure in the cell, temperature, laser power and the absorption volume. This allows for inclusion of pressure and temperature broadening effects.

Subsequent UV / visible emission from the prepared state was collected by being focused onto the inlet slits of the spectrometer (Figure 5.6) just as the lamp emission was collected (Figure 5.3). However, in this case, after preamplification, the signal entered an SRS Model SR250 Gated Integrator and Boxcar Averager (Figure 5.6). The boxcar was triggered off of the Pulse Energy BNC on the excimer laser's I / O panel. This output BNC provided a voltage proportional to the pulse energy of the laser, therefore triggering the boxcar at every laser pulse.

The boxcar functions as shown in Figure 5.9. Following the trigger, the boxcar waits for the set delay time to pass and then starts the gate. Any signal entering the boxcar during the set gate width is averaged over the number of samples, also set by the user. The averaged output can then be viewed and recorded by connecting it to one of the meters on the display module of the boxcar (Figure 5.10).

A Hewlett Packard Model 54501A Digitizing Oscilloscope was used to view the signal by setting the scope and boxcar up as shown in Figure 5.10. The scope was triggered off of the gate output of the boxcar and the signal coming into the boxcar was viewed on channel 1 of the scope. This method

allowed for visualizing the exact portion of the signal being averaged by the boxcar since the gate width was shown as a rectangular pulse on the scope's channel 4.



CO( $X^1\Sigma-a^3\pi$ , 0-2) transitions

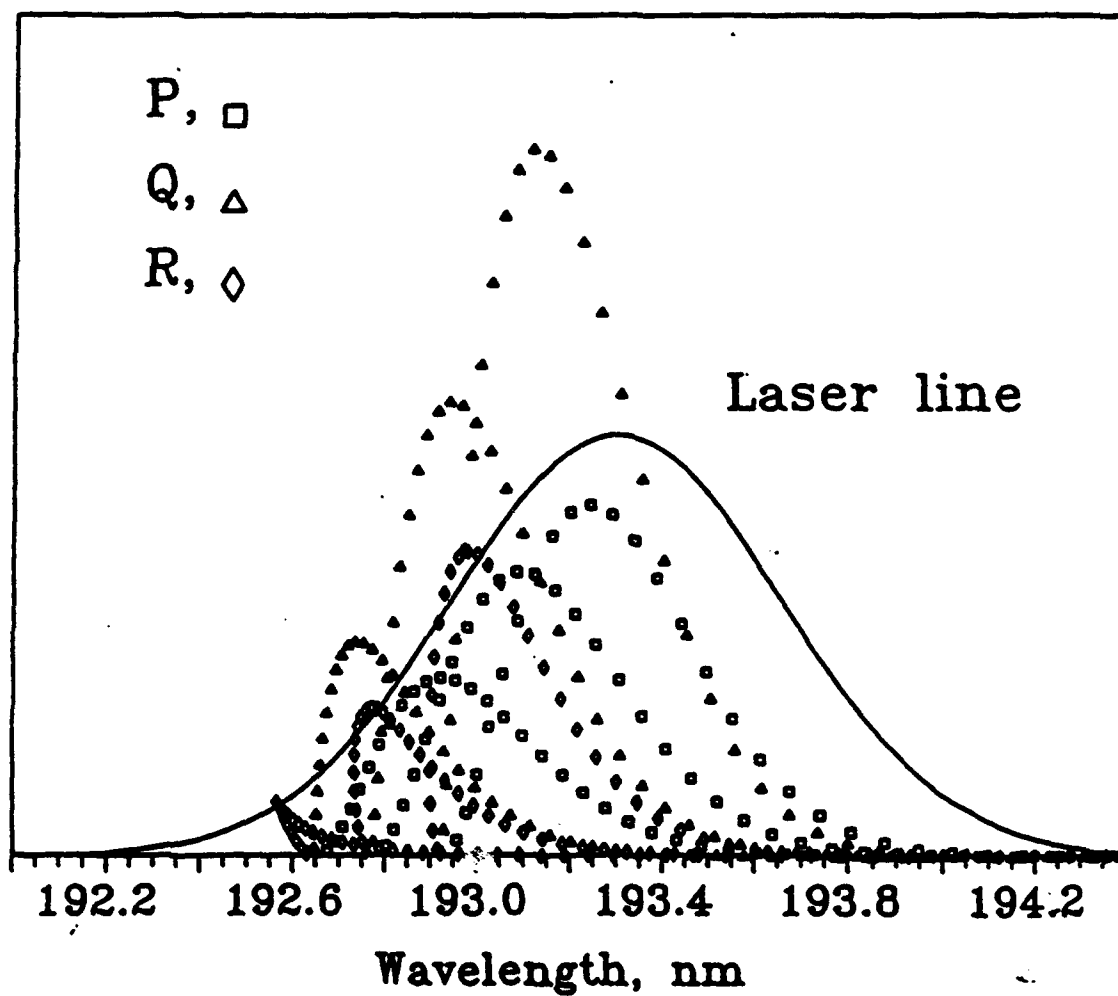


**Figure 5.7** CO( $X^1\Sigma^+$ )  $\rightarrow$  CO( $a^3\Pi$ ) absorption lines with the typical width of the pump laser line

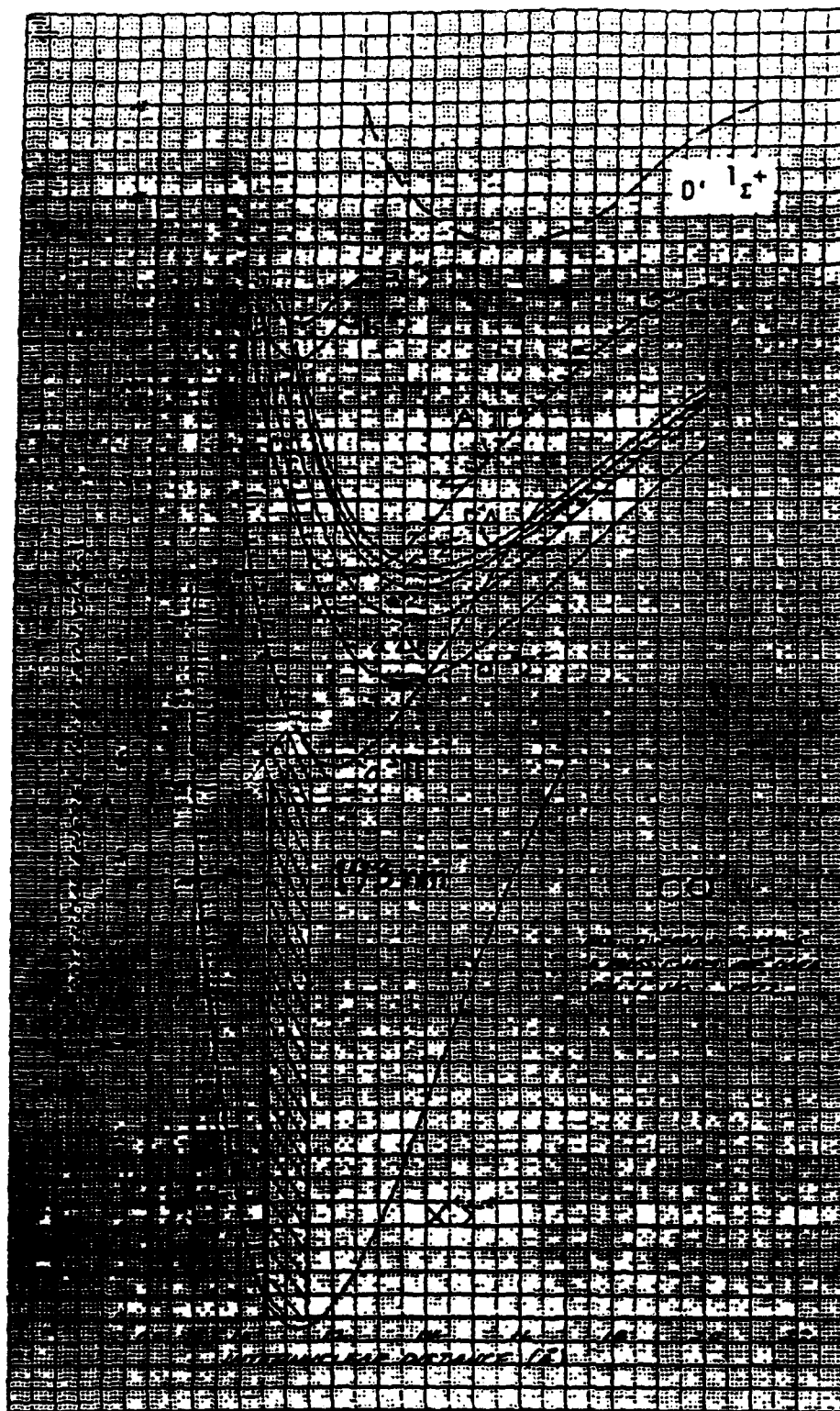
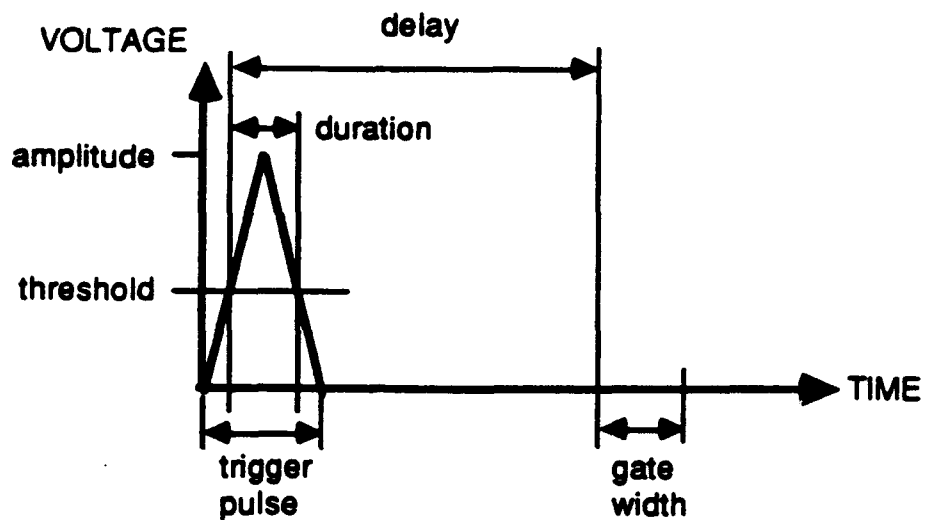


**Figure 5.8** Energy level diagram of CO illustrating the 193 nm pump laser transition



**Trigger:** amplitude - at least 0.5 volt , prefer <5 volts  
 threshold - 0.5 volt to 2.0 volts  
 duration -  $\geq 5$  ns  
 rise time -  $< 10 \mu\text{s}$   
 trigger rate - maximum 20 kHz

**Delay:** 1 ns to 10 ms (plus 25 ns trigger discriminator)

**Gate Width:** 2 ns to  $15 \mu\text{s}$

**Figure 5.9** Boxcar specifications with respect to time

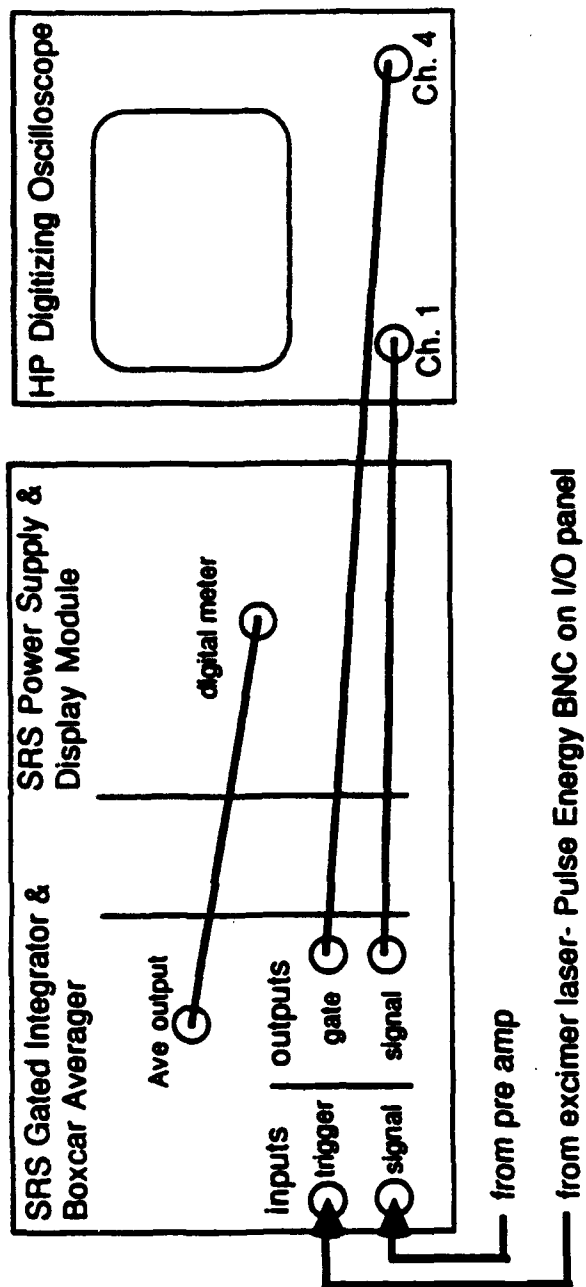


**Figure 5.10** Signal Processing Diagram for Boxcar and Oscilloscope

### 5.3 Experimental Results

This section discusses the experimental results obtained with the set-ups described in Section 5.2. Experimental conditions, and observations are presented with discussions of the possible energy transfer processes involved.

#### 5.3.1 Spectrometer Calibration and Determination of Scanning Function

Wavelengths were calibrated in the range 2500 to 5800 Å by scanning the emission of a HgAr lamp using the steady state setup described in Section 5.3.2. Reported wavelengths are accurate to  $\pm 2$  Å.

The line width scanning function of the spectrometer for a given slit opening was similarly determined. By scanning a known lamp line and measuring its full width at half of its maximum intensity (FWHM), an indication of the possible wavelength resolution was obtained for a given slit width. This was done for four slit sizes and the results are given in Table 5.2.

**Table 5.2.** Scanning Functions of the SPEX 1870 Spectrometer with 2500 Å Blaze Grating (1200 grooves/mm)

Slit Opening	FWHM (Å)
400 $\mu$	7
600 $\mu$	15 - 20
1 mm	30 - 60
2 mm	150

### 5.3.2 Results for Delay Setting of 1 $\mu$ sec

In order to establish which wavelengths were being emitted by the gas mixture in the cell, the time dependent set-up (Section 5.2.4, Figure 5.6) was used with the boxcar set at 1  $\mu$ sec delay. This delay was chosen after determining that the peak intensity of the signal at 2799.7 Å (with 2 mm slits) occurs at 1  $\mu$ sec. This wavelength had initially been considered due to being known as a strong CO 4th Positive band [19] and was found to be one of the strongest signals observed in these experiments.

With the boxcar set at 1  $\mu$ sec, a datum for a given wavelength was recorded by taking a time averaged reading of the signal emitted from the cell with and without the CO / Ar gas mixture flowing through the cell. By subtracting the baseline signal (the one taken with no gases in the cell), an emission signal intensity was determined. This was done for several wavelengths and the results are given in Figure 5.11.

# Results at 1 $\mu$ sec delay

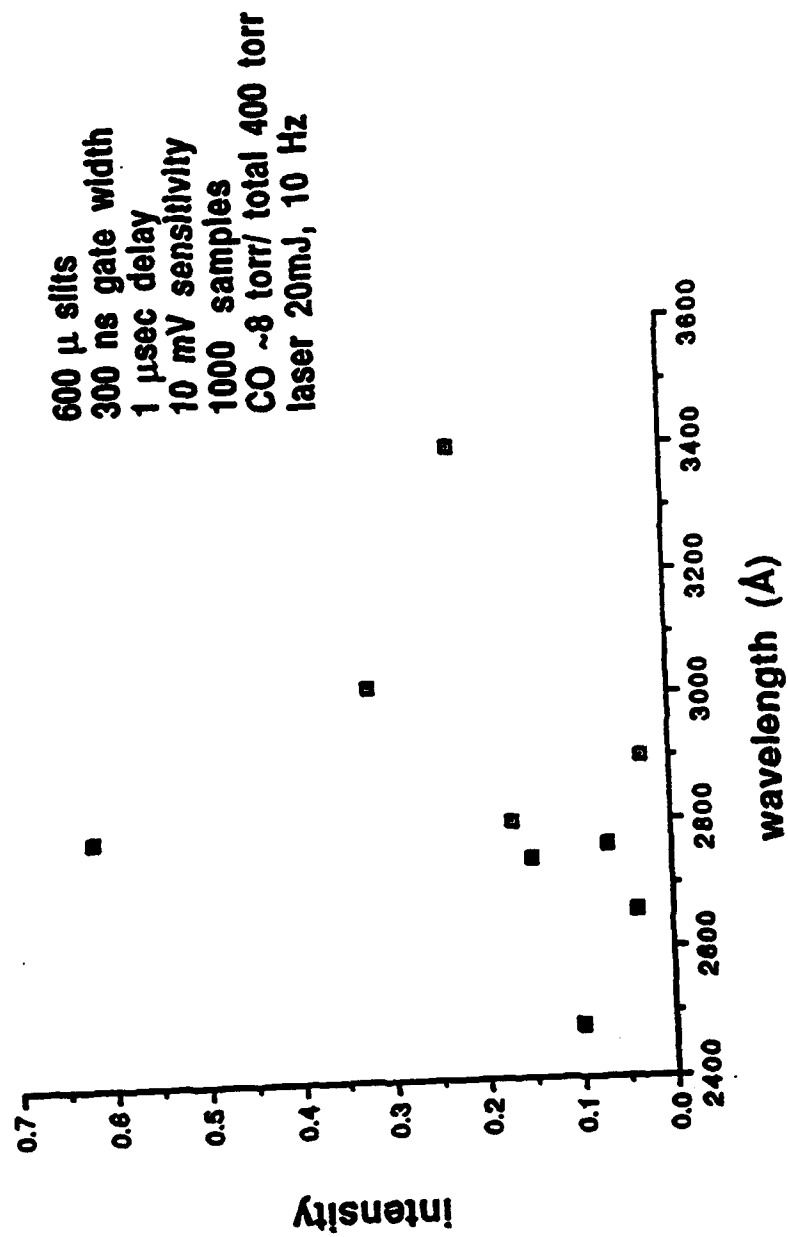


Figure 5.11 Results found at 1  $\mu$ sec delay

The amount of time required to take each reading was determined by dividing *the number of samples being averaged by the boxcar by the repetition rate of the laser (boxcar trigger rate)* . This number indicates the time constant of the exponential moving average being given by the boxcar. Since the signal reading from the boxcar approaches 99% of its value in 5 time constants, it is desired to wait at least this long before recording a data point. In this case, the typical running conditions of 10 Hz laser repetition rate and 1000 samples mandate that 9 or 10 minutes be required to take a data point.

In addition to the 1  $\mu$ sec delay time, 1000 samples and 10 Hz laser repetition rate, the typical conditions used while taking these readings were: 600  $\mu$  slits, 700 V PMT voltage, boxcar settings of 300 ns gate width and 10 mV sensitivity, and 20 mJ laser pulse energy. Wavelength selection was based on several factors. The purpose of taking these readings was to see what wavelengths were being emitted and from that, deduce what energy transitions in the molecules were occurring. For this reason, wavelengths corresponding to transitions found to give a strong emission in band systems that were expected to occur, given the level of excitation, were chosen. Two band systems in particular were explored; the Cameron bands ( $\text{CO}(a^3\Pi) \rightarrow \text{CO}(X^1\Sigma^+)$ ) and the 4th Positive bands ( $\text{CO}(A^1\Pi) \rightarrow \text{CO}(X^1\Sigma^+)$ ).

The choice of the former system follows from the fact that a vibrational level of the  $a^3\Pi$  is being prepared by the laser pulse. The 4th Positive system, however, was selected for several reasons. First, the  $A^1\Pi$  is the lowest lying excited singlet electronic state of CO and is low enough to be in the realm of possible interactions among the electronic states. In addition if the  $A^1\Pi$  were to be excited, the strongly allowed singlet - singlet 4th Positive system (10.69 nsec



lifetime) is a powerful radiator. Another reason for viewing 4th Positive lines is due to the fact that there is an overlap in the wavelengths of the Cameron bands and the 4th Positive. For this reason, 4th Positive bands at wavelengths longer than the longest Cameron band wavelength were checked so that any signal found in the overlap region could be identified. If a 4th Positive line is found outside of the overlap region, there is a good chance that other 4th Positive lines are emitting and this must be considered when evaluating the existence of Cameron bands.

In addition to wavelengths selected for their expected strength, some were chosen that were not expected to have a signal in order to provide a reference. To check for repeatability and to increase confidence in the results, the signal at several of the wavelengths was recorded again on several different days, the average of which is plotted in Figure 5.11. The level of detection in this setup was approximately 0.02 V boxcar output.

### Observations

It should be noted that the characteristic blue glow ( $C_2$  Swann Bands), commonly observed when CO is excited by infrared laser radiation, was never observed in any of the experiments discussed in this thesis. However, carbon deposition on the windows (#1, #3 in Figure 5.1) occurred in visible amounts significant enough to attenuate the incoming laser beam and reduce the emission signal. This required cleaning of the windows with methanol on a daily basis.

The fact that carbon was being formed most likely indicates one of two possibilities. First, multiphoton processes could be occurring causing the

dissociation of CO and the subsequent recombination of two carbon atoms to form C<sub>2</sub> which then attaches to the surfaces of the windows. A second possibility is that reaction:



is occurring where at least one of the reactants is CO(a<sup>3</sup>Π).

The feasibility of the first process occurring was tested. Multiphoton processes that Bokor et al. studied required a power density on the order of 10<sup>7</sup>-10<sup>9</sup> W/cm<sup>2</sup> [4] and the power density supplied by the laser when set at 20 mJ is only 10<sup>6</sup> W/cm<sup>2</sup>. Also, two CaF<sub>2</sub> windows were placed between the aperture and the cell to act as attenuators of the beam. This supplied approximately 25% attenuation; however, when the cell windows were removed for cleaning, there was still noticeable carbon deposition.

#### Identification of 1 μsec Results

This section will involve the discussion and possibilities for the identification of the results given in Figure 5.1. Identification of these experimental results was done by using the tabulation of observed spectra given in Pearse and Gaydon, "The Identification of Molecular Spectra" [9]. All relevant band systems of CO were checked in addition to the systems of other molecules. These include the Schumann - Runge system in O<sub>2</sub>, several systems in N<sub>2</sub>, the CN Violet system (known to be persistent in the event of an air leak into the system), the C<sub>2</sub> Swann system and the Fox-Herzberg system in C<sub>2</sub>. Also, atomic lines of oxygen, argon, carbon and nitrogen were checked.

Discussion will begin with the strongest line seen in this set of experiments, the 2785.4 Å. There was repeatedly a strong signal at this wavelength. Due to the scanning function at 600 μ slit width (Table 5.2), the monochromator set to this wavelength actually encompasses a range of about 2775 to 2795 Å. This line is attributed to the 4th Positive (CO(A<sup>1</sup>Π) v=4 --> CO(X<sup>1</sup>Σ<sup>+</sup>) v=18) transition for the following reasons. First, by looking at observed spectra in CO in Pearse and Gaydon [9], only this transition and that of the (1,1) transition (2793.1 Å) in the 3rd Positive system lie within the range stated above. The 3rd Positive transition was ruled out because a signal seen at 2800 Å, which is closer to 2793, was not as strong. The only other lines within 2775 to 2795 occur in a weak transition of the N<sub>2</sub> 4th Positive group and a transition in the C<sub>2</sub> Fox Herzberg system. The nitrogen line was ruled out due to the fact that, unless there is a considerable leak in the system, the amount of nitrogen in the cell should be negligible. As far as the carbon line goes, there was no other indication of any other lines in that system occurring, therefore, it was assumed not to be the source of the signal.

Other strong signals were found at 2478 ± 10 Å, 2742 ± 10 Å, 3020 ± 10 Å. Due to the presence of so many possible transitions lying within the given ranges, no conclusive identification was given. However, if only CO bands and carbon atom transitions are considered, the 2478 line could be accounted for either by the carbon atom transition (2478 Å) or by the (6 --> 17) 4th Positive transition (2483.8 Å). Similarly, the 2742 line could be due either of the (11--> 23) or the (7 --> 20) 4th Positive transition (2742.6 Å and 2740.0 Å, respectively). However, the source of the strong line at 3020 ± 10 Å is still unknown. It occurs beyond the 4th Positive system but before the CN Violet.

The closest line found to be near it is a transition in the Gaydon Herman system of  $N_2$ .

One question that needs to be addressed is, why isn't there an indication of any Cameron bands? Knowing that the Cameron system occurs from the radiation of the  $CO(a^3\Pi)$  and that the  $v=2$  level of the  $CO(a^3\Pi)$  has been prepared, it seems to follow that the Cameron bands would be observed. However, it is known that the Cameron bands are much weaker, by at least an order of magnitude, than the bands of the 4th Positive. For this reason, given the low level of signal seen at what has been attributed to a 4th Positive transition, the chance of picking up a signal an order of magnitude weaker is slim. However, there is a chance of picking up the radiation of the  $CO(a^3\Pi) v=2$  to  $CO(X^1\Sigma^+) v=0$  since this is the level of  $CO(a^3\Pi)$  being prepared.

### 5.3.3 Time Integrated Results

Several spectra were taken using the setup of Section 5.2.3. This mode of measurement allowed an overall look at a large range of wavelengths relatively quickly. However, as previously mentioned, any signal to be recorded in this way would have to be very strong and / or long lived. With this in mind, various spectra were recorded covering the range from 1700 to 5200 Å. Three obvious band systems were discovered (Figure 5.12).

Two of these are easily explained as the laser pulse in first and second order (1930, 3860 Å, respectively). However, these bands respond to shutting off the gas flow through the cell by decreasing in intensity, in other words when gases are in the cell, the signal is stronger indicating a contribution due to emission.

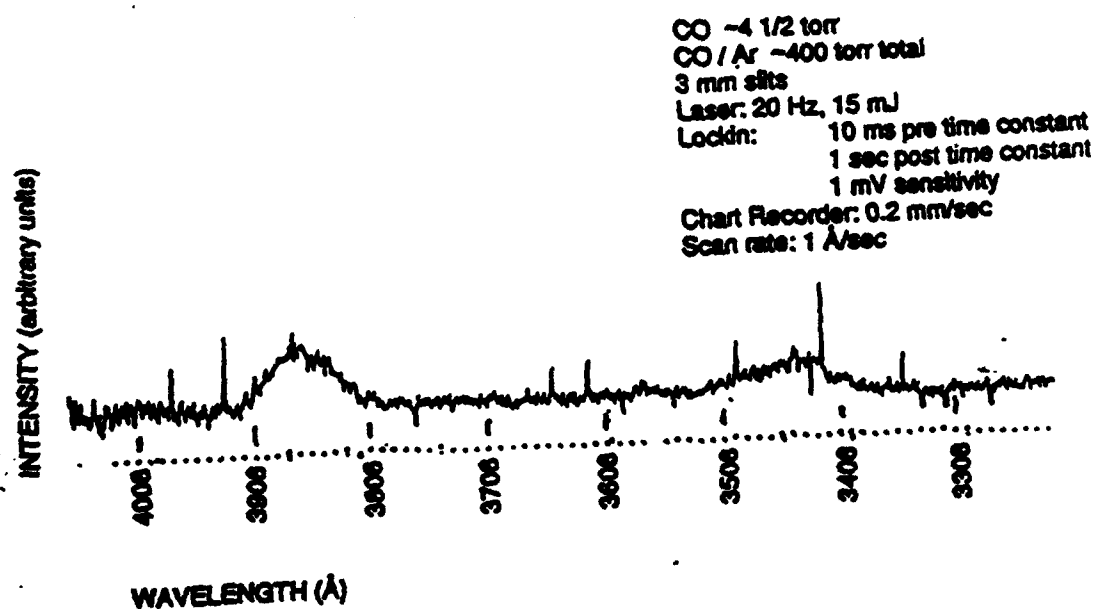
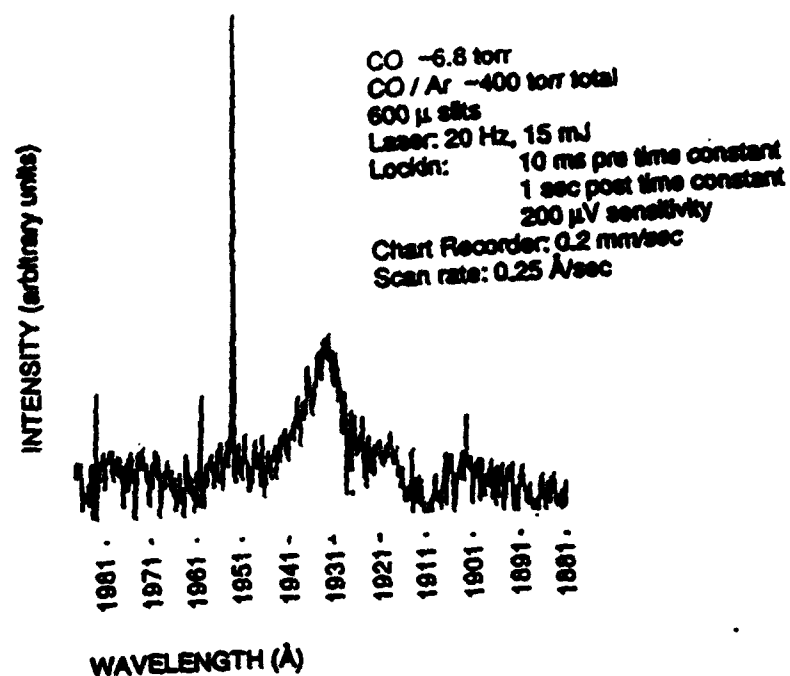


Figure 5.12 Quasi Steady State Results

Therefore, it is believed that the signals at 1930 and 3860 Å are due to a combination of the laser radiation and the induced fluorescence of CO on the  $\text{CO}(a^3\Pi) v=2$  to  $\text{CO}(X^1\Sigma^+) v=0$  transition.

The third band system discovered, upon further investigation, was found to consist of two smaller bands (Figure 5.13) peaked at around 3440 and 3490 Å. These systems do not occur when no gases are flowing through the cell. Similarly, when the CO is shut off, leaving Ar only the cell, the signal disappears. Considering the strength of the signal, near the same intensity of that of the laser pulse itself, it was suspected that the signal be due to a transition from a vibrational level near that of the prepared  $v=2$  in the  $a^3\Pi$ . By looking at the wavelengths of all possible transitions from the  $a^3\Pi$  (Appendix) and especially at those included in the locus of high transition probabilities, the Condon Parabola, the closest match was determined.

Although not right on the Condon Parabola, the two closest matching transitions were found to be (5  $\rightarrow$  14) at 3432 Å and the (7  $\rightarrow$  16) at 3483 Å. Keep in mind that the calculations give band origins, whereas the actual peak of the band (band head) may occur at a different wavelength. For example, the band origin calculated for the (2  $\rightarrow$  0) transition is 1928 Å and the actual band head occurs at a longer wavelength. Also, as one increases vibrational levels, the anharmonicity of the molecule has more of an effect. Therefore, the calculations (Appendix), which rely on constants fit to experimental data, have the potential of increasing error as the vibrational levels increase.

Here, another question must be addressed. If emission from the  $v=2, 5$ , and 7 levels of  $\text{CO}(a^3\Pi)$  is observed, why not from  $v=1, 3, 4$  and 6? According to the lower branch of the Condon Parabola (Table 5.A5) the favored transitions

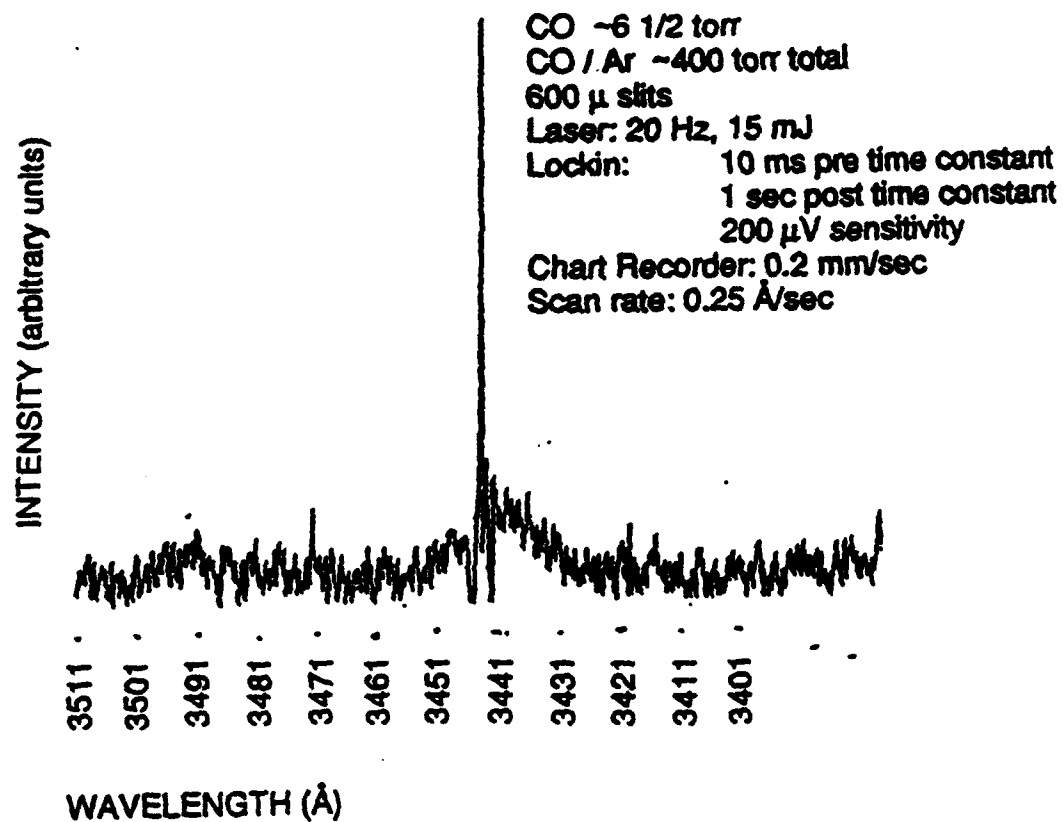


**Figure 5.13** 3440  $\text{\AA}$  system at higher resolution (600  $\mu$  slits) illustrating its two bands

originating from these states are as follows:  $v=1 \rightarrow 4$  or  $5$  (2394, 2517),  $v=3 \rightarrow 8$  (2694),  $v=4 \rightarrow 9$  or  $10$  (2716, 2865) and  $v=6 \rightarrow 12$  (2912). The upper branch of the Condon Parabola extends into the vacuum UV where any emission would be almost completely absorbed by the atmosphere, rendering it undetectable with the present set-up.

These wavelengths all fall within the range scanned during the time integrated measurements; however, no signal was observed. Also, all but the longest two wavelengths overlap the range of known 4th Positive lines [9]. The undetected emission from these wavelengths remains an unresolved question.

#### 5.3.4 Time Dependent Results

The final set of results was taken using the set-up described in Section 5.2.4. For each of the band systems discovered in quasi - steady state mode, a time dependent trace was obtained. However, due to equipment limitations, only qualitative conclusions may be drawn. The preamplifier currently used is a Thorn EMI Model A1. This preamp has four settings which trade off gain with instrument rise time. In order to amplify the signal to adequate levels for use by the boxcar, the rise time became unacceptably long, from 200 nsec to 20  $\mu$ sec depending on the setting. Thus, the true time dependence of the signal is masked, leaving only the possibility of qualitative comparisons between the signals obtained at the same gain setting.

It was found that the signal at 3860 Å rose sooner (Figure 5.14) and decayed faster (Figure 5.15) than 3440 Å. This indicates that the processes leading to the population of the originating vibrational states (in this



### Time Dependent Signal from CO / Ar Mixture

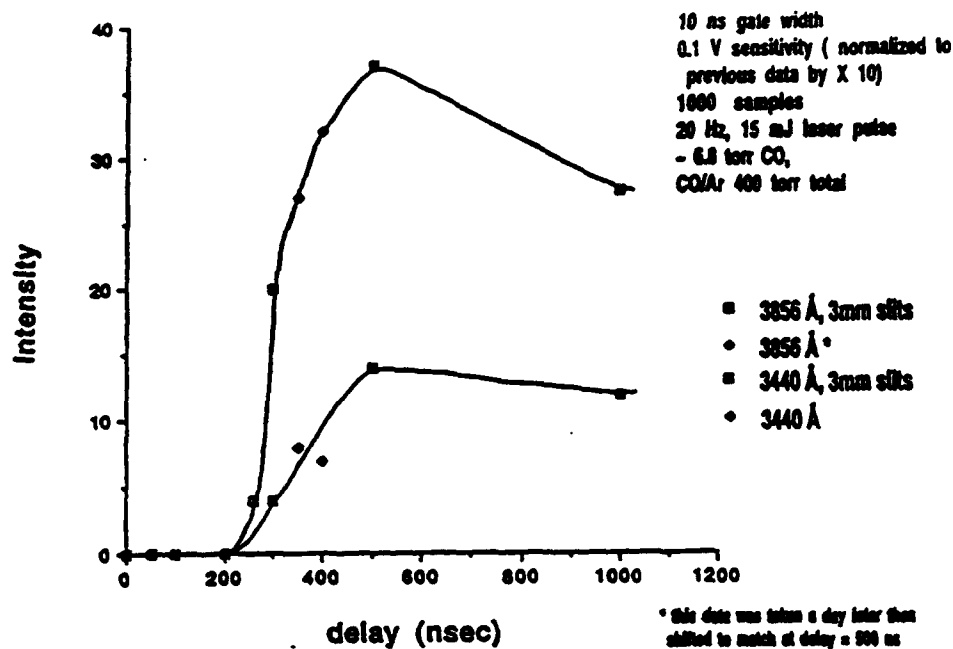


Figure 5.14 Relative rise times of the 3856 Å band and the 3440 Å band

### Time Dependent Signal from CO / Ar Mixture

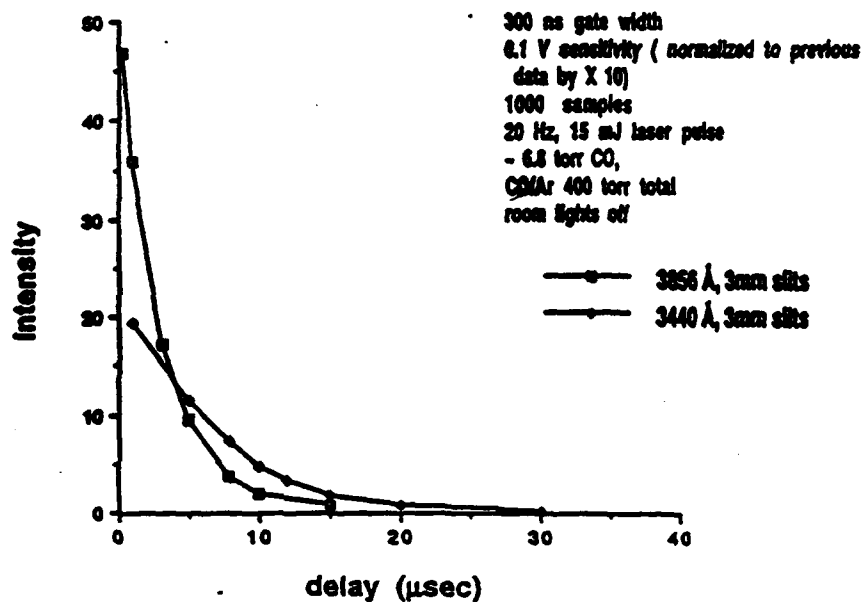


Figure 5.15 Relative decay times of the 3856 Å band and the 3440 Å band

case believed to be  $v = 5$  and  $7$  of the  $a^3\Pi$ ) take longer to complete than the process populating the  $v=2$  level. This is expected since the  $10$  nsec laser pulse populates the  $v=2$  state of the  $a^3\Pi$  before any subsequent transfer processes can occur. Therefore, following the creation of the  $v=2$ , its possible that upper vibrational levels of the  $a^3\Pi$  are populated by V-V pumping. Then its suggested that these levels are radiating back to the ground electronic state on the transitions given above.

## 5.4 Conclusions

In summary, signals at various wavelengths in the UV were observed following excitation by an excimer laser pulse which prepared the  $v=2$  state of the  $\text{CO}(a^3\Pi)$ . The wavelengths of the observed signals and the transitions to which they were attributed are given in Table 5.3.

**Table 5.3.** UV Emission from CO/Ar Mixture

Observed Wavelength ( $\text{\AA}$ )	Transition
$1930 \pm 10$	$\text{CO}(a^3\Pi) v=2 \rightarrow \text{CO}(X^1\Sigma^+) v=0$
$2785 \pm 10$	$\text{CO}(A^1\Pi) v=4 \rightarrow \text{CO}(X^1\Sigma^+) v=18$
$3440 \pm 10$	$\text{CO}(a^3\Pi) v=5 \rightarrow \text{CO}(X^1\Sigma^+) v=14$
$3490 \pm 10$	$\text{CO}(a^3\Pi) v=7 \rightarrow \text{CO}(X^1\Sigma^+) v=16$
$3860 \pm 10$	2nd Order of the 1930 signal

Other signals were observed, however no conclusive identification was given due to lack of supporting evidence. Qualitative time dependence of the 3860, the 3440 and the 1930  $\text{\AA}$  line was observed, the 1930 and the 3860 rose faster and decayed sooner than the 3440  $\text{\AA}$  signal. Equipment limitations forbade the quantitative study of the signal time dependence.

## APPENDIX

### Calculations and Tables of Transition Wavelengths

In order to view *all* possible vibrational transitions among electronic transitions in CO, instead of just those previously observed in experiments, tables were calculated using vibrational energy constants obtained from Huber and Herzberg [15]. The calculations are based on the anharmonic vibrational energy structure:

$$E(v) = T_e + w_e(v+0.5) - w_e x_e(v+0.5)^2 + \dots \quad (A1)$$

where higher order terms were included if data was available.  $E(v)$  is the energy of vibrational level  $v$  in  $\text{cm}^{-1}$ . The array of vibrational energies was then normalized such that zero energy corresponds to  $v=0$  of the ground electronic state. After the energy levels were tabulated (Tables A1-A4) it was simple to create a matrix of all the possible transition wavelengths. This was done for 3 electronic transitions in CO;  $b^3\Sigma \rightarrow a^3\Pi$  (observed as 3rd Positive bands),  $A^1\Pi \rightarrow X^1\Sigma^+$  (observed as 4th Positive bands), and  $a^3\Pi \rightarrow X^1\Sigma^+$  (observed as Cameron bands). Results are tabulated in Tables A5-A7 with the transitions lying on the Condon Parabola indicated.

Table 5.A1 Vibrational Energy Levels of CO( $X^1\Sigma^+$ )

CO ( $X^1\Sigma^+$ ) $v_m$	$G(v)$ (cm <sup>-1</sup> )	$E_v$ (eV)	$E_v - E_0$ (eV)
0	1081.58603	0.13408947	0
1	3224.85744	0.39983105	0.26573158
2	5941.84858	0.66227949	0.52818002
3	7432.02546	0.82145298	0.76736352
4	8496.05573	1.17735992	1.04326045
5	11533.0067	1.49000889	1.35590942
6	13545.3552	1.67940867	1.5453082
7	15530.768	1.82558829	1.79148882
8	17490.1213	2.16848995	2.03439748
9	19423.491	2.40820405	2.27410458
10	21330.9546	2.64468921	2.51059974
11	23212.591	2.87799321	2.74989274
12	25068.4805	3.10809299	2.97399352
13	26898.7045	3.33501167	3.2009122
14	28703.3457	3.55875848	3.42465901
15	30482.4874	3.77834576	3.64524429
16	32236.2137	3.99577795	3.86267848
17	33964.6094	4.21107153	4.07687206
18	35667.7592	4.42223503	4.28813556
19	37345.7478	4.63027894	4.49617947
20	38998.8598	4.83521374	4.70111427
21	40626.5788	5.03704981	4.90295034
22	42229.5877	5.23579742	5.10169795
23	43807.7677	5.43148665	5.29736718
24	45361.1986	5.62406738	5.48996791
25	46889.9579	5.81360923	5.67950976
26	48394.1206	6.00010149	5.86600202
27	49873.7586	6.18355307	6.0494536
28	51328.9403	6.36397247	6.22987299
29	52759.7301	6.54136765	6.40726818
30	54166.188	6.71574807	6.5816466
31	55548.3698	6.88711451	6.75301504
32	56906.3218	7.05547909	6.92137962
33	58240.0899	7.22094513	7.08674566
34	59549.7093	7.38321713	7.24911766
35	60835.2091	7.54259865	7.40849918
36	62096.6096	7.69899226	7.56489279
37	63333.9227	7.85239941	7.71829994
38	64547.1508	8.00282041	7.86872094
39	65736.2962	8.15028428	8.01618481
40	66901.3099	8.29469869	8.16059922
$\omega_m$	2109.51359		
$\omega_{m,m}$	13.28831		
$\omega_2$	0.010511		
$\omega_4$	6.74E-05		
$\omega_5$	9.60E-07		
$\omega_6$	-3.16E-08		

Table 5.A.2 Vibrational Energy Levels of CO( $\alpha^3\Pi$ )

CO( $\alpha^3\Pi$ ) $v=$	G(V) (cm <sup>-1</sup> )	E <sup>v</sup> (eV)	E <sup>v</sup> -E <sub>0</sub> (eV)
0	888.120128	0.19793309	0.00981040
1	2582.90013	0.82022816	0.22250362
2	4268.37813	0.82022816	0.43151318
3	5928.31013	0.73484424	0.63692181
4	7582.90013	0.93049852	0.8387189
5	9181.30013	1.13481671	7.03889308
6	10720.8101	1.3291728	7.23148017
7	12260.6781	1.62011674	7.42229412
8	13771.6001	1.70748846	7.60873682
9	15263.7201	1.89121876	7.76946613
10	16707.1301	2.07141849	7.97389586
11	18122.0701	2.2490884	8.15036677
12	19628.8281	2.42126418	8.32354155
13	20897.7401	2.5908878	8.49328487
14	22238.1801	2.76730597	8.66868334
15	23663.6101	2.92027315	8.82255082
16	24841.4001	3.07994886	8.99222593
17	26103.8381	3.23638784	9.18687802
18	27328.7201	3.39068163	9.29188821
19	28551.2101	3.53960849	9.44218888
20	29788.7401	3.68718093	9.5664083
CO ( $\alpha^3\Pi$ ) $v=0$		0.13400831	
Te =	4888.7	0.03687888	
We =	1743.4		
WeXe =	14.9		
We3 =	-0.04		
We4 =	0.002		

Table 5.A.3 Vibrational Energy Levels of CO( $A^1\Pi$ )

CO( $A^1\Pi$ ) $v=$	G(V) (cm <sup>-1</sup> )	E <sup>v</sup> (eV)	E <sup>v</sup> -E <sub>0</sub> (eV)
0	754.348	0.08382079	0.02777941
1	2236.218	0.272851	0.21150773
2	3886.128	0.48702089	0.39127382
3	5106.838	0.83338851	0.55784214
4	6508.308	0.80882634	0.74117896
5	7889.698	0.97819873	0.91248938
6	9267.388	1.14778807	0.93201889
7	10615.878	1.31619971	0.28046233
8	11989.788	1.48409302	0.41231885
9	13323.858	1.65192137	0.588174
10	14662.048	1.82034014	0.76469276
11	16049.518	1.9898487	0.9241373
12	17430.628	2.16112038	10.095373
13	18828.938	2.33481254	10.288852
14	20252.008	2.51082881	10.4461792
15	21701.398	2.69092792	10.8248806
16	23182.688	2.87428186	10.3085345
17	24700.378	3.06248376	10.9967084
18	26259.088	3.25570802	11.1899819
19	27863.358	3.45461289	11.3888656
20	29517.748	3.65973108	11.5938837
Te =			
We =	66078.7	0.0689521	
WeXe =	1518.2		
We3 =	18.4		
We4 =	0.76		

**Table 5.A4** Vibrational Energy Levels of CO( $b^3\Sigma$ )

CO ( $b^3\Sigma$ ) v =	Gv (cm <sup>-1</sup> )	Ev (eV)	Ev-Eo (eV)
0	1099.5	0.13632052	10.3938246
1	3299.5	0.40996155	10.6994656
2	5497.5	0.68160259	10.9391066
3	7696.5	0.95424363	11.2117477
4	9895.5	1.22688466	11.4843887
5	12094.5	1.4985257	11.7570297
6	14293.5	1.77216673	12.0296708
7	16492.5	2.04480777	12.3023118
8	18691.5	2.31744881	12.5749528
9	20890.5	2.59008984	12.8475939
10	23089.5	2.86273088	13.1202349
11	25288.5	3.13537191	13.392876
12	27487.5	3.40801295	13.665517
13	29686.5	3.68065398	13.938158
14	31885.5	3.95329502	14.2107991
15	34084.5	4.22593606	14.4834401
16	36283.5	4.49857709	14.7560811
17	38482.5	4.77121813	15.0287222
18	40681.5	5.04385916	15.3013632
19	42880.5	5.3165002	15.5740042
20	45079.5	5.58914124	15.8466453
Tab =	83814	10.3916034	
wob =	2199		
wasob =			

Table 5.A5 Vibrational Transitions of CO(a<sup>3</sup>Π) (across) --> CO(X<sup>1</sup>Σ<sup>+</sup>) (down)

v	wavelength (Å)	1	2	3	4	5	6	7	8	9	10
0	2062	1000	1030	1008	1013	1008	1013	1070	1028	1001	1009
1	2100	990	1011	1000	1000	1000	1000	1070	1000	1000	1000
2	2138	980	1000	990	990	990	990	1070	1000	1000	1000
3	2176	970	990	980	980	980	980	1070	1000	1000	1000
4	2214	960	980	970	970	970	970	1070	1000	1000	1000
5	2252	950	970	960	960	960	960	1070	1000	1000	1000
6	2290	940	960	950	950	950	950	1070	1000	1000	1000
7	2328	930	950	940	940	940	940	1070	1000	1000	1000
8	2366	920	940	930	930	930	930	1070	1000	1000	1000
9	2404	910	930	920	920	920	920	1070	1000	1000	1000
10	2442	900	920	910	910	910	910	1070	1000	1000	1000
11	2480	890	910	900	900	900	900	1070	1000	1000	1000
12	2518	880	900	890	890	890	890	1070	1000	1000	1000
13	2556	870	890	880	880	880	880	1070	1000	1000	1000
14	2594	860	880	870	870	870	870	1070	1000	1000	1000
15	2632	850	870	860	860	860	860	1070	1000	1000	1000
16	2670	840	860	850	850	850	850	1070	1000	1000	1000
17	2708	830	850	840	840	840	840	1070	1000	1000	1000
18	2746	820	840	830	830	830	830	1070	1000	1000	1000
19	2784	810	830	820	820	820	820	1070	1000	1000	1000
20	2822	800	820	810	810	810	810	1070	1000	1000	1000
21	2860	790	810	800	800	800	800	1070	1000	1000	1000
22	2898	780	800	790	790	790	790	1070	1000	1000	1000
23	2936	770	790	780	780	780	780	1070	1000	1000	1000
24	2974	760	780	770	770	770	770	1070	1000	1000	1000
25	3012	750	770	760	760	760	760	1070	1000	1000	1000
26	3050	740	760	750	750	750	750	1070	1000	1000	1000
27	3088	730	750	740	740	740	740	1070	1000	1000	1000
28	3126	720	740	730	730	730	730	1070	1000	1000	1000
29	3164	710	730	720	720	720	720	1070	1000	1000	1000
30	3202	700	720	710	710	710	710	1070	1000	1000	1000
31	3240	690	710	700	700	700	700	1070	1000	1000	1000
32	3278	680	700	690	690	690	690	1070	1000	1000	1000
33	3316	670	690	680	680	680	680	1070	1000	1000	1000
34	3354	660	680	670	670	670	670	1070	1000	1000	1000
35	3392	650	670	660	660	660	660	1070	1000	1000	1000
36	3430	640	660	650	650	650	650	1070	1000	1000	1000
37	3468	630	650	640	640	640	640	1070	1000	1000	1000
38	3506	620	640	630	630	630	630	1070	1000	1000	1000
39	3544	610	630	620	620	620	620	1070	1000	1000	1000
40	3582	600	620	610	610	610	610	1070	1000	1000	1000



Table 5.A6 Vibrational Transitions of CO(A<sup>1</sup>Π) (across) --> CO(X<sup>1</sup>Σ<sup>+</sup>) (down)

$v_2$	$v_1$	0	1	2	3	4	5	6	7	8
0	0	1742	1816	1878	1937	1992	2044	2092	2136	2178
1	1	1807	1880	1940	1997	2051	2101	2148	2191	2230
2	2	1872	1944	2003	2059	2112	2161	2207	2249	2288
3	3	1937	2008	2066	2121	2173	2221	2267	2308	2347
4	4	2002	2072	2129	2183	2234	2281	2326	2366	2405
5	5	2067	2136	2192	2245	2295	2341	2386	2425	2464
6	6	2132	2200	2255	2307	2356	2401	2445	2483	2521
7	7	2197	2264	2318	2369	2417	2461	2504	2541	2578
8	8	2262	2328	2381	2431	2478	2521	2563	2600	2636
9	9	2327	2392	2444	2493	2539	2581	2622	2658	2694
10	10	2392	2456	2507	2555	2600	2641	2681	2716	2751
11	11	2457	2520	2570	2617	2661	2701	2740	2774	2809
12	12	2522	2584	2633	2679	2722	2761	2799	2832	2866
13	13	2587	2648	2696	2741	2783	2821	2858	2890	2923
14	14	2652	2712	2759	2803	2844	2881	2917	2948	2979
15	15	2717	2776	2822	2865	2905	2941	2976	3006	3036
16	16	2782	2840	2885	2927	2966	3001	3035	3064	3093
17	17	2847	2904	2948	2989	3027	3061	3094	3122	3150
18	18	2912	2968	3011	3051	3088	3121	3153	3180	3207
19	19	2977	3032	3074	3113	3149	3181	3212	3238	3264
20	20	3042	3096	3137	3175	3210	3241	3271	3300	3326
21	21	3107	3160	3200	3237	3271	3301	3330	3358	3384
22	22	3172	3224	3263	3300	3333	3362	3390	3417	3443
23	23	3237	3288	3326	3362	3394	3422	3449	3475	3500
24	24	3302	3352	3389	3424	3455	3482	3508	3533	3558
25	25	3367	3416	3452	3486	3516	3542	3567	3591	3615
26	26	3432	3480	3515	3548	3578	3603	3627	3650	3673
27	27	3497	3544	3578	3610	3639	3663	3686	3708	3730
28	28	3562	3608	3641	3672	3700	3724	3746	3768	3789
29	29	3627	3672	3704	3734	3761	3784	3806	3827	3848
30	30	3692	3736	3767	3796	3822	3845	3866	3887	3907
31	31	3757	3800	3830	3858	3883	3905	3926	3946	3966
32	32	3822	3864	3893	3920	3944	3966	3986	4006	4025
33	33	3887	3928	3956	3982	4005	4026	4046	4065	4084
34	34	3952	3992	4019	4044	4066	4086	4105	4124	4142
35	35	4017	4056	4082	4106	4127	4146	4164	4182	4200
36	36	4082	4120	4145	4168	4188	4206	4224	4241	4258
37	37	4147	4184	4208	4230	4250	4268	4285	4302	4318
38	38	4212	4248	4271	4292	4311	4328	4344	4360	4376
39	39	4277	4312	4334	4354	4372	4389	4405	4420	4436
40	40	4342	4376	4397	4416	4433	4449	4464	4479	4494

Table 5.A6 (continued)

$\gamma_1$	$\gamma_2$	8	9	10	11	12	13	14	15	16	17	18
0	0	1322	1321	1320	1319	1318	1317	1316	1315	1314	1313	1312
1	0	1323	1322	1321	1320	1319	1318	1317	1316	1315	1314	1313
2	0	1324	1323	1322	1321	1320	1319	1318	1317	1316	1315	1314
3	0	1325	1324	1323	1322	1321	1320	1319	1318	1317	1316	1315
4	0	1326	1325	1324	1323	1322	1321	1320	1319	1318	1317	1316
5	0	1327	1326	1325	1324	1323	1322	1321	1320	1319	1318	1317
6	0	1328	1327	1326	1325	1324	1323	1322	1321	1320	1319	1318
7	0	1329	1328	1327	1326	1325	1324	1323	1322	1321	1320	1319
8	0	1330	1329	1328	1327	1326	1325	1324	1323	1322	1321	1320
9	0	1331	1330	1329	1328	1327	1326	1325	1324	1323	1322	1321
10	0	1332	1331	1330	1329	1328	1327	1326	1325	1324	1323	1322
11	0	1333	1332	1331	1330	1329	1328	1327	1326	1325	1324	1323
12	0	1334	1333	1332	1331	1330	1329	1328	1327	1326	1325	1324
13	0	1335	1334	1333	1332	1331	1330	1329	1328	1327	1326	1325
14	0	1336	1335	1334	1333	1332	1331	1330	1329	1328	1327	1326
15	0	1337	1336	1335	1334	1333	1332	1331	1330	1329	1328	1327
16	0	1338	1337	1336	1335	1334	1333	1332	1331	1330	1329	1328
17	0	1339	1338	1337	1336	1335	1334	1333	1332	1331	1330	1329
18	0	1340	1339	1338	1337	1336	1335	1334	1333	1332	1331	1330
19	0	1341	1340	1339	1338	1337	1336	1335	1334	1333	1332	1331
20	0	1342	1341	1340	1339	1338	1337	1336	1335	1334	1333	1332
21	0	1343	1342	1341	1340	1339	1338	1337	1336	1335	1334	1333
22	0	1344	1343	1342	1341	1340	1339	1338	1337	1336	1335	1334
23	0	1345	1344	1343	1342	1341	1340	1339	1338	1337	1336	1335
24	0	1346	1345	1344	1343	1342	1341	1340	1339	1338	1337	1336
25	0	1347	1346	1345	1344	1343	1342	1341	1340	1339	1338	1337
26	0	1348	1347	1346	1345	1344	1343	1342	1341	1340	1339	1338
27	0	1349	1348	1347	1346	1345	1344	1343	1342	1341	1340	1339
28	0	1350	1349	1348	1347	1346	1345	1344	1343	1342	1341	1340
29	0	1351	1350	1349	1348	1347	1346	1345	1344	1343	1342	1341
30	0	1352	1351	1350	1349	1348	1347	1346	1345	1344	1343	1342
31	0	1353	1352	1351	1350	1349	1348	1347	1346	1345	1344	1343
32	0	1354	1353	1352	1351	1350	1349	1348	1347	1346	1345	1344
33	0	1355	1354	1353	1352	1351	1350	1349	1348	1347	1346	1345
34	0	1356	1355	1354	1353	1352	1351	1350	1349	1348	1347	1346
35	0	1357	1356	1355	1354	1353	1352	1351	1350	1349	1348	1347
36	0	1358	1357	1356	1355	1354	1353	1352	1351	1350	1349	1348
37	0	1359	1358	1357	1356	1355	1354	1353	1352	1351	1350	1349
38	0	1360	1359	1358	1357	1356	1355	1354	1353	1352	1351	1350
39	0	1361	1360	1359	1358	1357	1356	1355	1354	1353	1352	1351
40	0	1362	1361	1360	1359	1358	1357	1356	1355	1354	1353	1352

Table 5.A6 (continued)

$V_1$	$V_2$	10	20
0	0	1000	1000
1	1	1110	1094
2	2	1148	1180
3	3	1160	1147
4	4	1184	1178
5	5	1200	1204
6	6	1220	1224
7	7	1230	1238
8	8	1240	1257
9	9	1250	1260
10	10	1260	1260
11	11	1270	1261
12	12	1278	1268
13	13	1284	1277
14	14	1297	1280
15	15	1301	1290
16	16	1307	1294
17	17	1309	1299
18	18	1310	1307
19	19	1310	1317
20	20	1310	1327
21	21	1318	1330
22	22	1328	1330
23	23	1334	1330
24	24	1338	1331
25	25	1342	1335
26	26	1346	1338
27	27	1350	1340
28	28	1354	1341
29	29	1358	1342
30	30	1360	1342
31	31	1374	1343
32	32	1378	1343
33	33	1380	1344
34	34	1385	1344
35	35	1388	1345
36	36	1390	1345
37	37	1390	1345
38	38	1390	1345
39	39	1390	1345
40	40	1390	1345

Table 5.47 Vibrational Transitions of CO( $b^3\Sigma$ ) (down) --> CO( $a^3\Pi$ ) (across)

$v$	wavelength ( $\mu$ )	1	2	3	4	5	6	7	8	9	10
0	2020	2078	2120	2200	2407	2693	2921	4173	4453	4708	5123
1	2092	2760	2828	2977	3239	3418	3609	3822	4068	4318	4604
2	2518	2829	2781	2892	3024	3177	3344	3526	3724	3941	4181
3	2303	2466	2624	2710	2836	2970	3116	3272	3442	3627	3829
4	2288	2360	2484	2589	2699	2799	2816	2862	2900	2969	3032
5	2157	2240	2329	2422	2521	2627	2740	2860	2990	3129	3277
6	2080	2186	2215	2286	2368	2469	2584	2691	2806	2927	3057
7	1970	2030	2112	2189	2269	2355	2445	2541	2642	2750	2864
8	1899	1952	2019	2099	2181	2269	2320	2409	2497	2593	2696
9	1813	1871	1932	1996	2063	2134	2208	2286	2367	2453	2544
10	1744	1797	1864	1918	1974	2039	2108	2178	2250	2328	2409
11	1678	1729	1781	1836	1892	1951	2012	2077	2144	2214	2288
12	1620	1669	1714	1764	1816	1870	1927	1986	2047	2111	2178
13	1584	1631	1672	1718	1766	1817	1869	1923	1989	2018	2079
14	1512	1563	1604	1637	1682	1730	1778	1828	1878	1932	1987
15	1493	1591	1640	1680	1722	1768	1816	1864	1904	1959	2007
16	1418	1463	1499	1527	1566	1609	1648	1691	1736	1781	1828
17	1372	1408	1442	1477	1514	1551	1590	1630	1671	1714	1757
18	1334	1366	1399	1431	1466	1500	1538	1574	1612	1651	1692
19	1290	1326	1360	1397	1410	1452	1488	1521	1557	1594	1631
20	1280	1286	1317	1346	1378	1407	1439	1472	1506	1540	1576

## References

1. T. G. Slanger, G. Black, E-V Energy Transfer Between Molecules, J of Photochemistry, 4 (1975) 329-339.
2. T. G. Schmalz, A Quantum Mechanical Model of Vibration - Electronic Energy Exchange During Collisions, J. Chem Phys, Vol 76, No 4, 15 Feb 1982.
3. Yu. Z. Ionikh, A. L. Kuranov, A. N. Lobanov, L. S. Starenkova, Vibrational Excitation of CO Molecules in the Reaction  $\text{CO}^*(a^3\Pi) + \text{CO} \rightarrow \text{CO}^v + \text{CO}^v$ , Opt. Spectrosc. (USSR) 60(4), April 1986.
4. J. Bokor, et al., Isotope Effect in Multiphoton UV Photolysis of CO, J. Chem. Phys., 72 (2), 15 Jan 1980, p. 965.
5. G. Meijer et al., State Selective Detection of CO Using a Tunable ArF Excimer Laser, J. Chem. Phys. 89 (4), 15 Aug 1988, p. 2588.
6. K. A. Peterson, R. C. Woods, Theoretical Dipole Moment Functions Involving the  $a^3\Pi$  and  $a'^3\Sigma^+$  States of CO, J. Chem. Phys., Oct 1990.
7. A. A. Markov et al, Determining the Excitation Function of the  $a^3\Pi$  State of the CO Molecule by Electron Impact, Opt. Spectrosc. (USSR) 72(2), Feb 92.
8. M. Drabbles, S. Stolte, G. Meijer, Production of an Intense Pulsed Beam of Oriented Metastable CO  $a^3\Pi$ , Department of Molecular and Laser Physics, University of Nijmegen, The Netherlands.
9. Pearse, Gaydon, The Identification of Molecular Spectra, John Wiley & Sons Inc., 4th edition, 1976.
10. Huber and Herzberg, Molecular Spectra and Molecular Structure ; IV - Tables of Diatomic Molecular Constants, 1979.

**6. NITRIC OXIDE STUDIES I:**  
**Vibrational and Electronic Excitation of NO**  
**in Optical Pumping Experiments\***

\*This chapter adapted from S. Saupe\*, I. Adamovich, M.J. Grassi, J.W. Rich,  
and R.C. Bergman, Chem. Phys. 174, 219 (1993)

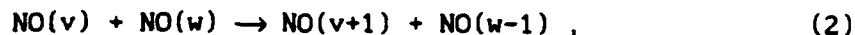
## 6.1. Introduction

Nonequilibrium molecular vibrational-mode energy distributions, maintained by the processes of vibration-to-translation (V-T) and vibration-to-vibration (V-V) collisional energy exchange in gases, have been widely studied for various species [1,2]. These processes and the resulting nonequilibrium energy distributions are of great importance in gas discharges, molecular lasers, supersonic gas flows and in the upper atmosphere. For some diatomic molecules, such as  $N_2$  and especially CO, which have very slow rates of V-T relaxation, there exist extensive experimental and theoretical data on this subject (see [1,2] and references therein).

Vibrational energy transfer in nitric oxide (NO) is much less studied, although it reveals some interesting features making it very attractive for investigation. First, this process has a very fast V-T self-relaxation rate; the rate constant,  $P_{v,v-1}$ , of the process:



for  $v=1$  and  $T=300$  K, is  $P_{10} = 2.5 \text{ ms}^{-1} \cdot \text{Torr}^{-1}$  [3], and is about 5 orders of magnitude faster than that of CO and  $N_2$ . Second,  $P_{10}$  has an anomalously weak temperature dependence with a minimum between 300 and 500 K (see a review of experimental data in [4]). Finally, recent measurements of the NO V-T rates using the stimulated emission pumping (SEP) technique by Yang, Kim and Wodtke [5] also show an unusual dependence of  $P_{v,v-1}$  on the vibrational quantum number. Detailed state-resolved experimental data on NO V-V rates are still not available, except for the rate constant of the process:



measured in [6] for  $v=w=1$  at room temperature,  $Q_{10}^{12}=124 \text{ ms}^{-1} \cdot \text{Torr}^{-1}$ .

Despite its fast V-T relaxation, NO does allow anharmonic vibration-vibration (V-V) pumping [7], such as has been experimentally found for  $\text{N}_2$  [8,9] and CO [10]. This nonequilibrium V-V pumping of NO has been observed in a glow discharge in NO/He and NO/ $\text{N}_2$  at  $T=250\text{--}350 \text{ K}$  [11], and also in CO laser optical pumping experiments [12-14] at  $T=300\text{--}400 \text{ K}$ , where the  $v=0 \rightarrow 1$  vibrational transition of NO was excited by a CO laser. Strongly nonequilibrium vibrational distribution functions (VDF) of NO have been measured up to level  $v=15$  in [11] and up to  $v=14$  in [14]. In addition, the NO  $\beta$  and  $\gamma$  bands, as well as the continuum spectrum of the  $\text{NO}_2$  recombination in the reaction:



were observed in [13]. Finally, new interesting results obtained in a NO/He radiofrequency afterglow [15] show well-pronounced vibrational bands in the first overtone NO infrared spectra up to  $v=17$ , at translational/rotational temperature  $T=250\text{--}300\text{K}$ , which indicate strong V-V pumping.

The present optical pumping experiment allows detailed investigation of NO vibrational and electronic energy transfer, as well as of vibrationally-induced chemical reactions. Its main advantage over glow discharge excitation methods is that vibrational levels above  $v=1$  are populated by the processes of V-V exchange only.

This chapter presents the results of our experiments on NO optical pumping and a theoretical discussion of the different energy



transfer processes involved. Also, new experimental data on V-T relaxation of NO as well as possibilities for further V-T/V-V rate measurements are reviewed, in light of the present results.

## 6.2. Experimental

The schematic of the experimental equipment used in these studies is shown in Fig. 6.1. Radiation from the CO gas laser (1) is focused into the flowing-gas absorption cell (5). A liquid nitrogen cooled flowing-gas CO laser with a 140 cm active length and a 20% transmitting mirror (2) is operated single-line using a gold-coated grating (3) with 290 grooves/mm. The central 20 mm ID glass laser tube with precooling coils is held in an insulated stainless-steel reservoir that contains the liquid nitrogen bath. A 2-a glow discharge is ignited in the tube. The laser delivers up to 8 W on the CO fundamental line P(11) 8 $\rightarrow$ 7,  $\lambda$ =5214 nm, which has a very close resonance with the NO line 1/2R(12.5) 0 $\rightarrow$ 1. The energy displacement between these lines is  $6.8 \cdot 10^{-3} \text{ cm}^{-1}$  from the mean of the NO  $\Lambda$ -doublet [16] (split by  $9.5 \cdot 10^{-3} \text{ cm}^{-1}$  [17]), and the laser line lies within the Doppler width of the lower-frequency  $\Lambda$ -component [13]. The laser parameters, optimized for the maximum power at this line, are listed in Table 6.1. In the present experiments the laser is operated in the cw regime.

The laser mirror and the grating holder are mounted on an optical table to improve the passive stability. No active stabilization is used. The achieved single-line stability is  $\pm 8\%$  over 3 hours. Short-time fluctuations are much smaller and not critical for the measurements.

The laser beam is focused into the pumping cell by a gold-coated mirror (4) of 30 cm focal length. The reflecting angle is kept small at  $15^\circ$  to reduce astigmatism. The focusing area is approximately  $0.1 \text{ mm}^2$ , which gives a power density of  $\sim 10 \text{ kW/cm}^2$ . The complete beam path is purged with dry nitrogen to avoid atmospheric water absorption.

An aluminum optical cell with 8 mm ID and an absorption length of 8 cm is used. It is sealed with  $\text{CaF}_2$  windows. A high gas velocity through the cell reduces the concentration of possible chemical products and also holds down the gas temperature which tends to be increased by the exothermic up-pumping process. To avoid back flows and turbulence in the pumped region, the gas inlet of the cell is designed with a smooth entry section. The gas mixture enters and leaves the cell through four symmetrical 6 mm tubing ports; it is flowing towards the laser beam. Except for the cell itself, all the tubing is stainless steel to avoid corrosion. The cell gas velocity reaches 7.2 m/s in the observed pumping region at a mass flow rate of 110 mg/s. This gives a residence time of  $t_r \sim 10 \text{ ms}$ .

The gases used are Matheson CP grade NO (99.9%) and Ar (99.9%). The pressures of NO and Ar in the cell can be varied over a wide range; for the present studies the NO partial pressure was in the range from 0.5 to 3 torr, with the NO-Ar mixture pressure being  $P_{\text{NO-Ar}} = 90 \text{ torr}$ . The absorbed laser power is determined by measuring the transmitted power behind the cell with and without NO. It changes from 1 W to 5.3 W for the range of gas pressure listed above, approximately linearly increasing with the NO partial pressure.

The fluorescence light from the cell is collected perpendicular to the laser beam. It is analyzed with a 1/3 m monochromator (6 of Fig. 6.1) and an InSb detector (7) in the infrared

or with a 1/2 m monochromator and a photomultiplier (8) in the UV and visible. In both cases, a mechanical chopper at a frequency of 227 Hz is used. A lock-in amplifier (9) records the signal; it is connected to a PC 486 (10) for data acquisition and processing.

### 6.3. Results

In these experiments, the absorption conditions are optimized to get maximum ultraviolet signal from the cell. The strongest UV emission is achieved with a mixture of 1.1 torr of NO diluted in argon at a total pressure of 90 torr. At a given NO partial pressure, the argon pressure shows a wider optimum range; the UV signal is not very sensitive to it. Measurements with NO pressures from 0.5 to 3 torr are analyzed while the total pressure is kept constant,  $P=90$  torr. Table 6.2 lists three selected cases of conditions.

Fig. 6.2 shows infrared emission spectra, generated by the optically pumped NO in the cell, for the three pumping conditions of Table 6.2. The first overtone,  $\Delta v=2$ , emission of NO bands is shown under low resolution and ranges from 2.6 to approximately 3.5  $\mu\text{m}$  wavelength. The approximate centers of some of the vibrational transitions are shown. Overlapping P and R-branches of different vibrational bands create the wavy structure of the signal. As can be seen, vibrational levels up to  $v=15$  are populated and radiating. Note that above level  $v=15$  there is still measurable infrared signal, but the signal-to-noise ratio here becomes worse, which makes the analysis of the spectrum difficult. The NO spectra shown are normalized to the same intensity at 2.8  $\mu\text{m}$  and demonstrate that the intensity distribution is remarkably

similar over the measured range of NO partial pressures.

The dashed line in Fig. 6.2 corresponds to a computer-generated synthetic spectrum, calculated for different NO vibrational distribution functions (VDF) until the best fit with the experimental curve of case II was obtained. Details of this standard procedure of inference of the NO VDF from partially-resolved IR emission spectra can be found in [11,18]. The spectrometer sensitivity used in this method is determined by a blackbody calibration. The most serious problem in the calculation of the synthetic spectrum is that there are no experimental measurements of the Einstein coefficients for spontaneous radiation of NO at high vibrational levels,  $v > 8$ . Fig. 6.3 shows the results of *ab initio* calculations of the Einstein coefficients by Billingsley [19], for  $\Delta v=1$  (curve 1) and  $\Delta v=2$  (curve 2). Curve 1', for  $\Delta v=1$ , is recommended in [20] up to  $v=13$ , and uses the Billingsley scaling with a more reliable experimental value for  $A_{10}$  of  $13.4 \text{ s}^{-1}$ . Curve 2', for  $\Delta v=2$ , is obtained in [20] from combining the direct measurements of ratios  $A_{v,v-2}/A_{v,v-1}$  (for  $v=2-13$ ) with curve 1'. Here we present the best fit, extrapolated up to  $v=15$ . The accuracy of these measurements, used in the present paper, decreases from  $\pm 6\%$  for  $v=2$  to  $\pm 20\%$  for  $v=13$ . The uncertainty in the inferred VDF is determined by this accuracy, since the population distributions are inversely proportional to the Einstein coefficients. The synthetic spectra are not very sensitive to rotational temperature variations within this accuracy. Another possible uncertainty is due to spatially inhomogeneous pumping conditions in the cell.

We believe the NO VDF in the cell attains steady-state at our experimental conditions,  $P_{\text{NO}} = 0.5-3 \text{ torr}$ ,  $t_r \sim 10 \text{ ms}$ . It has been shown in [13] that the IR radiation of the optically pumped NO reaches steady-

state after ~5 ms at  $P_{\text{NO}}=0.15$  torr, and after ~2 ms at  $P_{\text{NO}}=0.59$  torr, for a similar laser power density.

Fig. 6.4 presents the NO VDF obtained from the infrared spectrum of Fig. 6.2. It is obvious that the vibrational levels up to  $v=15$  are strongly overpopulated compared to a Boltzmann distribution at  $T=700$  K, which is a typical temperature in our experiments (see below). The VDF measured in earlier optical pumping experiments [14], at lower temperature  $T=300$  K, is also shown. By fitting the VDF's to the Treanor distribution [7] we obtained the vibrational temperature of the first level for both cases:

$$T_v = \frac{\theta}{\ln(f_0/f_1)} = 2500\text{K} , \quad (4)$$

where  $\theta = \omega_e(1-2\omega_e x_e)$  is the energy of the vibrational transition  $1 \rightarrow 0$  in K, and  $f_0$  and  $f_1$  are relative populations of levels  $v=0$  and  $v=1$ , respectively.

We also analyzed the visible/ultraviolet emission between 200 and 400 nm due to the  $\gamma$  and  $\beta$  bands of NO, emitted from the electronically excited states  $A^2\Sigma^+$  and  $B^2\Pi$ , respectively. A spectrum for the pumping conditions of case II is shown in Fig. 6.5. The  $\beta$ -bands extend into the violet and blue region and make the center of the pumped region visible to the eye. One can see a visible glow of about 1 mm in diameter and over 3-4 cm in length. Identification of different bands (some of them are indicated in Fig. 6.5) shows that only progressions  $v'=0, 1$  and  $2$  can be found in these spectra. For the cases I and III, the ultraviolet emission of  $\beta$  and  $\gamma$  bands is still present, but it is much weaker. The same transitions are observed as in case II, and the intensity ratios are very similar.

The electronic spectra are also used for the inference of the rotational temperature  $T_r$ , necessary for correct analysis of the obtained results. Fig. 6.6 shows a comparison of the experimental contour of the vibrational band  $0,2\gamma$  (case II) with the low resolution synthetic spectrum of this band for  $T_r = 500, 700$ , and  $900\text{K}$ . One can see that the agreement at  $700\text{K}$  is quite reasonable. Repeating this procedure for several non-overlapping bands, we infer the temperature  $T_r = 700 \pm 100\text{K}$  for all three cases of Table 6.2. Simple estimates show that the characteristic time of rotational relaxation at these conditions,  $\sim 10^{-8}$  s, is much shorter than the radiative lifetime of  $A^2\Sigma^+$  and  $B^2\Pi$  states ( $\sim 0.1\text{--}0.4 \mu\text{s}$  and  $3 \mu\text{s}$ , respectively, [21]) and the residence time,  $\sim 10$  ms. This allows assuming translation-rotation equilibrium,  $T = T_r$ .

## 6.4. Discussion

### 6.4.1 Vibrational excitation

First of all, the experimental results show that vibrationally excited NO molecules (at least up to level  $v=15$ ), as well as electronically excited molecules in  $A^2\Sigma^+$  and  $B^2\Pi$  states, are produced in the cell. Note that the cell is irradiated by a single CO laser line, which excites only the vibrational transition  $\text{NO}(X^2\Pi, v=0 \rightarrow 1)$ . This may be compared to the energy of the vibrational level  $v=0$  of the  $B^2\Pi$  state, which corresponds to  $v=35$  of the ground electronic state. The measured translational temperature  $T=700\text{K}$  is too low to account for this excitation by an equilibrium thermal population. Also, the laser energy fluence in the focal area does not exceed a value of  $\sim 10 \text{ kW/cm}^2$ , which

makes multiphoton excitation processes completely negligible. Therefore, the only possible explanation of the high vibrational excitation observed is the anharmonic V-V pumping of nitric oxide [7,22]. Basically, this mechanism involves single-quantum transitions, at least at the low vibrational levels.

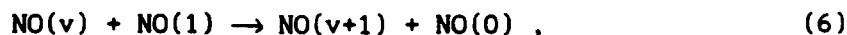
The NO VDF, measured in our experiments (see Fig. 6.4, reasonably corresponds to the Treanor distribution:

$$f_v = f_0 \exp \left\{ -v \cdot \left[ \frac{\theta}{T_v} - \frac{(v-1)\delta}{T} \right] \right\}, \quad v \geq v_0 = 0.5 + \frac{\theta \cdot T}{2\delta T_v} \quad (5)$$

at  $T=700\text{K}$  and  $T_v=2500\text{K}$  up to  $v=15 \sim v_0$ . In (5),  $v_0$  is the vibrational level at which the Treanor distribution has minimum,  $\delta=\omega_e x_e$  is the molecular anharmonicity in K. This confirms [7] that the VDF in this region is controlled by the V-V processes. The VDF, measured in [14] at a lower temperature,  $T=300\text{K}$ , reveals a similar structure. The Treanor curve at  $T=300\text{K}$ ,  $v \geq v_0=7$  lies much higher than the experimental VDF, which shows a significant influence of V-T relaxation.

As has been discussed in [11], the substantial V-V pumping of NO occurs because the V-V rates, at least among the lowest vibrational states, exceed the V-T relaxation rate, for example,  $Q_{10}^{12}/P_{10} \sim 50$ .

There remains a question, however, whether the vibrational levels at high  $v$ 's are populated in far-from-resonance V-V exchange processes:



or whether the near-resonant V-V exchange:



dominates. Recent measurements of the V-T rates in NO [5] have shown that at T=300 K the nonresonant V-V influence is negligible already at  $v=8$ , where the energy defect of the process (6) becomes significant. Nevertheless, the V-V pumping effect at room temperature does exist even at  $v=14$  (see Fig. 6.4). Thus, it becomes obvious that at T=300K the nonequilibrium VDF at  $v \geq 8$  is created by near-resonant V-V exchange (7). Note that the NO V-T relaxation rate only slightly rises with temperature; for example, the rate constant of the process (1) for  $v=1$ , increases approximately 20% from T=300 to 700 K (see [4]). In addition, the VDF's at these two different temperatures look very similar. Therefore, it is reasonable to conclude near-resonant V-V exchange is also a dominant process at T=700K, at least up to  $v=15$ .

For the conditions of the present experiment, the analytical diffusion theory of vibrational relaxation of diatomic molecules [23] predicts a gently decreasing plateau in the VDF above the Treanor minimum  $v_0$  (this is the so-called strong excitation regime):

$$f_v = \frac{\Gamma}{v+1} - \frac{P_{10}}{Q_{10}^{01}} \frac{T}{12\delta} \frac{\delta_{vv}^3}{\delta_{vt}} \frac{\exp(\delta_{vt} v)}{v+1} \approx \frac{\Gamma}{v+1} \quad (P_{10} \ll Q_{10}^{01}) \quad (8)$$

Here  $\Gamma$  is a constant to be found by matching the distributions of (5) and (8) at  $v=v_0$ ,  $\delta_{vt}$  and  $\delta_{vv}$  are parameters of the SSH [24] theory of V-T and V-V exchange, respectively:

$$P_{v+1,v} \sim (v+1) \cdot P_{10} \cdot \exp(\delta_{vt} \cdot v) \quad (9)$$

$$Q_{v+1,v}^{w,w+1} \sim (v+1) \cdot (w+1) \cdot Q_{10}^{01} \cdot \exp(-\delta_{vv} \cdot |v-w|) \cdot \left[ \frac{3}{2} - \frac{1}{2} \cdot \exp(-\delta_{vv} \cdot |v-w|) \right] \quad (10)$$



$$\delta_{VT} = \delta_{VV} \sim (1/\alpha) \cdot (\mu/T)^{0.5} \cdot \delta \quad (11)$$

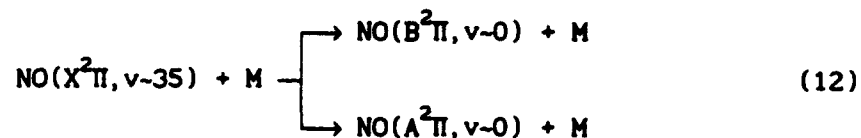
Qualitatively, this theory may be applied to the NO VDF. One can see that the VDF's in Fig. 6.4 at  $v > 8$  decrease much steeper than  $\sim 1/(v+1)$ . However, in the case of NO the ratio  $P_{10}/Q_{10}^{01} \sim 0.02$  is not so small as for  $N_2$  and CO; for this reason the second term in (8) becomes significant to give an exponential fall-off to the VDF. Also, numerical calculations for the conditions of the experiments [14], using master equation analysis [22], are shown in Fig. 6.7. Here  $\delta_{VT}$  and  $\delta_{VV}$  were taken from [13], rather than determined by the SSH-theory relations, (9-11). In [13], these two parameters were found by measuring the rise and decay time of the overall IR signal from the optically pumped NO (see discussion in Section 4 of [13]). The distribution function, created by all the V-V processes, follows the experimental VDF rather closely. At the same time (see Fig. 6.7), it is clear that non-resonant V-V are important only below  $v \leq 7$ . Note that V-V and V-T rates of [13] cannot be used for the simulation of the present experiments at  $T=700K$ , because they give an unrealistic temperature dependence.

#### 6.4.2 Electronic excitation

The mechanism for creation of the molecules in electronically-excited states observed is not so unambiguous as the ground state V-V, V-T processes. There exist three major possibilities:

a) collision-induced resonant vibration-to-electronic (V-E) energy transfer, following the V-V pumping of  $NO(X^2\Pi)$  up to level  $v=35$  as suggested in [13] (a similar process was experimentally observed in

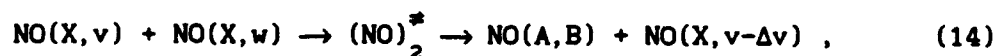
carbon monoxide [25]):



b) recombination of N and O atoms:



c) energy pooling in the process:

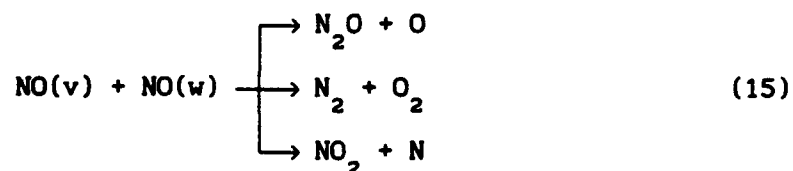


$$E_v + E_w \geq E_A, E_B$$

Here  $E_v$ ,  $E_w$  are energies of vibrationally excited molecules in the X-state;  $E_A$ ,  $E_B$  are energies of excitation of A and B states, respectively.

Note that the last two mechanisms (b and c) do not require the excitation of NO up to very high vibrational levels,  $v\sim 35$ .

The major mechanism of production of the atomic species in the cell is a vibrationally induced chemical reaction:



The activation energies of the three channels of the reaction (15) are  $E_1 \sim E_2 \sim 33$  kK and  $E_3 \sim 39$  kK, respectively [26], which correspond to NO vibrational levels  $v\sim 15$  and  $v\sim 17$ . Given the levels of NO vibrational excitation observed, such atom production is possible in the cell.

However, the formation of NO(A,B) in the recombination reaction (13) is very unlikely. If recombination occurs in the cell, the continuum fluorescence in reaction (3), much faster than (13), would appear, which we did not observe. We conclude that the residence time ~10 ms is too short to produce enough atomic species for any observable recombination to occur in reactions (3,13), following the vibrationally-induced reaction (15). The recombination continuum was observed previously, but only in a non-flowing cell [13], and in a slow-flowing cell with residence time ~ 0.2 sec [14].

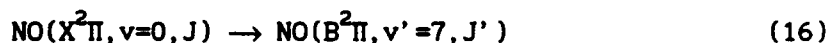
In addition, we did not identify any electronic transitions  $A, v' \rightarrow X, v''$  ( $v', v''\gamma$ ) and  $B, v' \rightarrow X, v''$  ( $v', v''\beta$ ) with  $v' > 2$ . Some of these transitions have substantial Franck-Condon (FC) factors  $f(v', v'')$  in the range of  $\lambda = 200-400 \mu\text{m}$  [21], comparable with the FC factors for the observed bands. For example, the transition  $5, 10\gamma$  ( $\lambda = 263 \text{ nm}$ , [27]) has a FC factor  $f(5, 10) = 0.210$ , while for the transition  $0, 3\gamma$  ( $\lambda = 259 \text{ nm}$ ) it is  $f(0, 3) = 0.147$ . Similarly, in  $\beta$  bands  $f(3, 10) = 0.0393$  ( $\lambda = 323 \text{ nm}$ ), while  $f(0, 8) = 0.0384$  ( $\lambda = 320 \text{ nm}$ ). One can conclude that the relative populations of NO(A,B,  $v > 2$ ) are small compared with those of  $v = 0-2$ , which mitigates against a purely recombinational mechanism of NO(A,B) formation.

Energy pooling (14) cannot be excluded on the basis of these experimental results. This process may occur if the total energy of colliding molecules exceeds the excitation energy of  $A^2\Sigma$  or  $B^2\Pi$  states, (which also makes possible the  $(\text{NO})_2^*$  transition complex formation in reaction (14), since its activation energy is lower [5]). In addition, the transition complex lifetime should be much greater than its period of vibration, to make possible the vibrational energy redistribution. The importance of this mechanism compared to resonant V-E transfer could be determined by measuring the rise time for populations of different

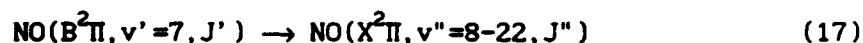
vibrational levels of the  $\text{NO}(X^2\Pi)$ , together with the rise time for the  $\text{NO}(A,B)$  population, using pulsed CO laser optical pumping.

#### 6.4.3 V-T and V-V rates measurements

The experimental data and the discussion presented above show that anharmonic V-V pumping of NO is possible despite its fast rate of V-T relaxation. In particular, at high vibrational levels  $v \geq 8$ , only near-resonant V-V exchange can compete with the V-T processes. The importance of this effect depends on the relative populations of the high vibrational levels and should be carefully checked in experiments involving vibrationally excited NO. For example, we consider the recent work by Yang, Kim and Wodtke [5], where NO V-T rates were measured using stimulated emission pumping (SEP), at  $v=8-22$ . In these experiments, one particular rotational level of NO was excited by a tunable narrowband ArF excimer laser (PUMP):



Then a high vibrational level of the X-state was prepared using a XeCl excimer pumped dye laser (DUMP):



The decay of the population of level  $v''$  was observed using laser induced fluorescence. The measurements were made at room temperature, with two different isotopes,  $\text{N}^{14}\text{O}^{16}$  and  $\text{N}^{15}\text{O}^{18}$ . The rotational levels, available for the PUMP transition (16), with the ArF laser, used in [5] ( $\omega = 51815 \pm 175 \text{ cm}^{-1}$ ), are  $J=24.5-32.5$  for  $\text{N}^{14}\text{O}^{16}$  and  $J=15.5-23.5$  for  $\text{N}^{15}\text{O}^{18}$ .

Simple estimates (see also [28]) show that, if both PUMP and DUMP pulses are saturated, the vibrational level  $v''$  is prepared with a maximum relative population of  $f_{v''} \sim 3 \cdot 10^{-4}$  and  $f_{v''} \sim 3 \cdot 10^{-3}$ , for light and heavy isotopes, respectively. Since the present paper shows that the effect of near-resonant V-V processes (7) on relaxation at  $v=10-15$  is very strong for  $f_v > 10^{-4}$  (see Fig. 6.4), the measured relaxation rate  $k(v'')$  should represent the combined action of both the V-T and the near-resonant V-V energy transfer.

The possible influence of near resonance V-V energy transfer was not discussed in [5]; it was not explicitly specified whether the laser pulses were saturated. Thus, the initial population of the level  $v''$ , as well as the possible influence of this V-V energy transfer, is uncertain. It appears, however, that the experiments of [5], using the heavy isotope  $N^{15}O^{18}$ , indicate that the measurements are not affected by V-V transfer. In the saturation regime the population of  $N^{15}O^{18}(v'')$  is about 10 times higher than that of  $N^{14}O^{16}(v'')$ . Since the rate of the near-resonant V-V exchange non-linearly depends on  $f_{v''}$ , this would give a much higher  $k(v'')$  for the heavy isotope. However, the measured  $k(v'')$  for  $N^{15}O^{18}$  is ~10-20% lower than that for  $N^{14}O^{16}$ . The only explanation, consistent with our measurements, is that the laser transitions in [5] were far from saturation, which made  $f_{v''}$  low enough to avoid the faster relaxation due to near-resonant V-V. This made possible reliable measurements of the V-T rate constants. Nevertheless, there is no doubt that the same experimental set-up [5] can be used for independent determination of the V-V rates, if it is operated in the saturation regime. It appears [28] that the lasers used in the experiments [5] are capable of producing sufficient pulse powers for saturation.

Some phenomenological measurements of the NO V-T and V-V

rates, using time-resolved optical pumping, were made in [13]. In these experiments, the IR radiation from the cell was not state-resolved, and only the overall signal intensity was monitored. This work used the functional dependencies (9,10) of the rates on the quantum number, where  $P_{10}$  and  $Q_{10}^{12}$  were measured in [3,6].  $\delta_{VT}$  and  $\delta_{VV}$  were considered as merely adjustable parameters, and the relations (9,10) are therefore not the results of SSH-theory, but only convenient parametrizations. The rate constants were determined by fitting the rise and decay of the IR signal, calculated using a master equation analysis [22], to the experimental curves. Of course, this procedure is reasonable for the inference of the rates only at low quantum numbers, presumably  $v \leq 10-15$ , because the IR radiation from upper states in these experiments is very weak, and the extrapolation to higher  $v$ 's, as well as to higher temperatures, has no firm basis. Fig. 6.8 shows the comparison of these inferred V-T rates [13] to the direct measurements [5]. One can see good agreement in the range of applicability of the procedure [13].

A more reliable and explicit method of inference of both the V-T and V-V rate constants would be a state- and time-resolved experiment with NO optical pumping, which would allow separate determination of the V-T, near-resonant V-V and non-resonant V-V rates. Again, this method would allow measurements at low  $v$ 's,  $v \leq 10-15$ , while the SEP technique cannot be used at  $v < 8$  because of strong Franck-Condon pumping [5]. These measurements are being pursued in our group.

The theoretical explanation of anomalously fast NO vibrational relaxation is still uncertain. An explanation given in [5] uses the basic arguments of adiabatic theory, developed in the 1960's (e.g. see [29]). This theory takes into account the strong attraction between two NO molecules. It reasonably explains the absolute value of  $P_{10}$  and its

temperature dependence, but it would give a much stronger dependence of  $P_{v,v-1}$  on  $v$ , then was actually found in [5]. On the other hand, non-adiabatic theory [30,31], predicting very weak quantum number dependence, gives no explanation of the  $P_{10}(T)$  rise at low temperatures  $T < 300$  K. Obviously, this problem requires further experimental studies and theoretical analysis.

## 6.5. Summary

Vibrational and electronic excitation of nitric oxide has been investigated in optical pumping experiments. It is shown that the mechanism of vibrational excitation is nonequilibrium V-V pumping, in particular near-resonant V-V exchange on high vibrational levels,  $8 \leq v \leq 15$ . This result shows the importance of the V-V processes even for fast relaxing diatomic molecules. Electronically excited NO molecules in  $A^2\Sigma$  and  $B^2\Pi$  states can be created both by resonant V-E energy transfer, following V-V pumping up to  $v \sim 35$ , and in an energy pooling process (14). The relative influence of chemical reactions appears to be small due to short residence time of the gas mixture in the cell.

Recent measurements of NO V-T rates are analyzed. It is suggested that direct V-V rate measurements at high  $v$ 's,  $v \geq 10$ , can be made using the SEP technique with pulse intensities giving saturation. Also, state and time-resolved infrared measurements in optical pumping are suggested as an efficient method of determination of the NO V-T and V-V rates at low  $v$ 's,  $v \leq 10-15$ .

## References

- [1] Nonequilibrium Vibrational Kinetics , ed. by M. Capitelli, Springer-Verlag, Berlin, 1986.
- [2] B. F. Gordiets, V. A. Osipov and L. A. Shelepin, Kinetic Processes in Gases and Molecular Lasers, London, Gordon and Breach, 1988.
- [3] J. C. Stephenson, J.Chem.Phys. 60, (1974), 4289.
- [4] L. Doyennette and M. Margottin-Maclou, J.Chem.Phys. 84, (1986), 6688.
- [5] X. Yang, E. H. Kim and A.M. Wodtke, J.Chem.Phys. 96, (1992), 5111.
- [6] J. C. Stephenson, J.Chem.Phys. 59, (1973), 1523.
- [7] C. E. Treanor, J. W. Rich and R. G. Rehm, J.Chem.Phys. 48, (1968), 1798.
- [8] W. M. Schaub, J. W. Nibler and A. B. Harvey, J.Chem.Phys. 67, (1977), 1883.
- [9] Yu. S. Akishev, A. V. Demyanov, I. V. Kochetov et al., Sov. High Temperature Physics, 20 (1977) 818.
- [10] J. W. Rich and R. C. Bergman, Chem.Phys, 44, (1979), 53.
- [11] R. C. Bergman, M. J. Williams and J. W. Rich, Chem.Phys, 66, (1982), 57.
- [12] J. Kosanetzky, H. Vormann, H. Dunnwald, W. Rohrbeck and W. Urban, Chem.Phys.Letters, 70, (1980), 60.
- [13] H. Dunnwald, E. Siegel, W. Urban, J. W. Rich, G. F. Homicz and M. J. Williams, Chem.Phys, 94, (1985) 195.
- [14] R. C. Bergman and J. W. Rich, unpublished.
- [15] S. DeBenedictis, Private communication, 1992
- [16] National Bureau of Standards Technical Note, 1321 (1988).
- [17] National Institute of Standards and Technology Special Publication, 821 (1991).
- [18] K. P. Horn and P. E. Oettinger, J. Chem.Phys., 54, (1971), 3040.
- [19] F. P. Billingsley II, J.Mol.Spectrosc., 61, (1976), 53.



- [20] W. T. Rawlins, M. E. Fraser, S. M. Miller and W. A. M. Blumberg, J.Chem.Phys., 96, (1992), 7555.
- [21] "Spectroscopic Constants for Selected Heteronuclear Diatomic Molecules" Aerospace Report No. TR-0074(4641)-6, Vol. II, prep. by S. N. Suchard, 1974.
- [22] J. W. Rich, Relaxation of Molecules Exchanging Vibrational Energy, Chap.4 in: E. W. McDaniel and W. L. Nighan, Applied Atomic Collision Physics, Vol.3, Gas Lasers, Academic Press, NY, 1982.
- [23] B. F. Gordiets and S. Zhdanok, Analytical Theory of Vibrational Kinetics of Anharmonic Oscillators, Chap. 3 in: Nonequilibrium Vibrational Kinetics, ed. by M. Capitelli, Springer-Verlag, Berlin, 1986.
- [24] K. F. Herzfeld and T. A. Litovitz, Absorption and Dispersion of Ultrasonic Waves, Academic Press, NY, 1959.
- [25] R. Farrenq, C. Rosetti, G. Guelachvili and W. Urban, Chem.Phys., 92, (1985), 389.
- [26] National Institute of Standards and Technology Chemical Kinetics Database, NIST Stand. Ref. Data, 1991.
- [27] R. W. B. Pearse and A. G. Gaydon, The Identification of Molecular Spectra, Chapman and Hall, London, 1976.
- [28] X. Yang and A.M. Wodtke, J.Chem.Phys. 92, (1990), 116.
- [29] J. B. Calvert and R. C. Amme, J.Chem.Phys., 45, (1966), 4710.
- [30] E. E. Nikitin, Optics and Spectroscopy, 9, (1960), 8.
- [31] E. E. Nikitin, Theory of Elementary Atom and Molecular Processes in Gases, Clarendon Press, Oxford, 1974.

Table 6.1. Laser parameters optimized for P(11) 8→7

Partial pressures (torr)	He	9.1
	N <sub>2</sub>	2.5
	CO	0.8
	Air	0.05
	Total	12.5
Gas velocity		5 m/s
Temperature		120 K
Discharge current		30 mA
Discharge voltage		13 kV

Table 6.2. Experimental regimes

Case	I	II	III
P <sub>NO</sub> , torr	0.5	1.1	2.9
Absorbed power, W	1.1	2.4	5.2

## Figure captions

Figure 6.1. The experimental set-up. 1, CO laser; 2, laser mirror, 3, grating; 4, focusing mirror; 5, absorption cell; 6, monochromator, 7, InSb infrared detector, 8, photomultiplier, 9, lock-in amplifier; 10, computer; 11, powermeter

Figure 6.2. The first overtone infrared NO spectra; solid lines - experimental spectra, dashed line - synthetic spectrum

Figure 6.3. Einstein coefficients for NO infrared spontaneous radiation; 1,2 - [19], 1',2' - [20]; 1,1' -  $\Delta v=1$ , 2,2' -  $\Delta v=2$

Figure 6.4. The experimental NO vibrational distribution functions (points); 1,2, Treanor distributions for  $T_v=2500K$ ,  $T=300K$ , and  $T_v=2500K$ ,  $T=700K$ , respectively; 3, Boltzmann distribution,  $T=700K$

Figure 6.5. The visible/ultraviolet NO spectrum

Figure 6.6. The experimental profile of the NO  $0,2\gamma$  band (points); the synthetic profile at different temperatures (lines)

Figure 6.7. Comparison of the master equation calculation with the experiment [14]

Figure 6.8. Comparison of the NO V-T rates measured by optical pumping [13] and by SEP [5] (the point for  $v=1$  is the result of [3])

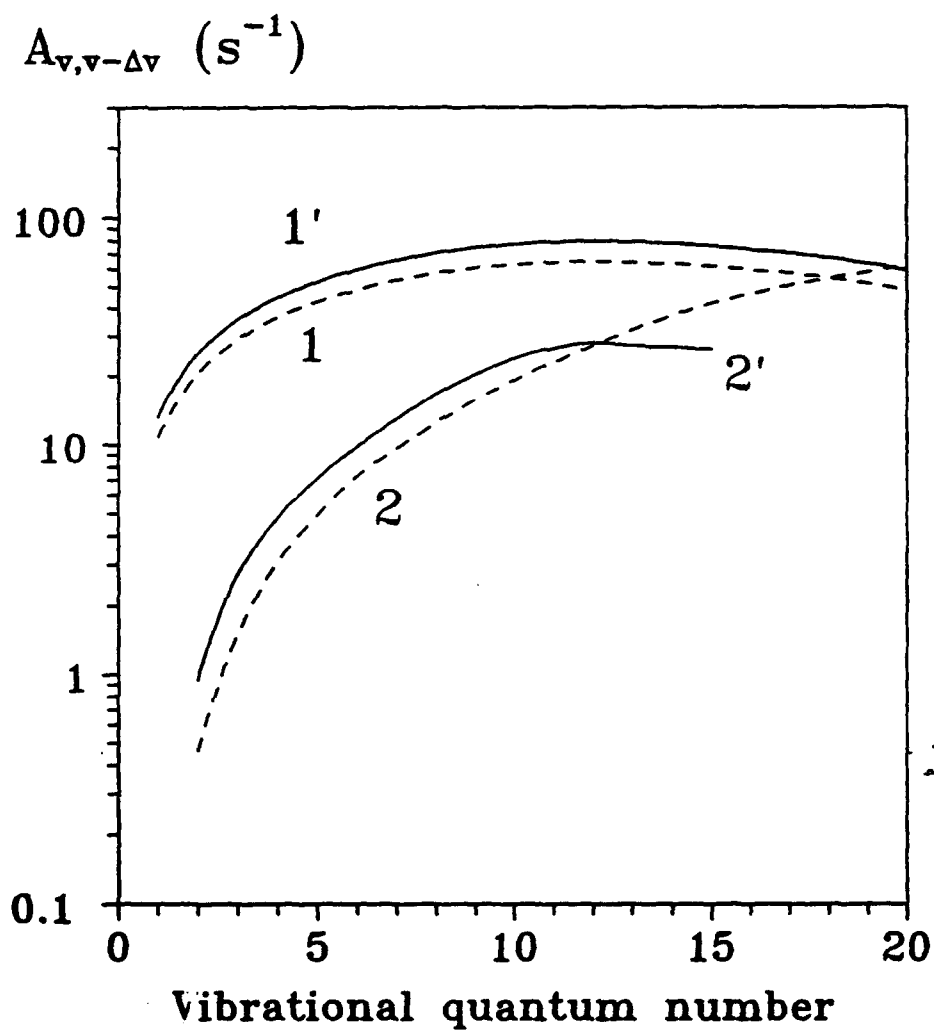


Figure 6.3. Einstein coefficients for NO infrared spontaneous radiation;

1,2 - [19], 1',2' - [20]; 1,1' -  $\Delta v=1$ , 2,2' -  $\Delta v=2$

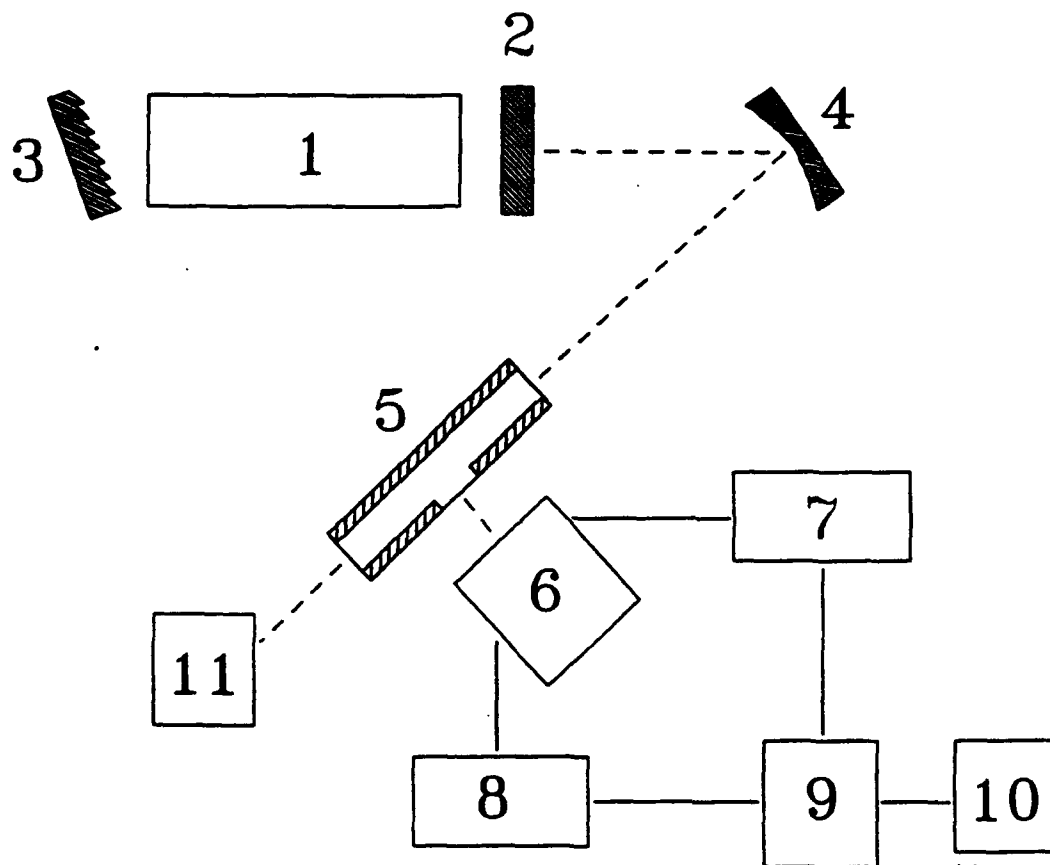


Figure 6.1. The experimental setup. 1, CO laser; 2, laser mirror, 3, grating; 4, focusing mirror; 5, absorption cell; 6, monochromator, 7, InSb infrared detector, 8, photomultiplier, 9, lock-in amplifier; 10, computer; 11, powermeter

# Emission intensity (normalized)

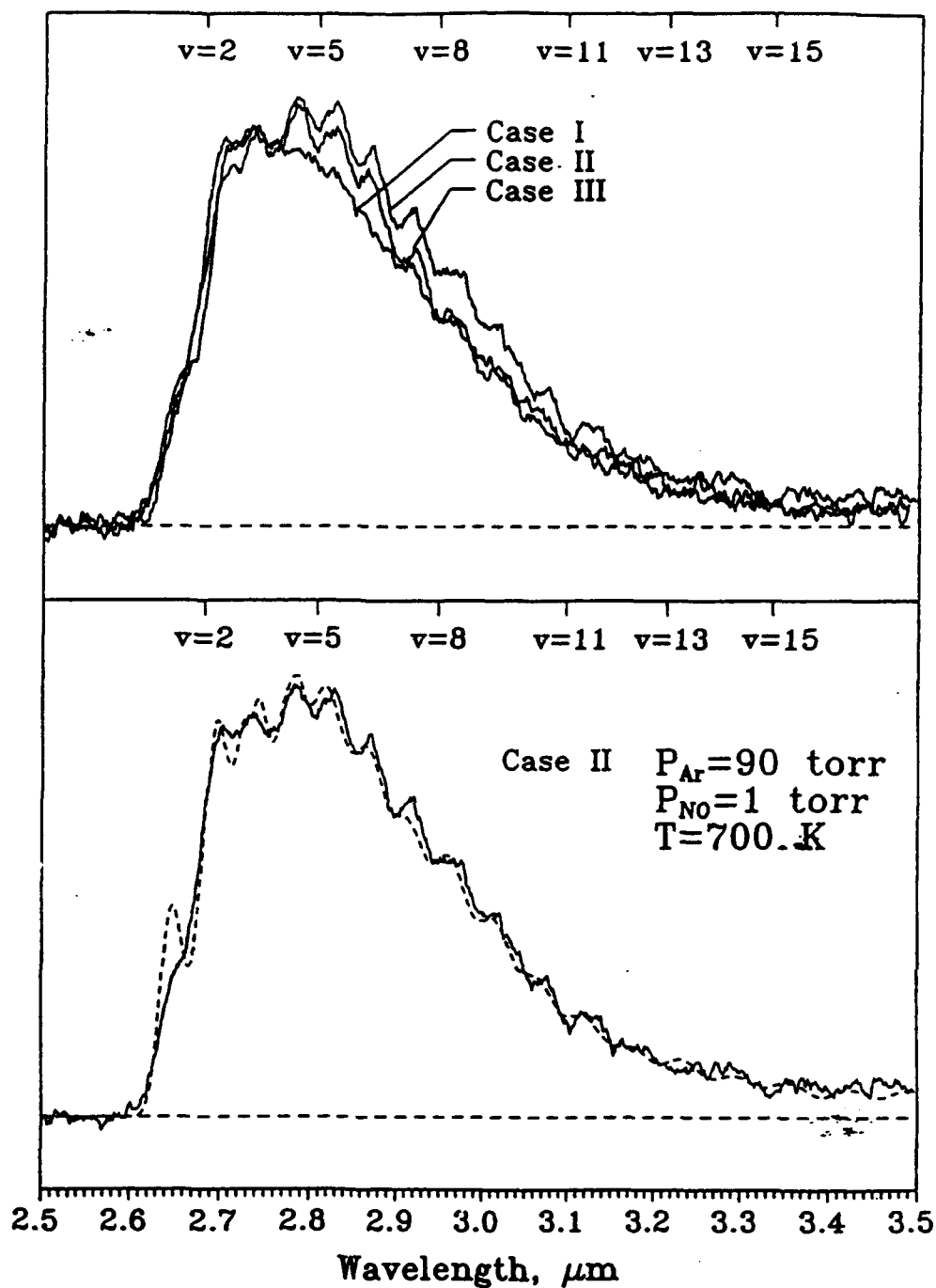


Figure 6.2. The first overtone infrared NO spectra; solid lines - experimental spectra, dashed line - synthetic spectrum

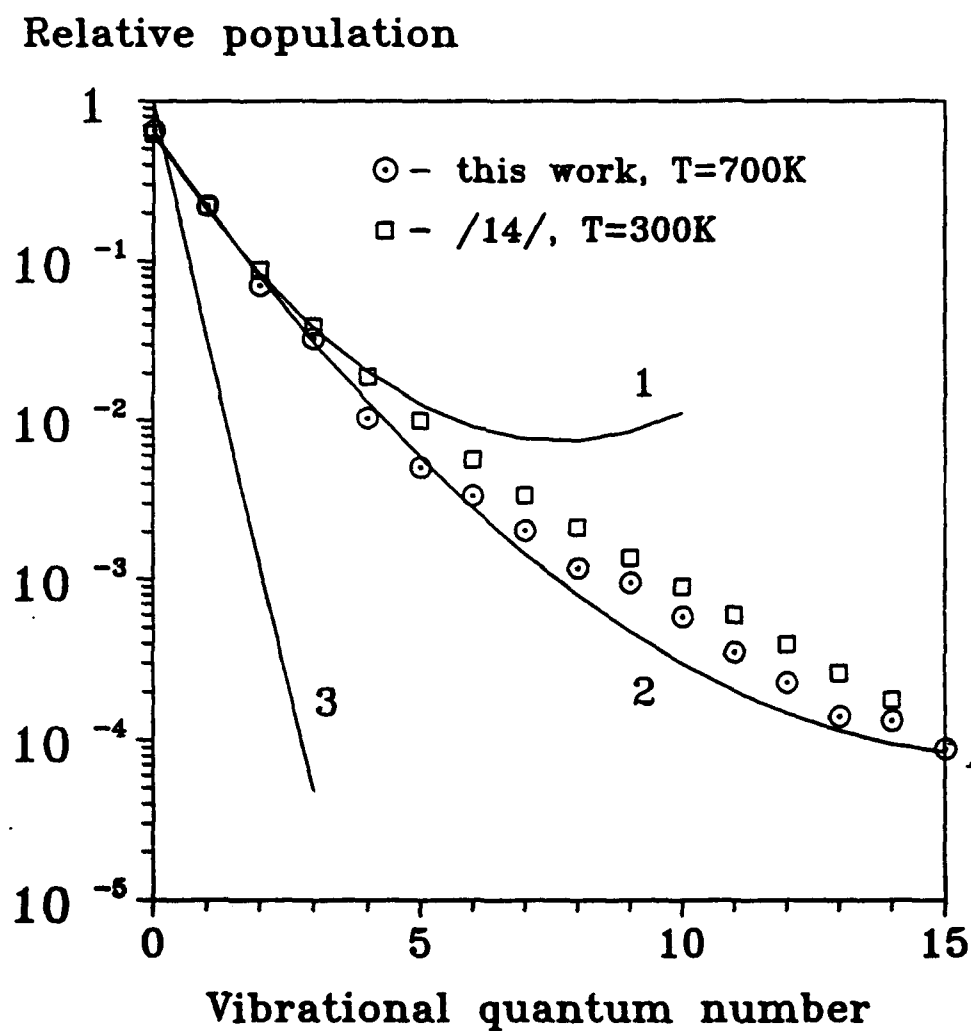


Figure 6.4. The experimental NO vibrational distribution functions (points); 1,2, Treanor distributions for  $T_v=2500K$ ,  $T=300K$ , and  $T_v=2500K$ ,  $T=700K$ , respectively; 3, Boltzmann distribution,  $T=700K$

Emission intensity

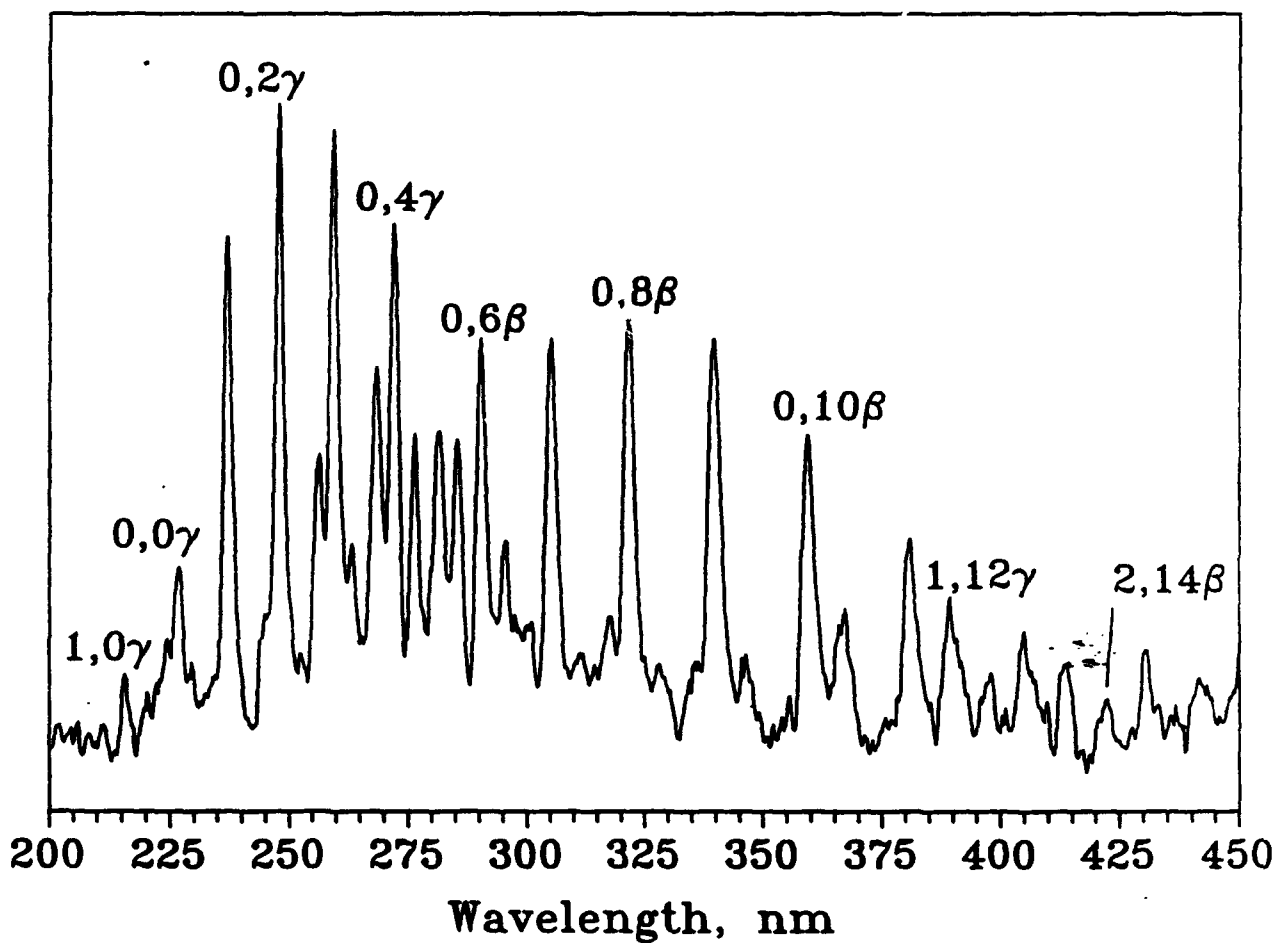


Figure 6.5. The visible/ultraviolet NO spectrum



## Emission intensity

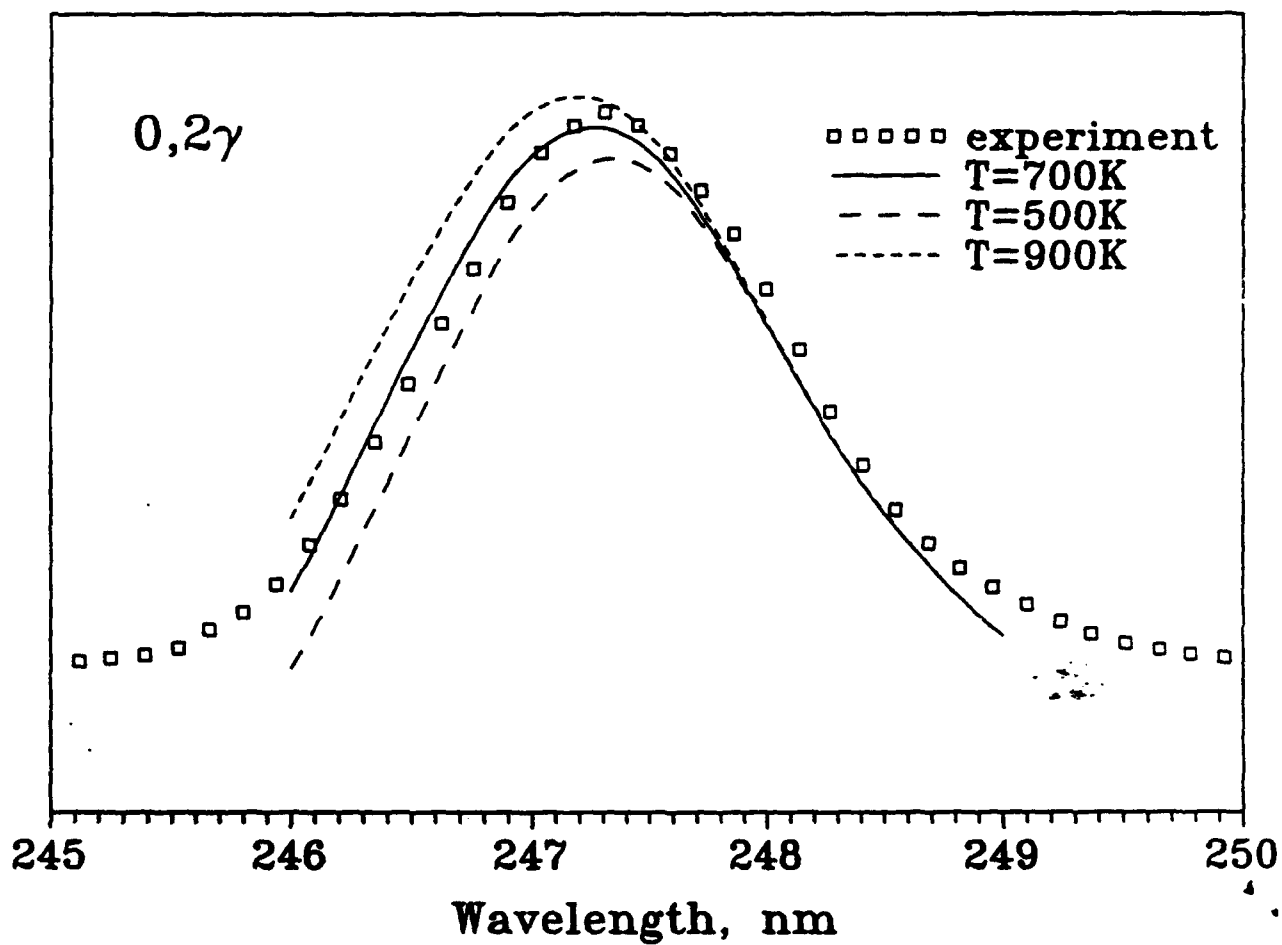


Figure 6.6. The experimental profile of the NO 0,2 $\gamma$  band (points); the synthetic profile at different temperatures (lines)

Relative population

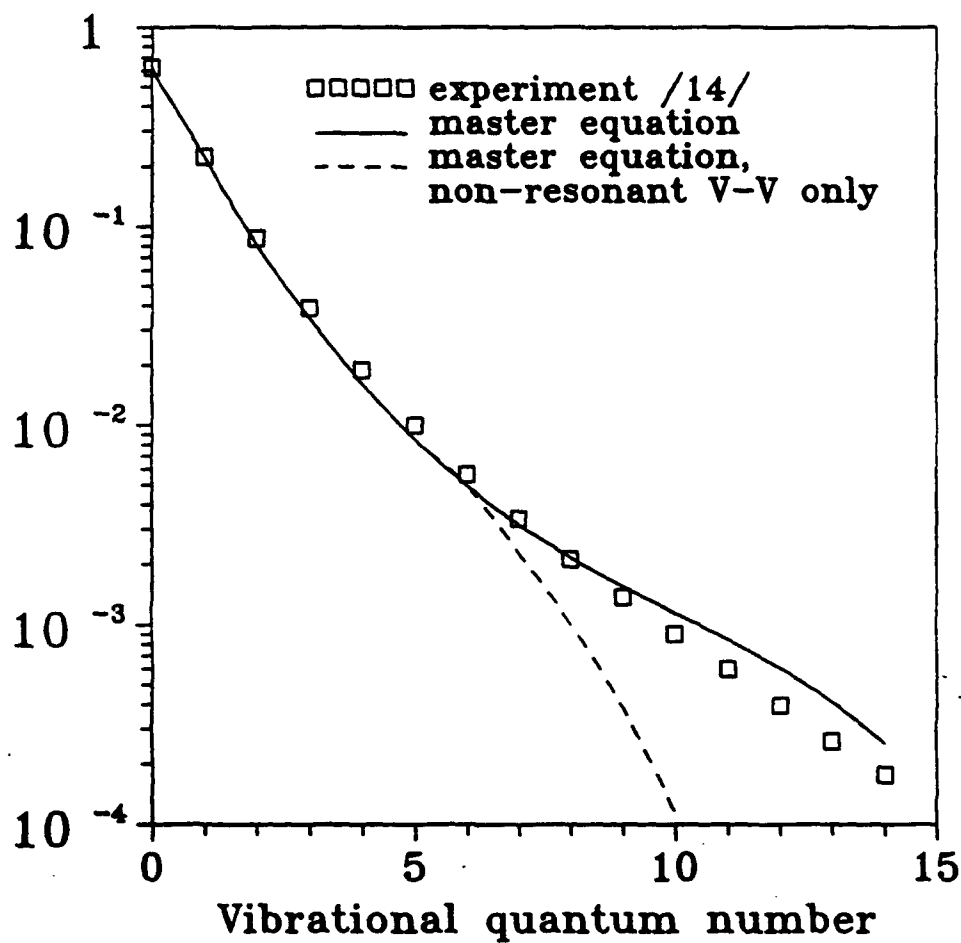


Figure 6.7. Comparison of the master equation calculation with the experiment [14]

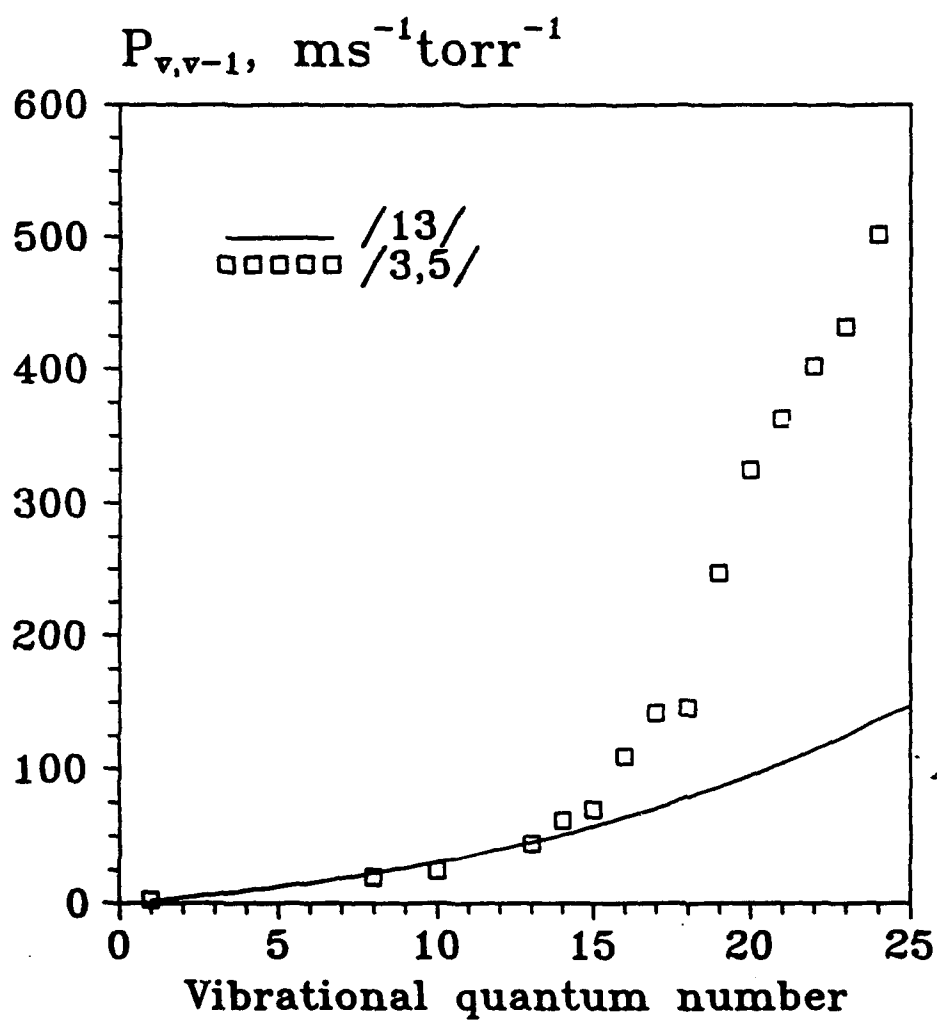


Figure 6.8. Comparison of the NO V-T rates measured by optical pumping [13] and by SEP [5] (the point for  $v=1$  is the result of [3])

**7. NITRIC OXIDE STUDIES II:**  
**Development of a 15 W c.w. Single Line CO Laser**  
**for NO Vibrational Excitation\***

\*This chapter adapted from M. Grassi, 15 W High-Efficiency Liquid-N<sub>2</sub>-Cooled Fast-Axial-Flow Electric Discharge Laser Operating Single-Line, M.S. Thesis, Department of Mechanical Engineering, OSU (1993)

## 7.1. INTRODUCTION

### History

A principal discovery that led to the development of today's powerful CO and CO<sub>2</sub> lasers is attributed to Legay-Sommaire and Legay when they showed that infrared emission from excited vibrational levels could be obtained by a collisional transfer of vibrational energy from active N<sub>2</sub> to some infrared-active molecules such as CO<sub>2</sub>, N<sub>2</sub>O and CO [1]. They also suggested that infrared laser action could be obtained by using vibrational-rotational infrared transitions of the ground electronic state of the CO molecule [2].

This was followed in the same year by Patel achieving the first CO laser, using active N<sub>2</sub> to excite the vibrational mode of CO [3]. Lasing action on the ground electronic state was produced in a low pressure CO pulsed discharge. The conditions for lasing were  $P_{CO} \approx .8$  Torr,  $V_{peak} \approx 15$  kV (pulse) and  $I_{peak} \approx 15$  A (pulse). Output was distributed among several vibrational-rotational lines of the CO fundamental vibrational infrared bands. The greatest power output from a single spectral line (0.1 mW) was on the  $v=7 \rightarrow 6$  P(11) transition. This laser was not cooled and operated at room temperature. The maximum power achieved in

the laser was 500 mW at 5% efficiency. Using a similar arrangement Legay-Sommaire et al reported continuous wave (cw) laser emission in 1965 with a total output power of 370 mW on 36 lines [4].

In 1968, Osgood and Eppers reported on the first high power CO laser; 20 W at 9% efficiency was attained. The improvement resulted from; 1) the addition of He and air to the N<sub>2</sub>-CO mix and, 2) cooling of the discharge tube with liquid N<sub>2</sub> [5,6]. In addition, in contrast to Patel and Legay et al's arrangement the gases were premixed before entering the optical cavity and then subsequently excited by electric discharge [7].

#### Present State

To date, powers in the kW region have been achieved using self-sustained direct current (dc) glow discharges in fast-axial-flow arrangements [8]. Other methods for producing high powers without the dc discharge exist, for example the supersonic gas-dynamically-heated laser of Watt [9]. In recent years, excitation by the use a capacitively-coupled radio frequency discharge has been applied to a fast-axial-flow arrangement by Sato and Taniwaki in a 1 kW laser [10]. Blow and Zeyfang have also used this method of excitation in the plenum of a supersonic nozzle [11].

Other methods of excitation which are being studied are electron-beam pre-ionized systems [12,13]. The Russians have

been the first to report on the operation of a large photoionized CO laser [14]. In this laser, electrons were created in the main laser tube by UV radiation from an auxiliary discharge. Best performance for delivering energy to the laser discharge was 12 J-liter-1-atm-1 with 11% conversion efficiency into laser output.

#### Comparison of CO Laser to Other Common Lasers

The CO laser, due to its wide spectral range of lasing lines from 4.8 to 8.4  $\mu\text{m}$  on the CO fundamental bands and from 2.8  $\mu\text{m}$  to 4.0  $\mu\text{m}$  on the second overtone, is between two other high power c.w. lasers in the infrared [15,16]. The hydrogen fluoride/deuterium fluoride laser operates in the 2.7- 3.5  $\mu\text{m}$  range and the CO<sub>2</sub> operates in the 9.4 -10.6  $\mu\text{m}$  range [17]. The CO laser is one of the most promising of the high power gas lasers from an efficiency standpoint. It has reached physical efficiencies as high as 47%, where physical efficiency is defined as:

$$\eta_{\text{phys}} = \frac{W_{\text{rad}}}{W_{\text{p}}} \quad (1.1)$$

where:

$W_{\text{rad}}$  - Laser output power

$W_{\text{p}}$  - Power supplied to the electric discharge

[Bhuamik,1970]. Unfortunately, a principle drawback to CO laser development, is that in order to achieve both high powers and efficiency, cryogenic cooling is needed [18].

Overall system efficiency defined as:

$$\eta_{\text{oss}} = \frac{W_{\text{rad}}}{W_p + W_{\text{circ}} + W_{\text{cool}}} \quad (1.2)$$

where:

$W_{\text{circ}}$  = Power required for circulating the laser gases

$W_{\text{cool}}$  = Power required for cooling active medium

$\eta_{\text{oss}}$  is, therefore, much lower than  $\eta_{\text{phys}}$ , primarily due to the  $W_{\text{cool}}$  term. However, compared to the efficiency of other lasers for industrial uses, most notably the  $\text{CO}_2$  laser, the overall efficiency is almost the same [19].

Another major advantage of the CO laser compared to the  $\text{CO}_2$  and other laser sources is its high efficiency in the 5 micron region. This is half the wavelength of the  $\text{CO}_2$  laser. The advantage of a smaller wavelength is that the laser beam is capable of better focusing, leading to greater intensities for the same laser power. For industrial applications, most notably the metal fabrication industries, the lower wavelength leads to higher absorption. Fiber optic power transmission is also possible with the 5 micron wavelength and more than 200 W has been transmitted through chalcogenide glass fibers [20]. This is an advantage over the  $\text{CO}_2$  laser since fiber optics have yet to be developed that are efficient in transmitting 10  $\mu$  wavelengths.



### Use in Kinetics and Spectroscopy

Despite the disadvantage of having to cryogenically cool the CO laser, the CO laser has been used with much success in the area of kinetics of vibrational distributions and rate constants for vibrational energy transfer [1]. The various diagnostic techniques which are used for this purpose are almost exclusively based on spectroscopy such as probe laser techniques, light scattering techniques and CARS. As much as the CO laser has proved to be successful it has an obvious weakness: the spectrum is discrete so it can only probe the same molecule or the transitions of another molecule that have good coincidence with one of the CO lines [21].

An ideal spectroscopic source would be tunable with good power. High pressure CO<sub>2</sub> waveguide lasers have been developed that are tunable but the range of tunability is limited to the 10  $\mu\text{m}$  region [22,23]. No tunable CO lasers have been built to date but much work has been done at the Institut für Angewandte Physik in Bonn for building a "stepwise-tunable" CO laser [23]. Recently this group has achieved cw-laser emission from a liquid nitrogen (LN<sub>2</sub>) cooled CO plasma on the overtone band  $\Delta v=2$ . This further increases the spectral range of the CO laser since this group achieved 150 rotational lines ranging from 2.86 to 4.07  $\mu\text{'s}$ . Unfortunately, maximum single line power was 50 mW [24].

As mentioned earlier the CO laser has been utilized in experiments involving vibrational energy transfer among small

polyatomic and diatomic molecules. Current research at the Molecular Energy Transfer Laboratory at OSU involves vibrational energy transfer and vibrational-to-electronic mode energy transfer in CO and NO when a CO laser is used to excite the molecular vibrational mode by resonant transfer of radiative energy to the molecule. Our experiments employ an absorption cell where a mixture of gaseous CO or NO in a diluent gas absorbs energy from a CO laser [25].

The CO laser has been used to achieve population inversions in pure solid  $\alpha$ -form CO at low temperatures (20-35 K). Legay-Sommaire and Legay using a conventional electric-discharge liquid-nitrogen-cooled CO-N<sub>2</sub>-He laser with a 3 m discharge length have observed strong vibrational inversions up to level  $v=23$  in isotopic  $^{13}\text{C}^{16}\text{O}$ ,  $^{12}\text{C}^{18}\text{O}$  and  $^{13}\text{C}^{18}\text{O}$  molecules [26]. In their experiment 50 mW on the laser line  $v=1\rightarrow 0$  P(11) or P(10) was used to pump  $^{12}\text{C}^{16}\text{O}$  molecules to the  $v=1$  level and this vibrational energy was then subsequently transferred to the heavier  $^{13}\text{C}^{16}\text{O}$ ,  $^{12}\text{C}^{18}\text{O}$  and  $^{13}\text{C}^{18}\text{O}$  isotopic molecules. One of the major problems they encountered was trying to grow a single  $\alpha$  crystal without any cracks. Chang and Ewing have overcome this problem by using a different crystal growing method and have obtained population inversions in isotopically enriched samples on a NaCl(100) substrate up to level  $v=30$  with a Q-switched laser similar to that of the Legays except operating single line on the  $v=3\rightarrow 2$  P(12) with  $300 \mu\text{J pulse}^{-1}$  at 50 Hz [27]. In their experiments  $\alpha$ -CO single-crystal slabs

were grown by epitaxially depositing gaseous CO on the (100) face of the NaCl single crystal. The success of the method was attributed to the identical crystal structure on the  $\alpha$ -CO and NaCl and close matchup of the lattice constants. The role of the substrate during the energy-transfer process was explored by monitoring the vibrational population distribution and relaxation lifetime as functions of the number of overlayers on the substrate surface. Results indicated that vibrational motions of the absorbed CO are poorly coupled to the NaCl(100) surface.

Ewing has also investigated collisional up-pumping of isotopic CO in liquid Ar [28]. A cw laser operating on the  $v=1-0$  and  $v=2-1$  transitions was used to pump the CO in the liquid Ar to the  $v=1$  level. Redistribution by collisional up-pumping to higher vibrational levels resulted and levels to  $v=20$  were detected. For some particular CO concentration, translational temperature, and lasing conditions the population of the vibrational level was inverted. The CO laser developed in the present research could be adapted for these liquid phase and surface experiments.

#### Motivation for Present Study

Motivation for building a new CO laser is that the CO laser that was originally being used was incapable of producing high power on the  $v=8-7$  P(11),  $\lambda=5214$  nm line or on other transitions that had good absorption by NO, see Table 7.1

Table 7.1: Absorption of CO laser radiation by a 2% NO/Argon mixture at P=118 atm, T=300 K and atmospheric absorption (km-kilometer)

CO Vibrational transition	Wavenumber $\text{cm}^{-1}$	Atmospheric Absorption coefficient $(1/(\text{atm}\cdot\text{km}))$ STP	NO Vibrational Transition	Wavenumber $\text{cm}^{-1}$	Energy Displacement $(10^3 \text{ cm}^{-1})$	Absorption Coefficient $(1/(\text{atm}\cdot\text{cm}))$
(6-5) P(20)	1921.6930		(1-0) 1/2 R(17.5)	1931.7321	-39.0	0.516033
(7-6) P(13)	1938.4010	.333	(1-0) 3/2 R(10.5)	1935.5005	-19.7	0.906250
(7-6) P(15)	1927.2959	.337	(1-0) 3/2 R(15.5)	1927.2752	20.7	1.549544
(8-7) P(11)	1917.0011	269	(1-0) 1/2 R(12.5)	1917.8723	-11.3	16.021993
(8-7) P(24)	1863.6346		(1-0) 3/2 R(2.5)	1863.6740	-39.4	0.741569
(9-8) P(9)	1900.0426	.259	(1-0) 1/2 R(6.5)	1900.0799	-37.3	2.526414
(9-8) P(13)	1884.3491	15.2	(1-0) 1/2 R(1.5)	1884.3016	47.5	1.259134
(9-8) P(13)	1884.3491	15.2	(1-0) 3/2 R(1.5)	1884.3332	35.9	0.771493
(9-8) P(25)	1824.1214		(1-0) 3/2 P(11.5)	1824.1953	-63.9	1.209456
(10-9) P(20)	1810.2603		(1-0) 3/2 P(12.5)	1810.2503	54.1	0.500304
(10-9) P(26)	1804.7445		(1-0) 1/2 P(19.5)	1804.7445	13.4	4.196132
(11-10) P(3)	1871.0469		(1-0) 1/2 P(1.5)	1871.0619	-15.0	4.327420
(11-10) P(6)	1860.1465		(1-0) 3/2 P(4.5)	1860.1097	36.0	1.110507

[30,31]. The principle objective for a new laser would be high power on a transition that had good resonance absorption by NO.

Other requirements of a new CO laser are that low vibrational band components, down to at least the  $v=2 \rightarrow 1$  transition, lase cw. This transition is needed in order to optically pump gaseous CO in an absorption cell. Other higher vibrational transitions such as the  $v=3 \rightarrow 2$  can be used to pump gaseous CO but this requires higher power for the same gas conditions [32]. The CO laser built by Mehmetli was excellent in this regard because it was able to lase on the  $v=1 \rightarrow 0$  with at least 70 mW Q-switched [33,34]. This laser was used by our group for many experiments and it would be convenient for operational purposes if another laser could be built that was also able to give good power on the lower transitions [25,25].

Another important requirement of a new laser is for it to be stable in cw operation on a single line. The new laser would have to be operable for hours at a time and be as inexpensive as possible to run, as well as being capable of easy, minimum, maintenance.

With these design objectives, a fast-axial-flow electric discharge arrangement was chosen. The reasons for choosing this type of setup are:

- 1) Higher power can be achieved yet the new design can remain very close to that of Mehmetli's CO laser. The idea was to improve upon the basic design since we knew it worked on the

v=1-0 transition.

2) With a fast-axial-flow design much time and cost could also be saved by not having to design for a laser where the active medium was entirely cooled through the wall of the discharge tube.

3) With the same layout the same optic holders could be used. The layout allows for the laser beam to be mechanically chopped, both intracavity for Q-switching, and after the output coupler for time resolved experiments.

The basic laser discharge and cooling system of Mehmetli's is shown in Figure 7.1. Many new ideas for cooling and design of the laser discharge tube were discussed (see the Recommendations and Discussion section for a new cooling tube arrangement). Much excellent work has been done in this area by Grigor'yan and his colleagues; and perhaps, if the time and funding had permitted, we would have opted to try such a design [36].

Section 7.2 will discuss the design of the new laser. It will also discuss the type of the optical resonator and other important details critical to the performance of the laser.

For the reader who is only interested in the performance of the laser, Section 7.3 discusses operation of the laser in the broad-band mode and single line mode. All gas conditions and other data on performance are included in this chapter. It contains most of the tables and figures pertaining to lasing

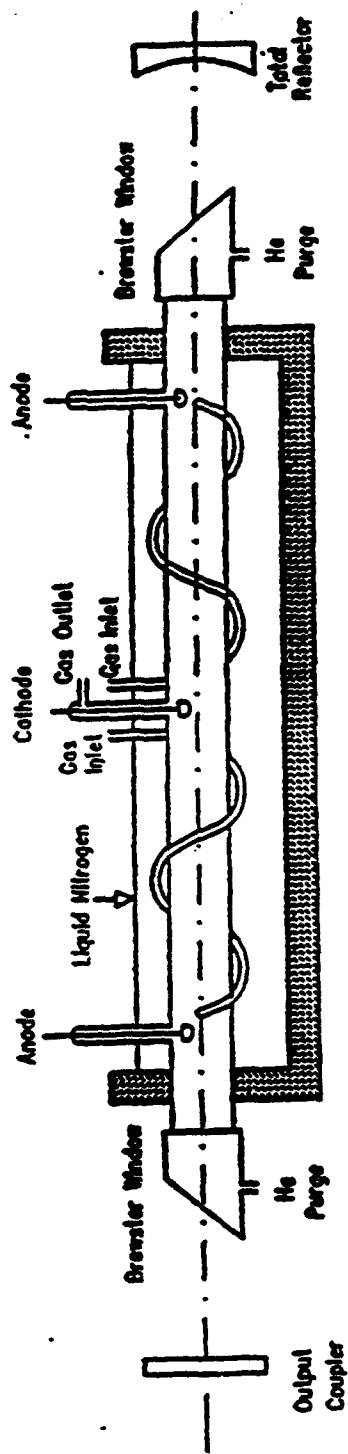


Figure 7.1: Molecular Energy Lab's CO laser constructed by Bulent Mehmetli [Meister]

conditions such as spectral laser scans and mode shape patterns.

Section 7.4 contains observations on running the laser and discusses how to tune the optics. This chapter need not be read in detail by those not interested in operating the laser.

Section 7.5 is a brief summary of the laser being used to pump NO. The thesis concludes with Chapter VI which gives an overall report on the laser's performance and discusses improvements to the existing setup and construction of a new laser tube.



## 7.2. DESIGN AND DESCRIPTION OF FAST-AXIAL-FLOW

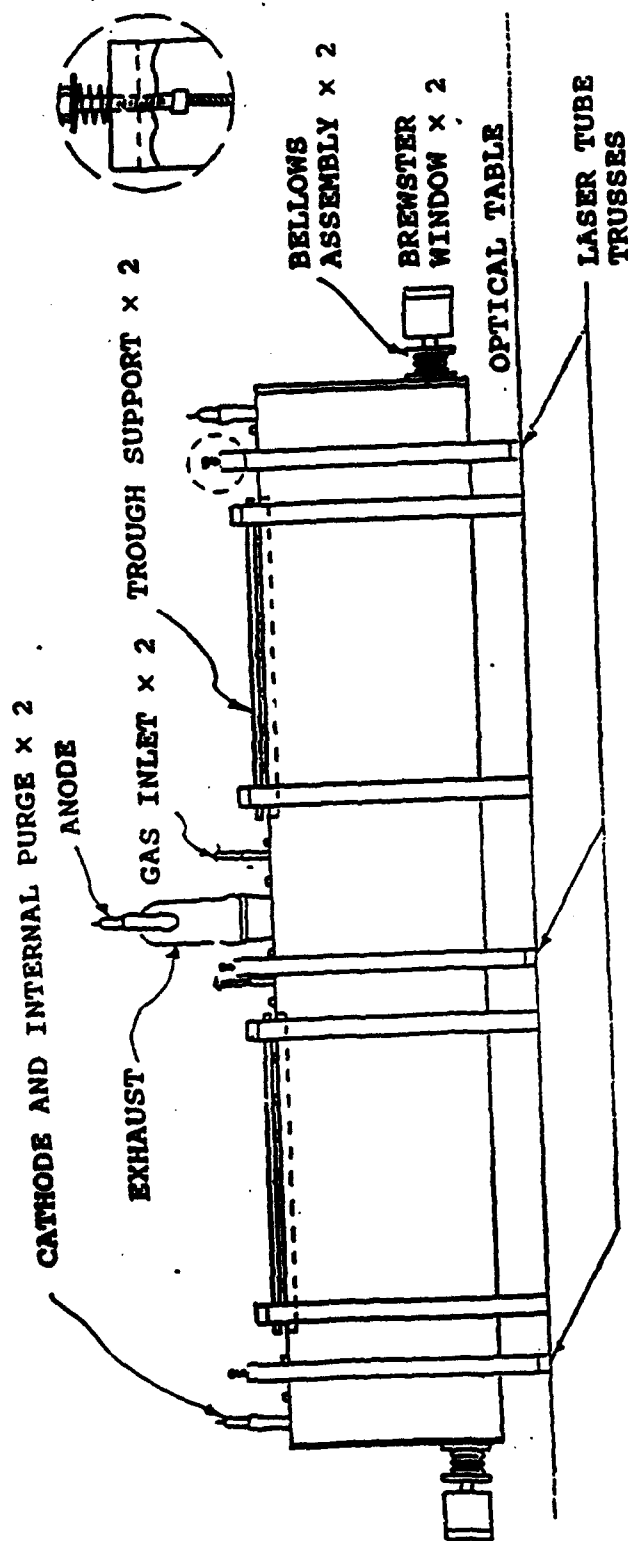
### ELECTRIC DISCHARGE CO LASER

#### General Description

A CO Electric Discharge Laser (EDL) utilizes a glow discharge to achieve lasing in a flowing gas medium. The active medium is a He:CO:N<sub>2</sub>:O<sub>2</sub> mixture. The typical laser is made of cylindrical glass tubing; a meter or so in length and a few cm in diameter. The gas mixture is passed through the tube and velocities can be several meters per second. In this chapter a specific design is discussed along with the actual construction.

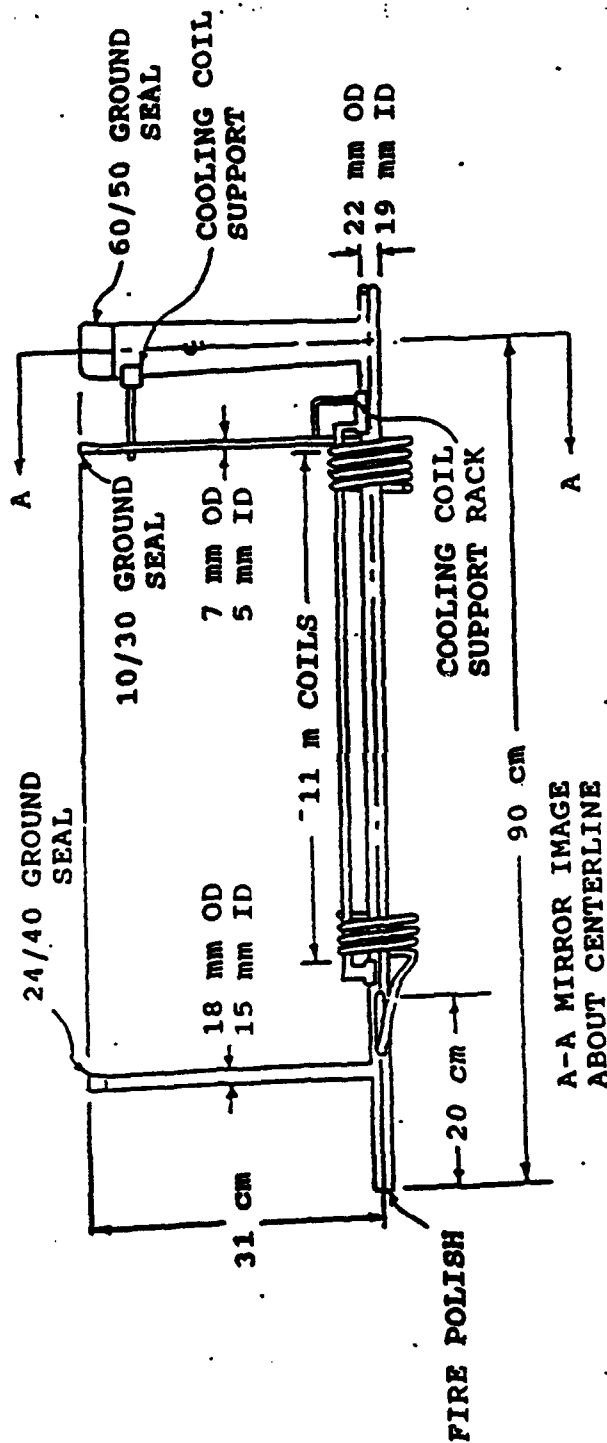
#### Laser Layout

For the new design a liquid-nitrogen-filled stainless steel trough surrounds the laser discharge tube. Laser gases, before entering the discharge tube, are precooled by coiled pre-cooling tubes which are also immersed in the trough. (The laser tube was designed for 400 watt cw output, which could be attained for higher gas flow rates than used here.) The laser is a 2 arm discharge with two entrances for incoming gas with a single exhaust. Figs. 7.2 and 7.3 show the laser's basic



NOTE: NOTE TO SCALE

Figure 7.2: Fast-Axial-Flow Electric Discharge (FAFED) CO laser basic layout. External view of trough and Brewster window assemblies.



EXHAUST TUBE - SHOULD TAPER FROM A 40 mm x 19 mm OVAL OPENING TO 60/50 GROUND SEAL FITTING. WALL THICKNESS AT MIDPOINT SHOULD BE  $\sim .75$  mm (OR SCORED) AND  $1.5 \pm .5$  mm ELSEWHERE. COOLING COIL SUPPORT IS NOT FUSED TO COOLING COIL, USE TEFLON TAPE TO LOOSELY CONNECT.

NOTES: MATR'L KIMBEL KG33 COOLING COIL SHOULD BE FORMED ON A 9 cm OD DRUM. TOTAL NO. OF COILS  $\sim 40$ . BE SURE THAT NO 2 COILS TOUCH. STRAIGHTNESS OF TUBE SHOULD NOT DEVIATE BY MORE THAN 1 mm FROM CENTERLINE.

Figure 7.3: Fast-Axial-Flow Electric Discharge CO laser tube

layout.

### Cooling tubes

The design of the cooling tubes depends on maximum mass flow rate. Many papers on Fast-Axial-Flow/Forced-Convective-Flow CO lasers were reviewed. The objective was to identify designs and flow rates that gave good power on transitions that had good absorption by NO, especially the  $v=8 \rightarrow 7$  P(11),  $\lambda=5214$  nm line [37]. Kan and Whitney's mass flow rates were chosen since their reported performance showed good power on the  $v=8 \rightarrow 7$  transitions, see Table 7.2. Best performance of their  $\text{LN}_2$  laser was reported at 400 W with a 35% output coupler. The mass flow rate was 2 g/sec with a He:CO: $\text{N}_2$  molar ratio of 950:36:14. Their laser tube was 1 m long with a 2.5 cm diameter bore. This mass flow rate was used to compute the number of coils required to cool the gas to  $\approx 78$  K. The calculations for the dimensions of the cooling tube are contained in Appendix B.

### Laser Discharge Tube

There was insufficient time to do a finite element analysis of the laser tube and best guesses or material availability was the rationale for some of the specification of this laser discharge tube. For the laser wall thickness, 1.5 mm was chosen because it was readily available. The overall dimensions of the laser tube were chosen as 19 mm for

Table 7.2: Kan and Whitney's spectral distribution of their laser in the convective and diffusion modes [Kan and Whitney]

Vibrational band	Forced convective flow		Diffusion mode	
	Transition	Relative normalized band intensity	Transition	Relative normalized band intensity
$v=5-4$	$P(12)$	0.1	...	...
$v=6-5$	$P(12)-P(13)$	0.8	...	...
$v=7-6$	$P(11)-P(13)$	1	$P(14)-P(16)$	0.5
$v=8-7$	$P(12)$	0.5	$P(15)-P(17)$	1
$v=9-8$	$P(11)-P(12)$	0.4	$P(13)-P(16)$	0.9
$v=10-9$	$P(10)-P(12)$	0.2	$P(13)-P(15)$	0.7
$v=11-10$	$P(10)-P(11)$	0.2	$P(14)$	0.2
$v=12-11$	$P(10)$	0.03	$P(14)-P(15)$	0.3
$v=13-12$	$P(9)-P(11)$	0.06	...	...
$v=14-13$	$P(9)-P(10)$	0.05	...	...
$v=15-14$	$P(9)$	0.02	...	...

the width mostly because of velocity requirements. The overall 1.8 meter length was chosen by the limit of the glass blower's oven size, and our optical bench size, see Figure 7.3 and Appendix A.

The injectors were designed so that swirl was introduced into the cavity. This has been shown to enhance the cooling at the walls. The design of these injectors, shown in Figure 7.4, is different from those used in Mehmetli's laser which is a copy of a design by Martin, see Figure 5 [38].

The nozzle is actually recessed from the tube and a small diffuser type of arrangement is used immediately after a capillary tube which is acting as the nozzle. This square edged nozzle makes calculations easy and the diameter tolerance of this capillary tube is excellent. A 2.0 mm inside diameter with a tolerance of  $\pm 0.1$  mm was used for the capillary tube/nozzle. This size was chosen because it was the same diameter as Mehmetli construction although there was considerable disagreement over what the inside diameter of this nozzle should be. Again, the idea was not to deviate too greatly from a construction that we knew worked on the  $v=1-0$  transition, yet we wanted to improve the design. Pressure measurements showed that Martin's orifice was not sonic at the gas conditions that were typically used. Being sonic at the orifice has its benefits in a CO laser construction. First, over a long period of operation, carbon and impurities from the discharge are much less likely to diffuse upstream past a

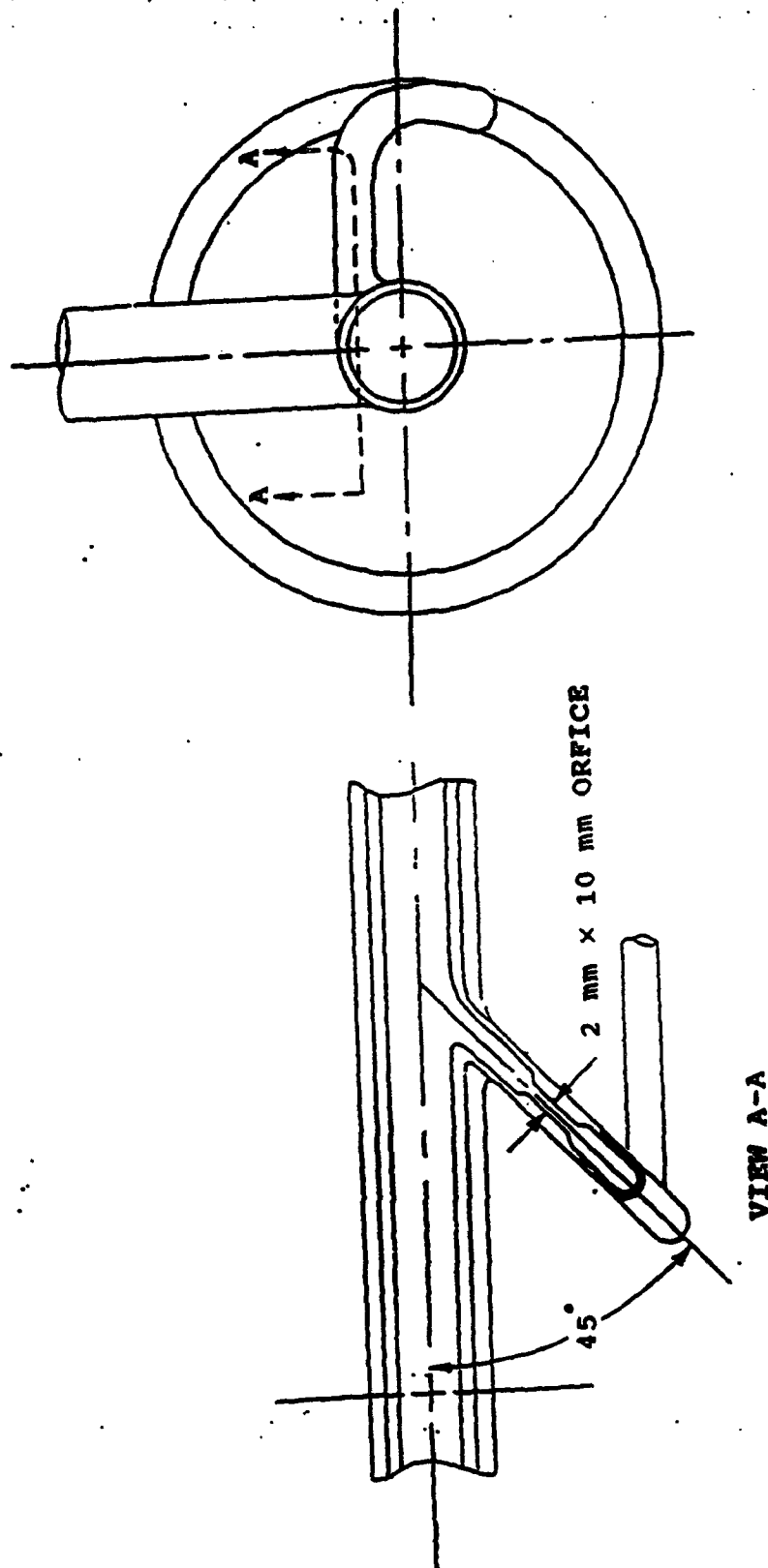


Figure 7.4: Fast Axial Flow gas swirl injector

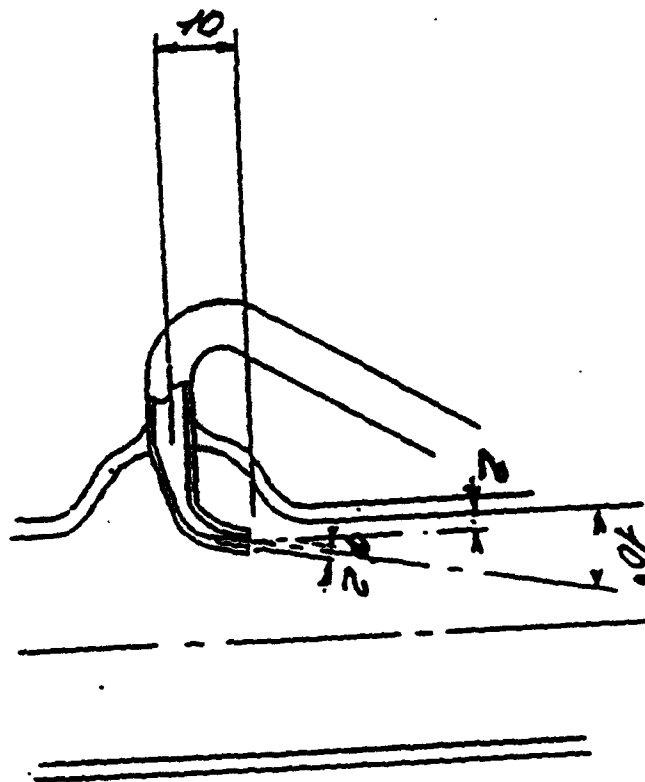


Figure 7.5: Injector used in  $V=1 \rightarrow 0$  laser by J.P. Martin and later used in Mehmetli's CO laser [Martin]



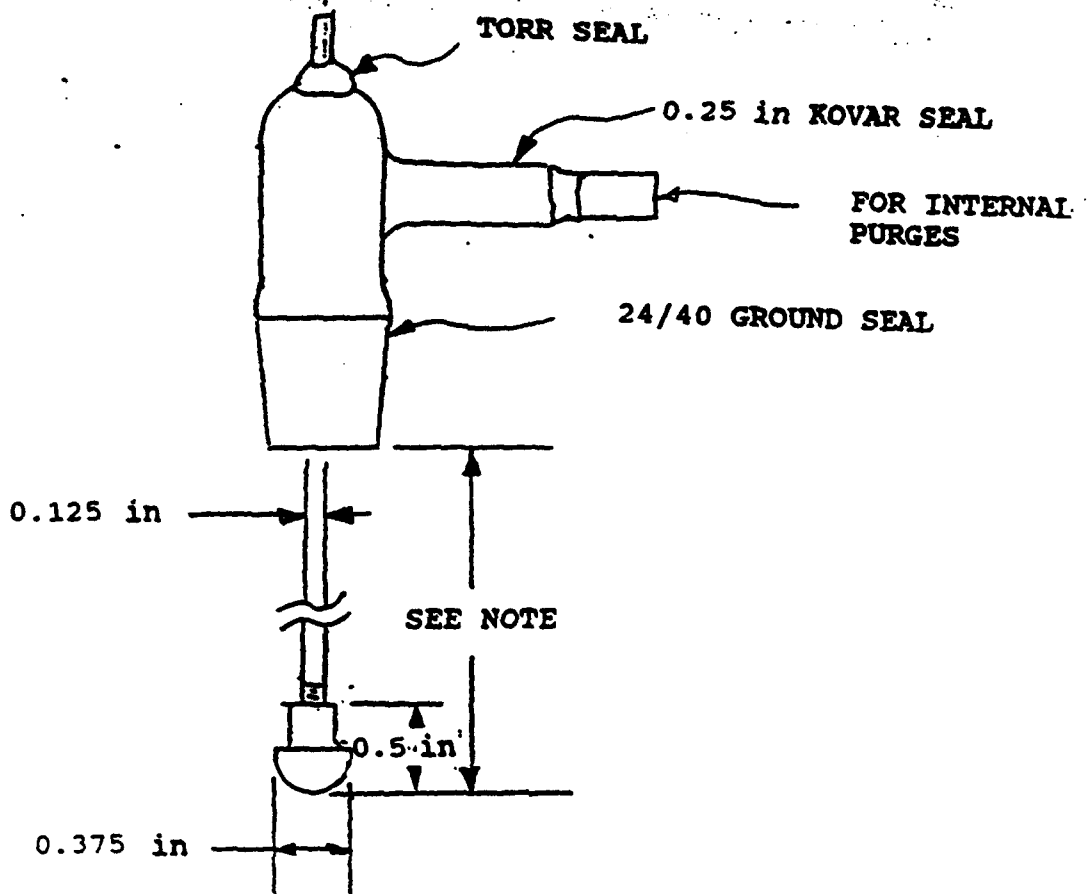
sonic injector and adhere to the cooling walls, decreasing the heat transfer coefficient. Second, since impurities are less likely to diffuse upstream under choked conditions they will not clog the nozzle. Thus the same amount of mass flow will be delivered; thereby, long term gas conditions are assured. Third, metering of the flow becomes easier because it is directly proportional to the upstream to downstream pressure ratio.

The benefits of the current injector design are that (1) it is easy for the glass blower to change the orifice and (2) the injector does not stick into the laser discharge area. Without the injector sticking into the laser cavity a smaller tube size could be used which is an integral part of the fast-flow-axial design.

One of the most important details of the current laser discharge tube is the design of the exhaust. With Mehmetli's design and similar designs such as those used by Urban's group in Bonn and those of Martin, the exhaust tube has been of equal or smaller size than the discharge tube diameter [25]. With the present design the inlet of the exhaust tube where it joins the discharge tube is twice the cross sectional area of the bore of the discharge tube. The exhaust tube then tapers to a 2-inch-round-diameter cross section. This is for two reasons. First the 2 inch diameter is the same inlet size as the vacuum pump. The second reason is that as the lasing gas medium leaves the discharge it is heating up to above room

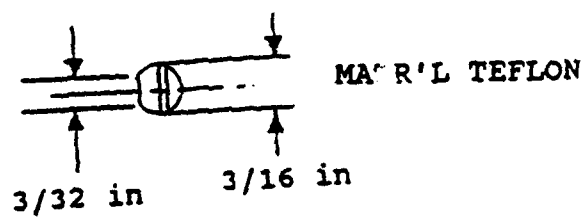
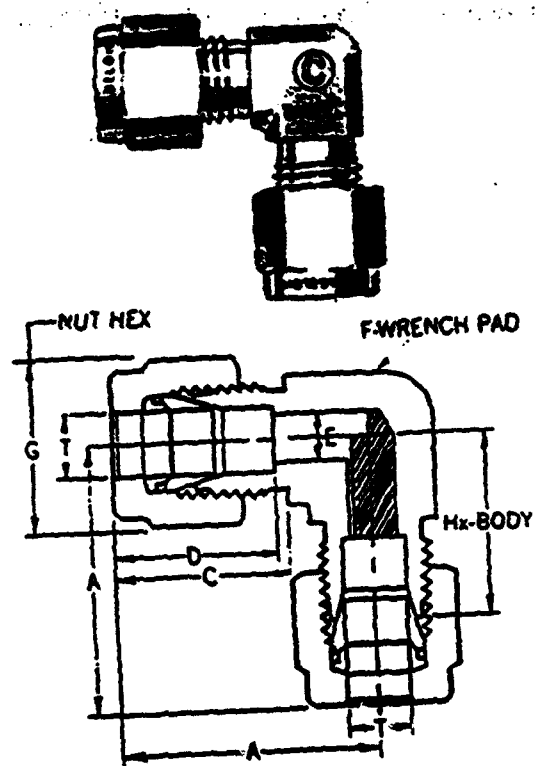
temperature by the combined effects of vibrational relaxation and heat transfer with the walls, thereby expanding its volume. The gas reaches room temperature approximately 4 inches above the  $\text{LN}_2$  level in the trough as no freezing of water vapor is seen after this point. In our experiments with absorption cells, we noted that even when ganging two vacuum pumps together the flow is not doubled from the cell exhaust since the flow rate is determined by the tube size (the pressure at the pump is constant). Therefore, it is very important that the gas exhaust construction is not the parameter which determines the pressure inside the laser discharge tube.

Ground tapered joints were used on all the fittings. These seal well, require no o-rings, and can therefore be used at colder temperatures allowing for closer proximity to the  $\text{LN}_2$ . The electrodes are Torr-sealed into the male taper. Part of this male taper for both anodes was a 1/4 in. inlet for the inner purges, see Figure 7.6. The inner purge 1/4 in. tube ends in a kovar seal. Swagelock 1/4 in 90° compression fittings are used to join 1/4 in. nylon inlet lines. One hidden aspect of the design is that inside the 1/4 in. Swagelock compression elbow a restrictor has been inserted to boost the pressure in the inlet lines, see Figure 7.7. This was done because we were having problems with the discharge arcing to ground through these lines. By using the restrictor the pressure in the lines was increased raising the resistivity to



NOTES- ELECTRODES ARE LOCATED 13 cm  
 FROM CENTERLINE OF LASER  
 DISCHARGE TUBE  
 ELECTRODE MATR'L IS STAINLESS  
 STEEL  
 MAKE 2 ELECTRODE HOLDERS AS  
 SHOWN AND ONE WITHOUT .25  
 KOVAR SEAL

Figure 7.6: Male taper joint construction showing details  
 of the internal purge and electrode  
 arrangement



T	CHARGE	A	A <sub>1</sub>	C	D	E	F	F <sub>1</sub>	G	Hx	Hx <sub>1</sub>
Tube	NUMBER					Minimum					
O.D.						Opening					
1/4	402-27	1.00	1.01	.70	.80	.19	1/8	7/16	7/16	.77	.73

Figure 7.7: Inner purge gas restrictor

prevent arcing back to ground.

Other notes concerning the laser discharge tube are that the tube is very heavy with 11 meters of cooling tube per side. The weight of these cooling tubes on the main tube causes it to be very flexible. Meticulous care in handling the tube is required. At no time should an arm be left unsupported, and supports should be (as a minimum) in at least three places; one near the exhaust and two at each end. The flexibility of the tube is somewhat advantageous because it allows for some thermal movement and (if the tube is constructed with some small offset) straightening of the tube. The glass blower will have a difficult time keeping the tube straight after installing the exhaust tube, thus some flexibility leaves a little leeway for adjustment.

#### Laser Tube Support System

The support of the laser tube was unlike the earlier laser design. In the previous design the laser tube was very rigid due to its 2.5-cm diameter and heavy wall thickness and was supported only at the ends. Due to the small diameter and wall thickness of the new tube and the weight of the cooling tubes this method was insufficient. End support alone could not be relied upon to support the tube. It was decided to hang the laser tube using stainless steel cables with glass saddles. The glass saddles were no more than half arcs made out of capillary tubes. The tube was then supported at three

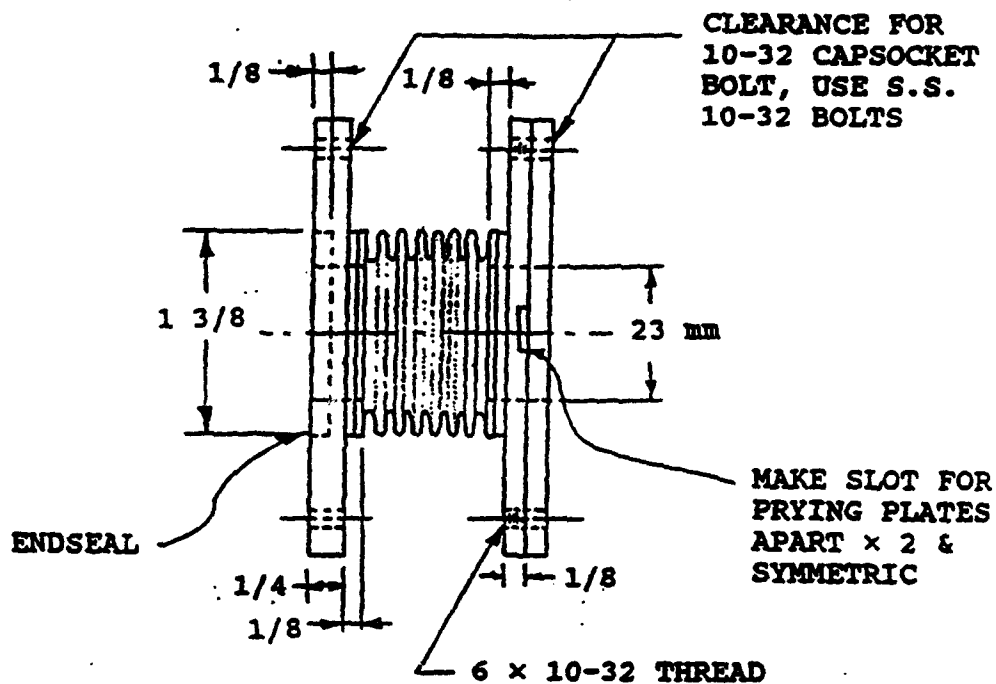
points as shown by the location of the laser discharge tube trusses in Figure 7.2. As was mentioned, it is important that the laser tube always be supported at least by three points. Three other saddles with support legs were constructed so that the laser tube prior to hanging would be supported. The cables were then, in turn, supported by three trusses that were attached to the optical table. A very important detail to the cable/hanging system is that each cable has a spring. It was reasoned if the trough shifted a small amount etc., when filled with  $LN_2$ , the cable could move without putting too much strain on the tube. Indeed, when the trough was filled with  $LN_2$  for the first time, the springs nearly contracted 6 mm (in the first trough arrangement the trough rested on styrofoam and it was the styrofoam that thermally contracted), see Figure 2. Spring tension was adjusted so the weight of one's finger on the laser tube when it is self-supporting is enough to cause further deflection in the spring. The force due to buoyancy should also be considered when the laser trough is filled with  $LN_2$ .

### Trough

A stainless steel trough was constructed, see Figure 7.2. 18 Gauge stainless steel was used and bent in the local tin shop. Removable aluminum reinforcements were used for rigidity and later for supporting the entire trough. This trough is a weaker part of the design. A more rigid unit

would have been preferred. Originally, the design had the unit sitting directly on styrofoam insulation which then rested on the optical table. This worked well for awhile but for long term operation thermal cycling of the foam would cause cracks leading to thermal instabilities. It was then decided to do a quick fix and the arrangement of supporting the trough vertically, as shown in Fig. 7.2, was chosen. The ribs that were used for rigidity, 1/4 by 1/2 inch, were then also used to support the trough. This worked, but the ribs deflect when the trough is filled to capacity with  $LN_2$ . Thicker ribs would certainly fix this problem. The end plates were sealed by using lead/tin soldering wire; 1-inch spacing was used for the end plate bolts so that a good seal would take place. It should be noted on assembly that a clockwise then counterclockwise tightening pattern should be used. No leaks have ever occurred using this method of sealing and this type of seal has considerably reduced the cost compared to prior designs which used indium wire to seal the end plates. A drain was also provided on the trough for removing  $LN_2$ . The drain consisted of a stainless steel braided hose for cryogenic use and was merely raised higher than the  $LN_2$  level during operation. The boil-off from this hose was used for external purges.

Bellows constructed of brass by Robertshaw were used to seal the laser discharge tube to the end plates. Teflon tape wrapped around the tube was then squeezed between the bellows



NOTES - BOLT HOLE PATTERN IS EQUALLY SPACED  
ABOUT CENTER  
BRASS MATR'L FOR PLATES  
ALL DIMENSIONS IN INCHES UNLESS  
OTHERWISE NOTED  
MAKE TEFLON WASHER FOR ENDSEAL  
1 3/8 x 1 x 3/16 TH'K  
BELLOWS; SERVOMETER CORP.  
(201) 785-4360 PART ST-100  
MUST BE SOLDERED ACCORDING TO  
MANUFACTURES SPECIFICATIONS.  
PLATES SHOULD BE CUSTOM BUILT  
FOR BELLOW TOLERANCES.

Figure 7.8: Cryogenic bellows end seal for connecting  
laser discharge tube to trough



end plates to form a leak proof seal, see Figure 7.8. This was also a change from indium wire and has performed superbly. Sealing between the bellows assembly and the end of the trough was accomplished by a teflon washer. This assembly performed flawlessly until the brass bellows developed microstructure cracks and leaked  $LN_2$ . Black oil was then sprayed into the bellows assembly and has since performed well. Cryogenic bellows were located and ordered but have not been tried. Further improvements to the laser should use these cryogenic type bellows.

### Electrodes

Type 306 stainless steel was used for the electrode material with excellent results. (It was felt that nickel electrodes were unnecessary.) The design we used is a threaded type as shown in Figure 7.6. When necessary an occasional cleanup with a piece of crocus paper resulted in like-new electrodes. The threaded assembly allows for easy removal; a necessity when cleaning the electrodes so that cracks would not develop in the torr-seal used to seal the electrode lead in the glass electrode holder. The electrodes were torr sealed so that the end of the electrode tips were located 13 cm from the centerline of the laser discharge tube.

### Power Supply

A Universal Voltronics, Model BAL-70-225-0S, high voltage power supply with a saturable reactor current limiter is currently being used to operate this laser. The unit is capable of 0-70 kVDC with a 0-225 mADC output current, which is, of course, of far greater power than needed for the present requirement. The supply current is divided equally between the two discharge arms of the laser. Because of the active medium's negative dynamic resistance, a 500 kOhm ballast resistor is in series with each arm [39]. The current is supplied by a cathode on each arm and collected by a common anode at the gas exhaust. Reported current and voltages in the tables are the power supply readings and the physical efficiency is calculated from equation 1.1 which has been simplified to:

$$\eta_{phys} = \frac{W_{rad}}{VI - \frac{I^2 R_b}{2}} \quad (2.1)$$

where:

V = Supply voltage

I = Supply current

R<sub>b</sub> = Ballast resistor value for one arm, 500 kOhm

W<sub>rad</sub> = Laser output power

All metallic pieces on the laser are grounded, except the kovar seal with brass compression fittings for the internal

purges located on the cathode male glass joint in Figure 7.6. Plexiglass boxes were constructed to prevent accidental contact with these pieces as well as with the wire connections to the electrode holder.

### Optics

A specially built grating by Zeiss was used in our laser to maximize performance in the 5200 nm region. A 28x28x10 mm size grating with a 25x25 mm ruled steel, gold-plated surface was chosen. Selection of the blaze angle was based on information supplied by the manufacturer and the article by Loewen et al [40]. Since the groove density is limited by the angle at which the first order is reflected (actually it is limited by the wavelength), a 290 grooves/mm line density was chosen (See Appendix C). This was a compromise between the lower cost associated with a smaller size grating and manufacturing tolerances on the blaze angle. Once the groove density was selected the blaze angle was chosen as 48.50°.

The grating is mounted in a holder that is a copy of a University of Bonn design and mounted to an Oriel 13031 rotation stage with 1.8 arc second sensitivity [25]. The holder allows for tilt in two planes, giving the entire grating and rotation stage three degrees of angular adjustment.

The TEM<sub>00</sub> mode was chosen for operation and design of the resonator. Intracavity irises used between the Brewster

windows and the mirrors help promote this mode by attenuating other modes. The output coupler/grating arrangement is of a half-symmetric resonator, Figure 7.9. The common hemispherical arrangement as shown in Figure 7.10 was not chosen for the resonator because; 1) grating inability to separate adjacent rotational transitions, and 2) the waist of the beam must cover a certain distance since the resolving power of grating is directly proportional to the width of the incoming beam. For a 2-meter cavity with a 19-mm bore the grating is able to separate wavelengths with a difference of approximately 40 nm, see Appendix D. The P branch vibrational-rotational transitions that occur in a CO vibrational band component are roughly spaced by 10 nm. The high angular sensitivity of the half-symmetric resonator is useful for rejecting the other close transitions. Other advantages of the half-symmetric resonator are: 1) the  $TEM_{00}$  mode fills the laser cavity more than the hemispherical resonator, and 2) the  $TEM_{00}$  mode fills the grating surface. For a 2-m half-symmetric resonator with a 10-m radius of curvature for the output coupler and a flat grating, a  $TEM_{00}$  waist size of 2.57 mm occurs at the grating surface, see Appendix E. The width required to collect 99% of the Gaussian beam can be shown to be  $\pi \cdot W_0$ . The width needed to eliminate diffraction effects needs to be at least  $4.6 \cdot W_0$ , where  $W_0$  is the  $TEM_{00}$  beam waist [41]. With these limits the optics were selected for the laser cavity. The optimum curvature for this laser is a 25 m

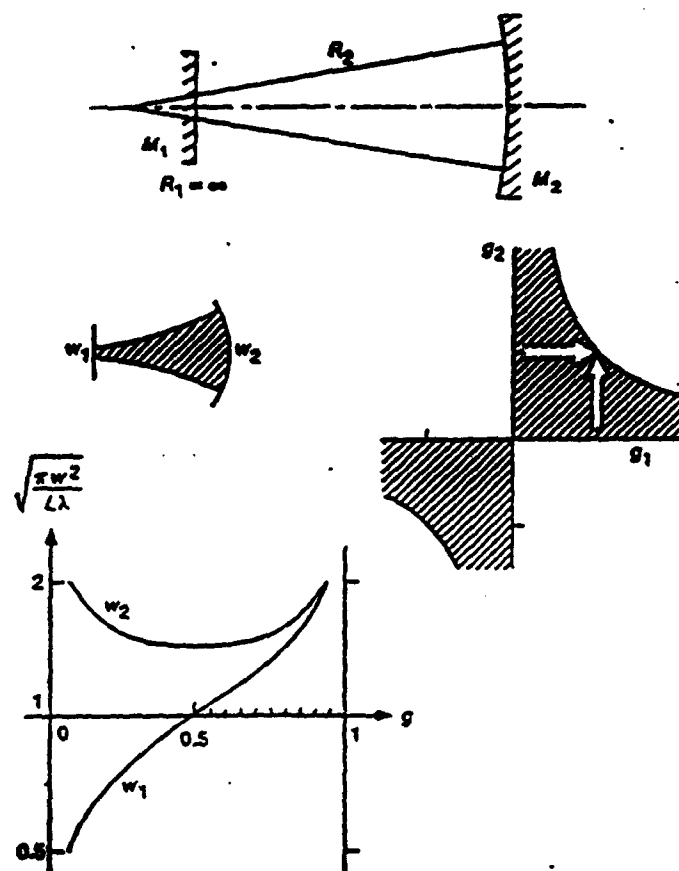


Figure 7.9: Half-symmetric resonator arrangement, stability diagram and waist size as a function of the well known  $g$  parameters [Seigman]

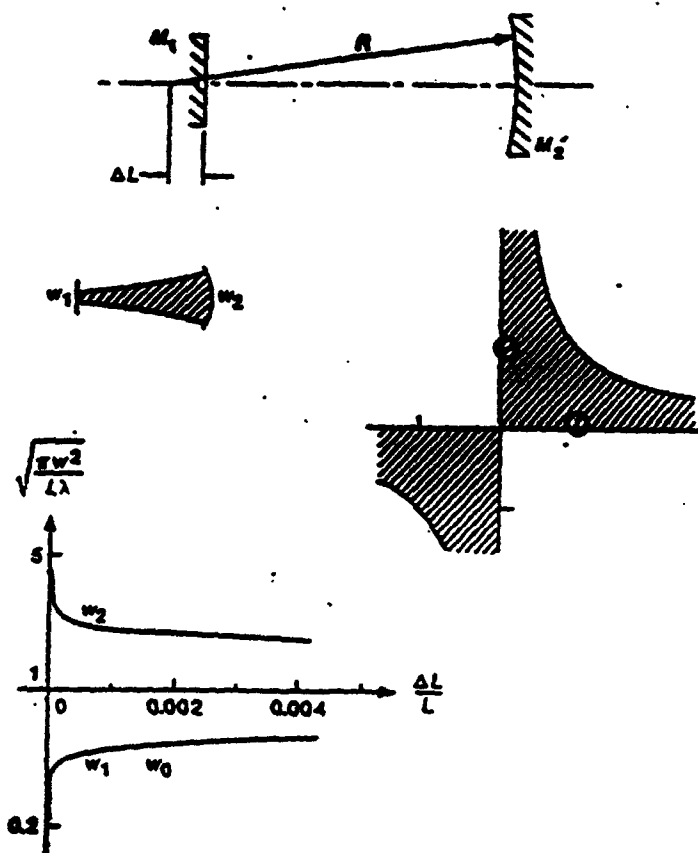


Figure 7.10: Near-hemispherical resonator arrangement, stability diagram and waist size as a function of the well known  $g$  parameters [Seigman]

Table 7.3. Parameters for selecting optimum output coupler

$R_2, m$ Output coupler	$g$	$w_0, mm$ waist at grating <3.48mm	$w_2, mm$ waist at output coupler <3.69mm	$gvol$ /pi/L  TEM <sub>00</sub> mode volume	Minimum laser tube dia., mm	Comment
5	0.6	2.016	2.602	1.332	11.96	
10	0.8	2.57	2.88	1.856	13.24	best, 15 mm tube
20	0.9	3.156	3.326	2.625	15.29	
25	0.92	3.355	3.497	2.934	16.08	best, 19 mm tube
30	0.933	3.524	3.643	3.210	16.76	$w_0$ >3.478

curvature, see Table 7.3. We did not select this radius because originally the laser was designed for a 15-mm inside diameter and the 10-m optic had already been ordered for this diameter. This turned out to be fortunate, because great care is needed in aligning this system. Our Oriel model 14501 gimbal mount used for the output coupler is rated at  $0.05^\circ$  sensitivity and is barely adequate for this optical arrangement, see Appendix D.

The typical Littrow configuration, as shown in Figure 11, was not used for this optical set-up since losses from the grating were not exactly known until after being manufactured. Instead, a novel arrangement, as shown in Figure 7.12, was used to reflect back the grating's losses from zeroth order. This arrangement will be referred to as the "semi-Littrow" reflector or arrangement. The original design of the optics did not include this setup and it was added only after experimental measurements indicated that high losses were occurring in zeroth order. Another Oriel gimbal mount was used with a 10-m curved silver first surface total reflector for  $10.6 \mu$ . This mirror, placed 16.5 cm from the center of the grating, reflected back zeroth order losses. It is assumed that the losses occurring on zeroth order are due to S polarization. Although a S and P efficiency curve was not supplied with the grating, it can be assumed that since the grating was designed for high reflectivity at  $5 \mu$  that it would be similar to Figure 7.13. Therefore, when the semi-



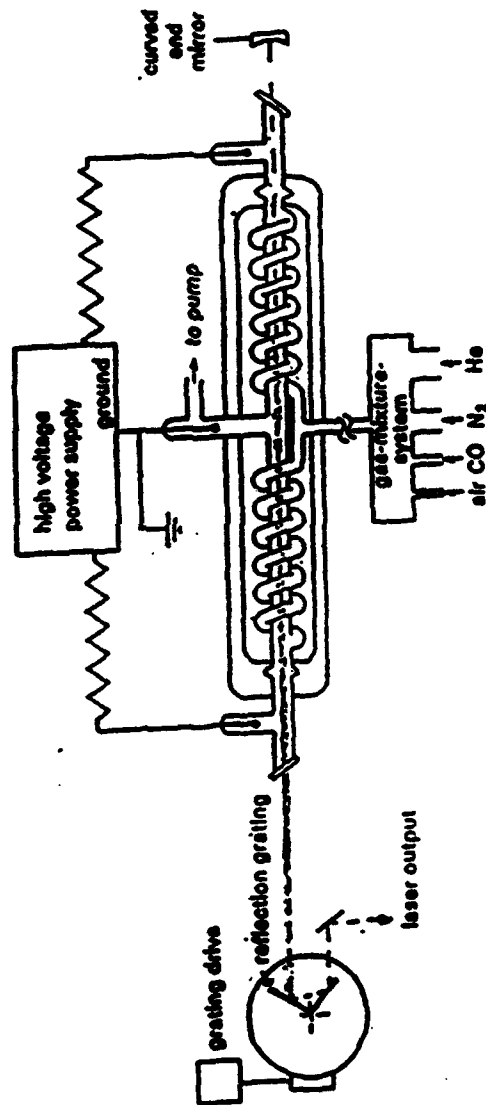


Figure 7.11: Typical Littrow configuration for a laser (Urban)

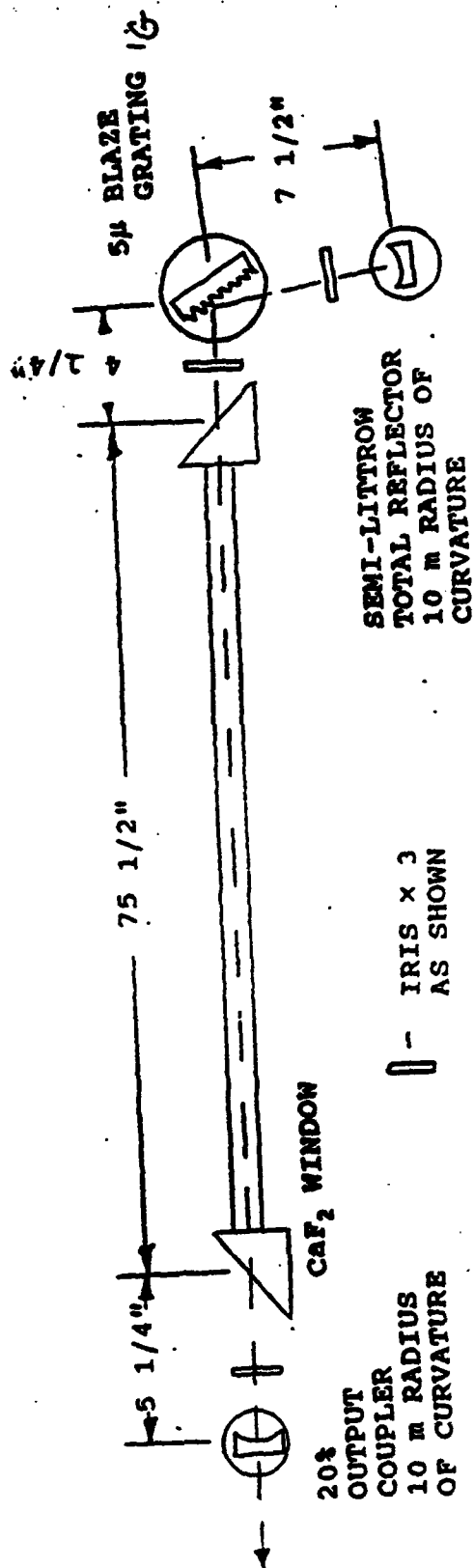


Figure 7.12: FAFED CO laser's optical resonator

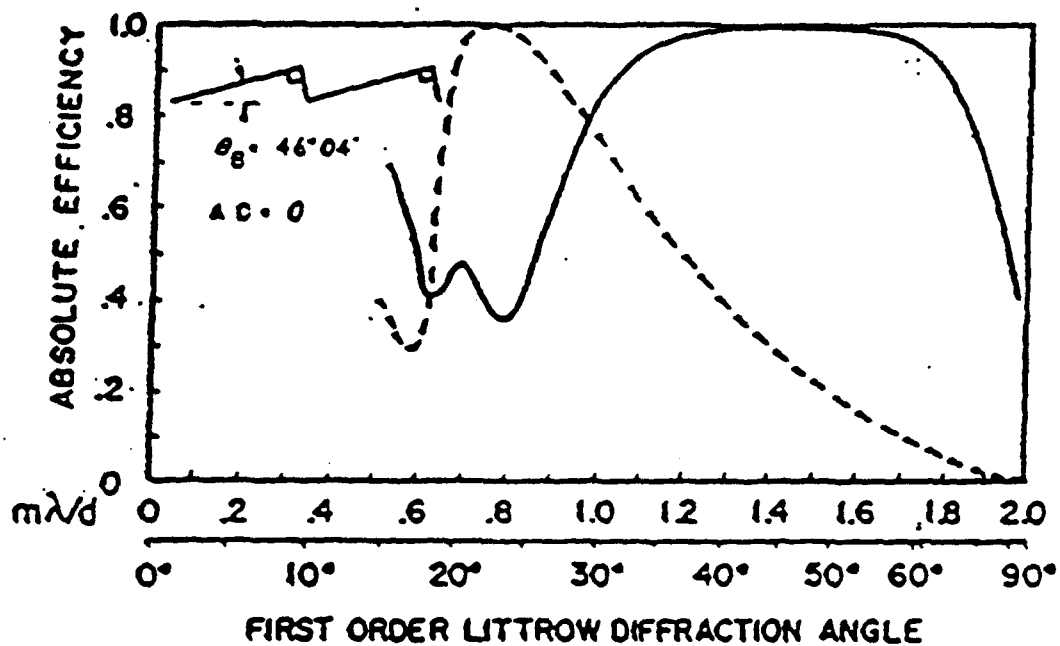


Figure 7.13: Typical grating first order efficiency curves for a  $46^\circ 04'$  blaze angle echelette grating, perfectly conducting with  $0^\circ$  between incident and diffracted beams. Solid curve, S plane; dashed curve, P plane [Loewen et al]

Littrow is being used the laser beam is no longer polarized and the cavity consists of two resonators; one for the S polarization and one for the P polarization.

The output coupler is a zinc selenide with a multi-layer dielectric coating made by Laser Optics. Reflectivity-transmitting has been optimized from 4.9 to 5.3  $\mu$  to give 80% reflectivity. The percent output was chosen based on the output couplers used by Kan and Whitney. They reported good performance with a 35% output coupler as well as a 20% output coupler. To be conservative a 20% output coupler was chosen for this laser.

The optics are mounted to a Newport Research Series 10x4x1 ft table. This table is mounted on NN series non-isolating support legs. To keep the optical table insulated from the LN<sub>2</sub>-filled trough, 1.5-inch-thick styrofoam was used to build a box around the trough. A 1/4-inch rubber mat was placed beneath the trough to keep cold gas from cooling the table surface. During operation oxygen may freeze out on the trough and drip onto the styrofoam. After many cycles the styrofoam cracks and the liquid oxygen drips on the rubber. For this reason aluminum trays were used to catch the liquid oxygen. A fan blows room air under the trough and keeps the trays warm.

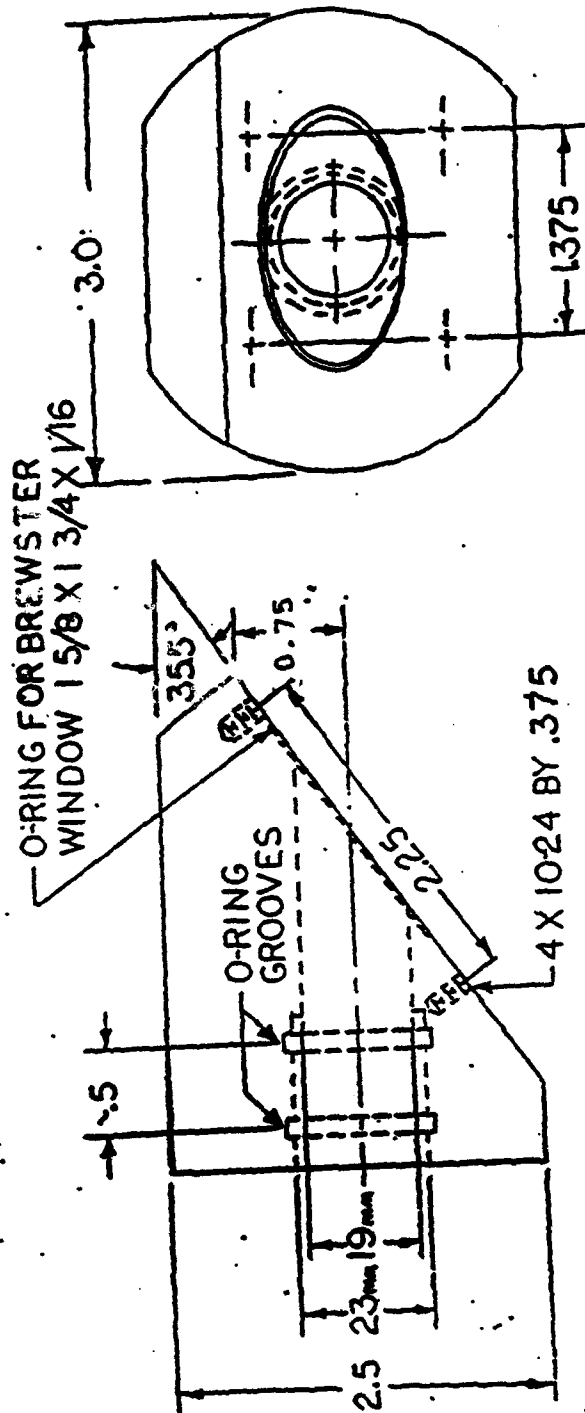
### Brewster Windows

CaF<sub>2</sub> windows placed at a Brewster angle of 35.5° as shown in Figure 7.14, are used to insure low losses for the S polarization at 5214 nm. The initial design of the optics did not take into account P polarization but from Figure 7.15 it can be seen that the losses are not that great.

UV grade CaF<sub>2</sub> windows were not used because prior experience has never indicated a need for these more expensive optics. With the operation of this laser, at the conditions which will be discussed later, we have noted a degradation due to UV radiation. For this reason UV grade should be specified if copying this laser design or for replacements.

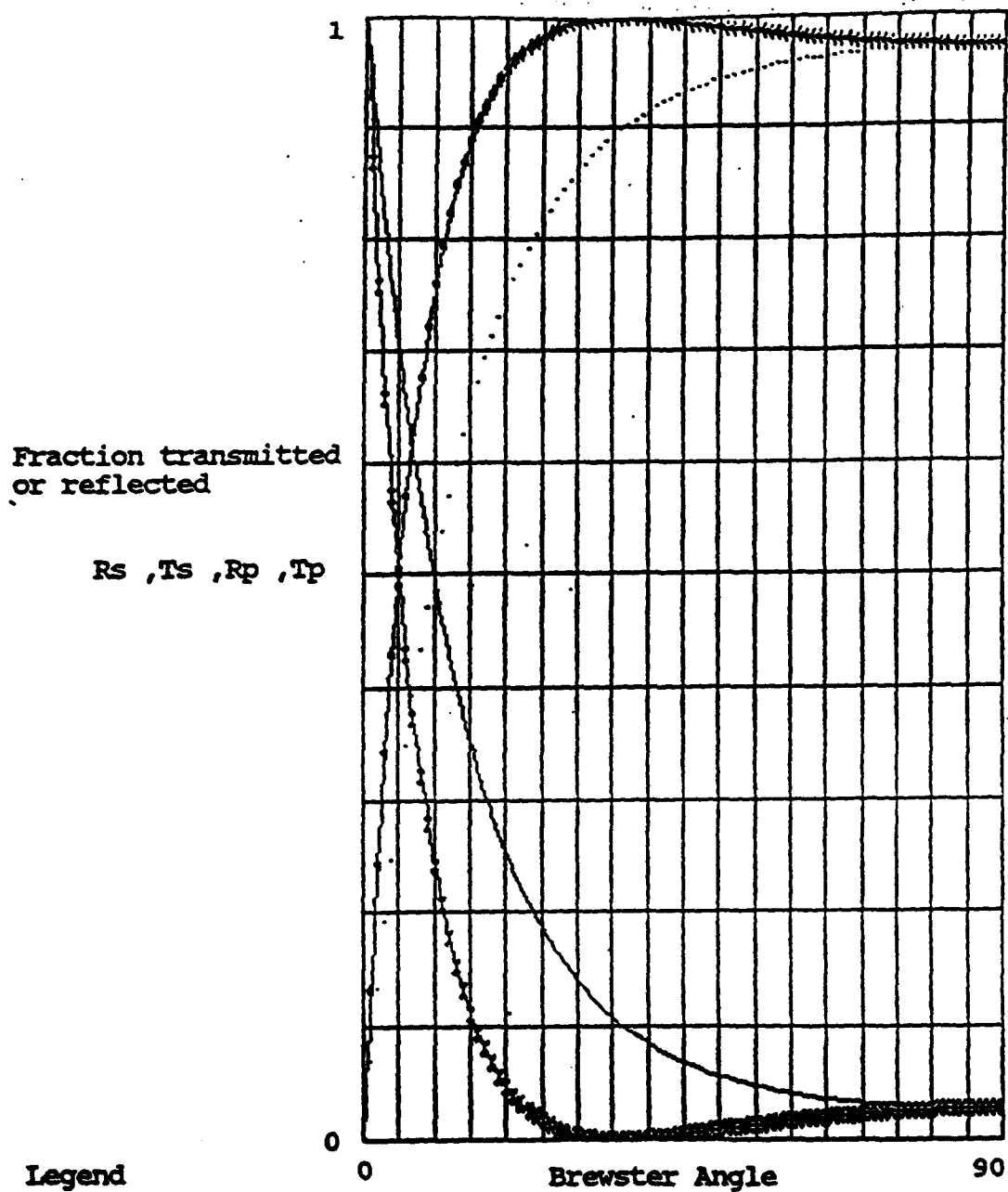
Brewster window holders were made of nylon. Double o-rings were used to seal the nylon Brewster window holder to the laser discharge tube. A single o-ring is used to seal the CaF<sub>2</sub> Brewster window holder. A flat was machined on the outer nylon surface to facilitate optical alignment. A machinist's level against this surface allows for excellent alignment for S and P polarization; a requirement for best performance with the grating.

Bolts with o-rings are used to retain the CaF<sub>2</sub> window when running in the vertical position. A four hole pattern is shown but only two are really necessary to keep the CaF<sub>2</sub> Brewster window from falling when the pump is turned off. Four retaining bolts should not be used in case the gas pressure inside the laser tube should exceed atmospheric



NOTES: O-RINGS FOR DISCHARGE TUBE  
SHOULD BE FIT ACCORDING TO  
MANUFACTURER  
MATERIAL-L-NYLON  
ALL DIMENSIONS IN INCHES  
UNLESS OTHERWISE NOTED

Figure 7.14: FAFED CO laser's Brewster window holder



Rp=reflection of P plane; line  
 Tp=transmission of P plane; dots  
 Rs=reflection of S plane; x's  
 Ts=transmission of S plane; diamonds

Figure 7.15: Fractional losses from incident S and P planes,  $\lambda=5200$  nm, on a  $\text{CaF}_2$  window ( $n_1=1$ ,  $n_2=3.975$ ) as a function of Brewster angle

conditions.

#### Gas Handling and Pressure Measurement

The gas handling system is as shown in Figure 7.16. The rotometers are listed in Appendix F with calibration curves.

A Leybold Heraeus SV280 vacuum pump rated at 198 cubic feet per minute is used. A 2-inch butterfly valve modified with a 2-foot handle is used to throttle the laser exhaust gases. This valve is difficult to control but very inexpensive and for one-time adjustments is very suitable. An ozone trap and high flow filter was built for the vacuum pump. Steel wool converts ozone to rust and a Fram 322 filter traps any fine particles. The box is sealed with a rubber gasket. Vacuum lines consist of PCV 2-inch schedule 40. Joints are PCV plastic and epoxy glued. This worked very well for our application. Two-inch couplings were used in the necessary places. Vibration isolation and flexibility between the glass tube and PCV was obtained using rubber tubing. This tubing would collapse under vacuum and reinforcing rings were made and fitted inside. A glass lip on the exhaust prevents slippage of the rubber tubing from the vacuum. Pressure measurements from the laser discharge tube were taken off the exhaust tube male connector as shown in Figure 7.17. It is assumed that the flow is not choked and the pressure as in the exhaust is the same pressure in the discharge tube.



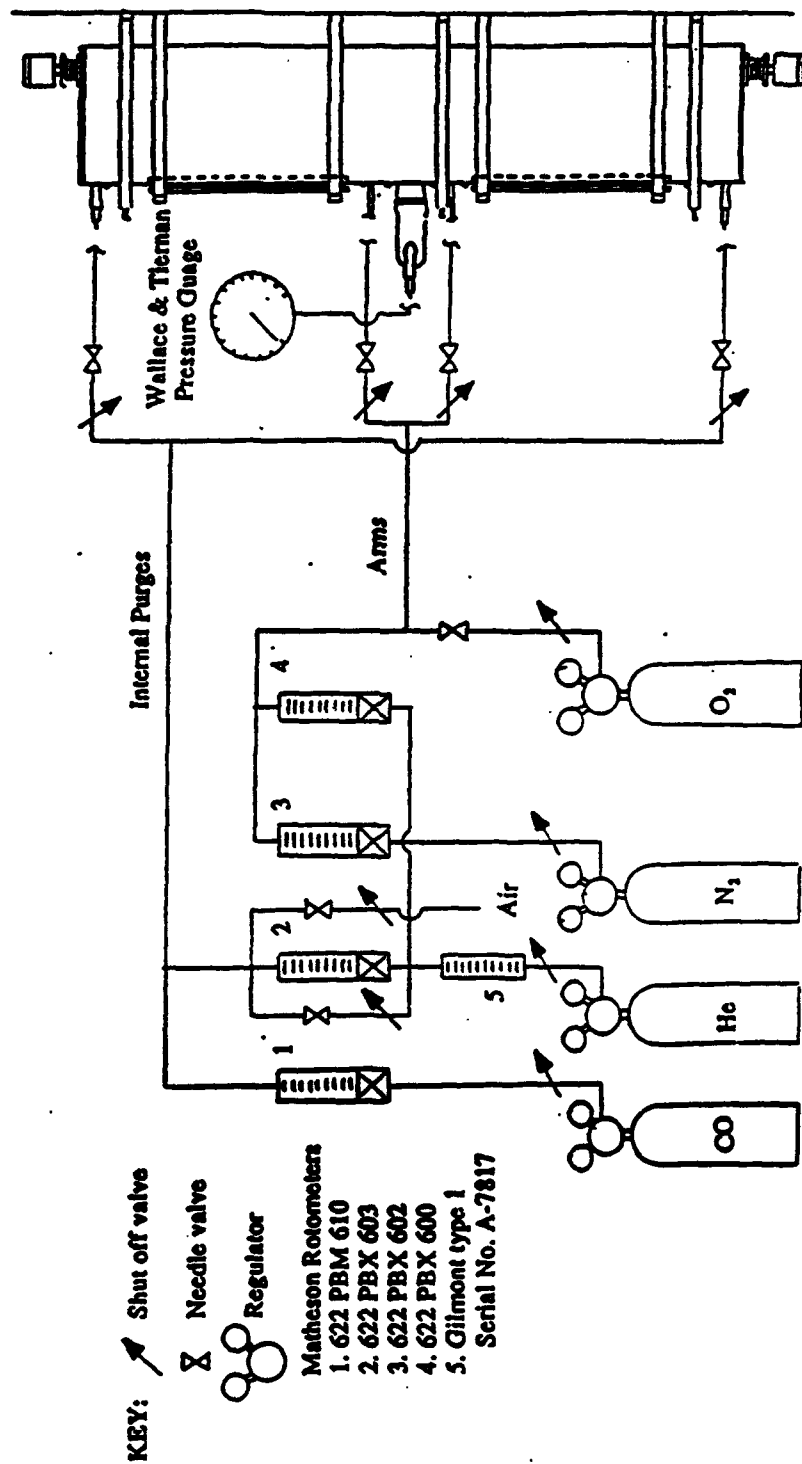


Figure 7.16: Gas handling and pressure measurement for FAFED CO laser

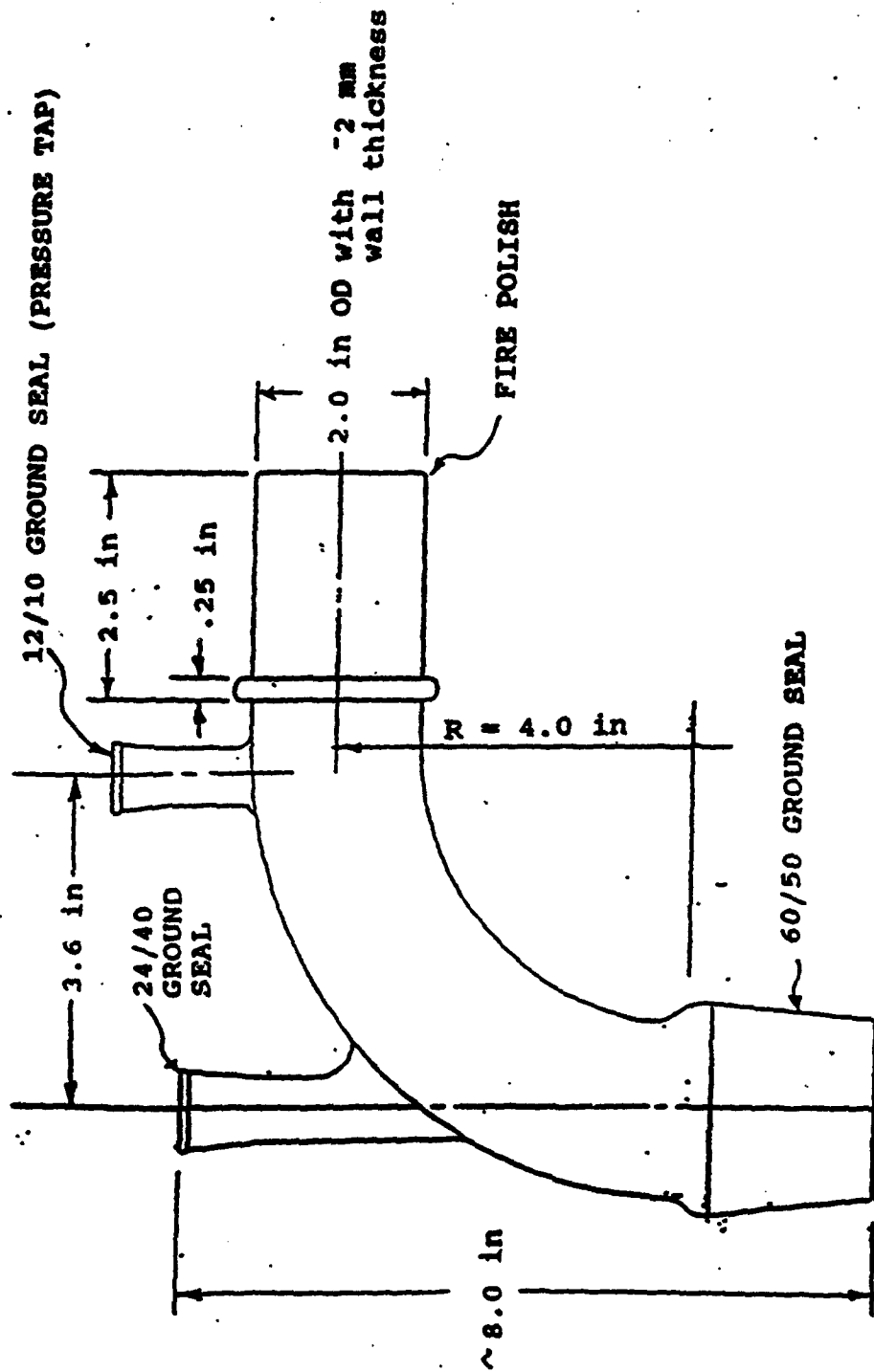


Figure 7.17: FAFED CO laser exhaust tube/common anode/pressure tap male taper joints

### 7.3. OPERATION

#### Broad-Band Performance

The laser was designed to lase with high power and good stability on the  $v=8 \rightarrow 7$  P(11) transition and to date only a few hours were spent checking the performance of the laser operating in a broad-band, or multiline mode. The optical setup for these runs was with the 10-m radius 80% output coupler with a flat silver first surface reflector made by II-VI Corp. The total reflector was optimized for the 10.6-micron region and was mounted in another Oriel gimbal mount at the location of the grating shown in Figure 7.12. Unfortunately, at this time the gas delivery system was not as indicated in Figure 7.16. The recorded measurements in Tables 7.4 and 7.5 were inferred from the recorded partial pressures and the measured CO mass flow rate.

Figure 7.18 shows a spectrum of the output during operation of the laser at the recorded partial pressures listed in Table 7.4. The  $v=2 \rightarrow 1$  P(12) transition is seen to be lasing even with a high percent output coupler. Total power was 12.5 watts and it was estimated that at least 0.81 Watt was on this line. Prior to this lasing the laser was also

**Table 7.4: Broad-band lasing conditions for  
0.8 W on the (2-1) P(12) transition**

<b>Date: 10-26-1992</b>		
<b>Gas</b>	<b>Partial Pressure (Torr)</b>	<b>mass flow rate (10<sup>3</sup> g/min)</b>
He internal purge	2.76	35.0
He	9.00	65.2
N <sub>2</sub>	2.75	143
CO	1.60	2.66
Air	0.01	0.89
<b>Total</b>	<b>9.56</b>	<b>247</b>
<b>He:CO:N<sub>2</sub>:Air Molar ratio</b>		
<b>729:99:171:1</b>		
<b>Discharge Conditions</b>		
<b>Current mADC</b>	<b>20</b>	
<b>Voltage kVDC</b>	<b>9.5</b>	
<b>Laser Power Broad Band W</b>	<b>12.5</b>	
<b>Physical Efficiency</b>	<b>13.9%</b>	

Table 7.5 : 92 W Broad-band lasing conditions

Date: 10-26-1992		
Gas	Partial Pressure (Torr)	mass flow rate (10 <sup>3</sup> g/min)
He internal purge	4.15	18.9
He	9.00	75.5
N <sub>2</sub>	2.75	138
CO	1.60	6.61
Air	0.01	0.89
Total	17.5	239
He:CO:N <sub>2</sub> molar ratio 751:92:157		
Discharge Conditions		
Current mADC	45	
Voltage kVDC	18	
Laser Power Broad Band W	92	
Physical Efficiency	30.3%	

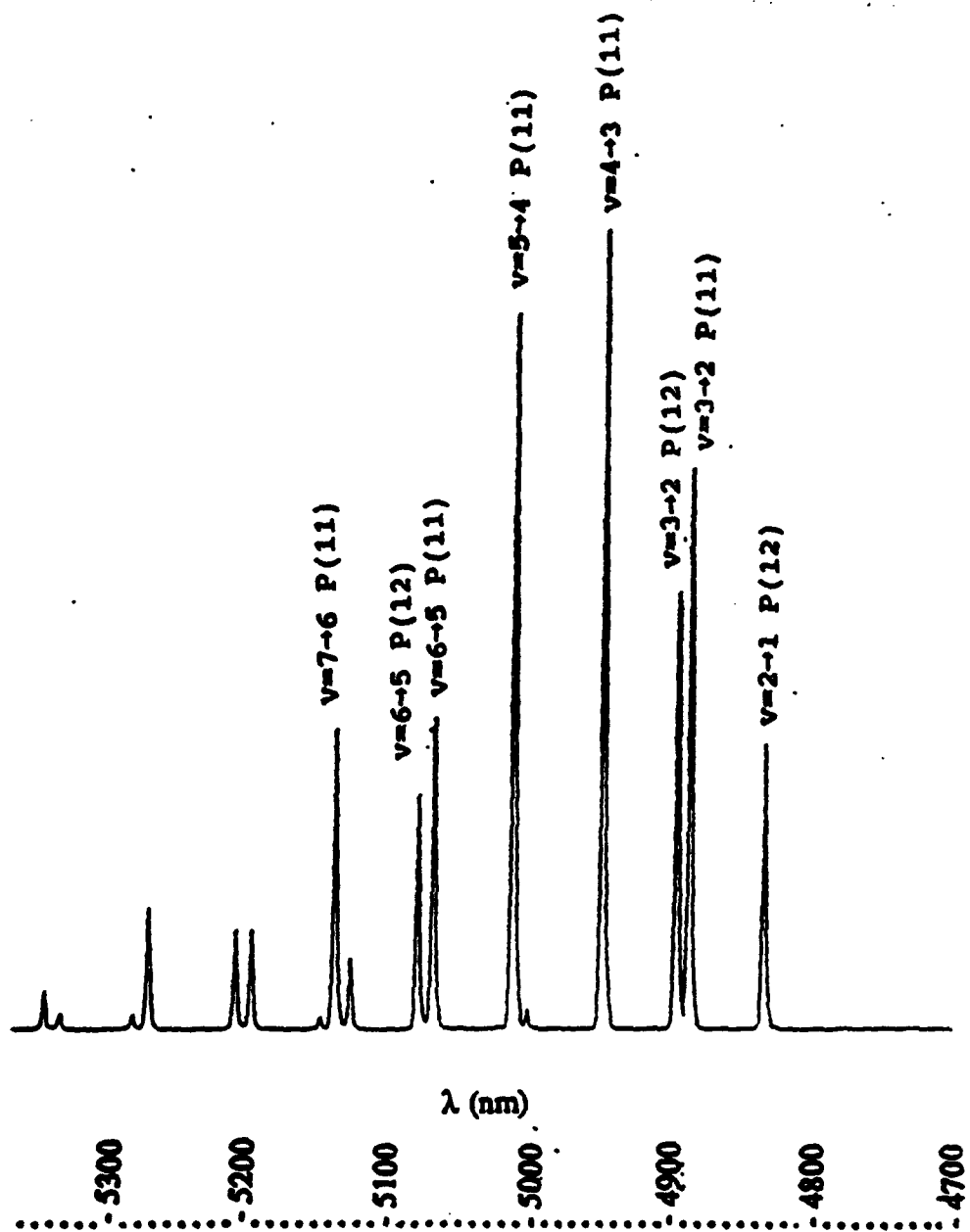


Figure 7.18: Typical all line operation of FAFED CO laser

checked for high power. No scan was made for the high power run and the partial pressures and discharge conditions are reported in Table 7.5. The measured power was 92 watts at a 30.3% physical efficiency. No further runs were made since we were operating with a new output coupler and did not want to damage it from high energy loading without any edge cooling. A comparison of mass flow rates between this run and the 35% output coupler-1g/sec power curve of Kan and Whitney (Figure 7.19) estimates this laser is using 2 orders less mass flow. This indicates the laser is capable of much higher power since the 92 watt conditions had the pump considerably throttled and output was with a 20% rather than higher output coupler.

#### Single Line Operation on the $v=8-7$ P(11) Transition

Much has been learned by operating this laser on the  $v=8-7$  P(11),  $\lambda=5214$  nm line. Most operational problems encountered running the laser can be pinpointed to the optics. The biggest problem has been amplitude stability on the  $v=8-7$  P(11) line. This instability has been caused by thermal contraction effects in the optical bench.

The present setup has evolved from a trough that used to sit directly on 2 inches of styrofoam. With that setup the trough was put under pretension by inverted trusses. Even though the trough was pre-loaded in this manner, once the trough was filled with  $LN_2$  it sank approximately 2-3 mm. After a week or more it stabilized around 3 mm. At this point in

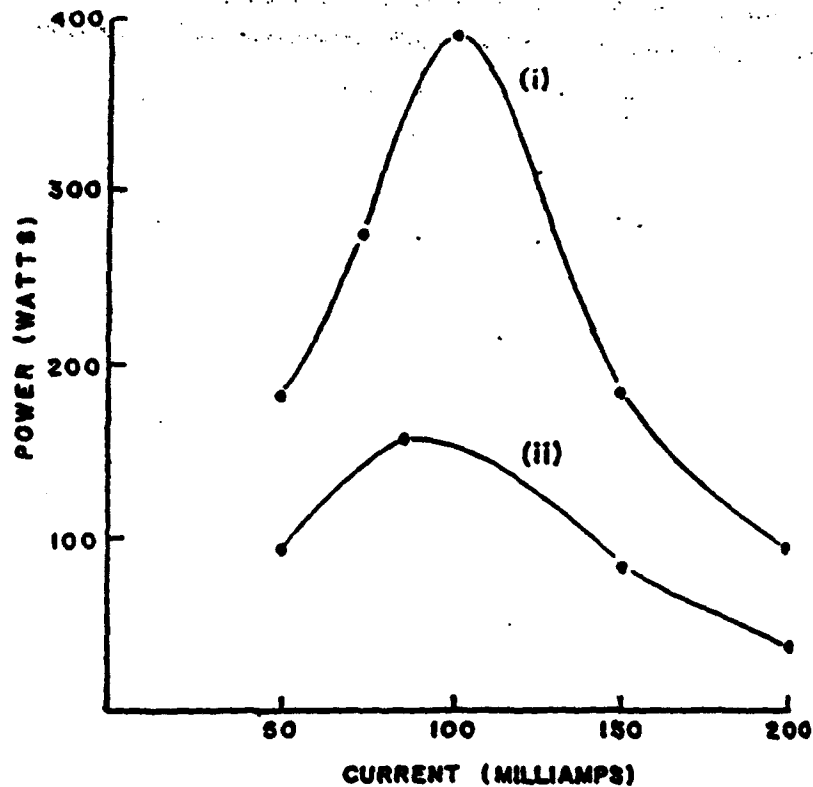


Figure 7.19: Variation of laser power as a function of discharge current for 2 different mass flow rates of Kan and Whitney's laser. (i) 2 g/sec, (ii) 1 g/sec with a 35% coupler He:CO:N<sub>2</sub> molar ratio of 950:36:14

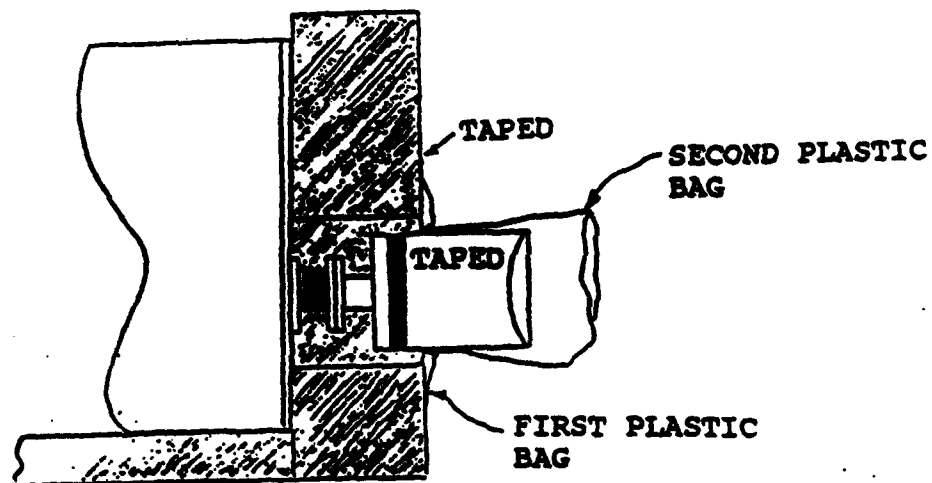


Figure 7.20: Present external purge arrangement



time stability was excellent. The laser was run for at least 3 hours a day with a  $\pm 8\%$  power deviation. After a month or more the styrofoam box started developing cracks from contact with liquid oxygen. Liquid oxygen would condense on the cooled stainless steel trough walls from air gaps around the styrofoam box and then drip onto the styrofoam causing the cracks. This caused the optical table to be thermally unstable.

The present setup, shown in Fig 7.2, has been evolved to resolve these problems. With this setup, even though there are cracks in the styrofoam, the optical table has remained thermally stable. As was mentioned earlier the supporting ribs for the trough are also now being used to support it. The ribs were not designed for this and some deflection occurs. The level of  $\text{LN}_2$  is maintained during operation at about 3-4 cm above the electrodes. This level is sufficient for cooling and keeps the deflection to a minimum.

Other problems have been with power attenuation of the laser line by absorption of atmospheric  $\text{H}_2\text{O}$ , see Table 7.1. External purges were made out of plastic for the optical path between the Brewster windows and the optics and flushed with dry  $\text{N}_2$  from a bottled supply. When the room humidity level is high, the line will not even turn on without these external purges. Care must be taken that the external purge system does not put any load on the optical system when thermally contracting, thereby causing misalignment. The setup that is

now being used is shown in Figure 7.20.

The gas and discharge conditions used to optimize power on the  $v=8-7$  P(11) transition are listed in Tables 7.6 and 7.7. Power has been as high as 8 watts without the semi-Littrow arrangement and 15 watts with it. Fig. 7.21 shows stability of the laser with the semi-Littrow arrangement and without it for the conditions of Table 7.7. Fig. 7.22 is a typical spectrum of the laser with and without the semi-Littrow for the lasing conditions of Table 7.6. The lines adjacent to the 5214 line  $v=8-7$  P(11) are from the  $v=9-8$  band and are lasing from zeroth order due to the high gain. These transitions are not present when operating without the semi-Littrow reflector. Even though not shown the scans taken with the semi-Littrow are scanned over a wide spectral range, from 4.1 to 5.4  $\mu$  to make sure no other lines are lasing. Scans taken without the semi-Littrow are from 5.15 to 5.8  $\mu$ .

Typical single line mode shapes are shown in Figure 7.23. These were obtained by holding a paper in the beam for a short time. One can see that the modes for good power  $>6$  w are multimode. To date good power has not been achieved unless it has been multimode.

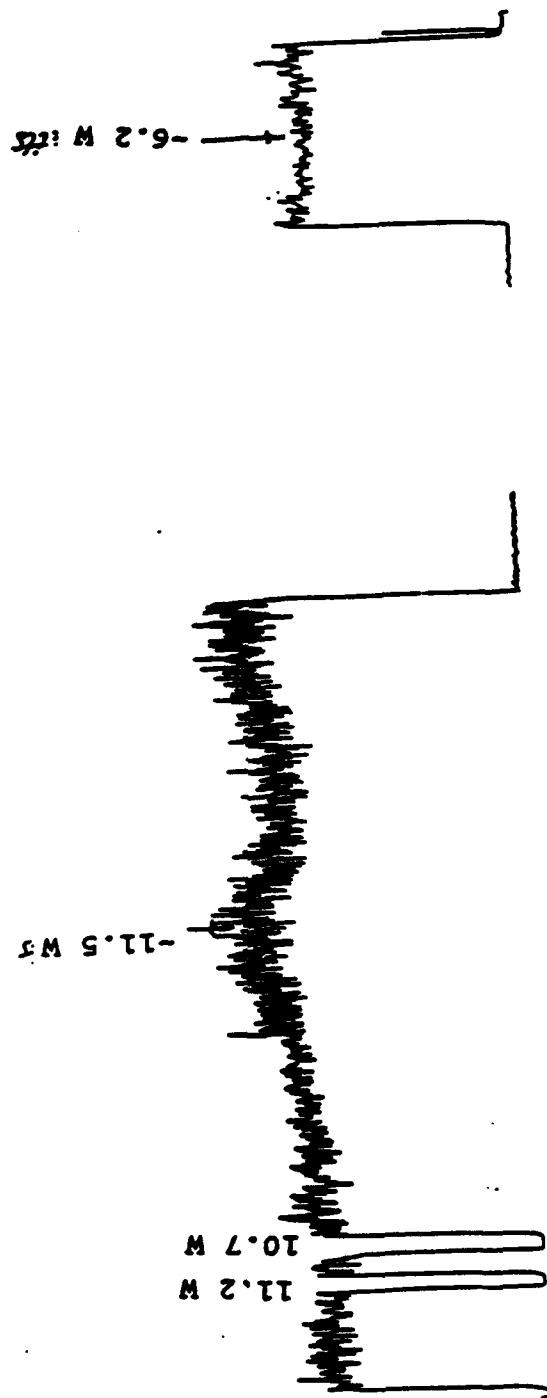
Table 7.6: 15 W Single line lasing conditions  
for the (8-7) P(11) transition

Date: 3-29-1993		
Gas	Partial Pressure (Torr)	mass flow rate (10 <sup>3</sup> g/min)
He internal purge	4.80	95.7
He	2.33	51.3
N <sub>2</sub>	2.22	267.9
CO	0.92	141.7
Air	0.08	11.87
Total	10.35	568
He:CO:N <sub>2</sub> :Air 689:89:214:8 molar ratio		
Discharge Conditions		
Current mADC	30	
Voltage kVDC	15	
Laser Power W	8.5	
Single Line	Semi-Littrow 15.5	
Physical Efficiency	3.78%	
Single Line	Semi-Littrow 6.89%	

Table 7.7: 10 W Single line lasing conditions  
for the (8-7) P(11) transition

Date: 5-16-1993		
Gas	Partial Pressure (Torr)	mass flow rate ( $10^3$ g/min)
He	3.92	154
N <sub>2</sub>	2.56	341
CO	1.09	193
Total	7.57	688
He:CO:N <sub>2</sub> molar ratio		518:143:339
Discharge Conditions		
Current mADC	30	
Voltage kVDC	15	
Laser Power W	6.3	
Single Line	Semi-Littrow 10.0	
Physical Efficiency	2.80%	
Single Line	Semi-Littrow 4.44%	

NOTE - NOT THE SAME SCALE



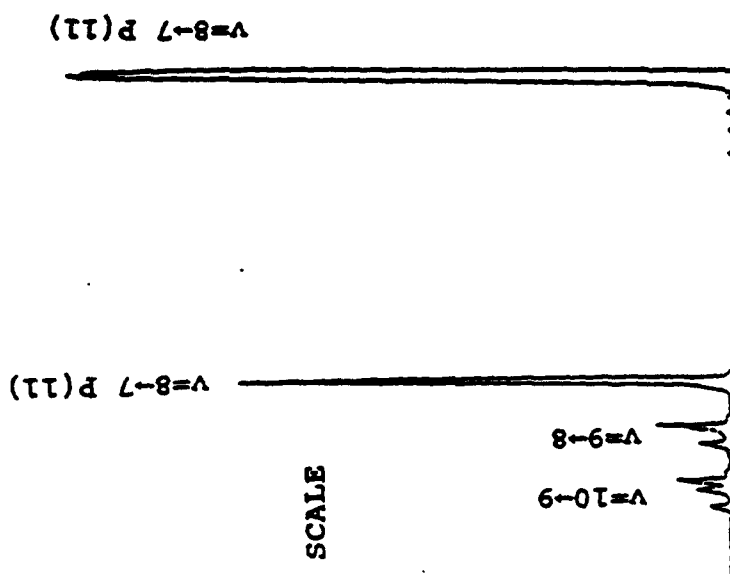
~10 MINUTES  
WITHOUT "SEMI-LITTROW"

~30 MINUTES WITH "SEMI-LITTROW"

Figure 7.21: Stability of FAFED CO laser with and without semi-Littrow zeroth order return


WITHOUT "SEMI-LITTROW"

WITH "SEMI-LITTROW"




NOTE - NOT THE SAME SCALE


Figure 7.22: Typical cw single line  $v=8-7$  P(11) line spectrum with and without semi-Littrow reflector




Without Semi-Littrow return.  
Combination of  $TEM_{0,0}$  and  $TEM_{1,1}$   
8.9 Watts, 21 Feb. 1993.



With Semi-Littrow return.  
Two separate resonators,  
S-plane is multimode and P-plane  
is in the  $TEM_{0,0}$ , 21 Feb. 1993.



With Semi-Littrow return adjusted  
to output coupler, 13.8 Watts,  
21 Feb 1993.



Without Semi-Littrow return.  
"Donut" mode is a combination  
of the  $TEM_{0,1}$  and  $TEM_{1,0}$ .  
7.2 Watts, 14 Feb. 1993.

Figure 7.23: Typical single line mode shapes with and without semi-Littrow zeroth order return

#### 7.4. DAILY OPERATING PROCEDURES

##### Leak Testing

As with the design of the laser, our lab procedure for running it has evolved over the course of this development project. It is essential to check the leak rate of the laser before running. Satisfactory leak rates for the entire system are  $\leq 1.4$  torr/hr: for the laser tube itself,  $\leq 1.0$  torr/hr.

It was noticed if any leak existed, giving rates higher than this, the pump down pressure before startup was sensitive enough to detect any leaks that would cause poor lasing performance. If the pump down pressure is not indicating a good vacuum, helium is added and the discharge is struck without any cooling. The discharge will appear whitish-purple in all regions of the laser tube if the leak rate is acceptable. If there is any sign of an orange discharge, this indicates air is getting into the system. For example, if only the output coupler arm has an orangish discharge from the cathode to the output coupler electrode, then the leak is from 1) the tapered joint or internal purge on this side, 2) a combination of this and a leak coming from the output coupler arm gas inlet, or 3) a combination of 1 and 2 with the



Brewster window assembly also leaking. The possible leak locations can be systematically and easily checked by using rubber stoppers to plug the end of the laser tube and the arm inlet. Such rubber stoppers can be used even for the 1/4-inch kovar seals. In the event the leak is coming from the taper seal it will be evident by examining the tapered joint for a channel forming in the vacuum grease. Suspect glass joints made on this tube. These can be examined by spraying liquid acetone onto the joint. Once the acetone enters the discharge from this leak a bright beautiful purple discharge will occur.

#### Laser Operation

After the vacuum pump has been turned on and the laser tube has been checked for leaks the  $N_2$  is turned on for the external purges. This keeps frost from forming on windows when the trough is being filled with  $LN_2$ . The helium discharge is left on with a low current setting as the trough is filled. The discharge allows one to see the level of the  $LN_2$  to prevent overfilling of the trough.

The  $N_2$  is added, followed by the CO and finally, the air. The current is increased as each gas is added to prevent extinguishing the discharge. Usually, if the discharge is quenched, there isn't any trouble restriking the discharge with all the gases in the laser tube. The current is usually set at  $\leq 20$  mAmps (the voltage should be  $\approx 11$  kV) for

alignment of the optics for the  $v=8-7$  P(11) line. It is found that if the current/voltage conditions exceed the above values, there is a possibility the line will not lase. This is caused by too little  $O_2$  in the active medium. By using an initially low current setting the CO is being prevented from dissociating. Once lasing action occurs the  $O_2$  can be optimized for higher currents.

The color of the discharge can be used as a diagnostic since it is an indication of the current/voltage conditions. The proper color is a dull "CO blue" in the arms and a bright "orangish-pink" in the internal purge area. If the discharge does not appear as such the line may not even lase. Improper conditions are a "bluish-white" in the arms and "purplish-white" or "pinkish-white" in the cathode electrode internal purge area. A discussion of the possible cause for this is found in Recommendations and Conclusions.

#### Adjustment of the Laser Optics

Prior to startup the optics and irises are aligned with two HeNe lasers. The  $CaF_2$  windows are 5 mm thick so they should be in place when aligning the optics and irises to the bore of the laser tube. The first HeNe laser is set up behind the grating and is used as a reference for all the optics. This HeNe laser is a permanent part of the optical arrangement and has a cage built around it to protect it from misalignment. The second HeNe laser is temporarily positioned

in front of the output coupler.

The grating setup is located on the optical table so that when turned to a position parallel to the axis of the laser tube the HeNe beam just grazes the face of the grating. The output coupler mount is also centered using this HeNe beam.

The grating is tuned so that when aligned, the different orders of the HeNe coming from the output coupler are in alignment with the irises. Orders around the  $\theta=50$  degree position (Littrow configuration, see Appendix C and Figure 7.32) should be especially well aligned since this is the region for the first order for  $\lambda=5124$  nm. The output coupler is aligned by using the HeNe laser located behind the grating. The reflections should align themselves on top of each other. If patterns such as those shown in Figure 7.24 are seen, they indicate that the laser or the mirrors are not exactly aligned. These are standing wave patterns and are indicative of a beam coming into a stable resonator at an angle.

A 1/3-m Spex spectrometer is used to detect the laser beam as well as emission from our experimental optical cell. Figure 7.25 shows the optical path layout. The HeNe is used to align the optics and to calibrate the Spex spectrometer.

The easiest way to tune the optics for the  $v=8-7$  P(11) line is to first align the output coupler and grating in zeroth order. This ensures, when the grating is tuned to the single line position, at least one of the two output coupler orientations is well aligned. These two orientations can be

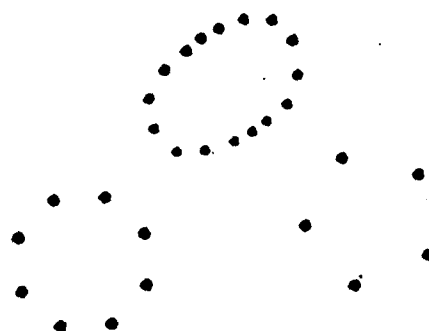
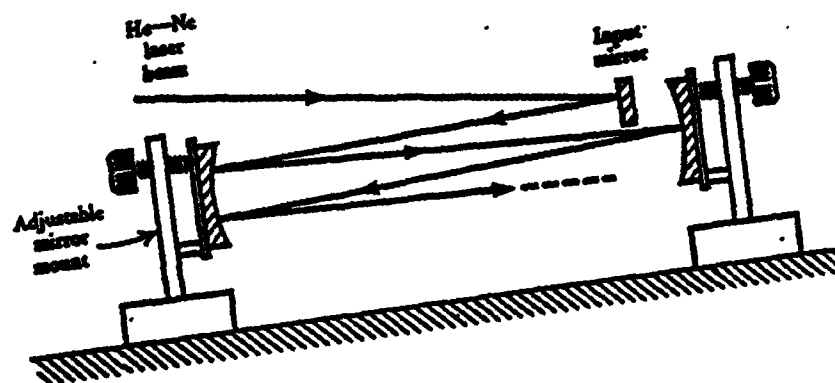
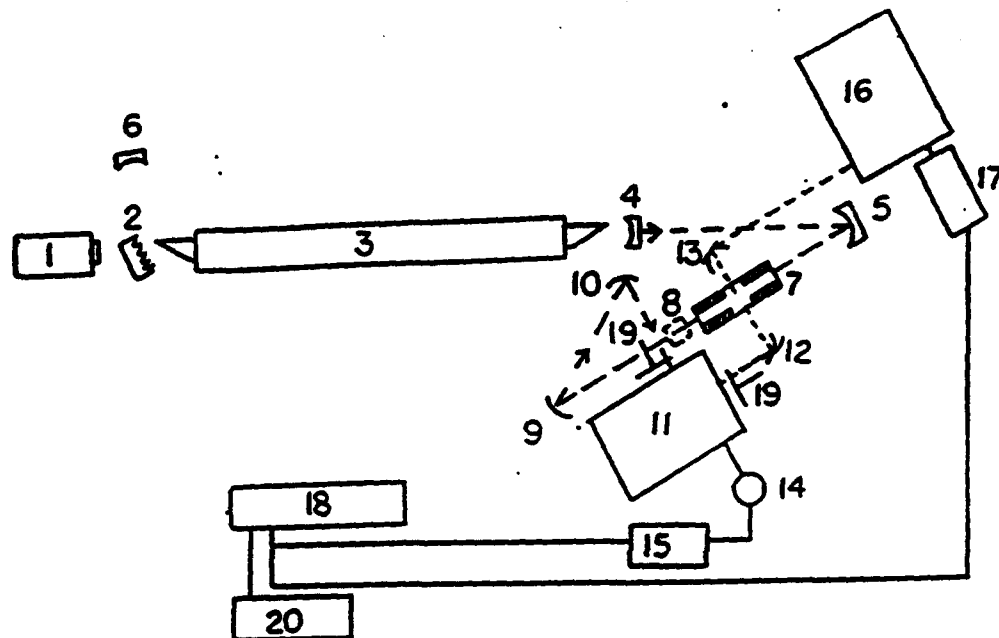


Figure 7.24: Standing wave patterns for a stable optical resonator [Seigman]



1. He Neon laser for alignment of optics and spectrometer
2. Zeiss grating, 5 micron blazed at 48.5 degrees
3. Fast-Axial-Flow Electric-Discharge CO Laser
4. Output Coupler 20% T at 5.2 microns, ZnSe 1.0" Diam. R=10 m, Laser Optics P/N 105-10070
5. Gold first surface 2.0 Diam., f=127 mm
6. Semi-Littrow zeroth order total reflector, 1.5" Diam. R=10 m, MaxR coating, Laser Optics P/N 105-70060
7. NO aluminum cell with CaF<sub>2</sub> windows [Sampe et al, 1993]
8. Laser power meter, Coherent Labmaster, model 200 thermopile
9. Laser Optics P/N 105-10070, 5% T at 4.7 microns, ZnSe 1.5" Diam. R=flat
10. Oriel first surface silver mirror, f=200mm P/N 44420
11. Spex .34 m spectrometer, model 340E, 4 & 2 micron blazed gratings
12. Two mirrors to invert an image that is horizontal to the table to be perpendicular, i.e. parallel with spectrometer entrance slit. Oriel f=75 and 300 mm, P/N 44370 and 44430
13. Same as 12 except f=300mm is a f=1.0 m Oriel P/N 43348
14. InSb IR detector E&G Jasco model J10D-M204-R1004-60
15. InSb Op-amp preamp circuit
16. Spex .5 m spectrometer with visible/uv grating model 1870
17. Thorn EMI photomultiplier, model VDN-048
18. SR510 Lock-in-amplifier
19. SR540 optical chopper
20. Computer for A/D data acquisition

Figure 7.25: Laser beam detection and optical cell setup

defined as the vertical and horizontal directions based on the output coupler face's normal vector. If the normal vector is aligned so that it is parallel with the optical table, it is the horizontal direction, and if aligned so that it points straight down the laser tube, it is the vertical direction. By aligning in the zeroth order, the vertical direction will be well aligned for the output coupler.

The spectrometer is then set to 5214 nm and the laser grating is turned until power is detected at this wavelength. The iris on the output coupler side is then closed down and the grating is tuned so that maximum power is seen.

Fine alignment of the output coupler and grating is not as easy with the half-symmetric resonator as with the hemispherical arrangement. Possible fine misalignments of the optics after the preliminary HeNe alignment are shown in Figure 7.25. With the laser discharge operating, some low cw power should be observed. The optics are then tuned to another position. If the power increases compared to the initial setting, the procedure is repeated until the power starts to decrease again and the direction of alignment is reversed.

When the laser has good power the laser line is scanned. It should appear as in Figure 7.22. If more than one line is seen to be lasing, as seen in Figure 7.27, the grating and output coupler are not properly aligned. This laser scan indicates in which direction to rotate the grating to turn off

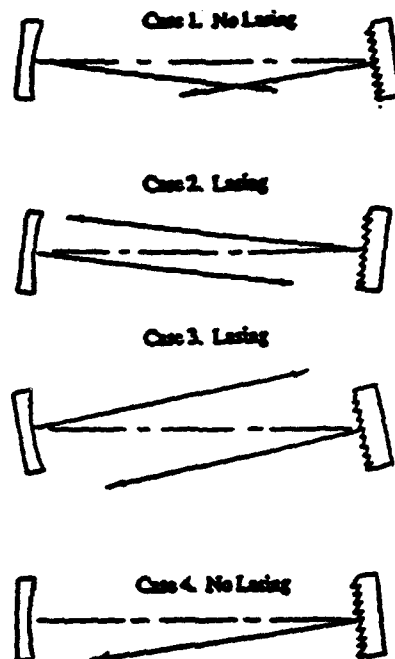


Figure 7.26 : Possible arrangements of the half-symmetric resonator prior to fine tuning

28 March 1993

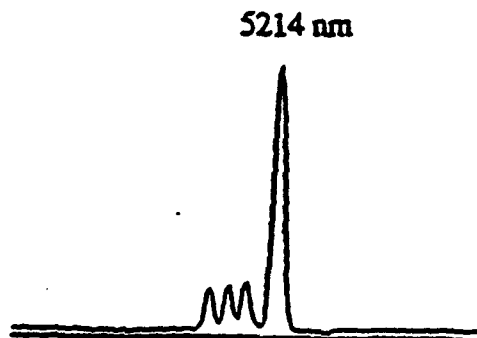


Figure 7.27 : Laser spectrum of misaligned half-symmetric resonator

these other lines:

Once the output coupler and grating have been aligned the semi-Littrow configuration is set up. This setup is not very precise and takes great care. The alignment procedure is to first align the horizontal direction (defined previously) of the semi-Littrow reflector by setting the reflector anywhere on the optical table and reflecting back a second HeNe alignment laser beam. The location of the reflector is then found by running the laser and marking the position of zeroth order losses.

Location of semi-Littrow reflector gimbal mount can now be accomplished by placing it where an iris marks the zeroth order losses. The difficulty with adjusting the present total reflector is that it has a 10-m curvature; a flat would be more effective. With the present total reflector, one can see as the semi-Littrow is adjusted the power at first is very high and then drops. There is a direct coupling between the losses on the grating due to the P-plane and the S-plane polarization. The equilibrium situation is a resonator that is based on the two 10 m curvature mirrors. It is, therefore, very difficult to tune this setup and some practice is required. Do not move the grating once the laser is already lasing on the 5214 line. This only misaligns the output coupler/grating optical resonator and it is better to only tune the semi-Littrow return.



### Final Notes and Observations on the Optics

Never try to tune the laser with the irises fully open. There is a possibility that the laser beam will be skewed with respect to the laser tube. This has happened and results in burning of the Brewster window holder.

In addition, losses from reflections off the Brewster window caused by the P-plane when lasing with the semi-Littrow configuration have caused burning of the Brewster window holder in the location indicated in Figure 7.28. For these reasons aluminum foil shaped as cylinders has been inserted into the Brewster window holders to protect the nylon. This has worked quite well.

As is typical with dielectric-coated ZnSe optics, in aligning the output coupler with the HeNe there are two reflections, one off the curved surface and the second off the flat (outer) surface. This was at first ignored, since the dielectric coating is supposed to be the surface that is reflecting in the  $5\text{-}\mu$  region. It was proposed that the second surface was actually reflecting some of incident laser radiation.

To test this idea, the reflector was put in backwards. The dielectric coated concave surface would now be seen as a convex surface by the laser beam, and this would be an unstable resonator. The only surface that could lase would be the flat surface. The laser did lase and the power recorded almost corresponded to the ratio of the intensities that were

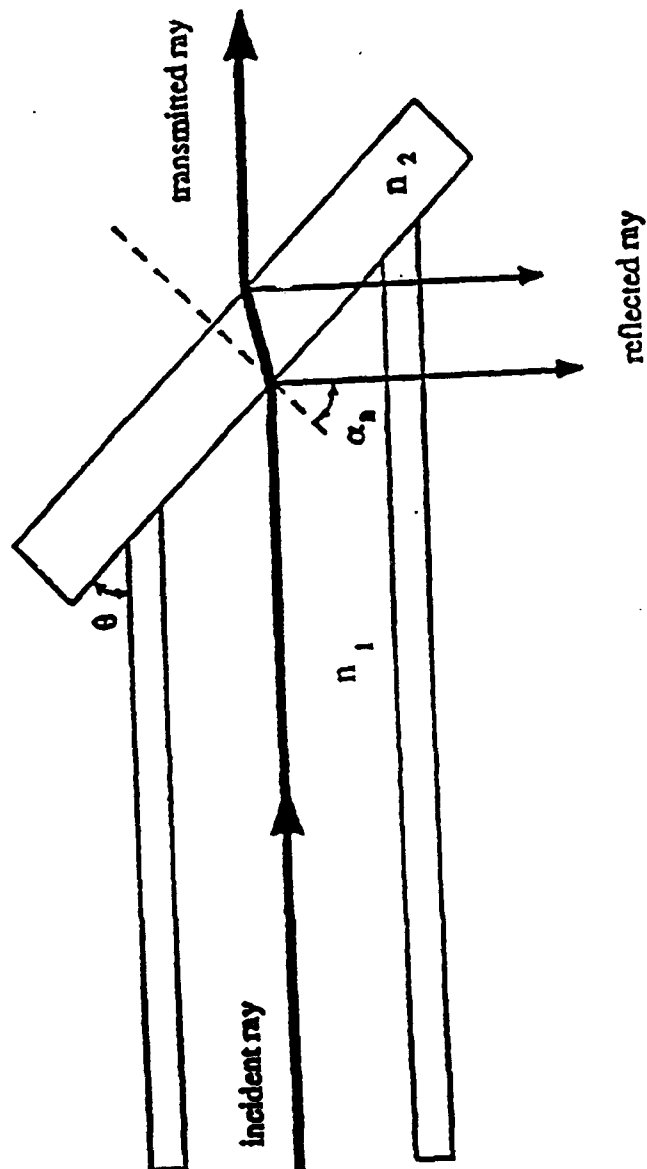


Figure 7.28: Losses of P-plane at the Brewster window set at a Brewster angle of  $35.5^\circ$ .

seen with the HeNe beam.

#### Further Comments on Laser Operation

The external purges should never be run on helium. Helium leaks through the Brewster window o-ring seal and if the discharge conditions are right, it will arc to ground through this path.

The lasing conditions that have been listed are the optimized discharge and gas conditions that we have found. A more detailed parametric investigation will probably give a more optimum gas condition for lasing on the  $v=7-8$  P(11) line.

Instead of adding air (for the oxygen) pure oxygen was tried. There was no difference in single line lasing performance. The partial pressure of water vapor in the air was either insignificant or the water froze out on the cooling tube wall. The latter is probably more plausible since the operating mass flow rate conditions are very small compared to the designed mass flow rate of the cooling tube. The amount of time the gas remains in the cooling tube is probably enough to remove all the water.

Some air is added to the internal purges and this added air keeps the electrodes very clean. The electrodes have not required cleaning since doing this. It is important not to add too much air to the gas conditions. Too much air is hard to detect from power measurements and a very fine metering valve is required. Ozone will freeze out on the laser walls,

especially around the cathodes. Solid ozone in the glass laser tube can be easily detected, as it is dark purple and readily visible. If solid ozone has formed, the laser can still be run but it is important not to restrike the discharge or turn the vacuum pump off. Our practice is to always leave the vacuum pump on until the laser tube has come to room temperature. If this is not done there is a great risk (which our group has experienced) that when the ozone evaporates it will blow the laser tube up.

#### Long Term Laser Operation

As was mentioned earlier, color spots on the  $\text{CaF}_2$  windows have been observed which can only be from UV. When the laser is running, if the lights are turned off fluoresce can be seen from the Brewster windows. It is possible that the UV damage is from long term running of the laser under the discharge conditions for lasing on the  $v=8 \rightarrow 7$  P(11) line.

The output coupler has also been checked after lasing performance decreased inexplicably. The coating has changed color in the area of the bore of the discharge indicating possible degradation in the infrared. This discoloration is probably due to laser infrared flux damage or perhaps UV.

After long term usage carbon and other deposits form on the walls of the laser discharge tube. Cleaning for about 2 hours with approximately 5.5 torr of air and with discharge conditions of  $\approx 10$  kVDC and  $\approx 20$  mADC, at room temperature,

cleans off some of the deposits. Using acetone to clean the tube works best, however, the optics have to be removed for this procedure so it is rarely done.

### 7.5. SINGLE LINE OPERATION TO PUMP NO-AR GAS MIXTURES

In current experiments being performed by our group, resonance absorption of the  $v=8 \rightarrow 7$  P(11),  $\lambda=5214$  nm transition is used to vibrationally excite NO in an optical cell with a flowing gas mixture of NO-Ar. The  $v=8 \rightarrow 7$  P(11) line has very close resonance with the NO line  $v=0 \rightarrow 1$  1/2R(12.5) with an energy displacement of only  $6 \cdot 10^{-3} \text{ cm}^{-1}$  from the mean of the NO  $\Lambda$ -doublet (split by  $\approx .01 \text{ cm}^{-1}$ ). The laser line lies within the Doppler width of the lower frequency  $\Lambda$ -component [43].

The experimental setup used is shown in Figure 7.25. Fluorescence, in the infrared and in the ultraviolet, is detected under steady-state pumping conditions. From quantitative analysis of the IR overtone spectrum,  $\Delta v=2$  (see Figure 7.29) the experimental vibrational distribution function of the ground state up to level  $v=15$  is inferred (see Figure 7.30). It is shown that the mechanism of vibrational excitation is anharmonic vibration-vibration pumping and in particular the higher vibrational levels  $v \geq 8$  are populated by near resonant vibration to vibration exchange processes. A detailed discussion of the pumping process in NO will not be discussed here, and the reader is referred to references [31,43,44].

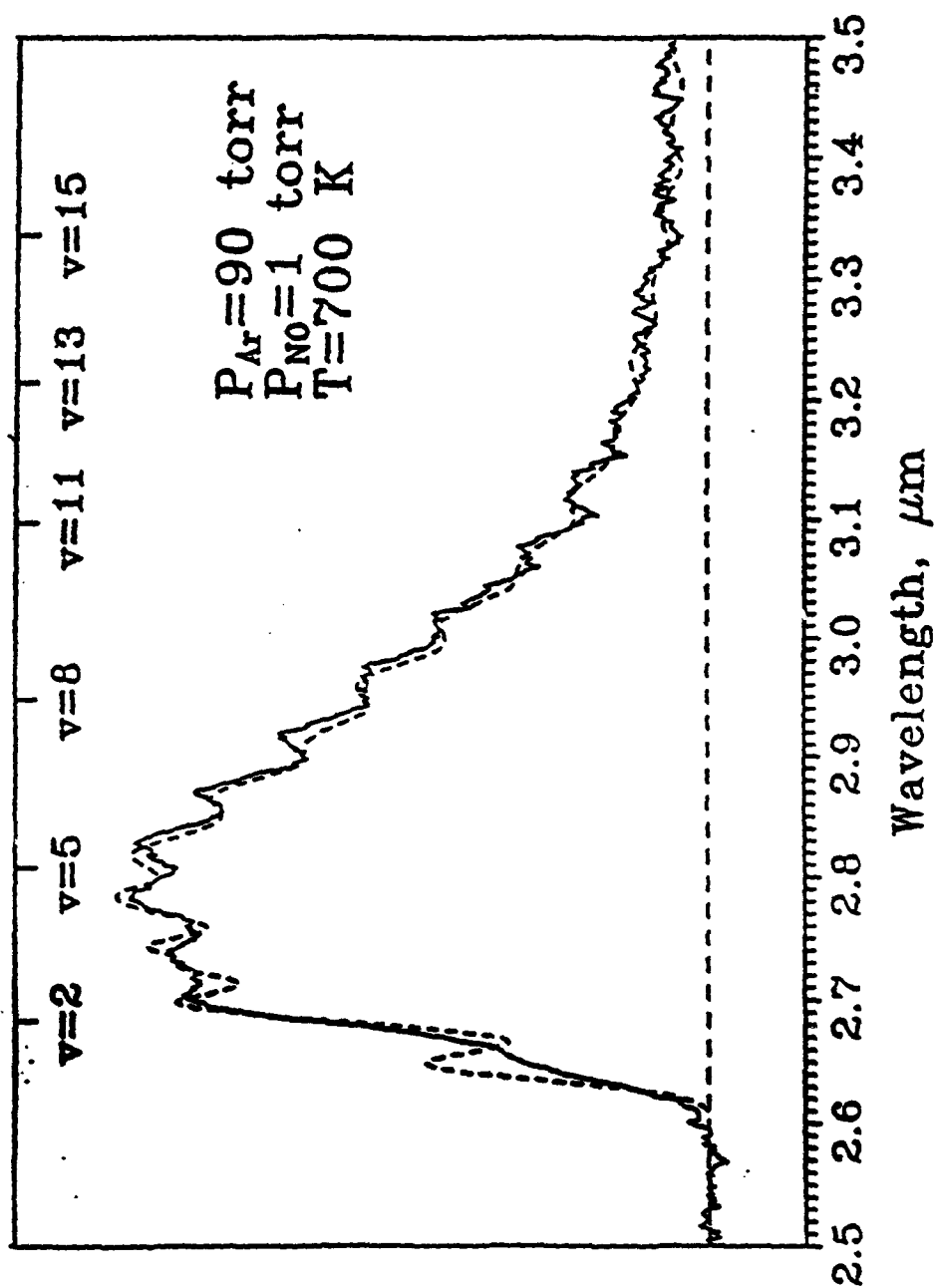


Figure 7.29: First overtone infrared NO spectra; solid line-experimental spectrum. dashed line-synthetic spectrum [Saupe et al.]

# Relative population

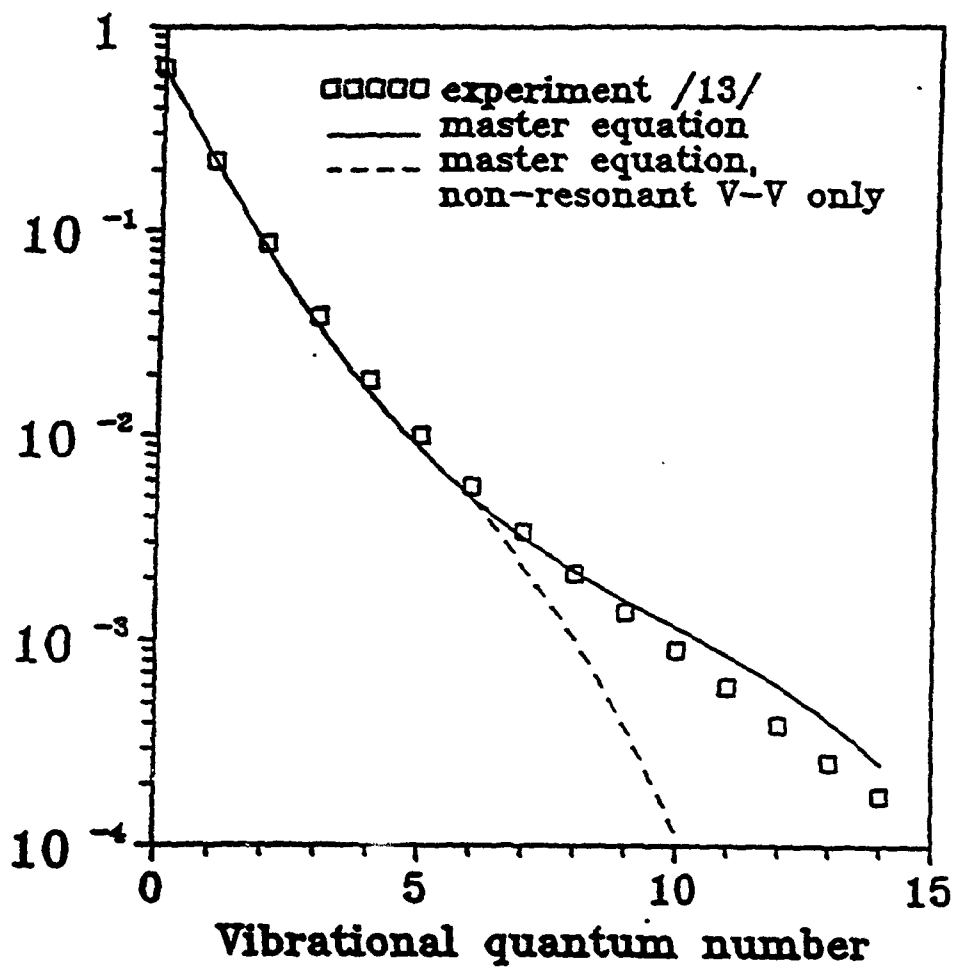


Figure 7.30: Experimental and master equation calculation of the NO vibrational distribution function



Emission intensity

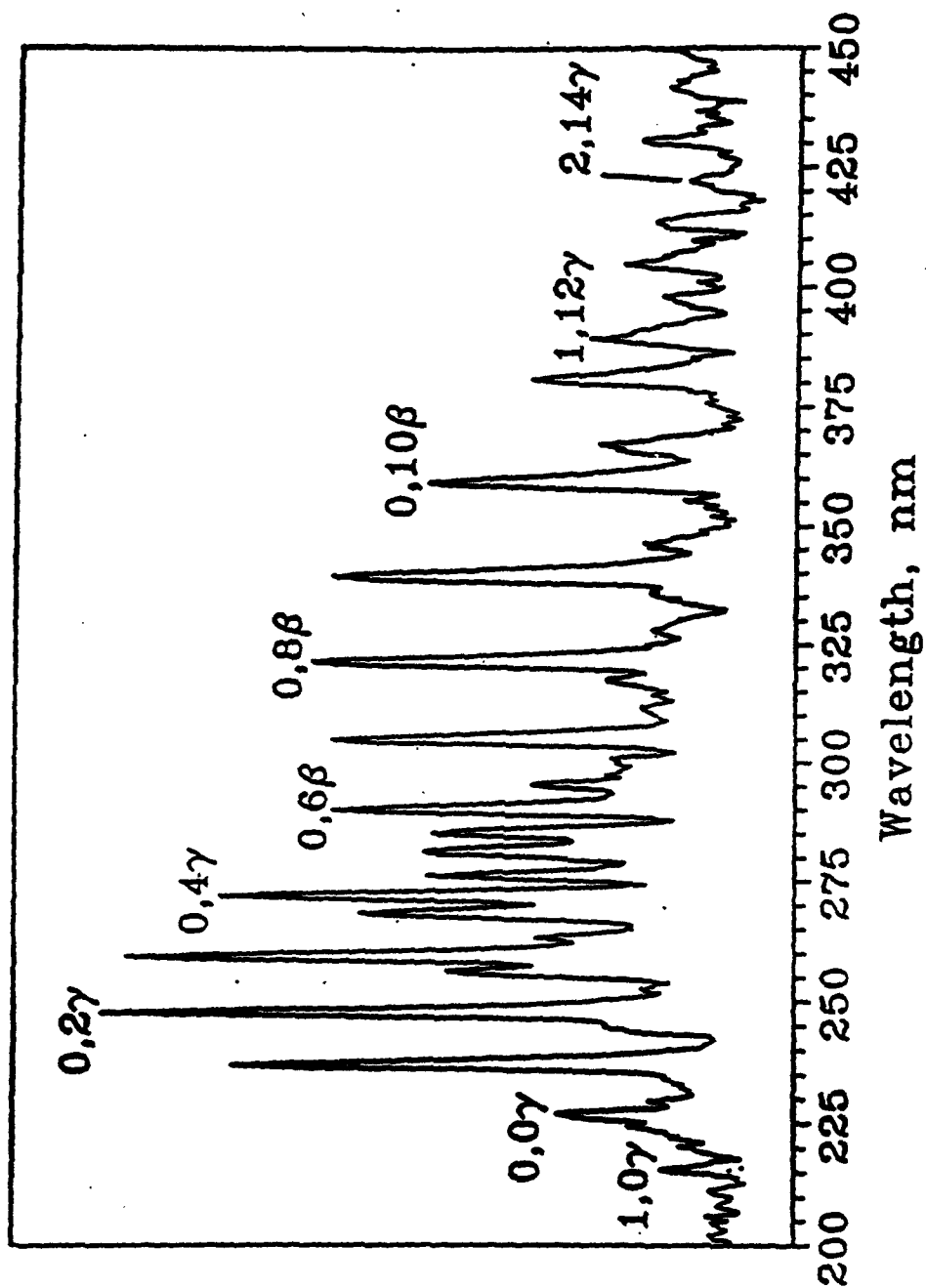


Figure 7.31: Visible/ultraviolet NO spectrum

The observed NO molecules in the electronically excited  $A^2\Sigma$  and the  $B^2\Pi$  states are shown in the visible/uv spectrum of Figure 7.31. It is suggested that these states are produced by both resonant vibrational-electronic energy transfer processes and in energy pooling reactions.

Current experiments that our group are conducting with NO-Ar gas mixtures are state/time-resolved infrared measurements. From these measurements we are hoping to infer the NO V-T and V-V rates for low v's,  $v \leq 10-15$ .

## 7.6. CONCLUSION AND RECOMMENDATIONS

A Fast-Axial-Flow Electric Discharge CO laser has been constructed to lase cw on the  $v=8 \rightarrow 7$  P(11),  $\lambda=5214$  nm transition. By resonant absorption on this line a NO-Ar mixture has been optically pumped and the vibration distribution function inferred from the second overtone emission.

Highest power achieved for the  $v=8 \rightarrow 7$  P(11) transition has been 15.5 watts using a semi-Littrow arrangement to return P-plane losses from a highly efficient S-plane grating. Physical efficiency with this single line operation has reached 6.9% and higher efficiencies can be obtained on stronger transitions. Compared to other EDL's of this type, which give single line power of 1-4 watts/meter on the strongest transitions, this laser gives more than 10 watts/meter on the  $v=8 \rightarrow 7$  P(11) transition [21]. Higher powers can probably be achieved if an optimized output coupler and different gas conditions are used.

Operation of the laser shows that the single line stability is at least  $\pm 8\%$  over a 3-hour period and has excellent short-time cw performance with or without the semi-

Littrow zeroth order return, see Figure 7.21.

A parametric study of lasing performance with different gas discharge conditions has not been done. The limited studies made of operating the laser under all line cw conditions indicate that with a low percentage output coupler the  $v=1-0$  can be made to lase, since the  $v=2-1$  was lasing with 0.8 W and a 20% output coupler. The laser was also shown to operate at higher powers and 92 watts all line cw has been achieved at a 30% physical efficiency, low-gas-flow, high-throttling condition. It should also be mentioned for these conditions the upper limit for the gas velocity in the discharge tube at 120 K was determined to be not more than 1.3 m/s and more likely 0.35 m/s. This indicates that the laser is operating in the diffusion mode and represents a significant gain for this regime. The most likely reason for this improvement is the exhaust design which prevents a choking condition.

Long term operation has shown that the biggest problem has been with thermal instability. This problem is solved by properly insulating the optical table from the laser LN<sub>2</sub> trough. Another long term operation problem has been a slow shift in the optimum operating conditions. Part of this problem has been from a drop in the air flow due to the metering valve which has become clogged by dust particles over a period of time. Symptoms of this problems have been CO dissociation leading to poor lasing and is seen when the

discharge turns "whitish" [45,46,47]. Another part of the problem is the output coupler specifications degrading with time. This can be best explained by noticing that the discharge conditions have shifted to higher currents and a lower voltage, characteristic of the optogalvanic effect [48]. Although small, this can be corrected by a new output coupler.

Suggestions for improving the current laser design are to change the output coupler curvature and increase to a  $\approx 35\%$  output coupler. Table 7.2 indicates that an output coupler, with a 25 m of curvature for the optical resonator, would fill the grating more resulting in higher resolving power, and the mode volume would increase by 36%. In such an output coupler, the substrate should also be biconcave because the beam is diverging at the output coupler with the half-symmetric resonator. This optic would require higher precision gimbal mounts than those currently being used. The "semi-Littrow" arrangement can also be improved by using a flat total reflector and either a true Littrow setup (Figure 7.11) or a semi-Littrow arrangement with a better gimbal mount. Current optical alignment uses no active feedback which is probably not needed since stability has been good without it. The Brewster angle which is set for no losses on the S-plane should be changed to 90 degrees. Fig. 7.15 shows that at 35.5 degrees overall efficiency is less for both S and P-plane than at 90 degrees, therefore, for the semi-Littrow configuration

which uses both S and P-plane a Brewster angle of 90 degrees would be better.

An alternative design for the laser tube is shown in Figure 7.32. The double jacket and cooling tube arrangement would allow for uniform thermal expansion. With this type of cooling, for the gases, the laser would not be as heavy and would require less support than the present design. Sonic injectors should also be used. Even more importantly, the vacuum arrangement would eliminate all thermal instabilities experienced with the optical table.

The last recommendation is a different gas handling system. Mass flow controllers are rather expensive and not really needed for one time adjustments. The present setup has good adjustability, but is still too sensitive to regulator pressure. Critical flow orificing should be used instead, such as the type produced by Host Systems. This type includes pre-manufactured vacuum tested mixing manifolds and the orifices are actually calibrated valves which can be changed depending on the size of flow and allow for controlled gas flow rate adjustment. This would save a lot of time in setting up the laser and would give accurate and repeatable mass flow rates.

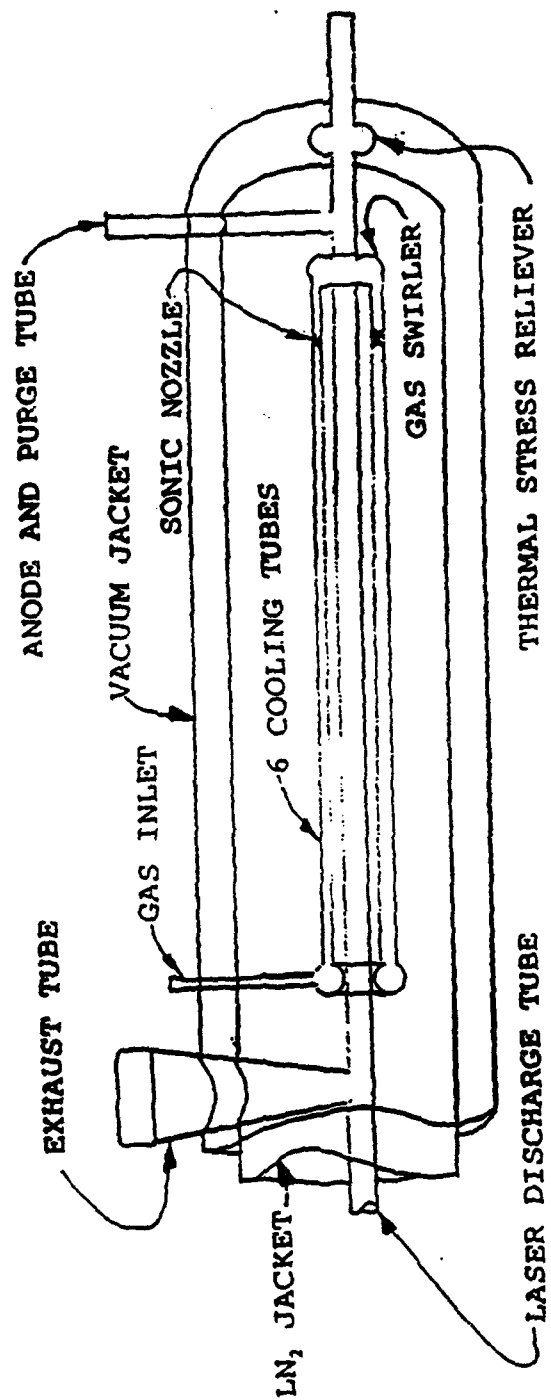


Figure 7.32: Alternate FAFED CO laser discharge tube and cooling system

## APPENDIX A

### SIZING OF VACUUM PUMP AND LASER DISCHARGE TUBE DIAMETER

The sizing of the vacuum pump and the discharge tube diameter are based on the mass flow rates reported by Kan and Whitney. The largest pump available to the program is rated at 198 ft<sup>3</sup>/min (5.61 m<sup>3</sup>/min). The calculations use this as the limiting volumetric flow rate.

From Kan and Whitney:

Reported gas mixture ratio of He:CO:N<sub>2</sub>=950:36:14.

Bore diameter of laser discharge tube=2.5cm.

Mean flow rate 120 m/sec in each arm (2 arm discharge) at a mass flow rate of 2 g/sec and 27 Torr (3599.7 Pa).

MWA = Molecular weight average g/mole

V = Volumetric flow rate, m<sup>3</sup>/sec

P = Pressure, Pa

R = Ideal gas constant, 8.314 N\*m/mole/K

T = Temperature, K

n = moles/sec

m = mass flow rate g/sec:

$$MWA = .95 \times 4 \frac{\text{g}}{\text{mole}} (\text{He}) + .05 \times 28 \frac{\text{g}}{\text{mole}} (\text{CO or N}_2) = 5.2 \frac{\text{g}}{\text{mole}} \quad (\text{A.1})$$



$$V = 2 \text{ arms} \times (120 \frac{\text{m}}{\text{sec}}) \left( \pi \left( \frac{0.25 \text{ m}}{2} \right)^2 \right) = .1178 \frac{\text{m}^3}{\text{sec}} \quad (\text{A.2})$$

so:

$$n = \frac{2 \text{ g/sec}}{5.2 \text{ g/mole}} = .384 \text{ mole/sec} \quad (\text{A.3})$$

and from ideal gas law:

$$PV = nRT \quad (\text{A.4})$$

$$(3599.7 \text{ Pa}) (.1178 \frac{\text{m}^3}{\text{sec}}) = (.384 \frac{\text{mole}}{\text{sec}}) (8.314 \frac{\text{Nm}}{\text{mole} \cdot \text{K}}) T$$

$T = 132 \text{ K}$ ; this seems reasonable for the discharge gas temperature. Now assume that the gas relaxes to  $270 \text{ K}$  and using ideal gas law  $V$  at the pump will be  $.239 \text{ m}^3/\text{sec}$  ( $= 507.4 \text{ ft}^3/\text{min}$ ).

This volumetric flow rate can be decreased by going to a smaller tube diameter. The discharge tube diameter required for the same mass flow rate for a  $198 \text{ ft}^3/\text{min}$  pump will be:

$$\text{bore diameter} = 25 \text{ mm} \sqrt{\left( \frac{198 \text{ ft}^3}{507.4 \text{ ft}^3} \right)} = 15.6 \text{ mm} \quad (\text{A.5})$$

The closest standard tubing size to this value is 15-mm tubing. This tubing size was unavailable at the time of construction and 19-mm tubing was substituted. Ideally, a 15-mm bore diameter should be used because the optics were chosen so that the  $\text{TEM}_{00}$  fills the laser volume, see Appendix E, and this would have given a higher mass flow rate.

With this size diameter and using the ideal gas equation, with an assumed temperature of  $130 \text{ K}$ , the mass flow rate for

the 198 ft<sup>3</sup> would be 1.6 g/sec. This value falls between the two curves of Figure 7.31 and this laser should be able to deliver at least 250 watts.

## APPENDIX B.

### DESIGN OF LASER DISCHARGE COOLING TUBES

The design of the laser discharge cooling tubes are based off Kan and Whitney's best lasing conditions. The relevant data has already been listed in Appendix A but will be repeated here. The calculation will only be an estimate of the tube length necessary for adequate cooling.

All data for this heat transfer calculation is taken from reference [49]. Assuming a constant temperature surface condition at the cooling wall the tube length can be found from:

$$\ln\left(\frac{T_w - T_{m,o}(x)}{T_w - T_{m,i}}\right) = -\left(\frac{PU}{mc_p}\right)x \quad (B.1)$$

where:

$T_w$  = liquid nitrogen temperature 77 K

$T_{m,o}(x)$  = mean temperature at exit, taken as 78 K

$T_{m,i}$  = mean temperature at the entrance, 300 K

$P$  = surface perimeter;  $\pi \times$  diameter for a round cooling tube  
(tube diameter that will be used is 0.005 meters i.d. and 0.007 o.d.)

$c_p$  = specific heat, taken for this case as an ideal gas

from Appendix A the molar ratio of the gases in the discharge tube are He:CO:N<sub>2</sub> = 0.95:0.036:0.014 therefore;

$$C_p = \left[ .95\left(\frac{1}{2}\right) + .05\left(\frac{1}{2}\right) \right] 8.314 \frac{\text{Nm}}{\text{mole K}} = 12.89 \frac{\text{J}}{\text{mole K}} \quad (\text{B.2})$$

or from equation A.1

$$C_p = \frac{12.89 \text{ J/mole K}}{5.2 \text{ g}} = 2.48 \frac{\text{J}}{\text{g K}}$$

$m$  = mass flow rate, taken as 2 g/sec

$x$  = length of cooling tube

$U$  = overall heat transfer coefficient defined as:

$$U = \frac{1}{\frac{1}{h_i} + \frac{r_i}{k_g} \ln\left(\frac{r_o}{r_i}\right) + \frac{r_o}{h_o}} \quad (\text{B.3})$$

where:

$h_i$  = inner heat transfer coefficient; from gases to cooling tube

$h_o$  = outer heat transfer coefficient; from cooling tube to the liquid nitrogen. This is a very complicated term to calculate and has been estimated to be approximately 500 W/(m<sup>2</sup>\*K) (This about the value for water on glass).

$r_i$  = inner tube radius, 0.0025 m

$r_o$  = outer tube radius, 0.0035 m

$k_g$  = conductivity of pyrex glass, 1.4 W/(m\*K)

These parameter for  $U$  are determined at the log mean temperature defined as:

$$\Delta T_{\text{lm}} = \frac{\Delta T_o - \Delta T_i}{\ln\left(\frac{\Delta T_o}{\Delta T_i}\right)} \quad (\text{B.4})$$

where:

$\Delta T_{\text{lm}}$  = log mean temperature = -41 degrees K.

Temperature for evaluating gas properties will be about 120 K

$$\Delta T_o = T_o - T_{m,o} = 77 - 78 = -1 \text{ K}$$

$$\Delta T_i = T_o - T_{m,i} = 77 - 300 = -223 \text{ K}$$

The inner heat transfer coefficient  $h_i$  can be determined from the Nussult number given by:

$$Nu_D = \frac{\left(\frac{f}{8}\right)(Re_D - 1000)Pr}{1 + 12.7\left(\frac{f}{8}\right)^{1/2}(Pr^{2/3} - 1)} = \frac{h_i ID}{k} \quad (B.5)$$

where:

ID = inside diameter of tube (as given above, 0.005 m)

$k$  = thermal conductivity of gas

valid for Prandtl numbers between  $0.5 < Pr < 2000$  and Reynold numbers between  $2300 < Re_D < 5 \times 10^4$ .

$f$  is the friction factor obtained either from a Moody diagram or for smooth tubes from the equation:

$$f = (.79 \ln Re_D - 1.64)^{-2} \quad (B.6)$$

The reynolds number is determined from:

$$Re_D = \frac{4\dot{m}}{\pi ID \mu} \quad (B.7)$$

where:

$\mu$  = dynamic viscosity taken for helium since it comprises most of the mix, (at 120 K  $106 \times 10^{-7} \text{ N}\cdot\text{s}/\text{m}^2$ )

the other properties of the gases were estimated to be:

$$Pr = 0.685$$

$$k = 78.3 \times 10^{-3} \text{ W/(m}^{\circ}\text{K)}$$

$Re_p$  is found to be 48000 from equation B.7 for 2 g/sec and  $f$  is, therefore,  $21.2 \times 10^{-3}$  from equation B.6.  $Nu_p$ , equation B.5, is thus found to be 99.6 and  $h_p$  is then estimated to be 1,560 W/(m $^{\circ}$ K).

Returning to equation B.3,  $U$ , the overall heat transfer coefficient is approximately 375 W/(m $^{\circ}$ K). The length of cooling tube necessary to cool 2 g/sec can now be determined from equation B.1 and is about 5 meters. This length is only a rough estimate and should not be considered as the upper limit. The length should be at least multiplied by 2 for a conservative design estimate, especially since (1) equation B.5 is at best 10% accurate, (2) the gas conditions could be different, i.e., a different gas molar ratio causing the specific heat to increase, and (3) the constant surface temperature condition may not be actually true. The length used in this tube was thus taken as 11 meters.

## APPENDIX C

### GRATING SELECTION

The grating was selected so that first order reflection would be very efficient at 5214 nm. The number of rulings determines the angle of reflection according to the grating equation, see Figure 7.33.

$$m\lambda = a(\sin\alpha \pm \sin\beta) \quad (C.1)$$

where:

$\alpha$  = angle of incident rays with respect to a normal to the grating.

$\beta$  = angle of diffraction with respect to normal. The plus sign signifies that  $\beta$  is on the same side of the normal as  $\alpha$  while the minus sign signifies that  $\beta$  is on the opposite side of the normal.

$a$  = grating constant or distance between successive grooves.

$m$  = the diffracted order, usually a small integer.

$\lambda$  = diffracted wavelength.

In the special but common case, when  $\alpha = \beta$  (Littrow configuration), the grating equation simplifies to:

$$m\lambda = 2a \sin\beta \quad (C.2)$$

The resolving power of a grating is directly proportional to the number of grooves. Unfortunately, this causes the first

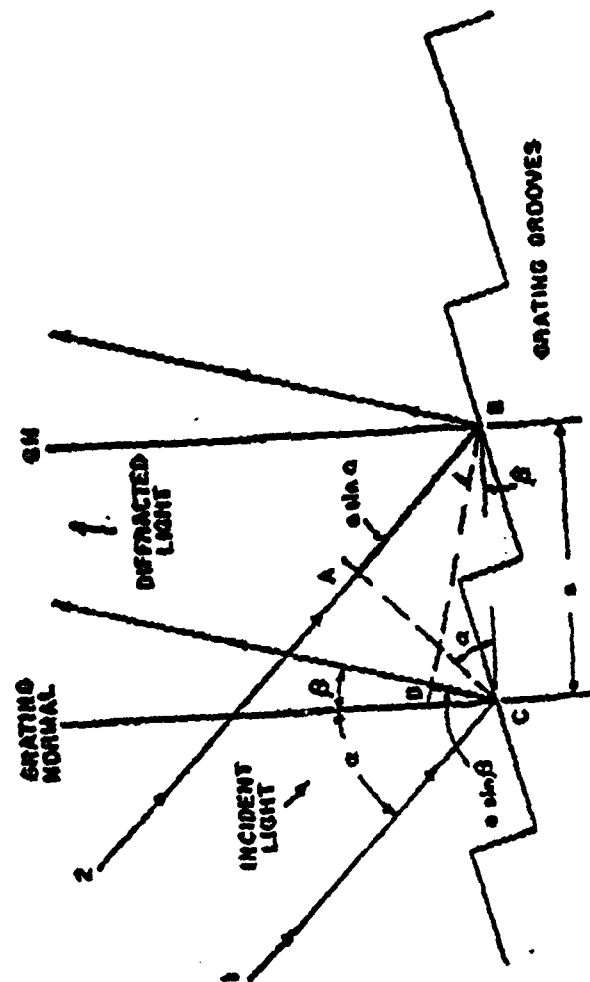


Figure 7.33: Diagram showing phase relation between rays diffracted from two adjacent grating grooves



order to occur at a larger angle of reflection, thereby requiring a larger ruled surface. The other major drawback is that as the angle of reflection increases so too must the blaze angle in order to have high efficiency in first order. The limits of manufacturing thereby determine the groove density since large blaze angles are difficult to manufacture. Based on information supplied by the manufacturer, a 48.5 degree blaze angle was chosen. The ruling was 290 grooves/mm so that from equation C.2 5214 nm would occur at 49.11 degrees. The required ruled surface was then based on this angle and the waist of the  $TEM_{00}$  mode, see Appendix E. The required ruled surface could therefore be selected as 25x25 mm.

In changing the bore of the laser tube from 15 mm to 19 mm, Appendix A, the size of the grating and the output curvature were not changed. If a new output coupler is selected to optimize the volume, Appendix E, a new wider grating would have to be selected.

## APPENDIX D

### RESOLVING CO ROVIBRATIONAL TRANSITIONS WITH THE GRATING

It is of great importance that the optical cavity be able to line select CO rovibrational transitions if the laser is to operate in the single line mode. The usual method of line selection is to use a grating that has the proper groove density and is operating in a specific order. The resolving power of a grating can be found by the equation:

$$\frac{\lambda}{\Delta\lambda} = mn \quad (D.1)$$

where  $\frac{\lambda}{\Delta\lambda}$  is the resolving power,  $m$  is the order, and  $n$  is the number of lines (groove density) of the grating.  $\Delta\lambda$  is based on the Rayleigh criterion shown in Fig. 7.34. The peak of one wavelength occurs at the minimum of the other line. It should also be pointed out that the  $n$  is the number of lines as seen by the incident beam on the grating. For this reason it is very important, for resolving transitions, that the mode waist be as large as possible in the resonator design, Appendix E.

By using a cavity length that is long enough to allow for enough separation between two different transitions,

single line operation of a laser can be achieved.

Due to the grating and the resonator cavity length (which is constrained by our optical table) line resolution in this laser optical design is limited. To alleviate this pitfall the bore of the laser tube is used to aperture other transitions and the resonator design is chosen to "reject" other possible close transitions. The optical resonator design, Appendix E, allows for some "line-tuning" by being optically unstable on close transitions. Close transitions will be somewhat skewed to the "true" optical axis and since the optical resonator is very sensitive to alignment these other close lines will not be optically favorable. Based on a 19-mm bore an estimate can be made of what possible wavelengths could lase:

$$\beta = \arctan\left(\frac{.019\text{m bore diameter}}{2.0\text{m resonator length}}\right) = .5 \text{ degrees} \quad (\text{D.2})$$

where  $\beta$  is same as as defined in equation C.1. By using equation C.2 5214 nm occurs at 49.11 degrees and at 49.61 degrees will be 5253 nm. From equation D.1, and Table 7.3 for the waist size  $n=1139$  lines ( $=2.57 \text{ mm} * [1/\cos(49.11)] * 290 \text{ rulings/mm}$ ),  $n=1$ ,  $\Delta\lambda=4.6 \text{ nm}$ . Thus the grating is able to distinguish between two incident beams that have a 3.5-nm wavelength difference. The CO transitions are listed in Table 7.8. It is important that no other CO P transition within  $\pm 4.6 \text{ nm}$  have good gain when operating on the 5214 nm line, since this line will also lase.

Fortunately, transitions that are close to the 5214-nm line are completely unfavorable for the higher power lasing conditions suitable for the 5214-nm line and thus operation is assured to be single line with this grating.

It was mentioned that the optical resonator design is used for "rejection" of other lines that could be lasing. An estimate of the optical resonator misalignment can be used to find the "rejection" qualities of the half-symmetric resonator. From experience with the optics and experimental observations for this cavity, the lasing could be turned off if the output coupler was rotated by 0.08 degree (rotation perpendicular to table). This would be the same as rotating the grating by 0.08 degree which corresponds to lasing on another line that is at most  $\pm 6$  nm from the 5214-nm line.

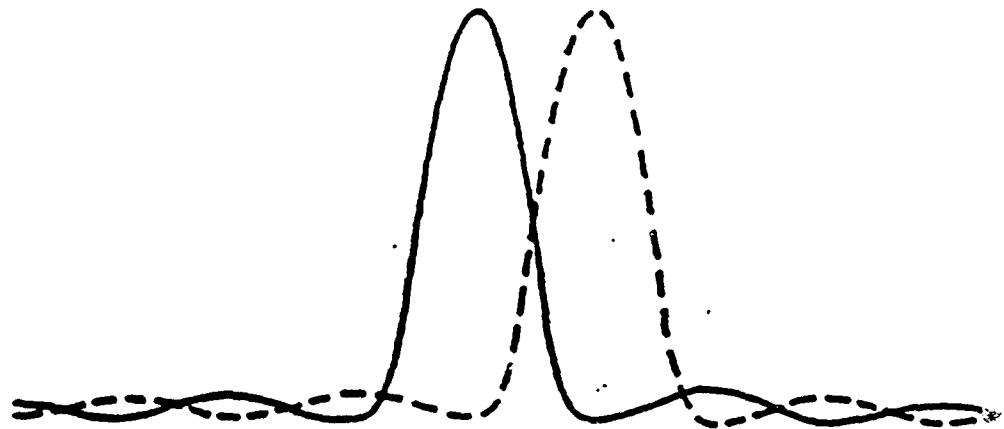


Figure 7.34 : Illustration of the Rayleigh criterion [Feynam]

## APPENDIX E

### LASER OPTICAL RESONATOR DESIGN

#### Design Criteria:

- 1) A half-symmetric resonator is selected for the resonator design for two reasons. The first reason is that the waist of the beam will be rather large at the grating. This is necessary so that the resolving power of the grating is maximized. Because of this, a hemispherical resonator design can not be used. The second reason is that the grating is not quite capable of resolving adjacent rotational transitions for this particular laser tube length, and thus the instability of this resonator design can be used to advantage for "rejecting" adjacent rovibrational transitions.
- 2) The laser bore was initially designed for a 15-mm diameter and later changed to 19 mm. The grating width was selected for the original 15-mm tube. The output coupler should, therefore, be designed to the grating width and not the new laser tube diameter.
- 3) Optics to be used should fit the existing gimbal mounts which are designed for 1" optics.
- 4) The mode used for calculations is the  $TEM_{00}$ . This should

also fill the volume of the laser tube as much as possible. The dimensions of the cavity are a length of 2.0 meters and bore size of 15 or 19 mm.

Calculations:

Following Siegmann [41], we define the g parameters:

$$g_1 = 1 - L/R_1 \quad (E.1)$$

$$g = g_2 = 1 - L/R_2 \quad (E.2)$$

Where:

L = resonator length

R<sub>1</sub> = grating curvature

R<sub>2</sub> = output mirror curvature

Letting R<sub>1</sub> the grating curvature, be infinity; and letting L=2.0 m, g<sub>1</sub>=1. The waists at the output coupler and the grating will therefore be [41]:

$$w_0^2 = w_1^2 = \frac{\lambda}{\pi} \sqrt{\frac{g}{1-g}} \quad \text{at the grating} \quad (E.3)$$

$$w_2^2 = \frac{\lambda}{\pi} \sqrt{\frac{1}{g(1-g)}} \quad \text{at the output coupler} \quad (E.4)$$

It can be shown that for a Gaussian beam that 99% of the beam is within  $\pi w_0$ , and to eliminate diffraction effects apertures should be at least  $4.6w_0$ . The curvature of the output coupler is then limited by the tube diameter for the 15-mm laser tube and by the grating width for the 19-mm laser tube since:

$$(25 \text{ mm}) \cos(50) \approx 16 \text{ mm}$$

as seen by the mode when operating at the 5124 nm line. The limit on  $w_1$  is 3.695 mm and  $w_0$  is 3.478 for the 19 mm tube and the 15 mm tube respectively.

The volume of the Gaussian beam (gvol) can be approximated by:

$$gvol \approx \left[ \frac{1}{2} \left( \frac{w_0 + w_1}{2} \right) \right]^2 \pi L \quad (E.6)$$

and should also be optimized when selecting the curvature. Table 7.3 lists the important parameters as a function of curvature.

Table 7.3 shows that the present design (19 mm tube) should use a 25-m curvature to optimize the volume and to take advantage of the the resolving power of the grating. For the 15-mm tube the radius of curvature is optimized at 10 m.

## REFERENCES

1. Capitelli, M., Nonequilibrium Vibrational Kinetics , Springer-Verlag, pp.233-269, 1986.
2. Legay, F., and Legay-Sommaire, N., Sur les possibilités de réalisation d'un maser optique utilisant l'énergie de vibration des gaz excités par l'azote activé , C.R. Acad. Sc. Paris, Vol. 259, p.99, 1964.
3. Patel, C.K.N., and Kerl, R.J., Laser Oscillation on  $X^1\Sigma^+$  Vibrational-Rotational Transitions of CO , Appl. Phys. Lett., Vol. 5, No. 4, pp.81-83, 1964.
4. Legay-Sommaire, N., Henry, L., and Legay, F., Réalisation d'un lase utilisant l'énergie de vibration des gaz excités par l'azote activé , C.R. Acad. Sc. Paris, Vol. 260, p.3339, 1965.
5. Osgood, R.M., Jr., and Eppers, W.C., Jr., High Power CO-N<sub>2</sub>-He Laser , Appl. Phys. Lett., Vol. 13, No. 12, pp.409-411, 1968.
6. Osgood, R.M., Jr., Eppers, W.C., Jr., and Nichols, E.R., An Investigation of the High-Power CO Laser , IEEE Journal of Quantum Electronics, Vol. QE-6, No. 3, pp.145-154, 1970.
7. Patel, C.K.N., Vibrational-Rotational Laser Action in Carbon Monoxide , Physical Review, Vol. 141, No. 1, pp.71-83, 1966.
8. Sato, S., Takahashi, K., Sugimoto, M., Saito, H., Fujioka, T., Noda, O., Kuribayashi, S., Imatake, S., Nagatomo, A., and Kondo, M., Five-Kilowatt Highly Efficient Electric Discharge CW CO Laser , Summ. Pap. Presented Conf. Laser Elect.r Opt. Summaries of Papers Presented at the Conference on Lasers and Electro-Optics, Baltimore MD, USA, Apr 24-28 1989. Publ. by IEEE, IEEE Service Center, Piscataway, NJ, USA, 1989 (IEEE cat n 89CH2638-5), p.274.
9. Watt, W.S., Carbon Monoxide Gas Dynamic Laser , Appl. Phys. Lett., Vol. 18, No. 11, p.487, 1971.



10. Sato, S., and Taniwaki, M., 1-kW, Capacitively Coupled Radio Frequency Discharge Excited CO Laser with a Closed-Cycle Fast Axial Flow , Appl. Phys. Lett., Vol. 61, No. 6, pp.621-623, 1992.
11. Bülow, H.V., and Zeyfang, E., Proc. SPIE, Vol. 1397, p.499, 1990.
12. Anan'ev, V.Yu., Danilychev, V.A., Ionin, A.A., Kotkov, A.A., Lytkin, A.P., and Sinitsyn, D.V., Pulsed Electron-Beam-Controlled Carbon Monoxide Laser Amplifiers. I. Amplification of Radiation from a CO Laser Operating in the Free-Running Regime , Sov. J. Quantum Electron., Vol. 19, No. 1, pp.4-9, 1989.
13. Anan'ev, V.Yu., Danilychev, V.A., Ionin, A.A., Kotkov, A.A., Lytkin, A.P., and Sinitsyn, D.V., Pulsed Electron-Beam-Controlled Carbon Monoxide Laser Amplifiers. II. Amplification of Radiation Pulses from an Electron-Beam-Controlled CO Laser with Controlled Spectral and Temporal Characteristics , Sov. J. Quantum Electron., Vol. 19, No. 1, pp.10-16, 1989.
14. Abrosimov, G.V., Vysikailo, F.I., Gurashvili, V.A., Moskvichev, S.G., Saenko, V.B., and Tyazhev, V.P., Cryogenic CO Laser Excited by a Photoionization Discharge , Sov. J. Quantum Electron., Vol. 20, No. 2, pp.109-112, 1990.
15. Urban, W., Infrared Lasers for Spectroscopy , Universität Bonn Report, 1987.
16. Urban, W., The CO-Overtone Laser A Spectroscopic Source in a Most Interesting Wavelength Region , Universität Bonn Report.
17. Weber, M.J., CRC Handbook of Laser Science Vol. I, Lasers and Masers , CRC Press Inc., 1982.
18. Treanor, C.E., Rich, J. W., and Rehms, R.G., J. Chem. Phys. 48, 1798, 1968.
19. Maisenhalder, F., High Power CO Lasers , Proceedings on High Power Lasers and Their Industrial Applications, Vol. 650, Divisional Meeting of the Quantum Electronics Division/European Physical Society, Innsbruck, Austria, 1986.
20. Sato, S., Igarashi, K., and Taniwaki, M., A Multihundredwatt CO Laser Power Delivery Through Chalcogenide Glass Fibers , Appl. Phys. Lett. 1992.

21. Urban, W., The Carbon Monoxide Laser as Spectroscopic Source , Laser Und Optoelektronik, Vol. 23, No. 1, pp.56-61, 1991.
22. Pearson, G.N., and Hall, D.R., Carbon Monoxide Laser Excited By Radio-Frequency Discharge , Appl. Phys. Lett., Vol. 50, No. 18, pp.1222-1224, 1987.
23. Kornilov, S.T., Protsenko, E.D., Tymper, S.I., and Chirikov, S.N., Waveguide CO Laser with a Wide Tuning Range of the Emission Frequency , Sov. J. Quantum Electron., Vol. 13, No. 9, pp.1280-1282, 1983.
24. Gromoll-Bohle, M., Bohle, W., and Urban, W., Broadband CO Laser Emission on Overtone Transitions  $\Delta v=2$  , Optics Communications, Vol. 69, pp.409-413, 1989.
25. Saupe, S., Private communication, October 1992..
26. Legay-Sommaire, N., and Legay, F., Observation of a Strong Vibrational Population Inversion by CO Laser Excitation of Pure Solid Carbon Monoxide , IEEE Journal of Quantum Electronics, Vol. QE-16, No. 3, pp.308-314, 1980.
27. Chang, H.C., and Ewing, G.E., Vibrational Energy Transfer and Population Inversion in CO Overlayers on NaCl(100) , J. Phys. Chem., Vol. 94, pp.7635-7641, 1990.
28. Anex, D.S., and Ewing, G.E., Transfer and Storage of Vibrational Energy in Liquids: Collisional Up-Pumping of Carbon Monoxide in Liquid Argon , J. Phys. Chem., Vol. 90, pp.1604-1610, 1986.
29. Urban, W., Lin, J.X., Subramaniam, V.V., Havenith, M., and Rich, J.W., Treanor Pumping of CO Initiated by CO Laser Excitation , Chem. Phys., Vol. 130, pp.389-399, 1989.
30. Hanson, R.K., Monat, J.P., and Kruger, C.H., Absorption of CO Laser Radiation by NO , J. Quant. Spectrosc. Radiat. Transfer, Vol. 16, pp.705-713. 1975.
31. Dönnwald, H., Siegel, E., Urban, W., Rich, J.W., Homicz, G., and Williams, M., Anharmonic Vibration-Vibration Pumping in Nitric Oxide by Resonant IR-Laser Irradiation , Chem. Phys., Vol. 94, pp.195-213, 1985.
32. Rich, J.W., and Bergman, R.C., Chem. Phys., Vol. 44, p.53, 1979.
33. Mehmetli, B.A., Electric-Discharge Conduction Cooled CO Laser , MS thesis, Mechanical Engineering Department, The Ohio State University, 1988.

34. Samimy, E., Optimization of Short Wavelength Operation in the CO Laser , MS thesis, Mechanical Engineering Department, The Ohio State University, 1989.
35. Adamovich, I., Saupe, S., Grassi, M., Schulz, O., Macheret, S., and Rich, J.W., Vibrationally-Stimulated Ionization of Carbon Monoxide in Optical Pumping Experiments , to be published in Chem. Phys., 1993.
36. Grigor'yan, G.M., Dymshits, B.M., and Ionikh, Yu.Z., Lasing Characteristics of a Longitudinal-Discharge Cryogenically Cooled CW CO Laser , Sov. J. Quantum Electron., Vol. 20, No. 6, pp.591-594, 1990.
37. Kan, T., and Whitney, W., Forced-Convective-Flow CO Laser ,Appl. Phys. Lett., Vol. 21, No. 5, pp.213-215, 1972.
38. Martin, J.P., Private communication to Rich, J.W. Mehmetli, B.A., Electric-Discharge Conduction Cooled CO Laser , MS thesis, Mechanical Engineering Department, The Ohio State University, 1988.
39. Witteman, W.I., The CO<sub>2</sub> Laser , Springer-Verlag, 1987.
40. Loewen, E.G., Neviere, M., and Maystre, D., Grating Efficiency Theory as it Applies to Blazed and Holographic Gratings , Applied Optics, Vol. 16, No. 10, pp.2711-2721, 1977.
41. Siegman, E., Lasers , University Science Books, Mill Valley, California, 1986.
42. McClatchy, R. A., Atmospheric Attenuation of CO Laser Radiation ,AFCRL-710370, Environmental Research Paper No. 359, 1971.
43. Saupe, S., Adamovich, I., Grassi, M.J., and Rich, J.W., Vibrational and Electronic Excitation of Nitric Oxide in Optical Pumping Experiments , to be published in Chem. Phys., 1993.
44. Kosanetzky, J., Vormann, H., Dunnwald, H., Rohrbeck, W., and Urban, W., IR Laser Induced UV Fluorescence in Nitric Oxide , Chem. Phys. Lett., Vol. 70, No. 1, pp.60-62, 1980.
45. Grigor'yan, G.M., Dymshits, B.M., and Ionikh, Yu.Z., Mechanism of the Influence of Oxygen on the Vibrational Distribution of Molecules in a CO Discharge , Opt. Spectrosc., Vol. 65, No. 4, pp.452-455, 1988.

46. Grigor'yan, G.M., Dymshits, B.M., and Ionikh, Yu.Z.,  
Influence of Oxygen on the Parameters of the Active  
Medium in an Electric-Discharge CO Laser , Sov. J. Quantum  
Electron., Vol. 19, No. 7, pp.889-893, 1989.
47. Mikaberidze, A.M., Ochkin, V.N., and Sobolev, N.N.,  
Dissociation of Carbon Monoxide in Discharge of Pumped  
CO-Laser , Translated by Humphrey, O.E. Jr, Techtran  
Corp., Post Office Box 729, Glen Burnie Maryland.
48. Grigor'yan, G.M., and Ionikh, Yu.Z., Optogalvanic Effect  
in a CO Laser , Sov. J. Quantum Electron., Vol. 21, pp.24-  
27, 1991.
49. Incropera, F.P., and Dewitt, D.P., Introduction to Heat  
Transfer , John Wiley & Sons, 1990.

## **8. ENERGY TRANSFER IN CO/OCS MIXTURES:**

### **The Possibility of c.w. Lasing<sup>\*</sup>**

**\*This chapter adapted from O. Shulz, On the Possibility of Creating c.w. Lasing in the Carbonyl Sulfide Molecule , M.S. Thesis, Chemical Physics Program, OSU (1992)**

## 8.1. LASING WITH THE CARBONYL SULFIDE MOLECULE

### A) The carbonyl sulfide molecule

The carbonyl sulfide molecule (OCS) is a linear triatomic molecule. It has been investigated widely and its energy levels and other properties are well known / Maki & Wells 91 /. There are three different modes of vibrational excitation. The vibration

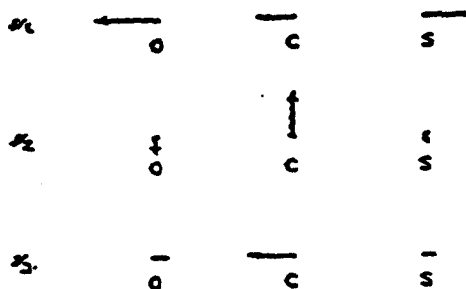


Fig. 8.1. The normal modes of OCS. Directions and length of arrows indicate relative motions of the nuclei for the three different vibrations.  $\nu_3$  is degenerated, a vibration of the same frequency perpendicular to the page is also possible. / Townes & Schawlow 55 /

corresponding to the symmetric stretch of the oxygen and sulfur atom has an energy of  $\nu_1 = 859.0 \text{ cm}^{-1}$ , its quantum number will be called  $n_1$ . The bending mode which is doubly degenerate corresponds to an energy of  $\nu_2 = 520.4 \text{ cm}^{-1}$ . The bending quantum number is named  $n_2$ . There is the possibility of an angular momentum associated with the bending mode if two bending vibrations perpendicular to each other are excited

simultaneously. Its rotational quantum number  $l$  can assume the values  $n_2, n_2-2, \dots, 1$  or  $0$ , depending on  $n_2$ .  $l$  is  $1$  for odd,  $0$  for even  $n_2$  / Kneubuehl & Sigrist 89/. The asymmetric stretch mode occurs at an energy of  $\nu_3 = 2062.2 \text{ cm}^{-1}$ .  $n_3$  will be used to describe its quantum number. A schematic of the vibrations is given in figure 1 / Townes &

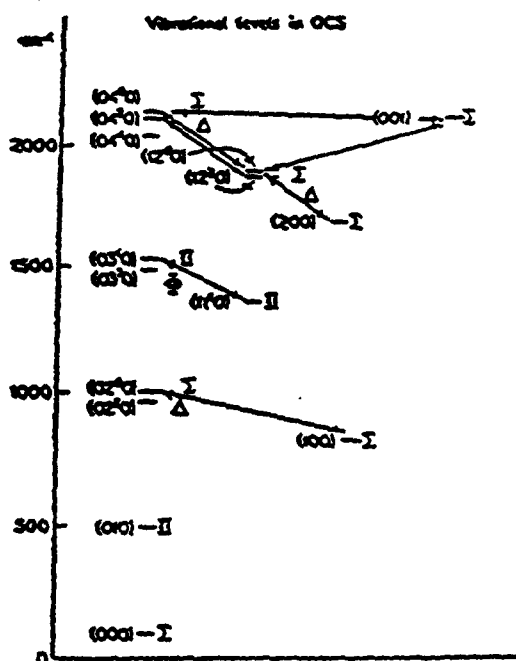


Fig. 8.2. Vibrational levels in OCS. Lines indicate possible interactions between nearby levels. / Townes & Schawlow 55 /

Schawlow 55 /.

Fig. 8.2 shows the different energy levels /Townes & Schawlow 55 /. In this work the vibrational excitation of a linear triatomic molecule will thus be described by the set of numbers  $(n_1, n_2, n_3)$ .

The energy for a linear triatomic molecule in a  $^1\Sigma$  electronic state is given by:

$$E = \sum_v (G_v + B_v J(J+1) - D_v [J(J+1) - l^2]^2 + H_v [J(J+1) - l^2]^3 + \dots) \quad (1.1)$$

/Maki & Wells 91/

The sum extends over the different vibrational levels  $v$ .  $G_v$  is the band center,  $B_v$ ,  $D_v$  and  $H_v$  are the rotational constants which depend on the state.  $J$  is the rotational quantum number for rotation about an axis perpendicular to the molecular axis and  $l$  the quantum number associated with the rotation about the molecular axis due to superpositions of bending modes perpendicular to each other. The constants in formula 1.1 are also given in the publication by Maki and Wells. The ones that are relevant for this work are summarized in Table 8.1.

Table 8.1. Rovibrational constants (in  $\text{cm}^{-1}$ ) for  $^{16}\text{O}^{12}\text{C}^{32}\text{S}$  / Maki & Wells 91 /

Vib. State	$G_v$	$B_v$	$D_v \cdot 10^8$	$H_v \cdot 10^{14}$
(00 <sup>0</sup> 0)	0	0.2028567408(8)	4.34064 (25)	-0.329(30)
(01 <sup>1</sup> 0)	520.422055(1470)	0.2032098348(21)	4.41148(31)	-0.260(38)
(10 <sup>0</sup> 0)	858.966932(48)	0.2022518316(60)	4.43350(36)	0.045(45)
(02 <sup>2</sup> 0)	1041.293318(239)	0.203559482(89)	4.48328(93)	-0.135(80)
(02 <sup>0</sup> 0)	1047.042048(11)	0.203480485(12)	4.41964(63)	-0.712(73)
(00 <sup>0</sup> 1)	2062.241(121)	2016415300(477)	4.40980(260)	4.551(470)
(04 <sup>4</sup> 0)	2084.378 374	2042480319(608)	4.5920(296)	-0.3
(04 <sup>2</sup> 0)	2099.524648(251)	2040519146(232)	4.49489(828)	-0.6
(04 <sup>0</sup> 0)	2104.827673(87)	2039680864(171)	4.30615(970)	-32.73(814)



To use the carbonyl sulfide molecule as a gain medium in a gas laser a population inversion has to be created. There are several rovibrational transitions in the OCS that can be used for that purpose / Deutsch 66, Schlossberg & Fetznerman 74 /. The most promising one results from the similarity of OCS to  $\text{CO}_2$ . Carbon dioxide is used in one of the most powerful gas lasers / Witteman 87, Dax 88/.

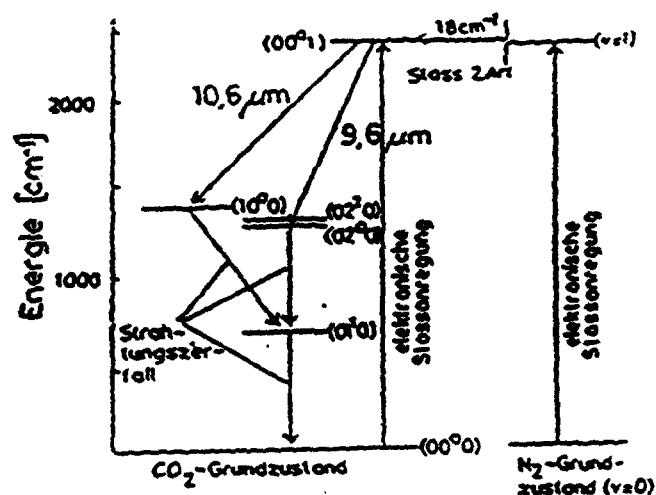


Fig. 8.3. Schematic  $\text{CO}_2$  -  $\text{N}_2$  laser energy transfer  
/ Kneubuehl & Sigrist 89 /

One can envision the OCS molecule as a  $\text{CO}_2$  molecule where one of the oxygen atoms is replaced by a sulfur atom. OCS has a vibrational mode structure similar to  $\text{CO}_2$ . This similarity leads to the idea that OCS could make a laser similar to the  $\text{CO}_2$  laser.

This proposed OCS laser would be very useful because there is a lack of fixed frequency lasers in the 8.3-micron range. If this hole is filled, the door would open for

more exact spectroscopic measurements in this region. Also the understanding of the OCS kinetics could be increased.

The CO<sub>2</sub> molecular laser is a gas laser which lases from the (001) state of the asymmetric stretch mode to the (02<sup>0</sup>0) state, the twice excited bending vibrational mode (9.6 μm band) and to the

first excited symmetric stretch state (100) (10.6 micrometer band). However, it should be mentioned that both the lower laser states mix because they are coupled in a

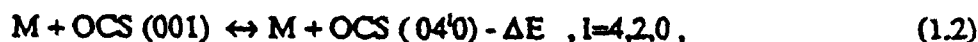
Fermi-Resonance due to their small separation in energy. A schematic is shown in

Fig. 8.3. In a CO<sub>2</sub> laser the upper laser level is populated by electron impact in a discharge and by near-resonant energy transfer from vibrationally excited nitrogen. N<sub>2</sub> is effective in storing vibrational energy since it surrenders that energy slowly in collisions and also does not radiate on transitions between vibrational levels of the same electronic state since it does not have an electric dipole moment. The lower laser levels are depopulated mainly by collision processes and also by spontaneous radiative decay. CO<sub>2</sub> lasers achieve up to 80 kW in the continuous wave mode of operation with a quantum efficiency of 15 to 20 % / Kneubuehl & Sigrist 89/.

However, there are differences between the CO<sub>2</sub> and the OCS, that have to be noted.

First, the Fermi resonance coupling of the (02<sup>0</sup>0) and (100) levels is not as strong as in CO<sub>2</sub> since this gap is larger than in CO<sub>2</sub>. In CO<sub>2</sub> this energy difference of the unperturbed states is about 7 cm<sup>-1</sup> (which is split up by the resonance to 102.8 cm<sup>-1</sup>) / Wittenman 87 / while in OCS the initial gap is already 181.9 cm<sup>-1</sup> / Maki & Wells 91/.

More important for the realization of an OCS laser is the fact, that the states  $(04^10)$ ,  $l=4,2,0$ , have a close coincidence with the desired upper laser level  $(001)$ . The band centers for this levels are found at  $2104.8$ ,  $2099.5$  and  $2084.3 \text{ cm}^{-1}$ , respectively. The  $(001)$  level in OCS is centered at  $2062.2 \text{ cm}^{-1}$ . So there is a possibility that the asymmetric stretch mode might be depopulated by intramolecular V-V transfer in collisions with other molecules or atoms in a reaction like:



in which a collision partner M collides with an OCS in the asymmetric stretch mode causing it to transfer to one of the bending modes  $(040)$ . The energy needed for this transition is a relatively small  $41$  to  $61 \text{ cm}^{-1}$  and comes from the kinetic energy of the collision partners. This V-V transfer alone is associated with a collision number of  $170$ , while in  $\text{CO}_2$  the total internal V-V transfer from the  $\nu_3$  to the  $4\nu_2, 3\nu_2, \nu_1 + \nu_2, 2\nu_1$  and  $\nu_1 + 2\nu_2$  modes is described by a collision number of  $25000$  / Mandich 80-1 /. The collision number gives the average number of collisions necessary to induce a specific transition. Therefore, this path of depopulation of the upper laser level is 2 orders of magnitude faster than the comparable one in  $\text{CO}_2$ .

Also it has to be noted that OCS possesses a permanent dipole moment of  $0.279 \text{ ea}_0$  / Itikawa 70 /.

## **B) Observed laser activity**

### **1. Pulsed laser activity at 8.3 $\mu\text{m}$**

In 1966, Thomas Deutsch observed pulsed laser activity at the transition from (001) to (100) in OCS in different mixtures with other gases / Deutsch 66 /.

The apparatus consisted of a water cooled 32-mm-inner-diameter tube and a resonator composed of a 25 m radius gold total reflector and a flat 1mm diameter pinhole which acted as a 1.5 % output coupler; 31 different transitions in that band lased in a pulsed discharge with pulse length of 1  $\mu\text{s}$  and 70 A peak amplitude in current. It was observed that the output increased monotonically with the gas mix sequence OCS, OCS-  $\text{N}_2$ , OCS - He, OCS - CO and OCS - CO - He. The increasing inversion ratio was also indicated by the presence of R - branch transitions in the last two mixtures. Typical gas mixtures contained about 0.3 torr OCS and 0.8 to 6.0 torr of He. The current threshold to achieve 8.3-micrometer lasing was 30 A. The partial pressures of the other gases are not given in the paper. In addition to the OCS laser action, lasing from CO molecules occurred also. Deutsch interprets the CO lasing by the formation of vibrationally excited CO due to decomposition of OCS. The increase in output by adding CO is explained by near resonant V - V transfer from vibrationally excited CO.

Several issues, raised by this paper, still remain unanswered. First, there is the question regarding the partial pressures of the gases in the lasing mixtures. Then one could

investigate the mixtures OCS - N<sub>2</sub> - He, OCS - CO - N<sub>2</sub> and OCS - CO - N<sub>2</sub> - He to investigate the effect of the additional excitation of CO by nitrogen. One could try to force additional transitions with the help of a wavelength selective resonator. Also there are questions remaining concerning the role of He. Why does helium increase the efficiency? What influence has the temperature on the laser output? To answer these questions, you need to have some information on the time development of the laser light for each mixture. / Deutsch 66 / is an important step towards an OCS continuous wave laser, without investigating the whole range of possibilities.

In 1975, Kildal and Deutsch / Kildal & Deutsch 75 / investigated two other ways to excite the OCS 8.3  $\mu\text{m}$  pulsed laser radiation.

First, CO was vibrationally excited by a frequency doubled pulsed CO<sub>2</sub> TEA laser. The energy is then stored in the CO molecule and transferred to OCS by near resonant V-V transfer. Lasing occurred with maximum pressures of 115 torr and a maximum efficiency of 2 %.

The second way of excitation was by direct optical pumping with five different frequency doubled lines of the CO<sub>2</sub> 9.6  $\mu\text{m}$  band ( P(26), P(28), P(30), P(32) and P(34)). Lasing occurred both near the pumped J values and near the J values corresponding to maximum thermal population. The maximum pressure and efficiency were 55 torr and 4 % , respectively.

In both cases 200 ns pulses containing up to 26 mJ were used.

These experiments once again demonstrates how important resonant V - V transfer from CO to OCS is for the process of populating the asymmetric stretch mode of OCS and

also points out the difficulties due to the close resonance of the (001) level to the (04<sup>0</sup>0) level. Unfortunately no information is given on the composition of the CO - OCS mixture used. Also no experiments have been conducted to investigate the impact of other gases such as helium on the performance. Nothing is said about the time development of the laser pulse.

## 2. OCS lasing at other wavelengths

In addition to lasing on the 8.3  $\mu\text{m}$  band pulsed laser action has been reported in the bending mode of OCS / Schlossberg & Fetterman 75 /. The (02<sup>0</sup>0)  $J=4$  state has been populated by a pulsed CO<sub>2</sub> laser operating on the P(22) of the 9.6  $\mu\text{m}$  band. Subsequent lasing with fairly high power has been observed down to the (010) state of OCS. The wavelength of the laser transitions were 18.983  $\mu\text{m}$  and 19.057  $\mu\text{m}$ .

## C) Continuous wave lasing at 8.3 $\mu\text{m}$

### 1. Excitation of the asymmetric stretch level

To achieve lasing it is necessary to create a population inversion. This means that ways have to be found to populate the higher laser level selectively, i.e., without populating the lower laser level or to depopulate the lower level selectively or both. As pointed out the OCS is supposed to lase from the (001) to the (100) level. There are four ways to populate the level (001) of OCS.

#### - Excitation by electron impact

The electron impact on OCS has been investigated by Sohn et al. / Sohn 86 /. They show that the cross section for excitation of the (001) level of OCS reaches its peak at

electron energies of 1.15 electron Volts (eV). In this case also the ratio of the cross sections for the excitation of the (001) level to that for the (100) level reaches a maximum. Sohn's results are shown in Table 8.2.

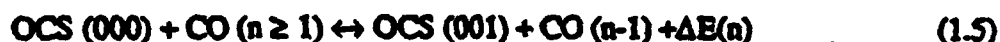
Table 8.2. Integral cross sections for  $e^- + \text{OCS}$  elastic scattering and vibrational excitation. All cross sections in  $10^{-16} \text{ cm}^2$ . / Sohn 87 /

Energy (eV)	Total	Elastic	Vibrational	OCS (100)	OCS (001)	OCS (010)
0.4	-	57.2	-	-	-	-
0.6	46.05	39.4	6.65	-	3	6.65
1.15	51.5	36.1	15.4	2	3.8	15.4
2.5	17	15.3	1.7	0.6	0.82	1.7
3	20.9	19.6	1.3	0.4	0.62	1.3
3.5	24.5	23	1.5	0.6	0.63	1.5

- At higher electron energies the cross sections and the ratio decrease. Once again these results are comparable to the similar results for the  $\text{CO}_2$  laser / Witteman 87 /.

- Excitation by vibration to vibration energy transfer

The asymmetric stretch mode is in close resonance to a number of vibrational transitions in other molecules. So there is the possibility of transferring energy in this mode by near resonant vibration to vibration V-V energy transfer. The first candidate for this mechanism is carbon monoxide in a reaction such as:



Probabilities for this reaction have been measured by Hancock and Smith and by M.

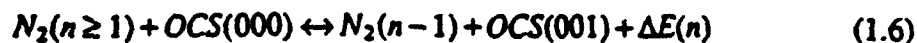
Lev-On et al. / Hancock 71, Lev-On 72 /. The number of collisions to transfer a

vibrational quantum from CO to OCS and the dependence of this number on the vibrational quantum number  $n$  of CO has been calculated from their data and is given in Table 8.3. These results, which are also confirmed

Table 8.3. Number of collisions required to cause V-V transfer from CO( $n$ ) to OCS, depending on CO vibrational quantum number  $n$ .  
after / Hancock 71, Lev-On 72 /

CO ( $n$ )	Collisions	CO ( $n$ )	Collisions
1	77	9	59
4	9	10	101
5	7	11	128
6	7	12	208
7	11	13	400
8	27		

by others / Hancock 74 /, show the very fast energy transfer to OCS. The observed variation with the CO vibrational excitation is due to two factors: the number of vibrational quanta available and the energy gap. The CO itself can be vibrationally excited by electron impact and by V-V transfer from  $N_2$  which itself is excited by electron impact / George 90 /. Both molecules reach higher vibrational levels due to Treanor pumping . This effect is favored at low temperatures / Treanor 68 /. Another possibility is the use of nitrogen. In collisions with vibrationally excited nitrogen, energy can also be transferred to OCS in the following reaction:





There are no data for this reaction in the gas phase, but one can expect this reaction to be important since  $\Delta E$  is a lot smaller than the average kinetic energy involved in the collision. This reaction has been observed in the liquid phase / Brueck 78/. Another hint is that OCS-N<sub>2</sub> mixtures gave more pulsed laser output than pure OCS / Deutsch 66 /.

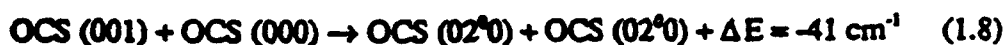
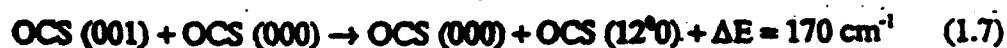
- Excitation by optical pumping

With the development of a CO laser operating at low vibrational levels an other opportunity for pumping the OCS (001) level is given. There is an accidental coincidence between the P<sub>1</sub>(13) (nomenclature P<sub>v</sub>(J''), quantum numbers for the lower levels are given) of CO and the R(5) line in the OCS (000) → (001) transition. The corresponding wavenumbers are 2064.58400(1) cm<sup>-1</sup> / Schneider 90 / and 2064.58404(13) / Maki & Wells 91 /, respectively. With the existing cw power of about 100 mW / Saupe 92 / on this CO laserline it might be possible to operate an optically pumped OCS laser. The optically pumped OCS laser would have the advantage that the lower laser level would not be populated by a discharge at all. This could simplify the creation of a population inversion.

2. Depopulation of the asymmetric stretch level

On the other hand, there are several mechanisms, apart from laser radiation in the 8.3 μm band, to depopulate the asymmetric stretch level of OCS. The spontaneous radiative lifetime of this level is 3.1 msec, which can be calculated from the transition moment of 345 Debye / Maki & Wells 91/. Also there are several opportunities for depopulation by

collisions. Most important is the redistribution of vibrational energy between OCS molecules with three main types of transfer processes:



M is a collision partner, e.g., OCS, CO or a rare gas. Rates for this processes have been measured by Hancock et al. / Hancock 74/. Their results are given in Table 8.4.

Table 8.4. Relaxation rates for OCS(001) / Hancock 74, Zittel 88 /

Collision process	rate constant (s <sup>-1</sup> torr <sup>-1</sup> )	Collisions per deactivation
OCS (001) + OCS	(4.7 +/- 0.6) * 10 <sup>4</sup>	160
OCS (001) + CO	(1.05 +/- 0.2)* 10 <sup>4</sup>	830
OCS (001) + Ar	(2.6 +/- 0.4)* 10 <sup>3</sup>	2,700
OCS (001) + He	(2.6 +/- 0.4) *10 <sup>3</sup>	2,700

### 3. Population of the symmetric stretch level

The lower laser level will be populated by three different ways. To maintain a population inversion population of this level should be avoided.

- Population by laser process.

This way of populating the lower laser level is unavoidable.

- Excitation by electron impact.

The results by Sohn, quoted in Table 8.2, point out that the symmetric stretch level of OCS is excited by electron impact as well as the higher asymmetric stretch level. As mentioned before, one must choose an electron energy that favors the population of the higher level over that of the lower one. Here 1.15 eV would be the appropriate electron energy.

-Excitation by internal V-V transfer processes.

The vibrational energy map for OCS by Mandich and Flynn shows that the (100) level of OCS can be populated by intramolecular energy transfer from the (020) levels / Mandich 80-1 /. From their work a collision number of 560 at 295 K can be calculated for this process. The (020) levels will be populated because of the mentioned transfer from the asymmetric stretch mode to the (040) levels. These levels will then relax in subsequential resonant processes such as:



The overall equilibration of the bending modes is very fast. The rate constant has been measured to be  $k_{2,eq} = (800 \pm 400) \times 10^3 \text{ s}^{-1} \text{ torr}^{-1}$  / Zittel 88 /. So once one populates the asymmetric stretch level, one also populates the lower laser level, the symmetric stretch

level, by subsequent intramolecular loss of vibrational energy. The close resonance of the (040) levels with the (001) level consequently has a negative impact on a possible population inversion in two ways: it depopulates the higher laser level and it populates the lower laser level. In the successful carbon dioxide laser no such process plays an important role.

#### 4. Depopulation of the symmetric stretch level

The lower laser level, the symmetric stretch level, will be depopulated by three major mechanisms.

First there will be relaxation into the rotational and the translational mode (V-T/R relaxation). The second process is V-V energy transfer to the twice excited bending mode which is separated by  $188 \text{ cm}^{-1}$ . This process is described by a collision number of  $1400 / \text{Mandich } 80-1 /$ . The last process is spontaneous radiative decay. The corresponding spontaneous lifetime is 1.2 seconds / due to Maki & Wells 91/. The total decay of the  $\nu_1$  state in pure OCS has been observed to be  $(1.7 \pm 0.2) 10^3 \text{ s}^{-1} \text{ torr}^{-1} / \text{Mandich } 80-1 /$ . Most likely this rate is faster in the presence of lighter gas, at least the part of it being associated with a V-T/R process.

## 8.2. EXPERIMENTAL SETUP

### A) Schematic Setup

A schematic of the setup is shown in Fig. 8.4. The experiments were conducted in a

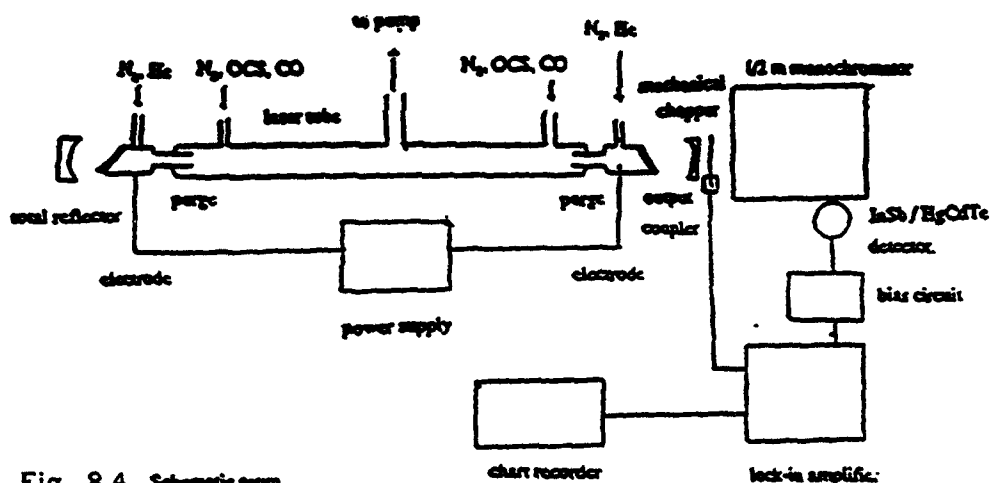


Fig. 8.4. Schematic setup

glass tube with a glass jacket to provide different means of cooling. In this glass tube there is an electric discharge which operates in a direct current mode. The glass tube is sealed by  $\text{BaF}_2$  Brewster windows which are purged. Just inside each purged end region there is a gas inlet. The gases are pumped out of the tube through a center port, as shown. The tube is mounted to an optical bench which also holds the resonator optics.

The resonator is composed of a total reflector and an output coupler and thus is not line selective. Gases entering the tube are mixed in a mixing volume. They can be measured by flowmeters and by partial pressures. Radiation leaving the tube can be investigated by means of a monochromator.

### B) The Resonator.

The resonator has been calculated to give a relatively large mode volume long length cavity to obtain a higher gain since one has to expect a small density of molecules in the upper laser level. The total reflector has a radius of curvature of  $R_v=10$  m, the output coupler has a reflectivity of 98 % centered at  $8.3 \mu\text{m}$  and a radius of curvature of  $R_{oc}=10$  m. Consequently the resonator is a symmetric one. The two reflectors are separated by  $L=180$  cm. One obtains the following resonator parameters, based on / Siegman 76 /:

$$g_{oc}=1-L/R_{oc}=0.82 \quad (2.1)$$

and simultaneously  $g_v=0.82$ . The resonator thus fulfills the stability condition:

$$0 \leq g_v g_{oc} \leq 1. \quad (2.2)$$

For  $8.3 \mu\text{m}$  the waist at the mirrors can thus be calculated to be:

$$w_{oc} = \sqrt{L \lambda / \pi \sqrt{g_{oc}(1-g_{oc})}} = 2.88 \text{ mm} \quad (2.3)$$

and with a symmetric expression one obtains  $w_v=2.88$  mm. Since the waist inside the resonator is everywhere inside the cavity smaller than the waist at the mirrors, there is no interference with the purges, which were selected to be 16 mm in diameter, at all.

Both mirrors are mounted to an optical rail supplied by Oriel Co. which is supposed to be very stiff. The rail itself is staged on the optical table by four vibration isolation feet. The table consists of steel beams and plates. This effort was made to vibrationally isolate the resonator. In order to achieve a better stability of the resonator additional improvements would be necessary.

The tube is closed by  $\text{BaF}_2$  optical flats which are mounted at the Brewster angle. A transmission curve for  $\text{BaF}_2$  is given in Fig. 8.5. There are two different thicknesses available, 3 mm and 6 mm.

$\text{BaF}_2$  refractive index vs. wavelength

$\lambda(\mu\text{m})$	$n$	$\lambda(\mu\text{m})$	$n$	$\lambda(\mu\text{m})$	$n$
0.26	1.51	0.85	1.47	8.00	1.43
0.30	1.50	3.24	1.46	8.60	1.42
0.36	1.49	5.14	1.45	9.20	1.41
0.48	1.48	6.50	1.44	9.80	1.40
				10.60	1.39

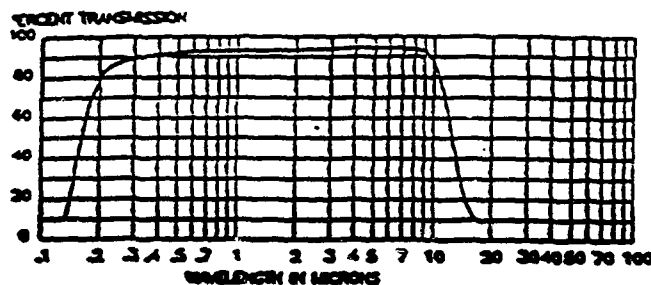


Fig. 8.5. Optical properties of  $\text{BaF}_2$  / Janos 89 /

Inside the discharge one has to expect the decomposition of OCS due to the reactions /

Barker 80 /



Therefore, one has to expect deposition of sulfur on the walls as observed earlier in direct current glow discharges / Yamada 87 /. To avoid sulfur deposition on the windows, they are separated from the main tube by a 16 mm diameter purge of 10 cm length. Helium and nitrogen are used as purge gases. The OCS is added 12 cm downstream from the helium and nitrogen. The experiments showed that this purges were very effective. While the main tube was covered with sulfur after a few minutes of discharge operation, no sulfur deposition ever could be observed in the purged volume.

The location of the decomposition of the carbonyl sulfide was monitored by the deposition of sulfur on the walls of the tube because the flow velocity was relatively small ( about 3.5 m/s). Therefore, the sulfur was deposited in the region where the decomposition of the carbonyl sulfide took place. It turned out that at high carbonyl sulfide partial pressures and high currents most of the deposition occurred in the region directly behind the carbonyl sulfide inlet. The conditions in this case were carbonyl sulfide partial pressures of about 1 torr and currents above 40 mA without any carbon monoxide added.

In discharges in pure carbonyl sulfide an almost complete decomposition of carbonyl sulfide in carbon monoxide and sulfur has been observed / Clark & De Lucia 80 /. The authors of this study also observed that rotational, translational and vibrational degrees of freedom reach approximately the same temperature in the discharge, although different times are needed to achieve this temperature.



The present experiment differs from a discharge in pure OCS by the addition of large amounts of He and CO. The He has the effect of significantly lowering the translational / rotational mode temperature by increasing the heat capacity of the gas mixture and by increasing the heat conduction to the walls. The added CO has the effect of shifting the equilibrium in equation (2.3), so less deposition of OCS into CO and S takes place. Also we note that a very small amount of OCS is retained in a large preponderance of CO.

This permits energy to be stored in the OCS / CO vibrational modes without thermalization from rapid V-T/R relaxation. This is similar to the  $N_2$  storage role in  $CO_2 - N_2$  laser mixture. The observed strong fluorescence from CO vibrational levels of at least up to  $v=5$  also proves that vibrational temperature in the CO is very much higher than the translational temperature. Therefore, the conclusions from Clark and De Lucia not necessarily apply to the discharge under investigation here.

At the conditions used later in the actual experiments (see Section 8.3). The partial pressure of carbonyl sulfide was about 0.01 torr and thus very much smaller than in the case described above. Also there was carbon monoxide added to about 0.1 torr partial pressure. Thus the decomposition of carbonyl sulfide was not as rapid as in the case of higher carbonyl partial pressures and lower carbon monoxide partial pressures. This could be concluded from the observation that the sulfur was deposited more uniformly on the tube wall. Also, the sulfur was deposited a lot slower in this cases. So there appears to be carbonyl sulfide in the whole tube and the decrease in carbonyl sulfide content towards the center of the tube where the exhaust was located seems to be very

moderate. The windows themselves are mounted on an nylon holder to allow

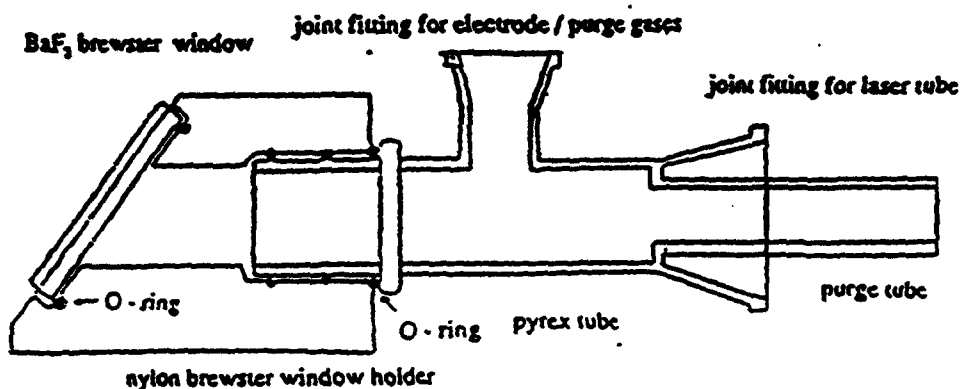


Fig. 8.6. Brewster window holder

replacement and cleaning. Fig. 8.6 shows a sketch of the Brewster window setup.

### C) Gas Handling System

A sketch of the gas handling system is displayed in Fig. 8.7. Helium and nitrogen are introduced into the tube through the purges while OCS, N<sub>2</sub> and CO enter the main tube just outside the purged areas. The flow is directed towards the center of the tube where the pump is connected. Pressures are measured at the gas outlet by a mechanical Wallace & Tiernan pressure gauge, model FA 180. This device allows pressure measurements with an accuracy of 0.01 torr.  $\mu$ . The flow of each gas can be regulated by metering valves and is measured by flowmeters. The gases entering the main tube are mixed in a mixing volume of about 225 cc.

A HYVAC 14 pump with a flow rate of 160 ltr / min is used. The flow velocity at a typical pressure of 5.00 torr in the laser tube has been measured to be about  $3.5 \frac{\text{m}}{\text{s}}$ .

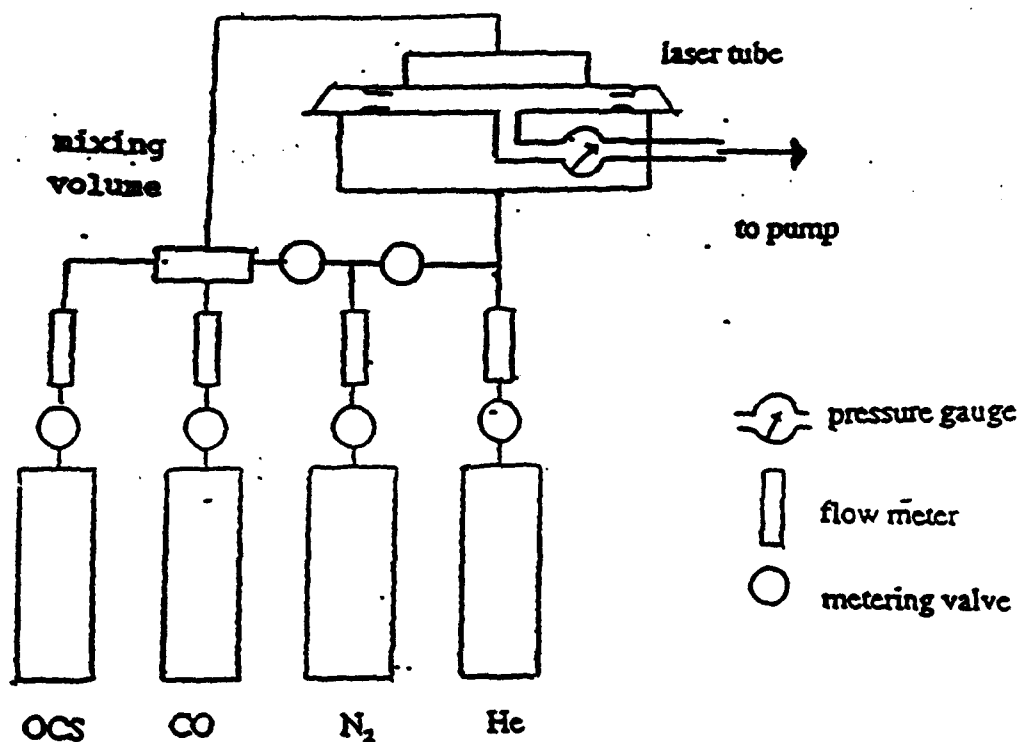


Fig. 8.7. Gas handling system for OCS laser setup.

#### D) The discharge

A one arm discharge extending between the purged areas is used to excite the gases. The electrodes are bullet shaped nickel pieces separated by 140 cm. A BRC -40-25-OS power supply by Universal Voltronics Corporation is used. No external ballast resistors are needed.

There is a optimum energy transfer from discharge electrons to the OCS(001) energy level if these electrons have an average energy of 1.15 eV / Sohn 87 /. With the analogy to the CO<sub>2</sub> laser this would correspond to an E/N ratio of about  $2.5 \cdot 10^{-16}$  V cm<sup>2</sup> / Witterman 87/. At the pulsed OCS laser by Deutsch / Deutsch 66 /, total

pressures of 1.1 to 6.3 torr have been used, requiring a voltage of 0.8 to 4.7 kV in our setup. The BRC-40-25-OS operates in this area and up to 20 kV.

#### **E) Cooling**

To allow cooling, the glass tube is supplied with an outer jacket of 7.5 cm diameter. It can be filled with a variety of coolants such as water, dry ice or liquid nitrogen. It is possible to have the coolants flow through this jackets.

#### **F) Radiation detection**

To analyze the radiation out of the tube, a 1/2 m monochromator manufactured by Spex, model 1870 is used. There are gratings blazed at 4  $\mu\text{m}$  and at 8  $\mu\text{m}$  available and two different infrared detectors. To detect the (001) state of OCS a liquid nitrogen cooled InSb detector by EG&G Judson, model J10D-M204-R01M-60 is used. The actual laser radiation at 8.3 microns is supposed to be detected by an liquid nitrogen cooled HgCdTe detector by the same manufacturer, model J15D12-M204-S01M-60. Response curves and electrical bias circuits for both detectors are given in the Appendix. The signal out of the detectors is analyzed by a phase-lock amplifier by Stanford Research Systems, model SR 510. A mechanical chopper is used to chop the radiation.

### 8.3. EXPERIMENTAL RESULTS.

#### A) Fluorescence from the upper laser level

##### 1. Procedure

To create a population inversion it is necessary to populate the upper laser level. The first part of this study consequently was to investigate how the different parameters that could be manipulated influenced this population. These parameters include the discharge current, the concentration of the different gases and the temperature. The easiest way to obtain information about the asymmetric stretch mode of the OCS is by monitoring the spontaneous emission to the ground state.

This transition has the strongest transition moment of the OCS transitions given by Maki and Wells (0.345 Debye / Maki & Wells 91 /, giving a spontaneous lifetime of 3 msec ).

The spontaneous lifetimes for the actual laser transition itself is not known but can be estimated, by the comparison with the CO<sub>2</sub> molecule, to be of the order of seconds. This transition consequently is a lot weaker. Adding to this is the fact that the infrared detectors are more sensitive for higher energy photons. Therefore, in total the (001) to (000) transition can be detected a lot better than the (001) to (100) transition. Nevertheless, this transition overlaps with the lower transitions of the CO  $\Delta v = 1$  band and can, therefore, with our equipment just be detected as a structure underneath the CO

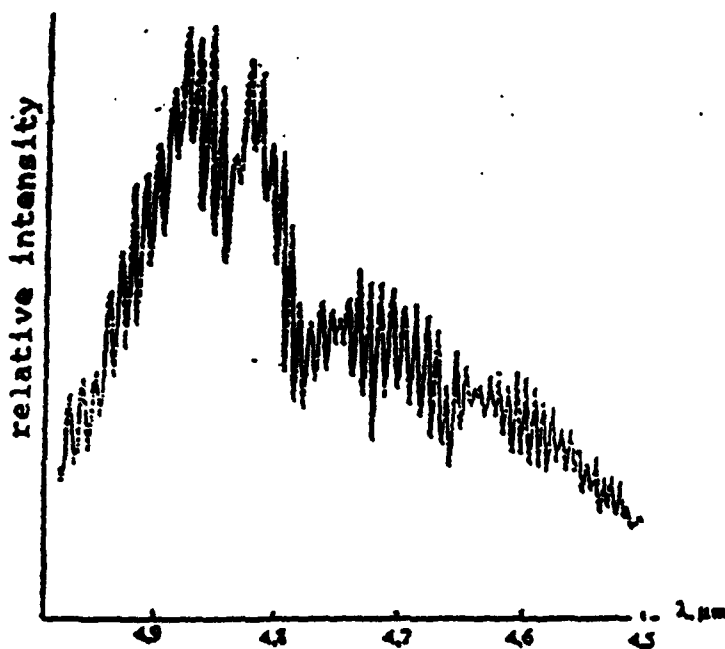


Fig. 8.8. CO-OCS spectrum

spectrum. The 1/2 meter spectrometer cannot resolve the single OCS rotational lines with the CO background since these lines are spaced closer than the CO lines and than the apparent width of the single CO lines, which is given by the instruments available. The spacing of the OCS

rovibrational lines is

approximately 1 nm while that of the CO lines is about 10 nm. The reason for that is of course that the OCS has a larger moment of inertia than CO.

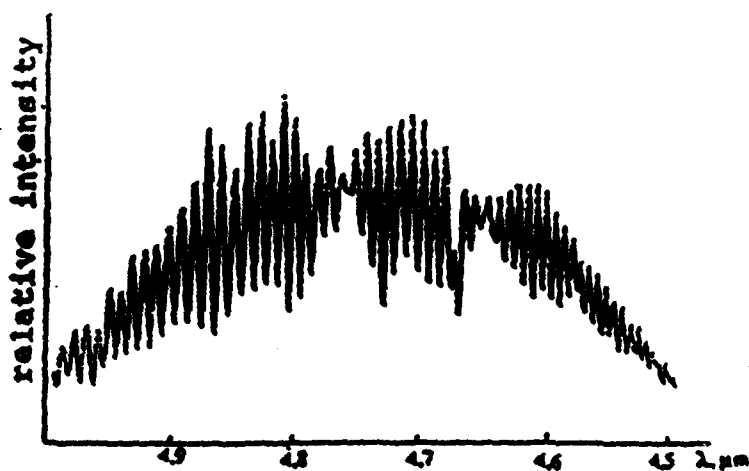


Fig. 8.9. Pure CO spectrum

To determine the real intensity of the OCS signal against the CO background the following procedure was applied. For every set of parameters two spectra were recorded, one with and one without OCS. The spectra

were taken observing the fluorescence from the discharge analyzing it with the half-meter monochromator and an InSb detector. Typical spectra for the cases with and without OCS are shown in Figs. 8.8 and 8.9. Then in both charts the intensity at 4.635, 4.832 and 4.873 microns corresponding to the CO transitions  $R_0(3)$ ,  $R_2(6)$  and  $R_2(10)$ , respectively, was determined. The latter two overlap with the OCS (001) to (000) transitions. It is assumed that the distribution of intensities among the CO lines does not significantly change when OCS is added. This might not exactly be true but it gives a good estimate since the energy transfer rates from the lower three CO vibrational levels, which are the ones under investigation here, should be in the same order of magnitude. The harmonic oscillator model / Landau 36 / suggests together with the work of Lev-On / Lev-On 72/ that approximately 77, 35 and 42 collisions are needed to transfer a vibrational quantum to OCS from the CO  $v=1,2,3$  level, respectively. At the same time collisions among CO molecules tend to rapidly redistribute the energy between the different CO vibrational levels toward a steady state distribution function. So one can imagine that the energy lost to the OCS is not lost by single CO vibrational states but by the CO population as a whole.

The procedure was to determine the ratios of the intensities at 4.6345 microns to that at 4.832 microns and to that at 4.873 microns in the OCS - free spectrum. In a second step these ratios and the signal at 4.6345 microns in the OCS-CO spectrum, where there is no OCS signal, were used to calculate which part of the signal at the two other wavelengths is due to CO. The rest of that signal has been attributed to OCS. This procedure

certainly does not give the exact OCS intensities. Nevertheless the possible systematic error introduced by this method will always be directed in the same direction. Probably this method will underestimate the OCS radiation since the overlapping CO transitions are more likely to transfer energy to OCS than the reference transition  $\text{CO } v=1 \rightarrow v=0$ . However, since all one is interested in is an estimate of the relative population of the OCS (001) level, this systematic error does not influence the interpretation of the results. To estimate the amount of the OCS in the (001) level, the average intensity of the two OCS lines has been divided by the partial pressure of the OCS in the lasertube. This value was named R, it can be called the relative population of the (001) level, given in arbitrary units.

## 2. Results

The dependance of the relative population of the OCS (001) level on the different controllable parameters has been investigated. It turned out that the optimum values found for each parameter were reproducible if the other parameters were varied within a reasonable range. In the following section the results of this investigation are presented.

### a) Carbonyl sulfide

As can be seen in Fig. 8.10, the relative intensity value R is more than inversely proportional to the OCS in the cell. It has to be pointed out that this behavior is not caused by the division with the partial pressure alone. The total radiation itself also increases with decreasing flow rate. It has also been observed that a high OCS concentration results in a smaller overall signal from the carbon monoxide population.



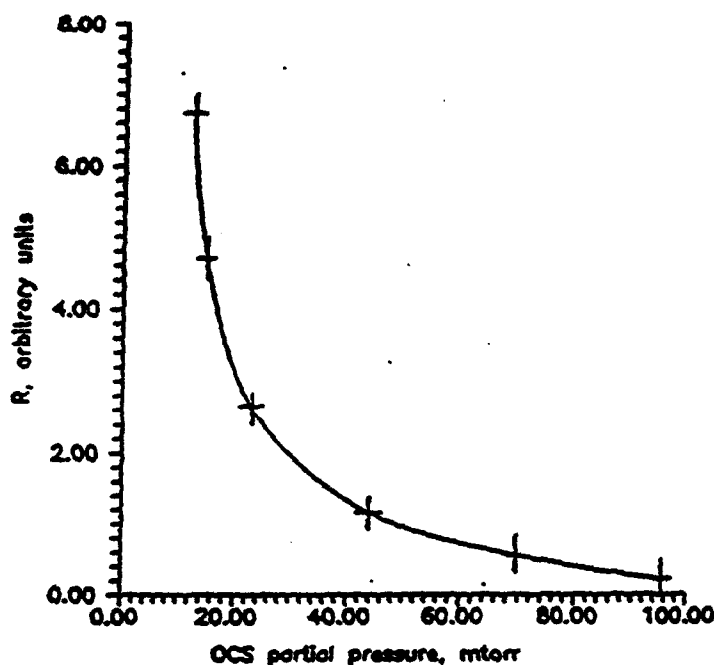


Fig. 8.10. Relative population of OCS (001) at different OCS partial pressures

The two curves in Fig. 8.11. point out the tremendous impact of the OCS concentration on the CO fluorescence signal. This result can be explained by two processes.

First, the smaller the OCS / CO concentration ratio, the more likely is a V-V energy transfer to the OCS by

vibrationally excited CO, because more excited CO molecules are available per OCS molecule. Since the OCS loses this energy relatively fast into other modes, a small OCS concentration also means that a smaller amount of energy is taken out of the CO molecules which, therefore, can continue to act as an energy reservoir for the OCS. As shown in Fig. 8.11 a high OCS partial pressure results almost in a complete loss of the CO energy reservoir.

On the other hand a higher number of OCS molecules means a higher probability for collisions among OCS molecules. OCS tends to give up vibrational energy in this collisions much more rapidly than in collisions with other molecules, as pointed out above. However the first effect mentioned is probably the dominant one.

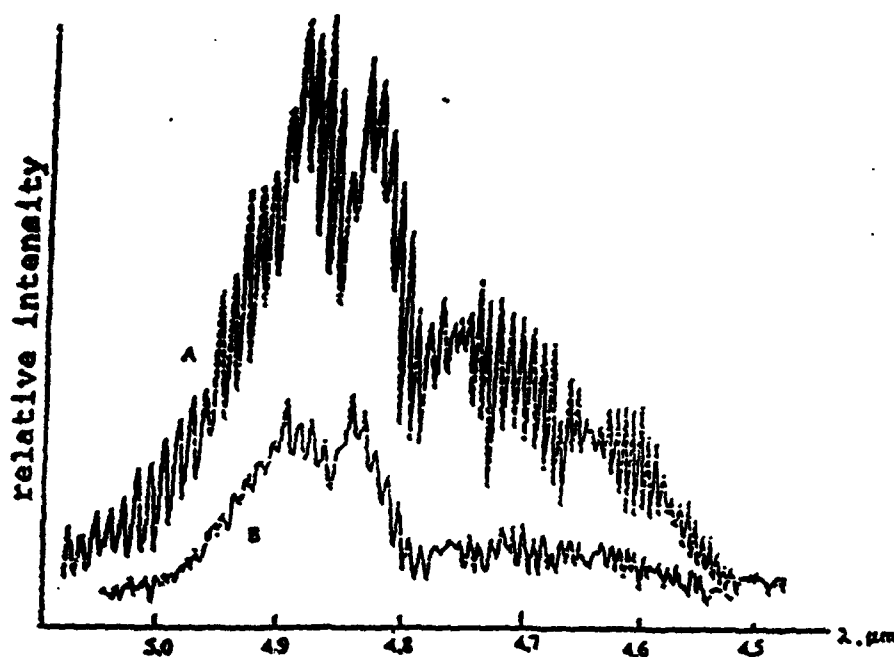


Fig. 8.11. Spectra of CO - OCS mixture for two different OCS partial pressures  
 Curve A : partial pressure 12.5 mtorr  
 Curve B : partial pressure 82.7 mtorr

It has to be noted that for all cases where OCS  $2062\text{ cm}^{-1}$  radiation has been observed, the OCS partial pressure was below 0.1 torr. Deutsch ran the OCS pulsed laser at typical pressures of 0.3 torr / Deutsch 66 /. So it can be seen that this laser was not running at optimum conditions for an OCS cw laser (if such a thing exists).

#### b) Current

The dependence on the current shows a maximum at currents around 22 mA as shown in Fig. 8.12. The voltage in this case was 6.0 kV. This gives  $E/N$  ratio of  $1.9 \times 10^{-16}\text{ V cm}^2$  at 5.3 torr total pressure. This  $E/N$  ratio would cause a rms kinetic energy of approximately 0.62 eV in a  $\text{CO}_2$  laser mix / Witteman 87 /. In a CO mix, which comes

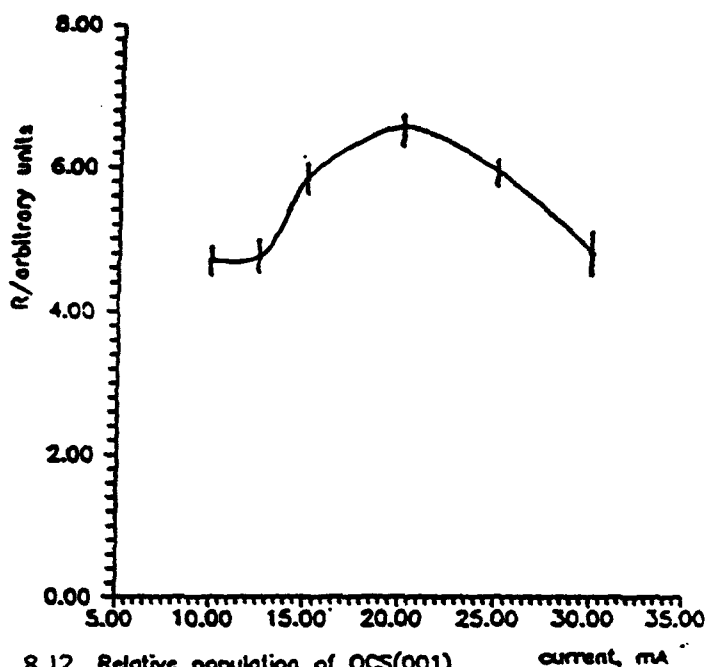


Fig. 8.12. Relative population of OCS(001) at different currents

closer to the present condition, this  $E/N$  ratio gives a rms of less than  $1.28 \text{ eV} / \text{Nighan 72 /}$ . This result also is in good agreement with the expectation of maximum excitation of the asymmetric stretch mode of OCS at an average kinetic electron

energy of  $1.15 \text{ eV} / \text{Sohn 86 /}$ . This shows that for the excitation of the OCS (001) level the mechanism of direct electron excitation cannot be neglected.

### c) Carbon monoxide

The dependence on the carbon monoxide partial pressure is given in Fig. 8.13. A slight preference for CO partial pressures around 0.1 torr is observed. Once again two effects seem to cause this. At lower CO concentrations, the OCS - CO ratio shifts towards the OCS and the energy loss due to OCS excitation becomes dominant. At higher CO pressures the number of excited nitrogen molecules decreases. Also the influence of the CO molecules on the electron energy distribution function increases. Fewer electrons will have the right energy to excite CO vibrations. Consequently less CO molecules with

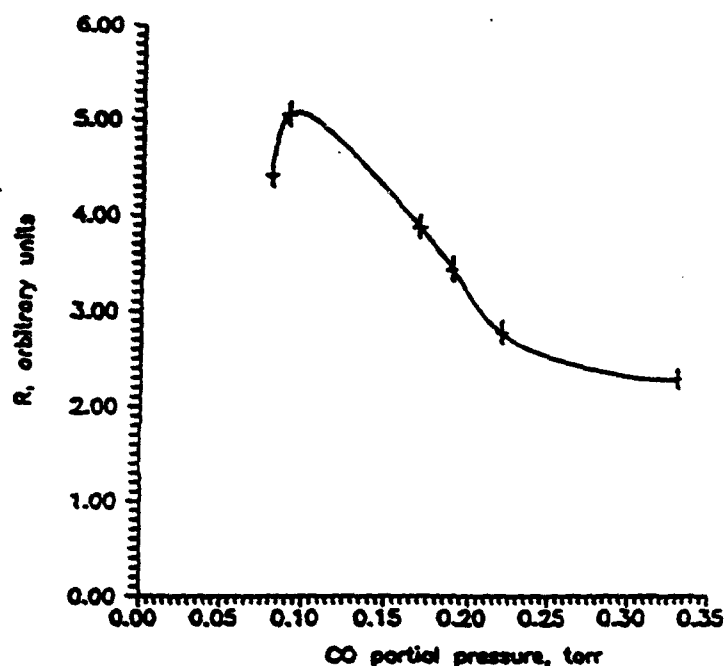


Fig. 8.13. Relative population of OCS (001) at different CO partial pressures

the favorable vibrational quantum levels of up to about  $v = 8$  are available. There might even be so much CO in the vibrational ground state that there is a considerable energy transfer from OCS to CO. Nevertheless it

seems that the CO concentration is not as critical as the parameters investigated previously.

#### d) Nitrogen

The nitrogen concentration was the least critical parameter. Fig. 8.14 shows that once a critical threshold is passed, there is no significant influence of the nitrogen partial pressure observed. This threshold is located at 0.07 torr. This may be caused by the fact that OCS-N<sub>2</sub> collisions play only a minor role due to a larger energy gap. Presumably, the influence of nitrogen on OCS is more indirect and occurs via CO excitation.

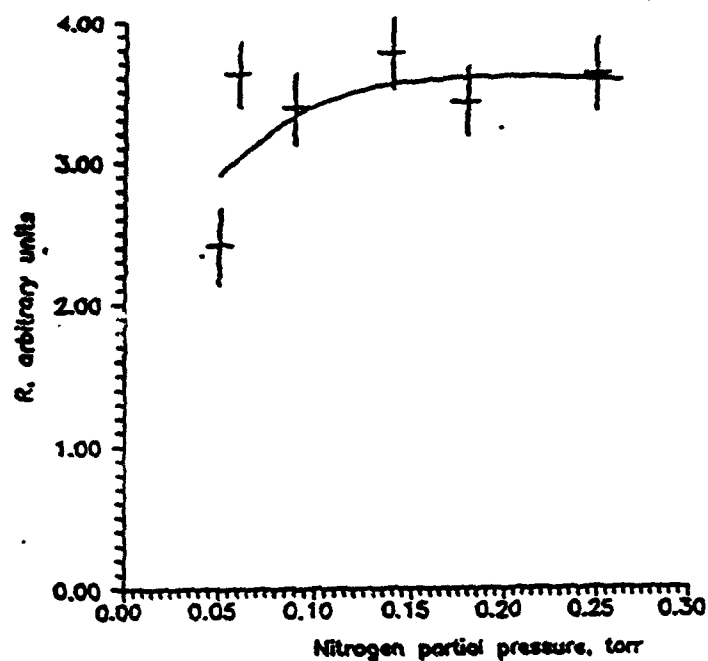


Fig. 8.14. Relative population of OCS (001) at different nitrogen partial pressures

c) Helium

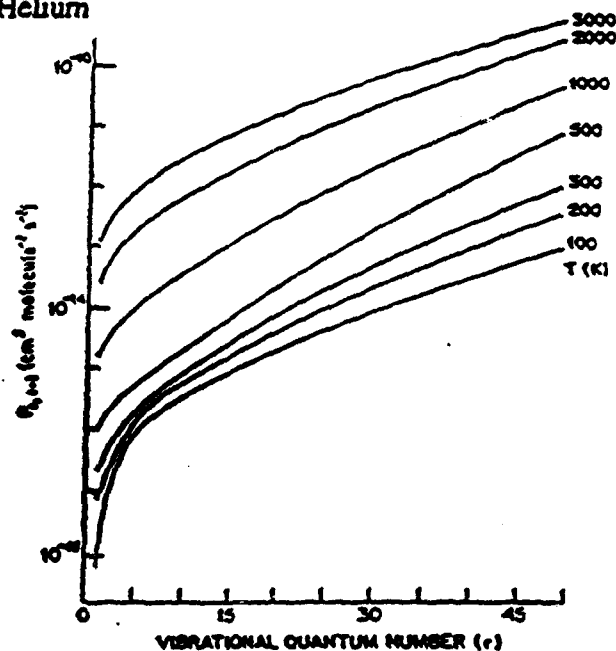


Fig. 8.15. CO-He vibrational-rotational energy transfer rates.  
/ Verter 76 /

Helium is used to support the discharge and is an effective coolant for the gases because it has a high thermal conductivity. The helium concentration is limited by the role it plays as a V-T/R relaxer for the OCS as well as for the CO.

As shown in Fig. 8.15 the V-T/R rate constant for carbon monoxide and helium increases with temperature as well as with quantum number. This can be explained by the fact that the higher vibrational quanta are smaller than the lower ones due to the anharmonicity of the CO potential / Rich 82 /. One can infer from Fig. 8.15 that for the low CO vibrational levels ( approximately  $v < 8$  ) which are needed for the energy transfer to carbonyl sulfide the temperature is not very important for the range accessible in this work ( 200 - 400 K ) and the rates are very small. The V-T/R rates for helium and asymmetric stretch mode of carbonyl sulfide have been measured to be  $8 \times 10^{-14} \text{ cm}^3 \text{ molecule}^{-1} \text{ s}^{-1}$  at 295 K / Zittel 88 / which is about 5 orders of magnitude higher than the

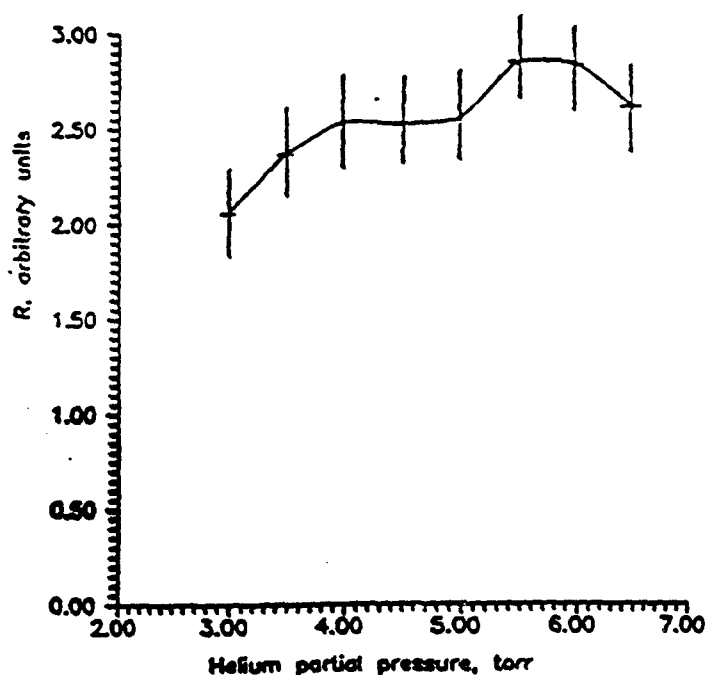


Fig. 8.16. Relative population of OCS (001) at different helium partial pressures

comparable rates for CO - He.

No temperature dependence

of this rate has been

measured. The reason for this

relatively high rate once again

is the possibility of

intramolecular transfer of

vibrational energy mainly to

the fourfold excited bending

mode. Since this reaction

requires only a small energy

of  $43 \text{ cm}^{-1}$ , one can expect the change of this rate with temperature to be very modest

because this energy will be available in almost all collisions occurring at the accessible temperatures. A temperature of 200 K already equals  $139\text{ cm}^{-1}$ . But even with this high V-T/R rates helium is, among the possible gases to support the discharge (He, Ar, Kr) the one with the smallest such rate. Nevertheless the helium concentration is not a very critical parameter. Fig. 8.16 displays a slight maximum at pressures around 5.5 torr.

f) Temperature

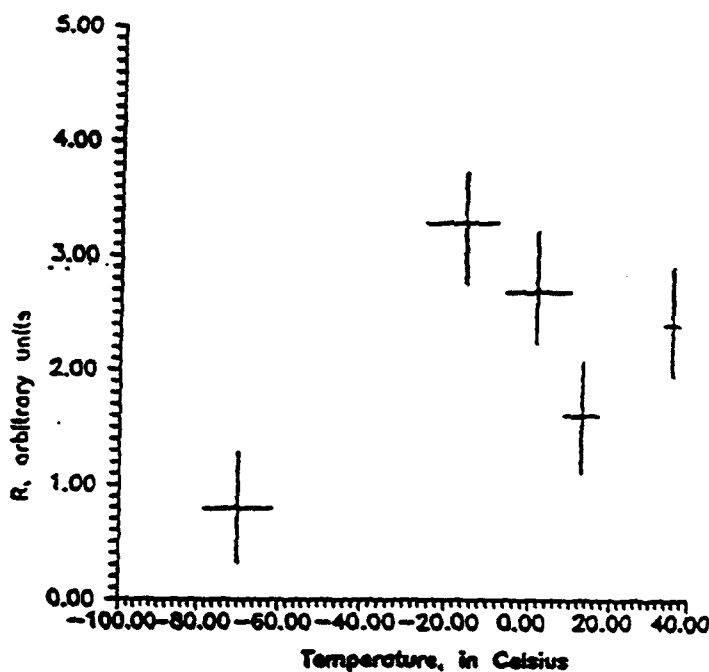


Fig. 8.17. Relative population of OCS (001) at different temperatures

Fig. 8.17 displays the influence of the temperature. Measurements have been made using liquid nitrogen (77 K), dry ice (frozen  $\text{CO}_2$ , 194 K) in acetone, and ice in water as coolants. As expected, OCS froze out as a white crystal at the  $\text{LN}_2$  temperatures, and no OCS radiation could be observed at these temperatures. A strong

dependence on the temperature could not be observed.

This is another clue for the important role of intramolecular V - V processes in the depopulation of the asymmetric stretch level. Typically, near resonant V-V energy

transfer shows an inverse temperature behavior while the V - T/R processes increase with rising temperatures / Rich 82 /. The negligible influence of the temperature on the OCS (001) population can be explained as follows. At low temperatures the V-V governed depopulation of the (001) level into the (04<sup>0</sup>0) level is more effective than at higher temperatures. This effect is compensated by the decreasing role of the V-T/R relaxation at lower temperatures. This decrease though should not be very steep as estimated above. The net effect is the very weak dependence on the temperature as observed.

### 3. Interpretation

The investigations show that the population of the asymmetric stretch level of OCS is influenced by all the parameters under investigation. For each parameter an optimum value could be determined. This optimum value is reproducible in every case for different sets of the other parameters if these are varied within a reasonable range. To summarize the above results one can recommend an current of 22 mA, a very low OCS partial pressure of about 17 mtorr, a Helium concentration of about 5.5 torr, a nitrogen concentration of about 0.1 torr and a carbon monoxide concentration of 0.1 torr also. Even if a population inversion can be achieved for an OCS partial pressure of 17 mtorr, it remains questionable whether this small amount of OCS can create an adequate small signal gain. The pulsed OCS laser realized previously operated with typical OCS pressures of 300 mtorr.

The results seem to confirm the expectations for the excitation of the OCS asymmetric stretch level. There is a dominant vibration to vibration energy transfer from



vibrationally excited CO to OCS. This is shown nicely by the facts that the OCS signal decreases when the CO reservoir is reduced as shown in the Fig. 8.11 and by the current which reaches its optimum value at a point where CO excitation is favored. However, direct excitation of the OCS (001) level by collisions with electrons cannot be neglected. One can almost think of the proposed gas mixture as a carbon monoxide laser containing small amounts of carbonyl sulfide.

The loss of the CO reservoir when the OCS concentration is increased above very slight amounts indicates how fast the OCS (001) level itself loses its energy. If the OCS would stay in the asymmetric stretch level for a time comparable to the time the CO remains vibrationally excited, the overall energy stored in the two molecules would remain the same even at higher OCS concentrations. An equilibrium at a higher total energy would be established. The experimental result indicates that the contrary is true. The OCS acts like an energy sink for the CO population. This could be caused either by the OCS being a fast vibration to translation (V-T) relaxer for the CO or by a fast internal redistribution of the energy inside the OCS or both. Information from the literature indicates that the latter is true as discussed in Section 8.1. The energy is lost by internal conversion from the asymmetric stretch level to the fourfold excited bending mode which is in close resonance.

Somewhat similar considerations apply to the  $\text{CO}_2$ - $\text{N}_2$  laser. In a  $\text{CO}_2$ - $\text{N}_2$  laser also the carbon dioxide partial pressure is limited by the amount of nitrogen available for optimum performance.

Unfortunately a good excitation of the higher laser level alone does not guarantee laser operation by itself if this level is depopulated very fast.

**B) The 8.3  $\mu\text{m}$  radiation in spontaneous emission.**

Efforts have also been made to observe the radiation from the asymmetric to the symmetric stretch mode at 8.3  $\mu\text{m}$  in spontaneous emission. For that purpose the grating in the monochromator has been changed from one blazed at 4 micrometers to one blazed at 8 micrometers. Also the InSb detector has been replaced by a HgCdTe detector. These efforts failed. The reason was that for this transition the spontaneous lifetime is about 3 orders of magnitude longer than for the direct transition to the ground state if the OCS behaves similar to  $\text{CO}_2$ . In  $\text{CO}_2$  one has to compare 3 msec with 5 sec / Wittman 87 /. Also, the HgCdTe detector is about 1 order of magnitude less sensitive to the 8.3  $\mu\text{m}$  radiation than the InSb is to the radiation around 5  $\mu\text{m}$  / EG&G 91 /.

**C) Attempts to achieve lasing**

To observe laser action the following procedure was applied. First, the resonator was adjusted. Two methods were used for this purpose. The first one was to adjust the resonator with a HeNe laser beam shone into the cavity through the output coupler which is partially transmitting in the visible and subsequent aligning of the mirrors so that the laser beam was reflected through the tube several times. The second method was to set up the laser as a  $\text{CO}_2$  laser. The total reflector has a reflectivity of 95 % for the 9.6 micrometer band and only 13 % for the 10.6 micrometer band. The  $\text{BaF}_2$  windows were replaced by NaCl ones (  $\text{CO}_2$  lasing with the  $\text{BaF}_2$  windows resulted in their destruction. The absorption of the high intra cavity powers by the  $\text{BaF}_2$  is too strong as seen from

Fig. 8.5. The window absorbs 10 % of the intra cavity radiation and breaks due to thermal shock / Janos 89 /. ) With a standard CO<sub>2</sub> laser mixture of 4.8 torr helium, 0.6 torr nitrogen and 0.5 torr carbon dioxide and a current of 40 mA an output power of 12.2 Watts could be achieved easily.

Then the barium fluoride windows were put back in place and it was tried to start the OCS laser with the so adjusted resonator. Gas mixture and other parameters found to be optimum for the population of the asymmetric stretch level were used to start with. From this point on all the parameters were varied within reasonable range. Also the adjustment of the resonator was checked each time. This experiments were very time consuming and disappointing because after the "readjustment" of the resonator at least the HeNe adjustment method was needed to realign the mirrors. Radiation was to be detected with a HgCdTe detector placed directly in front of the output coupler. No lasing could be detected at all.

Similar experiments using a mechanical chopper intracavity failed also.

#### 8.4. KINETIC MODEL

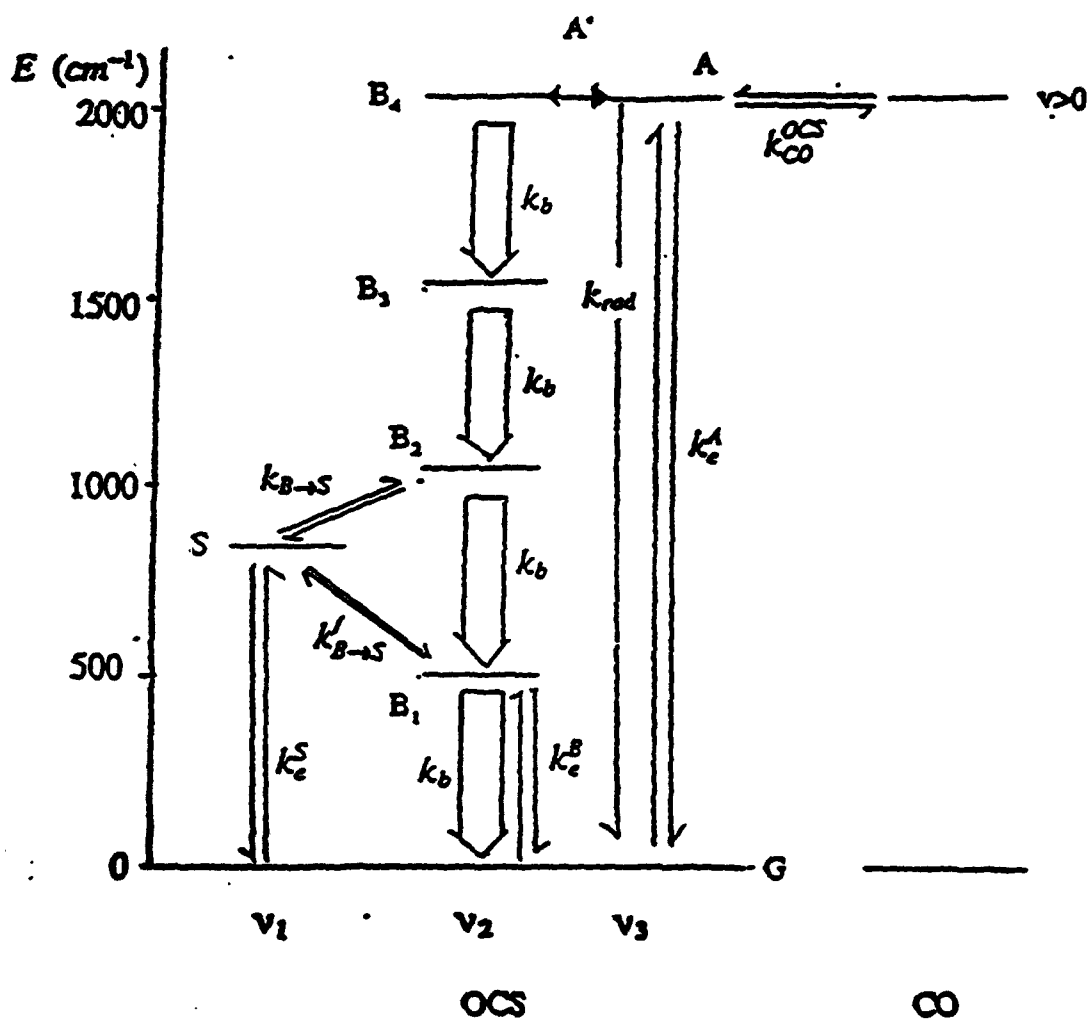


Fig. 8.18. Schematic of the pathways included in the code for the case of discharge and V-V transfer from CO.

Using the rates given in the literature, a simple kinetic model of the low lying vibrational states of carbonyl sulfide has been developed. The model describes the ground state, the lowest four states in the bending mode and the two projected laser levels, the first excited states of the symmetric and the asymmetric stretch mode. Equations (4.1) to (4.8) give the differential equations describing the time development of the populations for the different states as functions of the total number of OCS molecules. Fig. 8.18 shows the states and transitions included in the model:

$$\frac{dA}{dt} = \{k_{CO}^{OCS} N_{CO} + k_{N_2}^{OCS} N_{N_2} + k_e^A N_e\} G - \{k_{e,rev}^A N_e + k_{rad} + \sum_{i=1}^4 k_{A \rightarrow B}^i N_i\} A - \{k_{OCS}^{CO} N_{CO}' + k_{OCS}^{N_2} N_{N_2}'\} A + k_{B \rightarrow A} N_1 B_4 \quad (4.1)$$

The asymmetric stretch state (001) fractional population (A) is populated by excitation from the ground state(000) (G) by V-V energy transfer from vibrationally excited carbon monoxide molecules, described by the term  $k_{CO}^{OCS} N_{CO} G$ . On this term, the first factor is the rate, the second factor is the partial pressure of vibrationally excited CO molecules. Similar excitation occurs by vibrationally excited nitrogen molecules, the  $k_{N_2}^{OCS} N_{N_2} G$  term. The third term describes the excitation by electron collisions. The fourth term,  $k_{e,rev}^A N_e A$ , models the reverse process of the third, the deactivation of A by electron collisions. The loss due to spontaneous radiative decay is given by the fifth term. The sum in the sixth term describes the energy transfer to the (040) states ( $B_4$ ) due to collisions with the four different molecules present in the laser medium, i.e., carbonyl sulfide, carbon monoxide, nitrogen and helium. The two loss terms represent the

transfer of vibrational quanta to CO and nitrogen. The last term describes the transfer from the (040) states to the A state, using the abbreviation  $k_{B \rightarrow A} N_t$ . Here  $N_t$  stands for the total number of molecules in the mixture:

$$\frac{dB_4}{dt} = -k_b N_{OCS} B_4 + \sum_{i=1}^4 k_{A \rightarrow B}^i N_i A - k_{B \rightarrow A} N_t B_4 \quad (4.2)$$

Equation (4.2) models the behavior of the (040) states ( $B_4$ ). In addition to the terms already appearing in (4.1), this state is depopulated by relaxation into the third state of the bending mode. This is described by the term  $k_b N_{OCS} B_4$  where  $k_b$  describes the relaxation rate of the bending mode and  $N_{OCS}$  is the OCS partial pressure

$$\frac{dB_3}{dt} = k_b N_{OCS} B_4 - k_b N_{OCS} B_3 \quad (4.3)$$

The third state of the bending mode (03<sup>1</sup>0)  $B_3$  is populated by relaxation from  $B_4$  and depopulated by relaxation to  $B_2$ :

$$\frac{dB_3}{dt} = k_b N_{OCS} B_4 - k_b N_{OCS} B_3 - k_{B \rightarrow S} N_{OCS} G B_3 + k_{S \rightarrow B} N_{OCS} G S \quad (4.4)$$

The (02<sup>0</sup>) states  $B_2$  have in addition to the mechanisms similar to the ones in the third state of the bending mode a coupling to the symmetric stretch mode (S). This is given by the last two terms in equation (4.4) which describe the forward and the reverse processes:

$$\frac{dB_1}{dt} = k_b N_{OCS} B_2 - k_b N_{OCS} B_1 + k_e^b N_e G - k_{e,rev}^b N_e B_1 \quad (4.5)$$

The lowest state in the bending mode  $B_1$  once again undergoes the two typical processes for the bending mode. In addition to these processes electron excitation from the ground state is also possible as well as the reverse process

$$\frac{dS}{dt} = k_{B \rightarrow S} N_{OCS} G B_2 + k_e^S N_e G - k_{S \rightarrow B} N_{OCS} G S - k_{rad}^S S - k_{VT}^S N_i S - k_{e,rev}^S N_e S \quad (4.6)$$

The symmetric stretch state is populated by V-V processes from the second state of the bending mode as well as by electron excitation from the ground state. Depopulating mechanisms are the reverse process to the V-V coupling term in (4.4), spontaneous radiative decay and V-T relaxation to the ground state. Also there is relaxation induced by electron collision as described by the last term

$$\begin{aligned} \frac{dG}{dt} = & -G(k_e^A + k_e^S + k_e^B)N_e - \{k_{CO}^{OCS} N_{CO} - k_{N_2}^{OCS} N_{N_2}\}G + k_b N_{OCS} B_1 + k_{rad}^S S + \\ & + k_{VT}^S N_i S + \{k_{CO}^{CO} N_{CO}' + k_{N_2}^{N_2} N_{N_2}' + k_{rad}\}A \end{aligned} \quad (4.7)$$

The ground state  $G$  finally shows the reverse rates to all the rates connecting it to the other states that have been discussed above.

The conservation of particles demands:

$$G + A + S + B_1 + B_2 + B_3 + B_4 = 1 \quad (4.8)$$

Additional processes that are not included in the model are, for example, various coupling processes between the asymmetric stretch mode and the (12<sup>0</sup>) and (200) states as well as the coupling of the (200) state to the (04<sup>0</sup>) states. But these processes are characterized by fairly large energy mismatches so that they are probably less likely than the included ones. In any case there are no data available for these processes. More important is the neglect of the excitation of higher molecular energy states by electrons. No data are available for such processes, so electronic excitations had to be restricted to the lowest states of each vibrational mode. The neglect of processes involving any states above the (040) states also is a major simplification that can only be justified as an approximation. Finally interaction of particles with the walls is not included in the calculations. Nevertheless, this simple model gives some insight into the internal processes in the carbonyl sulfide molecule, as it includes the dominant paths among the lower states.

The above equations were solved using the fact that the time derivatives vanish for the steady-state case. Solving the remaining homogeneous set of linear equations gave the following populations for the excited levels in terms of the ground state population:

$$B_4 = \frac{G(k_{CO}^{OCS} N_{CO} + k_{N_2}^{OCS} N_{N_2}) \sum_{i=1}^4 k_{A \rightarrow B}^i N_i}{k_{A \rightarrow M} N + k_{rel} + \sum_{i=1}^4 k_{A \rightarrow B}^i N_i + k_{CO}^{CO} N_{CO}^{N_2} + k_{OCS}^{N_2} N_{N_2}} * \\ * [k_b N_{OCS} + k_{B \rightarrow M} N_i - \frac{k_{B \rightarrow M} N_i \sum_{i=1}^4 k_{A \rightarrow B}^i N_i}{k_{A \rightarrow M} N + k_{rel} + \sum_{i=1}^4 k_{A \rightarrow B}^i N_i + k_{CO}^{CO} N_{CO}^{N_2} + k_{OCS}^{N_2} N_{N_2}}] \quad (4.9)$$



$$B_3 = B_4 \quad (4.10)$$

$$B_2 = G \frac{k_4 N_{OCS} B_4 / G + k_2^2 N_e k_{2 \rightarrow 3} N_{OCS} / (k_{2 \rightarrow 3} N_{OCS} + k_{rad}^2 + k_{VT}^2 N_{OCS} + k_{r-m}^2 N_e)}{k_{2 \rightarrow 3} N_{OCS} + k_2 N_{OCS} - k_{2 \rightarrow 3} k_{2 \rightarrow 2} N_{OCS}^2 / (k_{2 \rightarrow 3} N_{OCS} + k_{rad}^2 + k_{VT}^2 N_{OCS} + k_{r-m}^2 N_e)} \quad (4.11)$$

$$B_1 = B_2 + \frac{k_{r-m}^2 N_e}{k_2 N_{OCS} + k_{r-m}^2 N_e} G \quad (4.12)$$

$$A = \frac{k_{CO}^{OCS} N_{CO} + k_{N_2}^{OCS} N_{N_2} + k_e^A N_e + k_{B \rightarrow A} N_{OCS} B_4 / G}{k_{r-m} N_e + k_{rad} + \sum_{i=1}^4 k_{A \rightarrow i}^i N_i + k_{CO}^{CO} N_{CO}' + k_{OCS}^{N_2} N_{N_2}'} G \quad (4.13)$$

$$S = \frac{k_{2 \rightarrow 3} N_{OCS} B_2 / G + k_2^2 N_e}{k_{2 \rightarrow 3} N_{OCS} + k_{rad}^2 + k_{VT}^2 N_{OCS} + k_{r-m}^2 N_e} G \quad (4.14)$$

A problem occurs since not all the rates needed in this model have been measured. Still, it is possible to obtain some insight with the measured rates and other estimations. The following is a short discussion of the values used and their importance:

All the known rates have been measured at room temperature and no temperature dependence is available for any rate.

$k_{CO}^{OCS} = 257 * 10^3 s^{-1} torr^{-1}$  / Hancock 74/ This very fast rate describes the dominant process for the population of the A level.

$k_e^A N_e = 25.7 * 10^3 s^{-1} torr^{-1}$ . This rate was obtained in a more complicated way out of Sohn's result (Table 8.2) and the assumption that the electrons show a Maxwellian velocity distribution. Detailed theory and measurement show that the actual electron velocity distribution departs from Maxwellian because the electrons are interacting with the gases

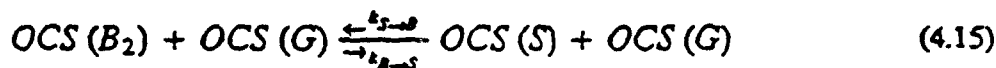
and are preferentially losing energy at certain velocities / Nighan 72 /. On the other hand Sohn only gives cross sections at selected energies and the average kinetic energy is only approximately known as discussed above. Therefore, the inclusion of the refinement of more accurate electron energy distributions is unrealistic. The overall cross section for exciting the different states was computed from the velocity distribution and the energy-resolved cross section with the total electron density determined from the current and the tube dimensions giving informations about the total electron density. The absolute value of this rate is not as important as the comparison with the electron excitation rates for the two other low lying states.

$k_{\text{exc}}^S N_e = 9 \cdot 10^3 \text{ s}^{-1} \text{ torr}^{-1}$  and  $k_{\text{exc}}^B N_e = 50.4 \cdot 10^3 \text{ s}^{-1} \text{ torr}^{-1}$ . The reverse rates were calculated by the demand for a detailed balance with an electron temperature given by the mean electron kinetic energy of  $1.28 \text{ eV} = 14848 \text{ K}$ .

$k_{\text{rad}} = 322 \text{ s}^{-1}$ . This is the inverse of the spontaneous lifetime given in Section 8.1. The bending mode relaxes with the already quoted overall bending relaxation rate constant  $k_b = (800 \pm 400) \cdot 10^3 \text{ s}^{-1} \text{ torr}^{-1}$  / Zittel 88 /. Once again this rate is just an overall rate including V-T/R and V-V processes in the bending mode. It has also been only measured in pure OCS. The influence of other gases on this rate is not known. Since the bending relaxation is in part a two-body process and it depends on the amount of OCS in the bending modes as far as the V-V part of this overall rate is concerned, there is considerable uncertainty in this rate. Therefore, we multiply this rate by the OCS partial pressure, because one can assume that the major fraction of the OCS molecules

remains in the ground state. In the numerical modeling these uncertainties must be investigated also.

The filling of the S state by the B<sub>2</sub> state is described by  $k_{S \rightarrow B_2} = 225 \text{ s}^{-1} \text{ torr}^{-1}$  for OCS as a collision partner. Helium gives a rate of  $108 \text{ s}^{-1} \text{ torr}^{-1}$ . The reverse rate is determined by the detailed balance requirement / Mandich 80 - 2/. This rate actually describes a two-body process:



In order to keep the equations linear, I make the assumption, which is justified by the calculations, that most of the OCS population remains in the ground state. Also one has to test the possibility that the OCS(G) molecule can be replaced by another collision partner. No rates are known except for the ones mentioned above with helium as collision partner.

I neglect the other possible relaxation channels, e.g. a possible coupling of the S and B<sub>1</sub> state, in this first model as well as the very slow radiative decay of the S state, which is described by  $k_{rad} = 0.83 \text{ s}^{-1}$  /after Maki & Wells 91 /.

The S state is coupled to the ground state by electron induced collisions only.

The most critical points are the rates of exchange between the A and the B<sub>4</sub> states. Here only net rates are measured (see Table 8.4). Since in the final formula describing the population of the A state the ratio, and not the difference between the forward and the reverse rates is used, further adjustments of the model have to be made.

There are two equations describing these two rates: The first one is the detailed balance requirement:

$$k_{A \rightarrow B}/k_{B \rightarrow A} = e^{-\frac{\Delta E}{kT}} = 0.82 \quad (4.16)$$

The result is given for room temperature. The second equation is the known difference between the forward and reverse rates:

$$\{k_{A \rightarrow B}A - k_{B \rightarrow A}B_4\}N_{OCS} = K_{overall} \quad (4.17)$$

The rate  $K_{overall}$  consists of a sum of the measured rates for the different collision partners times their partial pressures in the gas mixture. With these two equations it is possible to determine the two desired rates, which will depend on the gas mixture used if A and  $B_4$  are known. But A and  $B_4$  depend on these rates. So an iteration process had to be used. The model was calculated as described above with some input parameters fulfilling equation (4.16). Then the relative populations A and  $B_4$  were calculated with the complete model; with these values the two rates were recalculated according to (4.16) and (4.17). These new rates were used as the next input to the code.

This iteration process gave the following results:

First, the exchange of energy between the asymmetric stretch mode and the fourfold excited bending mode is very fast. Actually with this calculation no convergence could be noted.

The more important result is that the ratio of the populations of the asymmetric stretch mode and the (040) states is governed by the Boltzmann factor:

$$B_4/A = e^{-\frac{\Delta E}{kT}} = 0.82 \quad (4.18)$$

This conclusion results in a modification to the code. The A and B<sub>1</sub> states will be treated as one single state A' consisting of 55 % A and 45 % B<sub>1</sub>. Since the rate with which both "sub states" transfer energy to other states is by far slower than the internal transfer inside the new A' state, the ratio (4.18) will be obeyed at all times.

The modified model also includes a weak coupling of the B<sub>1</sub> and the S state which is discussed by Mandich / Mandich 80-2 /. This coupling is mainly introduced by helium, but other gases like carbonyl sulfide can also cause it. The rates for the transfer from the S to the B<sub>1</sub> state are given to be 29 s<sup>-1</sup> torr<sup>-1</sup> for OCS and 47 s<sup>-1</sup> torr<sup>-1</sup> for He. The reverse rate is determined by detailed balance.

The modified code incorporates the simplifications discussed above. It is described by the following equations:

$$\frac{dA'}{dt} = \{k_{CO}^{OCS} N_{CO} + k_{N_2}^{OCS} N_{N_2} + k_e^A N_e\} G - 0.55 \{k_{rad}^A + k_{e,rev}^A N_e + k_{OCS}^{CO} N_{CO}' + k_{OCS}^{N_2} N_{N_2}'\} A' - 0.45 k_b N_{OCS} A' \quad (4.19)$$

$$\frac{dB_3}{dt} = 0.45 k_b N_{OCS} A' - k_b N_{OCS} B_3 \quad (4.20)$$

$$\frac{dB_2}{dt} = k_b N_{OCS} B_3 - k_b N_{OCS} B_2 - k_{B \rightarrow S} N_{OCS} B_2 + k_{S \rightarrow B} N_{OCS} S \quad (4.21)$$

$$\frac{dB_1}{dt} = k_b N_{OCS} B_2 - k_b N_{OCS} B_1 + k_e^B N_e G - k_{e,rev}^B N_e B_1 + k_{S \rightarrow B}' N_i S - k_{B \rightarrow S}' N_i B_1 \quad (4.22)$$

$$\frac{dS}{dt} = k_{B \rightarrow S} N_{OCS} B_2 + k_e^S N_e G - k_{S \rightarrow B} N_{OCS} S - k_{e,rev}^S N_e S + k_{B \rightarrow S}' N_i B_1 - k_{S \rightarrow B}' N_i S \quad (4.23)$$

$$\frac{dG}{dt} = -\{k_{CO}^{OCS} N_{CO} + k_{N_2}^{OCS} N_{N_2} + [k_e^A + k_e^S + k_e^b] N_e\} G + .55\{k_{rad} + k_{e,rev}^A\} A' + \{k_{e,rev}^B N_e + k_b N_{OCS}\} B_1 + k_{e,rev}^S S \quad (4.24)$$

Also, equation (4.8) holds.

Solving the above equations yielded for the individual excited-state populations in terms of the ground state population:

$$A' = \frac{k_{CO}^{OCS} N_{CO} + k_{N_2}^{OCS} N_{N_2} + k_e^A N_e}{0.55\{k_{rad} + k_{e,rev}^A N_e + k_{CO}^{OCS} N_{CO}' + k_{N_2}^{OCS} N_{N_2}'\} + 0.45 k_b N_{OCS}} G \quad (4.25)$$

$$A = 0.55 A' \quad (4.26)$$

$$B_4 = 0.45 A' \quad (4.27)$$

$$B_3 = B_4 \quad (4.28)$$

$$S = \frac{k_e^B N_e + k_b k_{B \rightarrow S} N_{OCS} B_3 / (k_b + k_{B \rightarrow S}) G + k_{B \rightarrow S}' N_{OCS} (k_e^B N_e + \frac{k_b^2 N_{OCS}^2}{(k_b + k_{B \rightarrow S})^2}) / (k_{B \rightarrow S}' N_{OCS} + k_{e,rev}^B N_e + k_b N_{OCS})}{(k_{S \rightarrow B} N_{OCS} (\frac{k_b}{k_b + k_{B \rightarrow S}}) + k_{S \rightarrow B}' \times k_b N_{OCS} + k_{e,rev}^B N_e) / (k_b N_{OCS} + k_{e,rev}^B N_e + k_{B \rightarrow S}' N_{OCS}) + k_{e,rev}^S N_e} G \quad (4.29)$$

$$B_2 = \frac{1}{k_b + k_{B \rightarrow S}} (k_b B_3 + k_{S \rightarrow B} S) \quad (4.30)$$

$$B_1 = \frac{(k_{2-3} + k_3 k_{2-3} N_{OCS} / (k_3 + k_{2-3})) S / G + k_2^2 N_0 + k_2^2 N_{OCS} K (k_3 + k_{2-3}) B_3 / G}{k_3 N_{OCS} + k_{2-3} N_0 + k_{2-3} N_{OCS}} G \quad (4.31)$$

Using the preceding model results, calculations for different means of excitation are discussed:

- Excitation in pure OCS in a discharge.

The excitation of pure OCS in a discharge has been modeled by neglecting all terms describing interactions between OCS molecules and other types of molecules such as helium and carbon monoxide. Therefore, this run of the code does not include any

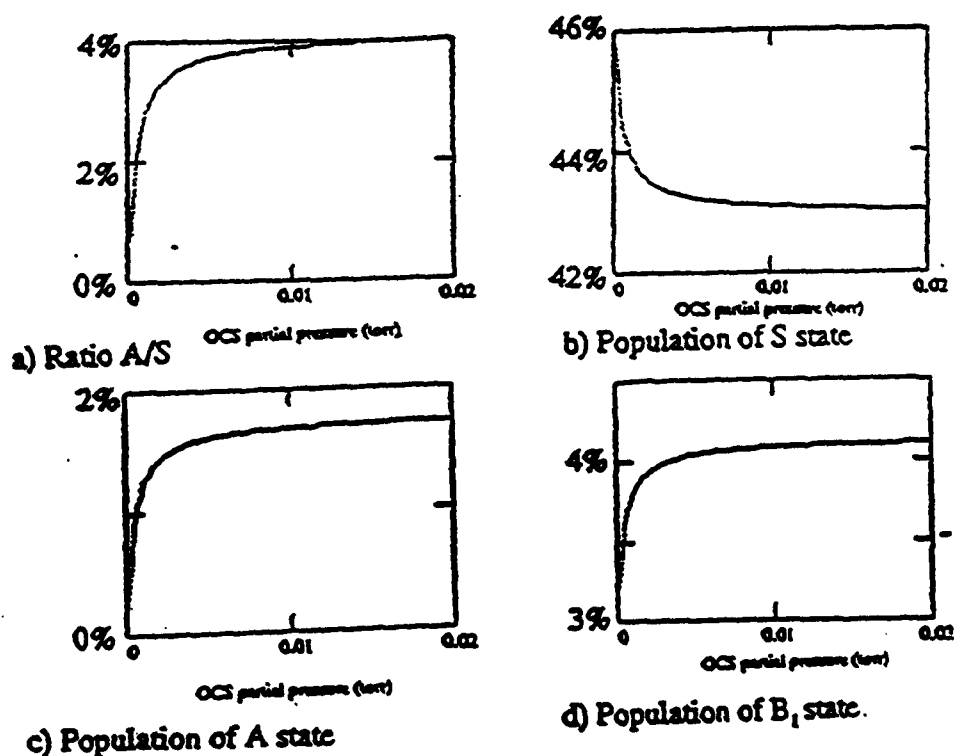


Fig. 8.19. Pure OCS discharge. Populations in % of the total OCS population.

pumping due to V-V transfer from CO. Fig. 8.19 shows some of the results. The first result is that there is no population inversion in OCS due to electron excitation. As a matter of fact the population of the S state is more than 20 times higher than that of the A state. There are several reasons for this. At first the rate for deactivation of the A state due to electron collision is higher than that for the two other states coupled to the ground state by the electron interaction because of the higher gap in energy. The second reason is that both the A and B<sub>1</sub> state are depleted due to the fast relaxation in the bending mode. The S state, on the other hand, is just weakly coupled to the bending mode and thus reaches the highest steady state population of the excited states. Fig. 8.19 gives the percentage of OCS molecules in the A, S and B<sub>1</sub> states as well as the ratio A/S.

- Excitation in pure OCS by optical pumping

The next situation under investigation is pure OCS that is optically pumped. Fig. 8.20 shows the population of the key states and the A/S rate, plotted against OCS partial pressure. No population inversion is predicted for this case also. However, the ratio of A/S is more favorable here than in the discharge case discussed above. It reaches values up to 40 % and is independent of the intensity of the pumping radiation. This can be readily explained because intensity of the pumping radiation only determines the population of the A state directly. Then the energy will redistribute inside the molecule. But all these redistributions are determined only by ratios of rates, not by the total amount of energy available. Once again the S state is the excited state with the highest population, because of the way it is coupled to the bending mode: About 90 % of this



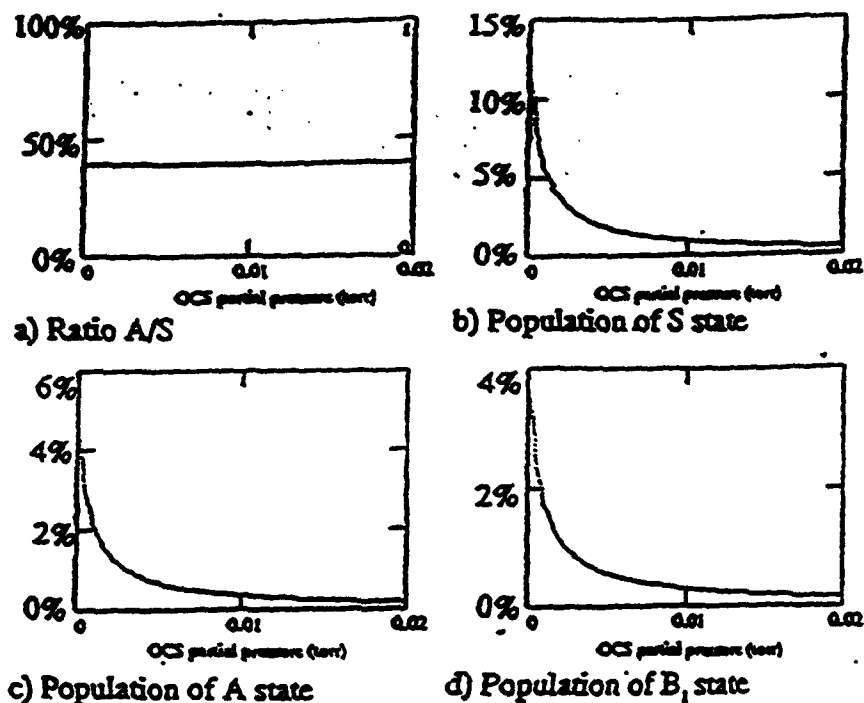


Fig. 8.20. OCS optically pumped. Populations in % of the total OCS population.

coupling in OCS is to the  $B_2$  level, the rest to the  $B_1$  level. So in a first approximation the S and the  $B_2$  state get into an equilibrium that favours the S population because this state has the lower energy. But the  $B_2$  state has almost the same population as the  $B_4$  state because all the energy relaxing through the bending mode also has to pass this state. The  $B_4$  state on the other hand contains 82 % the population of the A state. Therefore, the S state will obtain a higher steady-state population than the A state. Thus, no inversion occurs. The weaker coupling to the  $B_1$  state then lowers this difference because the S state has a higher energy than the  $B_1$  state. This change is not strong enough to change the overall picture, however.

To summarize, one can say that the energy entering the molecule in the A state gets lost in rapid decay through the bending mode. But since the bending mode is coupled to the S state this state will be populated also. Due to the nature of this interaction the S state will obtain a higher population than the B states and thus than the A state. These processes

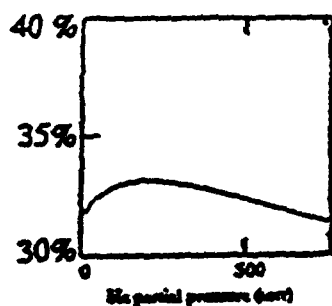
are independent of both the intensity of the pump radiation as well as the OCS concentration.

Since the coupling of the S

state with the B<sub>1</sub> state

increases in the presence of

Fig. 8.21. Ratio A/S depending on the He partial pressure. OCS optically pumped.



helium, as Mandich points out / Mandich 80-2 /, the influence of helium has been investigated also. Fig. 8.21 shows that helium tends even to decrease the ratio A/S. The reason for that is that He also increases the coupling to B<sub>2</sub> state.

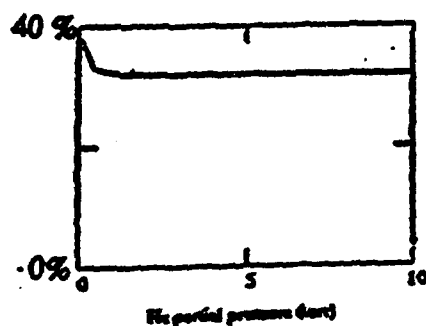


Fig. 8.22. Ratio A/S depending on the He partial pressure. OCS excitation by CO V-V transfer.

- Excitation by V-V energy transfer from CO

The next situation under investigation is the pumping of OCS by vibrationally

excited CO. The CO

excitation might be due to

optical pumping with a CO laser. For the code this case only differs from the direct optical pumping by the influence of the CO molecules on the rates connecting the different OCS levels. In this case the relative population of the states in consideration does not depend on the partial pressure of OCS. No inversion could be observed. For the case of 5.5 torr of helium and 0.1 torr of CO (10 % of which are vibrationally excited), the relative populations for the A, S, B<sub>1</sub> states are 5.5, 18, 4.5 %, respectively. The dependence of the ratio A/S is shown in Fig. 8.22 for varying He partial pressure and in

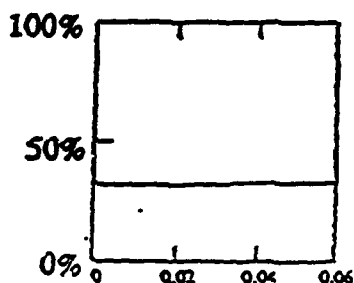


Fig. 8.23. Ratio A/S depending on the partial pressure of vibrationally excited CO (torr)

Fig. 8.23 for varying CO partial pressure.

- Excitation in an OCS - CO - N<sub>2</sub> - He mixture in a discharge

This is the actual situation occurring during the experiments performed. The calculations once again do not show a population inversion. The ratio A/S is displayed in Fig. 8.24 depending on the partial pressures of helium, carbon monoxide and carbonyl sulfide. The influence of the OCS partial pressure on different key states is shown in Fig. 8.25.

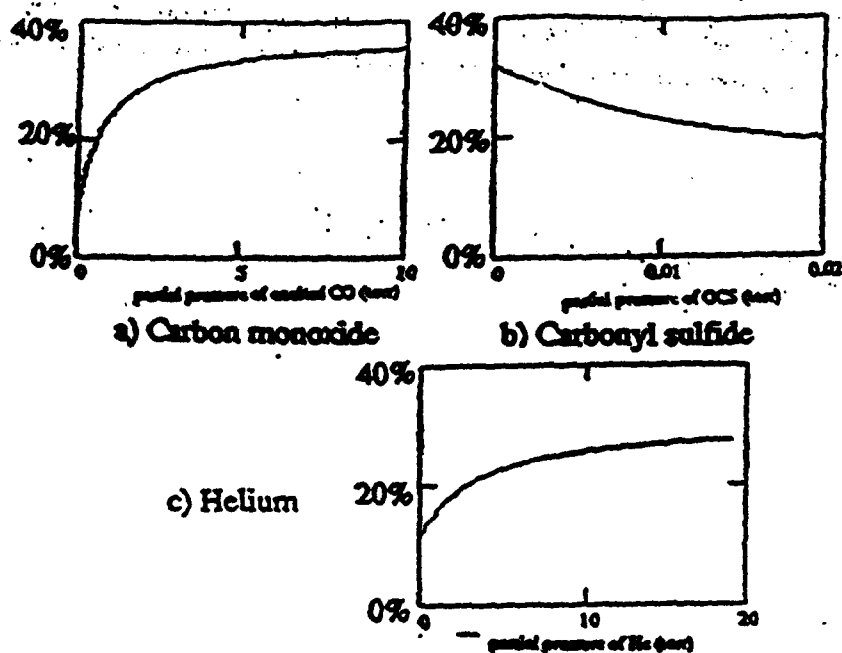


Fig. 8.24. Ratio A/S depending on the different gases in the experimental situation.

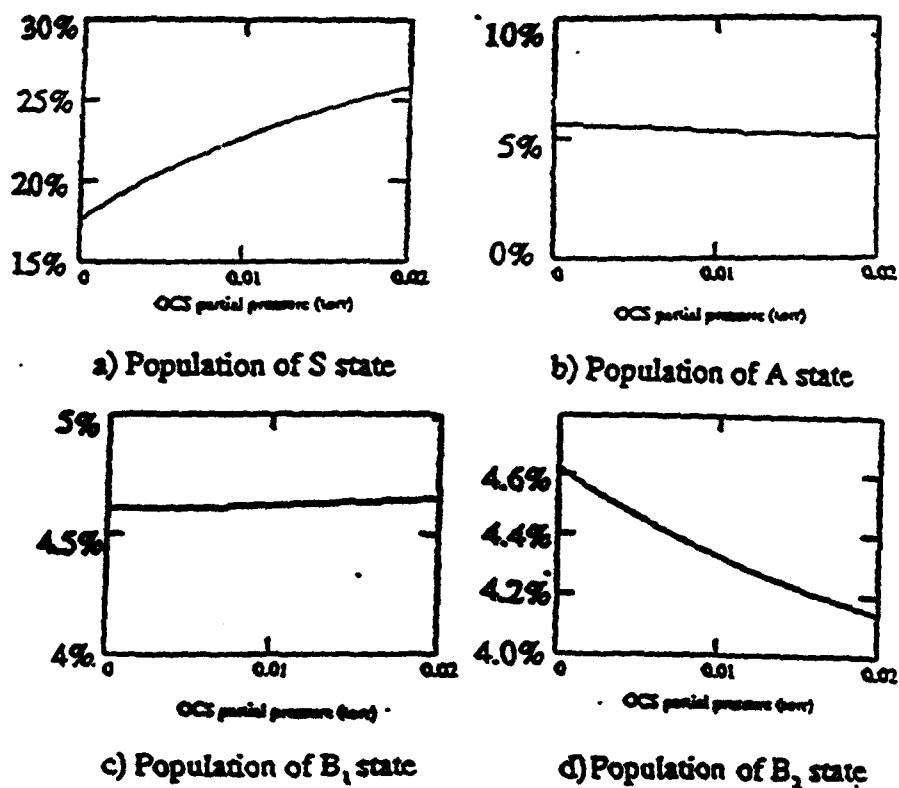
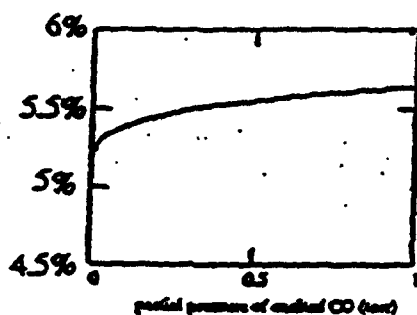
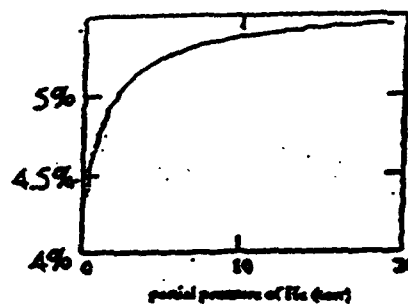


Fig. 8.25. Experimental situation. Populations in % of the total OCS population.



a) Carbon monoxide



b) Helium

Fig. 8.26. Relative A state population depending on the different gases in the experin situation.

Fig. 8.25 b) illustrates the population of the A state dependence on the OCS partial pressure. These figures can be compared directly with the experimental results. They show, at least qualitatively, the same behavior. As shown in Fig. 8.10 the relative population of the A state decreases with increasing OCS partial pressure. But the experimental decay is a lot faster than the calculated one. In the experiment the OCS depleted the CO reservoir which is shown to be the major source of A state excitation. In the calculation the CO excitation is fixed at 10 % of the also fixed CO partial pressure.

One should, therefore, take a look at the A state population depending on the CO available. Fig. 8.26 a) shows a sharp drop in the A state population with decreasing CO content. The calculations, therefore, seem to be in qualitative agreement with the experiment in this case. The influence on the CO partial pressure is not in agreement with the measured dependence on the CO partial pressure. The reason for this is probably the fact that in the calculations a fixed 10 % of the CO is excited and able to transfer energy to OCS. In the experimental situation, however, though the factor that

excite CO, namely current and nitrogen partial pressure, remain the same. Probably the fraction of CO being vibrationally excited decreases and so the total excitation of OCS decreases also, as discussed earlier.

The influence of the helium partial pressure as given in figure 16 can be compared with Fig. 8.26 b). The initial rise of the OCS A state is also observed in the experiment. But at higher pressure the model predicts a saturation while the experiments indicate a slight decay. The reason for this might be the influence of the helium on the vibrational distribution in carbon monoxide as well as on the electron energy distribution function. Such dependence on processes external to the OCS molecule is only included in the code as outside parameters. The experimental evidence for a decay is fairly weak. One can conclude that the model reproduces the most important feature of the influence of the helium on the A state population.

#### -Limitations of the model

There are two classes of weak points in the model. The first class consists of inaccurate measured rates, experimental uncertainties in rates or unknown rates. The most important uncertainty in this direction is the influence of the CO on the intramolecular rates of OCS. The model just assumes this to be the same as that of OCS itself. The same had to be done with nitrogen since no rates for OCS and nitrogen have been measured at all. But still a variation of this influence did not change the qualitative results of the code unless there would be a very substantial difference between the rates for different OCS-OCS transitions. A population inversion could just be achieved if there would be a

... faster rate connecting the S state with the B<sub>1</sub> than with the B<sub>2</sub> state. But this is not even true in the case of helium and there is no evidence such as a resonance between CO or N<sub>2</sub> with this transition.

The second class of weak points consists of ignoring interactions. For example, there are just seven states included in the model although there are reasons and evidence that more states are populated in OCS. The first state neglected is the second vibration in the symmetric stretch mode, but there are several other states, such as (120), that could be included also. The interaction of the electrons with higher levels is also neglected although these interactions have been measured in part / Sohn 87 /, and the observation of visible radiation from OCS proves their existence. But once again no sufficient data are available and the amount of OCS in higher states can probably be neglected. Also, most of the excitation would end up in the lower levels of the bending mode and, therefore, not improve the situation for a population inversion.

The next parameter which was ignored was the temperature. It was fixed to 295 K in the calculations. A temperature dependence has not been measured for any of the rates. Still, it is fairly unlikely that a change in temperature would give a population inversion, because the detailed balance requirement would favor the S state over the A state at every temperature. Once again it would make a difference if helium would increase the S to B<sub>1</sub> coupling at lower temperature. But this is also unlikely because this transition requires a fairly large amount of energy. Also, the experiments did not show a significant influence of the temperature on the A state population.

#### - Pulsed lasing in OCS

Although no time dependent calculations have been made, one can explain pulsed laser action in OCS with the measured rates. As seen before there exist several methods to populate the A state of OCS with a higher rate than the S state. These methods include optical pumping, V-V energy transfer and electron excitation. At very short times after populating the A state by one of these methods in a pulsed mode, the S state will not be populated at all or, in the case of electron excitation, populated much less than the A state. A population inversion can clearly be obtained. But as the A state relaxes through the bending mode, the S state will slowly fill up until equilibrium with the bending mode is reached. In the course of this relaxation the population inversion will vanish. So the OCS molecular laser appears to be a typical candidate for a pulsed laser.

#### - Comparison to CO<sub>2</sub>

In carbon dioxide the situation is very different. Here the S state is coupled strongly to the fast relaxing bending mode in Fermi resonance. The A state, on the other hand, is not coupled to the bending mode at all. Therefore, the situation is much better. The upper state has a relatively long lifetime while the lower laser level is coupled to the fastest relaxing mode in the molecule. This configuration guarantees the superior performance of the CO<sub>2</sub> laser.

#### - Conclusion

The model calculation seems to be in qualitative agreement with the experimental results and gives some insight in the intramolecular energy transfer mechanisms in carbonyl



sulfide. Various ways of excitation have been modeled and in no case could a population inversion be modeled.

This is explained by the strong coupling of the asymmetric stretch state to the bending mode which has the fastest overall relaxation rate by some orders of magnitude. The conclusion is that near-equilibrium exists among the four lowest levels in the bending mode and the asymmetric stretch state. The symmetric stretch state is coupled weakly to the second bending mode and therefore becomes populated, too. Due to the equilibration process between the latter two states the symmetric stretch obtains a higher population than the asymmetric stretch mode. Therefore no population inversion can be achieved in the steady-state regime.

These conclusions are not totally definitive. We cannot say that no OCS cw laser will ever be possible, since the code has several limitations. But one can certainly say that an OCS cw laser is very unlikely to exist.

### 8.5. CONCLUSION AND RECOMMENDATIONS

The energy transfer processes in carbonyl sulfide have been investigated both experimentally and with a kinetic model. A resonator has been set up to achieve amplification of the (001) to (100) transition in OCS. The theoretical as well as the experimental results suggest that no population inversion can be obtained. The reason for this is the fast energy transfer out of the asymmetric stretch mode through the bending mode. The coupling of the second level in the bending mode with the first level in the symmetric stretch mode results in a high population of the latter level. Therefore no population inversion can be achieved in the steady-state regime.

Still it would be interesting to do further experiments to obtain additional rates to improve the model. The coupling of the symmetric stretch mode with the bending mode in collisions with CO and N<sub>2</sub> has not been investigated yet. Also, the code introduces the possibility of a population inversion in OCS on another transition. In case of a very fast optical or V-V pumping of the asymmetric stretch mode with a rate comparable to the relaxation rate of the bending mode, the four lowest levels in the bending mode, the ground state and the (001) state could equilibrate. Then a population inversion of the

symmetric stretch level with the ground state would be achieved. Further investigations in this direction might be interesting.

## REFERENCES

- Barker 80** W. Barker and A.L. Mossman, Matheson Gas Data Book , Secaucus,NJ, 1980.
- Brueck 78** S.R.J. Brueck, Vibrational energy relaxation and exchange in liquid nitrogen - carbon monoxide - carbonyl sulfide mixtures , J. Chem. Phys., Vol. 68, No. 11, p. 4911, 1978.
- Clark & De Lucia 80** W.W. Clark, III and F.C. De Lucia, A spectroscopic investigation of the OCS discharge system , J. Chem. Phys., Vol. 74, No. 6, 1981.
- Dax 88** A. Dax, Aufbau eines Lamb-Dip-stabilisierten CO<sub>2</sub>-Lasers , Diplomarbeit, Institut fuer Angewandte Physik, Bonn, 1988.
- Deutsch 66** T.F. Deutsch, OCS molecular laser , Applied Physics Letters, Vol. 8, No.12, p.334, 1966.
- EG&G 91** EG&G Judson, manual, 1991.
- George 90** T. George, Entwicklung und Stabilisierung eines CO-Fundamentalbandenlasers , Diplomarbeit, Institut fuer Angewandte Physik, Bonn, 1990.

- Hancock 71** G. Hancock and I.W.M. Smith, Quenching of Infrared Chemiluminescence. 1. The Rates of De-Excitation of CO ( $4 \leq v \leq 13$ ) by He, CO, NO, N<sub>2</sub>, O<sub>2</sub>, OCS, N<sub>2</sub>O and CO<sub>2</sub>, Applied Optics, Vol. 10, No. 8, p. 1827, 1971.
- Hancock 74** J.K. Hancock et al., Measurement of the rate of excitation and deactivation of OCS(001), N<sub>2</sub>O(001), CS<sub>2</sub>(001) and C<sub>2</sub>N<sub>2</sub>(00100) using laser excited CO as a pumping source, J. Chem. Physics, Vol. 61, No. 8, p. 3017, 1974.
- Itikawa 70** Y. Itikawa, J. Phys. Soc. Japan, Vol. 28, p.1062, 1970, as quoted in Sohn 86.
- Janos 89** Janos Technology Inc., Precision Optics and Components, Townshend, Vermont, 1989.
- Kildal & Deutsch 75** H. Kildal and T.F. Deutsch, Optically pumped infrared V-V transfer lasers, Applied Physics Letters, Vol. 27, No. 9, p.500, 1975.
- Kneubuehl & Sigrist 89** F.K. Kneubuehl and M.W. Sigrist, Laser, 2. ueberarb. u. erw. Aufl., Stuttgart, Teubner, 1989.
- Landau 36** L.D. Landau and E. Teller, Zur Theorie der Schalldispersion, Physik. Z. Sovjetunion, Vol.10, p.34, 1936.
- Lev-On 72** M. Lev-On et al. Vibrational Energy Transfer between CO and COS: A Test of the Harmonic Oscillator Model, J. Chem. Phys. Vol. 37, No. 8, p.3575, 1972.
- Maki & Wells 91** A.G. Maki and J.S. Wells, Wavenumber Calibration Tables From Heterodyne Frequency Measurements, National Institute of Standards and Technology, Special Publication 821, Dec. 1991.

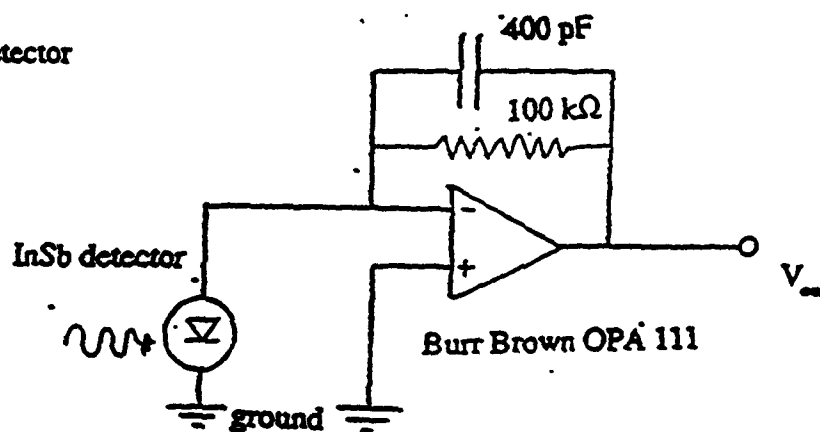
- |                            |  |
|----------------------------|--|
| Mandich 80-1               | M.L. Mandich and G.W. Flynn, Vibrational energy map for OCS , J. Chem. Phys. 73 (3), p.1265, 1980.   |
| Mandich 80-2               | M.L. Mandich and G.W. Flynn, Collisional relaxation of vibrationally excited OCS in rare gas mixtures , J. Chem. Phys., 73(8), p.3679, 1980.                                 |
| Nighan 72                  | W.L. Nighan, Electron Kinetic Processes in CO Lasers , Appl. Phys. Lett., Vol.20, No.2, p.96, 1972.  |
| Rich 82                    | J.W. Rich, Relaxation of Molecules Exchanging Vibrational Energy , in Applied Atomic Collision Physics, Vol. 3, p.99, 1982.  |
| Saupe 92                   | S. Saupe, private communication  |
| Schlossberg & Fetterman 74 | H.R. Schlossberg and H.R. Fetterman, Optically pumped vibrational transition laser in OCS , Applied Physics Letters, Vol. 26, No. 6, 1975, p.316.                            |
| Schneider 90               | M. Schneider et al., Heterodyne Frequency Measurements of $^{12}\text{C}^{16}\text{O}$ Laser Transitions near $2050\text{ cm}^{-1}$ , J. Mol. Spectrosc. Vol.139, Feb. 1990. |
| Siegman 76                 | A.E. Siegman, Lasers , University Science Books, Mill Valley, Ca., 1976.   |
| Sohn 86                    | W. Sohn et al., Low-energy electron impact of OCS and $\text{CS}_2$ , J. Phys. B: At. Mol. Phys, 20 (1987) 3217 - 3236.  |

- Townes & Schawlow 55      C.H. Townes and A.L. Schawlow, *Microwave Spectroscopy*, Dover Publications, Inc., New York first published in 1955 by McGraw-Hill Book Co, Inc.
- Treanor 68      C.E. Treanor et al., *Vibrational Relaxation of Anharmonic Oscillators with Exchange-Dominated Collisions*, J. Chem. Phys. Vol. 48, No. 4, p. 1798, 1968
- Verter 76      M.R. Verter and H. Rabitz, *Theoretical evaluation of vibrational transition and relaxation in CO-He*, J. Chem. Phys., Vol. 64, No. 7, p. 2939, 1976, as quoted in / Rich 82 /
- Witteman 87      W.J. Witteman, *The CO<sub>2</sub> Laser*, Springer Verlag, Berlin, 1987
- Yamada 87      K.T. Yamada and Wolfgang Klebsch, *High-Temperature Spectrum of OCS in a dc Discharge by Diode laser Spectroscopy*, J. Mol. Spectrosc., Vol. 138, p. 380, 1987
- Zittel 88      P.F. Zittel and M.A. Sedam, *Vibrational Relaxation of OCS (V<sub>3</sub>)*, Chemical Physics Letters, Vol. 148, No. 6, p. 486, 1988

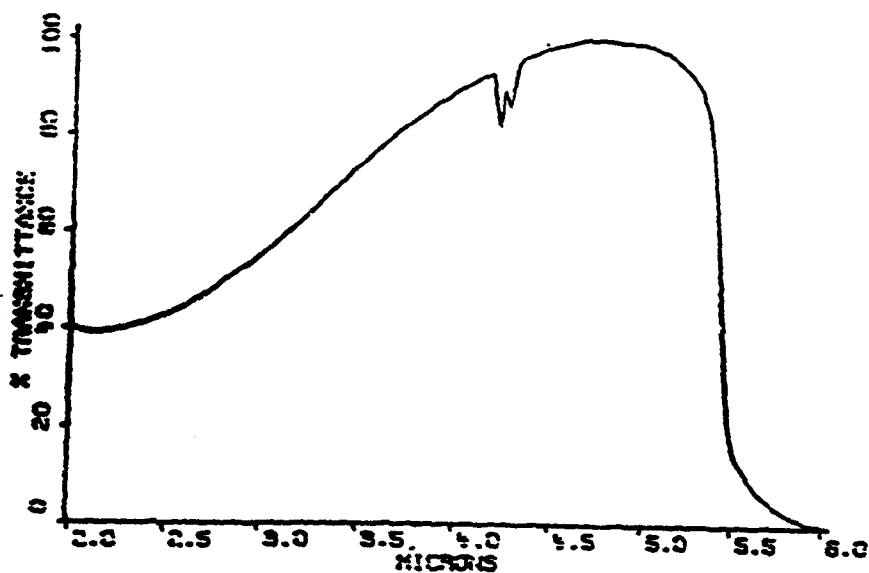
## Appendix

Bias circuits and response curves for the infrared detectors used.

- InSb detector



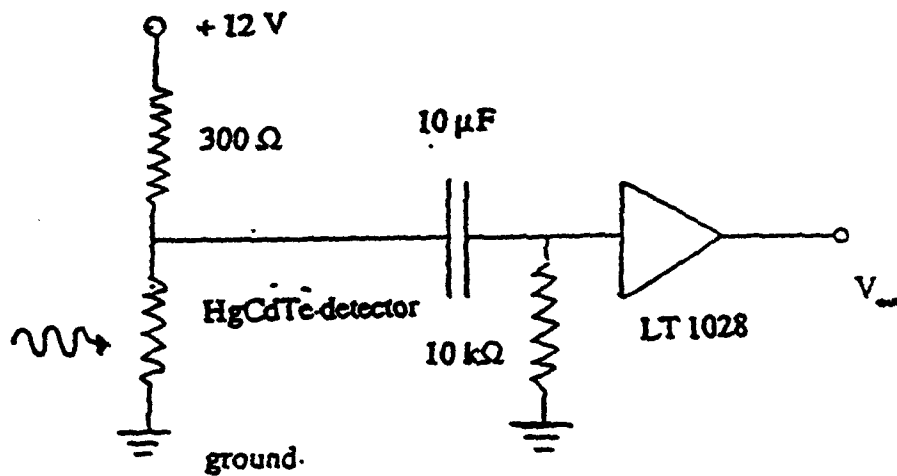
Operating circuit for J15D InSb detector



Relative response versus wavelength. Source: EG&G Judson  
(The curve is obviously taken in an  $\text{CO}_2$  contaminated environment)

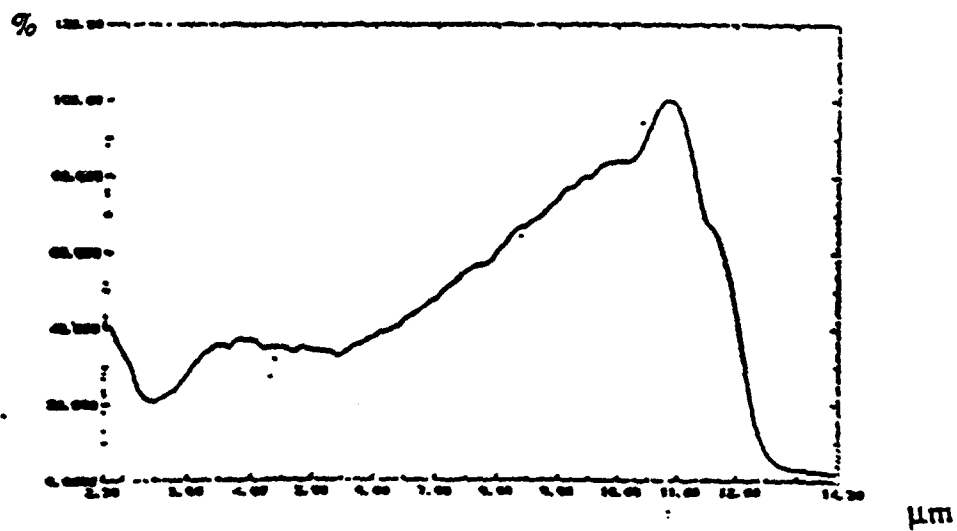


# HgCdTe detector



Operating circuit for J1SD HgCdTe detector

% RESPONSE vs. WAVELENGTH



HgCdTe detector. Relative response versus wavelength. Source: EG&G Judson

**9. MODELING STUDIES I:**  
**Strong Vibrational Nonequilibrium In Supersonic Nozzle Flows**

\* Contents of this Chapter adapted from A. Roany, C. Flament, J. W. Rich, V. V. Subramaniam, and W.W. Jr., "Strong Vibrational Nonequilibrium in Supersonic Nozzle Flows", AIAA J., 31,119-128 (1993).

## **Introduction**

Chemically reactive flows of compressible gases are extensively studied, with interest renewed by current hypersonic flight problems<sup>1-3</sup>, nonequilibrium molecular electric discharge reactors<sup>4</sup>, and investigations of new gas lasers<sup>5</sup>. In each of these applications, it is recognized that, in addition to chemical nonequilibrium, nonequilibrium of the molecular vibrational modes can often be a major influence. This is particularly the case in thermodynamic environments in which the translational and rotational molecular energy modes are maintained in equilibrium at a relatively low temperature, while the vibrational molecular mode(s) have high specific energies. Such environments are commonly realized in supersonic expansions of gases at high stagnation enthalpies, in molecular electric glow discharge plasmas, and in optically pumped molecular gases. In these cases, inelastic collisions exchanging vibrational energy can create extreme non-Boltzmann populations of vibrational energy states; these are so-called "vibration-vibration pumped" environments<sup>6,7</sup>. Historically, vibrationally nonequilibrium flow environments have been the subject of detailed modeling for certain gas and gas-dynamic laser species<sup>8-10</sup>. Such studies have, however, been largely confined to investigations of relatively low-lying vibrational states, and, in the case of chemical laser flows, to chemical processes directly relevant to pumping a vibrational population inversion.

The present study addresses the processes influencing the populations of very high vibrational quantum states of diatomic gas molecules in nonequilibrium gas dynamic flows. Specifically, while it is well-known that vibration-vibration pumping processes can populate high vibrational levels, the mechanisms which limit such up-pumping, which include chemical reaction and vibration-to-electronic mode energy transfer, are only beginning to be understood<sup>11-14</sup>. We report here detailed modeling studies of supersonic expansion flows of CO and N<sub>2</sub>, with energy transfer into low-lying excited electronic states. We discuss the nozzle conditions which create extreme upper vibrational state disequilibrium. A critical survey of recent theoretical and experimental vibration-state-specific energy transfer data for these species has been conducted, and relevant rate data incorporated into the kinetic model. Three major applications of the model are discussed :

- 1) Isotopic separation of <sup>13</sup>C by V-V pumping; related separation processes can occur in other molecules.
- 2) Possible vibration-to-electronic (V-E) energy transfer lasers, such as CO to NO, or N<sub>2</sub> to NO, and other systems.

### 3) Possible electronic-to-electronic (E-E) energy transfer lasers.

A computer modeling code has been developed and applied to these problems. The code includes kinetic equations for vibrational level populations of up to five diatomic molecular species, including excited electronic states of some of these species. The kinetic equations are fully coupled to the gas dynamic conservation equations.

The details of the model are outlined, including the governing equations, the specific kinetic rate models, and the method of computer integration used. We discuss gas dynamic nozzle design to maximize populations on very high vibrational levels. Then, we present computed results, and give a brief summary and review of model extensions currently in progress. An appendix gives the detailed analytic rate expressions used.

#### **Model**

##### **Assumptions:**

The rapid expansion through a two-dimensional planar nozzle is modeled with a quasi one-dimensional approach. The flow is assumed to be inviscid and compressible, and we are only interested in the steady state solution. The translational and rotational energy modes are supposed to be in full equilibrium along the nozzle, so that a single temperature can be defined for these modes. This approximation neglects the extremely short relaxation times for rotational and translational equilibration (processes typically requiring a few molecular collisions).

The vibrational energy modes can follow a non-Boltzmann distribution, and take into account the anharmonicity of the molecules. The diatomic molecules are electronically active and each electronic state is counted as a separate species. The monatomic species are treated as simple diluents that participate only in vibration-translation processes and chemistry.

##### **The balance equations:**

The mass conservation equation for quasi-one-dimensional flows is:

$$(1) \quad \rho u A = \text{constant}$$

where  $u$  is the streamwise gas velocity component along the nozzle,  $\rho$  the density of the gas, and  $A = A(x)$  is the cross sectional area of the nozzle.

The conservation equation governing the population of the  $v$ th vibrational state of the diatomic species  $i$  is:

$$(2a) \quad \frac{\rho u}{m_i} \frac{dY_{i,v}}{dx} = VV_i^v + VT_i^v + VE_i^v + EE_i^v + SRD_i^v + CHM_i^v$$

where  $m_i$  is the molecular mass of species  $i$ ,  $Y_{i,v} = \rho_{i,v} / \rho$  is the mass fraction of the vibrational state  $v$  of the species  $i$  and  $\rho_{i,v}$  is the density of the species  $i$  in the vibrational state  $v$ .

The right-hand side of this equation is the sum of various inelastic collision processes which change the vibration state or the chemical species. "VV" represents the sum of the rate processes changing vibrational state by molecular collisions which exchange vibrational mode energy (vibration-vibration exchange). VT and VE, represent changes of vibrational state by exchange of energy between vibrational modes and translational/rotational modes, and between vibrational and electronic modes respectively. "EE" represents the exchange of energy between two electronically excited molecules by nonradiative collisional processes. "SRD" represents the change of vibrational state by spontaneous radiative decay processes. Finally, "CHM" represents changes of state and species by chemical reactions. The details of these expressions are given in the Appendix.

The conservation equation governing the population of a monatomic species  $m$  is:

$$(2b) \quad \frac{\rho u}{m_m} \frac{dY_m}{dx} = CHM_m$$

The momentum and energy equations, where  $p$  is the pressure, and  $h$  the enthalpy per unit mass of the mixture, are given by:

$$(3) \quad \frac{dp}{dx} + \rho u \frac{du}{dx} = 0$$

$$(4) \quad \frac{d}{dx} \left[ h + \frac{1}{2} u^2 \right] = -q_r$$

where  $q_r$  is the energy sink due to radiative transitions which are expected to be optically thin.

#### Thermodynamic equations:

The average mass and pressure of the mixture, respectively, are:

$$(5) \quad \frac{1}{\mu} = \sum_{i,v} \frac{Y_{i,v}}{m_i} + \sum_m \frac{Y_m}{m_m}$$

$$(6) \quad p = \frac{\rho}{\mu} kT$$

where  $k$  is the Boltzmann constant.

The average enthalpy per unit mass of the mixture is:

$$(7) \quad h = \frac{5}{2} \frac{kT}{\mu} + \sum_{i,v} \frac{Y_{i,v}}{m_i} (kT + E_{i,v} + h_i^{\circ}) + \sum_m Y_m (Tc_m + h_m^{\circ})$$

where  $E_{i,v}$  is the internal energy of molecule  $i$  in vibrational level  $v$  for a given electronic state,  $Tc_i$  is the electronic energy and  $h_i^{\circ}$  is the heat of formation per unit mass of species  $i$ .  $E_{i,v}$  is given by:

$$(8) \quad E_{i,v} = Tc_i + \omega_{ei} \left( v + \frac{1}{2} \right) - \omega_{ei} x_{ei} \left( v + \frac{1}{2} \right)^2$$

$\omega_{ei}$  and  $x_{ei}$  are the spectroscopic constants (fundamental vibrational frequency and anharmonicity, respectively) for the molecule  $i$ .

#### System of O.D.E. solved:

Additional assumptions include constant average mass  $\mu$  (which is justifiable for the reactions under consideration here), there is only one monatomic species  $m$ , the radiation energy sink is negligible, the effect of the enthalpy of formation on the mixture total energy is negligible (the products are assumed to be in very small quantity).

With these assumptions, the previous equations can be written in terms of the derivatives of the molar fractions,  $X_{i,v} = Y_{i,v} \mu / m_i$  of the velocity  $u$ , and of the translational/rotational temperature  $T$ :

$$(9a) \quad \rho u A = \text{constant}$$

$$(9b) \quad X_m = 1 - \sum_{i,v} X_{i,v}$$

$$(9c) \quad \frac{dX_{i,v}}{dx} = \frac{\mu}{\rho u} \left( VV_i^v + VT_i^v + VE_i^v + EE_i^v + SRD_i^v + CHM_i^v \right)$$

$$(9d) \quad \frac{du}{dx} = - \frac{u}{(1 - M^2)} \left\{ \frac{dA}{A dx} + \Phi \right\}$$

$$(9e) \quad \frac{dT}{dx} = T \left\{ \frac{1}{A} \frac{dA}{dx} + \left( i - \frac{\mu u^2}{kT} \right) \frac{1}{u} \frac{du}{dx} \right\}$$

where  $M$  is the Mach number based on the frozen speed of sound and  $\Phi$  is a function which couples the equations of gas dynamics to the kinetics:

$$(10a) \quad M = \frac{u}{a}$$

$$(10b) \quad a^2 = \frac{kT}{\mu} \left\{ \frac{\frac{5}{2} + \sum_{i,v} X_{i,v}}{\frac{3}{2} + \sum_{i,v} X_{i,v}} \right\}$$

$$(10c) \quad \Phi = \frac{1}{\frac{5}{2} + \sum_{i,v} X_{i,v}} \left[ \sum_{i,v} \left( \frac{E_{i,v}}{kT} + 1 \right) \frac{dX_{i,v}}{dx} \right]$$

#### Numerical approach and applications:

The nozzle consists of two linear profiles for the subsonic and supersonic expansions. The zone near the throat has a parabolic shape. Immediately downstream of the throat, the supersonic expansion is straight-walled, with a specified expansion half-angle. The influence of an additional constant area channel, downstream of the expansion, is also studied; the location of this channel extension is varied parametrically. In our calculations, the stagnation conditions are chosen to be those generated by a shock tunnel, typically :  $T_0=2000$  K and  $P_0=100$  atm. The gas is chemically, vibrationally, and electronically active. The set of the fully coupled equations is solved using a "stiff" equation integrator : LSODE 15,16.

For the cases studied, which include several vibrationally active species, this system represents between 100 and 200 stiff equations. They have been integrated from the subsonic section through to the supersonic-hypersonic expansion. The integration through the throat represents a singularity; in some previous calculations, this has been avoided by assuming that the gas is in Boltzmann equilibrium at the throat. Our calculations show that the flow through the subsonic channel creates an out-of-equilibrium vibrational distribution of the molecules at the throat. The vibrational distribution of CO is plotted for a  $15^\circ$  half-angle expansion nozzle at two locations : at the nozzle inlet

where CO is at equilibrium, and at the throat (fig.9.1 and fig.9.2). Other run parameters are specified on the figure.

Since there is clearly a small, but not necessarily negligible nonequilibrium effect at the throat, we have chosen to integrate the system from the subsonic section to the supersonic expansion. An initial Mach number is calculated at the inlet of the nozzle; it is determined by considering the isentropic expansion of a non active gas ( $\gamma=1.4$ ). This inlet Mach number is changed each time the Mach number decreases during the expansion. An iterative scheme is then set up, using a halving method for calculating the new inlet Mach number.

### Design for high V-V up-pumping

#### Effect of the mixture:

When expanding pure CO through a  $15^\circ$  half-angle nozzle, the vibrational distribution of CO begins to show strong non-Boltzmann populations downstream of the throat. For example, as shown in fig.9.1, there is a considerable up-pumping of populations for levels lying between  $v=8$  and  $v=26$  at the nozzle outlet. As shown in fig.9.1 and fig.9.2, V-T relaxation is active downstream in the nozzle, and is increased if the stagnation temperature is raised from 2000 K to 3000 K. Argon is added to CO in order to decrease the V-T relaxation; this is possible because the V-T rate for Ar-CO is less than the V-T rate for CO-CO. Ar acts as a coolant in the mixture, and allows CO to be more strongly pumped on its vibrational levels below  $v=25$ , as shown on fig.9.3. It may be noted that partial vibrational population inversions of the type shown, produced in supersonic expansions of CO-Ar mixtures, constitute the typical "gas dynamic" CO laser environment<sup>17</sup>, which was first studied both theoretically and experimentally by McKenzie<sup>9</sup>.

In order to study the effect of the V-T relaxation and to assess the effect of possible impurities present in the mixture, we have calculated the CO vibrational distribution when the mixture consists of CO, Ar, and H<sub>2</sub>. Fig.9.4 shows the vibrational distribution of CO expanding in an optimized nozzle for several percentages of H<sub>2</sub> in the mixture. The CO-H<sub>2</sub> V-T relaxation is very fast, and as the percentage of H<sub>2</sub> increases CO is less excited on its high vibrational levels. It appears that, for less than 1% H<sub>2</sub>, CO remains highly excited. We are presently reviewing CO-H rate constants in order to investigate the relaxation of CO by atomic hydrogen during the expansion; H relaxes CO even more efficiently than H<sub>2</sub> does. Such studies are necessary since possible water vapor or hydrocarbon impurities can partially



dissociate under some nozzle plenum conditions, providing  $H_2$  and H which weaken the influence of V-V up pumping.

Dramatic nonequilibrium vibrational energy partition has been observed when expanding a mixture CO-N<sub>2</sub>-Ar. The average energy per particle is plotted on [fig.9.7.1](#) for CO and N<sub>2</sub> expanding along the nozzle. The energy is significantly transferred from N<sub>2</sub> to CO during the supersonic expansion, which enhances the excitation of the high energy levels in CO ([fig.9.5](#) and [fig.9.6](#)). This energy partition is a consequence of the well-known preferential transfer of vibrational energy from the more widely spaced vibrational quantum levels to the more closely-spaced vibrational quantum levels in V-V pumped systems<sup>6</sup>. In this example, the higher the frequency, more widely spaced N<sub>2</sub> levels transfer energy to the CO. It should be noted that the N<sub>2</sub> distribution of [fig.9.5](#), which now contains relatively low energy, displays the total population inversion over some states which characterizes so-called "weak pumping" cases<sup>46</sup>. In most subsequent calculations we use mixtures of CO-N<sub>2</sub>-Ar to provide highly pumped CO vibrational distributions.

#### Effect of the nozzle geometry:

In most numerical simulations, with a mixture providing pumped distributions of CO, the first few vibrational levels have a high density compared to levels of about  $v=25-30$ . In order to drain vibrational quanta from the low levels up to the high lying levels, one has to flow the mixture through a constant area channel, thus stopping the expansion in the supersonic section. The combination of the nozzle and the additional straight channel is referred to here as the "optimized nozzle". The location of the straight channel is found by considering the energy transfer curves ([fig.9.7.1](#) to [fig.9.7.3](#)). For the mixture CO-N<sub>2</sub>-Ar which we have considered above, the energy transfer curve ([fig.9.7.1](#)) shows a saturation in the transfer 20 cm after the throat; we choose this location for stopping the supersonic expansion with a straight channel. [Fig.9.5](#) and [fig.9.6](#) show the vibrational distribution of CO expanding in a nozzle without a straight channel (regular nozzle), and in an optimized nozzle respectively. The improvement is obvious; with the optimized nozzle, although the low levels are less populated, the distribution is pumped up to level  $v=38$  instead of  $v=30$  with the regular nozzle. The effect of the straight channel is also demonstrated on [fig.9.3](#) with a CO-Ar mixture.

Clearly, the present inviscid, shock-free calculations represent an optimum which can only be approached experimentally by a carefully contoured nozzle design with due allowance for boundary-

layer displacement. We note, however, that CO gas laser experiments in a relatively low density, planar 15° half-angle nozzle produce a supersonic near-isentropic core which approximates the velocity/temperature distribution given by the model<sup>18</sup>.

## **Results**

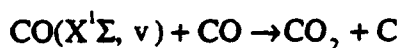
The following diatomic molecules are investigated. Unless indicated otherwise, molecules are in their electronic ground state:  $^{12}\text{C}^{16}\text{O}$ ,  $^{13}\text{C}^{16}\text{O}$ ,  $\text{CO}(a^3\Pi)$ ,  $\text{N}_2$ ,  $\text{NO}(X^2\Pi)$ ,  $\text{NO}(B^2\Pi)$ . Simplified energy level diagrams for the CO and NO species are given in [fig.9.12](#). Ar is added in most mixtures. C and  $\text{CO}_2$  appear as reaction products; they can relax active molecules by V-T transfer.

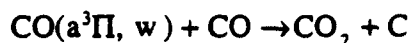
Both isotope separation and energy transfer laser applications involving excited electronic states (V-E, E-E, chemical reactions) require that relatively high vibrational levels of CO be populated. In most cases, we require a density of about  $10^{-5}N_0$  for vibrational levels of CO from  $v=20$  to  $v=35$ ,  $N_0$  being the number density of the vibrational ground state  $v=0$ . Our "optimized" nozzle expansion will cause energy transfer processes to give such high populations on the upper vibrational levels.

### **Isotope separation:**

The basic mechanism of the separation of  $^{13}\text{C}$  is the following: a vibrational energy transfer occurs from  $^{12}\text{CO}$  to  $^{13}\text{CO}$ ; [fig.9.7.2](#) and [fig.9.7.3](#) show the evolution of the average energy per particle along the nozzle for the two isotopes. The energy is clearly transferred from  $^{12}\text{CO}$  to  $^{13}\text{CO}$ . This is again an example of preferential transfer of vibrational energy favoring the lower-frequency, more closely spaced quantum levels of the  $^{13}\text{CO}$  <sup>6,7</sup>. The vibrational distributions of the two isotopes are plotted in [fig.9.8](#) and [fig.9.9](#), for the case when  $\text{N}_2$  and Ar are added to the mixture. The vibrational distribution of  $^{13}\text{CO}$  is pumped more efficiently than the  $^{12}\text{CO}$  distribution. The natural abundance of  $^{13}\text{CO}$  is 1.1%; the percentage of  $^{13}\text{CO}$  in CO versus the vibrational state is plotted in [fig.9.10](#). There is a preferential excitation in  $^{13}\text{CO}$  for some states occurring in the mixture; the maximum is at  $v=10$ ,  $^{13}\text{CO}$  representing about 8% of CO in the state  $v=10$ . The best case is obtained by using an optimized nozzle; the straight channel is located 20 cm after the throat.

An enrichment product can be obtained by considering the following reactions<sup>29</sup>, which take place all along the expansion :





The reactants are either  $^{12}\text{CO}$  or  $^{13}\text{CO}$ , and the products are  $^{12}\text{C}$ ,  $^{13}\text{C}$ ,  $^{12}\text{CO}_2$ , or  $^{13}\text{CO}_2$ . From earlier experiments<sup>19</sup>, the channel forming  $^{13}\text{CO}_2$  seems to be the most probable. We are presently introducing these chemical reactions and energy transfer into the first excited electronic state,  $\text{CO}(a^3\Pi)$ , in the code (see the following subsections). The model can be compared with experiments in which the  $\text{CO}_2$  produced during the expansion is removed with a liquid nitrogen trap, and the actual enrichment in  $^{13}\text{CO}_2$  is analysed<sup>20,21</sup>.

The effective activation energy of the preceding reactions is about 6 eV, which represents a vibrational level of about  $v=25$  for  $\text{CO}(X^1\Sigma)$ , or a low lying vibrational level of  $\text{CO}(a^3\Pi)$ . Thus, it is necessary to transfer as much energy as possible to  $^{13}\text{CO}$  in order to provide the required activation energy. It seems that if we can provide a fair density of  $^{13}\text{CO}(v>20)$ , a high enrichment can be reached.

The limit  $v>20$  is somewhat uncertain since the rate constants of the chemical reaction, and of the electronic transfer from  $\text{CO}(X^1\Sigma)$  to  $\text{CO}(a^3\Pi)$ , are not well known. Further experiments presently underway, when compared with the results of this study, should enable assessment of an efficient separation of  $^{13}\text{C}$ .

Monitoring the amount of C and  $\text{CO}_2$  produced, we have observed that only a small amount of these products are formed during the expansion. If we calculate the ratio of the density of  $\text{CO}_2$  produced to the total density of CO we find  $\text{CO}_2/\text{CO}$  between  $10^{-3}$  and  $10^{-6}$ , depending on the conditions we have considered. The yield of the chemical reactions is therefore very low; since the pressure of CO does not generally exceed 200 torr at the end of the expansion, it is unlikely that such a process could be practically used for isotope separation, unless one can use a very long straight channel and operate the supersonic expansion for several seconds. Nevertheless, short duration supersonic expansion experiments have been conducted, and substantial  $^{13}\text{C}$  enrichment fractions reported<sup>20,21</sup>, but yields are presumably small.

#### V-E energy transfer:

Processes similar to the ones discussed above occur when considering V-E transfer lasers. In such lasers, a highly vibrationally excited donor molecule transfers its energy in collisions to the electronic mode of a second, "acceptor" species<sup>22,23</sup>. The electronic configuration of the acceptor species is selected to obtain possible population inversion and subsequent laser gain on a visible or

near-ultraviolet radiative transition. In order to achieve the energy transfer from CO(v) to an acceptor electronic state lying above 6 eV, CO(v>25) has to be significantly populated. This constraint is not required when designing a CO gas dynamic laser since, in this case, one looks for a partial population inversion on lower vibrational levels.

At present, CO is chosen as a possible donor species, and the code is being run including the low-lying electronic energy states of CO. The details of the V-E transfer rate model used to couple the electronic states are given in the Appendix. Rates for transfer between CO( $X^1\Sigma$ ) and both CO( $a^3\Pi$ ) and CO( $A^1\Pi$ ) have been developed, and compared with data from available experiments<sup>13,24</sup>.

As previously discussed, a mixture of CO, N<sub>2</sub>, and Ar is used in order to enhance the V-E transfer from CO( $X^1\Sigma^+$ ) to CO( $a^3\Pi$ ). An optimized nozzle is used in the calculations, estimating the shape of the effective nozzle. The length of the 15° half-angle expansion is 15 cm, measured from the throat. A straight channel of 85 cm length follows the expansion. Higher electronic states are not considered in this model since it has been shown that the vibrational levels of the ground state CO( $X^1\Sigma^+$ ) above v=35 are not excited, and therefore only CO( $a^3\Pi$ ) is energetically accessible. Calculations were made for a 10%CO - 10%N<sub>2</sub> - 80%Ar mixture, with stagnation conditions T<sub>0</sub>=2000 K and P<sub>0</sub>=100 atm. Since state-resolved data for the V-V and V-T rates for the excited electronic state  $a^3\Pi$  in CO are unknown, the rate for the v<sup>th</sup> vibrational level of the excited state is presently assumed to be equal to the rate for the corresponding v<sup>th</sup> level of the CO ground state.

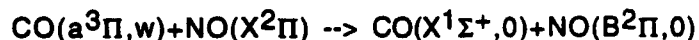
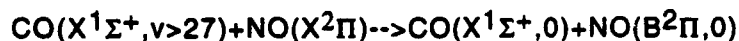
As described in the Appendix, the rate constant for the V-E transfer is a function of a resonance parameter C<sub>VE</sub> and a pre-exponential factor S<sub>VE</sub><sup>0</sup>. We have chosen C<sub>VE</sub>=13.58 x10<sup>-2</sup> in order to get the optimum of the transfer at resonance, where the energy defect between the two states is minimum. S<sub>VE</sub><sup>0</sup>, the amplitude of the transfer, is adjusted from 10<sup>-11</sup> cm<sup>3</sup>/s (gas kinetic) to 10<sup>-14</sup> cm<sup>3</sup>/s. At the same time, the formation of C and CO<sub>2</sub> is studied (see reactions above); the specific rate constant for these chemical reactions is k<sub>0</sub> (see Appendix), which varies between 10<sup>-15</sup> cm<sup>3</sup>/s and 10<sup>-17</sup> cm<sup>3</sup>/s. We have neglected back reaction rate processes; for the relatively small amounts of CO reacted, however, we can realistically study the amount of CO dissociated and the influence of the chemistry on the V-E transfer.

Fig.9.11 shows the vibrational state populations calculated with this model, for a 15° half-angle expansion of 15 cm length, followed by an 85 cm straight section, to A/A\*=16.5, M=5.5, P=151.2 torr and T=197 K. We have chosen the V-E coupling parameter of S<sub>VE</sub><sup>0</sup>=5 x10<sup>-13</sup> cm<sup>3</sup>/s,

and  $S_{VE}^0/k_0=100$ . This implies a V-E transfer rate approximately equal to the gas-kinetic collision rate, and a chemical reaction approximately 100 times slower than the V-E transfer. This choice of parameters approximately reproduces previously observed coupling between the two electronic states<sup>14,38</sup>. Fig.9.11 shows the influence on the  $X^1\Sigma^+$  vibrational population distribution of the V-E transfer into the  $a^3\Pi$  state. The large "dimple" beginning near  $v=28$  is due to this coupling; states near  $v=28$  are close to resonance for the V-E transfer from  $X^1\Sigma^+$  to  $a^3\Pi$ . Qualitatively similar effects on V-V pumped  $CO(X^1\Sigma^+,v)$  distributions have been measured experimentally in electric discharges by Farrenq et al.<sup>14</sup>. The coupling becomes very weak as  $S_{VE}^0$  is decreased below  $5 \times 10^{-14} \text{ cm}^3/\text{s}$ .

#### E-E energy transfer:

In order to model a CO-NO energy transfer laser, we have to study the transfer occurring between the electronic states of CO and NO (E-E transfer). A strong UV emission was reported in a previous study<sup>38</sup>, while CO was excited in a CO-NO mixture. The simplified model we have used in our calculations is as follows :



The two first electronic levels of CO transfer their energy to an excited electronic state of NO. This process is shown on the potential curves, on fig.9.12.

A related transfer is likely to occur from vibrationally excited levels of the electronic ground state of NO itself to  $NO(A^2\Sigma^+)$  and to  $NO(B^2\Pi)$ <sup>12</sup>. The band emission from these excited NO electronic states is the well-known  $\gamma$  band for the system  $NO(A^2\Sigma^+) - NO(X^2\Pi)$ , and the  $\beta$  band for the system  $NO(B^2\Pi) - NO(X^2\Pi)$ . We will only consider the  $\beta$  band in the following calculations. It is necessary to achieve a high density of  $CO(X^1\Sigma^+, v>27)$  and  $CO(a^3\Pi)$  if one wants to excite a fair amount of  $NO(B^2\Pi)$  in order to create a population inversion between  $NO(B^2\Pi)$  and  $NO(X^2\Pi)$ .

The mixture is: 10%CO - 10%N<sub>2</sub> - 80%Ar. The stagnation conditions are:  $T_0=2000 \text{ K}$  and  $P_0=100 \text{ atm}$ . The length of the 15° half-angle expansion is 15 cm; the straight channel is 85 cm long. At 80 cm from the throat, in the constant area channel, NO is injected in the mixture; the mixing is assumed to be instantaneous. Such an assumption implies that we have the maximum amount of NO in the mixture as soon as the gas reaches the mixing zone; this can be considered as the worst case since

NO is a very effective quencher. The mixing zone is 20 cm long; the population of each component of the mixture is monitored at the end of the mixing zone.

The detailed mechanism and rate constants for the reactions producing  $\text{NO}(\text{B}^2\Pi)$  are not known. The global parameter  $P_{EE}$  (see Appendix) is therefore varied from  $10^{-1}$  to  $10^{-6}$ . The amount of NO injected is 10% of the CO density. In order to study the possibility of a laser effect the small signal gain is calculated for the transition  $\text{NO}(\text{B}^2\Pi, v=0, J) \rightarrow \text{NO}(\text{X}^2\Pi, v=8, J+1)$  which corresponds to the largest Franck-Condon factor, or the most probable radiative transition. Standard expressions for Doppler-broadened gain<sup>38</sup> are used. The calculations show a population inversion between  $\text{NO}(\text{B}^2\Pi)$  and  $\text{NO}(\text{X}^2\Pi)$ ; the temperature achieved in the gas is 200 K. The gain (in  $\text{cm}^{-1}$ ) is plotted versus the rotational quantum number  $J$ , for several values of the transition probability  $P_{EE}$  on fig.13. The gain curves remain about the same for  $P_{EE} > 10^{-3}$ , showing the maximum gain that can be obtained under these conditions. It is likely that the gain is about  $10^{-3}$  for  $P_{EE}$  greater than  $10^{-4}$ . The wavelength of the transition is  $0.323 \mu\text{m}$ , in the UV range.

## Conclusion

A new vibrationally nonequilibrium code has been developed, which includes vibrational-state-specific population balances, the influence of excited electronic states, and some chemical reaction channels, for compressible flows of mixtures of diatomic gases. Recent theoretical and experimental rate data on vibration-to-vibration, vibration-to-electronic and electronic-to-electronic energy transfer processes have been reviewed and used in the model. Calculations for isotopic mixtures of CO molecules, V-E and E-E energy transfer in CO and NO are discussed in detail.

The code has been successfully applied to the design of a CO-NO energy transfer laser, and can be used with other donor-acceptor pairs such as NF-IF,  $\text{N}_2$ -NO, or other systems. Uncertainties remain in the model regarding some of the mechanisms involved and some of the transfer rate constants. Although the theoretical calculations show the feasibility of such lasers, validation by experiment is necessary; new processes and unexpected mechanisms can arise, due to the complexity of the electronic structures of the systems we are studying.

## Appendix

We introduce  $n_{i,v} = \rho_{i,v} / m_i$  the number density of the primary species  $i$ , in vibrational state  $v$ , in part/cc;  $n_{j,w} = \rho_{j,w} / m_j$  the number density of the secondary species  $j$  in vibrational state  $w$ , in

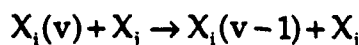
part/cc;  $n_i = \sum_v n_{i,v}$  the total number density of species  $i$ , in part/cc; and  $n_T = \sum_i n_i$  the total number density of the mixture. **Remark:** we have  $\rho = \sum_{i,v} \rho_{i,v} + \sum_m \rho_m = \mu n_T$  and  $X_{i,v} = n_{i,v} / n_T$

#### Vibration-translation term:

The VT term of equation (2) is written as:

$$VT_i^v = \sum_j n_j \{ P_{ij}^{v+1,v} [n_{i,v+1} - \exp(-\Delta E_i^v / kT) n_{i,v}] - P_{ij}^{v,v-1} [n_{i,v} - \exp(-\Delta E_i^{v-1} / kT) n_{i,v-1}] \}$$

where  $P_{ij}^{v,v-1}$  is the rate constant (in  $\text{cm}^3/\text{s}$ ) of the V-T transition:



$X_i(v)$  refers to species  $i$  in vibrational state  $v$ . The rate constant can be expressed as follows<sup>13,41</sup>:

$$P_{ij}^{v,v-1} = P_{ij}^0(T) \cdot \frac{v}{1 - x_{ei}^v} \cdot F_{ij}^{v,v-1}(\lambda_{ij}^{v,v-1})$$

$F$  is a function given by<sup>42</sup>:

$$F(\lambda) = \frac{1}{2} \cdot \left[ 3 - e^{-\frac{2}{3}\lambda} \right] \cdot e^{-\frac{2}{3}\lambda}$$

$$\lambda_{ij}^{v,v-1} = 2^{-\frac{3}{2}} \cdot \sqrt{\frac{\Theta_{ij}}{T}} \cdot \frac{|\Delta E|}{k\Theta_i}$$

$\Delta E$  is the energy difference between the products and the reactants in the V-T transition;

$\Theta_i = hc\omega_{ei} / k$  is the vibrational characteristic temperature of species  $i$ ;

$\Theta_{ij} = 16\pi^4 \mu_{ij} c^2 \omega_{ei}^2 l^2 / k$  is in Kelvin<sup>25,41</sup> where  $\mu_{ij}$  is the reduced mass,  $c$  is the speed of light and

$l = 0.2 \text{ \AA}$  is the range parameter. The ratio  $\Theta_{ij} / \Theta_i^2$  is given in table 1.

In the rate constant expression,  $P_{ij}^0(T)$  is a coefficient which allows fitting to experimental relaxation time data. It is expressed as :

$$P_{ij}^0(T) = \frac{(1 - x_{ei})kT}{\left\{ (\tau_{ij}^0 P) \cdot F_{ij}^{1,0} \cdot \left[ 1 - \exp\left(-\frac{\Theta_i}{T}\right) \right] \right\}}$$

Here, the Boltzmann constant  $k$  is in  $\text{erg/K}$ .  $\tau_{ij}^0 P$  is the vibrational relaxation time in  $\text{atm} \cdot \mu\text{s}$  and is given by:

$$\ln(\tau_{ij}^0 P) = A_{ij} + B_{ij} T^{-\frac{1}{2}} + C_{ij} T^{-\frac{3}{2}}$$

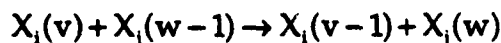
$A_{ij}$ ,  $B_{ij}$ ,  $C_{ij}$  are chosen in order to fit the experimental data (see table 9.1).

#### Vibration-vibration term:

The VV term, including only the single quantum transitions, is written as:

$$VV_i^v = \sum_j \sum_{w=0}^{\infty} \left\{ Q_{ij,w,w+1}^{v,v+1} \left[ n_{i,v+1} n_{j,w} - \exp(-\Delta E_{ij}^{v,w} / kT) n_{i,v} n_{j,w+1} \right] \right. \\ \left. - Q_{ij,w,w+1}^{v,v-1} \left[ n_{i,v} n_{j,w} - \exp(-\Delta E_{ij}^{v-1,w} / kT) n_{i,v-1} n_{j,w+1} \right] \right\}$$

$Q_{ij,w-1,w}^{v,v-1}$  is the rate constant (in cm<sup>3</sup>/s) of the V-V transition:



The rate constant is the sum of two terms, the first being the contribution of the short-range interactions, and the second the contributions of the long-range forces due to dipole-dipole interaction<sup>41,43-45</sup>. The rate constant has the following expression<sup>13</sup>:

$$Q_{ij,w-1,w}^{v,v-1} = Z_{ij} \left[ S_{ij,w-1,w}^{v,v-1} + L_{ij,w-1,w}^{v,v-1} \right] e^{-\frac{\Delta E}{2kT}}$$

$$Z_{ij} = 4\sigma_{ij}^2 \sqrt{\frac{\pi kT}{2\mu_{ij}}}$$

where  $Z_{ij}$  is the collision number and  $\pi\sigma_{ij}^2$  is the cross section.

The short-range contribution is given by<sup>41</sup>:

$$S_{ij,w-1,w}^{v,v-1} = S_{ij}^0 T \frac{v}{1-x_{ei}v} \frac{w}{1-x_{ej}w} F_{ij,w-1,w}^{v,v-1} \left( \lambda_{ij,w,w-1}^{v,v-1} \right)$$

$F(\lambda)$ ,  $\lambda$ , and  $\Delta E$  have the same definitions as above.

The long-range contribution is given by<sup>44,45</sup>:

$$L_{ij,w-1,w}^{v,v-1} = \frac{L_{ij}^0}{T} \left( \frac{g_i^{v,v-1}}{g_i^{1,0}} \right)^2 \left( \frac{g_j^{w-1,w}}{g_j^{1,0}} \right)^2 \exp\left(-\frac{\Delta E^2}{b_{ij}T}\right)$$

$S_{ij}^0$ ,  $L_{ij}^0$ , and  $b_{ij}$  are empirical parameters matched to experimental data (see table 9.1).  $b_{ij}$  is in erg<sup>2</sup>/K

and:

$$\left( \frac{g_i^{v,v-1}}{g_i^{1,0}} \right)^2 = \left[ \frac{a_i + 1}{a_i + 3 - 2v} \right]^2 \left[ \frac{v(a_i + 2 - 2v)(a_i + 4 - 2v)}{a_i(a_i + 3 - v)} \right] \\ \left( \frac{g_j^{w-1,w}}{g_j^{1,0}} \right)^2 = \left[ \frac{a_j + 1}{a_j + 3 - 2w} \right]^2 \left[ \frac{w(a_j + 2 - 2w)(a_j + 4 - 2w)}{a_j(a_j + 3 - w)} \right]$$

where  $a_i = 1/x_{ei}$  and  $a_j = 1/x_{ej}$  are the reciprocals of the anharmonicity factors.

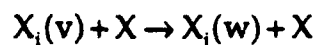
#### Vibration-electronic term:

The collision-induced V-E terms are retained only here:

$$VE_i^v = n_T \sum_{j=1}^{\infty} \sum_{w=0}^{\infty} S_{ij}^{v,w} \left\{ n_{j,w} + n_{i,v} \exp[-(E_j^w - E_i^v) / kT] \right\}$$



where  $S_{ij}^{v_i, v_j}$  is the rate constant (in  $\text{cm}^3/\text{s}$ ) for the collision induced vibration-to-electronic transition:



$X_i(v)$  and  $X_j(w)$  are two electronic manifolds of the same species. Their vibrational states are  $v$  and  $w$  respectively. It is assumed that collisions can induce the transition from  $X_i(v)$  to  $X_j(w)$  when the energies of these molecules are very close. Such resonance occurs between  $\text{CO}(X^1\Sigma)$  and  $\text{CO}(a^3\Pi)$  when the vibrational states of each electronic manifold are respectively  $v=27$  and  $w=0$ . The rate constant is modeled with a Gaussian function of the energy defect; the width and the maximum of the Gaussian rate are empirical parameters<sup>38</sup>:

$$S_{ij}^{v_i, w_j} = S_{VE}^0 \cdot \exp\left(-\left(\frac{\Delta E}{C_{VE}\omega_e}\right)^2\right) \cdot \exp\left(-\frac{\Delta E}{2kT}\right)$$

The vibrational spectroscopic constant,  $\omega_e$ , is taken to be the larger of the constants for the two electronic states involved. The adjustable parameters are  $S_{VE}^0$  and  $C_{VE}$ . In the case of  $\text{CO}(X^1\Sigma) \rightarrow \text{CO}(A^1\Pi)$  and  $\text{NO}(X^2\Pi) \rightarrow \text{NO}(B^2\Pi)$  transfers, values of these parameters were obtained by fitting kinetic rate models to V-V up-pumping experiments in optical cells<sup>12,13,24</sup>. For the case of  $\text{CO}(X^1\Sigma) \rightarrow \text{CO}(a^3\Pi)$ , there are no comparable data, although indication of the coupling has been seen in the experiments of Farrenq, et al.<sup>14</sup>. The range of validity of the resonance model above remains to be determined, in detailed state-resolved experiments. In table 9.2 the value of these parameters are indicated.

#### Electronic-electronic term:

The E-E transfer terms are written as:

$$EE_{\text{CO}(a^3\Pi, w)} = -k_{EE} n_{\text{CO}(a^3\Pi, w)} n_{\text{NO}(X^2\Pi)}$$

$$EE_{\text{CO}(X^1\Sigma^+, 0)} = k_{EE} [n_{\text{CO}(a^3\Pi, w)} + n_{\text{CO}(X^1\Sigma^+, v \geq 28)}] n_{\text{NO}(X^2\Pi)}$$

$$EE_{\text{CO}(X^1\Sigma^+, v \geq 28)} = -k_{EE} n_{\text{CO}(X^1\Sigma^+, v \geq 28)} n_{\text{NO}(X^2\Pi)}$$

$$EE_{\text{NO}(B^2\Pi, 0)} = -EE_{\text{NO}(X^2\Pi)} = EE_{\text{CO}(X^1\Sigma^+, 0)}$$

The rate constant for the electronic-electronic processes,  $k_{EE}$ , is expressed as follows<sup>38</sup>:

$$k_{EE} = P_{EE} \cdot Z_{\text{CO-NO}}$$

$P_{EE}$  is the probability of transfer and  $Z_{\text{CO-NO}}$  is the collision number. This number represents the number of collisions between CO and NO during one second in one cubic centimeter.  $P_{EE}$  is then the

percentage of collisions needed for the reaction to proceed.  $P_{EE}$  is treated as a parameter in the calculations, as discussed in the text. One can calculate  $Z_{CO-NO}$  (in  $\text{cm}^3/\text{s}$ ):

$$Z_{CO-NO} = 3.10^{-10} \sqrt{\frac{T}{300}}$$

#### Spontaneous radiative decay term:

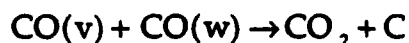
The spontaneous radiative transfer term is written as:

$$SRD_i^v = \sum_u [A_i^{v+u,v} n_{i,v+u} - A_i^{v,v-u} n_{i,v}]$$

The rates for the spontaneous radiative decay  $A$  have been calculated with the Einstein coefficients for radiative transitions between vibrational levels within the same electronic state, and with the Franck-Condon factors for the radiative transitions between vibrational levels of different electronic states<sup>26</sup>.

#### Chemical reactions Rate model:

We consider the reaction of CO during the expansion in the nozzle. The reactants can be CO isotopes in the two first electronic states,  $\text{CO}(X^1\Sigma)$  or  $\text{CO}(a^3\Pi)$ . The reaction is the following :



The activation energy of this reaction is  $E_a = 6 \text{ eV}$ .

The chemical terms are written as:

$$CHM_C = CHM_{CO_2} = \sum_{v,w} k_w^v n_{CO,v} n_{CO,w}$$

$$CHM_{CO,v} = CHM_{CO,w} = -k_w^v n_{CO,v} n_{CO,w}$$

The rate model<sup>27</sup> is the following :

$$k_w^v = k_0 \sqrt{\frac{T}{300}} \left( 1 - \frac{E_a}{E_{CO,v} + E_{CO,w}} \right)^2$$

where  $E_{CO,v}$  is the energy of  $\text{CO}(v)$  and  $k_0$  is an adjustable parameter.  $k_0 = 0$  when  $E_{CO,v} + E_{CO,w} \leq E_a$ .

The value of  $k_0$  is presently being inferred from experiments<sup>28,29</sup>. In the present calculation, the value  $k_0 = 5 \times 10^{-15} \text{ cm}^3/\text{s}$  is used.

#### Spectroscopic constants<sup>30</sup>:

All the spectroscopic constants are expressed in  $\text{cm}^{-1}$ . The spectroscopic constants have been determined by mass scaling of the constants of  $^{12}\text{CO}$  for  $^{13}\text{CO}$ .

#### Parameters used in the rate expressions:

The parameters used in the expression of the V-T and V-V rates are indicated in table 9.1. The rate constants involving  $^{13}\text{CO}$  are taken to be the same as for  $^{12}\text{CO}$ . For studying the effect of  $\text{H}_2$  in the mixture, the V-T rate  $\text{N}_2\text{-H}_2$  is assumed to be the same as for  $\text{H}_2\text{-CO}$ ;  $\text{H}_2$  is considered as a diluent and is not vibrationally active. We take n- $\text{H}_2$  in the model (the normal mixture ratio of o- $\text{H}_2$  and p- $\text{H}_2$ ).

#### Acknowledgement

This research was supported by 1) Pacific Applied Research, under prime contract from U. S. Strategic Defense Initiative Office/IST, and administered by Los Alamos National Laboratory, and by 2) Aero Propulsion and Power Laboratory, Aeronautical Systems Division, Wright Research and Development Center.

#### References

- <sup>1</sup> J. N. Moss, V. Cuda, and A. L. Simmonds, Nonequilibrium Effects for Hypersonic Transitional Flows, AIAA Paper 87-0404, January 1987.
- <sup>2</sup> Thomas R. A. Bussing, and Scott Eberhardt, Chemistry Associated with Hypersonic Vehicles, AIAA Paper 87-1292, June 1987.
- <sup>3</sup> S. P. Sharma and W. Gillespie, Nonequilibrium and Equilibrium Shock Front Radiation Measurements, *Journal of thermophysics and heat transfer*, Vol 5, July-September 1991, pp. 257-265.
- <sup>4</sup> V. D. Rusanov, A. A. Fridman, and G. V. Sholin, The Physics of a Chemically Active Plasma with Nonequilibrium Vibrational Excitation of Molecules, *Soviet Physics Uspekhi*, Vol. 24, June 1981, pp. 447-474.
- <sup>5</sup> E. W. McDaniel and W. L. Nighan, Applied Atomic Collision Physics, *Gas Lasers*, Vol. 3, Academic Press, New York, 1982.

- 6 C. E. Treanor, J. W. Rich and R. G. Rehm, Vibrational Relaxation of Anharmonic Oscillators with Exchange-dominated Collisions, *Journal of chemical physics*, Vol. 48, February 1968, pp. 1798-1807.
- 7 *Nonequilibrium Vibrational Kinetics*, ed.: M. Capitelli, Springer-Verlag, Berlin Heidelberg, 1986.
- 8 J. D. Anderson, Jr., *Gasdynamic Lasers: An Introduction*, Academic Press, New York, 1976.
- 9 R. L. McKenzie, Diatomic Gasdynamic Lasers, *Physics of Fluids*, Vol. 15, Dec. 1972, pp. 2163-2173.
- 10 E. M. Cherkasov and V. I. Chesnokov, Numerical Optimization of Parameters of CO Gasdynamic Lasers, *Soviet Journal of Quantum Electronics*, Vol. 18, March 1988, pp. 301-306.
- 11 C. Gorse, M. Cacciatore and M. Capitelli, Kinetic Processes in Non-equilibrium Carbon Monoxide Discharges. I. Vibrational Kinetics and Dissociation Rates, *Chemical Physics*, Vol. 85, 1984, pp. 165-176.
- 12 H. Dünwald, E. Siegel, W. Urban, J. W. Rich, G. F. Homicz, and M. J. Williams, Anharmonic Vibration-Vibration Pumping in Nitric Oxide by Resonant IR-laser Irradiation, *Chemical Physics*, Vol. 94, 1985, pp. 195-213.
- 13 R. L. Deleon and J. W. Rich, Vibrational Energy Exchange Rates in Carbon Monoxide, *Chemical Physics*, Vol. 107, 1986, pp. 283-292.
- 14 R. Farrenq and C. Rossetti, Vibrational Distribution Function in a Mixture of Excited Isotopic CO Molecules, *Chemical Physics*, Vol. 92, 1985, pp. 401-416.
- 15 A. C. Hindmarsh, LSODE and LSODI, Two Initial Value Ordinary Differential Equation Solvers, *ACM SIGNUM Newsletter*, Vol. 15, 1980, pp. 10-11.
- 16 E. S. Oran and J. P. Boris, *Numerical Simulation of Reactive Flow*, Elsevier Science Publishing Co., New York, 1987.
- 17 G. A. Andronov, A. G. Armer, V. A. Belavin, B. M. Dymshits, Ya. P. Koretskii, and V. F. Sharkov, Gasdynamic Laser Using a CO-Ar Mixture, *Soviet Journal of Quantum Electronics*, Vol. 7, Aug. 1977, pp. 1023-1024.
- 18 J. W. Rich, R. C. Bergman, and J. A. Lordi, Electronically Excited, Supersonic Flow Carbon Monoxide Laser, *AIAA Journal*, Vol. 13, Jan. 1975, pp. 95-101.
- 19 O. Dunn, P. Hartek, and S. Dondes, Isotopic Enrichment of Carbon-13 and Oxygen-18 in the Ultraviolet Photolysis of Carbon Monoxide, *Journal of Physical Chemistry*, Vol. 77, 1973, pp. 878-883.

- 20 V. M. Akulintsev, N. M. Gorshunov, Yu. P. Neshchimenko, A. A. Ostroglazov, A. A. Perov, G. A. Samsonov, A. A. Stepanov, and A. A. Shikanov, Separation of Carbon Isotopes in an Expanding Supersonic Flow, *Soviet Technical Physics Letters*, Vol. 8, March 1982, pp. 119-120.
- 21 V. M. Akulintsev, N. M. Gorshunov, Yu. P. Neshchimenko, and A. A. Shikanov, Isotope Separation in Nonequilibrium Chemically Reacting Supersonic Flows, *Soviet Physics: Technical Physics*, Vol. 29, Aug. 1984, pp. 918-920.
- 22 V. A. Kochelap, I. A. Izmailov and L. Yu. Mel'nikov, The Possibility of Population Inversion and Light Gain Due to Electronic Energy Transfer from  $N_2(A^3\Sigma_u^+)$ , *Chemical Physics Letters*, Vol. 157, Nos. 1-2, 1989, pp. 67-72.
- 23 N. G. Basov, V. F. Gavrikov, S. A. Pozdneev, and V. A. Shcheglov, Possible Expansion of the Spectral Emission Range of Electronic-Transition Chemical Lasers, *Soviet Journal of Quantum Electronics*, Vol. 17, Sept. 1987, pp. 1139-1153.
- 24 W. Urban, J.-X. Lin, V. V. Subramaniam, M. Havenith and J. W. Rich, Treanor Pumping of CO Initiated by CO Laser Excitation, *Chemical Physics*, Vol. 130, 1989, pp. 389-399.
- 25 J. T. Yardley, *Introduction to Molecular Energy Transfer*, Academic Press, New York, 1980.
- 26 P. H. Krupenie, The Band Spectrum of Carbon Monoxide, National Standard Reference Data Series, NSRDS-NBS 5, Washington, 1966.
- 27 V. D. Rusanov, A. A. Fridman, and G. V. Sholin, The Effect of Non-Boltzmann Population of Vibrationally Excited States on the Carbon Reduction in a Nonequilibrium Plasma, *Soviet Physics Doklady*, Vol. 22, No. 12, 1977, pp. 757-759.
- 28 C. Gorse, G. D. Billing, M. Cacciatore, M. Capitelli and S. De Benedictis, Non-equilibrium Vibrational Kinetics of CO Pumped by Vibrationally Excited Nitrogen Molecules: General Theoretical Considerations, *Chemical Physics*, Vol. 111, 1987, pp. 351-360.
- 29 S. De Benedictis, F. Cramarossa and O. V. Achasov, Homogeneous and Heterogeneous CO Chemical Kinetics in Liquid-nitrogen Cooled 5% CO-He Discharges, *Chemical Physics*, Vol. 124, 1988, pp. 91-101.
- 30 K. P. Huber and G. Herzberg, Constants of Diatomic Molecules, *Molecular Spectra and Molecular Structure*, Vol. 4, Van Nostrand Reinhold Co., New York, 1978.

- 31 G. D. Billing, Vibration-Vibration and Vibration-Translation Energy Transfer, Including Multiquantum Transitions in Atom-Diatom and Diatom-Diatom Collisions, *Nonequilibrium Vibrational Kinetics*, Springer-Verlag, Berlin Heidelberg, 1986.
- 32 M. Cacciatore, M. Capitelli and G. D. Billing, Theoretical Semiclassical Investigation of the Vibrational Relaxation of CO Colliding with N<sub>2</sub>, *Chemical Physics*, Vol. 89, 1984, pp. 17-31.
- 33 R. C. Millikan and D. R. White, Systematics of Vibrational Relaxation, *Journal of Chemical Physics*, Vol. 39, Dec. 1963, pp. 3209-3213.
- 34 D. F. McLaughlin and W. H. Christiansen, Isotope Separation and Yield Calculation for Vibrationally Enhanced Oxidation of Nitrogen, *Journal of Chemical Physics*, Vol. 84, March 1986, pp. 2643-2648.
- 35 L. L. Poulsen and G. D. Billing, Vibrational Deactivation of CO(v=1) by p-H<sub>2</sub>. The Importance of the Higher-order Multipole Moments, *Chemical Physics*, Vol. 89, 1984, pp. 219-222.
- 36 G. D. Billing, Vibration/Vibration Energy Transfer in CO Colliding N<sub>2</sub>, *Chemical Physics*, Vol. 50, 1980, pp. 165-173.
- 37 Yu. Akishev, A. V. Dem'yanov, I. V. Kochetov, A. P. Napartovich, S. V. Pashkin, V. V. Ponomarenko, V. G. Pevgov, V. B. Podobedov, Determination of Vibrational Rate Constants in N<sub>2</sub> by Gas Heating, *Teplofizika Vysokikh Temperature*, Vol. 20, No. 5, 1982, pp. 818-827.
- 38 J. W. Rich, R. C. Bergman, M. J. Williams, Vibration to Electronic Energy Transfer Laser, Calspan Report n°6678-A-2, Buffalo, N. Y., April 1984.
- 39 J. C. Stephenson, Vibrational Relaxation of NO X<sup>2</sup>Π(v=1) in the Temperature Range 100-300°K, *Journal of Chemical Physics*, Vol. 60, June 1974, pp. 4289-4294.
- 40 W. D. Breshears and P. F. Bird, Vibrational Relaxation of Nitric Oxide at 500-1,900 K, *Nature*, Vol. 224, Oct. 1969, pp. 268-268.
- 41 R. N. Schwartz and K. F. Herzfeld, Vibrational Relaxation Times in Gases (Three-dimensional Treatment), *Journal of Chemical Physics*, Vol. 22, May 1954, pp. 767-773.
- 42 J. Keck and G. Carrier, Diffusion Theory of Nonequilibrium Dissociation and Recombination, *Journal of Chemical Physics*, Vol. 43, Oct. 1965, pp. 2284-2298.
- 43 W. Q. Jeffers and J. D. Kelley, Calculations of V-V transfer Probabilities in CO-CO Collisions, *Journal of Chemical Physics*, Vol. 55, 1971, pp. 4433-4437.

- 44 R. D. Sharma and C. A. Brau, Energy transfer in Near-resonant Molecular Collisions Due to Long-range Forces with the Application to Transfer of Vibrational Energy from  $\nu_3$  Mode of  $\text{CO}_2$  to  $\text{N}_2$ , *Journal of Chemical Physics*, Vol. 50, Jan. 1969, pp. 924-930.
- 45 J. W. Rich, J. A. Lordi, R. A. Gibson and S. W. Kang, Supersonic Electrically Excited Laser Development, Calspan Report No. WG-5164-A-3, Buffalo, N. W., June 1974.
- 46 A. A. Likalter and G. V. Naidis, On the Vibrational Relaxation of Diatomic Molecules at Intermediate Excitation, *Chemical Physics Letters*, Vol. 59, No. 2, 1978, pp. 365-368.

Table 9.1: Parameters used in the V-T and V-V rate models

species	A <sub>jk</sub>	B <sub>jk</sub>	C <sub>jk</sub>	$\Theta_{jk} / \Theta_j^2$	S <sub>jk</sub> <sup>0</sup>	L <sub>jk</sub> <sup>0</sup>	b <sub>jk</sub>	ref.
CO-CO	-15.23	280.5	-549.6	45.6 x10 <sup>-02</sup>	1.64 x10 <sup>-06</sup>	1.614	7.78 x10 <sup>-31</sup>	[13,31]
CO-N <sub>2</sub>	-7.934	147.7	0	3.295 x10 <sup>-02</sup>	7.006 x10 <sup>-08</sup>	1.897 x10 <sup>-02</sup>	3.69 x10 <sup>-30</sup>	[32,36]
N <sub>2</sub> -N <sub>2</sub>	-12.539	258.9	-390.9	18.495 x10 <sup>-02</sup>	9.37 x10 <sup>-08</sup>	0	1	[31,33,37]
CO-Ar	10.38	0	0	1.335 x10 <sup>-03</sup>	-	-	-	[13]
N <sub>2</sub> -Ar	-15.62	168.95	0	1.335 x10 <sup>-03</sup>	-	-	-	[34]
CO-H <sub>2</sub>	-4.71	62.87	0	3.4175 x10 <sup>-02</sup>	-	-	-	[35]
NO-NO	3.451	-26.182	0	48.78 x10 <sup>-02</sup>	2.428 x10 <sup>-05</sup>	0	1	[12]
NO-CO	-0.658	13.274	0	47.19 x10 <sup>-02</sup>	3.37 x10 <sup>-06</sup>	0	1	[38,39,40]
NO-N <sub>2</sub>	6.4338	0	0	3.525 x10 <sup>-02</sup>	1.55 x10 <sup>-08</sup>	0	1	[38,39,40]
NO-Ar	10.38	0	0	1.335 x10 <sup>-03</sup>	-	-	-	this work

Table 9.2: Parameters used in the V-E rate model

transitions	C <sub>VE</sub>	S <sub>VE</sub> <sup>0</sup>	ref.
CO(X <sup>1</sup> Σ <sup>+</sup> )-CO(a <sup>3</sup> Π)	13.58 x10 <sup>-02</sup>	5.0 x10 <sup>-13</sup>	this work
CO(X <sup>1</sup> Σ <sup>+</sup> )-CO(A <sup>1</sup> Π)	5.49 x10 <sup>-02</sup>	9.94 x10 <sup>-13</sup>	[13]
NO(X <sup>2</sup> Π)-NO(B <sup>2</sup> Π)	8.0 x10 <sup>-02</sup>	3.938 x10 <sup>-10</sup>	[12]



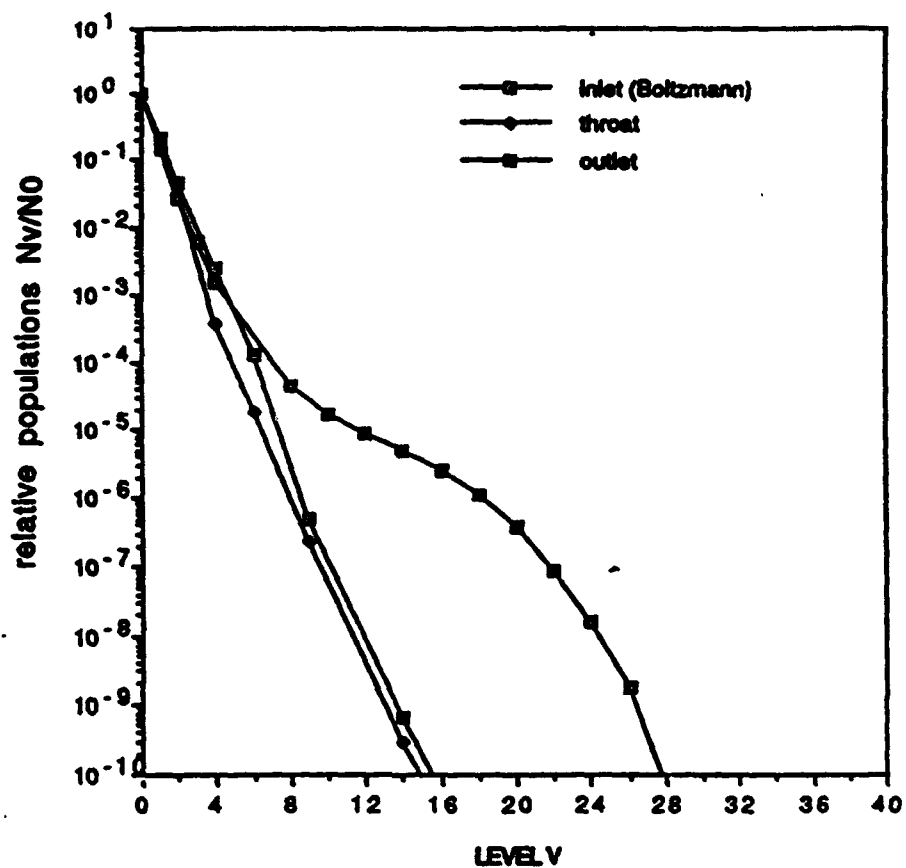


**Figure 9.1: Normalized Vibrational Populations vs. Vibrational Quantum Number.**  
 Pure CO,  $P_0=100$  atm,  $T_0=2000$  K  
 outlet:  $P=17.5$  torr,  $T=199$  K,  $M=7.1$ ,  $A/A^*=110$ .

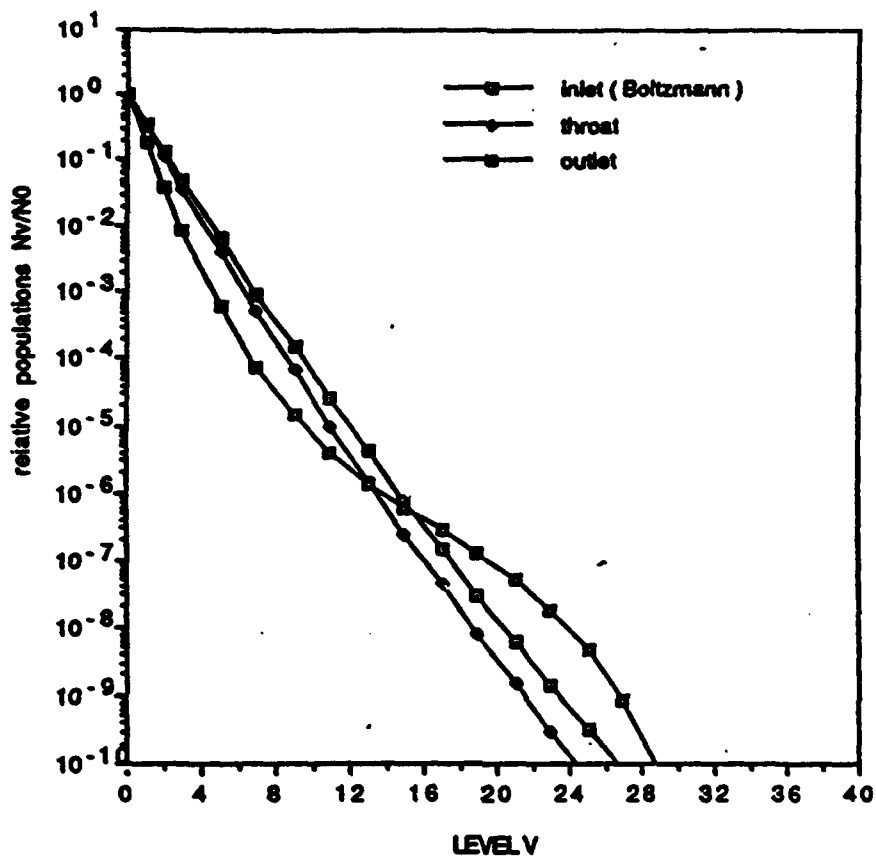


**Figure 9.2: Normalized Vibrational Populations vs. Vibrational Quantum Number.**  
 Pure CO,  $P_0=100$  atm,  $T_0=3000$  K  
 outlet:  $P=17.7$  torr,  $T=327$  K,  $M=6.9$ ,  $A/A^*=110$ .

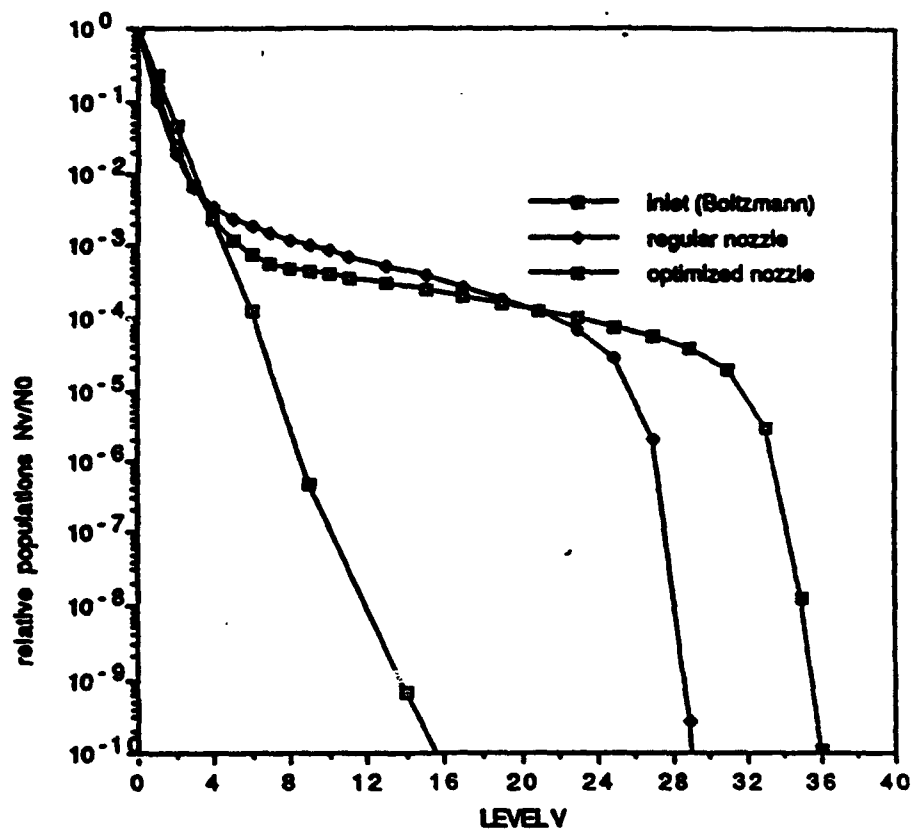


**Figure 9.3: Normalized Vibrational Populations vs. Vibrational Quantum Number.**  
 20%CO-80%Ar  $P_0=100$  atm  $T_0=2000$  K  
 reg. noz. outlet:  $P=5.7$  torr,  $T=59$  K,  $M=11.5$ ,  $A/A^*=111$   
 opt. noz. outlet:  $P=31.4$  torr,  $T=116$  K,  $M=7.8$ ,  $A/A^*=41$ .

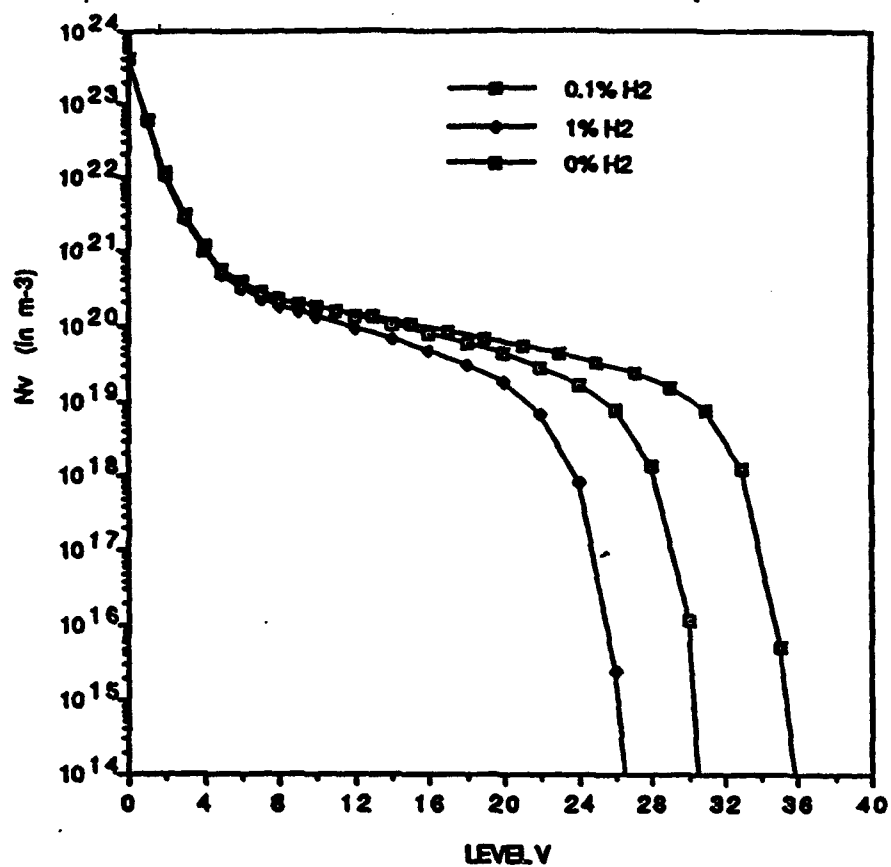


**Figure 9.4:** Vibrational Populations vs. Vibrational Quantum Number.  $\text{H}_2$  impurity influence. CO-Ar- $\text{H}_2$ , optimized nozzle.

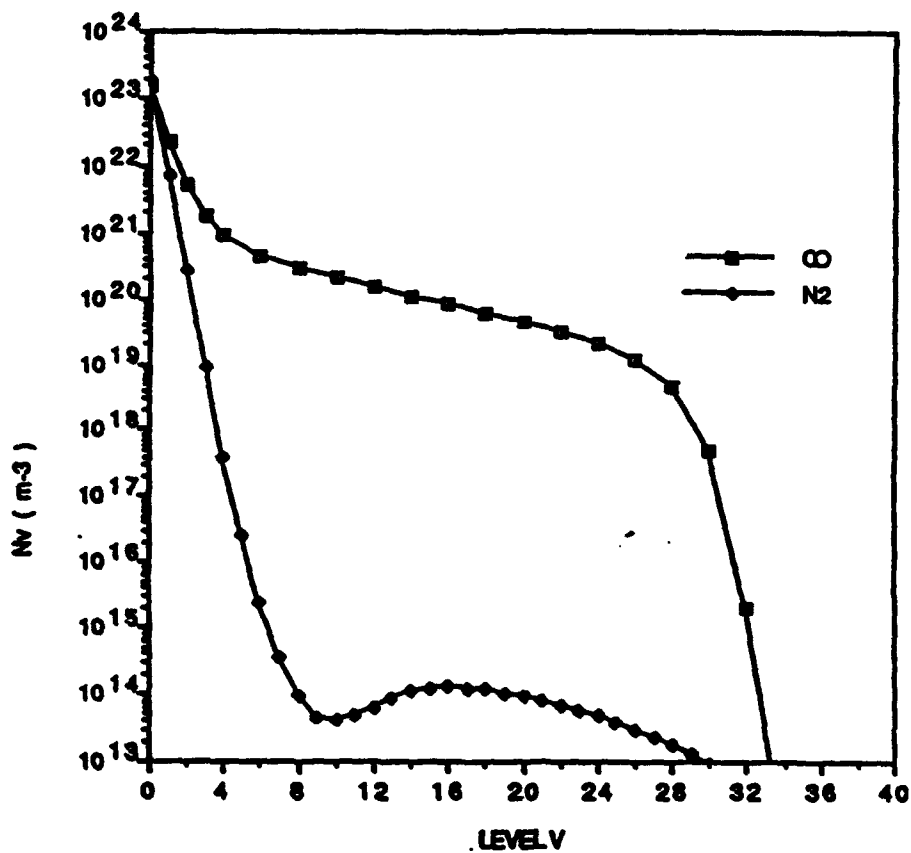


**Figure 9.5: Vibrational Populations  
vs. Vibrational Quantum Number.**  
20%CO-20%N<sub>2</sub>-60%Ar, reg. nozzle.  
outlet: P=8.7 torr, T=90.9 K, M=9.1, A/A\*=111.

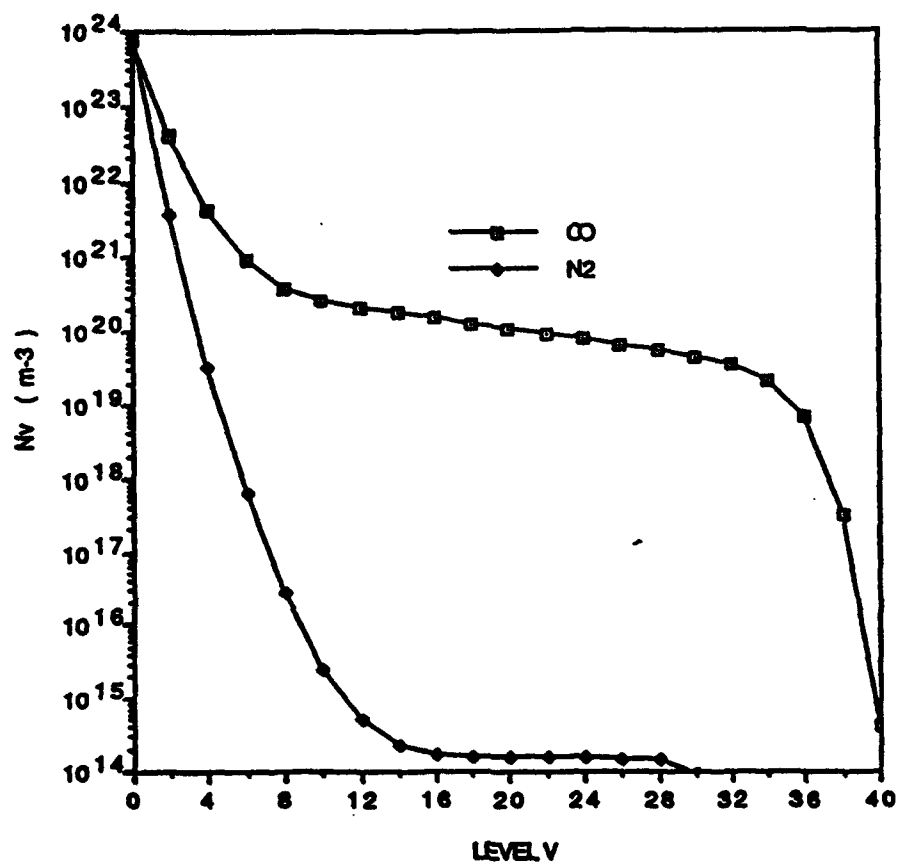


**Figure 9.6: Vibrational Populations  
vs. Vibrational Quantum Number.**  
 20%CO-20%N<sub>2</sub>-60%Ar; opt. nozzle.  
 P=103 torr, T=209 K, M=5.8, A/A\*=22.

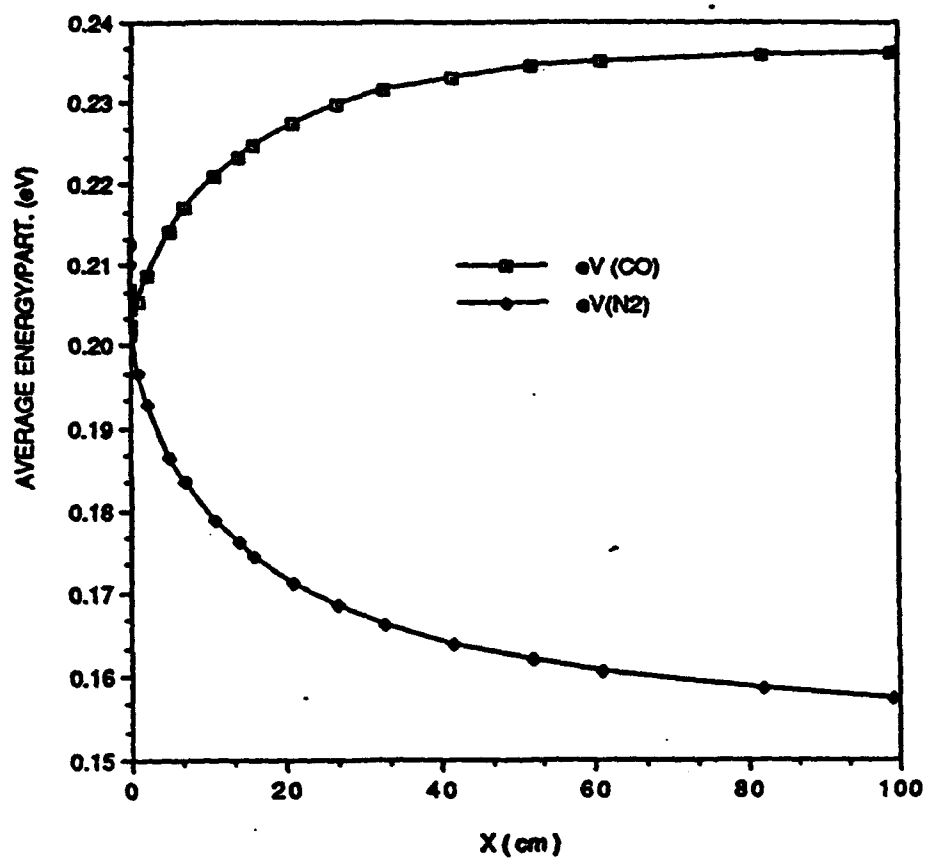


**Figure 9.7-1: Average Vibrational Mode Energy vs. Nozzle Position. Mixture CO-N<sub>2</sub>-Ar.**

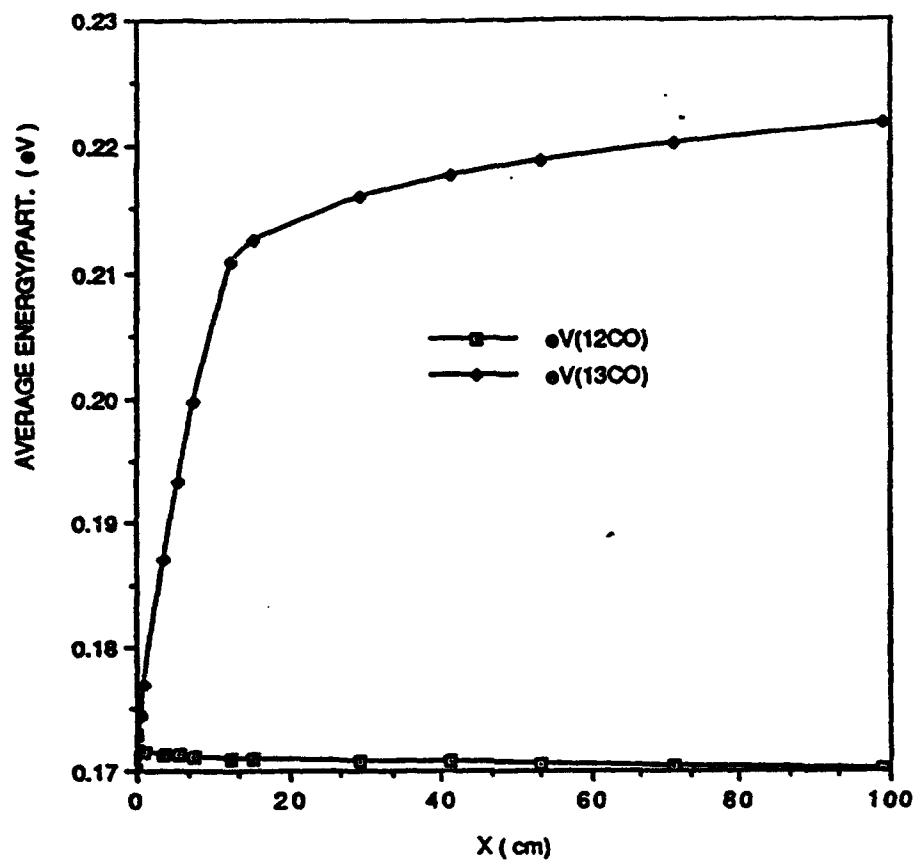


**Figure 9.7-2: Average Vibrational Mode Energy vs. Nozzle Position. Mixture  $^{12}\text{CO}$ - $^{13}\text{CO}$ -Ar.**



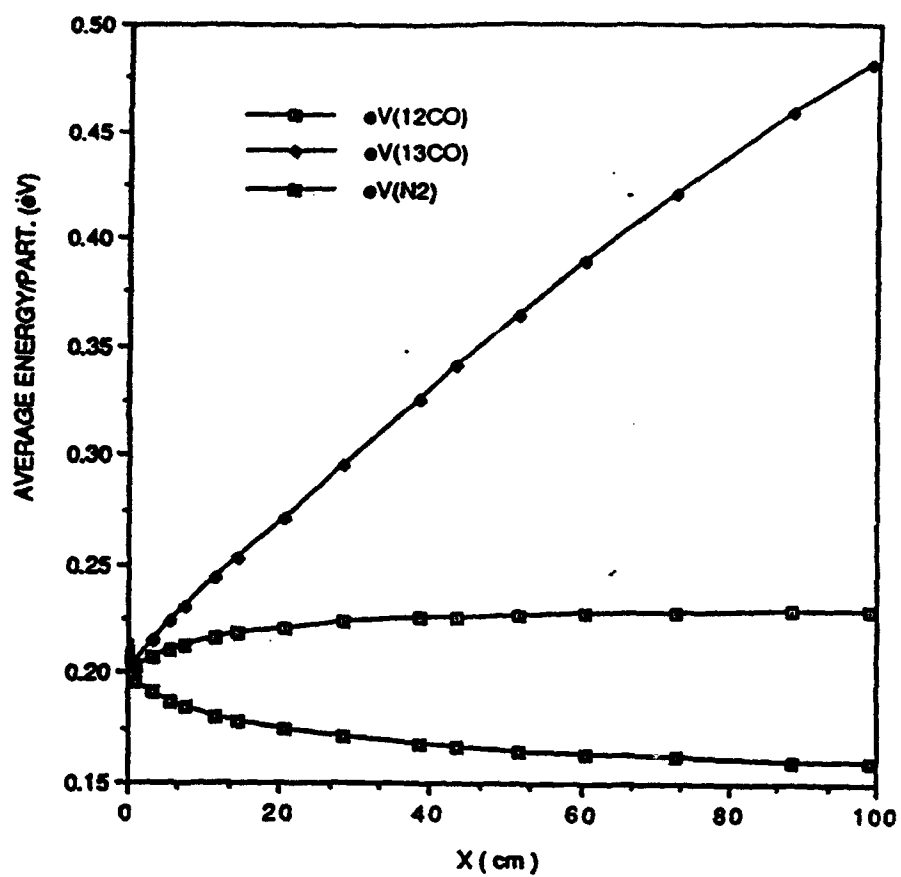


**Figure 9.7-3:** Average Vibrational Mode Energy vs. Nozzle Position. Mixture  $^{12}\text{CO}$ - $^{13}\text{CO}$ - $\text{N}_2$ -Ar.

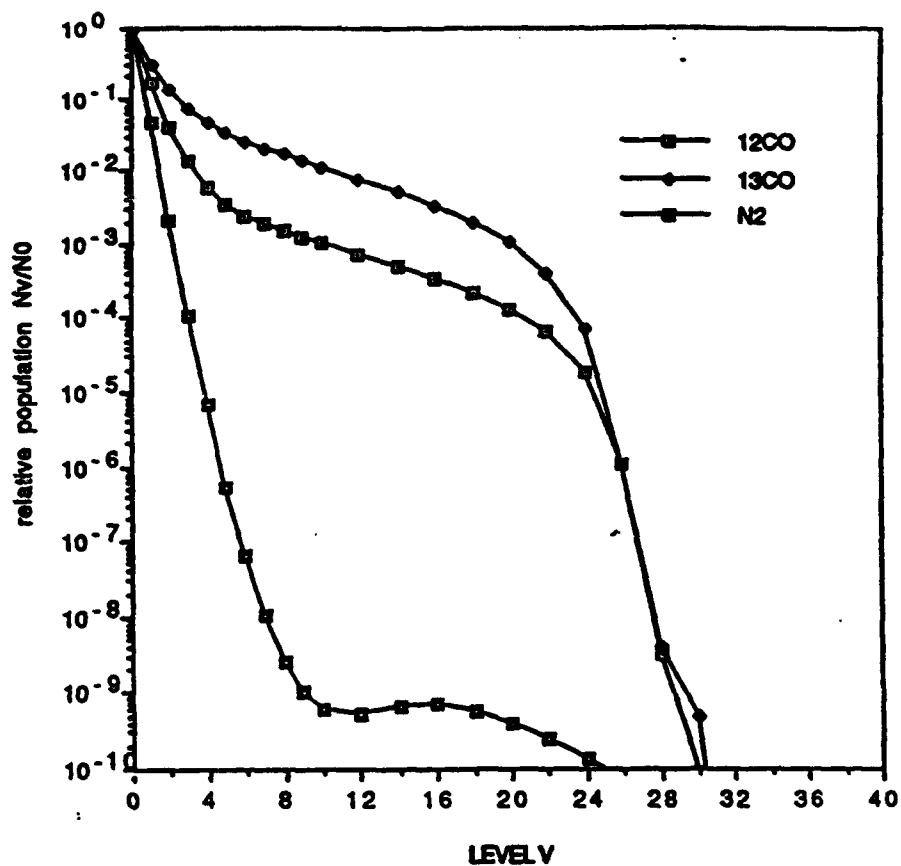


**Figure 9.8:** Normalized Vibrational Populations  
vs. Vibrational Quantum Number.  
25%CO-25%N2-50%Ar.  
outlet: P=8.2 torr, T=109 K, M=8.4, A/A\*=111.

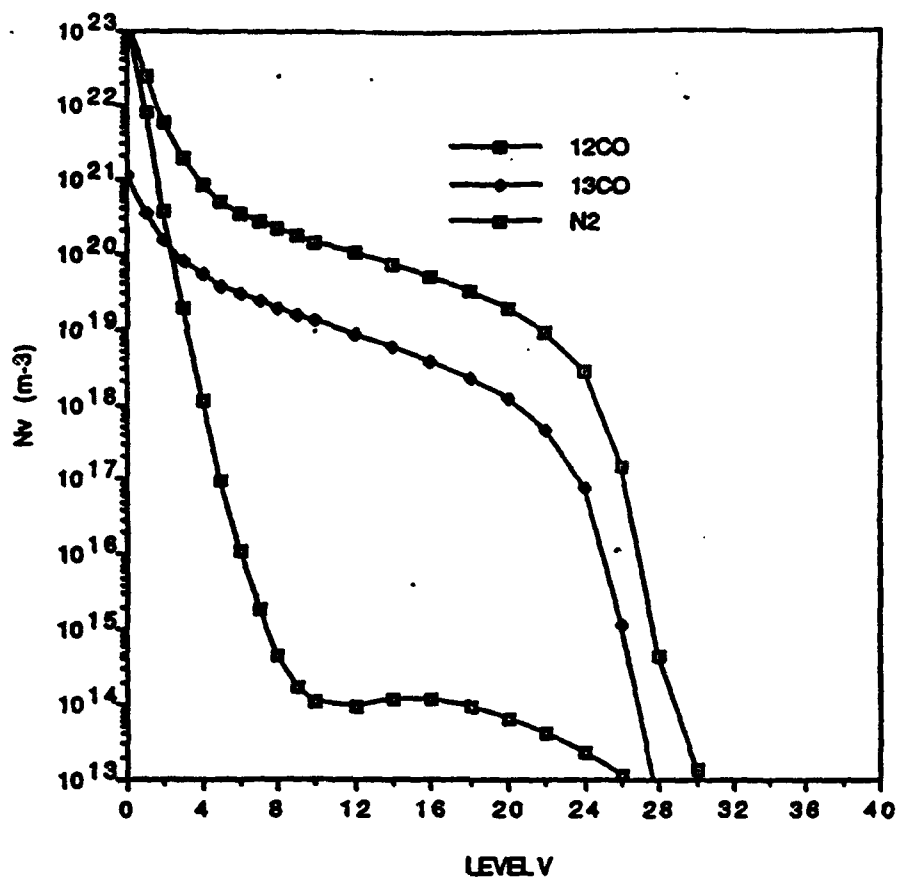


**Figure 9.9: Vibrational Populations  
vs. Vibrational Quantum Number.  
25%CO-25%N2-50%Ar.  
outlet: P=8.2 torr, T=109 K, M=8.4, A/A\*=111.**

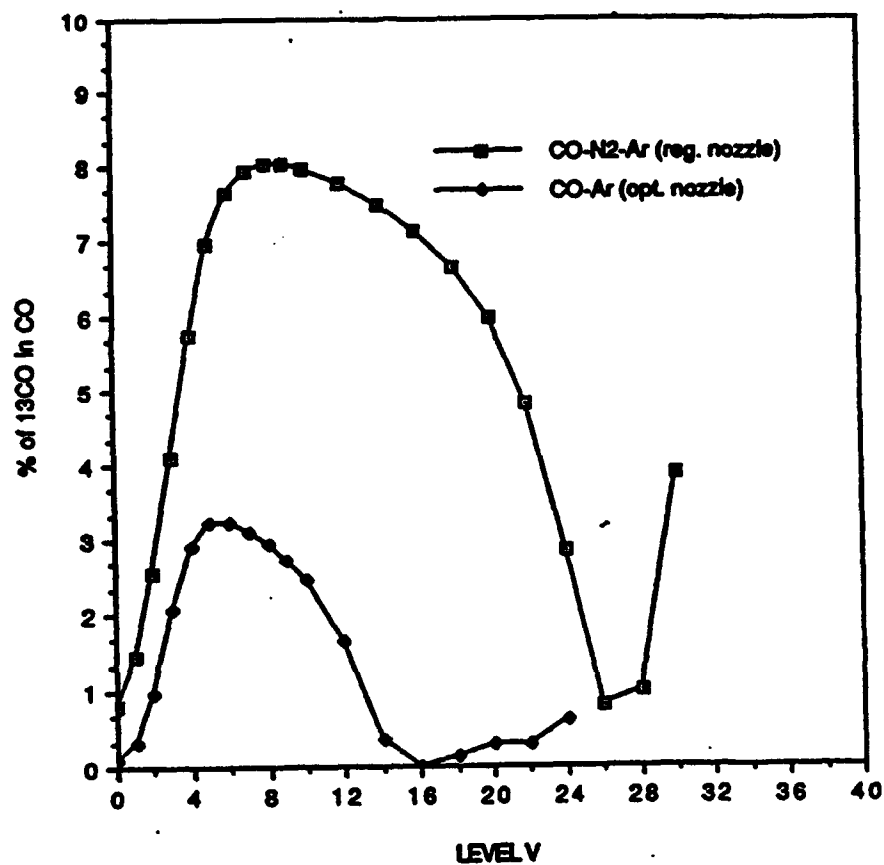


**Figure 9.10:**  $^{13}\text{C}$  Isotopic Enrichment vs. Vibrational Quantum Number. Natural abundance: 1.1%.

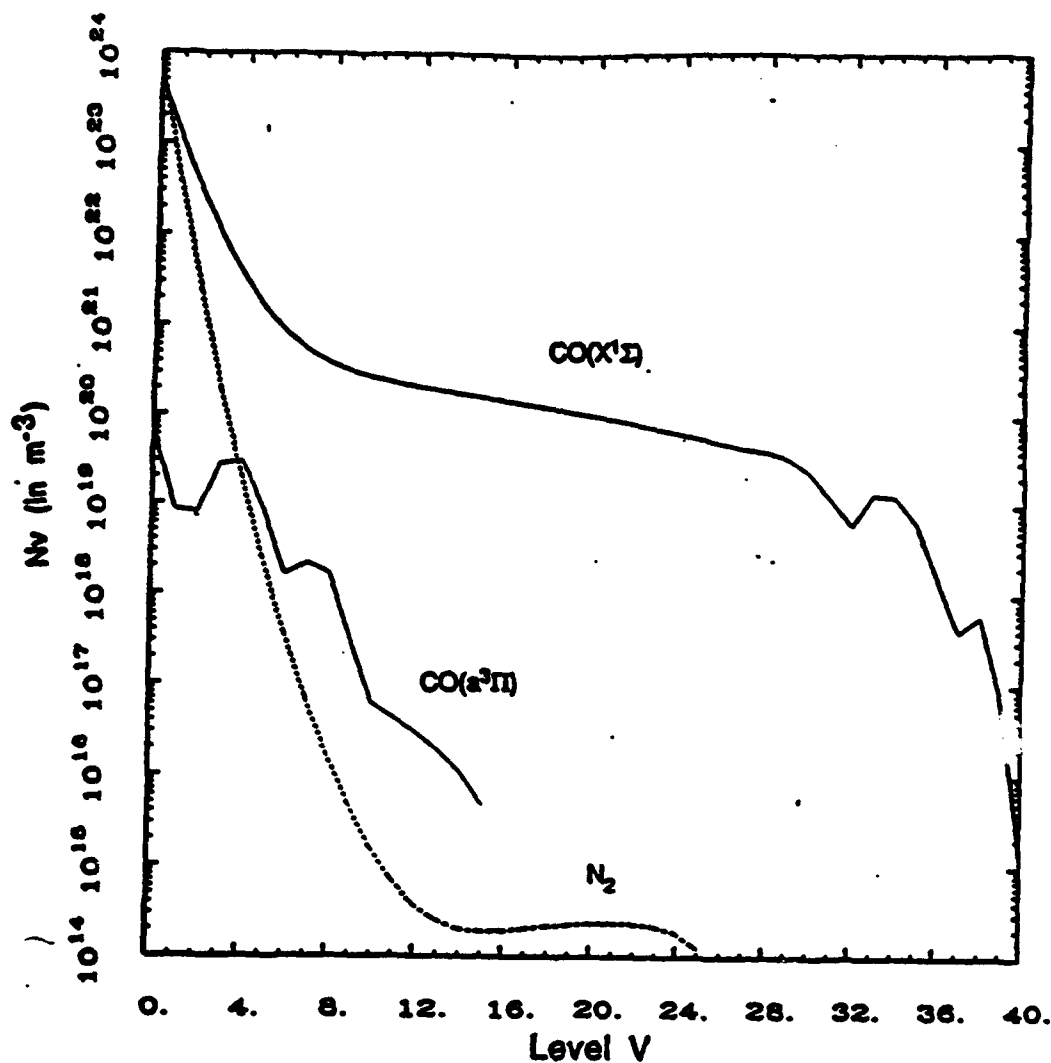


**Figure 9.11: Vibrational Populations vs. Vibrational Quantum Number.**  
 Influence of Excited Electronic States. 10%CO-10%N2-80%Ar.  
 $S_{VE}^0 = 5 \times 10^{-13} \text{ cm}^3/\text{s}$  and  $S_{VE}^0/k_0 = 100$ .

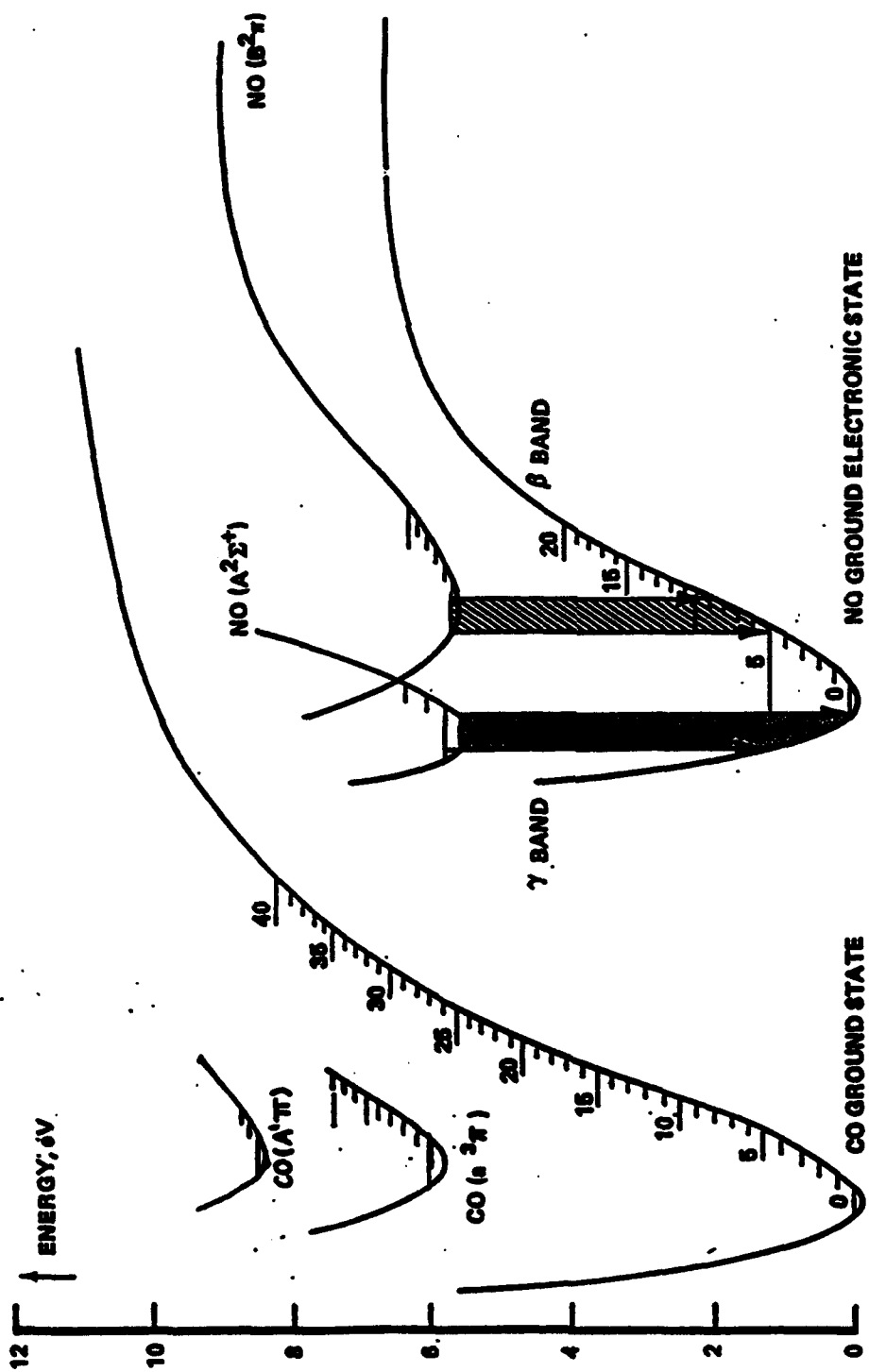


Figure 9.12: CO and NO energy levels

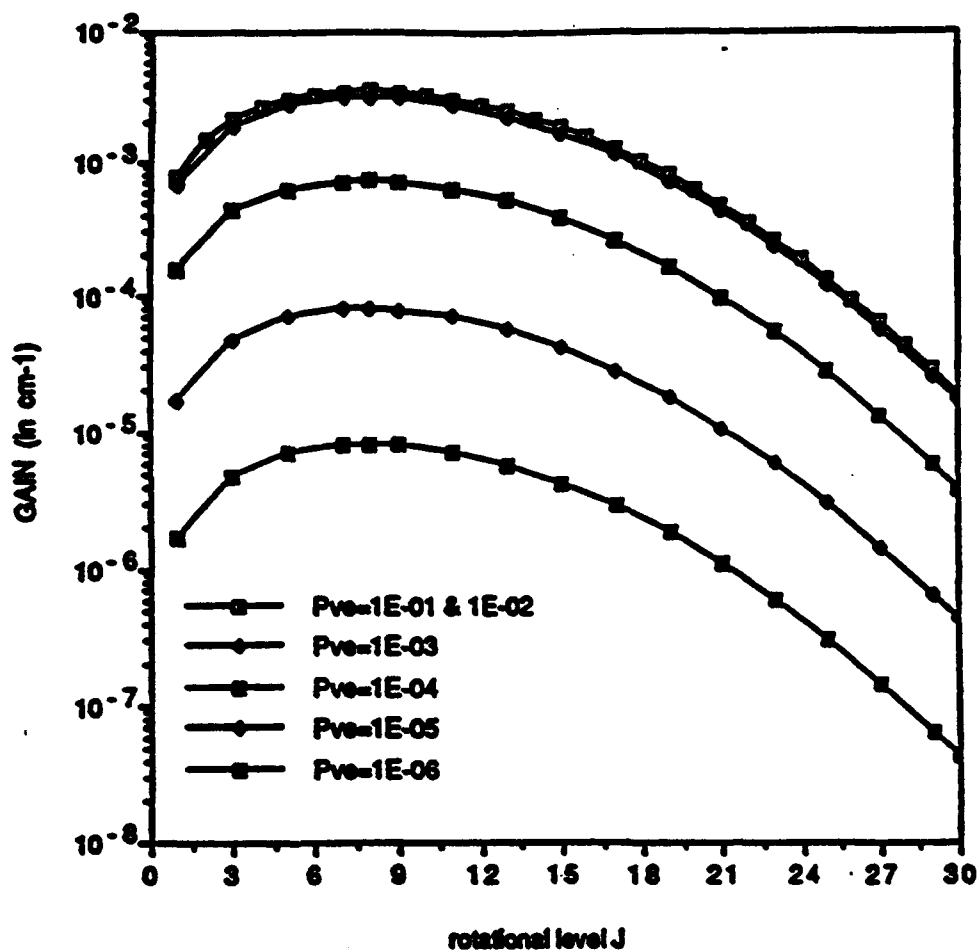


Figure 9.13: CO/NO V-E/E-E Transfer Laser.  
 Small Signal Gain for NO- $\beta$  at 200 K.  
 $\text{NO}(\text{B}^2\Pi, v=0, J) \rightarrow \text{NO}(\text{X}^2\Pi, v=8, J+1)$

**10. MODELING STUDIES II:**

**Nonequilibrium Dissociation Rates Behind Strong Shock Waves  
(classical model)\***

\*This chapter adapted from S.O. Macheret and J.W. Rich, Chem. Phys. 174,  
25 (1993)



## 10.1. INTRODUCTION

Prediction of chemical reaction rates in high temperature gases where the vibrational mode is not in equilibrium with translational/rotational modes remains a persistent problem in chemical physics. With renewed interest in hypersonic gas dynamic phenomena [8-11, 42], such prediction is especially important for dissociation rates of gases behind strong shock waves.

Specifically, gas temperature  $T$  behind bow shocks accompanying reentry spacecraft can reach tens of thousands Kelvins, while vibrational temperature  $T_v$  is considerably (up to an order of magnitude) lower. Under these conditions, nonequilibrium dissociation coupled with vibrational relaxation is crucially important for determining temperature, pressure, chemical composition, and heat fluxes. This has prompted many researchers to construct theoretical models for the dissociation rate coefficient as a function of the translational/rotational and vibrational temperatures.

A major feature of dissociation at  $T > T_v$  and very high  $T$  which makes it qualitatively different from that at low or moderate  $T$  and  $T_v > T$ , and complicates theoretical analysis, is that at very high gas temperatures even molecules in low vibrational levels can dissociate in a single collision, due to the availability of large collision energies. In addition, vibration-vibration (VV) and vibration-translation (VT) energy exchange at such high temperatures are incompletely understood. Common predictive theories of VV and VT rates based on the adiabatic approximation (such as SSH theory [1]) fail at such temperatures.

Early nonequilibrium dissociation models of Hammerling et. al. [2] and Treanor and Marrone [3] were based on several assumptions: (a)

dissociating molecules were modeled by a truncated harmonic oscillator; (b) the vibrational distribution function was assumed to be quasi-Boltzmann with vibrational temperature  $T_v$ ; (c) rotation of molecules was neglected; (d) the dissociation probability was considered to become non-zero as soon as the sum of vibrational ( $E_v$ ) and translational ( $E_t$ ) energies exceeded the dissociation (chemical bond) energy  $D$ ; and (e) dissociation from each vibrational level was assumed to proceed with equal probability provided the translational energy was sufficient.

It was apparent almost immediately, however, that these models were not totally satisfactory and provided an inadequate description of experimental data. For this reason, Marrone and Treanor [4] relaxed assumption (e): to account for preferential dissociation of higher vibrational levels, they suggested that the probability of dissociation of a molecule with vibrational energy  $E_v$  (again, provided translational energy is enough) be proportional to  $\exp(-(D-E_v)/U)$ , where  $U$  is an empirical adjustable parameter. After averaging over vibrational and translational energy distributions, Marrone and Treanor obtained a formula for the rate coefficient  $k(T_v, T)$  which was found to describe satisfactorily experimental data available at that time, provided that the parameter  $U$  was taken about  $1/6$  to  $1/3$  of dissociation energy  $D$ .

Later, Kuznetsov [5, 6, 7] developed a model retaining the abovementioned assumptions (a)-(d), but assuming that the probability of dissociation is zero for molecules below some vibrational level  $N$ , and the probabilities for all levels above  $N$  are equal (in a sufficiently energetic collision). The numerical value of  $N$  was an adjustable parameter. One can note that, since Marrone-Treanor factor  $\exp(-(D-E_v)/T)$  is small at  $E_v < D-U$  and close to unity at  $E_v > D-U$ , Kuznetsov's model is almost the same as that of Marrone and Treanor.

The Marrone-Treanor model has been widely adopted over many years. However, since it sometimes yielded results appreciably deviating from new experimental data, Park [8, 9, 10, 42] suggested an empirical formula for the rate coefficient of nonequilibrium dissociation in the form:

$$k(T_v, T) = AT_a^n \exp\left(-\frac{D}{T_a}\right), \quad (1)$$

where  $A$ ,  $n$  are parameters of the Arrhenius expression for thermal (equilibrium) rate constant, and  $T_a$  is the "average" temperature:

$$T_a = T^s T_v^{1-s} \quad (2)$$

Initially [8, 9], Park suggested  $s=0.5$ . Later, he found that a better fit to computer modeling of vibrational relaxation and dissociation using SSH rates would be provided by using  $s=0.7$  [10].

Since SSH theory, being essentially a near-adiabatic perturbation model and neglecting rotational effects, can not be correctly applied to multiple-jump vibrational transitions at high collision energies and temperatures, then the dissociation modelling in Ref.[10] as well as in [11] is not adequate. In addition, as pointed out in Ref.[11], choosing parameters of the interaction potential slightly different from those used in Ref.[10] can dramatically change the results. (For example, the "bottleneck" effect observed in [10] disappears.) Therefore, Park's model is not based on any microscopic dynamical theory and should be considered as a convenient empirical correlation formula.

In parallel with these simple analytical rate expressions, an extensive literature exists on computer modeling of collision-induced dissociation (CID). Classical [12], quasiclassical [13, 14], and various

quantum calculations [15-33] have been performed to determine dissociation cross-sections for a given vibrational energy of a diatomic molecule and a given kinetic energy of an incident atom. With rare exceptions, these calculations have been specifically for the  $H_2$  molecule colliding with either H or rare gas atoms. Those studies reveal sometimes interesting features in dependence of cross-sections on energies, but their accuracy is still considerably limited by uncertainties of potential energy surfaces other than those performed for the H-H-H potential surface.

With development of computational techniques and hardware, it became possible, in some cases, to perform almost complete modelling of dissociation of a given molecule at a given temperature. Such a study was done, for example, in Ref. [14], where steady-state dissociation of hydrogen in Ar atmosphere was examined for thermal equilibrium conditions at 4500 K. First, several cross-sections for energy transfer and CID were calculated by the quasiclassical trajectory method. Then these cross sections were extrapolated by the information-theory approach [43] for other vibrational and rotational levels and other collision energies. Finally, a master equation was solved with a complete matrix of cross sections, and vibrational populations and dissociation rate were calculated to within a factor of 6.

Although such studies provide important information about high-temperature dissociation phenomena, they can not embrace all possible temperatures and gases. Therefore, there is a need for simple analytical formulae determining rate coefficients and average energy removed per dissociation act as functions of  $T_v$ ,  $T$ , and some easily-determined molecular parameters.

We have seen that existing formulae for the rate coefficient are

either semiempirical (Marrone-Treanor [4]) or empirical (Park [8-10, 42]). In this paper, we present an analytical formula for the rate coefficient based on a very simplified but realistic model of energy transfer in elementary collisions. Several features make this problem solvable.

First, due to the exponential cut-off provided by translational/rotational and vibrational distribution functions, the most important - exponential - part of rate coefficient dependence on  $T_v$  and  $T$  is determined by the threshold energy, i.e., the minimum translational energy above which the dissociation can occur at a given vibrational energy. Second, at higher temperatures (above the characteristic temperature of vibration) and for medium-mass atoms, collision dynamics can be well described by classical mechanics. Third, at the high collision energies which are necessary to dissociate a molecule from low vibrational levels, the collision time is considerably less than the period of vibration, making such a collision close to the impulsive limit.

## 10.2. THRESHOLD LINE CONCEPT

It is well known that the exponential temperature dependence in the Arrhenius formula for thermal reaction rates stems from two simple model assumptions: (1) the reaction cross section  $\sigma$  is zero when the reagent energy  $E$  is below certain threshold  $E_0$  and non-zero when  $E > E_0$ ; (2) energy distribution is Maxwell-Boltzmann with temperature  $T$ . Then, integrating the product of  $\sigma$  and relative velocity with that distribution, we get:

$$k_{\text{Arr}} = A T^n \exp\left(-E_0/T\right) \quad (3)$$

where factors A and n are determined by the cross section behavior above the threshold. Temperature T in this equation and in all subsequent equations throughout this paper is expressed in units of energy.

Suppose now that vibrational and translational/rotational modes are in disequilibrium. For example, one could simply consider the vibrational distribution to be quasi-Boltzmann with some temperature  $T_v$  different from translational (gas) temperature T, and neglect rotation. What then would be the generalization of the Arrhenius formula (1)?

For each vibrational energy,  $E_v$ , the reaction cross section becomes non-zero when kinetic (translational) energy exceeds a certain minimum (threshold) value,  $E_t$ , the latter depending on  $E_v$ :

$$E_t = F(E_v) , \quad (4)$$

where the function  $F(E_v)$  is determined by particular details of collision dynamics. We will refer to the function (4) as a threshold function, or threshold line.

Integrating the product of the cross section  $\sigma(E_v, E_t)$  and relative velocity weighted by distribution functions gives the rate coefficient:

$$k(T_v, T) = (8\mu T/\pi)^{-1/2} \int_0^D \left( \int_{F(E_v)}^{\infty} \sigma(E_v, E_t) E_t \exp(-E_t/T) d\frac{E_t}{T} \right) e^{-E_v/T_v} d\frac{E_v}{T_v} \quad (5)$$

where  $\mu$  is the collision reduced mass.

Due to the exponential cut-off provided by the factor  $\exp(-E_t/T)$ , the internal integral in eqn (5) is determined by the vicinity of the lower integration limit:

$$\int_{F(E_v)}^{\infty} \sigma(E_v, E_t) E_t \exp(-E_t/T) d\frac{E_t}{T} = g(E_v, T) \exp(-F(E_v)/T) \quad (6)$$

where:

$$g(E_v, T) = \sigma(E_v, F(E_v) + \epsilon_1 T) \left( F(E_v) + \epsilon_2 T \right), \quad (7)$$

$\epsilon_1, \epsilon_2$  being numerical factors of the order of 1.

Inserting (6) into (5), we get:

$$k(T_v, T) = (8\mu T/\pi)^{-1/2} \int_0^D g(E_v, T) \exp\left(-\frac{E_v}{T_v} - \frac{F(E_v)}{T}\right) d(E_v/T_v) \quad (8)$$

Again, since the function  $g(E_v, T)$  is less steep than the exponential function in the eqn (8), we can substitute  $g$  by its value  $g^*$  at the point contributing the most to the integral, to get:

$$k(T_v, T) = k_0 \int_0^D \exp\left(-\frac{E_v}{T_v} - \frac{F(E_v)}{T}\right) d(E_v/T_v) \quad (9)$$

where the preexponential factor:

$$k_0 = g^* (8\mu T/\pi)^{-1/2}$$

depends on  $T_v$  and  $T$ , but this dependence is less steep than exponential.

The integral (9) can be evaluated by the method of steepest descent. Namely, we must find a point  $E_v^*$  maximizing the exponent in the integrand. For a monotonically decreasing convex threshold function (4) whose derivative  $F'(E_v)$  takes any negative value, the maximum of the integrand corresponds to the solution of equation:

$$F'(E_v) = -\frac{T}{T_v} \quad (10)$$

If from analysis of collision dynamics we determine the threshold function (4), then solution of equation (10) will give us  $E_v^*$ , the vibrational energy contributing the most to dissociation rate, or, roughly, the mean vibrational energy removed per dissociation act. Then the rate coefficient would be:

$$k(T_v, T) \propto \exp \left( -\frac{E_v^*}{T_v} - \frac{F(E_v^*)}{T} \right) \quad (11)$$

The concept of the threshold line and the procedure of calculating rate coefficients by eqns (4)-(11) have been first suggested by Macheret et.al. [34, 35] for endoergic exchange reactions  $AB+C \rightarrow A+BC$ . Using a classical collinear model at the impulsive limit, Macheret et al., obtained simple formulae for energy consumption as a function of the ratio  $T/T_v$ , and for the rate coefficient  $k(T_v, T)$ . From the previous considerations, however, it is clear that the threshold line concept and eqns(4)-(11) are quite general and valid for nonequilibrium reactions of any kind, including collision-induced dissociation  $AB+C \rightarrow A+B+C$  or  $AB+CD \rightarrow A+B+CD$ .

Before proceeding with particular dynamic calculations, we make two comments:

Dissociation is possible in principle if the reacting system has enough energy, that is,  $E_v + E_t \geq D$ . That does not mean, however, that the threshold line is simply  $E_t = D - E_v$ . Due to dynamic restrictions (such as the simple rebound effect, as we will see later), the true threshold line must lie, at least in part, above the straight line  $E_t = D - E_v$ . Of course, this is strictly true in a classical-mechanical model; a real quantum-mechanical system can react as soon as it has enough energy. However, as we move closer to the classical limit (higher energies, heavier masses), the reaction cross section in the region  $D - E_v < E_t \leq F(E_v)$



must become smaller and smaller, thereby shifting the effective threshold closer to its classical value  $E_t = F(E_v)$ .

Another comment concerns generalization of eqns (4)-(11). First, it may happen, as we will see later, that the absolute value of the derivative  $F'(E_v)$  is limited, and eqn (10) has no solutions at certain  $T/T_v$ . This is due to the oscillator phase effect (see eqns (13)-(17) and the discussion immediately following them). In that case, the integral (5) would be determined mainly by the vicinity of  $E_v = D$ . Second, generalization of the threshold line concept and eqns (8)-(11) to non-Boltzmann vibrational distributions and to including participation of the rotational mode would be simple and straightforward. In fact, we will do exactly this in following sections.

### 10.3. DIATOM-ATOM COLLINEAR IMPULSIVE COLLISIONS

To calculate the rate coefficient and energy consumption, we need to consider some reasonable model of collision dynamics and determine for it the threshold function.

Let us consider first a collinear collision of a homonuclear diatomic molecule, modelled as a classical oscillator, with a structureless particle (atom). We chose the collinear geometry not only because of its simplicity. It is well known that rotational energy is not as effective as vibrational in promoting dissociation due to the effect of the centrifugal barrier [7, 36]. For this reason, we can, in the first approximation, disregard the rotation of the dissociating molecule. For the same reason, in non collinear collisions the component of incident velocity normal to the molecule axis could be used only to excite "inefficient" rotation. In other words, the maximum

efficiency of collisional energy transfer into internal (vibrational) energy, which is exactly what we need to determine the threshold function, corresponds to a head-on, collinear collision.

We next make the very important assumption that the collision is impulsive, that is, instantaneous. To be more specific, the ratio of the characteristic collision time to the period of vibration, that is, the Massey parameter, is considered to be small. This is the opposite to the near-adiabatic approximation commonly used in Landau-Teller or SSH theories of vibrational relaxation. Qualitatively, it is obvious that the Massey parameter should be small for high collision energies. Indeed, if we consider, for example, collision of two nitrogen molecules, then for the relative kinetic energies of the order of 10 eV (which is necessary to dissociate a molecule from low vibrational levels where, as we will see, the threshold function is nontrivial), and characteristic radius of repulsive intermolecular forces  $r_0 \approx 0.1-0.2$  Å, the collision time, as can be easily verified, is about 0.1 of the vibrational period. Note that the validity of the impulsive approximation at or above 10-eV translational energy does not mean that gas temperature should be around 10 eV (110000 K). Even at much lower temperatures  $T$  (but  $T > T_v$ ), the translational energy contributing the most to the dissociation ( $E_t^*$ , see eqn (22)) is of the order of the bond energy  $D$ . Of course, the impulsive approximation is violated for dissociation from very high vibrational levels. However, in that case we will obtain the correct result (see eqn (28) below) coinciding with that of the "ladder" model. Summarizing, we can state that the impulsive approximation should work satisfactorily even at temperatures well below several eV. Thus, the most essential temperature limitation is imposed on our model by the classical approximation: temperatures  $T$  and  $T_v$  must

exceed the characteristic temperature, that is, the vibrational quantum expressed in temperature units (i.e., a few thousand Kelvin or a few tenths of eV).

A classical collinear model at the impulsive (hard-sphere) limit for an atom-diatom collision has been first suggested and extensively studied by Benson et al. [37]. However, Benson et al. were interested mainly in applying this model to the problem of VT relaxation, and they did not try to obtain a formula for dissociation rate at  $T_v < T$ . Later, Fan [12] did apply Benson's hard-sphere model, among other models, to calculations of collision-induced dissociation. But since Fan was trying only to explain experiments by Tully et al. [38] on dissociation of CsBr bombarded by a high-energy Xe molecular beam, he also did not attempt to derive a general formula for  $k(T_v, T)$ . Here, we combine Benson's model of energy exchange with our threshold line concept to derive a formula for the nonequilibrium rate coefficient.

The collinear diatom-atom collision is shown in Fig. 10.1. If we denote the mass of each of two atoms constituting the molecule as  $m$ , the mass of an incident atom as  $M$ , the relative kinetic energy in the center-of-mass system as  $E_t$ , and initial vibrational energy as  $E_v$ , then the atom initial velocity  $u$ , the molecule initial velocity  $v$ , and the amplitude vibrational velocity  $v_0$  of each atom are:

$$u = \frac{2m}{M} \left( \frac{ME_t}{m(M+2m)} \right)^{1/2} ; \quad v = \left( \frac{ME_t}{m(M+2m)} \right)^{1/2} ; \quad v_0 = \left( E_v/m \right)^{1/2} \quad (12)$$

Here the center-of-mass velocities  $u$ ,  $v$  are determined by the obvious momentum and energy relations:  $2mv = Mu$ ;  $E_t = 2mv^2/2 + Mu^2/2$ .

In the center-of-mass system velocities of two atoms constituting the molecule are:  $v - v_0 \cos \varphi$  ("left" atom in Fig. 10.1) and  $v + v_0 \cos \varphi$

("right" atom in Fig. 10.1). Here  $\varphi$  denotes the phase of molecule oscillations at the moment of collision. Of course,  $\cos\varphi$  changes from -1 to +1,  $\cos\varphi=1$  corresponding to the equilibrium distance and maximum velocities of oscillations.

Calculations of the energy transferred in diatom-atom impulsive collision can be done similarly to Benson's derivations [37]. The incident atom collides with the nearest atom of the molecule ("right" atom in Fig. 10.1). Applying conservation of energy and momentum equations, one can determine velocities after collision. Considering then velocities relative to the center of mass of the receding molecule, the final internal (vibrational) energy of the molecule -  $E'_V$  - can be calculated, to give:

$$E'_V = E_V + \frac{M^2 m(u+v)^2}{(M+m)^2} - \frac{Mm}{(M+m)^2} \left( 2m(u+v)v_0 \cos\varphi + (M+2m)v_0^2 \cos^2\varphi \right) \quad (13)$$

Dissociation occurs if  $E'_V$  is equal to or greater than  $D$  - the chemical bond energy. Hence, for given masses  $M$  and  $m$  and initial vibrational energy  $E_V$  (i.e., amplitude vibrational velocity  $v_0$ ) we must find the minimum kinetic energy  $E_t$ , or the minimum relative velocity  $(u+v)$  for the right-hand side of eqn (13) to be equal to  $D$ . The most convenient way to do this is to notice that the maximum  $E'_V$ , i.e., the maximum efficiency of kinetic-to-vibrational energy transfer for given masses and initial energies  $E_V$  and  $E_t$ , corresponds to the minimum value of the expression in square brackets in eqn (13). This bracketed expression,  $y$ , is simply a quadratic function of  $x=\cos\varphi$  with local minimum at the point:

$$x_0 = - \frac{m(u+v)}{(M+2m)v_0} \quad (14)$$

If  $x_0 \geq -1$ ,  $y_{\min}$  corresponds to  $x = x_0$ . However, since  $x = \cos\varphi \geq -1$  always, then in the case  $x_0 < -1$   $y_{\min}$  will correspond to the point  $x = \cos\varphi = -1$ . Therefore, the optimum value of the oscillator phase is:

$$\cos\varphi_{\text{opt}} = \begin{cases} -1 & , \text{ if } \frac{(M+2m)v_0}{m(u+v)} \leq 1 \\ -\frac{m(u+v)}{(M+2m)v_0} & , \text{ if } \frac{(M+2m)v_0}{m(u+v)} \geq 1 \end{cases} \quad (15)$$

Substituting this formula into eqn (13), setting  $E'_v = D$  and solving for  $E_t$ , we obtain the desired threshold function:

$$E_t = F(E_v) = \begin{cases} (\sqrt{D} - \sqrt{\alpha E_v})^2 / (1 - \alpha) & , \text{ if } E_v \leq \alpha D \\ D - E_v & , \text{ if } E_v > \alpha D \end{cases} \quad (16)$$

where:

$$\alpha = \left( \frac{m}{M+m} \right)^2 \quad (17)$$

The threshold line (16) is shown in Fig. 10.2. The behavior of this line is remarkable. When the initial vibrational energy of the molecule is high enough, collision-induced dissociation can occur as soon as the minimum energy requirement is satisfied:  $E_t + E_v \geq D$ . There exists an optimum phase of molecule oscillations at the moment of collision, which ensures the minimum threshold. As the vibrational energy is lowered, the cosine of the optimum phase shifts toward -1 according to eqn (15). However, when the initial vibrational energy  $E_v$  falls below certain value, i.e.,  $E_v < \alpha D$ , the cosine of the optimum phase can no longer decrease and ensure the energetically minimum threshold. So, the cosine stays at -1 (eqn (15)), and the threshold kinetic energy

$E_t$  must be higher than  $(D-E_v)$ .

In fact, the effect we have just obtained can be called the "preferential dissociation" from the higher vibrational levels. This "preferential dissociation" was intuitively felt by Marrone and Treanor [4] and Kuznetsov [5,6] and reflected in their semiempirical models (see Introduction). In our model, however, this effect naturally emerges as a consequence of a realistic, although simplified, microscopic dynamics.

The parameter  $\alpha$  explicitly depends on the ratio  $m/M$  (formula (17)), and it increases with this ratio. Thus, for collision-induced dissociation in the atmosphere of a light gas (large  $m/M$ ), threshold kinetic energy is substantially larger than  $(D-E_v)$  for almost all vibrational levels except very high ones. The physical meaning of this behavior is clear. A light incident particle can transfer only a small fraction of its energy into vibrational mode of a target molecule. Therefore, single-collision dissociation from low vibrational states is inhibited, and the dissociation will occur mainly from high levels with only small collisional energy transfer. This mass effect will be also discussed in later sections in connection with formulae for the rate coefficient.

On the other hand, if  $m/M$  is very small, then the translational energy threshold for almost all vibrational levels except very low ones coincides with the energetically minimum  $(D-E_v)$  values. We will see, however, that it is exactly the region below the "cut-off" energy  $\alpha D$  that determines the dissociation rate coefficient at sufficiently high  $T/T_v$ .

#### 10.4. DISSOCIATION RATE COEFFICIENT AND ENERGY CONSUMPTION FOR DIATOM-ATOM COLLISIONS

As we now have an explicit expression (16), (17) for the threshold function, we need an analytical form for the vibrational distribution function in order to get the dissociation rate.

It is well known that in the quasi-steady-state region of vibrational relaxation behind a shock wave, the population of low vibrational levels can be characterized by a vibrational temperature  $T_v$  different from the gas temperature  $T$  [7, 42]. The main process responsible for forming the vibrational distribution function (VDF) at low levels is quasi-resonant vibration-vibration (VV) energy exchange which results in a Treanor VDF [39]. At high temperatures, however, the deviation of the Treanor VDF from a quasi-Boltzmann one is small, and, therefore, the VDF at low vibrational energies is quasi-Boltzmann. With increasing vibrational energy the rate of vibration-translation (VT) relaxation grows, and above a certain energy  $E_1$  it prevails over VV exchange, thus establishing Boltzmann-like VDF with the slope characterized by the gas temperature  $T$ . At still higher energies, the VDF is depleted by rapid dissociation from the highest levels. Such a behavior of the VDF has been known for a long time; most recently, it was observed in computer modeling [10, 11].

From what has been just said, an analytical form for the VDF is:

$$f(E_v) = \begin{cases} T_v^{-1} \exp\left(-\frac{E_v}{T_v}\right) & , \text{ if } E_v \leq E_1 \\ T_v^{-1} \exp\left(-\frac{E_1}{T_v} - \frac{E_v - E_1}{T}\right) & , \text{ if } E_v > E_1 \end{cases} \quad (18)$$

Of course, this formula does not take into account the depletion of very high levels mentioned above. However, even in the "ladder" model considering dissociation from the highest vibrational level, the effect of the depletion decreases the dissociation rate by only a factor of about 3 [7, 14]. Since, as we will show later, it is the VDF at low levels that influences dissociation at sufficiently high  $T/T_v$ , then the depletion effect must be even less important in our model, and the distribution function (18) is a physically sound approximation.

The energy  $E_1$ , separating the regions of quasi-Boltzmann distributions with temperatures  $T_v$  and  $T$ , is a very important parameter of the VDF (18). To calculate  $E_1$ , a knowledge of VV and VT rates is required. If one knows the dependence of these rates on vibrational energy, then, making VV and VT rates equal to each other and solving the equation thus obtained, one could calculate  $E_1$ . Kuznetsov [7,40] has evaluated  $E_1$  using SSH formulae for VV and VT rates and obtained a very interesting result: within the range of validity of the SSH theory, i.e. at gas temperatures  $T$  from room temperature up to a few thousand Kelvin, the ratio  $E_1/D$  depends only weakly on temperature and molecular parameters, staying close to 0.5. For higher temperatures, there is no analytical theory of VV and VT rates, and the energy  $E_1$  should be determined by quantum-mechanical or quasiclassical computation of these rates for a given molecule. In the present paper, we will consider the ratio  $E_1/D$  as a parameter which, most probably, is about 0.5.

Now, having both the threshold function (16) and VDF (18), we can derive the desired formula for the dissociation rate coefficient. The derivations are performed in exactly the way we obtained eqn (9) from eqn (5), with one generalization: instead of Boltzmann VDF used in the eqn (5) we now take the VDF from eqn (18). Taking also the explicit



expression for the threshold function  $F(E_v)$  from eqn (16), we arrive at the formula:

$$k(T_v, T) = k_0 T_v^{-1} \left( \int_0^{\alpha D} \exp \left( -\frac{E_v}{T_v} - \frac{(\sqrt{D} - \sqrt{\alpha E_v})^2}{(1-\alpha)T} \right) dE_v + \right. \\ \left. + \int_{\alpha D}^{E_1} \exp \left( -\frac{E_v}{T_v} - \frac{D-E_v}{T} \right) dE_v + \right. \\ \left. + \int_{E_1}^D \exp \left( -\frac{E_1}{T} - \frac{E_v-E_1}{T} - \frac{D-E_v}{T} \right) dE_v \right) \quad (19)$$

Here  $k_0$  is a preexponential factor, similar to that in eqn (9), whose dependence on  $T$  and  $T_v$  is less steep than exponential.

An important assumption has been made in deriving formula (19), namely, we assumed:

$$E_1/D > \alpha \quad (20)$$

As was said above, the ratio  $E_1/D$  is about 0.5. The mass parameter  $\alpha$  is determined by formula (17) and simply depends on the mass ratio  $M/m$ . If  $m=M$ , then  $\alpha=0.25$ . As can be easily verified from formula (17),  $\alpha$  can exceed 0.5 only for the case of dissociation in an atmosphere of light atoms or molecules:  $M/m < \sqrt{2} - 1 \approx 0.4$ . Hence, with the exception of dissociation in a helium or hydrogen environment, condition (20) should be valid. We will return to the case when (20) is violated later, but now we proceed with analysis of the formula (19).

The three integrals in (19) have a very clear physical meaning: they correspond to dissociation from low, intermediate, and high vibrational levels, respectively. Therefore, it is convenient to write the rate coefficient  $k(T_v, T)$  as the sum of rate coefficients corresponding to dissociation from low ( $k_l$ ), intermediate ( $k_i$ ), and high

( $k_h$ ) levels:

$$k(T_v, T) = k_l(T_v, T) + k_i(T_v, T) + k_h(T_v, T) \quad (21)$$

### Dissociation from low vibrational levels

The first integral in (19) can be evaluated by the simplest version of the steepest descent method. Maximum value of the integrand corresponds to the following vibrational ( $E_v^*$ ) and translational ( $E_t^* = F(E_v^*)$ ) energies:

$$E_{v,1}^* = \frac{\alpha D}{\left(\alpha + (1-\alpha)T/T_v\right)^2}; \quad E_{t,1}^* = \frac{(1-\alpha)D}{\left(\alpha T_v/T + (1-\alpha)\right)^2} \quad (22)$$

Evaluation of the integral itself yields:

$$k_1(T_v, T) = k_0 \Psi \exp\left(-\frac{D}{\alpha T_v + (1-\alpha)T}\right) \quad (23)$$

where:

$$\Psi = \left(\frac{\pi \alpha (1-\alpha) T T_v D}{\left(\alpha T_v + (1-\alpha)T\right)^3}\right)^{1/2} \quad (24)$$

The rate coefficient (23) has a simple form. The "effective" temperature in the denominator of the exponent is a weighted average of vibrational and translational temperatures, the "weights" being determined by mass ratio of colliding particles (see formula (17)). For example, when  $M=m$ , the contribution of  $T_v$  is  $\alpha=0.25$ , and the contribution of  $T$  is  $1-\alpha=0.75$ . With increasing mass  $M$  of a collision partner, the  $T_v$  contribution decreases while the  $T$  contribution grows.

One might note that formula (23) is somewhat similar to Park's formulae (1), (2). Indeed, both contain some combination of  $T_v$  and  $T$ . However, there are several basic differences. First, the temperature combinations are different. Second, our formula (23) has been derived from a physical model, and the key parameter  $\alpha$  is a specifically identifiable as a simple mass ratio, while Park's model is purely empirical. Finally, formula (23) represents only one limiting case in our theory (dissociation from low vibrational levels), and we will discuss when it can be applied.

One might note that the evaluation of the integral by the steepest descent method introduces a simplification additional to the assumptions already made. However, the integral can be evaluated exactly and expressed through the well-known function:

$$\operatorname{erf}(x) = \frac{2}{\sqrt{\pi}} \int_0^x \exp(-t^2) dt \quad (25)$$

This would give again formula (23) with more exact expression for the  $\Psi$  factor:

$$\begin{aligned} \Psi = & \frac{(1-\alpha)T}{\alpha T_v + (1-\alpha)T} \left[ \exp\left(-\frac{\alpha T_v D}{(1-\alpha)T[\alpha T_v + (1-\alpha)T]}\right) - \exp\left(-\frac{\alpha(1-\alpha)D(T-T_v)^2}{T_v T[\alpha T_v + (1-\alpha)T]}\right) \right] + \\ & + \left[ \frac{\pi \alpha(1-\alpha) T T_v D}{(\alpha T_v + (1-\alpha)T)^3} \right]^{1/2} \left[ \operatorname{erf}\left(\frac{\alpha T_v D}{(1-\alpha)T[\alpha T_v + (1-\alpha)T]}\right)^{1/2} + \operatorname{erf}\left(\frac{\alpha(1-\alpha)D(T-T_v)^2}{T_v T[\alpha T_v + (1-\alpha)T]}\right)^{1/2} \right] \end{aligned} \quad (26)$$

Later we will check the accuracy of the steepest descent evaluation of the integral by comparing rate coefficients calculated with eqn (24) or (26) for the  $\Psi$  factor.

## Dissociation from intermediate and high vibrational levels

Evaluation of the second and third integrals in eqn (19) is trivial, and it yields:

$$k_1(T_v, T) = k_0 \frac{\exp(-D/T)}{1 - T_v/T} \left[ \exp\left(-\alpha D \left(\frac{1}{T_v} - \frac{1}{T}\right)\right) - \exp\left(-E_1 \left(\frac{1}{T_v} - \frac{1}{T}\right)\right) \right] \quad (27)$$

$$k_h(T_v, T) = k_0 \frac{D-E_1}{T_v} \exp\left(-\frac{E_1}{T_v} - \frac{D-E_1}{T}\right) \quad (28)$$

It is worth noting that  $k_h$  in the form (28) is very similar to the rate coefficient obtained by Kuznetsov [7, 40] for the "ladder" model of dissociation.

## Evaluation of the preexponential factor $k_0$ and numerical estimates

Exact evaluation of the preexponential factor  $k_0$  requires more detailed investigation of collision dynamics, particularly post-threshold behavior of reaction cross-sections. This is beyond the scope of the present paper. However, at this point we can impose a condition which  $k_0$  must satisfy. Namely, for thermal equilibrium at  $T_v=T$ , the rate coefficient, that is, the sum (21) of  $k_1$ ,  $k_i$  and  $k_h$ , must coincide with the Arrhenius rate constant (3) with experimentally measured parameters  $A$  and  $n$ , and  $E_0=D$ .

Note that eqn (27) for  $k_1$  formally gives an uncertainty 0/0 at  $T_v=T$ . However, calculating the limit of  $k_1$  as  $T_v \rightarrow T$  gives a finite value. With this comment, demanding that the sum (21) be equal to the

Arrhenius rate constant (3) at  $T_v=T$  gives an expression for  $k_0$  at this limit:

$$k_0 = \frac{A T^{n+1}}{(1-\alpha)D + \sqrt{\pi\alpha(1-\alpha)}DT} \quad (29)$$

if the  $\Psi$  factor is evaluated by the eqn (24), and:

$$k_0 = \frac{A T^{n+1}}{(1-\alpha) \left[ D + T \left( \left( \frac{\pi\alpha D}{(1-\alpha)T} \right)^{1/2} \operatorname{erf} \left( \frac{\alpha D}{(1-\alpha)T} \right)^{1/2} + \exp \left( - \frac{\alpha D}{(1-\alpha)T} \right) - 1 \right] \right]} \quad (30)$$

if the  $\Psi$  factor is evaluated by the eqn (26).

The formulae just obtained give a value of  $k_0$  only at  $T_v=T$ . However, since the main dependence of the rate coefficient  $k(T_v, T)$  on  $T_v$  is due to the exponential factor, we can, in the first approximation, disregard the  $k_0$  dependence on  $T_v$  and use eqn (29) or (30) to estimate the preexponential factor for all  $T_v$  at a given  $T$ .

We have made numerical calculations of the dissociation rate coefficient of nitrogen at a fixed translational temperature  $T=10000$  K and for different vibrational temperatures. The parameters were set to  $\alpha=0.25$  (i.e.,  $m=M$ ) and  $E_1/D=0.5$ ; the Arrhenius rate parameters  $A$  and  $n$  were taken from Ref.[10]. Calculations were made both by "exact" evaluation of  $\Psi$  and  $k_0$  (eqns (26),(30)) and by using the steepest descent method (eqns (24),(29)). Fig. 10.3 depicts the rate coefficient calculated by the present model; for comparison, rate coefficients given by the Park and the Marrone-Treanor empirical models are also shown. Fig. 10.4 shows the contribution of dissociation from low, intermediate and high vibrational levels to the overall dissociation rate, expressed as:

$$\chi_l = k_l/k ; \chi_i = k_i/k ; \chi_h = k_h/k \quad (31)$$

Fig. 10.4 is illustrative of the physical processes of dissociation. It is clear that at sufficiently low vibrational temperatures there are very few molecules having energies close to the dissociation energy  $D$ . Therefore, the only dissociation processes that can occur under such conditions are those with large collisional energy transfer from the "hot" translational energy reservoir. Increasing vibrational temperature produces more molecules on high vibrational levels and enhances the role of dissociation from these levels with relatively small collisional energy required. Exactly this behavior is reflected in Fig. 10.4. When vibrational temperature is less than about one-half of the translational temperature, dissociation occurs predominantly from low vibrational levels ( $k_l \gg k_i, k_h$ ). At higher  $T_v$ , the contribution of  $k_l$  continuously falls, while the contribution of  $k_h$  and  $k_i$  grows. At equilibrium,  $T_v = T$ , the proportion between the three contributions well reflects the widths of the energy intervals which we called low, intermediate, and high levels:  $k_l:k_i:k_h \approx (\alpha D):(E_1 - \alpha D):(D - E_1) = 0.25:0.25:0.5$ . In other words, at thermal equilibrium each vibrational level contributes almost equally to the overall dissociation rate.

We can now better understand Fig. 10.3. At sufficiently high vibrational temperatures dissociation from high levels is dominant, and the slope of the curve  $\log k(T_v)$  is dictated by the parameter  $E_1/D = 0.5$ . At the same time, the slope of the curve calculated with Park's formula is determined at sufficiently high  $T_v$  by the parameter  $1-s$ . Therefore, making  $s$  equal to 0.5 should give a good agreement between Park's model and ours at high vibrational temperatures, which is indeed clearly seen in Fig. 10.3. Lowering vibrational temperature leads to predominant role of the dissociation from low vibrational levels, where the slope of the

curve  $\log k(T_v)$  is determined by the mass parameter  $\alpha$  (see eqn (23)). Since for the case of equal masses  $\alpha=0.25$  (see eqn (17)), then making the Park's empirical parameter  $s$  equal to 0.7, so that  $1-s=0.3$ , should give a good enough agreement with our model, which is again clearly seen in Fig. 10.3.

#### Vibrational energy removed in dissociation

Analysis of nonequilibrium shock flows requires not only rate coefficients, but also the mean energy removed from the vibrational mode in each dissociation act. The present model allows this energy,  $E_{rem}$ , to be calculated:

$$E_{rem} = k_0 T_v^{-1} \left( \int_0^{\alpha D} E_v \exp \left( -\frac{E_v}{T_v} - \frac{(\sqrt{D}-\sqrt{\alpha E_v})^2}{(1-\alpha)T} \right) dE_v + \right. \\ \left. + \int_{\alpha D}^{E_1} E_v \exp \left( -\frac{E_v}{T_v} - \frac{D-E_v}{T} \right) dE_v + \right. \\ \left. + \int_{E_1}^D E_v \exp \left( -\frac{E_1}{T} - \frac{E_v-E_1}{T} - \frac{D-E_v}{T} \right) dE_v \right) k(T_v, T) \quad (32)$$

The second and third integrals in (32) can be evaluated exactly, and the first one - by the method of steepest descent, to give:

$$\begin{aligned}
E_{\text{rem}} = & \frac{k_0}{k(T_v, T)} \left[ \alpha D \left( \frac{T_v}{\alpha T_v + (1-\alpha)T} \right)^3 \left( \frac{\pi \alpha (1-\alpha) T T_v D}{\alpha T_v + (1-\alpha)T} \right)^{1/2} \exp \left( - \frac{D}{\alpha T_v + (1-\alpha)T} \right) + \right. \\
& + \frac{\left[ 1 + \alpha D \left( \frac{1}{T_v} - \frac{1}{T} \right) \right] \exp \left( - \alpha D \left( \frac{1}{T_v} - \frac{1}{T} \right) \right) - \left[ 1 + E_1 \left( \frac{1}{T_v} - \frac{1}{T} \right) \right] \exp \left( - E_1 \left( \frac{1}{T_v} - \frac{1}{T} \right) \right)}{\left( \frac{1}{T_v} - \frac{1}{T} \right)^2} \times \\
& \times \exp \left( - D/T \right) + \frac{1}{2} \left( D^2 - E_1^2 \right) \exp \left( - \frac{E_1}{T_v} - \frac{D-E_1}{T} \right) \Bigg] . \quad (33)
\end{aligned}$$

where  $k_0$  and  $k(T_v, T)$  are the preexponential factor and the overall rate coefficient calculated earlier.

The mean energy removed per dissociation act as a fraction of the dissociation energy  $D$  is plotted in Fig. 10.5 vs. vibrational temperature at different constant gas temperatures. In accordance with the previous discussion, the contribution of high vibrational levels to the overall dissociation rate grows with increasing  $T_v$ . This naturally leads to a continuously increasing  $E_{\text{rem}}/D$ , as seen in Fig. 10.5. Since, as pointed out in the previous subsection, at thermal equilibrium ( $T_v = T$ ) all vibrational levels contribute almost equally to the dissociation rate, then the value of  $E_{\text{rem}}/D$  should be close to  $1/2$  at  $T_v = T$ , which is indeed seen in Fig. 10.5.

#### Extension to the case $(E_1/D) < \alpha$ . Mass effect

Now we will briefly show how the results just obtained can be extended to the case  $(E_1/D) < \alpha$ , that is, when condition (20) is violated. The general expression for the rate coefficient in this case is similar



to eqn (19), only with different limits of integration:

$$\begin{aligned}
 k(T_v, T) = k_0 T_v^{-1} & \left( \int_0^{E_1} \exp \left( -\frac{E_v}{T_v} - \frac{(\sqrt{D} - \sqrt{\alpha E_v})^2}{(1-\alpha)T} \right) dE_v + \right. \\
 & + \int_{E_1}^{\alpha D} \exp \left( -\frac{E_1}{T_v} - \frac{E_v - E_1}{T} - \frac{(\sqrt{D} - \sqrt{\alpha E_v})^2}{(1-\alpha)T} \right) dE_v + \\
 & \left. + \int_{\alpha D}^D \exp \left( -\frac{E_1}{T_v} - \frac{E_v - E_1}{T} - \frac{D - E_v}{T} \right) dE_v \right) \quad (34)
 \end{aligned}$$

These integrals can be evaluated in a way similar to the integrals evaluated before for eqn (19). Instead of doing this, we will discuss qualitatively results that would be obtained.

The third and second integrals together give the rate coefficient for dissociation from high and intermediate levels in about the same form as eqns (27), (28), with slightly different preexponential factors. As to the first integral (dissociation from low levels), it can again yield the rate coefficient in the form (23) provided the energy  $E_{v,1}^*$  lies within the limits of integration, that is, when:

$$\frac{T}{T_v} > \frac{\sqrt{\alpha D/E_1} - \alpha}{1 - \alpha} \quad (35)$$

In order for dissociation from low levels to play any significant role, the temperatures must at least satisfy the inequality (35), which may be a strict limitation. This reflects the mass effect.

As was mentioned above, the mass parameter  $\alpha$  can be greater than  $E_1/D$  for dissociation in collisions with light species. It is obvious that a light incident particle can lose only a small part of its kinetic

energy in a collision with a molecule. In other words, if initial vibrational energy is low, then, in order to produce dissociation, kinetic energy of the light particle must be substantially higher than that in the case of equal masses, thereby diminishing the probability of such a dissociation. If, however, the molecule already has large vibrational energy, then the required additional kinetic energy is small and can be delivered in a single collision. Thus, diminishing the mass  $M$  of a collision partner and hence increasing the parameter  $\alpha$  would favor dissociation from higher vibrational levels.

This effect is clearly confirmed by the threshold line (16), (17) (see also Fig. 10.2), where the "cut-off" parameter  $\alpha D$  shifts toward higher energies with decreasing  $M$ . It would be also confirmed by calculations of the rate coefficient in the case  $\alpha > (E_1/D)$ . Indeed, in this case, for low-level dissociation to prevail, the ratio  $T/T_v$  must satisfy the inequality (35). For example, for nitrogen dissociation in collisions with hydrogen atoms, when  $M/m=1/14$ , so  $\alpha=0.87$ , then with  $E_1/D=0.5$  the inequality (35) gives:  $T/T_v > 3.5$ . At higher  $T_v$  the dissociation from low levels can play only a minor role. In addition, as can be seen from eqn (23) for  $k_1$ , increasing parameter  $\alpha$  enhances the  $T_v$  contribution to the rate-determining combination  $\alpha T_v + (1-\alpha)T$ , which results in sharper decrease of  $k_1$  with decreasing  $T_v$  and widens the temperature range of prevailing dissociation from high vibrational levels.

## 10.5. DISSOCIATION IN DIATOM-DIATOM COLLISIONS

So far we considered dissociation only in diatom-atom collisions. However, in a real gas which is not largely dissociated, molecules

collide mainly with molecules. In this section, we extend our theory to dissociation in diatom-diatom collisions.

Let us consider first a collinear collision of two diatomic homonuclear molecules, one consisting of atoms of mass  $m$  each and initially having vibrational energy  $E_v$ , and the other consisting of atoms of mass  $M$  each and non-vibrating. This collision is shown in Fig. 10.6a. The reason for considering a collision partner with zero initial vibrational energy is that when vibrational relaxation is not yet completed, so that  $T_v < T$ , collisions with non-excited molecules are by far more probable than collisions with excited ones. More exact justification will be provided later in this section.

The same procedure as was used in analysis of diatom-atom collisions now results in a formula for the final internal energy  $E'_v$  of the "left" molecule exactly coinciding with the eqn (13) for diatom-atom case. Only velocities  $u$  and  $v$  are different from (12), namely:

$$u = \frac{m}{M} \left( \frac{ME_t}{m(M+m)} \right)^{1/2} ; \quad v = \left( \frac{ME_t}{m(M+m)} \right)^{1/2} \quad (36)$$

Now we are able to obtain the desired threshold function, but due to the difference between (12) and (36), it is somewhat different from the function (16):

$$E_t = F(E_v) = \begin{cases} (\sqrt{D} - \sqrt{\alpha E_v})^2 / (1 - \sqrt{\alpha}) , & \text{if } E_v \leq \alpha D \\ (1 + \sqrt{\alpha})(D - E_v) , & \text{if } E_v > \alpha D \end{cases} \quad (37)$$

This threshold line is depicted in Fig. 10.7. One can see that, in contrast to the threshold line for the diatom-atom case (Fig. 10.2),

this line lies entirely above the energetically minimum line  $E_t + E_v = D$ .

The physical reason for this behavior is simple. Since (at least, in the impulsive limit considered) the collision actually occurs only between the two atoms closest to each other, kinetic energy of the "far" atom of the incident molecule can not be used for the desired excitation and dissociation. Hence, to produce dissociation, a higher translational energy  $E_t$  is required as compared to the diatom-atom case.

Is it possible to suggest some other mechanism that would yield a lower threshold line coinciding in some part with the energetically minimum line  $E_t + E_v = D$ ? To do this, the atom of an incident molecule immediately hitting the dissociating molecule must be supplied with additional energy from a source other than translational motion. And such a source does exist: rotational motion.

Obviously, the rotational energy will be used with maximum efficiency if rotational velocity of the atom hitting the dissociating molecule is added to its velocity in translational motion. In this sense, the collinear configuration is the worst, because there is no component of rotational velocity along the dissociating molecule axis.

Therefore, we need to abandon the collinear model and consider possible non collinear geometry. Again, since we are looking for the lowest possible threshold and therefore need to have the maximum possible rotational velocity component along the axis of dissociating molecule, it is clear that the best configuration is when the incident molecule axis is perpendicular to the axis of the dissociating molecule, as shown in Fig. 10-6b.

Repeating derivations that led to eqns (16), (37), but with additional rotational velocity  $v_r = \sqrt{E_r/M}$  of the incident atom, we obtain a generalized threshold function, that is, the minimum translational

energy necessary to produce dissociation, as a function of initial vibrational energy of the dissociating molecule and rotational energy ( $E_r$ ) of its collision partner:

$$E_t = F(E_v) = \begin{cases} \left( \sqrt{D - \sqrt{\alpha} E_v} - \sqrt{(\sqrt{\alpha} - \alpha) E_r} \right)^2 / (1 - \sqrt{\alpha}) & , \text{ if } E_v \leq \alpha D \\ \left( \sqrt{(1 + \sqrt{\alpha})(D - E_v)} - \sqrt{\sqrt{\alpha} E_r} \right)^2 & , \text{ if } E_v > \alpha D \end{cases} \quad (38)$$

Naturally, at  $E_r = 0$  this formula reduces to (37), but at  $E_r > 0$  the threshold value of  $E_t$  is lower than that given by eqn (37), as was expected.

Now we proceed with calculations of the rate coefficient. For convenience, we will show intermediate results for microscopic rate coefficients, that is, averaged only over translational and rotational energy distributions, but not averaged yet over vibrational one.

As before, we neglect dependence of preexponential factors on energy and/or temperature, and use the method of steepest descent to evaluate integrals.

Integration over translational energy with the threshold function (38) gives:

$$k(E_v, E_r, T) = \begin{cases} k'_0 \exp \left( - \frac{\left( \sqrt{D - \sqrt{\alpha} E_v} - \sqrt{(\sqrt{\alpha} - \alpha) E_r} \right)^2}{(1 - \sqrt{\alpha}) T} \right) & , \text{ if } E_v \leq \alpha D \\ k'_0 \exp \left( - \frac{\left( \sqrt{(1 + \sqrt{\alpha})(D - E_v)} - \sqrt{\sqrt{\alpha} E_r} \right)^2}{T} \right) & , \text{ if } E_v > \alpha D \end{cases} \quad (39)$$

Now we integrate over rotational energy, assuming the rotational distribution function to be quasi-Maxwellian with some temperature  $T_r$ :

$$k(E_v, T_r, T) = \begin{cases} k'_0 \exp \left( - \frac{(\sqrt{D} - \sqrt{\alpha} E_v)^2}{(1-\alpha)(T + \sqrt{\alpha} T_r)} \right) & , \text{ if } E_v \leq \alpha D \\ k''_0 \exp \left( - \frac{(1+\sqrt{\alpha})(D - E_v)}{T + \sqrt{\alpha} T_r} \right) & , \text{ if } E_v > \alpha D \end{cases} \quad (40)$$

Here  $k'_0$  and  $k''_0$  are preexponential factors similar to  $k_0$ .

For comparison, we show what the microscopic rate coefficient looks like in the case of diatom-atom collisions (threshold function (16)):

$$k(E_v, T_r, T) = \begin{cases} k_0 \exp \left( - \frac{(\sqrt{D} - \sqrt{\alpha} E_v)^2}{(1-\alpha)T} \right) & , \text{ if } E_v \leq \alpha D \\ k_0 \exp \left( - \frac{D - E_v}{T} \right) & , \text{ if } E_v > \alpha D \end{cases} \quad (41)$$

Rotational relaxation in gases is very fast. To establish an equilibrium between rotational and translational energy distributions requires only a few collisions. Therefore, in virtually all practically important situations  $T_r = T$ . But then eqn (40) becomes exactly the same as (41).

Thus, absolutely all results previously obtained for dissociation rates in diatom-atom collisions are valid for diatom-diatom collisions, with  $M$  meaning the mass of each of the incident molecule atoms. Only, instead of translational energy consumption in dissociation, we have now consumption of translational-rotational energy combined.

An important qualitative conclusion we can draw is that the actual mechanism of collision-induced dissociation in diatomic gases at  $T_v < T$  necessarily implies non-collinear collisions with large rotational

energy of a collision partner and relative translational energy simultaneously transferred to the dissociating molecule's vibrational mode.

If, for some reason, rotational temperature is less than translational, then from comparison of eqn (40) with (41) one can notice that the diatom-diatom rate coefficient would reduce to the diatom-atom one if we introduce an effective "kinetic" temperature  $T_k$  as a weighted average of translational and rotational temperatures:

$$T_k = \frac{T + \sqrt{\alpha} T_r}{1 + \sqrt{\alpha}} \quad (42)$$

Substituting the  $T_k$  defined above for  $T$  in all equations for the diatom-atom case, formulae for the diatom-diatom case can be obtained.

Now we are able to justify the previously made assumption about zero vibrational energy of the collision partner of the dissociating molecule. Considering a collinear collision with the collision partner having vibrational energy distributed with temperature  $T'_v$ , one can get the microscopic rate coefficient in the form (40), but with  $T'_v$  instead of  $T_r$ . In other words, such dissociation would proceed with an "effective" temperature:

$$T_{\text{eff}} = \frac{T + \sqrt{\alpha} T'_v}{1 + \sqrt{\alpha}} \quad (43)$$

which should be substituted for  $T$  in the diatom-atom formulae. Consequently, during the entire period of nonequilibrium dissociation, when  $T'_v < T$ , and  $T_r = T$ , the "effective" temperature determined by eqn (43) will be less than  $T_k = T$  given by eqn (42), and the corresponding "collinear" rate coefficient will be negligible compared with that of "rotational" mechanism.

However, at thermal equilibrium, when  $T_v = T'_v = T_r = T$ , both "effective" temperatures are equal to each other and to the gas temperature  $T$ . Therefore, at high-temperature thermal equilibrium, collision-induced dissociation proceeds via both near-collinear collisions, with large vibrational energy of a collision partner and translational energy transferred to the vibrational mode of the dissociating molecule, and non-collinear collisions, with large rotational and translational energy transferred to the dissociating bond.

## 10.6. CONCLUSIONS

In this report, we suggest a theoretical model for analytical calculations of dissociation rates behind shock waves where the vibrational temperature is less than the gas temperature. The key role in our theory belongs to a threshold function - the minimum translational energy needed for collision-induced dissociation as a function of initial vibrational and rotational energy. This function has been shown to determine the most important, exponential, part of the rate coefficient temperature dependence. Then the threshold function method was combined with a simple dynamical model of energy transfer - the classical impulsive limit - to obtain formulae for the rate coefficient.

These explicit formulae for  $k(T_v, T)$  and for the mean vibrational energy removed in dissociation constitute the main result of this work.

The theory agrees in its qualitative aspects and in some particular cases with major earlier work. For example, we have shown that for sufficiently high vibrational energy  $E_v$  the threshold translational energy is simply  $(D - E_v)$ , while for low  $E_v$  the



translational threshold actually exceeds  $(D-E_v)$ . Thus, the model provides a theoretical basis for the qualitative idea of "preferential dissociation" from higher vibrational levels put forward by Marrone and Treanor [4].

In one particular case, when dissociation proceeds mainly via low vibrational levels, our formula for  $k(T_v, T)$  contains a weighted average of the temperatures  $T_v$  and  $T$  (eqn (11)). This is similar to the model of Park (eqns (1), (2)), although the present formula has a different kind of average and it is derived theoretically rather than empirically.

In the opposite case, when dissociation from high vibrational level is dominant, the present result coincides with two-temperature dissociation rate obtained by Kuznetsov [7, 40] in a "ladder" approximation with dissociation occurring only from the highest vibrational level.

Since the theory is analytical, it gives an opportunity to analyze results easily, and to examine dependence on parameters and limiting cases. Several qualitative results are worth mentioning:

It has been shown that during vibrational relaxation behind strong shock waves the mechanism of dissociation changes: from prevailing dissociation from low vibrational levels at high temperature ratio  $T/T_v$  to almost equiprobable dissociation from all levels at  $T/T_v$  approaching 1. Accordingly, the functional dependence on  $T$  and  $T_v$  of the rate coefficient and of the mean vibrational energy removed also changes.

The formulae exhibit an explicit dependence of dissociation rates on the mass ratio of the dissociating molecule and its collision partner. In particular, we have shown that decreasing the mass of the collision partner makes dissociation from high vibrational levels more favorable.

Finally, it has been demonstrated that dissociation in a molecular gas at  $T > T_v$  occurs predominantly via non collinear collisions with simultaneous transfer of large rotational and translational energy to the vibrational mode of the dissociating molecule.

The theory contains several simplifying assumptions, such as neglecting quantum effects, using the impulsive collision limit, and disregarding the energy (and/or temperature) dependence of preexponential factors. These assumptions are reasonable approximations over a large range of temperatures encountered behind strong shock waves, as discussed in earlier sections. We can qualitatively indicate the temperature range of validity of our theory. For the classical description to be correct, vibrational and translational temperatures must exceed the characteristic vibrational temperature (i.e., a few thousand Kelvin, or 0.2-0.3 eV). On the other hand, neglecting the energy dependence of preexponential factors and evaluating integrals by the steepest descent method is correct if both temperatures  $T_v$  and  $T$  are substantially less than the dissociation energy  $D$  (i.e. 5-10 eV).

Immediate improvement of the present theory would be made by accurate derivations of preexponential factors. This work is currently underway.

## REFERENCES

1. R.N.Schwartz, Z.I.Slawsky and K.F.Herzfeld, J.Chem.Phys. 20 (1952) 1591.
2. P.Hammerling, J.D.Teare and B.Kivel, Phys.Fluids 2 (1959) 422.
3. C.E.Treanor and P.V.Marrone, Phys.Fluids 5 (1962) 1022.
4. P.V.Marrone and C.E.Treanor, Phys.Fluids 6 (1963) 1215.
5. N.M.Kuznetsov, Dokl.Akad.Nauk SSSR 233 (1977) 413.
6. N.M.Kuznetsov and A.M.Samusenko, Dokl.Akad.Nauk SSSR 250 (1980) 1181.
7. N.M.Kuznetsov, Kinetics of Unimolecular Reactions [in Russian], (Nauka, Moscow, 1982).
8. C.Park, J.Thermophys.Heat Transfer 2 (1988) 8.
9. C.Park, J.Thermophys.Heat Transfer 3 (1989) 233.
- 10.S.P.Sharma, W.M.Huo and C.Park, J.Thermophys.Heat Transfer 6 (1992) 9
- 11.D.B.Landrum and G.V.Candler, AIAA Paper No.92-2853 (1992).
- 12.H.Fan, J.Chem.Phys., 55 (1971) 4628.
- 13.J.C.Gray, G.A.Fraser and Truhlar D.G., J.Chem.Phys. 73 (1980) 5726.
- 14.K.Haug, D.G.Truhlar and N.C.Blais, J.Chem.Phys. 86 (1987) 2697.
- 15.R.D.Levine and R.B.Bernstein, Chem.Phys.Lett. 11 (1971) 552.
- 16.C.Rebick and R.D.Levine, J.Chem.Phys. 58 (1973) 3942.
- 17.G.Wolken, J.Chem.Phys. 63 (1975) 528.
- 18.E.W.Knapp, D.J.Diestler and Y.W.Liu, Chem.Phys.Lett. 49 (1977) 379.
- 19.E.W.Knapp and D.J.Diestler, J.Chem.Phys. 67 (1977) 4969.
- 20.L.W.Ford, D.J.Diestler and A.F.Wagner, J.Chem.Phys. 63 (1975) 2019.
- 21.K.C.Kulander, J.Chem.Phys. 69 (1978) 5064.
- 22.L.L.Johnson and R.E.Roberts, Chem.Phys.Lett. 7 (1970) 480.
- 23.I.Rusinek and R.E.Roberts, J.Chem.Phys. 65 (1976) 872; *ibid.* 68 (1978) 1147.

24. I. Rusinek, J.Chem.Phys. 72 (1980) 4518.
25. L.H.Beard and D.A.Micha, J.Chem.Phys. 73 (1980) 1193.
26. J.Manz and J.Romelt, Chem.Phys.Lett. 77 (1981) 172.
27. J.A.Kaye and A.Kuppermann, Chem.Phys.Lett. 78 (1981) 546.
28. L.H.Barg and A.Askar, Chem.Phys.Lett. 76 (1980) 609.
29. M.I.Haftel and T.K.Lim, Chem.Phys.Lett. 89 (1982) 31.
30. C.Leforestier, G.Bergeron and P.Hiberty, Chem.Phys.Lett. 84 (1981) 385.
31. G.Bergeron, P.Hiberty and C.Leforestier, Chem.Phys. 93 (1985) 253.
32. C.Leforestier, Chem.Phys. 87 (1984) 241.
33. C.Leforestier, in: The Theory of Chemical Reaction Dynamics, ed. D.C.Clary (NATO ASI Series, Series C: Mathematical and Physical Sciences, vol.170 ), (D.Reidel, Dordrecht-Boston-Lancaster-Tokyo, 1985) p.235.
34. S.O.Macheret, V.D.Rusanov, A.A.Fridman and A.A.El'kin, Dokl.Akad.Nauk SSSR 305 (1989) 137; *ibid.* 305 (1989) 403.
35. S.O.Macheret, A.A.Fridman and A.A.El'kin, Khim. Fizika (Sov.J.Chem.Phys.) 9 (1990) 174.
36. N.M.Kuznetsov, Dokl.Akad.Nauk SSSR 229 (1976) 1155.
37. S.W.Benson, G.C.Berend and J.C.Wu, J.Chem.Phys. 38 (1963) 25.
38. F.P.Tully, Y.T.Lee and R.S.Berry, Chem.Phys.Lett. 9 (1971) 80.
39. C.E.Treanor, J.W.Rich and R.G.Rehm, J.Chem.Phys. 48 (1968) 1798.
40. N.M.Kuznetsov, Teoreticheskaya i Eksperimental'naya Khimiya 7 (1971) 22.
41. H.Jeffreys and B.Swirles, Methods of Mathematical Physics (Cambridge University Press, Cambridge, 1966).
42. C.Park, Nonequilibrium Hypersonic Aerothermodynamics (Wiley, 1990).
43. A.Ben-Shaul, R.D.Levine and R.B.Bernstein, J.Chem.Phys. 57 (1972) 5427

## FIGURE CAPTIONS

Fig. 10.1. Collinear diatom-atom collision. Arrows indicate velocities of atoms.

Fig. 10.2. Threshold line  $E_t = F(E_v)$  for dissociation in diatom-atom collisions.

Fig. 10.3. Dissociation rate coefficient for  $N_2-N_2$  or  $N_2-N$  collisions versus vibrational temperature at constant translational temperature  $T=10000$  K. 1, 1' - Park model [8]-[10] with  $s=0.5$  (1) and  $s=0.7$  (1'); 2, 2' - Marrone-Treanor model [4] with  $U=D/6$  (2) and  $U=D/3$  (2'); 3, 3' - present theory with "exact" evaluation of  $\Psi$  and  $k_0$  (3) and using the steepest descent method (3').

Fig. 10.4. Relative contribution of dissociation from low (1), intermediate (2), and high (3) levels to the overall nitrogen dissociation rate at constant  $T=10000$  K. Solid lines - "exact" evaluation of  $\Psi$  and  $k_0$ , dashed lines - calculations using the steepest descent method.

Fig. 10.5. Average energy removed from vibrational mode in a single dissociation act as a fraction of dissociation energy versus vibrational temperature at different gas temperatures.

Fig. 10.6a. Diatom-diatom collision in collinear geometry.

Fig. 10.6b. Diatom-diatom collision in perpendicular geometry.

Fig. 10.7. Threshold line for dissociation in collinear diatom-diatom collisions.

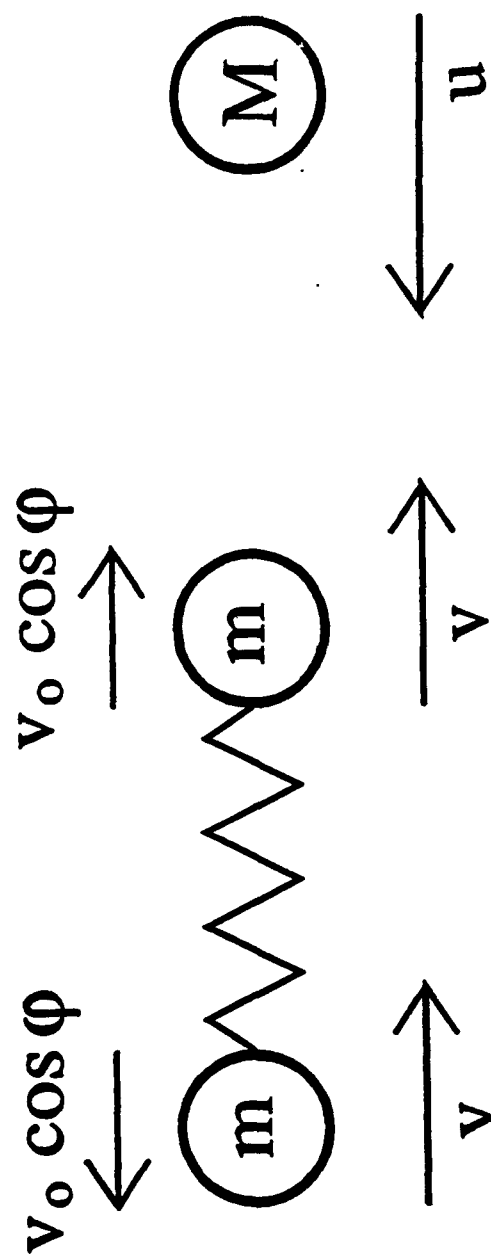


Fig. 10.1. Collinear diatom-atom collision. Arrows indicate velocities of atoms.

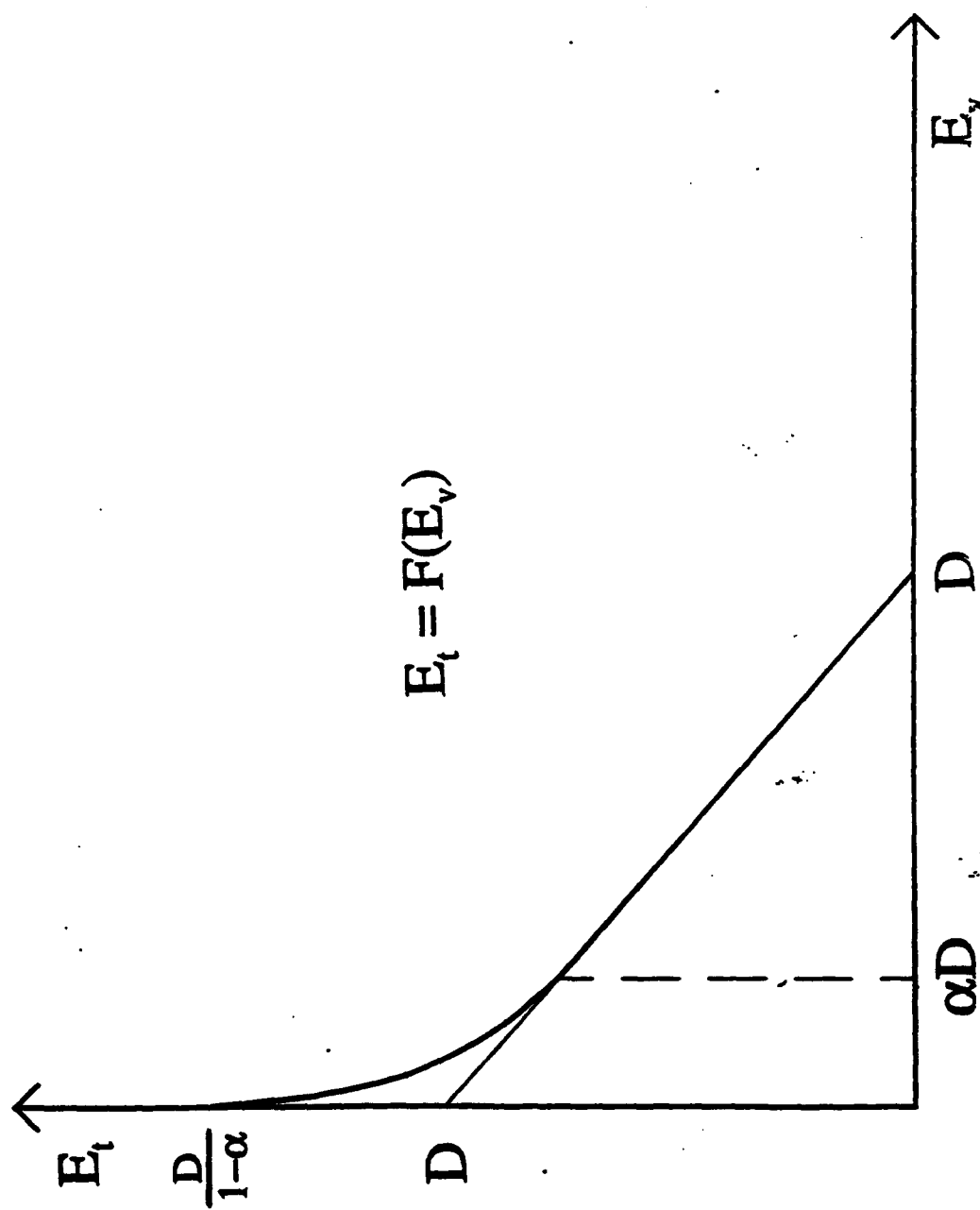


Fig. 10.2. Threshold line  $E_t = F(E_v)$  for dissociation in diatom-atom collisions.

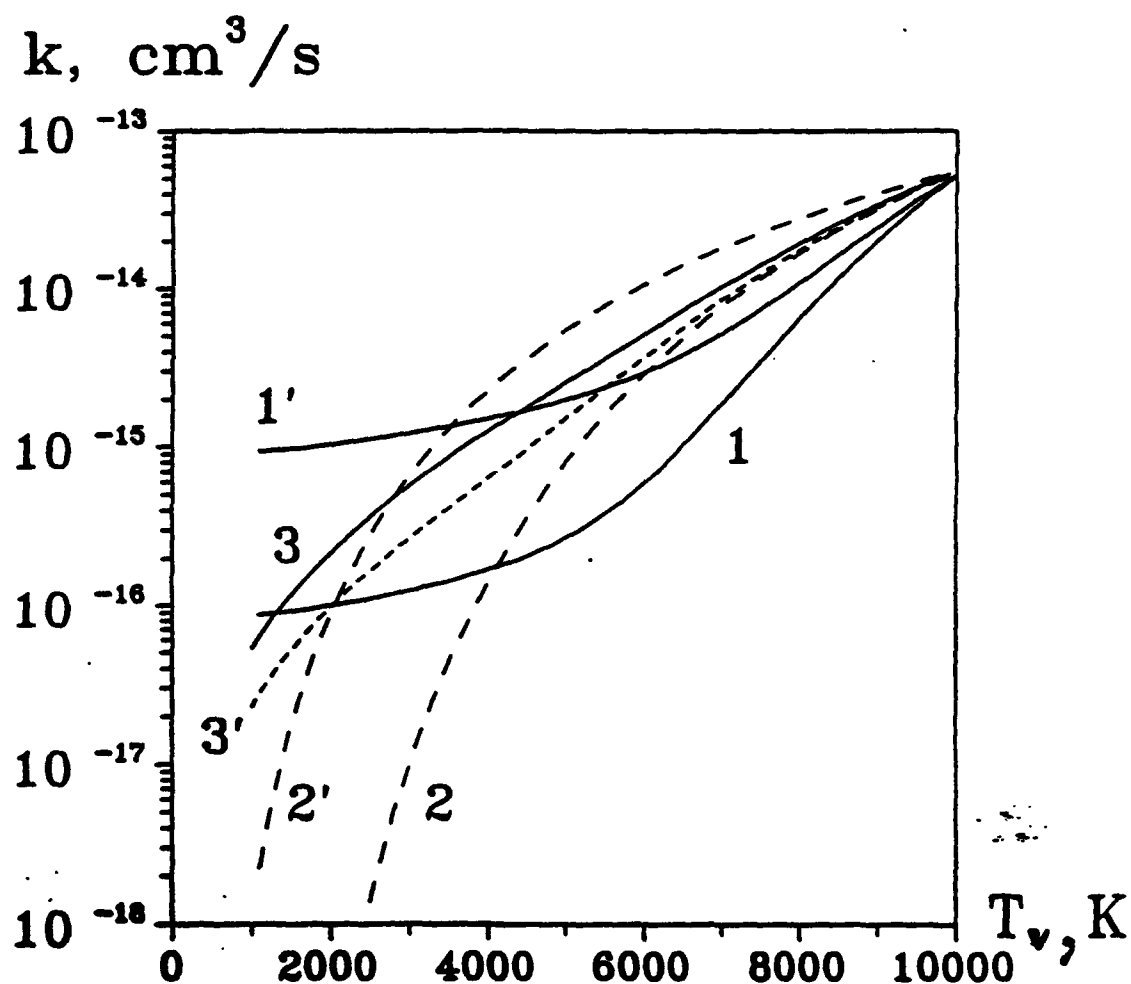


Fig. 10.3. Dissociation rate coefficient for  $N_2-N_2$  or  $N_2-N$  collisions versus vibrational temperature at constant translational temperature  $T=10000$  K. 1, 1' - Park model [8]-[10] with  $s=0.5$  (1) and  $s=0.7$  (1'); 2, 2' - Marrone-Treanor model [4] with  $U=D/6$  (2) and  $U=D/3$  (2'); 3, 3' - present theory with "exact" evaluation of  $\Psi$  and  $k_0$  (3) and using the steepest descent method (3').



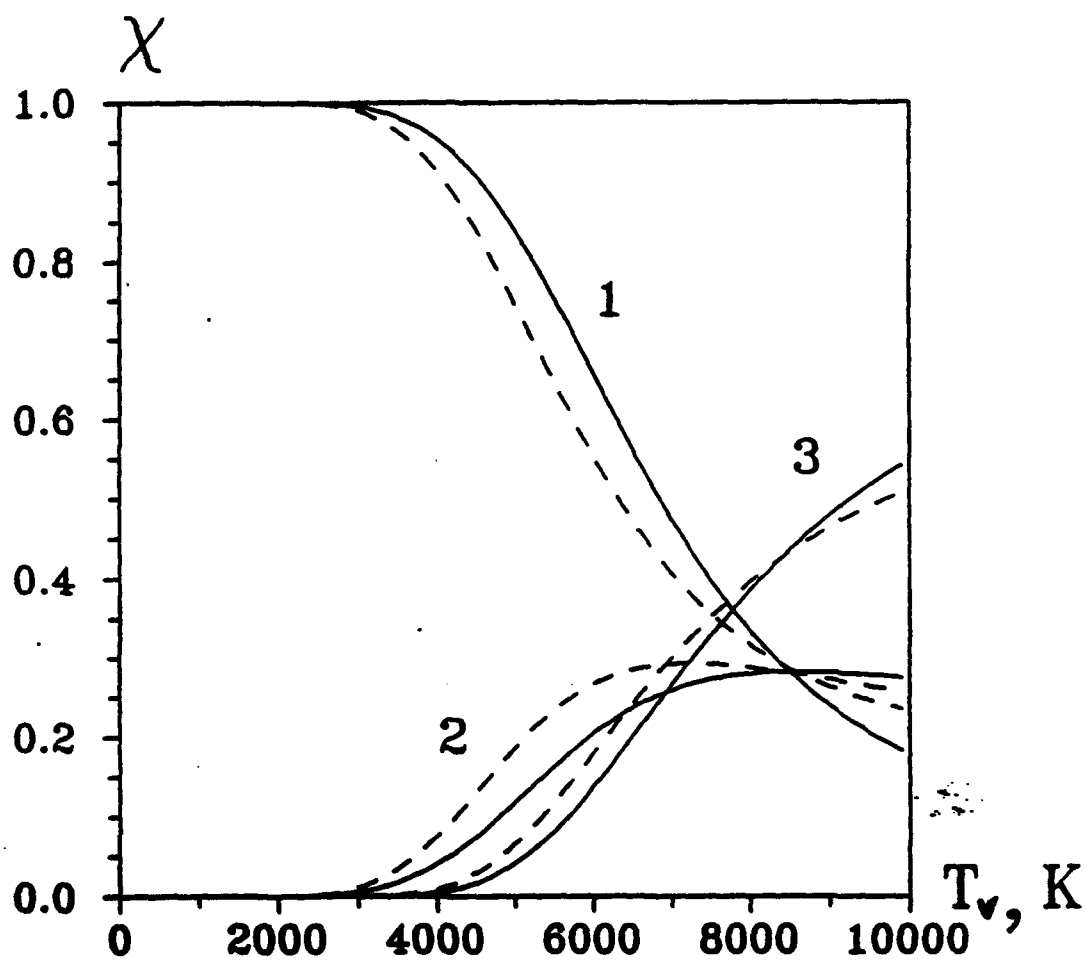


Fig. 10.4. Relative contribution of dissociation from low (1), intermediate (2), and high (3) levels to the overall nitrogen dissociation rate at constant  $T=10000$  K. Solid lines - "exact" evaluation of  $\Psi$  and  $k_0$ , dashed lines - calculations using the steepest descent method.

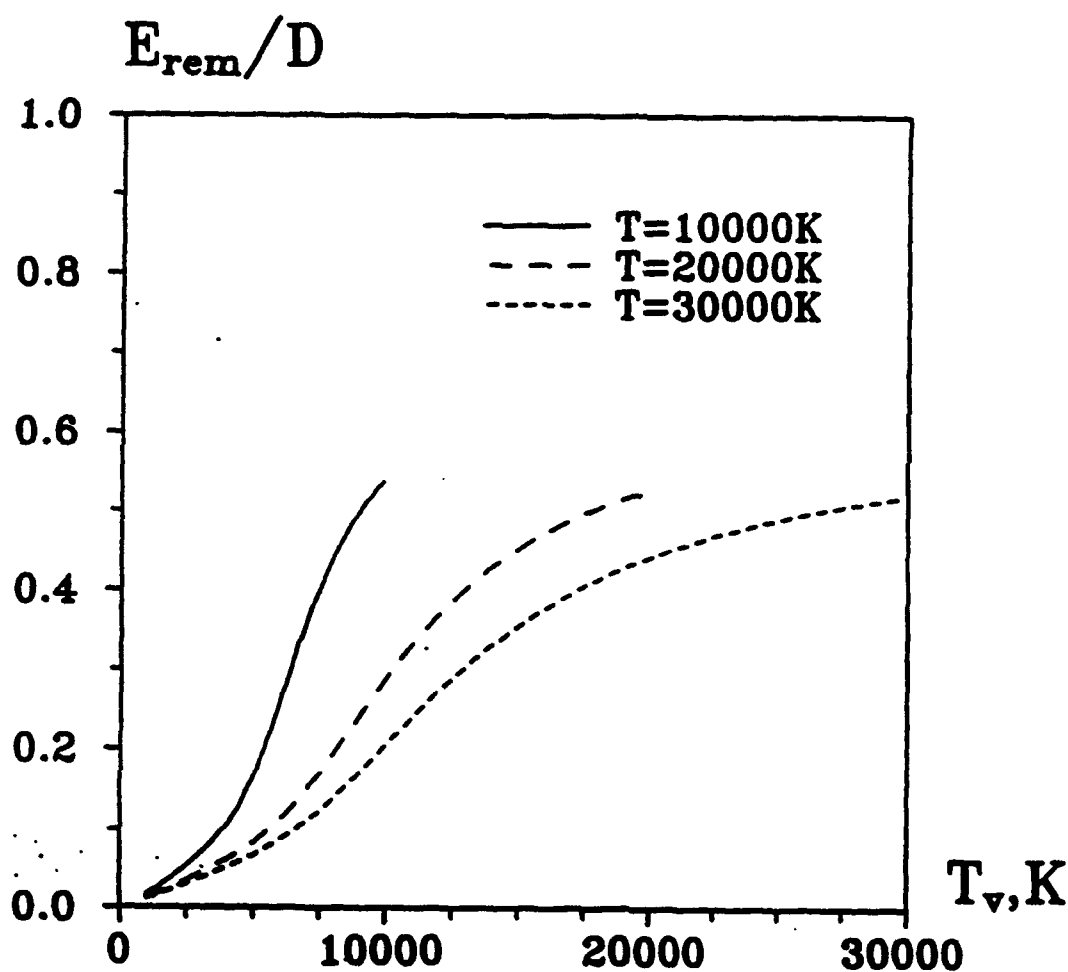


Fig. 10.5. Average energy removed from vibrational mode in a single dissociation act as a fraction of dissociation energy versus vibrational temperature at different gas temperatures.

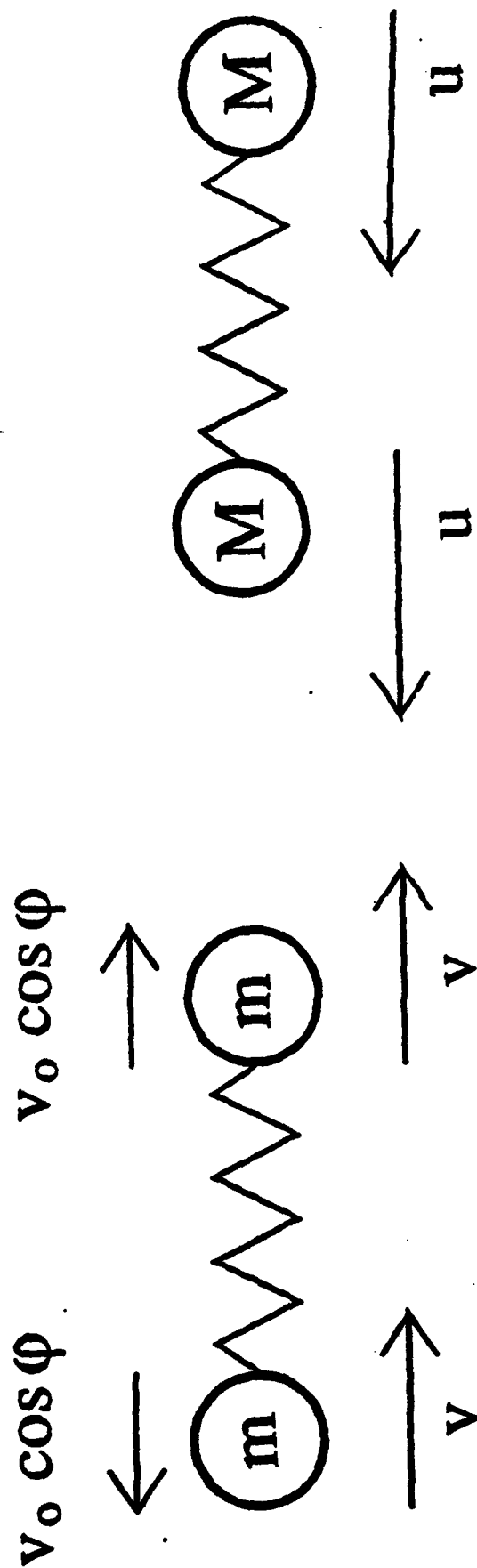


Fig. 10.6a. Diatom-diatom collision in collinear geometry.

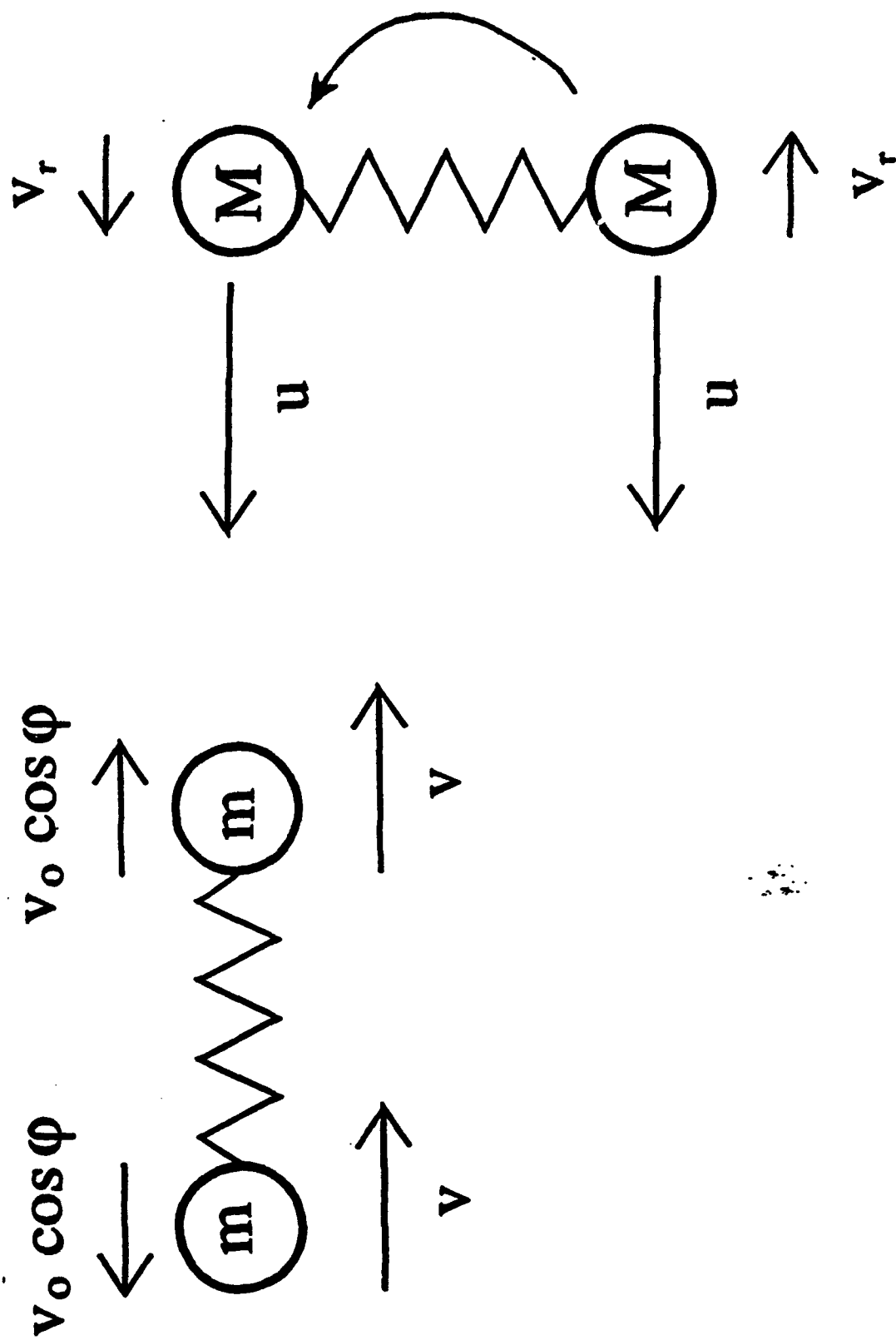


Fig. 10.6b. Diatom-diatom collision in perpendicular geometry.

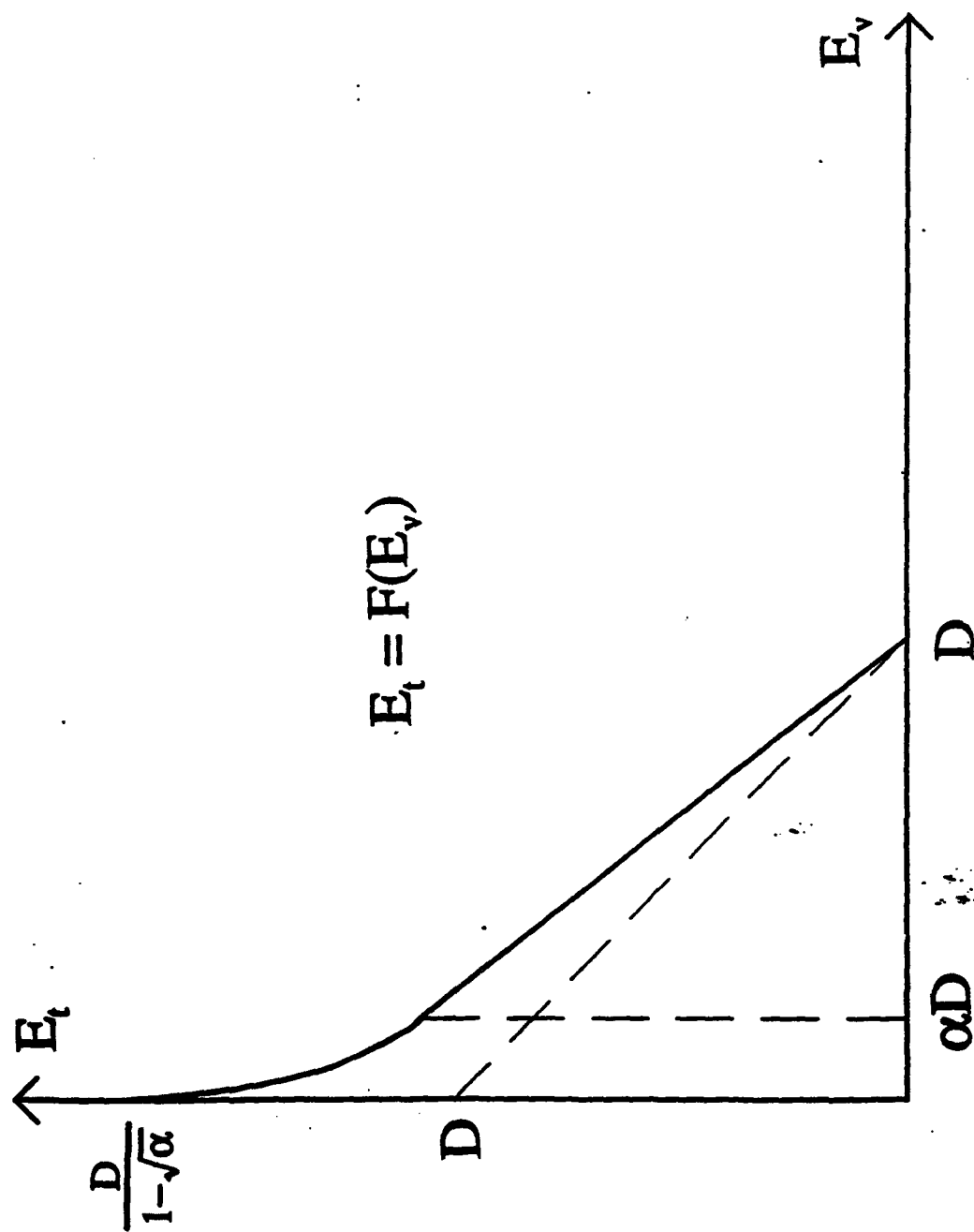


Fig. 10.7. Threshold line for dissociation in collinear diatom-diatom collisions.